Best Practices Handbook for the Collection and Use of Solar Resource Data for Solar Energy Applications: Fourth Edition

Edited by Manajit Sengupta,[1] Aron Habte,[1] Stefan Wilbert,[2] Christian Gueymard,[3] Jan Remund,[4] Elke Lorenz,[5] Wilfried van Sark,[6] and Adam R. Jensen[7]

1 National Renewable Energy Laboratory
2 German Aerospace Center (DLR)
3 Solar Consulting Services
4 Meteotest AG
5 Fraunhofer Institute for Solar Energy Systems (Fraunhofer ISE)
6 Utrecht University, Copernicus Institute of Sustainable Development
7 Technical University of Denmark (DTU)

This update was prepared in collaboration with the International Energy Agency.

NREL is a national laboratory of the U.S. Department of Energy
Office of Energy Efficiency & Renewable Energy
Operated by the Alliance for Sustainable Energy, LLC

This report is available at no cost from the National Renewable Energy Laboratory (NREL) at www.nrel.gov/publications.

Contract No. DE-AC36-08GO28308

Technical Report
NREL/TP-5D00-88300
September 2024

Best Practices Handbook for the Collection and Use of Solar Resource Data for Solar Energy Applications: Fourth Edition

Edited by Manajit Sengupta,[1] Aron Habte,[1] Stefan Wilbert,[2] Christian Gueymard,[3] Jan Remund,[4] Elke Lorenz,[5] Wilfried van Sark,[6] and Adam R. Jensen[7]

1 National Renewable Energy Laboratory
2 German Aerospace Center (DLR)
3 Solar Consulting Services
4 Meteotest AG
5 Fraunhofer Institute for Solar Energy Systems (Fraunhofer ISE)
6 Utrecht University, Copernicus Institute of Sustainable Development
7 Technical University of Denmark (DTU)

Suggested Citation
Sengupta, Manajit, Aron Habte, Stefan Wilbert, Christian Gueymard, Jan Remund, Elke Lorenz, Wilfried van Sark, and Adam R. Jensen. 2024. *Best Practices Handbook for the Collection and Use of Solar Resource Data for Solar Energy Applications: Fourth Edition*. Golden, CO: National Renewable Energy Laboratory. NREL/TP-5D00-88300. https://www.nrel.gov/docs/fy24osti/88300.pdf. https://doi.org/10.2172/2448063.

NREL is a national laboratory of the U.S. Department of Energy
Office of Energy Efficiency & Renewable Energy
Operated by the Alliance for Sustainable Energy, LLC

This report is available at no cost from the National Renewable Energy Laboratory (NREL) at www.nrel.gov/publications.

Contract No. DE-AC36-08GO28308

Technical Report
NREL/TP-5D00-88300
September 2024

National Renewable Energy Laboratory
15013 Denver West Parkway
Golden, CO 80401
303-275-3000 • www.nrel.gov

ISBN 979-8-218-51537-9

NOTICE

This work was authored in part by the National Renewable Energy Laboratory, operated by Alliance for Sustainable Energy, LLC, for the U.S. Department of Energy (DOE) under Contract No. DE-AC36-08GO28308. Funding provided in part by U.S. Department of Energy Office of Energy Efficiency and Renewable Energy Solar Energy Technologies Office. The views expressed herein do not necessarily represent the views of the DOE or the U.S. Government. This report was also supported by the Swiss Federal Office of Energy under contracts no. SI/501984-01 and SI/502607-01 and by the German Federal Ministry for Economic Affairs and Climate Action under contract no. 03EE1010(A-E) (SOLREV) based on a resolution of the German Bundestag.

Cover Photos by Dennis Schroeder: (clockwise, left to right) NREL 51934, NREL 45897, NREL 42160, NREL 45891, NREL 48097, NREL 46526.

Foreword

Solar energy technologies—such as solar photovoltaics (PV), solar heating and cooling, and concentrating solar power—provide solutions to the growing need for clean energy to mitigate climate change, improve air quality, and reduce dependence on non-renewable fuels. During the past few years, the use of solar energy has strongly progressed, in particular thanks to the impressive development and deployment of PV. PV deployment reached more than 1 TW of installed capacity worldwide in 2022, and it has emerged as one of the most cost-competitive energy technologies overall. The markets for the various solar energy systems continue to increase—the solar PV market turnover in 2022 was estimated to be more than $U.S. 200 billion worldwide. Reliable and precise historical estimates and future projections of the solar resource are relevant not only to predict the energy output of solar installations and power systems but also, increasingly, to determine their expected competitiveness and economic return.

This fourth edition of the *Best Practices Handbook for the Collection and Use of Solar Resource Data for Solar Energy Applications* has been prepared under the leadership of the National Renewable Energy Laboratory (NREL) together with a team of worldwide experts that consists of 51 authors from 11 countries working within the framework of the International Energy Agency's (IEA's) Photovoltaic Power Systems Programme (PVPS) Technology Collaboration Programme Task 16 on "Solar Resource for High Penetration and Large-Scale Applications." This project is a joint task with the IEA's Solar Power and Chemical Energy Systems (SolarPACES) Technology Collaboration Programme. Building on the previous work under the IEA's Solar Heating and Cooling Technology Collaboration Programme, this handbook is a prominent example of technology collaboration across the different solar energy technologies and the respective IEA technology collaboration programs.

This fourth edition of the handbook follows only three years after the previous edition, which was published in 2021, and it marks the rapid evolution in the field of solar resource assessment and forecasting. It reflects the considerable progress that has occurred since then in the measurement and modeling of solar radiation and related topics. For instance, this edition features a data quality and solar resource variability chapters. Particular emphasis is on the progress of forecasts using all-sky images as well as on probabilistic and regional forecasts, which increasingly use machine learning. For the practitioner, an important Chapter 11 deals with the application of solar resource data to solar energy projects, including performance modeling.

With comprehensive coverage of the state of the art in solar resource assessment and forecasting, this handbook serves as a reference document for a wide range of target audiences—from science to solar energy professionals. Understanding the nature of solar radiation, its variations across the world, and forecasting its evolution over time will increasingly contribute to making solar energy more predictable. As the contribution of solar energy to the energy supply increases over time, the improved predictability is crucial for the optimization of future energy systems.

The IEA PVPS Technology Collaboration Programme is pleased to publish the fourth edition of this handbook together with NREL. Most importantly, I would like to acknowledge the leadership of NREL, in particular, Aron Habte and Manajit Sengupta; the IEA PVPS Task 16/IEA SolarPACES Task 5 experts; and the support of the U.S. Department of Energy.

I hope this handbook finds many interested readers and contributes to the further deployment of solar energy worldwide.

Daniel Mugnier
Chair, IEA PVPS Technology Collaboration Programme

August 2024

Preface

Jan Remund[1] and Manajit Sengupta[2]
[1] *Meteotest, Switzerland*
[2] *National Renewable Energy Laboratory, USA*

As the world looks for carbon-free sources to meet energy demands associated with heat, electrical power, and transportation, energy from the sun stands out as the single most abundant energy resource on Earth. Harnessing this energy is the challenge as well as an opportunity for achieving a carbon-free energy supply by 2050 to fulfil the 1.5°C target set by the Intergovernmental Panel on Climate Change[1] and recommended in the 2015 Paris Agreement. Reducing carbon dioxide emissions per energy unit and rapidly accessing the huge potential of solar energy will have the largest effects on achieving the 1.5°C target.

Photovoltaics (PV), solar heating and cooling, and concentrating solar power (CSP) are the primary forms of energy applications using sunlight. These solar energy systems use different technologies, collect different fractions of the solar resource, and have different siting requirements and production capabilities. Reliable information about the solar resource is required for every solar energy application. This holds true for small installations on a rooftop as well as for large, gigawatt-size, utility-scale solar power plants; however, solar resource information is the most critical in the latter case because such projects require substantial investments, sometimes exceeding $1 billion in construction costs. Before such projects can be undertaken, the best possible information about the quality and reliability of the fuel source (i.e., solar radiation) must be made available. This implies that project developers need to have reliable and accurate information about the solar resource available at specific locations, including historic trends in the seasonal, daily, hourly, and (preferably) subhourly variability to predict the daily and annual performance of a proposed power plant. Without this information, a bankable financial analysis is not possible.

In response to a meeting of prominent CSP developers and stakeholders hosted by the U.S. Department of Energy (DOE) in September 2008, the National Renewable Energy Laboratory (NREL) produced a handbook to provide best practices for the use of solar resource data, which was titled *Concentrating Solar Power: Best Practices Handbook for the Collection and Use of Solar Resource Data*.[2] The content was based on the experiences of scientists and engineers from industry, academia, and DOE for identifying the sources, quality, and methods for applying solar and meteorological data to CSP projects.

During this time, the International Energy Agency's (IEA's) Solar Heating and Cooling (SHC) Technology Collaboration Programme was hosting tasks on solar resource knowledge management (Task 36, 2005–2011; Task 46, 2011–2016). This work was then followed by the IEA's Photovoltaic Power Systems Programme (PVPS) Task 16. These tasks have brought together the world's foremost experts in solar energy meteorology. This group of experts agreed there is a need to maintain a collective document to disseminate the knowledge that was being developed through these tasks. It was decided that combining the efforts of the experts involved in the IEA tasks to build on the information in NREL's original version of the handbook would

[1] See https://www.ipcc.ch/report/ar4/syr/.
[2] See https://www.nrel.gov/docs/fy10osti/47465.pdf.

provide the best use of resources and deliver a handbook of outstanding quality to users. It was also decided that the handbook would incorporate additional solar technologies, such as PV, along with additional aspects of energy meteorology that had become extremely important, such as solar forecasting. As a result, in 2017, NREL published a second edition of the handbook under a revised title, *Best Practices Handbook for the Collection and Use of Solar Resource Data for Solar Energy Applications*.[3] This served as the final deliverable for IEA SHC Task 46. An update in 2021 concluded the work of the first phase of IEA PVPS Task 16 between 2017 and 2020. This document is the result of the collaboration in the third period (2020–2023), presented here as the fourth edition of the handbook. As before, this edition is available in two formats, published by NREL and the IEA PVPS.

The solar PV industry has rapidly developed throughout the last few years based on ongoing technical evolution, technology cost reduction, and enhanced growth rates. PV installation sizes as well as penetration levels have grown—further enhancing the needs for accurate solar data for planning and operation. Induced by these needs, there have been significant enhancements in the body of knowledge in the areas of solar resource assessment and forecasting. This fourth edition of the handbook updates and enhances the preceding versions and presents the state of the art in a condensed form for all of its users.

In the coming years, another stage of solar penetration will be reached, and solar energy will become a major share of the production and the backbone of the electric grid. This growth will increase the needs for high-quality and reliable resource data as well as for studies about optimal integration, including firming PV power.

The handbook's structure has been updated since the previous editions. Many chapters now include executive summaries and an overview figure. Chapter 1 lays out the need for high-quality and reliable solar resource data to support the rapidly growing industry, and Chapter 2, as before, provides a basic tutorial on solar resources.

Chapter 3 presents a comprehensive overview of best practices for measuring solar radiation, including information gained under collaborative work completed during the IEA PVPS Task 16. Chapter 4 is a new chapter describing data quality assessment. Chapter 5 describes additional meteorological variables (besides radiation) that are required for accurate performance analysis. Chapter 6 is also a new chapter giving insights on solar resource variability. Chapter 7 summarizes techniques used to develop estimates of solar resources from weather satellite data and numerical model predictions.

Chapter 8 describes an updated list of commonly used models and datasets available in both the public and private sectors, and Chapter 9 provides an update on recent developments in the ability to forecast the solar resource over time horizons spanning from minutes to hours ahead and days ahead.

Chapter 10 provides important information on both measured and modeled solar data uncertainty. All this information leads to Chapter 11, which provides data application techniques for the various stages of project development, from prefeasibility to routine operations, as shown in the figure in the executive summary of that chapter. The outlook for future work is summarized in Chapter 12.

[3] See https://www.nrel.gov/docs/fy18osti/68886.pdf.

Acknowledgments

The authors acknowledge the U.S. Department of Energy (DOE) Office of Energy Efficiency and Renewable Energy (EERE) Solar Energy Technologies Office (SETO) for supporting this research. Specifically, the authors are grateful to Dr. Anastasios Golnas, the technology manager for the Photovoltaics (PV) team, and Dr. Inna Kozinsky, a science and technology advisor on the SETO Photovoltaics team, for their support and encouragement. The authors also thank the International Energy Agency Photovoltaic Power Systems Programme Task 16, without which this publication would not have been possible. Finally, the authors thank the National Renewable Energy Laboratory Communications Office for their tireless work during the publication process.

Special thanks to the following experts who spent hours of their valuable time reviewing the chapters and making excellent suggestions that significantly improved the quality of this handbook:

- Stephen Wilcox – Solar Resource Solutions, LLC, USA
- Thomas Stoffel – Solar Resource Solutions, LLC, USA
- Daryl Myers – National Renewable Energy Laboratory, USA, retired
- Jose Lorenzo Balenzategui Manzanares – PVLab-CIEMAT, Spain
- Anne Forstinger – CSP Services GmbH, Germany
- Nate Blair – National Renewable Energy Laboratory, USA
- Justin Robinson, Julie Chard, and Alex Bryan – GroundWork Renewables, Inc., USA
- Augustin Laguarrda – Facultad de Ingeniería, Universidad de la República, Uruguay
- Sue Ellen Haupt – National Center for Atmospheric Research, USA
- Jonathan Leloux – LuciSun, Belgium
- Ana Garcia – Centro Nacional de Energías Renovables (CENER), Spain
- Björn Müller – Enmova GmbH
- Tomas Cebecauer – Solargis, Slovakia
- Jose Antonio – Universidad De Malaga, Spain
- Merlinde Kay – University of New South Wales (UNSW), Australia.

This work was authored in part by the National Renewable Energy Laboratory, operated by Alliance for Sustainable Energy, LLC, for the U.S. Department of Energy (DOE) under Contract No. DE-AC36-08GO28308. Funding provided by U.S. Department of Energy (DOE) Office of Energy Efficiency (EERE) and Renewable Energy Solar Energy Technologies Office (SETO). The views expressed in the article do not necessarily represent the views of the DOE or the U.S. Government. The U.S. Government retains and the publisher, by accepting the article for publication, acknowledges that the U.S. Government retains a nonexclusive, paid-up, irrevocable, worldwide license to publish or reproduce the published form of this work, or allow others to do so, for U.S. Government purposes.

This report was also supported by the Swiss Federal Office of Energy under contract no. SI/501486-01 and SI/501984-01, by the German Federal Ministry for Economic Affairs and Energy under contract no. 03EE1010 and 03EE1011 (SOLREV) based on a resolution of the German Bundestag, and by the Danish Energy Agency through grant no. 134232-510237.

List of Acronyms

1P	one-in-portrait
2P	two-in-portrait
ABI	Advanced Baseline Imager
ACR	absolute cavity radiometer
AERONET	Aerosol Robotic Network
AGRI	Advanced Geostationary Radiation Imager
AHI	Advanced Himawari Imager
AI	artificial intelligence
AM	air mass
AMI	Advanced Meteorological Imager
AMO	Atlantic Multidecadal Oscillation
AnEn	analog ensemble
ANN	artificial neural network
AOD	aerosol optical depth
API	application programming interface
APOLLO	AVHRR Processing scheme Over cLouds, Land, and Ocean
ARM	Atmospheric Radiation Measurement
ÅS	Ångström scale
ASI	all-sky imager
ATF	atmospheric transmission factor
AU	astronomical unit
AutoML	auto machine learning
AVHRR	Advanced Very-High-Resolution Radiometer
BFIR	back-to-front irradiance ratio
BHI	beam horizontal irradiance
BIPM	Bureau International des Poids et Mesures (International Bureau of Weights and Measures)
BOM	Australian Bureau of Meteorology
BPV	bifacial photovoltaic
BRDF	bidirectional reflectance distribution function
BTDF	bidirectional transmittance distribution function
BSA	black-sky albedo
BSRN	Baseline Surface Radiation Network
BTI	beam tilted irradiance
CAL	cloud albedo
CAMS	Copernicus Atmosphere Monitoring Service
CART	classification and regression tree
CCD	charge-coupled device
CDF	cumulative distribution function
CDR	Climate Data Record
CdTe	cadmium telluride
CENER	El Centro Nacional de Energías Renovables (National Renewable Energy Centre of Spain)
CERES	Clouds and the Earth's Radiant Energy System
CF	climate forecast

CFSR	Climate Forecast System Reanalysis
CIEMAT	Centro de Investigaciones Energéticas, Medioambientales y Tecnológicas
CIMO	Commission for Instruments and Methods of Observation
CLARA	Cloud, Albedo, and surface RAdiation data set
CLARA-A2	CM SAF Cloud, Albedo and Surface Radiation Data Set from AVHRR Data, Edition 2
CLARA-A3	CM SAF Cloud, Albedo and Surface Radiation Data Set from AVHRR Data, Edition 3
CLAVR-x	Clouds from AVHRR Extended System
CM SAF	EUMETSTAT Satellite Application Facility on Climate Monitoring
CMA	Chinese Meteorological Administration
CMIP	Coupled Model Intercomparison Project
CMV	cloud motion vector
CNN	convolutional neural network
CNRS	Centre National de la Recherche Scientifique (National Center for Scientific Research)
CO_2	carbon dioxide
COD	cloud optical depth
convLSTM	convolutional long short-term memory
COSMO	Consortium for Small-scale MOdeling
COV	coefficient of variation
CPP	cloud physical properties
CPV	concentrating photovoltaics
CRPS	continuous ranked probability score
CRPSS	CRPS skill score
CSD-Clim	clear-sky-dependent climatology
CSIRO	Commonwealth Scientific and Industrial Research Organization
CSP	concentrating solar power
CST	concentrating solar thermal
DEM	digital elevation model
DHI	diffuse horizontal irradiance
DIR	direct horizontal irradiance
DISORT	DIScrete Ordinates Radiative Transfer
DL	deep learning
DLI	daily light integral
DLR	Deutsches Zentrum für Luft- und Raumfahrt (German Aerospace Center)
DNI	direct normal irradiance
DOE	U.S. Department of Energy
DRY	design reference year
DSCOVR	Deep Space Climate Observatory
DTI	diffuse tilted irradiance
DTU	Technical University of Denmark
ECMWF	European Center for Medium-Range Weather Forecasts
ENDORSE	ENergy DOwnstReam Services
ENSO	El Niño-Southern Oscillation
ENTSO-E	European Network of Transmission System Operators for Electricity

EPC	engineering, procurement, and construction
EPIC	Earth Polychromatic Imaging Camera
EPS	Ensemble Prediction System
ERA5	ECMWF ReAnalysis v5
ESMAP	Energy Sector Management Assistance Program
ESRA	European Solar Radiation Atlas
ESRL	Earth System Research Laboratory
ET	extraterrestrial
ETOPO	NOAA's Earth TOPOgraphy
ETR	extraterrestrial radiation
ET-RR	Expert Team on Radiation References
ETS	extraterrestrial spectrum
EUMETSAT	European Organisation for the Exploitation of Meteorological Satellites
FARMS	Fast All-sky Radiation Model for Solar applications
FARMS-NIT	Fast All-sky Radiation Model for Solar applications with Narrowband Irradiances on Tilted surfaces
FCI	Flexible Combined Imager
FLASHFlux	Fast Longwave and Shortwave Radiative Fluxes
FOV	field of view
FPF	firm power forecast
Fraunhofer IEE	Fraunhofer Institute for Energy Economics and Energy System Technology
Fraunhofer ISE	Fraunhofer Institute for Solar Energy Systems
FY-4	FengYun-4
GARCH	Generalized AutoRegressive Conditional Heteroskedasticity
GEBA	Global Energy Balance Archive
GEM	Global Environmental Multiscale
GEOS	Goddard Earth Observing System
GFS	Global Forecast System
GHI	global horizontal irradiance
GIS	geographic information system
GK-2A	GEO-KOMPSAT-2A
GML	Global Monitoring Laboratory
GNI	global normal irradiance
GOES	Geostationary Operational Environmental Satellite
GOME2	Global Ozone Monitoring Experiment–2
GPU	graphics processing unit
GTI	global tilted irradiance
GUM	Guide to the Expression of Uncertainty in Measurements
GVF	ground view factor
HARMONIE	HIRLAM ALADIN Regional Mesoscale Operational NWP In Europe
HIRLAM	High-Resolution Limited Area Model
HRRR	High-Resolution Rapid Refresh
ICDR	Interim Climate Data Record
ICON	ICOsahedral Nonhydrostatic
IDW	inverse distance weighting

IEA	International Energy Agency
IEC	International Electrotechincal Commission
i-EM	Intelligence in Energy Management
IFE	Institutt for Energiteknikk
IFS	Integrated Forecasting System
INSAT	Indian National Satellite
IODC	Indian Ocean Data Coverage
IPC	International Pyrheliometer Comparison
IPCC	Intergovernmental Panel on Climate Change
IPS	international pyrheliometric scale
IPSL	Institute Pierre-Simon Laplace
IR	infrared
IRENA	International Renewable Energy Agency
IS	interval score
ISCCP	International Satellite Cloud Climatology Project
ISIS	Integrated Surface Irradiance Study
ISO	International Organization for Standardization
IT	information technology
ITCZ	Intertropical Convergence Zone
IWV	integrated water vapor
JPSS	Joint Polar Satellite System
KNMI	Royal Netherlands Meteorological Institute
LAT	Local Apparent Time
LCOE	levelized cost of energy
LMD	Laboratoire de Météorologie Dynamique (Laboratory of Dynamic Meteorology)
LRS	land constraints, radiation, and slope
LSA	Land Surface Analysis
LST	Local Standard Time
LSTM	long short-term memory
MACC	Monitoring Atmospheric Composition and Climate
MAD	mean absolute deviation
MADCast	Multisensor Advection Diffusion nowCast
MAE	mean absolute error
MBD	mean bias deviation
MBE	mean bias error
McICA	Monte Carlo Independent Column Approximation
MDMS	Meteorological Data Management System
MERRA-2	Modern-Era Retrospective analysis for Research and Applications, Version 2
MESOR	Management and Exploitation of Solar Resource Knowledge
METEOSAT	Meteorological satellite
MetOp	Meteorological Observation
METSTAT	METeorolgoical-STATistical model
MFG	Meteosat First Generation
MIDC	Measurement and Instrumentation Data Center

MISR	Multi-angle Imaging SpectroRadiometer
ML	machine learning
MODIS	Moderate Resolution Imaging Spectroradiometer
MOS	model output statistics
MSE	mean square error
MSG	Meteosat Second Generation
MTG	Meteosat Third Generation
MTS	Meteorological Statistical Model
MTSAT	Multi-functional Transport Satellite
NA-ME-E	Northern Africa-Middle East-Europe
NAO	North Atlantic Oscillation
NASA	National Aeronautics and Space Administration
NCAR	National Center for Atmospheric Research
NCEP	National Center for Environmental Protection
NetCDF	network common data form
NIP	Normal Incidence Pyrheliometer
NIR	near-infrared
NIST	National Institute of Standards and Technology
NOAA	National Oceanic and Atmospheric Administration
NREL	National Renewable Energy Laboratory
NSRDB	National Solar Radiation Database
NWC-SAF	Nowcasting Satellite Application Facility
NWP	numerical weather prediction
O&M	operations and maintenance
OMI	Ozone Monitoring Instrument
ONI	Oceanic Niño Index
ORNL	Oak Ridge National Laboratory
OSI-SAF	Ocean and Sea Ice Satellite Application Facility
PAR	photosynthetically active radiation
PATMOS-x	Pathfinder Atmospheres Extended
PDF	probability density function
PDO	Pacific Decadal Oscillation
PeEn	persistence ensemble
PHYGNN	physics-guided neural network
PIMENT	Laboratory of Physics and Mathematical Engineering for Energy and the Environment
PMOD	Physikalisch-Meteorologisches Observatorium Davos (Physical Meteorological Observatory in Davos)
POA	plane of array
POE	probability of exceedance
POWER	Prediction of Worldwide Energy Resources
PPFD	photosynthetic photon flux density
PR	performance ratio
PSM	Physical Solar Model
PSP	precision spectral pyranometer
PV	photovoltaic

PVGIS	Photovoltaic Geographical Information System
PVPS	Photovoltaic Power Systems Programme
PW	precipitable water
PWV	precipitable water vapor
PyPI	Python Packaging Index
QC	quality control
QEERI	Qatar Environment and Energy Research Institute, Hamad Bin Khalifa University
QM	quantile mapping
R/FR	red/far-red ratio
RAMS	Regional Atmospheric Modeling System
RBR	red-to-blue ratio
REST2	Reference Evaluation of Solar Transmittance, 2 bands
RGB	red-green-blue
RHI	reflected horizontal irradiance
RL	Rayleigh limit
RMSD	root mean square deviation
RMSE	root mean square error
RNN	recurrent neural network
RPOA	rear plane of array
RRTM	Rapid Radiation Transfer Model
RRTMG	Rapid Radiation Transfer Model for General Circulation Models
RSI	rotating shadowband irradiometer
RSP	rotating shadowband pyranometer
RSR	rotating shadowband radiometer
RTI	reflected tilted irradiance
SAF	Satellite Application Facility
SAM	System Advisory Model
SARAH	CM SAF Surface Solar Radiation Data Set - Heliosat
SARAH-E	CM SAF Surface Solar Radiation Data Set - Heliosat – East
SAURAN	Southern African Universities Radiometric Network
SC	solar constant
SCIAMACHY	Scanning Imaging Absorption Spectrometer for Atmospheric Chartography
SD	standard deviation
SDS-WAS	Sand and Dust Storm Warning Advisory and Assessment System
SDU	sunshine duration
SERI	Solar Energy Research Institute
SEVIRI	Spinning Enhanced Visible and InfraRed Imager
SHC	Solar Heating and Cooling Programme
Si	silicon
SI	Système International (international system of units)
SICCS	Surface Insolation under Clear and Cloudy Skies
SICLONE	Système d'Information pour l'analyse et la prévision des Configurations spatio-temporelLes des Occurrences NuageusEs
SID	surface incoming direct radiation
SIS	solar surface irradiance

SMARTS	Simple Model of the Atmospheric Radiative Transfer of Sunshine
SMHI	Swedish Meteorological and Hydrological Institute
SO_2	sulfur dioxide
SolarPACES	Solar Power and Chemical Energy Systems
SolarPILOT	Solar Power tower Integrated Layout and Optimization Tool
SOLEMI	Solar Energy Mining database
SOLIS	SOlar Irradiance Scheme
Suomi-NPP	Suomi National Polar-Orbiting Partnership
SPECTRL2	Bird Simple Spectral Model version 2
SPF	smart persistence forecast
SPRAY	Solar Power Ray-Tracing Tool
SRB	Surface Radiation Budget
SRRL	Solar Radiation Research Laboratory
SRTM	Shuttle Radar Topography Mission
SS	Smithsonian scale
SSE	Surface meteorology and Solar Energy
STC	standard test condition
STE	solar thermal electricity
STRAL	Solar Tower Ray-Tracing Laboratory
SUNY	State University of New York
SURFRAD	Surface Radiation Budget Network
SVF	sky view factor
SZA	solar zenith angle
TDY	typical direct normal irradiance year
TGY	typical global horizontal irradiance year
TMM	typical meteorological month
TMY	typical meteorological year
TOA	top of atmosphere
TOD	total optical depth
TRY	typical reference year
TRYNSYS	Transient System Simulation Tool
TSI	total solar irradiance
TSO	transmission system operator
UPS	uninterruptible power supply
UT	Universal Time
UTC	Coordinated Universal Time
UV	ultraviolet
UXO	unexploded ordnance
VPP	virtual power plant
WEST	Western Energy Supply and Transmission
WHO	World Health Organization
WMO	World Meteorological Organization
WPS	web processing service
WPVS	World Photovoltaic Scale
WRC	World Radiation Center
WRDC	World Radiation Data Center

WRF	Weather Research and Forecasting
WRMC	World Radiation Monitoring Center
WRR	World Radiometric Reference
WSA	white-sky albedo
WSG	World Standard Group

Table of Contents

List of Figures

List of Tables

1 The Importance of Solar Resource Information for Solar Power

Manajit Sengupta[1]
[1] *National Renewable Energy Laboratory, USA*

Solar radiation is the fuel for all solar energy technologies. For any solar generation source, knowledge of the quality and future reliability of the fuel is essential for determining the financial viability of any new project. This information is also important during operations for accurate control, analyses, and integration of the generation to the grid. The variability of the supply of sunlight represents the single-greatest uncertainty in a solar power plant's predicted performance. Solar resource information is needed for various stages of a plant's development and operation, such as:

- Historical long-term data for site selection during feasibility studies
- Prediction of power plant output for plant design and financing
- Real-time measurement and solar forecasting for plant and grid operations.

Site selection requires information about numerous parameters for prospective project locations, including current land use, grid access, and proximity to load centers. The top priority, however, is determining if adequate solar resource exists for a proposed project. For site selection, average annual solar irradiation at the site is the first meteorological selection criterion. Other meteorological parameters, such as ambient temperature, wind speed and surface albedo, also play an important role. Further, lower seasonal and interannual variability could also be advantageous because of a more consistent match to the power demand. As weather patterns can change from one year to another, many years of data are required to determine reliable average irradiation conditions and interannual variability. For this purpose, satellite-derived, high-quality historic solar radiation datasets covering at least 10 years are usually considered necessary for the site selection of large solar energy systems. As humanity encounters a changing climate, new solar development will have to account for the possibility of changes and variability in solar resource that might not be represented in historical data. Output from climate models is currently being investigated for use in predicting future solar generation and understanding resource adequacy under high deployment of photovoltaics.

As flat-priced electricity feed-in tariff regulations get phased out, the economic yield of solar power systems increasingly depends on the solar production at specific times of the day as well as during various times of the year. Thus, for solar projects with variable prices, the temporal distribution of solar irradiance to estimate potential yields among competing sites might be critical even during site selection. This becomes even more important as storage solutions are integrated with new solar generation facilities. At early stages of project development, it is sufficient to study the temporal variability of the energy output throughout the year and typical daily cycles. As an alternative to multiple-year datasets, typical meteorological year (TMY) data for each site might be sufficient at this stage, particularly for smaller installations; however, the TMY cannot characterize interannual variability and might have limited use for certain projects.

If an appropriate site is identified, the development of a larger solar energy project will require more precise and detailed datasets. For site-specific techno-economic optimization of a solar

system, the availability of high-resolution data is always beneficial. These data generally exist in the form of satellite-derived or reanalysis-based time series. To finance large solar power plants, datasets that are validated by ground measurements on or near the site are essential to reduce the yield risk. In addition to accurate solar radiation measurements, specialized meteorological stations usually provide additional environmental parameters that help to optimize the sizing and proper selection of plant components.

Accurate solar and meteorological stations are also valuable during the commissioning of larger plants because reliable measurements form the basis for acceptance testing to demonstrate proof of fulfillment of technical specifications for heat or electric output. Although temporary measurement equipment can be used for acceptance testing, reliable measurements are essential for estimating real-time plant output to ensure high efficiency of the plant throughout its service life. The evaluation of plant output as a function of solar irradiance is the most important indicator of power plant performance. A reduction in overall efficiency implies a degradation of one or more power plant components or poor maintenance or operation. Although remotely sensed data can be used for smaller systems, where performance accuracy can be relaxed, larger solar systems usually rely on ground-based measurements, which might be combined with near-real-time satellite-derived solar radiation data. Local ground measurements also assist in site-specific model validation and improvements of solar forecasts.

Proper and accurate solar forecasts are important for the optimized use of solar power plants, both economically and operationally. They help to improve system operations, such as the optimal use of a storage tank in a solar thermal water heating system, a molten salt system for high-temperature applications, or a battery system in a photovoltaic (PV) system. With the fast growth of grid-connected solar electrical systems, solar radiation forecasts have become highly important for safe grid operations and the efficient dispatch of power plant resources. Short-term solar forecasts in areas of high solar penetration enable efficient dispatch, while day-ahead forecasts enable accurate unit commitment, leading to efficient planning of reserves.

This handbook covers all pertinent aspects of solar radiation that are relevant for the planning and operation of PV plants, solar thermal heating and cooling systems, concentrating solar thermal plants, and the electric grid. Chapter 2 introduces solar radiation concepts that are essential for understanding the behavior of sunlight. Chapter 3 discusses the measurement of solar radiation and the best practices that must be followed to acquire defensible solar measurements. Chapter 4 provides users with information about how to control the quality of measurements and how to assess that quality after measurements have been taken. Chapter 5 provides users with information on meteorological parameters that are either used for modeling solar irradiance, solar energy production, or PV reliability. Chapter 6 provides information about the variability of solar radiation at various timescales. As solar radiation is inherently variable, this chapter is particularly important for those who seek to develop methods to balance grid operations. Chapter 7 provides users with information about solar radiation modeling, including how satellite-based models predict solar radiation and how solar radiation can be modeled at various orientations at which solar energy converters are deployed. Chapter 8 provides users with information about various sources of solar data and models. This chapter is a useful repository of links for users looking for either solar datasets or models to manipulate solar data for their applications. Chapter 9 covers solar forecasting at various timescales and is an extremely important chapter for grid operators seeking to reduce the cost of grid operations under fast-

growing deployments of solar energy. Chapter 10 provides users with an understanding of uncertainty in solar measurements and modeled solar data, both historical and forecast. Chapter 11 provides users with information about how to use both measured and modeled solar data for modeling solar energy both during development and operation of solar energy plants. Chapter 12 provides users with an outlook of what is on the horizon for the International Energy Agency (IEA) Photovoltaic Power Systems Programme (PVPS) Task 16, primarily based on the challenges and gaps that have been identified by experts.

Some emerging topics, such as the application of machine learning in solar energy applications and the impact of climate change on plant performance and resource adequacy, are briefly mentioned in the handbook. As we move toward decarbonization of the grid, and ultimately of all energy use, it is expected that these topics will be expanded upon and presented in more detail in future editions of the handbook. Readers should note that this handbook is the result of significant effort by the foremost international experts in the field. Therefore, this handbook ensures that the material presented here is well vetted and is the most current understanding of the state of the art.

2 Overview of Solar Radiation Resource Concepts

Aron Habte,[1] Thomas Stoffel,[2] Christian Gueymard,[3] Daryl Myers,[4] Philippe Blanc,[5] Sara Bham, [5] Stefan Wilbert,[6] Frank Vignola,[7†] and Nicholas Riedel-Lyngskær[8]

[1] *National Renewable Energy Laboratory, USA*
[2] *Solar Resource Solutions, LLC, USA*
[3] *Solar Consulting Services, USA*
[4] *National Renewable Energy Laboratory, USA, retired*
[5] *MINES Paris–PSL, Center Observation, Impacts, Energy, France*
[6] *German Aerospace Center (DLR), Germany*
[7] *University of Oregon, USA*
† *Deceased*
[8] *Technical University of Denmark (DTU), Denmark*

Executive Summary

Obtaining data time series or temporal averages of the solar radiation components—most importantly, global horizontal irradiance (GHI) and direct normal irradiance (DNI)—that relate to a conversion system is the first step in selecting the site-appropriate technology and evaluating the simulated performance of specific system designs. Photovoltaic (PV) systems and thermal flat-plate collectors (fixed or tracking) can use all downwelling radiation components, as well as radiation reflected from the ground if in the collector's field of view. The reflected component is of particular importance for bifacial PV systems and related to the albedo of the ground. Systems with highly concentrating optics rely solely on DNI. Low-concentration systems might also be able to use some sky diffuse radiation.

Describing the relevant concepts and applying a consistent terminology are important to the usefulness of any handbook. This chapter discusses standard terms that are used to illustrate the key characteristics and components of solar radiation—the fuel for all solar technologies.

Beginning with the sun as the source, this chapter presents an overview of the effects of Earth's orbit and atmosphere on the possible types and magnitudes of solar radiation available for energy conversion. An introduction to the concepts of measuring and modeling solar radiation is intended to prepare the reader for the more in-depth treatments in Chapters 3–10. This overview concludes with a topic of terrestrial spectral irradiance, which is used as a basis for performance evaluation of various PV technologies and characterization of absorptance, reflectance, and transmittance, and spectral response evaluation of PV materials.

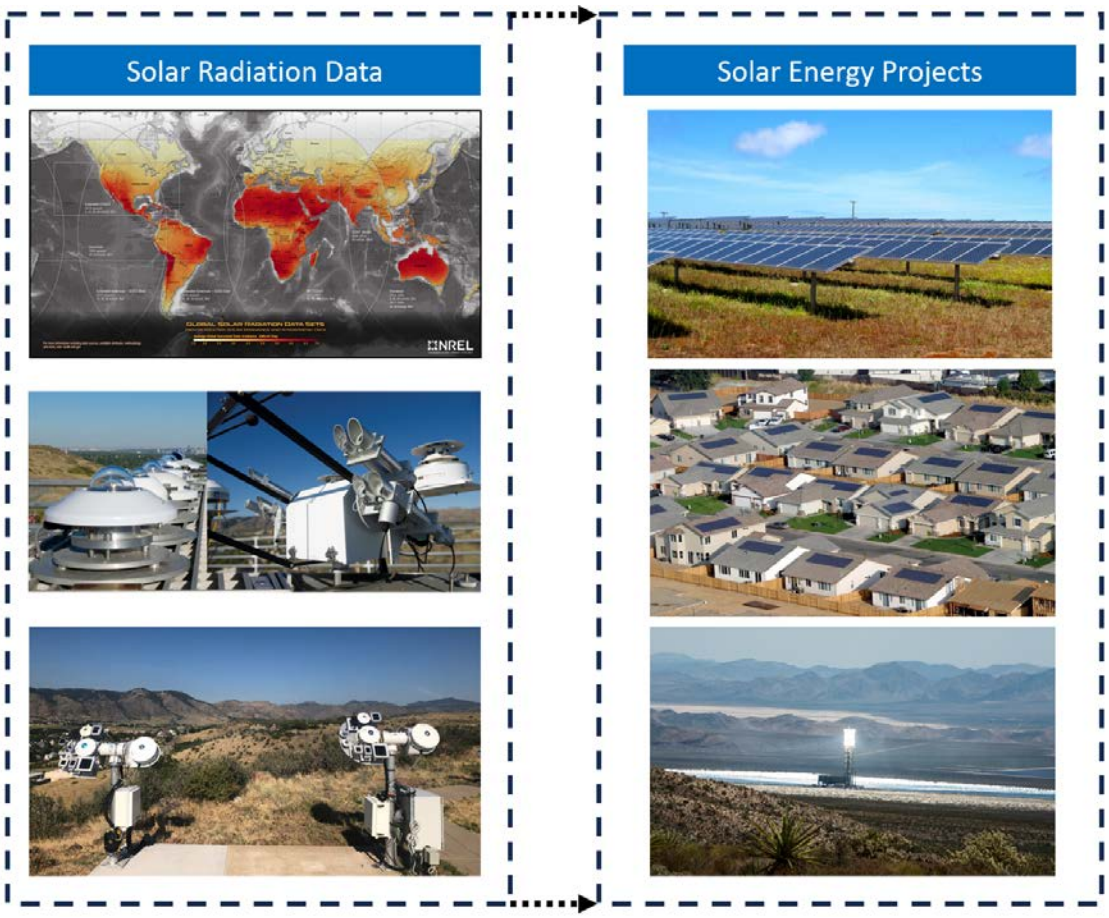

Figure ES 2-1. Example solar radiation data and application to solar energy projects

Image by NREL

2.1 Extraterrestrial Irradiance Spectrum

Any object with a temperature above absolute zero Kelvin emits radiation. With an effective surface temperature of ≈5800 K, the sun behaves like a quasi-static blackbody and emits radiation over a wide range of wavelengths, with a distribution that is close to that predicted by Planck's law (Figure 2-1). This constitutes the solar spectral power distribution, or solar spectrum. For terrestrial applications, the useful solar spectrum, also called the shortwave spectrum (≈290–4000 nm), includes the spectral regions called ultraviolet (UV), visible, and near-infrared (NIR) (Figure 2-1). The latter is the part of the infrared spectrum that is below 4000 nm in the solar spectrum. In contrast, the longwave (or far-infrared) spectrum extends beyond 4 μm, where the planetary thermal emission is dominant. Based on a recent determination (Gueymard 2018b), most spectral irradiance (98.5%) of the extraterrestrial spectrum (ETS) is contained in the wavelength range from 290–4000 nm. In what follows, broadband solar radiation will always refer to this spectral range, unless specified otherwise.

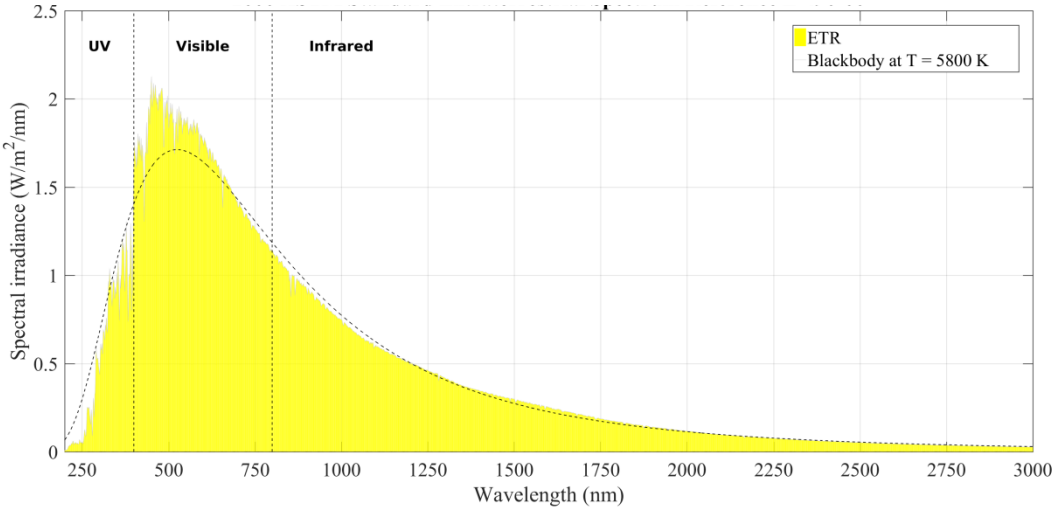

Figure 2-1. Reference ETS (ASTM E490-22) and 5800-K blackbody distribution using Planck's law

Image by Philippe Blanc, MINES Paris–PSL University

Various ETS distributions have been derived based on ground measurements, extraterrestrial measurements, and physical models of the sun's output. All distributions contain some deviations, as evidenced by the historical perspective offered by (Gueymard 2018b; 2004; 2006). A more recent generation of ETS distribution, based on spectral measurements from space, was published (Gueymard 2018b) and was eventually adopted to become the current standard extraterrestrial spectrum, as now mandated by ASTM Standard E490 (ASTM E490 2022) (Figure 2-1).

2.2 Solar Constant and Total Solar Irradiance

The total radiant power emitted by the sun is nearly constant to within ±0.2%. The solar irradiance at 1 AU (astronomical unit, approximate average sun-Earth distance) distance from the sun is called the total solar irradiance (TSI) and used to quantify the solar output. TSI was commonly called the solar constant (SC) until slight temporal variations were discovered (Fröhlich and Lean 2004; Kopp and Lean 2011). The SC is now defined as the long-term mean TSI. Small but measurable changes in the sun's output and TSI are related to the sun's magnetic activity. There are cycles of approximately 11 years in solar activity, which are accompanied by a varying number of sunspots (cool, dark areas on the sun) and faculae (hot, bright spots). TSI increases during high-activity periods because the numerous faculae more than counterbalance the effect of sunspots. From an engineering perspective, these TSI variations are relatively small, so the SC concept is still useful and eminently appropriate in solar applications.

Figure 2-2 shows the latest version of a composite TSI time series based on multiple spaceborne instruments that have monitored TSI since 1978 using a variety of absolute scales (Gueymard 2018a). Estimates are also used from 1976–1978 to make this time series start at the onset of solar cycle 21. The solar cycle numbers are indicated for further reference. (Solar cycle 25 has started in December 2019 and is expected to peak in 2024 or 2025.) Figure 2-2 shows the SC (always evaluated at 1 AU) as a horizontal solid line.

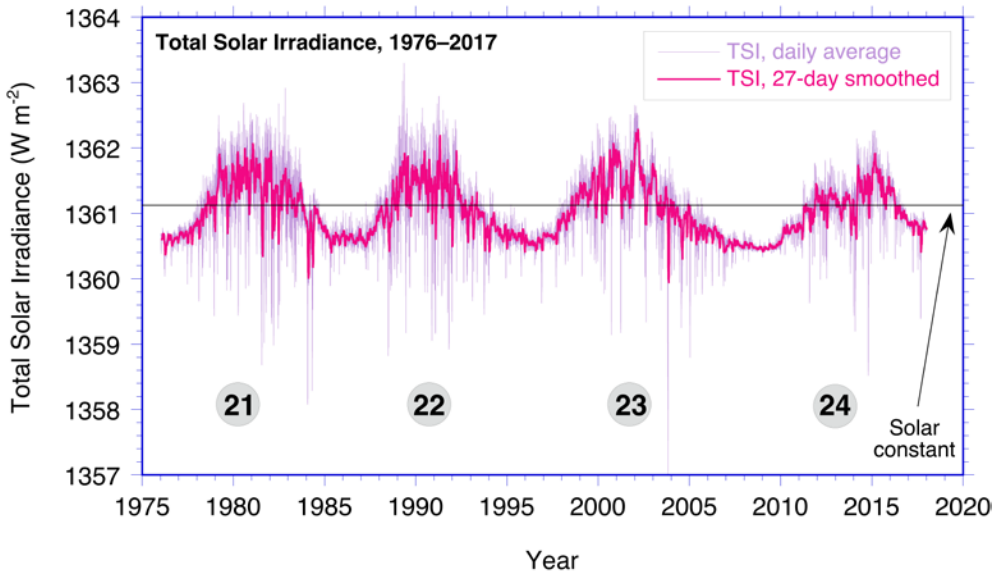

Figure 2-2. Four solar cycles show the temporal variations of TSI in a composite reconstruction of the 1976–2017 time series based on observations from spaceborne radiometers after corrections and gap-filling.

The thick line indicates the 27-day moving average (corresponding to the 27-day mean solar rotation period), and the circled numbers refer to the solar cycle designation. The horizontal line shows the SC (1361.1 W/m^2). Image based on data published in (Gueymard 2018a)

On a daily basis, the passage of large sunspots results in lower TSI values than the SC. The measured variation in TSI resulting from the sunspot cycle is at most ±0.2%, only twice the precision (i.e., repeatability—not total absolute accuracy, which is approximately ±0.5%) of the most accurate radiometers measuring TSI in space. There is, however, some large variability in a few spectral regions—especially the UV (wavelengths less than 400 nm)—caused by solar activity.

Historic determinations of SC have fluctuated throughout time (Gueymard 2006; Kopp 2016). At the onset of the 21st century, it was assumed to be 1366.1 ± 7 W/m^2 (Gueymard 2004) More recent satellite observations using advanced sensors and better calibration methods, however, have shown that the SC is somewhat lower: ≈1361 W/m^2. After careful reexamination and corrections of decades of past satellite-based records, (Gueymard 2018a) proposed a revised value of 1361.1 W/m^2, which has since been adopted as the new standard value according to ASTM E490 (2022). The magnitude of this change is the result of better measurements and methodology rather than a change in the output of the sun.

According to astronomical computations such as those made by the National Renewable Energy Laboratory's (NREL's) solar position software,[1] using SC ≈1361 W/m^2, the seasonal variation of ±1.7% in the sun–Earth distance causes the irradiance at the top of the Earth's atmosphere to vary from ≈1409 W/m^2 (+3.5%) near January 3 to ≈1315 W/m^2 (–3.3%) near July 4. This seasonal variation is systematic and deterministic; hence, it does not include the daily (somewhat random) or cyclical variability in TSI induced by solar activity, which was discussed previously.

[1] See https://midcdmz.nrel.gov/spa/.

This variability is normally less than ±0.2% and is simply ignored in the practice of solar resource assessments.

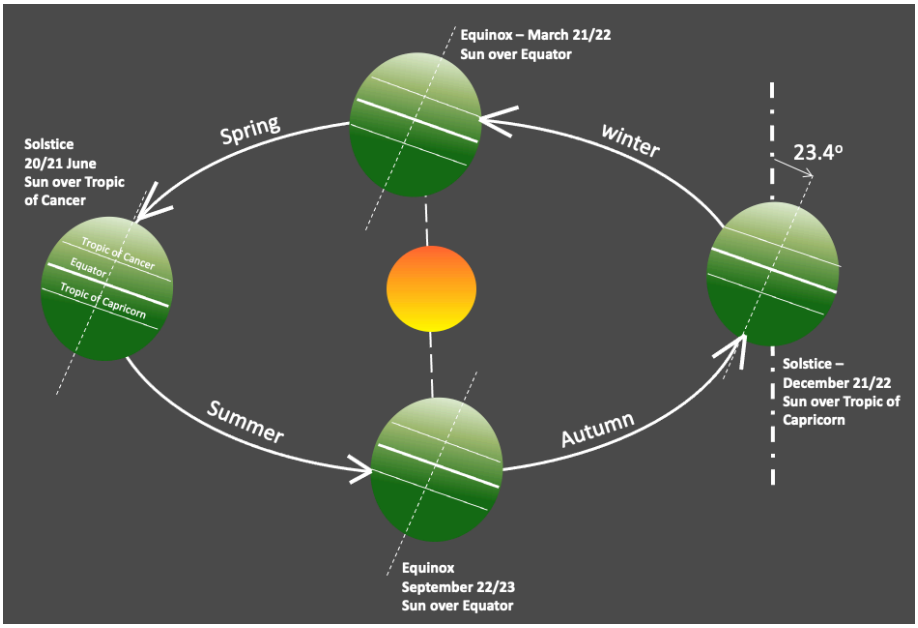

Figure 2-3. Schematic of the Earth's orbit. The Earth's orbit around the sun is slightly elliptic.

Note: The seasons are represented for the Northern Hemisphere. *Image by NREL*

2.3 Sun-Earth Distance and Extraterrestrial Radiation

The amount of radiation exchanged between two objects is affected by their separation distance. The Earth's elliptical orbit (eccentricity 0.0167) brings it closest to the sun in January and farthest from the sun in July, as just mentioned. The average Sun–Earth distance is close to the new definition of the AU, which is exactly 149,597,870,700 m, as introduced in 2012 by the International Astronomical Union and recognized as a Système International (SI) unit in 2014 by the International Bureau of Weights and Measures (BIPM).[6] Figure 2-3 shows the Earth's orbit in relation to the Northern Hemisphere's seasons, caused by the average ≈23.4° tilt of the Earth's rotational axis with respect to the plane of the orbit. The solar irradiance available at the top of atmosphere (TOA) is called the extraterrestrial radiation (ETR). ETR (Eq. 2-1) is the power per unit area, or flux density, in Watts per square meter (W/m^2), radiated from the sun and available at the TOA. Just like ETS, ETR (e.g., Figure 2-4) varies with the Sun–Earth distance (r) and annual mean distance (r_0):

$$\mathrm{ETR} = \mathrm{TSI}\left({}^{r_0}/_{r}\right)^2 \tag{2-1}$$

As indicated in Section 2.2, it is customary to neglect temporal variations in TSI so that TSI can be replaced by SC in Eq. 2-1 for simplification. The Sun–Earth distance correction factor, $(r_0/r)^2$, in Eq. 2-1 can be obtained from sun position algorithms, such as those described in Section 2.4.1.

[6] See https://www.bipm.org/documents/20126/41483022/SI-Brochure-9-EN.pdf/2d2b50bf-f2b4-9661-f402-5f9d66e4b507.

Daily values of sufficient accuracy for most applications can also be found in tabulated form (e.g., [Iqbal 2012]).

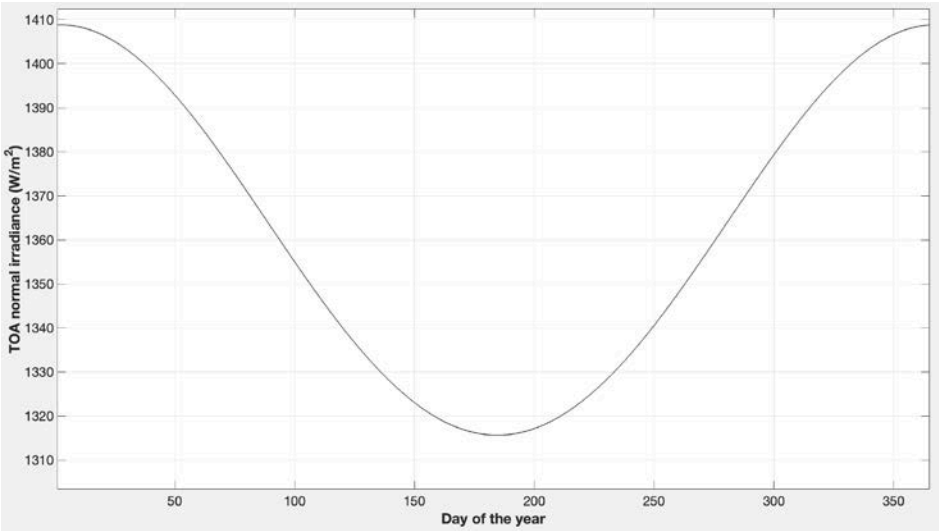

Figure 2-4. ETR (i.e., the solar normal irradiance available at the TOA)

Image by NREL

From the TOA, the sun appears as a very bright small disk surrounded by a completely black sky, apart from the light coming from stars and other celestial bodies. The angle describing the size of the sun disk can be determined from the distance between the Earth and the Sun, and the latter's visible diameter. It varies by ±1.7%, because the Sun–Earth distance varies. A point at the top of the Earth's atmosphere intercepts a cone of light from the hemisphere of the sun facing the Earth with a total angle of 0.53°±1.7% (i.e., 0.266° half the apex angle on a yearly average). Because the divergence angle is very small, the rays of light emitted by the sun are nearly parallel; these are called the solar beam. The interaction of the solar beam with the terrestrial atmosphere is discussed next.

2.4 Solar Radiation and the Earth's Atmosphere

The Earth's atmosphere can be seen as a continuously variable filter for the solar ETR as it reaches the surface. Figure 2-5 illustrates the attenuation of solar radiation by atmospheric constituents such as ozone, oxygen, water vapor, aerosols, or carbon dioxide. The amount of atmosphere the solar photons must traverse, also called the atmospheric path length or air mass (AM), depends on the relative position of the observer with respect to the sun's position in the sky (Figure 2-5). By convention, air mass one (AM1) is defined as the amount of atmospheric path length observed when the sun is directly overhead. As a first approximation, and for low zenith angles, air mass is geometrically related to the solar zenith angle (SZA). Actually, the air mass is approximately equal to the secant of SZA, or 1/cos(SZA). Air mass 1.5 (AM1.5) is a key quantity in solar applications and corresponds to SZA = 48.236° (Gueymard, Myers, and Emery 2002). Air mass two (AM2) occurs when SZA is ≈60° and has twice the path length of AM1. By extrapolation, one refers to the value at the TOA as AM0 (Myers 2013).

The cloudless atmosphere contains gaseous molecules and particulates (e.g., dust and other aerosols) that reduce the ETR as it progresses farther down through the atmosphere. This

attenuation is caused mostly by scattering (a change of a photon's direction of propagation) and also by absorption (a capture of radiation). Finally, clouds are the major elements that modify the ETR (also by scattering and absorption) on its way to the surface or to a solar collector.

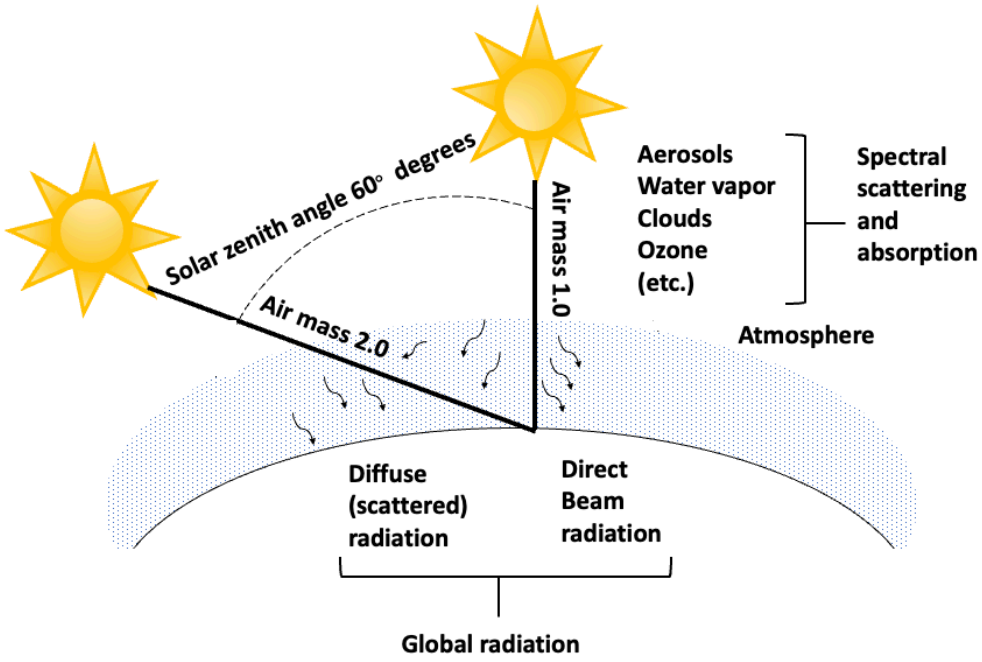

Figure 2-5. Illustration of air mass, the SZA, and absorption and scattering in the atmosphere. Scattering of the direct beam photons from the sun by the atmosphere produces diffuse radiation that varies with air mass.

Image by NREL, modified from Dunlap et al. (1992)

Absorption converts part of the incoming solar radiation into heat and raises the temperature of the absorbing medium. Scattering redistributes the radiation in the hemisphere of the sky dome above the observer, including a part that is reflected back into space. The longer the path length through the atmosphere, the more radiation is absorbed and scattered. The probability of scattering and absorption increases as the path (air mass) from the TOA to the ground increases.

Part of the radiation that reaches the Earth's surface is eventually reflected into the atmosphere. A fraction of this returns to the surface through a process known as backscattering. The actual geometry and flux density of the reflected and scattered radiation depend on the reflectivity and physical properties of the surface and constituents in the atmosphere, especially clouds and aerosols.

Based on these interactions between the radiation and the atmosphere, the terrestrial solar radiation is divided into two components: *direct beam radiation*, which refers to solar photons that reach the surface without being scattered or absorbed, and *diffuse radiation*, which refers to photons that reach the observer after one or more scattering events with atmospheric constituents. These definitions and their usage for solar energy are discussed in detail in Section 2.5.

Ongoing research continues to increase our understanding of the properties of atmospheric constituents, ways to estimate them, and their impact on the magnitude of solar radiation in the atmosphere at various atmospheric levels and at the surface. This is of great importance to those who measure and model solar radiation fluxes (see Chapters 3–7).

2.4.1 Solar Position in the Sky

The position of the sun in the sky depends in particular on the position of the Earth relative to its orbit around the sun, the rotation of the Earth, and the direction of the Earth's axis of rotation relative to the plane of the Earth's orbit (Figure 2-3). The Earth rotates around an axis through the geographic north and south poles, inclined at an average angle of ≈23.4° to the plane of the Earth's orbit. The axial tilt of the Earth's rotation results in daily variations in solar geometry during any year. At mid-latitudes (latitudes 23.4° to 66.6°, both north and south) near midday, the sun is relatively low above the horizon during winter and high in the sky during summer. In the summer of the Northern Hemisphere, days are longer than winter days because the North Pole is facing the sun in summer and directed away from the sun in winter. All these changes result in changing geometry of the solar position in the sky with respect to time of year and specific location. Similarly, the resulting yearly variation in the solar ETR contributes to seasonal variations in climate and weather at each location. The solar position in the sky corresponds to topocentric angles, as follows:

- The solar elevation angle is defined as the angle formed by the direction of the sun and the local horizon. It is equal to 90°–SZA.
- The solar azimuth angle is defined as the angle formed by the projection of the direction of the sun on the horizontal plane defined eastward from true north, following the International Organization for Standardization (ISO) 19115 (ISO 19115-1:2014) standard. For example, 0° or 360° = due north, 90° = due east, 180° = due south, and 270° = due west.

An example of apparent sun path variations for various periods of the year is depicted in Figure 2-6). Because of their significance in performing any analysis of solar radiation data or any radiation model calculation, the use of solar position calculations of sufficient accuracy is necessary, such as those derived from NREL's Solar Position Algorithm[7] (Reda and Andreas 2004; 2007). This algorithm predicts solar zenith and azimuth angles in addition to other related parameters such as the Sun–Earth distance and the solar declination. All this is possible in the period from 2000 B.C. to 6000 A.D. with an SZA standard deviation of only ≈0.0003° (1"). To achieve such accuracy during a long period, this algorithm is very time consuming, with approximately 2300 floating operations and more than 300 direct and inverse trigonometric functions at each time step. To realize the stated accuracy over many millennia, the algorithm requires input values for the target date of differences between clock time and the apparent solar time due to variations in the Earth's rotational speed. Other algorithms exist, differing in the attained accuracy and in their period of validity. They use various strategies to limit the number of functions and operations, such as reducing the period of validity while maintaining high accuracy (Blanc and Wald 2012; Grena 2008; Blanco, Milidonis, and Bonanos 2020) or keeping a long period while reducing accuracy (Michalsky 1988b; 1988a).

[7] See http://www.nrel.gov/midc/spa/.

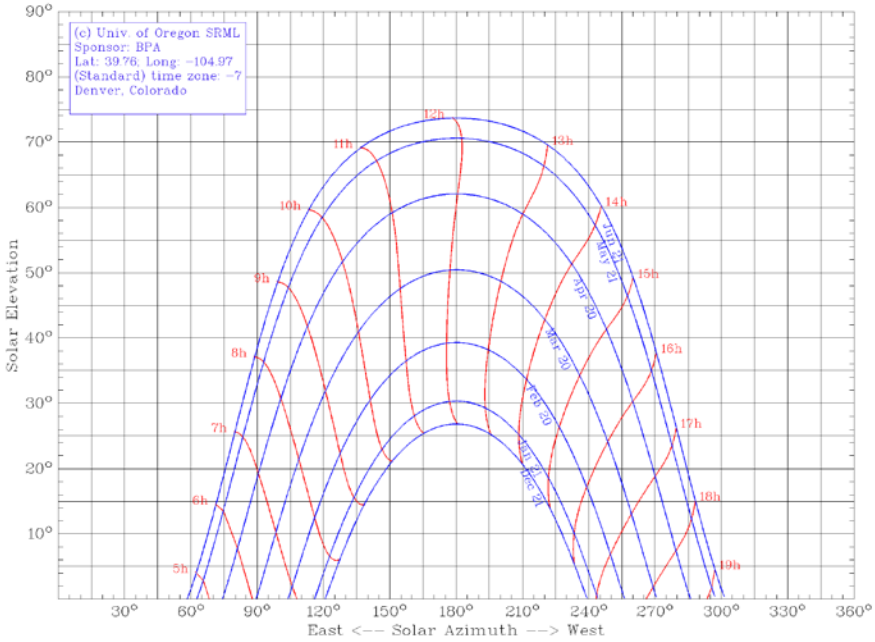

Figure 2-6. Apparent sun path variations during a typical year in Denver, Colorado

Image from the University of Oregon Solar Radiation Monitoring Laboratory (http://solardata.uoregon.edu/sunChartProgram.php)

2.5 Solar Resource and Irradiance Components for Solar Energy Applications

Solar radiation, when going through the atmosphere, can be transmitted, absorbed, reflected, or scattered in varying amounts by atmospheric constituents (aerosols, water vapor, ozone, other gases), depending on wavelength.

Consider first the downwelling broadband irradiance components reaching a horizontal surface. *Broadband* means that this irradiance is integrated over the whole shortwave spectrum, ranging from ~290 nm to 4000 nm, expressed in W/m^2. These complex interactions of the Earth's atmosphere with solar radiation result in three fundamental irradiance components of interest, notably to solar energy conversion technologies (Figure 2-7):

- DNI: solar direct or beam irradiance from a small solid angle centered on the sun position.
- Diffuse horizontal irradiance (DHI): scattered solar downwelling irradiance on a horizontal plane from the sky dome, excluding the same small solid angle as the direct component.
- GHI: solar downwelling irradiance on a horizontal plane from the whole dome, also called the total hemispheric irradiance.

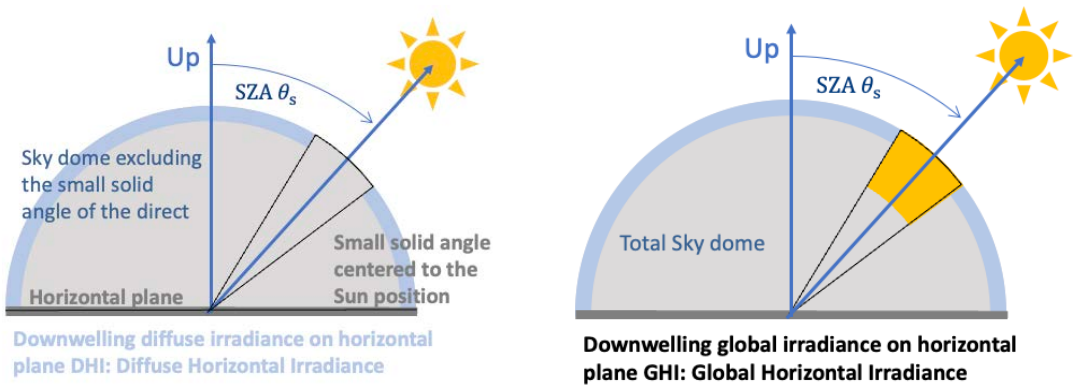

Figure 2-7. Depictions of three fundamental irradiance components

Image by Philippe Blanc, MINES Paris–PSL University

These basic solar components are related to each other by a fundamental expression called the closure equation:

$$GHI = DNI \bullet \cos(SZA) + DHI \tag{2-2}$$

The difference between the global and diffuse horizontal irradiance is often denoted as the *beam* horizontal irradiance (BHI = DNI • cos(SZA)) rather than direct horizontal irradiance to avoid acronym confusion with *diffuse* horizontal irradiance.[8]

GHI is measured at a relatively large number of stations in the world (see Chapter 8); however, the quality of such data remains to be verified at most of these stations. Assuming that good-quality GHI data are available at a station of interest, how can the analyst derive the two other components—DNI and DHI?

There are two possible solutions to this frequent situation. The first is to obtain time series of GHI, DNI, and DHI from a reputable source of satellite-derived data. The modeled and measured GHI data can then be compared for quality assurance and possible improvements of the modeled data (using site adaptation; see Chapter 7, Section 7.6) or, conversely, to determine the quality of the measured data. Both measured and modeled GHI values might unfortunately incorporate systematic biases. Understanding the magnitude and nature of these biases and how they can affect the calculation is important when determining the uncertainty in the results (see Chapter 10).

The second method for determining DNI and DHI from GHI data consists of using one of numerous "separation" or "decomposition" models, as further discussed in Chapter 7, Section 7.3.1. Considerable literature exists on this topic. (Gueymard and Ruiz-Arias 2016) reviewed 140 such models and quantified their performance at 54 high-quality radiometric stations over all continents using data with high temporal resolution (1 minute, in most cases). Other studies have followed, proposing and/or validating potentially better models (Starke et al. 2021; Tan, Wang, and Zhang 2023; Yang 2022; Yang et al. 2024; Ruiz-Arias and Gueymard 2024a; 2024b). All current models of this type, being empirical in nature, are not of "universal" validity and thus might not be optimized for the specific location under scrutiny, particularly under adverse situations (e.g., subhourly data, high surface albedo, or high aerosol loads) that can trigger

[8] An alternate set of acronyms indeed exists in the literature, whereby DHI or DIR represents the direct horizontal irradiance and DIF is the diffuse horizontal irradiance.

significant biases and random errors; hence, the most appropriate way to deal with the component separation problem cannot be ascertained at any given location. The solar radiation scientific research community continues to validate the existing conversion algorithms and to develop new ones.

In general, the higher the time resolution, the larger random errors in the estimated DNI or DHI will be. Even large biases could appear at subhourly resolutions if the models used are not appropriate for short-interval data. This issue is discussed by (Gueymard and Ruiz-Arias 2016; 2014), who showed that not all hourly models are appropriate for higher temporal resolutions and that large errors might occur under cloud-enhancement situations. Another avenue of research is to optimally combine the estimates from multiple models using advanced artificial intelligence techniques (Aler et al. 2017; Tan, Wang and Zhang 2024).

2.5.1 Irradiance vs. Radiance

To better understand the different components of broadband irradiance on any tilted plane (Figure 2-8), one should consider the downwelling and upwelling broadband radiances at the surface, expressed in W/(sr•m^2). The downwelling radiance describes the angular distribution of the downwelling solar radiation from the sky to the surface. The upwelling radiance describes the angular distribution of the downwelling solar radiation reflected by the surface. The downwelling and upwelling irradiance incident on a tilted plane is the result of the integral of the downwelling and upwelling radiance with respect to the hemisphere facing that plane. The upwelling irradiance is generally named the surface-reflected irradiance, or just ground-reflected irradiance if no water surfaces are involved.

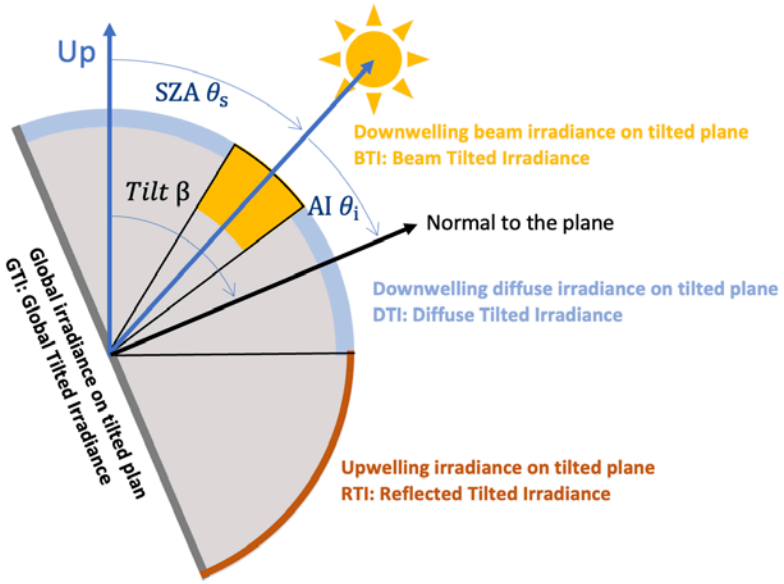

Figure 2-8. Solar radiation components incident on a tilted plane (oriented hemispherical irradiance)

Image by Philippe Blanc, MINES Paris–PSL University

Following Figure 2-8, the different components of irradiance on a tilted plane are:

- Beam tilted irradiance (BTI): downwelling solar irradiance incident on the tilted surface, from the downwelling radiance restricted to the same small solid angle as DNI:

$$BTI = DNI \cdot \cos(AI) \quad (2\text{-}3)$$

  where AI is the angle of incidence of the sunbeams for that specific tilted surface.
- Diffuse tilted irradiance (DTI): downwelling solar irradiance incident on the tilted surface, considering the solid angle of sky dome facing the tilted plane, but excluding the same small solid angle as for DNI.
- Reflected tilted irradiance (RTI): upwelling solar irradiance reaching the tilted surface from the surface-reflected upwelling radiance, considering the solid angle of the ground facing the tilted plane.
- Global tilted irradiance (GTI): defined as the sum of the diffuse, direct, and reflected irradiance incident on the tilted surface. GTI is also referred to as the plane-of-array (POA) irradiance in the photovoltaic (PV) literature.

In the theoretical case when the sky diffuse radiance can be considered isotropic (i.e., constant downwelling radiance in all directions, except for the small solid angle of the direct component), and if the surface's reflectance is also assumed isotropic (Lambertian) with a given albedo, ρ, a simplified relationship is obtained:

$$GTI = DNI \cdot \cos(AI) + DHI \cdot SVF + \rho \cdot GHI \cdot GVF \quad (2\text{-}4)$$

where SVF is the sky view factor between the collector and the visible part of the sky, and GVF is the ground view factor between the collector and the visible part of the foreground surface, according to:

$$SVF = (1+\cos(tilt))/2 \quad (2\text{-}5)$$

$$GVF = (1-\cos(tilt))/2 \quad (2\text{-}6)$$

The tilt angle is written as "tilt" in these equations and defined as illustrated in Figure 2-8. Eq. 2-5 and 2-6 are strictly valid *only* under the assumptions of isotropy for both the sky and reflected radiance, and of a reflecting surface of an infinite dimension. These assumptions are convenient to simplify calculations (Kamphuis et al. 2020), but rarely fully accurate in nature. For a more accurate calculation, anisotropic models of downwelling sky radiance (e.g., (Gueymard and Kocifaj 2022)), of sky diffuse irradiance (see Chapter 7), and of bidirectional reflectance distribution function (BRDF) (e.g., [Ross 1981]; see also Chapter 7) need to be used that correspond well to the current sky and ground conditions.

2.5.2 Direct Normal Irradiance and Circumsolar Irradiance

By definition, DNI is the irradiance on a surface perpendicular to the vector (i.e., normal incidence) from the observer to the center of the sun caused by radiation that was not scattered by the atmosphere out of the region appearing as the solar disk (WMO 2018). This strict definition is useful for atmospheric physics and radiative transfer models, but it results in a complication for ground observations: it is not possible to observe whether a photon was scattered if it reaches the observer from the direction in which the solar disk is seen. Therefore, DNI is usually interpreted in a less stringent way in the world of solar energy. Direct solar radiation is understood as the "radiation received from a small solid angle centered on the sun's

disk" (ISO 9488 2022). The size of this "small solid angle" for DNI measurements is recommended to be $5 \cdot 10^{-3}$ sr (corresponding to ≈2.5° half angle) (WMO 2018). This recommendation is approximately 10 times larger than the angular radius of the solar disk itself based on no-atmosphere geometry, whose yearly average is 0.266°. This relaxed definition is necessary for practical reasons because instruments for DNI measurement (pyrheliometers) need to track or follow the sun throughout its path of motion in the sky, and small tracking errors are to be expected. The relatively large field of view (FOV) of 5° (or 2.5° half angle) of pyrheliometers reduces the effect of such tracking errors.

To understand the definition of DNI and how it is measured by pyrheliometers in practice, the role of circumsolar radiation—scattered radiation coming from the annulus surrounding the solar disk—must be discussed. (The reader is referred to the detailed review, based on both experimental and modeling results, found in [Blanc et al. 2014].) Because of forward scattering of direct sunlight in the atmosphere, the circumsolar region closely surrounding the solar disk (solar aureole) looks very bright and can affect the observed *sunshape* (Buie, Monger, and Dey 2003). The sunshape—a quantity not to be confused with the "shape of the sun"—is the azimuthally averaged radiance profile as a function of the angular distance from the center of the sun normalized to 1 at the apparent sun's disc center. The radiation coming from this region is called circumsolar radiation. For the typical FOV of modern pyrheliometers (5°), circumsolar radiation contributes a variable amount, depending on atmospheric conditions, to the DNI measurement. Determining the magnitude of the circumsolar radiation is of interest in concentrating solar thermal (CST) applications because DNI measurements are typically larger than the beam irradiance that can be used in concentrating systems. This causes an overestimate of CST plant production because the FOV of the concentrators (typically of the order of 1° or less) is much smaller than the FOV of the pyrheliometers that are used on-site to determine the incident DNI.

The circumsolar contribution to the observed DNI can be quantified if the radiance distribution within the circumsolar region and the so-called penumbra function of the pyrheliometer are known. The latter is a characteristic of the instrument and can be derived from the manufacturer's data. The former, however, is difficult to determine experimentally with current instrumentation. For instance, a method based on two commercial instruments (a "sun and aureole measurement" system and a sun photometer) has been presented (Gueymard 2010; Wilbert et al. 2013). Other instruments that can measure circumsolar irradiance are documented in (Wilbert, Pitz-Paal, and Jaus 2012; Wilbert et al. 2018; Kalapatapu et al. 2012; Wilbert 2014).

To avoid additional measurements, substantial modeling effort is required and might involve estimation of the spectral distribution (Gueymard 2001). Some specific input data are rarely accessible in real time, particularly when a thin ice cloud (cirrus) reduces DNI but considerably increases the circumsolar contribution. Despite these difficulties and because of the special needs of the solar industry, new specialized radiative models have been developed recently to evaluate the difference between the true and apparent DNI using various types of observations (Eissa et al. 2018; Räisänen and Lindfors 2019; Sun et al. 2020; Xie et al. 2020). More research is being conducted to facilitate the determination of the circumsolar radiation at any location and any instant as part of solar resource assessments. Further information on circumsolar radiation can be found in Chapter 5, Section 5.10.

2.5.3 Diffuse Irradiance

The atmosphere absorbs and scatters some radiation out of the direct beam before it reaches the Earth's surface. Scattering occurs in essentially all directions, away from the specific path of the incident beam radiation. This scattered radiation constitutes the sky diffuse radiation in the hemisphere above the surface. In particular, the Rayleigh scattering theory explains why the sky appears blue (short wavelengths, in the blue and violet parts of the spectrum, are scattered more efficiently by atmospheric molecules) and why the sun's disk appears yellow-red at sunrise and sunset (blue wavelengths are mostly scattered out of the direct beam, whereas the longer red wavelengths undergo less scattering, resulting in a red shift). The broadband sky radiation in the hemisphere above the local surface is quantified as the DHI. A more technical and practical definition of DHI is that it represents all radiation from the sky dome except what is considered DNI; hence, in practice, DHI is the total irradiance from the whole-sky hemisphere minus the 2.5° annulus around the sun center.

DHI includes radiation scattered by molecules (Rayleigh effect), aerosols (Mie effect), and clouds (if present). It also includes the backscattered radiation that is first reflected by the surface and then re-reflected downward by the atmosphere or clouds. The impact of clouds is difficult to model because they have optical properties that can vary rapidly over time and can also vary considerably over the sky hemisphere. Whereas a single and homogenous cloud layer can be modeled with good accuracy, complex three-dimensional cloud scenes present more challenges (Hogan and Shonk 2013).

2.5.4 Global Irradiance

The total hemispherical solar irradiance on a horizontal surface, GHI, is the sum of DHI and the projected DNI to the horizontal surface, as expressed by Eq. 2-2. This fundamental equation is used for data quality assessments, some solar radiation measurement system designs, and atmospheric radiative transfer models addressing the needs for solar resource data. Because GHI is easier—and less expensive—to measure than DNI or DHI, most radiometric stations in the world provide only GHI data.

2.5.5 Front and Rearside Plane-of-Array Irradiance and Albedo

POA refers to the receiving surfaces of one or more planar solar collectors, all with the same orientation or on the same tracking device such that one POA description applies to all. POA irradiance is the fuel for monofacial PV and flat-plate thermal collectors, whereas the rear plane-of-array (RPOA) irradiance is only useful for bifacial PV collectors. In the PV literature, GTI is typically referred to as the POA irradiance, or even just POA.

Consider now the broadband irradiance components on a tilted plane. The orientation of this tilted plane is defined by the two spherical angles that describe the orientation of the surface's normal vector: azimuth (ψ) and zenithal angle (θ), also simply referred to as tilt. A horizontal plane has a tilt of 0°, whereas a vertical plane has a tilt of 90°. A plane has two faces defined by opposite normal vectors. In particular, the horizontal irradiance components defined above implicitly consider the normal toward the sky (up) with $\theta = 0°$. For a horizontal plane facing the ground, the upward global irradiance is referred to as reflected horizontal irradiance (RHI).

For a bifacial PV module with a tilt θ and azimuth ψ, the tilt of its backside is 180-θ with the same azimuth ψ. As mentioned above, the corresponding global irradiance incident on that backside is usually denoted as RPOA. Similar to POA, the RPOA irradiance is composed of the three same components: direct, diffuse, and reflected tilted irradiance (Figure 2-9). Obviously, the direct irradiance cannot be incident on the front and back sides at the same time.

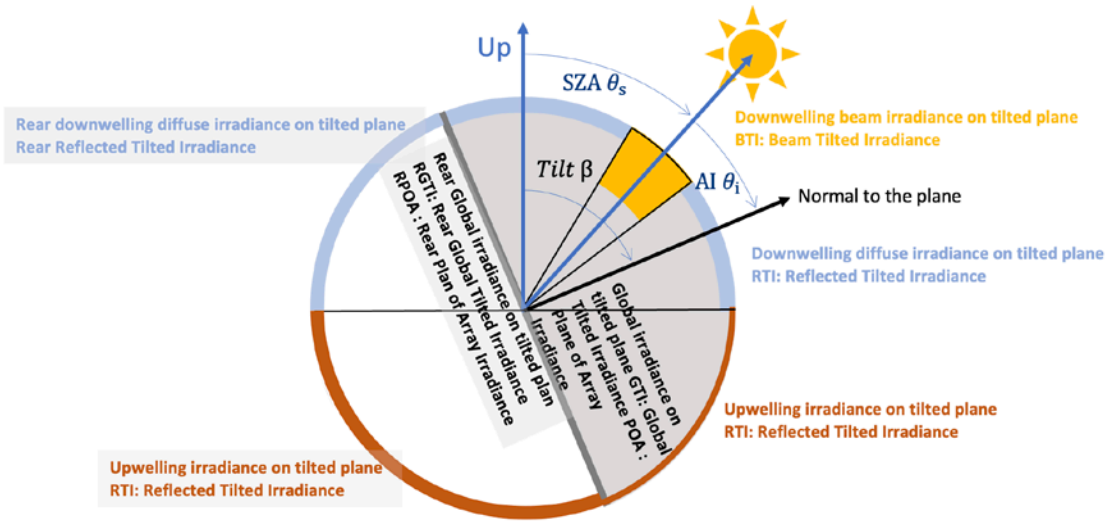

Figure 2-9. Solar radiation components (oriented hemispherical irradiances) incident on the front and back of a tilted plane

Image by Philippe Blanc, MINES Paris–PSL University

2.5.5.1 Albedo

The ratio of the total irradiance reflected to the total irradiance received by a surface is called the "bihemispherical reflectance," which is also customarily known as "albedo" (ρ). In contrast, the term "reflectance" is used when directionality is involved (e.g., to describe the effect of specular reflecting surfaces such as a concentrating mirror). More discussion on these definitions appears in (Gueymard et al. 2019). For solar energy applications, the albedo definition can be mathematically expressed as the RHI emanating from a surface normalized by the GHI that is incident onto it:

$$\rho = {}^{\mathrm{RHI}}/_{\mathrm{GHI}}. \tag{2-7}$$

This definition holds for either spectral or broadband fluxes. Only the latter case is discussed further here because of its predominant interest in solar applications, but further information on spectral albedo can be found in Chapter 3. The albedo's physical possible values range from 0–1 (sometimes expressed in percentage). In nature, most land areas not covered by ice or snow have an albedo in the approximate range from 0.15–0.45. Water bodies usually have a low albedo, typically near 0.05. At the other extreme, areas covered with fresh snow or clean ice have a very high albedo, which can exceed 0.85. Figure 2-10 shows the distribution of the mean values of albedo of the land areas in the world. According to this, 75% of the values are included in the range approximately between 0.14 and 0.39. High values around 0.8 correspond to the regions with fresh snow or clean ice. The median value is ≈0.2, which has traditionally been a standard constant value for albedo in solar applications.

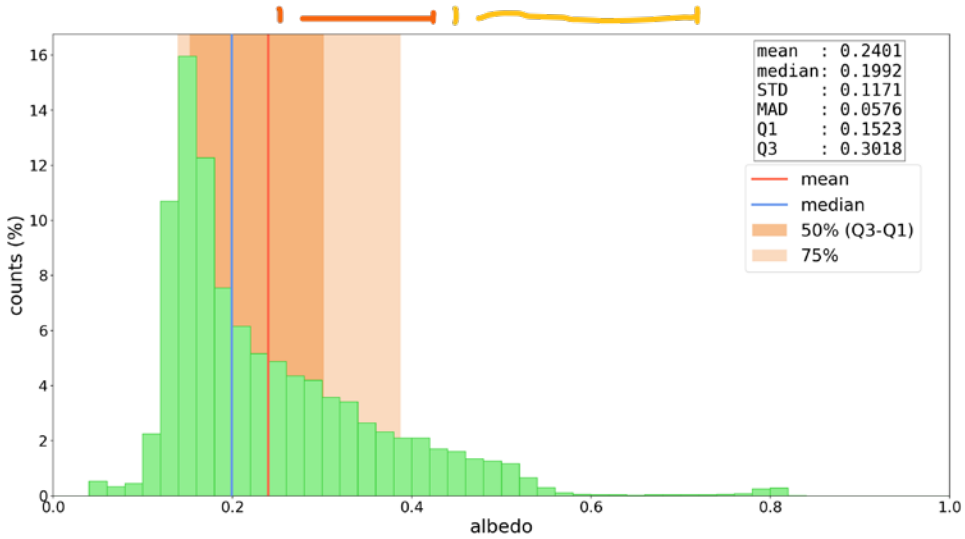

Figure 2-10. Distribution of annual mean values of albedo in land areas of the world (no oceans or large water bodies included) obtained from a combination of MODIS products and ERA5 reanalysis

The vertical red line shows the mean; the vertical blue line indicates the median. The interquartile range ("50% (Q3–Q1)") is shown in dark orange. The range showing 75% of the data is marked in light orange ("75%"). Some descriptive statistical values are also provided in the textbox: mean, median, standard deviation (STD), median absolute deviation (MAD), and the first and third quartile (Q1 and Q3).

One difficulty is that albedo is not merely a true constant surface property but rather a property of the coupled surface-atmosphere system. In particular, surface albedo is a function of the inherent surface characteristics, atmospheric state, and illuminating conditions (Wang et al. 2015). For that reason, in general albedo presents a high variability both in space (at scales from a few centimeters to hundreds of kilometers) and time (at scales from minutes to daily, seasonal, and even interannual) (e.g., dry regions with sparse vegetation or spots of snow cover—see, e.g., [Berg et al. 2020; Gueymard et al. 2019; 2021]).

Figure 2-11 shows an example of the temporal variability of the albedo of a specific site at different timescales. Under clear skies, the diurnal albedo evolution is a function of solar position because the reflection process is never purely isotropic (Lambertian) in the real world. Conversely, albedo tends to be constant under dense overcast conditions because the direct beam component is zero, and the incident illumination is nearly isotropic. Additionally, daily albedo time series vary on a daily, seasonal, and interannual basis.

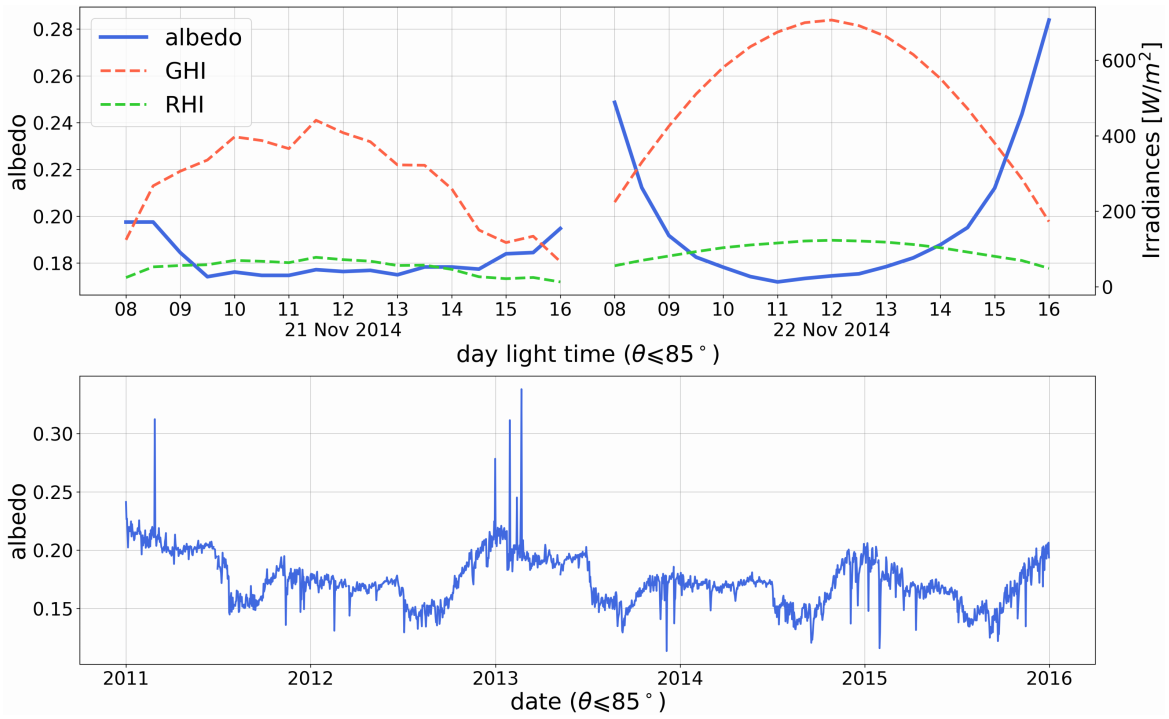

Figure 2-11. (Top) Example of diurnal variation of albedo (30-minute intervals) for (left) cloudy-sky conditions and (right) clear conditions, derived from the total incident and reflected horizontal irradiances, GHI and RHI, measured at the AmeriFlux radiometric station of Walnut Gulch Kendall Grasslands in Arizona, United States. (Bottom) Five years of daily mean albedo recorded at the same station, illustrating its seasonal and interannual variability.

The variations of the surface characteristics are typically related to the vegetation's phenological state, the surface's roughness and wetness, and the presence of snow or ice. Additionally, the albedo's spatiotemporal variability is impacted by both the atmospheric state and the ambient illumination conditions through the GHI's direct and diffuse components. In this respect, it is possible and convenient to define two theoretical illumination scenarios. The extreme situation in which there is only pure direct beam illumination—resulting in an ideally black sky dome—corresponds to the conceptual case of "directional-hemispherical reflectance," also known as *black-sky albedo* (BSA). The opposite theoretical situation is that under purely isotropic diffuse illumination, referred to as *white-sky albedo* (WSA). Overall, RHI can be expressed as a combination of these individual components as:

$$\mathrm{RHI} = \mathrm{BSA} \cdot \mathrm{BHI} + \mathrm{WSA} \cdot \mathrm{DHI} \tag{2-8}$$

where BHI and DHI denote the direct and diffuse horizontal irradiances, respectively. Assuming that the diffuse illumination is purely isotropic, the actual surface albedo—sometimes referred to as *blue-sky albedo*—can be interpolated as a weighted linear combination of its components (Lewis and Barnsley 1994; Lucht, Schaaf, and Strahler 2000; Román et al. 2010):

$$\rho = \mathrm{WSA} \cdot K + \mathrm{BSA} \cdot (1 - K) \tag{2-9}$$

where K is the diffuse fraction, DHI/GHI. Under overcast conditions, usually only the diffuse component is present ($K \approx 1$), hence $\rho \approx$ WSA. This approximation is convenient and typically used

in most solar energy applications because of practical constraints and lack of detailed data on BSA. Most often, WSA is considered a constant value over time, such as 0.2, but that might constitute an oversimplification.

Both BSA and WSA can be determined by respective spatial and angular integrations of the surface's BRDF. This is the conceptual foundation to determine the reflectance of the target surface according to the geometry of the source-surface-observer directions of radiation. It is a function of wavelength (λ) and of the structural and optical properties of the surface. The BRDF attempts to describe the behavior of the naturally anisotropic scattering of the solar radiation at the surface-air interface. Because of the complexity, diversity, and variability of BRDF distributions, mathematical models are used in practice to generate a parametric representation of it (Lucht, Schaaf, and Strahler 2000). In addition to the precise determination of the angular reflectance in any direction, the BRDF framework is used in a large range of applications related to satellite remote sensing.

In solar energy applications, determining surface albedo is fundamental for various reasons (Gueymard et al. 2019). First, radiative transfer models require albedo to account for the multiple reflections between the surface and the atmosphere (referred to as the backscattering effect) and to ultimately evaluate DHI and GHI (Ruiz-Arias and Gueymard 2018; Sun et al. 2020; Xie, Sengupta, and Dudhia 2016). Second, in the frequent case when the incoming solar irradiance is modeled based on satellite imagery, the surface albedo also constitutes a key independent variable to estimate the dynamic range of cloud reflectance (Perez, Cebecauer, and Šúri 2013). Third, most solar applications involve planar solar thermal collectors or PV modules that are tilted with respect to the horizontal, in which case the ground-reflected irradiance that is incident on the tilted plane must be determined. This is particularly important in increasingly popular bifacial PV technology, which directly exploits the reflected irradiance as the primary source of energy for each module's rear side. This makes bifacial PV modules markedly more sensitive to the albedo magnitude and variations than monofacial modules; hence, reliable information about the surface albedo has become important to determine the most suitable PV technology at any site, to obtain reliable simulations of the envisioned system's energy output, and to assess the economic feasibility of any solar power project. Difficulties exist because the calculation of the reflected irradiance on a tilted surface is generally performed following several simplifying assumptions that do not apply in practice (Gueymard et al. 2019; Kamphuis et al. 2020). A detailed discussion on these practical aspects is presented in Section 3.4.

There are three main sources of data on surface albedo: (1) ground measurements using albedometers (two pyranometers placed horizontally in opposite up and down directions, measuring GHI and RHI, respectively); (2) satellite estimates based on monitoring the reflected radiance emanating from the Earth's surface-atmosphere system; and (3) predictions based on a reanalysis model. All present distinct characteristics with advantages and limitations.

In-situ albedo measurements are described in Chapter 3, Section 3.3.2. Various albedo products from the other two sources have been proposed and cover various geographic areas and periods at diverse spatiotemporal resolutions. An exhaustive table of openly accessible sources is available in (Gueymard et al. 2019), along with their main characteristics. In addition, some specialized proprietary databases of surface albedo exist and are accessible through service providers. Modeled albedo databases are described in Chapter 5.

When using albedo databases to evaluate the specific albedo at a site during the design phase of a projected solar energy system, some critical questions arise: (1) Will the historical albedo at hand be conserved in the future, considering possible changes in the surface characteristics caused by the system's construction (e.g., vegetation removal)? (2) How is the albedo of the specific site under scrutiny related to the albedo of the area (e.g., grid cell) for which information is available from these databases? The first question must be answered on a case-by-case basis by the designer. To address the second question, an analysis of the spatial variability of the albedo over the area around the site must be conducted. Analyses show that this spatial variability can be high in many cases (Gueymard et al. 2021; Wang et al. 2015), which complicates the matter because the use of spatial interpolation or extrapolation over inhomogeneous areas could result in incorrect results.

2.5.5.2 Rear Plane-of-Array Irradiance

RPOA consists primarily of scattered light from multiple sources including the ground, sky, and neighboring PV rows (Figure 2-12). RPOA depends mostly on the surface albedo beneath the PV array, the height and tilt of the array, and the fraction of diffuse light in the sky hemisphere. Research has shown that RPOA on the back of a 37° fixed-tilt system above light sandy soil is 130–150 W/m^2 when the frontside is illuminated with the air mass 1.5 global (AM1.5G) reference spectrum (1000 W/m^2) (Monokroussos et al. 2020; Deline et al. 2017; IEC 61215-1 2021). Therefore, about 12% of the total irradiance received by a bifacial PV system (BPV) under reference conditions is RPOA, most of which is ground-reflected light.

It is possible, and at times cost-effective, to increase the albedo of the original surface over which a BPV system is being built using a high-reflectance product, such as a white membrane, to maximize RPOA. In contrast, floating BPV systems are somewhat at a disadvantage because of the low albedo of water (typically 0.05–0.07). Such systems would thus substantially benefit from the addition of appropriate reflectors (Ziar et al. 2021).

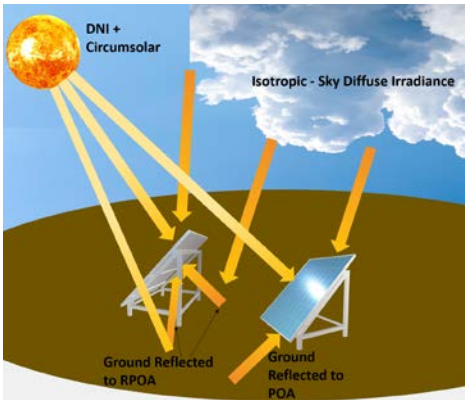

Figure 2-12. Contributions to illumination of the front and rear of BPV modules, including direct, sky diffuse, and ground-reflected radiation

Image by NREL

2.5.6 Terrestrial Solar Spectra

Many solar energy applications rely on collectors or systems that have a pronounced inhomogeneous spectral response. The performance of solar cells that constitute the building blocks of PV systems are affected by the spectral distribution of incident radiation. Each solar

cell technology has a specific spectral dependence (see Section 3.2.6). To allow for the comparison and rating of solar cells or modules, it is thus necessary to rely on reference spectral conditions. To this end, various international standardization bodies—ASTM, the International Electrotechnical Commission (IEC), and ISO—have promulgated standards that describe such reference terrestrial spectra. In turn, these spectra are mandated to test the performance of any solar cell using either indoor or outdoor testing methods. Currently, all terrestrial standard reference spectra are for an air mass of 1.5 (noted AM1.5). The reason for this, as well as historical perspectives on the evolution of these standards, are discussed by (Gueymard, Myers, and Emery 2002). The standard reference spectra of relevance to the solar energy community are the following:

- ASTM G173: for DNI and GTI on a 37°-tilted surface
- ASTM G197: for the direct, diffuse, and global components incident on surfaces tilted at 20° and 90°
- IEC 60904-3: similar to an older edition of ASTM G173, with only slightly different values, lower by 0.29%
- ISO 9845-1: replicating an older edition of ASTM G173, additionally proposing 171 subordinate spectra related to various atmospheric conditions (Jessen et al. 2018).

In addition, (CIE 241:2020 2020) proposes a number of recommended reference solar spectra for industrial applications at various air masses, and ASTM G177 defines a "high-UV" spectrum at an air mass of 1.05 for material degradation purposes.

It is emphasized that these reference spectra correspond to clear-sky situations and are difficult to realize experimentally (Gueymard 2019). Spectroradiometers are now available that measure the spectral irradiance at high temporal resolution (e.g., each minute) under all possible sky conditions. Moreover, there are models, such as the Fast All-sky Radiation Model for Solar applications with Narrowband Irradiances on Tilted surfaces (FARMS-NIT) (Xie and Sengupta 2018; Xie, Sengupta, and Wang 2019), that can provide modeled narrowband or spectral irradiance for fixed-tilt and single-axis tracking systems under all-sky conditions. The availability of measured and/or modeled spectral data is critical to testing solar energy systems under field conditions (see Chapters 3, 5, and 7).

References

Aler, R., I. Galván, J.A. Ruiz-Arias, and C.A. Gueymard. 2017. "Improving the Separation of Direct and Diffuse Solar Radiation Components Using Machine Learning by Gradient Boosting." *Solar Energy* 150: 558–69. https://doi.org/10.1016/j.solener.2017.05.018.

ASTM E490. 2022. "ASTM E490-22 Standard Solar Constant and Zero Air Mass Solar Spectral Irradiance Tables." ASTM International. https://doi.org/10.1520/E0490-00AR19.

Berg, L.K., C.N. Long, E.I. Kassianov, D. Chand, S-L Tai, Z. Yang, L.D. Riihimaki, et al. 2020. "Fine-Scale Variability of Observed and Simulated Surface Albedo Over the Southern Great Plains." *Journal of Geophysical Research: Atmospheres* 125 (7). https://doi.org/10.1029/2019JD030559.

Blanc, P., B. Espinar, N. Geuder, C.A. Gueymard, R. Meyer, R. Pitz-Paal, B. Reinhardt, et al. 2014. "Direct Normal Irradiance Related Definitions and Applications: The Circumsolar Issue." *Solar Energy* 110: 561–77. https://doi.org/10.1016/j.solener.2014.10.001.

Blanc, P., and L. Wald. 2012. "The SG2 Algorithm for a Fast and Accurate Computation of the Position of the Sun for Multi-Decadal Time Period." *Solar Energy* 86 (10): 3072–83. https://doi.org/10.1016/j.solener.2012.07.018.

Blanco, M.J., K. Milidonis, and A.M. Bonanos. 2020. "Updating the PSA Sun Position Algorithm." *Solar Energy* 212: 339–41. https://doi.org/10.1016/j.solener.2020.10.084.

Buie, D., A. G. Monger, and C. J. Dey. 2003. "Sunshape Distributions for Terrestrial Solar Simulations." *Solar Energy* 74 (2): 113–22. https://doi.org/10.1016/S0038-092X(03)00125-7.

CIE 241:2020. 2020. "Recommended Reference Solar Spectra for Industrial Applications." https://doi.org/10.25039/TR.241.2020.

Deline, C., S. MacAlpine, B. Marion, F. Toor, A. Asgharzadeh, and J.S. Stein. 2017. "Assessment of Bifacial Photovoltaic Module Power Rating Methodologies—Inside and Out." *IEEE Journal of Photovoltaics* 7 (2): 575–80. https://doi.org/10.1109/JPHOTOV.2017.2650565.

Dunlap, M.A., G. Cook, B. Marion, C. Riordan, and D. Renne. 1992. "Shining On: A Primer on Solar Radiation Data.", NREL/TP-463-4856; ON: DE92010555, https://doi.org/10.2172/5181287.

Eissa, Y., P. Blanc, H. Ghedira, A. Oumbe, and L. Wald. 2018. "A Fast and Simple Model to Estimate the Contribution of the Circumsolar Irradiance to Measured Broadband Beam Irradiance under Cloud-Free Conditions in Desert Environment." *Solar Energy* 163: 497–509. https://doi.org/10.1016/j.solener.2018.02.015.

Fröhlich, C., and J.L. Lean. 2004. "Solar Radiative Output and Its Variability: Evidence and Mechanisms." *The Astronomy and Astrophysics Review* 12: 273–320, https://doi.org/10.1007/s00159-004-0024-1.

Grena, R. 2008. “An Algorithm for the Computation of the Solar Position.” *Solar Energy* 82 (5): 462–70. https://doi.org/10.1016/j.solener.2007.10.001.

Gueymard, C.A. 2001. “Parameterized Transmittance Model for Direct Beam and Circumsolar Spectral Irradiance.” *Solar Energy* 71 (5): 325–46. https://doi.org/10.1016/S0038-092X(01)00054-8.

———. 2004. “The Sun’s Total and Spectral Irradiance for Solar Energy Applications and Solar Radiation Models.” *Solar Energy* 76 (4): 423–53. https://doi.org/10.1016/j.solener.2003.08.039.

———. 2006. “Reference Solar Spectra: Their Evolution, Standardization Issues, and Comparison to Recent Measurements.” *Advances in Space Research* 37 (2): 323–40. https://doi.org/10.1016/j.asr.2005.03.104.

———. 2010. “Spectral Circumsolar Radiation Contribution To CPV.” *AIP Conference Proceedings* 1277 (1): 316–19. https://doi.org/10.1063/1.3509220.

———. 2018a. “A Reevaluation of the Solar Constant Based on a 42-Year Total Solar Irradiance Time Series and a Reconciliation of Spaceborne Observations.” *Solar Energy* 168: 2–9. https://doi.org/10.1016/j.solener.2018.04.001.

———. 2018b. “Revised Composite Extraterrestrial Spectrum Based on Recent Solar Irradiance Observations.” *Solar Energy* 169: 434–40. https://doi.org/10.1016/j.solener.2018.04.067.

———. 2019. “The SMARTS Spectral Irradiance Model after 25 Years: New Developments and Validation of Reference Spectra.” *Solar Energy* 187: 233–53. https://doi.org/10.1016/j.solener.2019.05.048.

Gueymard, C.A., and M. Kocifaj. 2022. “Clear-Sky Spectral Radiance Modeling under Variable Aerosol Conditions.” *Renewable and Sustainable Energy Reviews* 168: 112901. https://doi.org/10.1016/j.rser.2022.112901.

Gueymard, C.A., V. Lara-Fanego, M. Sengupta, and A. Habte. 2021. “Surface Albedo Spatial Variability in North America: Gridded Data vs. Local Measurements.” *Solar Energy* 227: 655–73. https://doi.org/10.1016/j.solener.2021.05.012.

Gueymard, C.A., V. Lara-Fanego, M. Sengupta, and Y. Xie. 2019. “Surface Albedo and Reflectance: Review of Definitions, Angular and Spectral Effects, and Intercomparison of Major Data Sources in Support of Advanced Solar Irradiance Modeling over the Americas.” *Solar Energy* 182: 194–212. https://doi.org/10.1016/j.solener.2019.02.040.

Gueymard, C.A., D. Myers, and K. Emery. 2002. “Proposed Reference Irradiance Spectra for Solar Energy Systems Testing.” *Solar Energy* 73 (6): 443–67. https://doi.org/10.1016/S0038-092X(03)00005-7.

Gueymard, C.A., and J.A. Ruiz-Arias. 2014. “Performance of Separation Models to Predict Direct Irradiance at High Frequency: Validation over Arid Areas.” EuroSun 2014 Conf., Aix-les-Bains, France. https://doi.org/10.18086/eurosun.2014.08.06.

———. 2016. “Extensive Worldwide Validation and Climate Sensitivity Analysis of Direct Irradiance Predictions from 1-Min Global Irradiance.” *Solar Energy* 128: 1–30. https://doi.org/10.1016/j.solener.2015.10.010.

Hogan, R.J., and J.K.P. Shonk. 2013. “Incorporating the Effects of 3D Radiative Transfer in the Presence of Clouds into Two-Stream Multilayer Radiation Schemes.” *Journal of the Atmospheric Sciences* 70 (2): 708–24. https://doi.org/10.1175/JAS-D-12-041.1.

IEC 61215-1. 2021. “IEC 61215-1:2021 Terrestrial Photovoltaic (PV) Modules - Design Qualification and Type Approval - Part 1: Test Requirements.”

Iqbal, M. 2012. *An Introduction to Solar Radiation*. Elsevier.

ISO 9488. 2022. “ISO 9488:2022 Solar Energy — Vocabulary.” https://www.iso.org/obp/ui/en/#iso:std:iso:9488:ed-2:v1:en.

ISO 19115-1:2014. 2014. “Geographic Information — Metadata — Part 1: Fundamentals.” ISO. https://www.iso.org/standard/53798.html.

Jessen, W., S. Wilbert, C.A. Gueymard, J. Polo, Z. Bian, A. Driesse, A. Habte, A. Marzo, P. R. Armstrong, F. Vignola, L. Ramírez. 2018. “Proposal and Evaluation of Subordinate Standard Solar Irradiance Spectra for Applications in Solar Energy Systems.” *Solar Energy* 168: 30–43. https://doi.org/10.1016/j.solener.2018.03.043.

Kalapatapu, R., M. Chiesa, P. Armstrong, and S. Wilbert. 2012. “Measurement of DNI Angular Distribution with a Sunshape Profiling Irradiometer.” Proc. SolarPACES Conference, Marrakech, Morocco: 11–14.

Kamphuis, N.R., C.A. Gueymard, M.T. Holtzapple, A.T. Duggleby, and K. Annamalai. 2020. “Perspectives on the Origin, Derivation, Meaning, and Significance of the Isotropic Sky Model.” *Solar Energy* 201 (May): 8–12. https://doi.org/10.1016/j.solener.2020.02.067.

Kopp, G. 2016. “Magnitudes and Timescales of Total Solar Irradiance Variability.” *J. Space Weather Space Clim.* 6: A30. https://doi.org/10.1051/swsc/2016025.

Kopp, G., and J.L. Lean. 2011. “A New, Lower Value of Total Solar Irradiance: Evidence and Climate Significance.” *Geophysical Research Letters* 38 (1). https://doi.org/10.1029/2010GL045777.

Lewis, P., and M. J. Barnsley. 1994. “Influence of the Sky Radiance Distribution on Various Formulations of the Earth Surface Albedo.” International Symposium on Physical Measurements and Signatures in Remote Sensing, Int. Sco. for Photogramm. and Remote Sens., Val d'Isere, France.

Lucht, W., C.B. Schaaf, and A.H. Strahler. 2000. “An Algorithm for the Retrieval of Albedo from Space Using Semiempirical BRDF Models.” *IEEE Transactions on Geoscience and Remote Sensing* 38 (2): 977–98. https://doi.org/10.1109/36.841980.

Michalsky, J.J. 1988a. “Errata.” *Solar Energy* 41 (1): 113. https://doi.org/10.1016/0038-092X(88)90122-3.

———. 1988b. “The Astronomical Almanac’s Algorithm for Approximate Solar Position (1950–2050).” *Solar Energy* 40 (3): 227–35. https://doi.org/10.1016/0038-092X(88)90045-X.

Monokroussos, C., Q. Gao, X.Y. Zhang, E. Lee, Y. Wang, C. Zou, L. Rimmelspacher, J. Castro, M. Schweiger, and W. Herrmann. 2020. “Rear-Side Spectral Irradiance at 1 Sun and Application to Bifacial Module Power Rating.” *Progress in Photovoltaics: Research and Applications* 28: 755–766. https://doi.org/10.1002/pip.3268.

Myers, D.R. 2013. *Solar Radiation: Practical Modeling for Renewable Energy Applications*. CRC Press. https://doi.org/10.1201/b13898.

Perez, R., T. Cebecauer, and M. Šúri. 2013. *Semi-Empirical Satellite Models, Chapter 2 in: Solar Energy Forecasting and Resource Assessment, Edited by: Kleissl, J*. Elsevier, https://doi.org/10.1016/C2011-0-07022-9.

Räisänen, P., and A.V. Lindfors. 2019. “On the Computation of Apparent Direct Solar Radiation.” *Journal of the Atmospheric Sciences* 76 (9): 2761–80. https://doi.org/10.1175/JAS-D-19-0030.1.

Reda, I., and A. Andreas. 2004. “Solar Position Algorithm for Solar Radiation Applications.” *Solar Energy* 76 (5): 577–89. https://doi.org/10.1016/j.solener.2003.12.003.

———. 2007. “Corrigendum to ‘Solar Position Algorithm for Solar Radiation Applications’ [Solar Energy 76 (2004) 577–589].” *Solar Energy* 81 (6): 838. https://doi.org/10.1016/j.solener.2007.01.003.

Román, M.O., C.B. Schaaf, P. Lewis, F. Gao, G.P. Anderson, J.L. Privette, A.H. Strahler, C.E. Woodcock, and M. Barnsley. 2010. “Assessing the Coupling between Surface Albedo Derived from MODIS and the Fraction of Diffuse Skylight over Spatially-Characterized Landscapes.” *Remote Sensing of Environment* 114 (4): 738–60. https://doi.org/10.1016/j.rse.2009.11.014.

Ross, J. 1981. *The Radiation Regime and Architecture of Plants Stands*. Tasks for Vegetation Science. Junk Pub. https://books.google.com/books?id=NSJnNAEACAAJ.

Ruiz-Arias, J.A., and C.A. Gueymard. 2018. “Worldwide Inter-Comparison of Clear-Sky Solar Radiation Models: Consensus-Based Review of Direct and Global Irradiance Components Simulated at the Earth Surface.” *Solar Energy* 168: 10–29. https://doi.org/10.1016/j.solener.2018.02.008.

Ruiz-Arias, J.A., and C.A. Gueymard. 2024a. “GISPLIT: High-performance global solar irradiance component-separation model dynamically constrained by 1-min sky conditions.” *Solar Energy* 269: 112363. https://doi.org/10.1016/j.solener.2024.112363.

Ruiz-Arias, J.A., and C.A. Gueymard. 2024b. “Solar irradiance component separation benchmarking: The critical role of dynamically-constrained sky conditions.” *Renewable and Sustainable Energy Reviews* 202: 114678. https://doi.org/10.1016/j.rser.2024.114678.

Starke, A.R., L.F.L. Lemos, C.M. Barni, R.D. Machado, J.M. Cardemil, J. Boland, and S. Colle. 2021. “Assessing One-Minute Diffuse Fraction Models Based on Worldwide Climate Features.” *Renewable Energy* 177: 700–714. https://doi.org/10.1016/j.renene.2021.05.108.

Sun, Z., J. Li, G. Shi, J. Manners, and J. Li. 2020. “Fast Scheme for Determination of Direct Normal Irradiance. Part II: Parameterization of Circumsolar Radiation.” *Solar Energy* 199: 256–67. https://doi.org/10.1016/j.solener.2020.02.029.

Tan, Y., Q. Wang, and Z. Zhang. 2023. “Algorithms for Separating Diffuse and Beam Irradiance from Data over the East Asia-Pacific Region: A Multi-Temporal-Scale Evaluation Based on Minute-Level Ground Observations.” *Solar Energy* 252: 218–33. https://doi.org/10.1016/j.solener.2023.01.061.

Tan, Y., Q. Wang, and Z. Zhang. 2024. “Hybrid model improves the ability to separate the diffuse component of minute-scale global solar radiation.” *Modeling Earth Systems and Environment*. https://doi.org/10.1007/s40808-024-02098-w.

Wang, D., S. Liang, T. He, Y. Yu, C. Schaaf, and Z. Wang. 2015. “Estimating Daily Mean Land Surface Albedo from MODIS Data: Estimating Daily Mean Albedo from MODIS.” *Journal of Geophysical Research: Atmospheres* 120 (10): 4825–41. https://doi.org/10.1002/2015JD023178.

Wilbert, S., B. Reinhardt, J. DeVore, M. Röger, R. Pitz-Paal, Christian A. Gueymard, and R. Buras. 2013. “Measurement of Solar Radiance Profiles With the Sun and Aureole Measurement System.” *Journal of Solar Energy Engineering* 135 (4). https://doi.org/10.1115/1.4024244.

Wilbert, S. 2014. “Determination of Circumsolar Radiation and Its Effect on Concentrating Solar Power.” Ph.D. Thesis, Rheinisch-Westfälischen Technischen Hochschule Aachen. http://publications.rwth-aachen.de/record/444996/files/5171.pdf.

Wilbert, S., R. Pitz-Paal, and J. Jaus. 2012. “Circumsolar Radiation and Beam Irradiance Measurements for Focusing Collectors.” COST ES1002 WIRE Workshop on Remote Sensing Measurements for Renewable Energy, DTU Risoe, Denmark. https://elib.dlr.de/78602/1/ES1002_CircumSolarSWilbert_final.pdf.

Wilbert, S., M. Röger, J. Csambor, M. Breitbach, F. Klinger, B. Nouri, N. Hanrieder, et al. 2018. “Sunshape Measurements with Conventional Rotating Shadowband Irradiometers.” *AIP Conference Proceedings* 2033 (1): 190016. https://doi.org/10.1063/1.5067201.

WMO (World Meteorological Organization). 2018. “Guide to Instruments and Methods of Observation.” *World Meteorological Organization WMO*. https://library.wmo.int/.

Xie, Y., and M. Sengupta. 2018. “A Fast All-Sky Radiation Model for Solar Applications with Narrowband Irradiances on Tilted Surfaces (FARMS-NIT): Part I. The Clear-Sky Model.” *Solar Energy* 174: 691–702. https://doi.org/10.1016/j.solener.2018.09.056.

Xie, Y., M. Sengupta, and J. Dudhia. 2016. "A Fast All-Sky Radiation Model for Solar Applications (FARMS): Algorithm and Performance Evaluation." *Solar Energy* 135: 435–45. https://doi.org/10.1016/j.solener.2016.06.003.

Xie, Y., M. Sengupta, Y. Liu, H. Long, Q. Min, W. Liu, and A. Habte. 2020. "A Physics-Based DNI Model Assessing All-Sky Circumsolar Radiation." *iScience* 23 (3): 100893. https://doi.org/10.1016/j.isci.2020.100893.

Xie, Y., M. Sengupta, and C. Wang. 2019. "A Fast All-Sky Radiation Model for Solar Applications with Narrowband Irradiances on Tilted Surfaces (FARMS-NIT): Part II. The Cloudy-Sky Model." *Solar Energy* 188: 799–812. https://doi.org/10.1016/j.solener.2019.06.058.

Yang, D. 2022. "Estimating 1-Min Beam and Diffuse Irradiance from the Global Irradiance: A Review and an Extensive Worldwide Comparison of Latest Separation Models at 126 Stations." *Renewable and Sustainable Energy Reviews* 159: 112195. https://doi.org/10.1016/j.rser.2022.112195.

Yang, D., Y. Gu, M.J. Mayer, C.A. Gueymard, W. Wang, J. Kleissl, M. Li, Y. Chu, and J.M. Bright. 2024. "Regime-Dependent 1-Min Irradiance Separation Model with Climatology Clustering." *Renewable and Sustainable Energy Reviews* 189: 113992. https://doi.org/10.1016/j.rser.2023.113992.

Ziar, H., B. Prudon, F-Y Lin, B. Roeffen, D. Heijkoop, T. Stark, S. Teurlincx, et al. 2021. "Innovative Floating Bifacial Photovoltaic Solutions for Inland Water Areas." *Progress in Photovoltaics: Research and Applications* 29 (7): 725–43. https://doi.org/10.1002/pip.3367.

3 Measuring Solar Radiation

Stefan Wilbert,[1] Thomas Stoffel,[2] Daryl Myers,[3] Stephen Wilcox,[2] Aron Habte,[4] Frank Vignola,[5,†] Anton Driesse,[6] Vicente Lara-Fanego,[7] Christian Gueymard,[8] Nicholas Riedel-Lyngskær,[9] Josh Peterson,[5] Robert Höller,[10] Birk Kraas,[11] Anne Forstinger[11]

[1] *German Aerospace Center (DLR), Germany*
[2] *Solar Resource Solutions, LLC, USA*
[3] *National Renewable Energy Laboratory, USA, retired*
[4] *National Renewable Energy Laboratory, USA*
[5] *University of Oregon, USA*
[6] *PV Performance Labs, Germany*
[7] *SolarGIS, Slovakia*
[8] *Solar Consulting Services, USA*
[9] *Technical University of Denmark (DTU), Denmark*
[10] *University of Applied Sciences Upper Austria, Austria*
[11] *CSP Services GmbH, Germany*
† Deceased

Executive Summary

Accurate measurements of the incoming irradiance are essential for solar power plant project design, implementation, and operations. Large and medium solar energy systems require ground-measured irradiance data for:

- Site resource analysis, yield assessment, financing
- System design
- Plant operation and performance control.

Ground-based irradiance measurements are also essential for developing, testing, and enhancing models to estimate and forecast solar radiation resources. This includes performing a site adaptation of long-term resource datasets and applying recent measurements for the creation of a forecast. Solar irradiance measurements are only available at a limited number of stations, so a specific measurement campaign must typically be performed at (or around) the location of each specific new project. Depending on the solar technology that will be used in the project, different radiometers are of interest. Pyranometers are used to measure global horizontal irradiance (GHI), global tilted irradiance (GTI) (also referred to as plane-of-array [POA] irradiance when measured on a photovoltaic [PV] array), diffuse horizontal irradiance (DHI), rear plane of array (RPOA), or reflected horizontal irradiance (RHI). Pyranometers can measure the resource used by PV and flat-plate solar systems. RPOA, DHI, and RHI are particularly relevant for bifacial PV (BPV). As an alternative or in addition to measuring RPOA with a pyranometer directly, this RPOA can also be estimated based on RHI, GHI, and DHI. In this approach, RHI is divided by GHI to calculate the local surface albedo that is then used to derive the ground-reflected contribution to RPOA. DHI is utilized along with so-called view factors to obtain the diffuse radiation's contribution to RPOA. In the case of PV systems, PV reference cells are also of interest, as they might replace GTI and RPOA pyranometers for monitoring applications. To measure DHI, a sun-shading device such as a tracked shading ball for the pyranometer is often used, which complicates the measurements compared to the other above-mentioned radiation components, because a solar tracker is needed. For systems based on concentrating collectors, direct normal irradiance (DNI) measurements are required. DNI is also of interest for large and tracked PV installations. Such measurements can be collected with pyrheliometers that are mounted on solar

trackers. The protective windows of these instruments are prone to soiling, and their signal is affected more by soiling than that of pyranometers. Thus, pyrheliometers require more frequent maintenance. To avoid expensive maintenance-intensive and failure-prone solar trackers for DNI and/or DHI measurements, alternative instruments are available. Such instruments are comparably cheaper and require less maintenance, but cannot reach the same high accuracy as well-maintained tracker systems equipped with a pyrheliometer and two pyranometers of the highest accuracy class, even if their operations and maintenance (O&M) is optimum.

To generate reliable irradiance measurement data, it is important not only to select the most appropriate sensors, but also to ensure their correct installation, operation, and maintenance. The station's design must avoid unwanted effects caused by shading or other influences from, for example, traffic, industrial activity, insects, animals, strong winds, or vandalism. The frequent periodic inspection of the station by trained personnel, including required corrections and cleaning of the sensors, is typically a simple task, but essential for measurement accuracy. In operating solar power plants, conflicts of interest resulting from the expected difficulty for a single contractor to reconcile two different objectives (high solar plant efficiency and high irradiance data quality) should be avoided. This is because, for instance, measurement errors caused by soiled radiometers or wrong radiometer installation can lead to an overestimation of solar system efficiency. The calibration of radiometers also contributes significantly to overall uncertainty and must be repeated periodically according to the instrument specifications and international standards. The provided recommendations are based on the relevant international standards and are complemented by exemplary station plans and checklists for the various steps needed for accurate solar irradiance measurements.

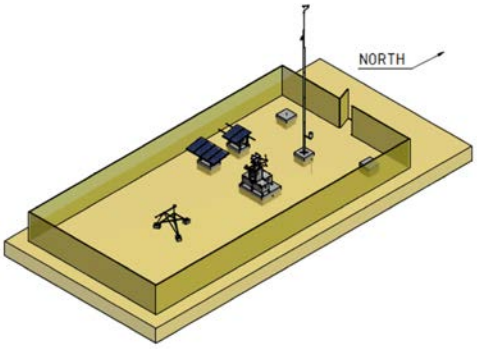

Figure ES-3-1. Exemplary plan for a high-accuracy radiometric station with a solar tracker, albedo measurement, wind mast, PV soiling measurements, and a PV power supply positioned for minimal shading effects.

Image from CSP Services

3.1 Introduction

Solar power plant project design, implementation, and operations require accurate measurements of the incoming irradiance. Because accurate solar irradiance measurements are relatively time-consuming and expensive compared to other meteorological variables like temperature, they are publicly available for only a limited number of permanent or semipermanent stations. This is true especially for direct normal irradiance (DNI) or diffuse horizontal irradiance (DHI). Large and medium solar energy projects thus typically require the installation of an on-site station to collect ground-measured irradiance data for:

- Site resource analysis and site adaptation of long-term resource datasets for yield assessment and financing
- System design
- Plant operation and performance control.

More generally, ground-based irradiance measurements at various sites are also essential for:

- Developing and testing models that use remote satellite-sensing techniques or available surface meteorological observations to estimate the solar resource
- Developing solar resource forecasting techniques and enhancing their quality by applying recent measurements to generate the forecasts
- Other disciplines not directly related to renewable energy, such as climate studies or accelerated weathering tests.

This chapter discusses the available radiometers and their calibrations and provides recommendations on the required measurands and instruments for different applications, their installation, station design, and operations and maintenance (O&M). Further, detailed exemplary station plans and checklists are provided for the various tasks that are connected to radiation measurement campaigns.

3.2 Radiometer Types

Instruments designed to sense any form of radiation are called radiometers. The earliest developments of instrumentation for measuring solar radiation were designed to meet the needs of agriculture (in terms of bright sunshine duration to understand evaporation) and to determine the sun's output or "solar constant." During the 19th and 20th centuries, the most widely deployed instrument for indirectly estimating solar radiation was the Campbell-Stokes sunshine recorder (Iqbal 2012; Vignola, Michalsky, and Stoffel 2020). This analog device focuses the direct beam with a simple spherical lens (glass ball) to create burn marks during clear periods (when DNI exceeds ≈120 W/m^2) on a sensitized paper strip placed daily in the sphere's curved focus plane. By comparing the total burn length to the corresponding day length, records of the percentage of possible sunshine from stations around the world became the basis for characterizing the global distribution of solar radiation (Löf, Duffie, and Smith 1966). The earliest pyrheliometers (from the Greek words for fire, sun, and measure) were based on calorimetry and used by scientists to measure brief periods of DNI from various experimental sites, generally at high elevation to minimize the effects of a thick atmosphere on the transmission of radiation from the sun (e.g., in an attempt to derive the solar constant). By the early 20th century, scientists had developed pyranometers (from the Greek words for fire, sky,

and measure) to measure global horizontal irradiance (GHI) and better understand the Earth's energy budget (Vignola, Michalsky, and Stoffel 2020).

This section summarizes the types of commercially available radiometers most commonly used to measure solar radiation in the context of solar energy technology applications. Solar resource assessments are traditionally based on broadband measurements (i.e., encompassing the whole shortwave spectrum [0.29–4 μm]). Spectrally selective measurements made using spectroradiometers (described in Chapter 5, Section 5.7) are needed to evaluate the spectral distribution of this irradiance and ultimately investigate the performance of photovoltaic (PV) cells that have a significant spectral dependence.

3.2.1 Pyrheliometers and Pyranometers

Pyrheliometers and pyranometers are two types of radiometers used to measure solar irradiance. Their ability to receive solar radiation from two distinct portions of the sky distinguishes their designs. As described in Chapter 2, pyrheliometers are used to measure DNI, and pyranometers are used to measure GHI, DHI, global tilted irradiance (GTI or plane of array [POA]), or the in-plane rear-side irradiance (RPOA). Another important measurement involving pyranometers is that of reflected horizontal irradiance (RHI), which is necessary to estimate the surface albedo per Eq. 2-3 (Table 3-1). Figure 3-1 summarizes some key attributes of these two types of radiometers.

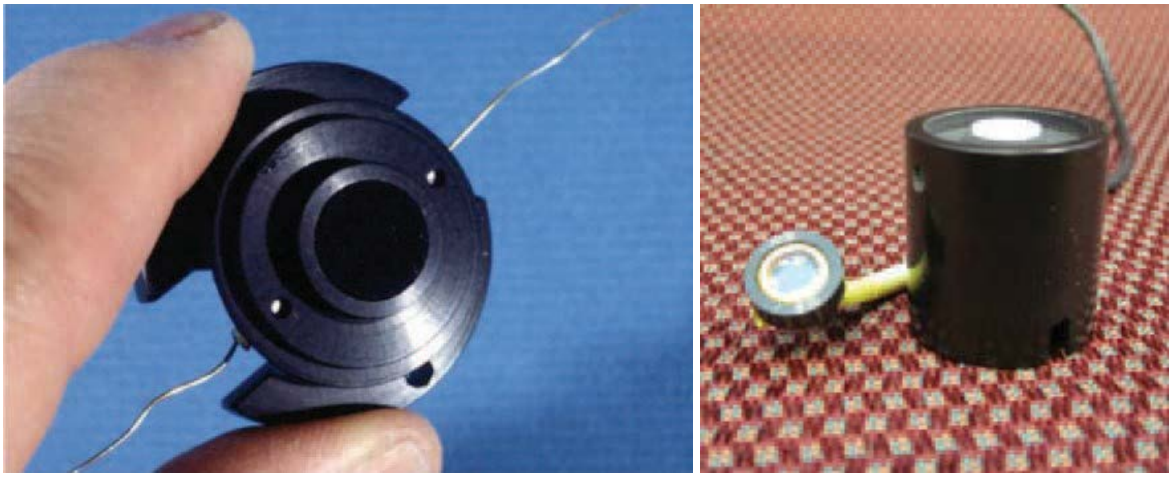

Figure 3-1. (Left) Thermopile assembly used in an Eppley Laboratory Inc. model PSP and (right) a typical photodiode detector.

Photos used with permission from LI-COR Inc.

Table 3-1. Overview of Solar Radiometer Types and Their Applications

Radiometer Type	Measurement	Field of View (Full Angle)	Installation
Pyrheliometer	DNI	5–6°	Mounted on a two-axis solar tracker for alignment with the solar disk
Pyranometer	GHI	2π steradians	Mounted on a stable horizontal surface free from local obstructions[a]
Pyranometer	DHI	2π steradians	Mounted on a two-axis solar tracker fitted with a shading attachment or on a manually adjusted shadowband platform to block DNI from the detector's surface[a]
Pyranometer	GTI (POA)	2π steradians	Mounted in the plane of the PV module array or flat-plate solar collector (fixed or tracked along one or two axes)[a]
Pyranometer	RPOA	2π steradians	Mounted in the plane of the rear side of the PV module array oriented toward the ground (fixed or tracked along one or two axes)[a]
Pyranometers	Albedo	2π steradians (for each pyranometer)	Two pyranometers mounted horizontally measuring the downward and upward irradiance (Section 3.3.2)[a]

[a] Optionally, thermopile pyranometers are installed with a powered ventilator and heating system to reduce contamination of optical surfaces and thermal errors. The base (heatsink) of most thermopile pyranometers must be shielded from direct sunlight.

Pyrheliometers and pyranometers commonly use either a thermoelectric or photoelectric passive sensor to convert the sensed solar irradiance (W/m^2) into a proportional electrical signal (microvolts [μV] DC). Thermoelectric sensors have an optically black coating that allows for a broad and uniform spectral response to all solar radiation wavelengths (Figure 3-1, left), covered by a window (flat for pyrheliometers and domed for pyranometers) having a flat transmittance from approximately 300–3,000 nm or wider. The most common thermoelectric sensor used in radiometers is the thermopile. There are all-black thermopile sensors used in pyrheliometers and pyranometers, as well as black-and-white thermopile sensors used exclusively in pyranometers. In all-black thermopile sensors, the surface exposed to solar radiation is completely covered by the absorbing black coating. The absorbed radiation creates a temperature difference between the black side of the thermopile (i.e., "hot junction") and the other side (i.e., "reference" or "cold junction"). Often the "cold junction" is attached to a large thermal mass that serves as a heatsink. The base of the pyranometer often serves as the heatsink. The temperature difference causes a voltage signal. One drawback of this design is that the hot junction radiates to the sky, thus creating radiative imbalance, referred to as "thermal offset." Consequently, the signal of all-black thermopile pyranometers is somewhat too low during the day and negative at night, particularly under cloudless conditions because the sky is then colder than if covered by clouds. The magnitude of this underestimation depends on the meteorological conditions, the measured radiation component, and the instrument's design and specifications, and is about 0–20 W/m^2 for unventilated and about half of that for ventilated pyranometers (Sanchez, Cancillo, and Serrano 2016; Sanchez, Serrano, and Cancillo 2017). Some recent instruments rely on innovative features that almost completely eliminate their offset.

In black-and-white thermopiles, the surface exposed to radiation is partly black and partly white. In this case, the temperature difference between the black and the white surfaces creates the voltage signal. This design has the advantage of eliminating the thermal offset issue. Despite having a relatively small thermal mass, the 95% response times of thermopile radiometers are not negligible for some applications, with the output signal typically lagging the changes in solar flux by 1–30 seconds.[7] Some instruments include a signal postprocessing that tries to compensate for this time lag. Most instruments of this type include electronic circuitry to introduce a temperature compensation to the signal, thus reducing the need for any ulterior temperature correction. Recently, new smaller thermopile sensors with response times as low as 0.2 seconds have been made commercially available as well. A detailed analysis of radiometer response times is found in Driesse (2018).

In contrast to thermopiles, common photoelectric sensors generally respond to only the visible and near-infrared spectral regions from approximately 350–1100 nm (Figure 3-1, right; Figure 3-2). Pyranometers with photoelectric sensors are sometimes called silicon (Si) pyranometers or photodiode pyranometers. Their non-flat spectral sensitivity and their limited spectral range lead to significant spectral errors, as the solar spectrum varies in a way that cannot be fully captured by photoelectric sensors even with elaborate postprocessing and complex calibrations. On the other hand, these sensors have very fast time-response characteristics on the order of microseconds.

For both thermopile and photelectric detectors used in commercially available instruments, the electrical signal generated by exposure to solar irradiance magnitudes of approximately 1000 W/m^2 is ≈10 mV DC (assuming no amplification of the output signal and an appropriate shunt resistor for photodiode sensors). This rather low-level signal requires proper electrical grounding and shielding considerations during installation, as well as a highly accurate voltage measurement (Section 3.5.4).

Most manufacturers now also offer pyrheliometers and pyranometers with built-in amplifiers and/or digital outputs. Such digital instruments have several advantages and are described in Section 3.4.3.

[7] The given response time represents the time it takes the instrument to reach 95% of the final value. Typically, a steplike change of the incoming irradiance is used to determine the response time.

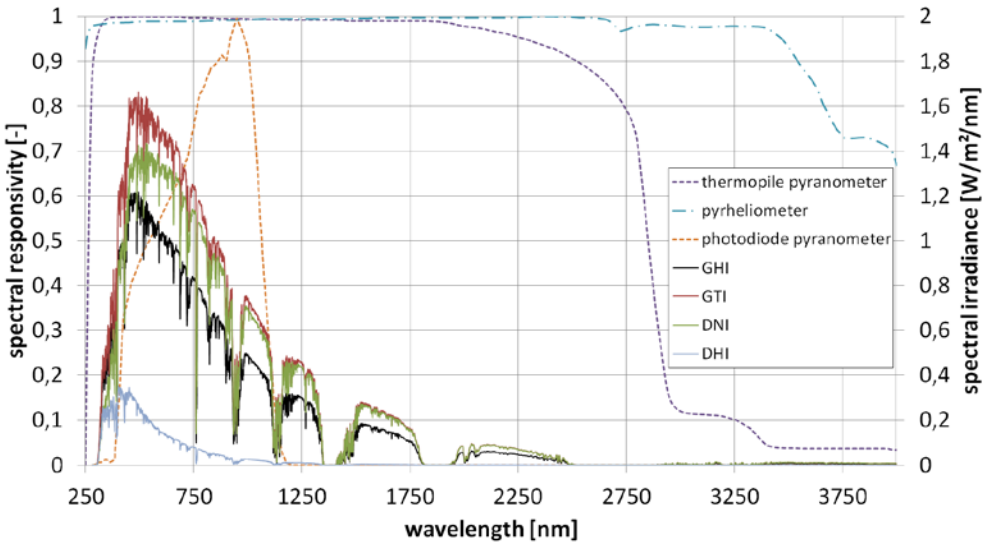

Figure 3-2. Spectral response of Kipp & Zonen CM21 thermopile pyranometer, CHP1 pyrheliometer, and LI-COR pyranometer LI200SA plotted next to the GHI, GTI, DNI, and DHI spectra for ASTM G-173 conditions at AM1.5.

Image by the German Aerospace Center (DLR)

3.2.1.1 Pyrheliometers

Pyrheliometers are typically mounted on automatic two-axis solar trackers to maintain the instrument's alignment with the solar disk and to fully illuminate the detector from sunrise to sunset (Figure 3-3 and Figure 3-4). Alignment of the pyrheliometer with the solar disk is determined by a simple diopter—a sighting device in which a small spot of light (the solar image) falls on a mark in the center of a target located near the rear of the instrument, serving as a proxy for alignment of the solar beam to the detector. A small tracking error is acceptable as long as the solar image is at least tangent to the diopter target. Modern sun trackers use software to compute and precisely track the sun position. These calculations require that the sun tracker is assembled and positioned correctly (horizontally leveled, with correct azimuth and elevation orientation). Therefore, tracking errors occur if the tracker is not installed and positioned correctly (e.g., imperfect leveling). A solid, stable mounting platform is required so that wind and vibration, nearby personnel or traffic, as well as thermal expansions due to temperature variations, do not induce any significant tracking errors. Sun sensors can help reduce the remaining tracking errors during periods with direct irradiance. The sun sensor tracks the sun and typically uses a four-quadrant sensor placed behind a pinhole or a lens to detect the tracking error. The tracking error is then sent to the tracker software so that it can be corrected. Because of all these requirements and their associated costs, solar trackers are only used at high-quality or research-class stations.

By convention, and to allow for small variations in tracker alignment, view-limiting apertures inside the pyrheliometer's collimating tube allow for the detection of radiation in a narrow annulus of sky around the sun (WMO 2018), called the circumsolar region. This circumsolar radiation component is the result of forward scattering of radiation near the solar disk, itself caused by cloud particles, atmospheric aerosols, and other constituents that can scatter solar radiation. All modern pyrheliometers should have a 5° field of view (FOV), following the World Meteorological Organization (WMO) (WMO 2018) recommendations. (An FOV-related design

characteristic of pyrheliometers is their penumbra function; see Chapter 2, Section 2.5.2 and references therein.) The FOV of older instruments could be larger, however, such as 5.7°–10° full angle. Depending on the FOV and tracker alignment, pyrheliometric measurements include varying amounts of circumsolar irradiance contributions to DNI. Although this is usually a very small contribution to the measurement, it can affect the measurement under atmospheric conditions of intensified scattering. To determine the amount of circumsolar irradiance and its spatial distribution over the FOV, a few methods are available (see Chapter 2, Section 2.5.2 and Chapter 5, Section 5.10).

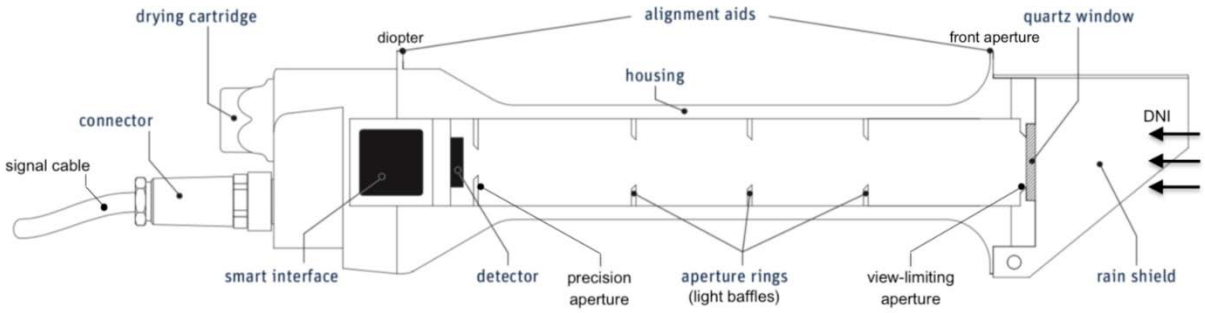

Figure 3-3. Schematic of a Kipp & Zonen B.V., model SHP1—a "smart" pyrheliometer.

Image modified from Kipp and Zonen (2017)

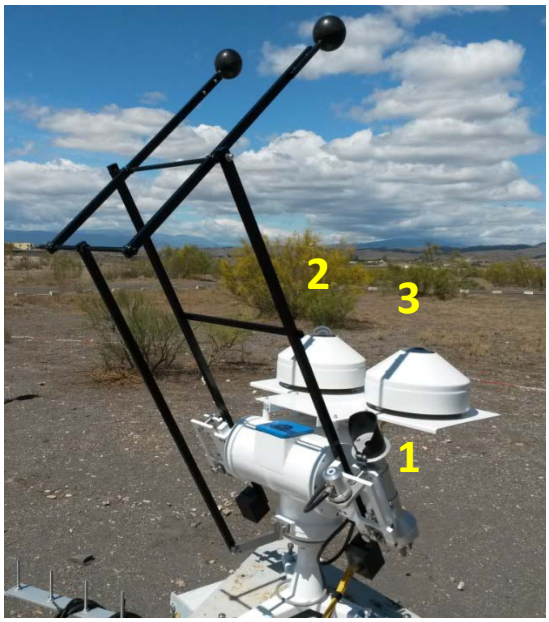

Figure 3-4. A pyrheliometer (1), a shaded pyranometer (2), and a shaded pyrgeometer (3) (see Section 3.2.4) mounted on an automatic solar tracker.

Photo from DLR

The most accurate measurements of DNI under stable conditions are accomplished using an electrically self-calibrating absolute cavity radiometer (ACR). This advanced type of radiometer is the basis for the World Radiometric Reference (WRR), the internationally recognized detector-based measurement standard for DNI (Fröhlich 1991). The WMO World Standard

Group of ACRs is shown in Figure 3-5. By design, ACRs have no windows and are therefore generally limited to fully attended operation during dry conditions to protect the integrity of the receiver cavity (Figure 3-6). Removable windows and temperature-controlled all-weather designs are available for automated continuous operation of these radiometers; however, the installation of a protective window nullifies the "absolute" nature of the DNI measurement. The window introduces additional measurement uncertainties associated with the optical transmittance properties of the window (made from either quartz or calcium fluoride) and the changes to the internal heat exchange resulting from the sealed system. Moreover, ACRs need some periods of self-calibration during which no exploitable measurement is possible. This creates discontinuities in the high-accuracy DNI time series that could be measured with windowed ACRs, unless a regular pyrheliometer is also present to provide the necessary redundancy (Gueymard and Ruiz-Arias 2015). Combined with their very high cost of ownership and operation, this explains why ACRs are normally not used to measure DNI in the field.

A unique 10-month comparison of outdoor measurements from 33 pyrheliometers, including ACRs, under a wide range of weather conditions in Golden, Colorado, indicated that the estimated measurement uncertainties at a 95% confidence interval ranged from ±0.5% for windowed ACRs to +1.4%/–1.2% for commercially available instruments (Michalsky et al. 2011). Interestingly, the results also suggested that the measurement performance during the comparison was better than indicated by the manufacturers' specifications. These results, however, were obtained under laboratory conditions—as opposed to field conditions—and thus the instruments were remarkably well attended in terms of calibration, daily cleaning, and maintenance. Soiling of the protective window can degrade the accuracy of pyrheliometers. Some recent designs include a window heater to limit the effect of dew, raindrops, and soiling, but frequent cleaning is desirable anyway.

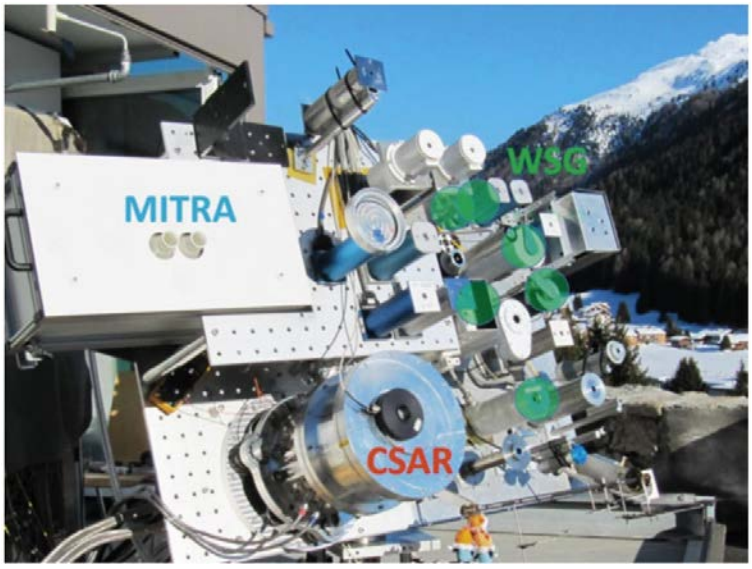

Figure 3-5. The World Standard Group of ACRs (marked in green) used to define the WRR or DNI measurement standard.

Photo from the Physical Meteorological Observatory in Davos/World Radiation Center

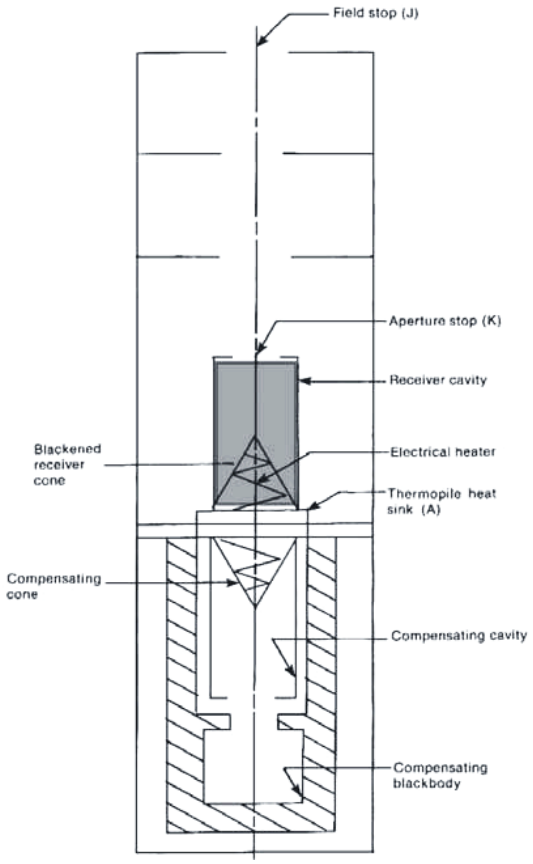

Figure 3-6. Schematic of the Eppley Laboratory Inc. automatic Hickey-Frieden model of an ACR.

Image modified from Reda (1996)

3.2.1.2 Pyranometers

A pyranometer has a thermoelectric or photoelectric detector with a hemispherical FOV (180° or 2π steradians) (Figure 3-4 and Figure 3-7). This type of radiometer is mounted horizontally to measure GHI. In this horizontal mount, the pyranometer has a complete view of the sky dome. Ideally, the mounting location for this instrument is free of natural or artificial obstructions on the horizon. Alternatively, the pyranometer can be mounted at a tilt to measure GTI (or POA), as in the case of latitude-tilt or one-axis tracking systems, or vertically for building applications. In an upside-down position, it senses RHI. The local albedo is simply obtained by dividing the latter by GHI, as further discussed in Sections 2.5.5.1 and 3.3.2.

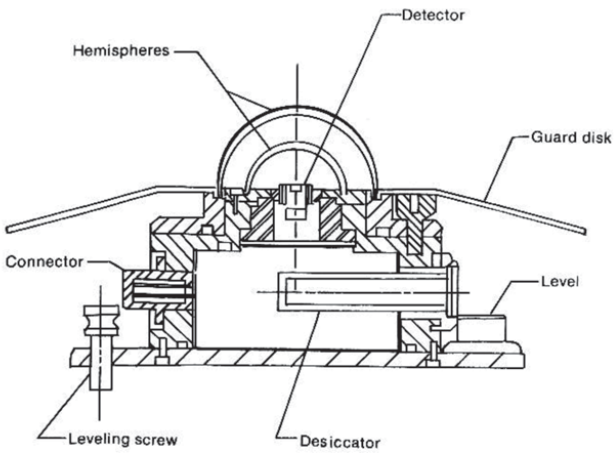

Figure 3-7. Schematic of the Eppley Laboratory Inc. PSP.

Image by the National Renewable Energy Laboratory (NREL)

Thermoelectric pyranometer detectors are mounted under one or two protective dome(s) (usually made of optical glass or precision quartz in some high-end models) and/or a diffuser. Both designs protect the detector from the weather and provide optical properties consistent with receiving hemispheric solar radiation. Pyranometers can be fitted with ventilators that constantly blow air—sometimes heated—from under the instrument and over the dome (Figure 3-8). The ventilation and heating reduces the potential for contaminating the pyranometer optics caused by dust, dew, frost, snow, ice, insects, or other materials. Ventilation also beneficially mitigates the thermal offset characteristics of pyranometers with single all-black detectors (Vignola, Long, and Reda 2009). The ventilation devices require a significant amount of electrical power (5 to 20 W), particularly when heated, adding to the required capacity for on-site power generation in remote areas and to the periodic maintenance such as cleaning of the intake air filter or replacement of the fan. Both DC and AC ventilators exist, but DC ventilators are preferable (Michalsky, Kutchenreiter, and Long 2017). Further, external heating can cause errors in thermopile-based measurements so that it should be restricted to conditions requiring heating and to low or no irradiance periods (dusk to dawn), if possible, if the heating is not combined with ventilation. Some pyranometer models are equipped with recirculating ventilation between the two glass domes. The air might also be heated to suppress dew and frost formation, and that heating can be done throughout the day with little to no impact on measurement accuracy. This approach reduces the power consumption significantly relative to an external heating and ventilation device because of the lower heat loss achieved by recirculating the air. Whereas this maintains most of the beneficial ventilation/heating effects, dust settling or insects/birds perching on the glass dome is not reduced.

Photoelectric pyranometers generate a signal from a photodiode as short-circuit current. The fast response of such photodiode pyranometers makes them important for applications where fast and intense transients are involved, such as the measurement of cloud enhancement or ramping events. Photodiode pyranometers employ a diffuser above the detector (Figure 3-9) to achieve an approximate hemispherical response while omitting the glass dome to reduce cost. The application of a diffuser rather than a transparent glass dome makes the instrument measurably more dust-tolerant (Maxwell et al. 1999). Whereas thermoelectric pyranometers tend to be spectrally flat, photoelectric sensors are spectrally selective because of their photodiode detector.

The long-term stability of photodiode pyranometers can vary differently from thermopile-based pyranometers, as shown in Figure 3-10 and as further analyzed in Geuder et al. (2014). Evaluation of this stability is obviously contingent on the calibration procedure remaining constant over long periods. Not all institutions use the same procedure, so slight discontinuities can occur if the instrument is not always calibrated at the same institution. These instrument-specific behaviors dictate the need for regular calibrations as recommended by the manufacturers.

Figure 3-8. Kipp & Zonen model CM22 pyranometers installed in ventilated CV2 enclosures.

Photo by NREL

Figure 3-9. Selected photodiode sensors with different diffusor geometries.

Photos by DLR

Pyranometers can also be used to measure diffuse radiation. The required device for this measurement is known as a diffusometer. It consists of a pyranometer and a shading attachment that blocks the direct radiation on its way to the sensor. Shading balls, shading disks, shading rings, or shadowbands are used for that purpose. Shading balls (Figure 3-4) and shading disks must track the sun; they cover only a small part of the sky corresponding to the angular region defined for measuring DNI (normally 5°). Shadowbands and shading rings must be manually adjusted on a daily basis to properly shade the sun and cover a larger fraction of the sky; they are further described in Sections 3.2.5 and 3.2.5.2.

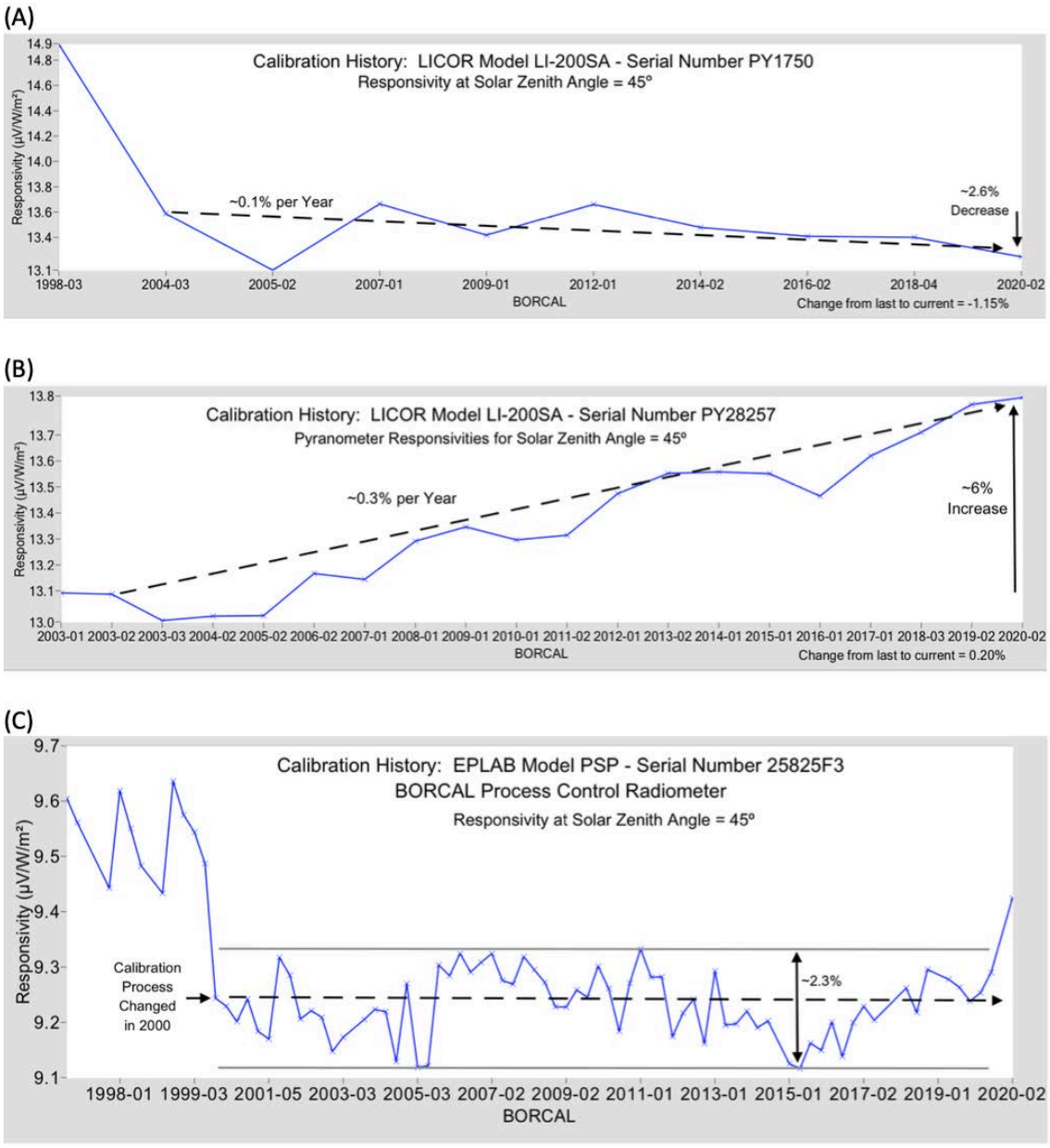

Figure 3-10. Example of long-term calibration responsivity changes for two photodiode-based pyranometers (A and B) with an acrylic diffuser and a thermopile-based pyranometer (C) based on results from periodic NREL Broadband Outdoor Radiometer Calibration events.

Image by NREL

3.2.2 Pyrheliometer and Pyranometer Classifications

Radiometer classification is useful for selecting the correct instrument for a particular use case and interpreting the data. Both the International Organization for Standardization (ISO) and WMO have established instrument classifications and specifications for the measurement of solar irradiance. The current ISO 9060 (ISO 9060 2018) classification is recommended because of some shortcomings in the WMO classification and the previous version of ISO 9060.

Several instrument properties are used as the basis for these pyrheliometer and pyranometer classifications. The latest specifications for these radiometers are found in ISO 9060:2018 and are summarized in Table 3-2 and Table 3-3 based on (Apogee 2019). The standard provides not only acceptance intervals but also corresponding guard bands, which are useful because the measurements on which the sensor specifications are based have nonnegligible uncertainties.

The acceptance intervals provided by ISO 9060 give a general idea of the differences in data quality between instrument classes; therefore, the radiometer classes can be understood as accuracy classes. The 2018 standard also notes, however, that the acceptance intervals shown in the tables cannot be used for uncertainty calculations for measurements obtained at conditions that are different from those defined for the classification. For example, the temperature response limits are defined for the interval from −10°C to 40°C relative to the signal at 20°C. A measurement at 10°C will be connected to a different temperature response error than a measurement at 0°C or even more so at −20°C. For the other parameters, the same principle applies. In particular, the spectral clear-sky irradiance error used for the classification can deviate from the spectral irradiance error for other conditions, such as cloudy conditions or other air masses. For pyranometers, it must also be considered that the spectral error for diffuse or tilted radiation is different from the spectral error for global horizontal radiation. A more detailed discussion of the clear-sky spectral error can be found in Wilbert et al. (2019).

The most important changes in the current ISO 9060 compared to the previous 1990 version (ISO 9060 1990) are as follows:

- Simple names are used for the four classes (AA, A, B, C), including Class AA that is introduced mainly for ACRs.
- The clear-sky spectral error is used to classify the spectral properties of the radiometers, allowing photodiode-based radiometers to also be included in the ISO classification. Previously, spectral selectivity was used, which excluded photodiode radiometers. The spectral selectivity is defined by ISO as the deviation of the spectral responsivity from the average spectral responsivity between 0.35–1.5 µm.
- Additional radiometer classes are defined relative to their response time and their spectral responsivity. If the 95% response time is less than 0.5 seconds, the term “fast response” can be added to the name of the class. Similarly, “spectrally flat” radiometers are defined using spectral selectivity. If a radiometer has a spectral selectivity less than 3%, the term “spectrally flat” can be added to the name of the class (e.g., “spectrally flat Class A”).
- For Class A pyranometers, individual testing of temperature response and directional response is required.
- The final signal of a sensor can be used for classification after the application of specific correction functions (e.g., for temperature response) if these corrections are applied within the measurement system (processor within instrument or control unit). Processing errors are also used as a classification criterion.

Including photodiode radiometers was considered helpful because only fast-response (a few microseconds) photodiode sensors can be used for accurate monitoring of extremely rapid fluctuations of solar irradiance. Under such circumstances—typically caused by ramping and cloud-enhancement events—side-by-side thermopile and photodiode radiometers can disagree by a significant margin (Gueymard 2017a; 2017b). Further, because the most accurate way to

determine GHI involves the combination of DNI and DHI measurements (Michalsky et al. 1999; ISO 2018), the shading balls, shading disks, shading masks, and rotating shadowbands are also defined in the current ISO 9060.

Table 3-2. ISO 9060:2018 Specifications Summary for Pyrheliometers Used to Measure DNI

Pyrheliometer Classification List				
Parameter	**Name of Class, Acceptance Interval**			
Name of Class	**AA**	**A**	**B**	**C**
Roughly Corresponding Class From ISO 9060:1990	*Not Defined*	*Secondary Standard*	*First Class*	*Second Class*
Response time for 95% response	No requirement	<10 s	<15 s	<20 s
Zero offset: (a) Response to 5-K/h change in ambient temperature	±0.1 W/m^2	±1 W/m^2	±3 W/m^2	±6 W/m^2
(b) Complete zero offset including effect (a) and other sources	±0.2 W/m^2	±2 W/m^2	±4 W/m^2	±7 W/m^2
Non-stability: Percentage change in responsivity per year	±0.01%	±0.5%	±1%	±2%
Nonlinearity: Deviation from the responsivity at 500 W/m^2 because of change in irradiance from 100 to 1000 W/m^2	±0.01%	±0.2%	±0.5%	±2%
Clear-sky DNI spectral error	±0.01%	±0.2%	±1%	±2%
Temperature response: Percentage deviation because of change in ambient temperature within interval from −10°C to 40°C relative to 20°C	±0.01%	±0.5%	±1%	±5%
Tilt response: Percentage deviation from the responsivity from 0° to 90° at 1000 W/m^2 irradiance	±0.01%	±0.2%	±0.5%	±2%
Additional signal-processing errors	±0.1 W/m^2	±1 W/m^2	±5 W/m^2	±10 W/m^2

Even within each instrument class, there can be some measurement uncertainty variations. The user is expected to research various instrument models to gain familiarity with the design and measurement performance characteristics in view of a particular application (Myers and Wilcox 2009; Wilcox and Myers 2008; Gueymard and Myers 2009; Habte et al. 2014). Further, the accuracy of an irradiance measurement depends on the instrument itself as well as on its alignment, maintenance, data logger calibration, appropriate wiring, and other conditions or effects that degrade performance. The accuracy of radiometers is further discussed in Chapter 10.

Table 3-3. ISO 9060:2018(E) Specifications Summary for Pyranometers

Pyranometer Classification List			
Specification	**Class of Pyranometer**		
	A	**B**	**C**
Roughly Corresponding Class From ISO 9060:1990	*Secondary Standard*	*First Class*	*Second Class*
Response time: 95% response	<10 s	<20 s	<30 s
Zero offset: (a) Response to −200 W/m^2 net thermal radiation	±7 W/m^2	±15 W/m^2	±30 W/m^2
(b) Response to 5-K·h^{-1} change in ambient temperature	±2 W/m^2	±4 W/m^2	±8 W/m^2
(c) Total zero offset including the effects of (a), (b), and other sources	±10 W/m^2	±21 W/m^2	±41 W/m^2
Non-stability: Change in responsivity per year	±0.8%	±1.5%	±3%
Nonlinearity: Percentage deviation from the responsivity at 500 W/m^2 because of change in irradiance from 100 to 1000 W/m^2	±0.5%	±1%	±3%
Directional response for beam radiation (range of errors caused by assuming that the normal incidence responsivity is valid for all directions when measuring, from any direction, a beam radiation that has a normal incidence irradiance of 1000 W/m^2)	±10 Wm^{-2}	±20 W/m^2	±30 W/m^2
Clear-sky GHI spectral error	±0.5%	±1%	±5%
Temperature response: Deviation because of change in ambient temperature within the interval from −10°C to 40°C relative to 20°C	±1%	±2%	±4%
Tilt response: Percentage deviation from the responsivity at 0° tilt because of tilt change from 0° to 180° at 1000-W/m^2 irradiance	±0.5%	±2%	±5%
Additional signal-processing errors	±2 W/m^2	±5 W/m^2	±10 W/m^2

Parallel to the ISO 9060 classification just described, WMO also offers its own similar classification. The WMO characteristics of operational pyrheliometers and pyranometers are presented for three radiometer classifications:

- High quality: near state of the art, suitable for use as a working standard, maintainable only at stations with specialized facilities and staff
- Good quality: acceptable for network operations
- Moderate quality: suitable for low-cost networks in which moderate to low performance is acceptable.

The difference between the WMO and the outdated ISO 9060:1990 classifications is in the definition of spectral selectivity. The wavelength range used in the former is from 300 to 3000 nm, in contrast with 350–1500 nm in the latter. The WMO limits for the selectivity for the different classes are the same or even stricter, as in the case of the highest pyranometer class. This led to the unfortunate situation that, apparently, no weather-proof pyrheliometer fulfills the requirements of the WMO classes even though the spectral errors of Class A field pyrheliometers are small. (Clear-sky spectral errors are approximately 0.1% [Wilbert et al. 2019].) Typical pyranometers of the highest class in ISO 9060 (for both the 1990 and the 2018 versions) are also excluded from the WMO classification (Wilbert et al. 2019).

Due to the mentioned issues of the WMO classification and the outdated 1990 version of the ISO 9060 classification, using the most recent version of ISO 9060 is recommended.

3.2.3 Pyrheliometer and Pyranometer Calibrations

As stated, the signal of field radiometers is a voltage or a current that is ideally proportional to the solar irradiance reaching the detector. A calibration factor is required to convert the current or voltage to solar irradiance. The calibration factor, $C_{cal,}$ is the inverse of the responsivity, Rs. For example, the responsivity of a thermopile pyrheliometer is given in µV per W/m^2. The irradiance, E, can be obtained from the voltage signal, $V_{pyr,}$ and the instrument's responsivity as:

$$E = V_{pyr}/Rs = V_{pyr} \cdot C_{cal} \tag{3-1}$$

These responsivities can vary over time, which requires periodic recalibrations, as demonstrated by the time-series plot of the determined responsivities of two pyrheliometers shown in Figure 3-11. The temporal variability can be caused by changes in the instrument (e.g., degradation), the specific meteorological conditions at the time and location of calibration, the stability of the calibration reference radiometer(s), the performance of the data acquisition system, and other factors included in the estimated uncertainty of each calibration result. The application of calibrations and the frequency of recalibrations is described in ISO/TR 9901 (2021), ASTM G183 (2023), and IEC 61724-1 (2021). A yearly or alternate-year recalibration cycle is recommended. As the calibration uncertainty might be higher than the relative change in calibration factor, ISO TR9901 provides three different options to use recalibration results.

1. The new responsivity is applied for all data after the calibration.
2. The new responsivity is only seen as a confirmation of the old responsivity if the change is small compared to the calibration uncertainty.
3. The new responsivity is applied for all data after a specific point in time that might be even before the calibration, maybe because of a certain event.

Note that the calibration uncertainty that must be considered for the overall measurement uncertainty will be different, depending on the used option. For research purposes, an alternate

method is sometimes used, by which the irradiance during the period between two successive calibrations is calculated with a calibration factor that varies daily in a linear way between its two determinations (Abreu et al. 2023).

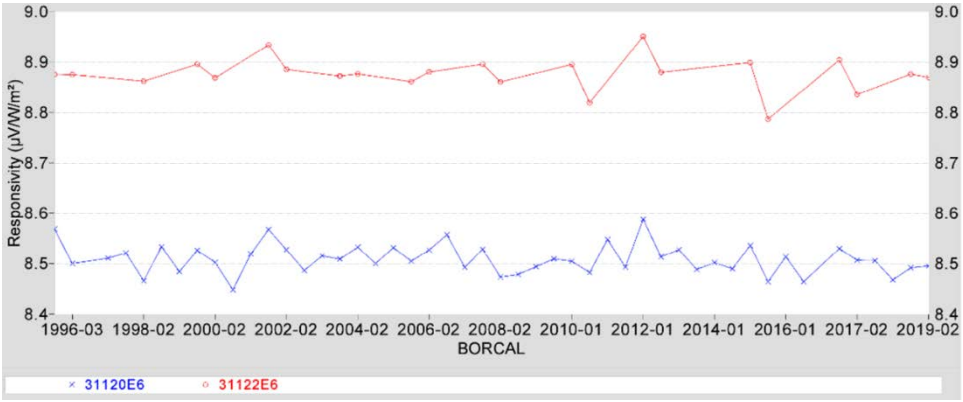

Figure 3-11. Calibration histories for two pyrheliometer control instruments spanning 23 years of Broadband Outdoor Radiometer Calibration events.

Image by NREL

The calibration of pyrheliometers and pyranometers is described in detail in international standards ASTM G167 (ASTM G167 2023), ASTM E816 (ASTM E816 2023), ASTM E824 (ASTM E824 2018), ASTM G183 (ASTM G183 2023), ISO 9059 (ISO 9059 1990), ISO 9846 (ISO 9846 1993), and ISO 9847 (ISO 9847 2023). The calibration method described in ISO 9059 for pyrheliometers is based on simultaneous solar irradiance measurements with the test and reference pyrheliometers. ISO 9846 describes a calibration method for a pyranometer using a reference pyrheliometer and another method based on a reference pyrheliometer and a reference pyranometer. ISO 9847 describes pyranometer calibrations using a reference pyranometer. While an updated version of ISO 9847 has been published in 2023, the two other ISO standards are currently under revision.

Pyrheliometers are calibrated following ISO 9059 by comparing the output signal (e.g., a voltage) of the tracked test pyrheliometer to the reference DNI from one or a group of reference pyrheliometers. For each simultaneous measurement pair, a preliminary responsivity can be calculated as the ratio of the test instrument's output signal to the reference DNI (Figure 3-12, right). After rejecting outliers and data collected during unstable conditions, an average responsivity can be determined. Because the responsivity of some older pyrheliometers shows a noticeable correlation with the solar zenith angle (SZA), specific angular responsivities can also be derived (Figure 3-12). For this calibration method, it is important that clouds do not mask the sun or the circumsolar region. The calibration can be affected if significant levels of circumsolar radiation prevail during the calibration. This risk increases with the instrument's FOV; hence, Linke turbidities should be less than 6, according to the standard method. The Linke turbidity coefficient, T_L, is a measure of atmospheric attenuation under cloudless conditions. It represents the number of clean and dry atmospheres that would result in the same attenuation as the real cloudless atmosphere. One method to derive the Linke turbidity from DNI is presented in Ineichen and Perez (2002).

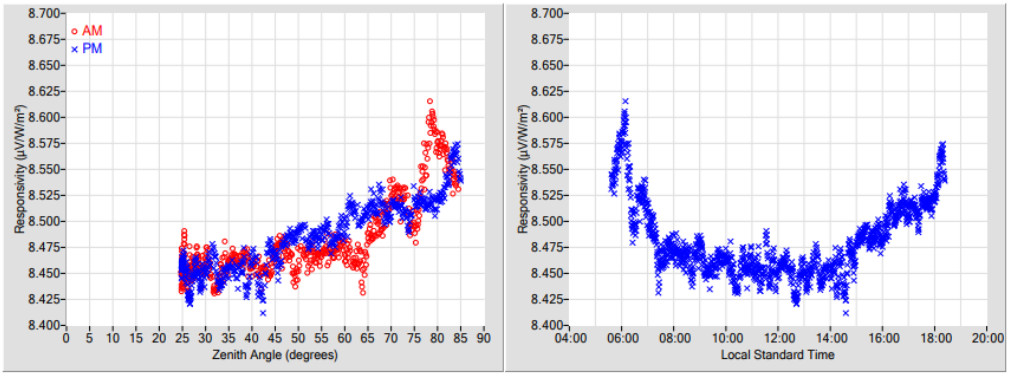

Figure 3-12. Pyrheliometer calibration results for an Eppley Normal Incidence Pyrheliometer (NIP) summarizing (left) *Rs* compared to SZA and (right) *Rs* compared to local standard time.

Image from NREL (2022)

The WRR must be used as the traceable reference for the calibration of all terrestrial broadband radiometers, as stipulated by the *Système International* (SI). This internationally recognized measurement reference is a detector-based standard maintained by a group of electrically self-calibrating ACRs at the World Radiation Center by the Physical Meteorological Observatory in Davos, Switzerland (Figure 3-5). The present accepted inherent uncertainty in the WRR is ±0.3% (Finsterle et al. 2011). All radiometer calibrations must be traceable to WRR, but that does not mean that all radiometers are calibrated *directly* against WRR. The calibration chain from the WRR to a field instrument can have several steps. For example, reference ACRs are used as national and institutional standards, and these instruments are calibrated by comparison to the WRR during international pyrheliometer comparisons conducted by the World Radiation Center once every 5 years. In turn, standard pyrheliometers are calibrated against these national standards with a well-defined uncertainty (Balenzategui et al. 2022).

The WRR was established by WMO in 1978. From a historical perspective, it is the latest in a series of "pyrheliometric scales," after the Ångström scale (ÅS; created in 1905), the Smithsonian scale (SS; created in 1913), and the international pyrheliometric scale (IPS; created in 1956). The relative differences among these scales can introduce a data bias on the order of 2%. The user should be aware of this potential bias in data measured before 1979, which are still useful to establish long-term trends, in particular (see Chapter 6). A correction is necessary to harmonize older datasets to the current scale, according to:

- WRR = 1.026 (ÅS 1905)
- WRR = 0.977 (SS 1913)
- WRR = 1.022 (IPS 1956).

Moreover, old irradiance data were typically reported in either one of two deprecated units: Langley (symbol: Ly) or calorie (symbol: cal). The conversion to SI units is: 1 Ly = 1 cal·cm^{-2} = 4.184 × 10^{4} J·m^{-2}, or 1 Ly·min^{-1} = 1 cal·cm^{-2}·min^{-1} = 697.33 W·m^{-2}.

Over the last three decades, elaborate laboratory studies (involving advanced cryogenic radiometers) and experimental intercomparisons have been conducted to compare the radiometric watt per square meter (defined experimentally by the WRR scale) to the electric watt per square meter (defined by SI in an absolute sense), as described in some reports (e.g.,

Fehlmann et al. 2012; Walter et al. 2017) and summarized in Balenzategui, Fabero, and Silva (2019). The goal is to ultimately realize an official transition from the WRR scale to the electric SI scale for worldwide radiation measurements in the future. The current difference between the two scales is estimated at ≈0.3%, but it will take more studies and international consultation under the WMO auspices[8] to confirm this, and finally transform the wording in all calibration certificates from "traceability to WRR" to "traceability to SI." Resolving this discrepancy is important because the calibration of PV reference cells and power rating of PV modules are normally done with traceability to SI units. In certain situations in which the utmost accuracy is required, an adjustment of 0.3% can be made to account for the difference; however, in the vast majority of field applications, other sources of uncertainty are far larger and the difference between these scales can be safely ignored. In parallel, this scale difference also slightly impacts the calculation of nondimensional ratios between a terrestrial irradiance component and its extraterrestrial counterpart, such as the ubiquitous clearness index (see Chapter 7), because the current solar constant value is derived from space measurements traceable directly or indirectly (i.e., after suitable corrections) to SI. If daily fluctuations in extraterrestrial irradiance of up to ±0.2% are also factored in (per Chapter 2), it is possible that systematic errors of up to ≈0.5% are introduced in various calculations, depending on solar activity.

Pyranometers calibrated against traceable WRR reference radiometers make these pyranometer calibrations traceable to WRR. Pyranometers can be calibrated outdoors with three different methods. One option, as described in ISO 9846, is to compare the DNI output from a reference pyrheliometer (preferably ACR) to that derived from the test pyranometer using the shade-unshade method. The successive voltages, V_{unshade} and V_{shade}, are proportional to GHI (unshaded) and DHI (shaded), respectively. Using the reference DNI and the relationship between GHI, DHI, and DNI, as described by Eq. 2-2a, the responsivity, *Rs*, of the pyranometer under test for one measurement sequence can be derived:

$$Rs = [(V_{\text{unshade}} - V_{\text{shade}})/\cos(\text{SZA})]/\text{DNI} \tag{3-2}$$

This method is described in more detail by (Reda, Stoffel, and Myers 2003). For this calibration method, virtually constant atmospheric conditions during the pair of shaded and unshaded measurements are required. Cloud cover must be very low, and the angular distance between clouds and the sun must be high. In addition to cloud cover, aerosol and water vapor variations could affect the calibration. This explains why only data collected for a low T_L (less than 6) should be used for the calibration.

Another option offered by ISO 9846 consists in comparing the voltage signal of the test pyranometer obtained in the GHI (unshaded) measurement configuration to that of the GHI calculated from independent DNI and DHI measurements from a reference pyrheliometer (e.g., ACR) and a shaded reference pyranometer. The *Rs* of a pyranometer under calibration for one simultaneous set of three measurements can be computed from their unshaded signal (V_{unshaded}):

$$Rs = V_{\text{unshaded}}/[\text{DNI} \cdot \cos(\text{SZA}) + \text{DHI}] \tag{3-3}$$

[8] An Expert Team on Radiation References (ET-RR) exists within WMO to supervise the future transition from WRR to SI. It is currently anticipated that the switch to SI would not occur before the WMO general meeting of 2027.

Computing *Rs* this way is called the component-summation calibration technique. Again, T_L should be less than 6, and a high angular distance of clouds from the sun should exist during the whole calibration period.

The third option to calibrate pyranometers outdoors is described in ISO 9847. It compares a test pyranometer to a reference pyranometer while both sensors are in the same measurement position (either GHI or GTI). The *Rs* is then obtained as the ratio of the test signal to the reference irradiance. For outdoor pyranometer calibrations using a reference pyranometer, the sky conditions are less precisely defined than for the other methods described. The calibration interval is adjusted depending on the sky conditions.

The indoor calibration methods from ISO 9847 use irradiance measurements under an artificial light source. For the first option, measurements are taken simultaneously after ensuring that the test and the reference pyranometer receive the same irradiance from an integrating sphere. This is done by switching pyranometer positions during the calibration procedure. The other option is to take consecutive measurements by mounting the test and the reference instrument one after the other in the same position under a direct beam. The indoor calibrations are carried out in a controlled environment independent from external meteorological conditions. If measurements with the reference and test pyranometers are made after each other, however, instabilities of the artificial light source increase the calibration uncertainty compared to outdoor calibrations. If simultaneous measurements are used, an additional uncertainty contribution comes from the fact that the test and the reference pyranometer might not receive the same irradiance from the artificial light source, though some of this error can be mitigated by switching the positions of the instruments during the calibration procedure. Further, the incident angle of the radiation is usually not well defined for indoor calibrations. Because of the pyranometer's directional errors (Table 3-3), this is another source of calibration uncertainty; therefore, in general, thorough outdoor calibrations with accurate reference instruments have lower uncertainties than indoor calibrations.

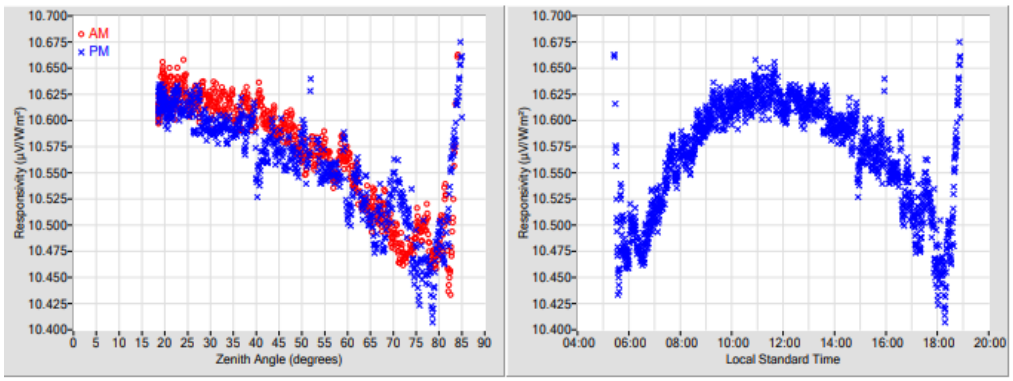

Figure 3-13. Pyranometer calibration results for a Kipp & Zonen CMP22 showing (left) *Rs* vs. SZA and (right) *Rs* vs. local standard time.

Image from NREL (2022)

The shade/unshade and component-summation techniques, when conducted throughout a wide range of SZAs, show that the pyranometer responsivity is correlated with SZA. The variation of *Rs* as a function of SZA is like a fingerprint or signature of each individual pyranometer (Figure 3-13). This means that the angular responsivities of different specimens of the same model can

differ. Variations of pyranometer *Rs* can be symmetrical with respect to solar noon, or they can be highly skewed, depending on the mechanical alignment of the pyranometer, detector surface structure, and detector absorber material properties. For GHI and DHI measurements, the *Rs* for a 45° incidence angle is normally used. To improve the accuracy of GHI measurements, using an SZA and azimuth angle-dependent calibration factor for each individual measurement is also possible. This method, however, is applicable only to conditions with high direct radiation contribution to GHI, because the variation of responsivity with SZA is mostly caused by direct radiation and the associated cosine dependence. For situations when thick clouds mask the sun, or for DHI measurements, the angular distribution of the incoming irradiance cannot be approximated well by one incidence angle. For DHI measurements, it is recommended to use the *Rs* for a 45° incidence angle.

For accurate photodiode pyranometer calibration, further considerations beyond these standards are recommended because of the uneven spectral response. In particular, a specific calibration method is discussed in Section 3.2.5 for photodiode instruments equipped with a rotating shadowband.

3.2.4 Correction Functions for Systematic Errors of Radiometers

Some pyrheliometer and pyranometer measurement errors are systematic and can be reduced by applying correction functions. An example is the correction of directional errors, as mentioned just above. Some manufacturers provide one calibration constant for a pyranometer and additional correction factors for different intervals of SZA. This treatment of the incidence angle dependence has the same effect as using an incidence-angle-dependent responsivity. In practice, this approach is rarely used because of its additional complexity and dependence on sky conditions.

Moreover, an additional temperature correction can be applied if the internal temperature of pyranometers or pyrheliometers is measured using a temperature-dependent resistor close to the sensor. Correction coefficients are often supplied by the manufacturer.

Measurements from only black (as opposed to black-and-white) thermoelectric pyranometers can be corrected for the expected thermal offset using additional measurements from pyrgeometers (Figure 3-4, right). Usage of pyrgeometers allows for the determination of the downward longwave irradiance between approximately 4.5 and 40 μm, based on their sensor (thermopile) signal and body temperature. The thermopile is positioned below a coated Si window that is transparent only to the specified infrared radiation wavelength range while excluding all visible, near-infrared, and far-infrared radiation. Most pyrgeometers must be positioned below a shading ball or disk to limit window heating by DNI. Ventilation units are also used for pyrgeometers, as in the case of pyranometers. If no pyrgeometer is available, which is the general situation,[9] a less-accurate correction for the thermal offset can be made based on estimations of the thermal offset from the typically negative measurements collected during the night (Dutton et al. 2001; Gueymard and Myers 2009; Vignola, Long, and Reda 2009). Correction functions for photodiode pyranometers are presented in Section 3.2.5.

[9] Unfortunately, because they can also be useful to estimate the temperature of PV modules.

3.2.5 Systems for Determining Solar Irradiance Components

A measurement system that independently measures the three basic solar components—GHI, DNI, and DHI—offers the significant advantage that data quality tests relying on the closure equation can be performed (see also Eq. 2-2a):

$$DNI = (GHI - DHI) / \cos(SZA) \quad (3\text{-}4)$$

This can be applied for data quality control and data flagging. Alternatives to solar trackers with a pyrheliometer and two pyranometers exist that reduce the overall cost of such a system and its operation while offering potentially acceptable data accuracy, depending on application. These alternatives are designed to reduce the complexity compared to an automatic solar tracker with pyrheliometer and shaded pyranometer and to reduce the overall power consumption. Such alternatives are described next.

3.2.5.1 Rotating Shadowband Irradiometers

Rotating shadowband irradiometers (RSIs) use a fast pyranometer that is periodically shaded by a small motorized shadowband, which rapidly sweeps across the detector's FOV (Figure 3-14). The RSI's principle of operation is to alternatively sense GHI when unshaded and DHI when shaded. The DNI is calculated using the fundamental closure equation relating these three components, Eq. 3-4.

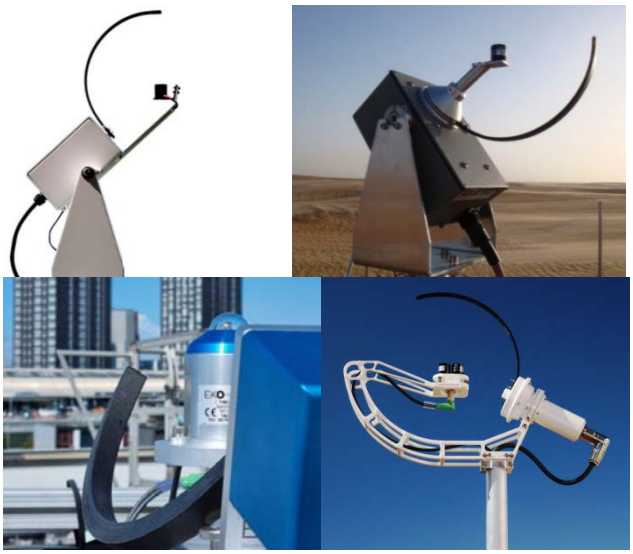

Figure 3-14. Four commercially available RSIs (clockwise from top left): Irradiance Inc. model RSR2; Reichert GmbH RSP 4G; EKO RSB (Pó 2023); and CSP Services GmbH Twin-RSI.

Photos by (clockwise from top left) Irradiance Inc.; CSP Services; EKO; and CSP Services

RSIs are also referred to as rotating shadowband radiometers or rotating shadowband pyranometers, depending on instrument manufacturer. RSI is a generic term that refers to all such instruments measuring irradiance by use of a rotating shadowband. There are two types of RSIs: those with continuous rotation and those with discontinuous rotation.

The operational principle of RSIs with continuous rotation is shown in Figure 3-15. At the beginning of each rotation cycle, the shadowband is below the pyranometer in its rest position.

The rotation is performed with constant angular velocity and takes approximately 1 second. During the rotation, the irradiance is measured with a high and constant sampling rate (approximately 1 kHz). This measurement is called a burst or sweep. At the beginning of the rotation, the pyranometer measures GHI. The moment the center of the shadow falls on the center of the sensor, it approximately detects DHI; however, the shadowband covers some portion of the sky, so the minimum of the burst is less than DHI. Thus, so-called shoulder values are determined by curve analysis algorithms. Such algorithms use the maximum of the absolute value of the burst's slope to find the position of the "shoulder values." The difference between GHI and the average of the two shoulder values is added to the minimum of the curve to obtain the actual DHI. Subsequently, DNI is calculated using GHI, DHI, and SZA (Eq. 3-4). All the RSIs shown in Figure 3-14 (except for the EKO RSB 2) work with a continuous rotation.

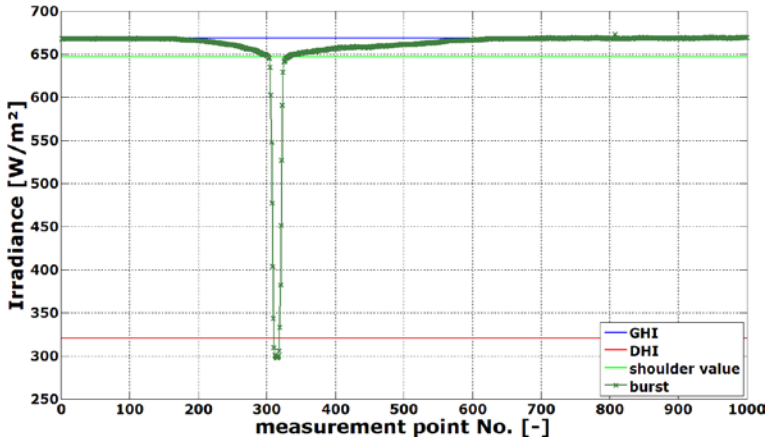

Figure 3-15. Burst (sweep) with sensor signal and the derived GHI, shoulder values, and DHI.

Image from Wilbert (2014)

RSIs with discontinuous rotation measure not the complete burst, but only four points. First, the GHI is measured while the shadowband is in the rest position. Then the shadowband rotates from the rest position toward the position just before it begins shading the diffuser, stops, and a measurement is taken. Then it continues the rotation toward the position at which the shadow lies centered on the diffuser, and another measurement is taken. The last point is measured in a position at which the shadow has just passed the diffuser. The measurement with the completely shaded diffuser is used equivalently to the minimum of the burst (Figure 3-15). The two measurements made when the shadow is close to the diffuser are used equivalently to the shoulder values to estimate the portion of the sky blocked by the shadowband.

These two types of RSIs have advantages and disadvantages. An RSI with continuous rotation needs a detector with a fast response time (≈10 µs). Because a thermopile sensor cannot be used, typically a Si-photodiode is used instead. The instruments shown in Figure 3-14 (except bottom left) use the Si-based LI-COR pyranometer models LI-200SA or LI-200R. Because of the variable spectral response of such Si sensors (Figure 3-2), the measurement accuracy of highest-class thermopile pyranometers cannot be reached. Correction functions (also called adjustment functions) for systematic spectral, cosine, and temperature errors must be applied to reach the accuracy required in resource assessments, albeit still not on par with the accuracy of thermopile instruments and with potentially varying performance under various climatic/spectral composition conditions (Geuder et al. 2016). Several research groups have developed correction

functions that reduce systematic errors in the readings of RSI instruments built around a LI-200SA or LI-200R sensor. Whereas temperature correction is similar in all versions (King and Myers 1997; Geuder, Pulvermüller, and Vorbrugg 2008), the methods for the spectral and cosine corrections vary. King and Myers (1997) proposed functional corrections depending on air mass and SZA, primarily targeting GHI. This approach was further improved by Augustyn et al. (2002) and Vignola (2006), including diffuse and subsequently direct beam irradiance. The combination of the GHI correction of Augustyn et al. (2002) and of the diffuse correction from Vignola (2006) provides a complete set of corrections for LI-200SA-based RSIs. Independently, another method for DNI, GHI, and DHI correction was developed using functional corrections that include a particular spectral parameter obtained from GHI, DHI, and DNI (Geuder, Pulvermüller, and Vorbrugg 2008). Secondary corrections with dependence on air mass and SZA were also added. Other sets of correction functions have also been presented in Geuder et al. (2011); Vignola et al. (2017; 2019); Lezaca, Meyer, and Heinemann (2018); and Forstinger et al. (2020).

RSIs with discontinuous rotation allow sufficiently long measurement times for each of the four points so that a fast-response thermopile detector can be used instead of a photodiode detector; thus, a more accurate pyranometer can be used and, most importantly, the spectral error inherent to photodiodes can be avoided. However, the discontinuous rotation is associated with alignment and timing issues compared to the continuous rotation. Whereas RSIs with continuous rotation are not affected by small azimuth alignment errors (within approximately ±5°), the azimuth alignment of RSIs with discontinuous rotation is crucial for their accuracy. Moreover, the accuracy of the sensor's coordinates and sweep time is more important for the discontinuous rotation. If the shadowband stops in the wrong position, the DHI measurement is incorrect. Further, the longer duration of the DHI measurement procedure with a discontinuous rotation can also increase the measurement uncertainty. The four-point measurement takes longer than the continuous sweep; thus, if GHI and the sky radiance distribution change during the four-point measurement, the data used to determine DHI will have a larger uncertainty.

DHI is typically determined by scheduling a sweep one to four times per minute. This frequency constitutes an effective trade-off between desirable sampling frequency and instrument wear. In contrast, GHI measurements can be sampled at a higher frequency whenever the shadowband does not rotate—for example, every second. The temporal variation of GHI also contains some information about any concomitant change in DNI. Different algorithms are used to determine the averages of DHI and DNI between two DHI measurements using the more frequent GHI measurements. Temporal variations detected by the higher-frequency GHI measurement can be used to trigger an additional sweep of the shadowband to update the DHI measurement under rapidly changing sky conditions.

The initial higher uncertainty of RSIs compared to ISO 9060 Class A pyrheliometers and pyranometers is often compensated by some unique advantages. Their simplicity/robustness, low soiling susceptibility (Pape et al. 2009; Geuder and Quaschning 2006; Maxwell et al. 1999), low power demand, and comparatively lower cost (instrumentation and O&M) provide significant advantages compared to thermopile sensors and solar trackers, especially at remote sites without electric power from the grid.

The accuracy of RSIs is approximately 2.5%–4% for GHI and 3%–9% for DNI, if proper calibration and correction functions are used (standard uncertainty, 1 sigma [Forstinger et al. 2022]). The lower uncertainty limit is only reached if the calibration conditions correspond well to the measurement conditions and for deployment at sunny sites. For comparison, in well-maintained stations with Class A thermopile pyrheliometer and pyranometers, a standard uncertainty of about 1.5% for DNI and 2% for GHI can be reached (see Chapter 10 for further discussion). The correction functions and the condition-specific calibration reduce the uncertainties compared to uncorrected measurements that are based only on the manufacturer calibration of the photodiode pyranometer. Most instrument providers also offer postprocessing software or services that include these correction functions. Users should ask the manufacturer whether such postprocessing is part of the instrument package and is readily available.

Special calibration techniques are applicable to the case of RSIs. LI-200SA or LI-200R pyranometers come with pre-calibration values of sensitivity from the manufacturer (LI-COR) for GHI, based on outdoor comparisons with an Eppley PSP with an accuracy stated as better than 5% (LI-COR 2001). Considering that the PSP has only limited performance (Gueymard and Myers 2009), an additional calibration (e.g., either by the RSI manufacturer or on-site using GHI, DHI, or DNI measured independently) of the RSIs can noticeably improve their accuracy and is strongly recommended (Wilbert et al. 2016). Because of the rather narrow and inhomogeneous spectral response of the photodiodes and the combined measurement of DHI and GHI, only some aspects of the existing ISO standards for pyrheliometer and pyranometer calibrations can be transferred to RSI calibration. Calibrating RSI instruments involves independently field-calibrating them, depending on the correction algorithm with either a global calibration constant or two or three individual constants for DNI, DHI, and GHI. Each of these steps is challenging because each irradiance component has a distinct spectral composition that can change during the day or from one location to another. Because of the spectral response of the Si detectors and/or the diffusers, it is problematic to calibrate an RSI based on only a few short series of measurements. The current best practice is to consider a long enough calibration period (e.g., 8 weeks) to include the wide variety of meteorological conditions expected at the site where the RSI is planned to be used.

Further information on RSIs can be found in Wilbert et al. (2023). More information about RSIs with discontinuous rotation can be found in Harrison, Michalsky, and Berndt (1994). Further general information on the accuracy of RSIs can be found in Chapter 7.

3.2.5.2 Other Instruments Used To Derive Diffuse Horizontal Irradiance and Direct Normal Irradiance

Beside RSIs, there are other instruments that can be used to derive DHI or DNI without a solar tracker. Several of these instruments, as well as an RSI, are currently in the process of benchmarking at CIEMAT's Plataforma Solar de Almería in Tabernas and other sites (Blum et al. 2023). The reference data stems from a solar tracker with ISO 9060 Class A spectrally flat pyrheliometer and pyranometers. The tested systems are shown in Figure 3-16 and described below.

Figure 3-16. Alternative radiometers to derive DNI or DHI without a solar tracker (from left to right): Delta-T SPN1, EKO MS-90, PyranoCam (all-sky imager plus CMP21 pyranometer [Blum et al. 2022]), and Sunto Technology CaptPro.

Images by DLR

The Delta-T SPN1 senses both DHI and GHI with an array of seven fast-response thermopile radiation detectors that are distributed in a hexagonal pattern under a glass dome. The detectors are positioned under diffuser disks and a special hemispherical shadow mask. The shape of the mask is designed such that for any position of the sun in the sky there will always be one or more detectors that are fully shaded from the sun and exposed to approximately half the diffuse radiance (for completely overcast skies). Moreover, one or more detectors are exposed to the full solar beam under any sun position. The minimum and the maximum readings of the seven detectors are used to simultaneously derive GHI and DHI. With this principle of operation and the closure equation, GHI, DHI, and DNI can be obtained without any moving parts and without needing alignment other than horizontal leveling. However, a well-defined azimuthal orientation of the sensor might enable further accuracy enhancements obtained by correction functions in the future. Further, the SPN1's low power demand (temperature-controlled dome prevents dew and frost) increases its suitability for operation at remote sites compared to DNI or DHI measurements involving two-axis trackers. Test results indicate that the accuracy of the SPN1's GHI is comparable with RSIs, but its DNI and DHI readings have higher errors than those measured with RSIs (Vuilleumier et al. 2017; Blum et al. 2023). The SPN1 performance results obtained at six different locations worldwide can be found in (Badosa et al. 2014). An additional comparison with conventional radiometers is presented by (Habte et al. 2016).

Another option for DNI measurements without tracking is the EKO MS-90 instrument (Figure 3-16), which is based on an earlier sunshine recorder sensor (MS-093). The revised design uses a rotating mirror within a fixed glass tube tilted to latitude (−58° to +58°). The mirror reflects the direct beam onto a broadband pyroelectric detector that senses DNI four times per minute. The performance of the MS-90 specimen deployed at NREL has been assessed under both clear-sky and all-sky conditions (Habte and Beuttell 2022).

In the last years, all-sky imagers have also been used to derive solar irradiance (Kurtz and Kleissl 2017; Blum et al. 2022). If only the camera image alone is used, the accuracy of such estimates is still too low for their application in resource assessment. However, the combination of a thermopile pyranometer with an all-sky imager demonstrated accuracies for DHI and DNI similar to RSIs in tests at six different sites in different climates (Blum et al. 2023). In this method, a calibration factor for the sky images is determined using the collocated pyranometer while the camera detects thick clouds that mask the sun so that there is no direct radiation and DHI is equal to GHI. The site dependence of the accuracy of this method is expected to be better than that of RSIs because the color information of the imagery can be used to detect variations in

the solar spectrum, which is not possible with RSIs. All-sky imagers can also be used to document the actual sky conditions and to evaluate further meteorological parameters of interest, such as cloud cover (Kazantzidis et al. 2012), aerosol optical depth (Kazantzidis et al. 2017), or precipitation (Kazantzidis et al. 2012). Moreover, all-sky imagers can also provide short-term radiation forecasts; hence, these instruments are further discussed in Chapter 9, Section 9.3.1 in the context of solar forecasting.

Exemplary results of the benchmark of these instruments are shown in Figure 3-17. The results suggest two groups of instruments with similar accuracy. A higher accuracy is found for both RSIs and the imager-pyranometer combo compared to SPN1 and MS90. Besides their performance in terms of accuracy, these sensors' robustness and reliability are of high importance for their general applicability, particularly at remote sites.

For completeness and clarification, further options that are currently not recommended for DHI or DNI measurements should be mentioned. The Sunto Technologies "all-out" radiometer (Figure 3-16) uses various photodiodes in different orientations and tilts, and derives DNI and DHI from those signals. During a test conducted recently at CIEMAT's Plataforma Solar de Almería in Tabernas, Spain, that sensor showed significant deviations (root mean square deviation [RMSD] of 18% for DNI and 48% for DHI), and malfunctioned after a few months of operation (Blum et al. 2023). Similar approaches have also been proposed with various PV reference cells (Gostein et al. 2020), but their accuracy is not known.

Additionally, the widely used shading rings for thermopile pyranometers should be mentioned. Shading rings cover the complete solar path during a day as seen from a pyranometer. They are built a little bit wider than the 5° used for shading balls to cover the sun's path on several consecutive days so that readjustments of the shading ring position are not required every day. Because a shading ring blocks a significant part of sky diffuse radiation, correction functions are necessary to determine the actual DHI from the instrument's voltage. This explains why the accuracy of such a DHI determination is less than that of a DHI measurement with a shading disk or a shading ball, despite the near-daily personnel effort required for the adjustments. Therefore, these shading rings are not recommended when a new solar resource assessment station is projected and high-quality data are required. Nevertheless, many existing stations worldwide have provided long time series of data based on that configuration, which can thus be of value in various solar energy (or other) applications. In such cases, it is important to know whether the data stream has already been corrected for the shading ring's sky obstruction, and whether appropriate quality control tests have been applied (Nollas, Salazar, and Gueymard 2023). Finally, many attempts have been made to estimate the daily integrated values of GHI or DNI from the vast archive of measurements obtained with legacy Campbell-Stokes sunshine recorders (Stanhill 1998; Painter 1981), but such modeled data have only a low temporal resolution and are not sufficiently accurate for most applications.

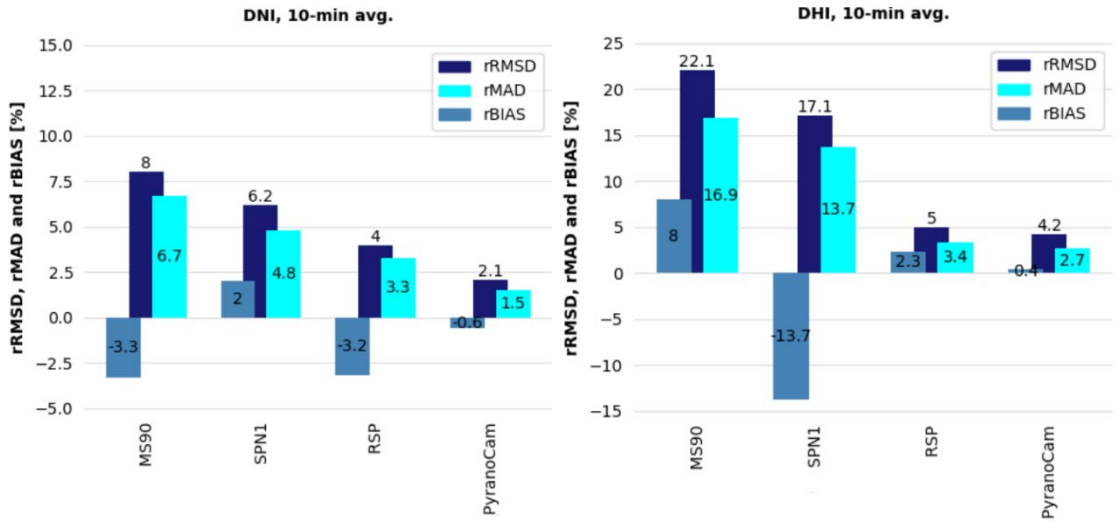

Figure 3-17. RMSD, mean absolute deviation (MAD), and bias for a radiometer benchmark in Tabernas conducted in 1 year.

Image by DLR

3.2.6 Photovoltaic Reference Cells for Outdoor Measurements of the Photovoltaic-Matched Irradiance

Solar PV cells can be advantageously used as radiometer elements; when they are mounted in a suitable enclosure for measurement purposes, they are referred to as PV reference cells. Commercial products in this category are quite diverse, as shown in Figure 3-18. Their active cell area ranges from approximately 4 to 225 cm^2 (from left to right).

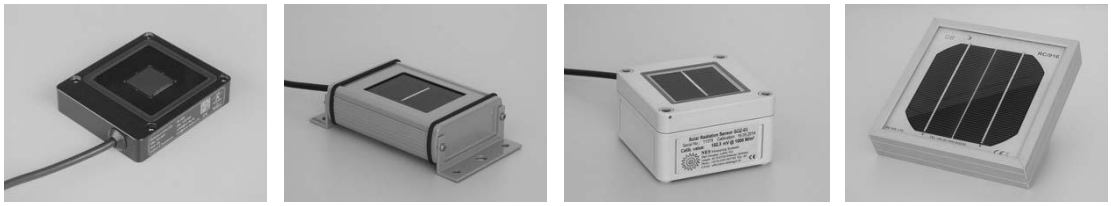

Figure 3-18. A variety of commercial outdoor PV reference cells.

Photos by Anton Driesse, PV Performance Labs

Although they can be physically diverse, PV reference cells share four main characteristics:

- The output signal (usually the voltage measured across an internal shunt resistor) is proportional to the short-circuit current of the detector's PV cells. The cell does not produce electrical power in this configuration, but the measured short-circuit current represents the amount of radiation that could be converted to electric power.
- The detector's PV cells are protected by a flat, transparent window, which creates reflections at the air-window interface, and consequently lower irradiance readings for radiation coming at higher angles of incidence. If reference cells were used as pyranometers, this would be considered a very poor directional response. However, this can also be seen as an advantage because this makes the reference cell readings more closely track the power output of a PV plant—especially when the window material

matches the glass used in the plant's PV modules. Figure 3-19 shows the variations in the angular response from four reference cells that are currently available commercially.

- Like photodiode pyranometers, the spectral response of PV reference cells is narrow and nonuniform (Figure 3-20). The spectral response is mainly defined by the PV cell used in the sensor. This differs substantially from the response of spectrally flat pyranometers, but allows the reference cells to track the PV plant output more closely. This works best when the technology of the reference cell—and its spectral response—matches the modules in the PV plant. In some reference cells, a filter glass is used to absorb some of the near-infrared light before it reaches the Si detector (PV cell), thereby creating an overall spectral response that more closely matches another cell type, such as amorphous Si or cadmium telluride.
- In practice, the output signal of reference cells has a pronounced temperature dependency: the short-circuit current increases with temperature. This dependency is primarily a byproduct of both the spectral response and its temperature dependency, and therefore varies by technology (for instance, it is ≈0.04%/K for crystalline Si cells). Note that this is not the same as the much larger effect of temperature on PV module power. That is because PV modules operate at the maximum power point rather than in short circuit, and because their voltage and efficiency decrease significantly as temperature increases. Reference cell products nearly always include a temperature sensor, and they might offer temperature-corrected and/or uncorrected irradiance signals as output.

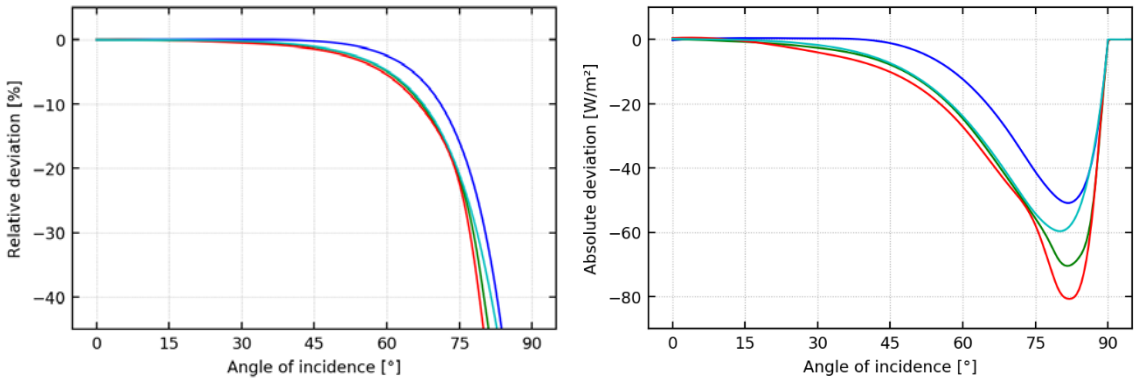

Figure 3-19. Deviations of directional response for four commercial reference cells relative to the ideal cosine response.

Measurements and graphics from Anton Driesse, PV Performance Labs

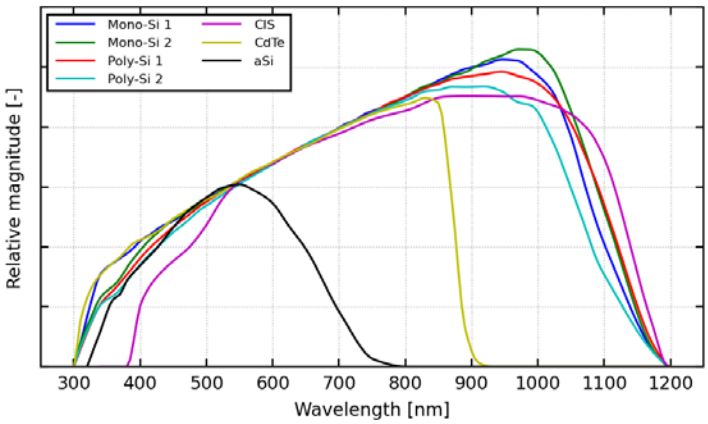

Figure 3-20. Spectral response functions for selected PV devices.

Image from Anton Driesse, PV Performance Labs

In the context of this handbook, only PV reference cells designed for long-term continuous outdoor measurements are of interest. This includes PV resource applications (Habte et al. 2018), for which a key issue is the method of calibration (Section 3.2.6.2). Other types of reference cells exist for indoor use only and do not have a protective window. It is also possible to use a regular full-sized PV module as a radiometer by measuring its short-circuit current. This method would behave like reference cells, but is outside the scope of this overview because of its many degrees of freedom.

It is clear from the discussion above that reference cells are fundamentally different from most other types of radiometers discussed in this handbook. These differences must be known beforehand because they directly influence which type of radiometer is best suited for a given measurement objective. For instance, PV reference cells are not intended to measure the broadband irradiance (GHI or GTI), but to measure a quantity that equals, or closely approximates, the irradiance that is usable by PV modules and systems. This measurement is referred to here as PV-matched irradiance, and sometimes also called "effective irradiance" or "PV resource." That quantity is such that the spectral response and directional response of reference cells approximate those of the PV modules of interest—or approximately match them to a useful degree. Overall, PV reference cells constitute a helpful source of solar resource data, especially for PV monitoring. Nevertheless, they still cannot replace broadband measurements in the context of general solar resource assessments. It is possible, however, that new, improved resource assessment methods specialized for PV applications will be developed and will rely partly or primarily on PV reference cells.

Further considerations of the adequate applications for reference cells and PV-matched irradiance are offered in Sections 3.4.1 and 3.4.2.

3.2.6.1 Standardization of Photovoltaic Reference Cells

Because of their measurement characteristics, reference cells are not consistent with ISO or WMO pyranometer classifications (ISO 9060 2018; WMO 2018). Although many standards apply to PV reference cells directly or indirectly, there is no standard akin to ISO 9060 that would describe precisely and completely how reference cells should behave. In other words, there exists a definition of an ideal pyranometer but not of an ideal reference cell. Nevertheless,

IEC 60904-2 (IEC 60904-2 2023) describes many useful requirements (e.g., linearity better than 0.5% and acceptance angle >160°) and recommendations for PV reference devices ranging from single cells to whole modules. One of the most important aspects of this standard is the extensive documentation requirement, which states that calibration reports must include spectral responsivity, temperature coefficient, and many other details about the device itself, as well as the calibration method and equipment used. Currently, most manufacturers of PV reference cells for outdoor use do not claim to abide by this standard.

There is also a de facto World Photovoltaic Scale (WPVS) reference cell standard. This was first established in 1997 by a group of laboratories seeking to establish a reference scale similar to the WRR (Osterwald et al. 1999). WPVS cells conform to IEC 60904-2 and fulfill several very specific additional design criteria (e.g., physical dimensions and connections) that improve long-term stability and repeatability of measurements. Their high cost is more easily justified in a laboratory setting than for fieldwork; nevertheless, outdoor versions of WPVS cells are available.

3.2.6.2 Calibration of Photovoltaic Reference Cells

The responsivity of PV reference cells varies with wavelength, intensity and direction of the incident light, and temperature of the cell. The calibration value is the response of the device (usually measured in millivolts) under a precisely defined spectral irradiance: the AM1.5 global spectrum (IEC 60904-3, [IEC 60904-3 2019]) with a broadband irradiance of 1000 W/m^2 and a device temperature of 25°C. When combined, these conditions are referred to as the standard test conditions (STCs), which apply equally to PV module ratings. A reference cell's response is normally linear with irradiance; therefore, the value of the response under the STCs is equal to the responsivity of the device in mV per 1000 W/m^2 or μV/(W/m^2).

IEC 60904-4 (IEC 60904-4 2019) describes four different methods for performing the calibration of primary reference devices with traceability to WRR using SI units, so the relationship of reference cells to broadband radiometers is well defined, but only for normally incident irradiance. All these methods consider the narrow spectral response of PV devices by calculating a spectral mismatch factor, which compensates for the fact that the light used during calibration does not normally correspond precisely to the AM1.5 global reference spectrum. Similar methods are found in ASTM E1125-16 (ASTM E1125 2020).

IEC 60904-2 describes how secondary or field reference cells can be subsequently calibrated by comparison to a primary reference device using either natural or simulated sunlight. When the spectral response of the primary reference cell is the same as that of the cell being calibrated, there is no spectral mismatch to be considered. Similar methods are found in ASTM E1362-15 (ASTM E1362 2019).

Primary reference cells are usually calibrated at precisely 25°C so that no temperature correction is required; moreover, when identical devices are used for secondary or field calibrations, the effect of temperature cancels out. When there are differences in devices or device temperatures, however, a correction must be done as part of the calibration. Measurement procedures to determine the temperature coefficient are covered by IEC 60891 (IEC 60891 2021); essentially, they consist of measuring the response over a wide range of temperatures and determining the slope of a linear fit.

In all calibration situations, the direction of the incident light is predominantly normal to the plane of the cell, implying a relatively small fraction of diffuse irradiance under very clear conditions. This minimizes the influence of the directional dependence, but in recent work this aspect has been analyzed more comprehensively, and the use of an angular mismatch factor has been proposed to further improve calibration consistency (Plag et al. 2018). More generally, however, any calibration adjustments for temperature, spectrum, or direction tend to have a small impact overall compared to the strong effects of temperature, spectrum, and direction in field measurements.

The responsivity of reference cells is subject to drift (e.g., <0.3% per year [Viel 2006]), so recalibrations are recommended. IEC 61724-1 (2021) recommends a recalibration interval of maximum 2 years for accuracy Class A monitoring, and the interval recommended by the manufacturer should not be surpassed. Lower-accuracy monitoring systems can be recalibrated according to the manufacturer's recommendation (e.g., every 3 years [Viel 2006]).

3.2.6.3 Recent and Ongoing Research

The key to the effective use of PV reference cells is to understand their special characteristics and to apply that knowledge when collecting, interpreting, and using the data they produce. One active area of research is to quantify these characteristics for product categories, product models, and individual instruments (Figure 3-21) (Driesse et al. 2015; Vignola et al. 2018; 2022). Directly related to this are studies attempting to apply this knowledge of characteristics to instrument calibration, uncertainty analysis, and modeling (Driesse and Stein 2017). In a recent comparison of commercial reference cells for outdoor use, it was found that the majority of calibration factors provided by manufacturers were quite accurate when compared to calibrations performed indoors at NREL (Driesse 2021). Nevertheless, that study confirmed previous observations to the effect that other characteristics, such as directional and spectral response, are not well documented and vary from model to model. These variations currently add to the uncertainty in short- and long-term integrated energy values measured using reference cells (Driesse, Gotseff, and Sengupta 2022), so efforts continue to promote further standardization (Habte et al. 2018). A specific proposal for the standardization of reference cells with emphasis on outdoor use, referred to as the Baseline Performance Reference, is found in Driesse, Habte, and Sengupta (2023).

Figure 3-21. Test facility to quantify PV reference cell characteristics and compare them with other types of radiometers.

Photo by PV Performance Labs

3.3 Rear Plane-of-Array Irradiance and Surface Albedo Measurements

The RPOA, that is, the irradiance that is incident on the rear side of BPV modules, is becoming increasingly important because of the large quantity of bifacial modules being deployed. Methods of various complexity are being developed to determine the RPOA from models using inputs of either spectral or broadband albedo information (Berrian and Libal 2020; Chudinzow et al. 2019; Hansen et al. 2017; Monokroussos et al. 2020; Patel et al. 2019; Arguez and Vose 2011; Sun et al. 2018). In practice, however, it is recommended to follow the RPOA measurement guidelines formulated in standard IEC 61724-1 (IEC 2021c).

RPOA consists primarily of scattered light from multiple sources including the ground, sky, and neighboring PV rows. RPOA depends strongly on the albedo of the surface below the PV array, the height and tilt of the array, and the diffuse light emanating from the fraction of the sky hemisphere viewed by the array's rear side. Research has shown that the RPOA incident irradiance on the back of a 37° fixed-tilt system above light sandy soil is 130–150 W/m^2 when the front side is illuminated with the AM1.5G reference spectrum (1000 W/m^2) (Deline et al. 2017; Monokroussos et al. 2020; IEC 61215-1 2021). Therefore, ≈12% of the total irradiance received by a BPV system under reference conditions is RPOA, most of which is ground-reflected light. Under realistic conditions, this fraction is highly variable depending on the system's geometry, surface type, and atmospheric conditions.

RPOA can be measured directly or modeled based on albedo and irradiance data. Simple models for the RPOA typically use 2D or 3D view factor methods, whereas more advanced methods are based on raytracing or computer graphics. All methods require albedo, GHI and DHI, the PV system geometry (i.e., pitch, tilt, width, and height) and the solar position as inputs. The 2D view factor method has low computational demands as compared to raytracing, which makes it the most common method presently used to calculate RPOA in PV yield predictions. A disadvantage of the 2D view factor approach is that it is incapable of simulating complex geometries (e.g., PV mounting system), and therefore adjustment factors must be applied to the simulated RPOA before the data can be used in PV yield predictions. For single-axis trackers, case studies have shown that the results using the 2D view factor and 3D raytracing techniques are within approximately 2% and 1% of the measured bifacial gain, respectively (Riedel-Lyngskær, Berrian, et al. 2020).

3.3.1 Measurement of Rear Plane-of-Array Irradiance

Studies on RPOA measurement have appeared only within the last few years, and as such, the best practice guidelines for irradiance monitoring in BPV systems are still evolving. The many challenges surrounding RPOA measurements are discussed comprehensively in Gostein et al. (2021). Rear-side edge-brightening effects (Pelaez et al. 2019), nonuniform irradiance patterns that change with conditions (Deline et al. 2020; Janssen et al. 2017), and structural shading effects (Pelaez, Deline, Stein, et al. 2019; Zhao et al. 2021) make it difficult to identify an RPOA sensor location that is representative of a PV array's average back-side intensity. For this reason, the use of multiple RPOA sensors distributed on the back side is common.

The spectral albedo of most natural materials is significantly different from the distribution of the incident solar spectrum, which creates large spectral mismatch factors for spectrally selective

sensors placed on the back side (Mouhib et al. 2022; Blakesley et al. 2020; Gostein, Marion, and Stueve 2020; Riedel-Lyngskær et al. 2022). These spectral effects make RPOA sensor type selection non-trivial (i.e., thermopile pyranometer vs. photodiode sensor vs. PV reference cell). The literature contains some RPOA measurement comparisons of pyranometers and reference cells mounted on different system types above various reflecting surfaces (Babal et al. 2020; Asgharzadeh et al. 2019; Pelaez et al. 2020; Riedel-Lyngskær, Berrian, et al. 2020; Riedel-Lyngskær et al. 2022). The difference between the pyranometer (flat spectral response) and reference cell (peaked spectral response) RPOA readings depends strongly on the spectral distribution of the local albedo compared to that of the PV material. The larger the difference of the RPOA spectrum from the GTI standard spectrum, the greater the spectral mismatch of Si PV devices will tend to be. For instance, the back-side spectral mismatch has been calculated for Si cells above different surfaces in Riedel-Lyngskær et al. (2022). Spectral mismatch factors greater than 1.20 (20%) were obtained over the studied vegetation, compared to near-unity factors for snow. This can be explained by the large difference between the broadband value of albedo for vegetation (≈0.2) and its value (≈0.5) in the NIR close to the peak (around 900 nm) of the Si spectral response curve. In comparison, the albedo of snow is more spectrally uniform (Figure 3-22).

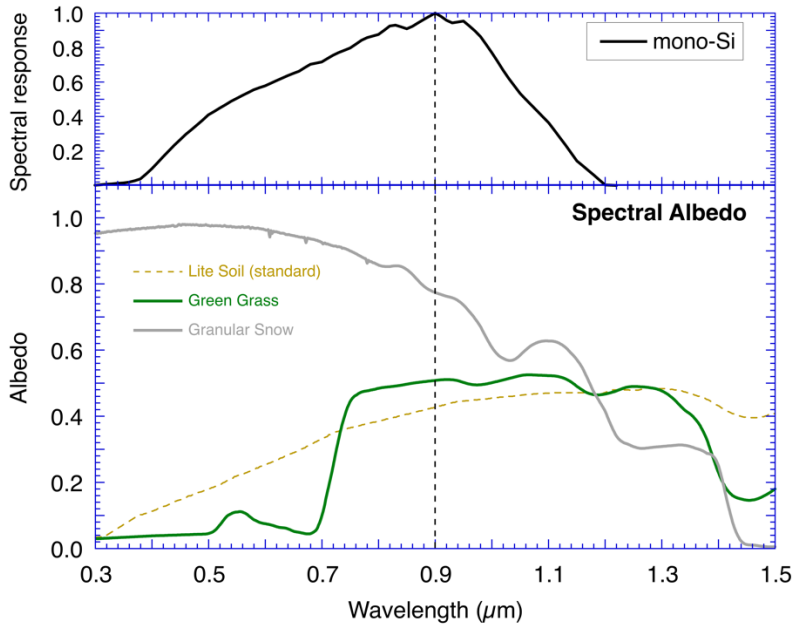

Figure 3-22. Spectral response of monocrystalline Si (top plot) and spectral albedo of three typical surfaces (Lite Soil, Green Grass, and Snow) extracted from the SMARTS library (bottom plot). The Lite Soil surface is used to define the AM1.5G standard spectrum.

Image by C. A. Gueymard

Some authors have proposed the use of full-size reference modules for irradiance monitoring of BPV systems (Riedel-Lyngskar et al. 2022; Braid et al. 2022). The advantage of this approach is that a PV panel used as a large-area sensor responds to the nonuniform irradiance and spectral effects much in the same way as the power-generating panels in the array. Moreover, Pelaez, Deline, Stein, et al. (2019) and Korevaar et al. (2020) showed how ray-trace modeling can be used to identify the position of a single small-area RPOA sensor that is representative of the back-side array.

Much of the PV community's present knowledge surrounding RPOA measurement practices and considerations is codified in the latest revision of IEC 61724-1 (IEC 61724-1 2021) for PV monitoring. The key recommendations made in this IEC standard for RPOA measurements include:

- Sensors should be mounted at the same tilt angle as the modules while minimizing shade on the modules.
- Sensors should be positioned to avoid end-row brightening effects, localized shading, or enhanced illumination phenomena.
- Multiple sensors should be installed to measure the spatially nonuniform illumination profile throughout the day.

An example for the RPOA measurement in a BPV park is shown in Figure 3-23. The relative RPOA measurement errors due to objects in the RPOA pyranometer's FOV can be comparably high. In one example, metallic roofs 50 m away from a pyranometer added ~5 W/m² to RPOA in the afternoon. For a coincident RPOA of 50 W/m², this 10% relative error is highly visible in the RPOA time series.

IEC 61724-1 does not recommend a specific number of RPOA sensors per array, but only specifies a minimum number of sensors within a solar park depending on the BPV system size for the accuracy Class A monitoring setup defined in this standard. The minimum number of RPOA sensors in Class A monitoring systems is three times greater than for GTI. For example, 12 RPOA sensors are needed for a 200-MW BPV park. Logically, the number of sensors and their precise placement within an array are not mandated because the RPOA nonuniformity depends on ground properties and the array's height, tilt angle, and pitch, making general recommendations difficult. The IEC standard states that bifacial reference cells can be used to determine the effective rear-to-front irradiance ratio, but it does not recommend the use of any specific sensor type for RPOA measurements (i.e., thermopile pyranometers, photodiode detectors, or reference cells). Nevertheless, the standard states that spectrally corrected RPOA measurement is optional, but does not provide clear guidance about how or when to make the implied corrections. Further information on the measurand and instrument selection for RPOA is provided in Sections 3.4.1.2 and 3.4.2.2.

Figure 3-23. Example of multiple pyranometers (circled in red) used for RPOA monitoring of a south-facing, fixed-tilt BPV system (left). Close-up view of RPOA sensor mounting (right). Note that the array's length runs east-west and that the sensors are placed several meters away from the western or eastern array edges.

Photos by Nicholas Riedel-Lyngskær

The left part of Figure 3-24 shows exemplary diurnal GTI and RPOA measurements on a clear day near the vernal equinox (March 25, 2020) in Roskilde, Denmark (55.6°N, 12.1°E). Time-series measurements related to an equator-facing 25° fixed-tilt system and a horizontal single-axis tracker are shown. Both systems are in the middle of a multi-row field, and the RPOA sensors are mounted as shown in Figure 3-23 to avoid edge-brightening effects. Under clear conditions and a common broadband albedo value (≈0.2), the figure shows that the front-side GTI is roughly an order of magnitude greater than its back-side counterpart (i.e., RPOA). The right part of Figure 3-24 shows 1 year of back-to-front irradiance ratios (BFIR) for the equator-facing fixed-tilt system. RPOA is here the average irradiance from two pyranometers mounted on the back of the system (Figure 3-23). The histogram borders show the annual distributions of BFIR and GTI, whereas the color scale shows the density of BFIR and GTI observations clustered into 10 quantiles. The annual median BFIR is 7.4% for this fixed-tilt system. Note that the mean BFIR is skewed because of the high BFIRs that can occur when GTI is low. The broadband albedo at the site (normally ≈0.2 in the absence of snow) is comparable to many natural ground surfaces. Therefore, the distributions of annual BFIR shown in Figure 3-24 (right) might be similar to that in many utility-scale BPV parks.

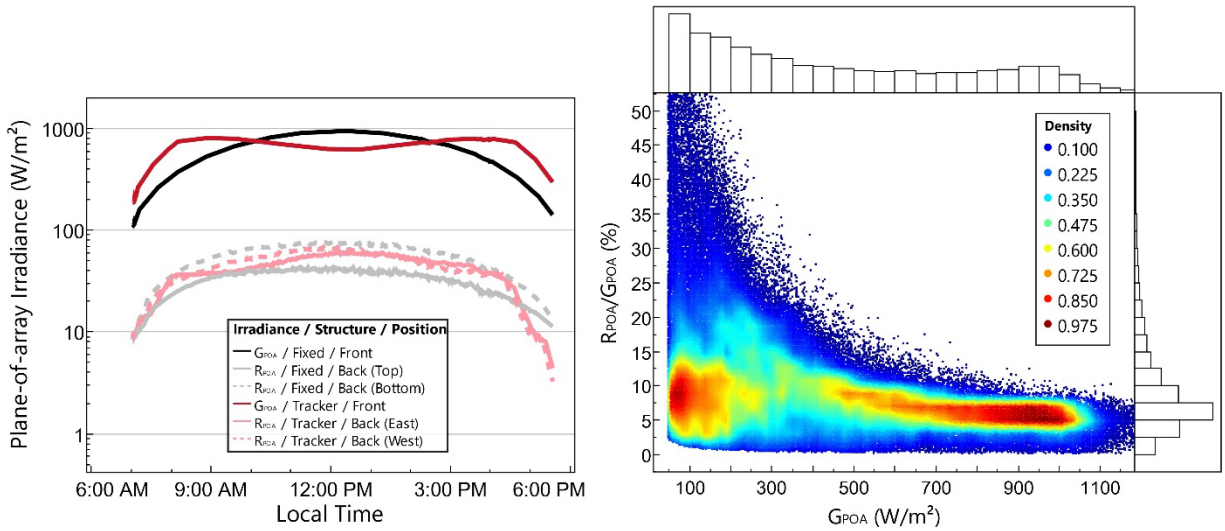

Figure 3-24. Diurnal plot of GTI (labeled as GPOA) and RPOA for fixed-tilt and single-axis tracker systems (left). Rear-to-front-side irradiance ratio versus POA from 1 year of measurements on a fixed-tilt bifacial system (right).

Figures by Nicholas Riedel-Lyngskær

Nonuniform irradiance patterns on the back side of BPV modules are created mainly from reflected irradiance near the array edges and from shading by the supporting structure. RPOA's nonuniformity is also a complicated function of surface albedo, array height, tilt angle, and sky conditions. Field measurement campaigns of RPOA have been carried out on fixed-tilt systems (Deline et al. 2017; Pelaez, Deline, MacAlpine, et al. 2019; Kenny et al. 2018; Rossa, Martínez-Moreno, and Lorenzo 2021). Additionally, several studies have examined the RPOA nonuniformity via simulation (Pelaez, Deline, Greenberg, et al. 2019; Kreinin et al. 2010; Hansen et al. 2017; McIntosh et al. 2019; Asgharzadeh et al. 2018). These studies have demonstrated that the nonuniformity of RPOA is caused by brightening at array edges (e.g., the east and west edges of an equator-facing fixed-tilt system) as well as dimming in areas shaded by structural support members (e.g., tracker torque tubes). Sensitivity studies have also shown that RPOA's homogeneity tends to improve with increasing array height and row spacing and with an increased fraction of sky diffuse irradiance. The nonuniformity of RPOA tends to be highest for low-ground-clearance systems above high surface albedo during clear-sky conditions.

The spatially nonuniform nature of the incident irradiance on the back side means that the position of RPOA sensors can affect the bifacial performance ratio (PR_{BIFI}) calculations. PR_{BIFI} is an indicator of the energy output of a BPV system relative to the energy input available to it (i.e., both GTI and RPOA). The recommended formulae to calculate PR_{BIFI} have been compiled in IEC 61724-1.

Raytracing simulations using typical meteorological year data from over 700 locations have recently been performed to identify suitable RPOA sensor positions for single-axis tracker designs (Riedel-Lyngskær and Andersen 2024). The red circles in Figure 3-25 show the simulated positions that have been found within ±5% of the annual average back-side irradiance at 70% of the locations studied. The one-in-portrait (1P) tracker is the only design for which the bottom of the torque tube has been found representative of the annual average RPOA.

When assessing BPV performance at short time scales (e.g., intraday), it is recommended to install one RPOA sensor on the eastern half and one on the western half; this adequately captures diurnal RPOA variations such as those shown in Figure 3-24. Both the 1P and two-in-portrait (2P) designs show representative sensor positions at precisely half the distance between the torque tube and panel edge, whereas representative RPOA positions on 2P designs with a gap over the torque tube ($2P_{gap}$) are 10%–20% further from the torque tube. The results for fixed-tilt bifacial systems are likely to vary from those for the single-axis tracker shown in Figure 3-25. Korevaar et al. (2020) performed raytracing simulations to identify representative RPOA sensor locations for fixed-tilt systems. They found that a sensor placed 68% from the lowest edge gives readings that are most representative of the mean annual RPOA.

Lastly, the electrical measurements of a 6.5-kWp BPV array are used to demonstrate how the RPOA sensor positions can induce uncertainty in PR_{BIFI} calculations, and to validate the recommended RPOA positions for the $2P_{gap}$ design shown in Figure 3-25. The PV system analyzed here is mounted on a 2P single-axis tracker above grass in Roskilde. An array of 10 c-Si reference cells is mounted on the back of the tracker for high spatial resolution RPOA measurements. Six months of performance data are used to calculate the hourly PR_{BIFI} distributions at the 10 reference cell positions located on the eastern half of the tracker system (Figure 3-26). The western and eastern halves of a 2P tracked system should normally yield symmetrical results, so long as the ground clearances and albedo are similar (Riedel-Lyngskær, Petit, et al. 2020). Figure 3-26 shows that PR_{BIFI} can vary by ≈3% when the two most distant RPOA sensor locations are considered. The reference cell closest to the torque tube (i.e., the axis of rotation) receives the least irradiance, and, therefore, RPOA data from this location will yield the highest PR_{BIFI} values. The opposite is true of the reference cell farthest from the torque tube. This sensor tends to receive the most irradiance, thereby resulting in the lowest PR_{BIFI} values. The horizontal red line in Figure 3-26 shows the average PR_{BIFI} of all sensor locations, which closely corresponds to the PR_{BIFI} value obtained when the RPOA sensor is mounted 60% of the distance between the torque tube edge and array edge.

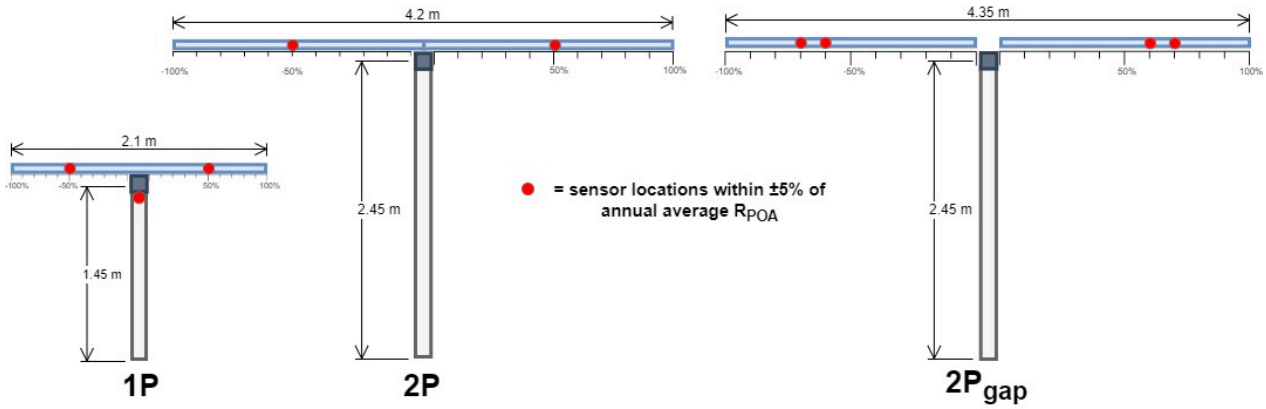

Figure 3-25. Spatial diagram showing three common single-axis tracker designs (1P, 2P, and 2P with a gap over the torque tube). The red dots on each tracker show the discrete points that were found within ±5% of the annual average back-side irradiance at 70% of the locations studied.

Figure by Nicholas Riedel-Lyngskær

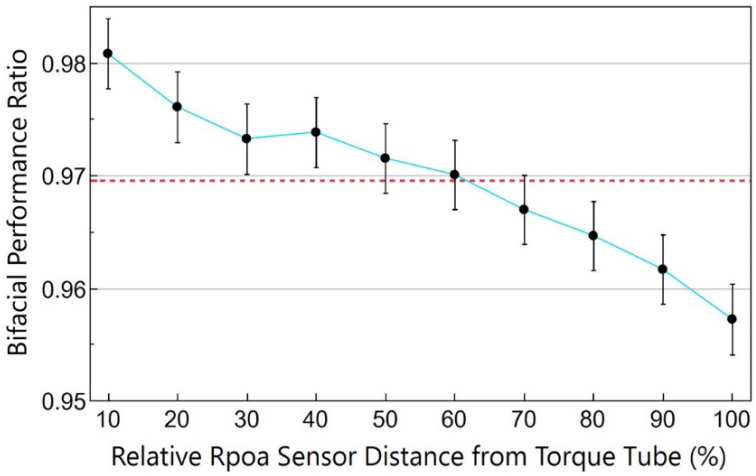

Figure 3-26. Measured hourly bifacial performance ratios of a 6.5-kWp single-axis tracker system using RPOA data from 10 different sensors positions in Roskilde, Denmark (55.6°N, 12.1°E). The black dots show the mean PR_{BIFI} at each sensor position. The error bars show the interquartile ranges at each position, and the horizontal red line shows the grand mean of all sensor positions.

Figure by Nicholas Riedel-Lyngskær

3.3.2 Surface Albedo Measurements

As discussed in Section 2.5.5.1, the surface albedo is the ratio between the total irradiance reflected and the total irradiance received by a horizontal surface (i.e., RHI/GHI). This quantity affects GTI for all tilted collectors, and is particularly relevant for the calculation of RPOA. RHI and GHI are measured by means of two independent pyranometers facing downward and upward, respectively. This two-pyranometer arrangement, if attached together on a boom, makes up an albedometer, as shown in Figure 3-27. On a different spatial scale, the surface albedo is also routinely estimated by remote sensing, using reflectance observations from satellite sensors (Chapter 5).

Figure 3-27. Albedometer equipped with a glare screen for the down-facing RHI pyranometer.

Photo by University of Applied Sciences Upper Austria

The albedo value is representative of the surface just below the albedometer at any given moment in the case of ground-based measurements, or of a much larger pixel in the case of satellite-based estimates (Gueymard et al. 2021). Ultimately, the desired quantity is the spatially averaged albedo of the whole surface below the PV system. If that surface presents significant spatial inhomogeneities, the limited representativeness of the spatially averaged albedo value—or, even more so, that obtained from a single albedometer—increases the uncertainty of the albedo assessment. Therefore, the surface representativeness of albedo is a key factor that directly influences how it should be measured, either with radiometers installed just above the surface (typically at a height of 1.5–2 m) or from satellite-based sensors. This is of practical relevance to BPV projects, as the surface of interest is precisely delimited by the boundaries of the solar field.

In the case of ground-based observations, the surface area for which the measured albedo value is representative is delimited by the FOV of the down-facing pyranometer and by shading objects within this FOV. As a rule of thumb, no shading object should exist at distances less than 13 m or 10 m when the albedometer is at a height of 2 m or 1.5 m, respectively. Moreover, the vertical mounting structure or vertical pole should face away from the equator relative to the instruments. The majority of the energy captured by the downward-facing instrument measuring RHI comes from a limited circular area centered around the instrument position. The installation height of the instrument determines the radius of that area. Figure 3-28 illustrates a scheme of the geometry involved in measuring albedo. As an example, the surface is split into two distinct areas: one with albedo ρ_a sustained by a cone defined by the instrument's height h, view angle θ_a, and radius r, and the surroundings with a potentially different albedo ρ_s. This example assumes that the ground is an ideal diffusely reflecting surface. Hence, the emitted radiance, $L_{\text{reflected}}$, as seen from the RHI pyranometer is constant for all θ and φ, and is proportional to ρ GHI. With this simplifying assumption, the observed RHI can be expressed as follows:

$$\text{RHI} = \int_{\varphi=0}^{2\pi} \int_{\theta=0}^{\frac{\pi}{2}} L_{\text{reflected}} \cos\theta \sin\theta \, d\theta \, d\varphi$$

$$= \text{GHI}\left(\rho_a \int_0^{\theta_a} \cos\theta \sin\theta \, d\theta + \rho_s \int_{\theta_a}^{\frac{\pi}{2}} \cos\theta \sin\theta \, d\theta\right) \quad (3\text{-}5)$$

which results in:

$$\text{RHI} = \text{GHI}\left(\rho_a \sin^2\theta_a + \rho_s(1 - \sin^2\theta_a)\right) \quad (3\text{-}6)$$

Therefore, the total reflected irradiance measured by the instrument is a weighted average of the radiant energy flux reflected by the two areas, where the weighting factor is $\sin^2\theta_a$, corresponding to the area defined by the partial FOV of the instrument when sensing the particular area of albedo ρ_a.

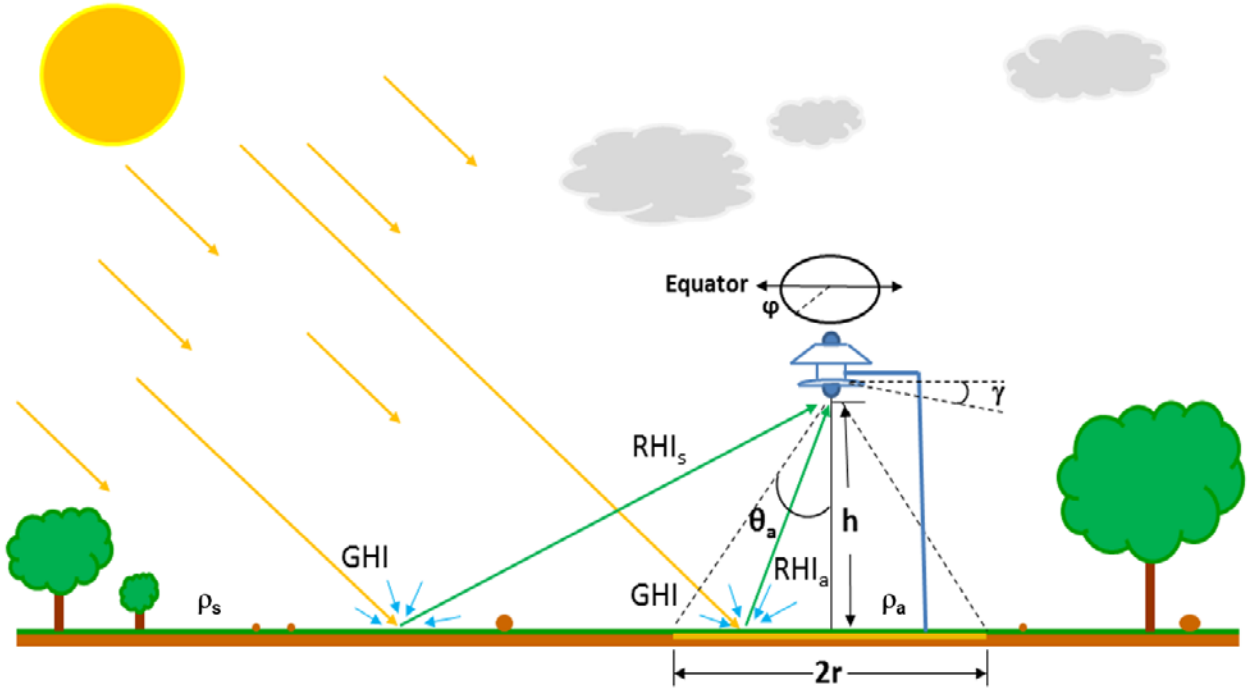

Figure 3-28. Schematic of an albedometer installed at height *h* above a part of ground surface with albedo ρ_a. The FOV of the instrument has a half-angle θ_a, corresponding to a radius *r* at its base. The surrounding surface area has an albedo ρ_s. The obstructed angle by a possible glare screen (used to block direct beams when the sun is near the horizon) is γ.

Image by SolarGIS

Assuming that ρ_a and ρ_s in Eq. (3-6) are identical, the contribution of the circle defined by θ_a relative to RHI is $F = \sin^2\theta_a$. Therefore, the surface closer to the instrument contributes much more to the measured energy than the farthest one, as could be expected. Since $r = h \cdot \tan(\theta_a)$, it is possible to evaluate the size of the area with a relative contribution F:

$$r = h \tan\left(\sin^{-1}\sqrt{F}\right) \tag{3-7}$$

Figure 3-29 shows the contribution of the surface to the measured RHI as a function of the radius of the area below the sensor for different installation heights. For the typical installation heights in PV projects (1.5–2 m), the contribution to the measured RHI increases rapidly with the radius, reaching values above 85% below 5 m. Similar visualizations have been published previously, as in Gostein et al. (2021).

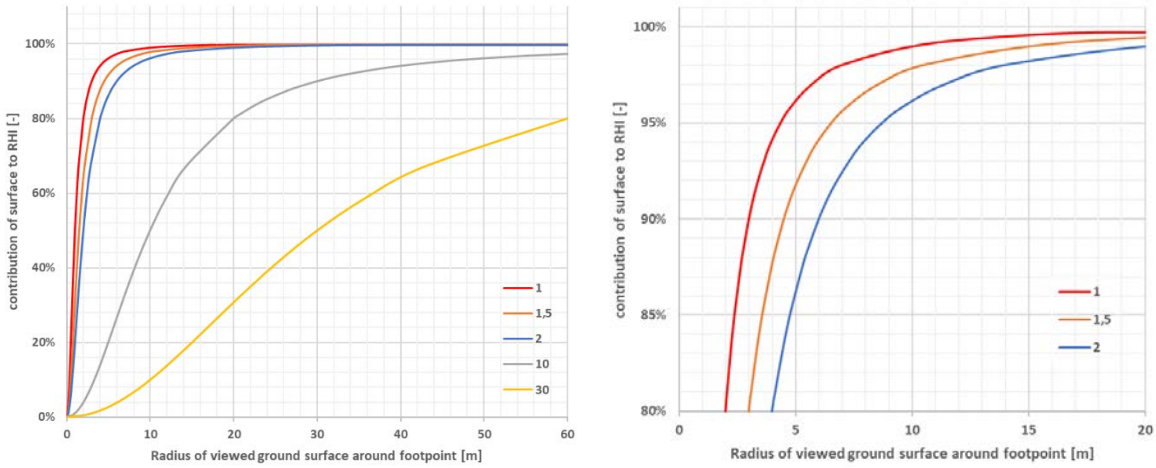

Figure 3-29. Percentage contributions of the circle-shaped area centered at the instrument's footpoint to the measured RHI as a function of its radius for different installation heights (legend shows height in m). The right plot shows a close-up of the left plot for selected installation heights.

Table 3-4 gathers the radius of the circular areas under the albedometer for different installation heights and contributing factors *F*. Thus, for instance, 99% of the total reflected energy measured by an albedometer installed 1.5 m above ground comes from a circle-shaped area with a radius of 14.9 m (700 m^2). For the sake of comparison, the land area required for a PV plant of 5 MWp would be approximately 10^5 m^2 (assuming a fixed-tilt system and a 2-ha/MW coverage factor). Hence, an area of 700 m² could accommodate ≈35 kW of PV.

If the instrument is equipped with a glare screen blocking an angle of 5°, it can sense ($\sin^2(90°–5°)$) = 99.2% of RHI, and the radius of the observed area can be directly calculated as $r = h \cdot \tan(90°–5°)$. The last row in Table 3-4 shows the results for this glare screen and installation heights up to 30 m.

Table 3-4. Radius of the Circle-Shaped Area Under an Albedometer for Different Instrument Heights and Contributing Factors *F*

h [m]	1	1.5	2	3	10	20	30	Viewing Half-Angle for F [°]
r [m], (F = 90%)	3	4.5	6	9	30	60	90	71.6
r [m], (F = 95%)	4.4	6.5	8.7	13.1	43.6	87.2	130.8	77.1
r [m], (F = 99%)	9.9	14.9	19.9	29.8	99.5	199.0	298.5	84.3
r [m], (glare screen with 5°, F = 99.2%)	11.4	17.1	22.9	34.3	114.3	228.6	342.9	85

3.3.2.1 Impacts of Albedo Errors on Bifacial Photovoltaic Yields

To evaluate the importance and value of correctly measuring the surface albedo, it is useful to provide some examples of potential errors in yield calculations caused by erroneous albedo assumptions. For this purpose, a simplified calculation was carried out in Blum and Wilbert (2023) for a BPV plant in Brandenburg, Germany, using default configurations in the PVWatts® simulation software.[10] If the PV plant is built over 50% dry grass (assumed albedo ≈0.21) and 50% sand (albedo ≈0.45) the average albedo would be ≈0.33, but for the example, the albedometer is supposed to be incorrectly installed over the sandy area. Using this albedo value of 0.45 instead of 0.33, the yearly yield is overestimated by 2.7%. A similar example for a PV park in Hamilton, Canada, assuming a combination of 50% wet soil (albedo ≈0.15) and 50% aged snow (albedo ≈0.7) in winter and purely wet soil during the rest of the year, leads to a 5.6% yield overestimation if a single albedometer above the snowy area is used (Blum and Wilbert 2023).

Similarly, in Lara-Fanego et al. (2022), a particular modeled PV plant was analyzed and it was found that the deviation in the annual energy production can be as high as 2.5% for an uncertainty in the albedo estimation of 0.10. Another study of the effect of albedo changes on the yield for six PV parks was presented in Merodio et al. (2023) resulting in albedo sensitivity coefficients between 0.18% and 0.3% yield change per 0.01 albedo change, which is in line with the other examples above.

3.3.2.2 How To Determine a Representative Albedo Value for PV Modeling

Obtaining representative albedo measurements for PV modeling of a planned or existing installation is not trivial. ISO TR 9901 and IEC 61724-1 provide rough recommendations for albedo measurements, but several issues are not addressed in these documents. The following recommendations are more elaborate, but refer to these documents whenever relevant.

Representativeness of the Measurement Location and Duration

Of all the parameters to consider when selecting the most appropriate location for installing an albedometer, representativeness is the most important. Ultimately, the objective is to characterize the surface albedo for the entire area covered by the bifacial modules. Therefore, if a single albedometer is used, it must be placed where the optical conditions of the surface to be sensed and the larger area occupied by the whole solar field are of similar nature and fit each other well. The spatial variability of ground albedo can be quite remarkable, especially over large areas (Gueymard et al. 2021; Wang et al. 2015). It might be necessary to characterize the albedo of different zones, preferably using a few albedometers. The ground maintenance beneath the RHI pyranometer should mimic the maintenance practices that are carried out/planned during the PV plant operation. Satellite-based estimates are also useful because they can provide historical time series for almost any part of the planet and can be site-adapted with ground observations (Lara-Fanego et al. 2022). Because the instantaneous albedo depends on the illumination conditions of the moment, as explained in Section 2.5.5.1, and because vegetation and other ground properties might change drastically even over short periods of time, a marked temporal variation pattern might appear. In particular, seasonal effects and faster (daily, minutely) changes caused by changing sun position, or variable sky conditions and ground properties (e.g., snow, soil

[10] Access the tool at pvwatts.nrel.gov/.

humidity, or vegetation) are clearly visible. This is stated in ISO TR 9901, which also introduces the recommended practice of carrying out samplings that are then combined with long-term data, such as satellite data. Currently, despite the high spatial and temporal variability of surface albedo, most PV modeling software only use one estimate of the local albedo for the whole solar field and each month, or even season or year. Nonetheless, albedo time series cannot be simply characterized by short-term (days or weeks) measurement campaigns, even if the collected data are subsequently used to site-adapt long-term time series provided by a satellite (Lara-Fanego et al. 2022). The required duration of measurement campaigns to ensure proper albedo characterization depends on the characteristics of each location. Ideally, at least 1 year is recommended to correctly analyze seasonal albedo variability. At favorable sites, such as snow-free and monsoon-free areas that are permanently arid, it is possible to obtain a reliable statistical description with only several weeks or months of ground-based albedo measurements.

When dealing with inhomogeneous surfaces at small scale—for instance, near or within a solar power plant—another aspect of the albedo determination is that various surfaces exhibit pronounced directional effects, thus negating the assumed Lambertian (i.e., isotropic) behavior. To remedy this situation, particularly in the case of BPV applications, methods have been proposed to evaluate the angular effects of composite surfaces on the overall effective albedo (Ziar et al. 2019).

Finally, when measuring albedo at a site during the design phase of a projected solar system, another critical question arises: Will the historical albedo at hand be conserved in the future, considering possible changes in the surface characteristics caused by the system's construction (e.g., vegetation removal) or other factors? This question must be answered on a case-by-case basis by the designer. Similarly, after the construction of a PV plant, the ground is often bare, and it takes several months or longer for the vegetation to reach the long-term expected ground conditions, which may also differ from the previous conditions due to the change in microclimate caused by the solar array. This is of particular importance when preparing acceptance tests of PV plants.

Mounting Structure and Height

The height of the albedo measurement should be high enough to achieve a sufficient measurement area with low shading effects, but low enough to facilitate easy maintenance; therefore, heights between 1.5 m and 2 m are recommended, at least if the expected snow heights allow this. In most cases, a height of 1.5 m is preferred for practical reasons because the radiometers' maintenance is easier, and the required object-free area within the FOV of the RHI pyranometer is less. This recommendation is in line with ISO TR 9901, which recommends heights between 0.5 m and 2 m, and with IEC 61724-1, which recommends heights above 1 m. Note that ASTM E1918–21 (ASTM E1918 2023) is not appropriate in solar applications because of the recommended measurement height of only 0.5 m along with a short measurement period.

Conversely, heights of 10 m or more are helpful to evaluate the albedo over a larger ground area, with the goal of comparing such data with airborne or spaceborne observations, for instance. Such heights bring along complex maintenance procedures, however (because of the requirement of frequent cleaning, in particular) so that this setup is rather limited to scientific applications. The albedometer's mounting structure should be between the RHI pyranometer and the nearest pole to reduce the impact of the mounting structure as much as possible.

Objects and Shadows in the FOV of the RHI Pyranometer

Obstructions, reflections, or shading that might affect albedo measurements should be avoided. If objects, such as small bushes or rocks, are under most of the PV modules, it is recommended that such objects are also present under the RHI pyranometer in a similar distribution. If these objects are not present under the RHI pyranometer, their effect on the albedo measurements should be estimated and used to correct them. Only objects that are not characteristic of the surface under the PV modules and that are not specifically included in the PV simulation model should be considered obstructions. Reflections might be related to metal buildings (e.g., silos) and wind turbine masts (e.g., in the case of hybrid wind and solar plants). Finding a location without obstructions, reflections, or shading can be a complex puzzle if the instrument needs to be located inside a small, fenced area or PV park along with other instruments and structural elements. A useful tool for analyzing shadow casting is the online Sundial tool of the Solar Radiation Monitoring Laboratory of the University of Oregon.[11] NREL's SAM PV simulation model can also be used to analyze complex shading effects.[12] According to IEC 61724-1, the area that should be free of objects and shadows is defined as ±80° from the RHI pyranometer. This shadow-free FOV corresponds to an 8.5-m radius if the instrument is at a height of 1.5 m, yielding $F = 97\%$. In practice, it is often difficult to find fully object- and shadow-free areas of such a large extension, particularly if fences are needed (the extra length of fences that would be needed to avoid shadows is costly).

For an RHI pyranometer at a height of 1.5 m, a 5-m radius or more without other objects is recommended, and it can be accepted that shadows fall in this area at times (5-m radius at 1.5 m height corresponds to a FOV of ±73.3° and $F = 91.8\%$). If a larger radius than 5 m is feasible, this is advantageous. Requiring that the area below the pyranometer is always shadow-free might be impossible, meaning some shadows are usually unavoidable, particularly when the sun is low. Measurements taken while a significant part of the area below the RHI pyranometer is shaded should be sorted out. For instance, all albedo data points for SZA>85° can be systematically rejected when calculating the mean daily albedo. Other authors recommend excluding data with SZA > 60° (Merodio et al. 2023). This prevents egregious errors caused by both shading and the imperfect cosine response of pyranometers at large SZAs. A more specific filtering and rejection of suboptimal data can be done based on geometric considerations for the given layout of objects and RHI sensor. For instance, shading is acceptable at least within a half-hour of sunrise or sunset, as allowed by IEC 61724-1 for GTI measurements for PV monitoring, but longer intervals with shading can also be acceptable, depending on their impact on the daily or long-term mean albedo. The valid albedo measurements that have passed that quality control step should be for a long enough period.

Instrumentation for Albedo Measurements

The selection of the two radiometers constituting an albedometer is an important consideration. IEC 61724-1 does not specify the instrument type for RHI measurements, but only for GHI measurements (see Section 3.4.2). The most common setup includes two spectrally flat pyranometers according to ISO 9060, but IEC 61724-1 does not require that both are of the same model or even accuracy class. However, the accuracy of 1-minute data is affected if, for example, a fast-response GHI pyranometer and a slow-response RHI pyranometer are used.

[11] Access the tool at solardat.uoregon.edu/SunDialProgram.html.
[12] Access the tool at sam.nrel.gov/about-sam.html.

Because of the albedo's spectral dependence, the application of two spectrally flat pyranometers allows for the highest accuracy (e.g., ISO TR 9901). This setup also avoids complications related to the calibration conditions, which deviate strongly for the RHI pyranometer because it is typically calibrated in the upward position, that is, based on GHI. The use of non-spectrally flat pyranometers (i.e., photodiodes) for RHI and/or GHI introduces additional spectral errors for the albedo measurement, which might be higher than the typical spectral errors in DHI or GHI measurements. This issue is further addressed in Chapter 4, Section 4.2.10. Using a reference cell to sense RHI is another possibility, but this would result in a quantity different from the true albedo, meaning further research and adaptations of the PV simulation models would be required before such a setup could be applied.

To avoid any RHI overestimation caused by direct sunlight or specular reflections interfering with the down-facing pyranometer dome, a glare screen should always be used to protect the RHI pyranometer.

Further Considerations for Albedo Measurements

Once the solar field has been installed, the artificial shadows cast by the modules and their supporting structures typically affect the surface albedo. These effects should be modeled internally in the PV simulation software.

The albedo of a horizontal surface cannot be measured properly by tilted (POA) pyranometers (Dittmann et al. 2019). Similarly, measuring the albedo of a steep slope is prone to error because the GHI measurement then contains part of the ground-reflected radiation, and the RHI measurement might contain diffuse sky radiation. A method has been recently proposed to address this issue (Ramtvedt and Næsset 2023).

To guarantee that the instruments perform optimally, the specific recommendations of the manufacturer concerning the installation, calibration, and the O&M of the radiometric instrumentation should be followed. In addition, the two radiometers constituting an albedometer are susceptible to soiling. Care is needed to protect the albedometer from flying debris during ground maintenance (e.g., mowing). Efforts should be made to regularly clean both instruments.

Temporal and Spatial Averaging of Albedo Measurements

Customarily, albedo data are measured at high temporal resolutions, just like GHI or GTI. However, the albedo data's temporal resolution is typically degraded to become usable in PV modeling. The average value of albedo over a period of time "*p*", ρ_p, is defined as (Wang et al. 2015):

$$\rho_p = \frac{\mathrm{RHI}_p}{\mathrm{GHI}_p} \tag{3-8}$$

where GHI_p and RHI_p represent the average global and reflected irradiations over the same period, respectively. When RHI is not known, but the albedo and the global irradiance at a determined time "*t*", GHI_t and ρ_t, are known, the average albedo value can be determined as:

$$\rho_p = \frac{\int_p \rho_t \, \mathrm{GHI}_t \cdot dt}{\int_p \mathrm{GHI}_t \cdot dt} \tag{3-9}$$

For example, in a practical case of a daily period and n valid measurements for which SZA is less than, for example, 85°, the daily mean value of albedo, ρ_d, can be directly estimated as the following weighted average:

$$\rho_d = \frac{\sum_{i=1}^{n} \mathrm{RHI}_i}{\sum_{i=1}^{n} \mathrm{GHI}_i} = \sum_{i=1}^{n} w_i \cdot \rho_i \tag{3-10}$$

where the weights w_i are:

$$w_i = \frac{\mathrm{GHI_i}}{\sum_{i=1}^{n} \mathrm{GHI_i}} \tag{3-11}$$

If the underlying albedo time series is not complete (because of data gaps, insufficient data quality, or shadows) gap-filling of the albedo time series should be considered. If areas of different albedo are present over the complete extent of a large PV plant, several albedo stations would be needed. Weighted averages of these area-specific albedos can then be used to obtain the spatially averaged albedo, particularly for use with PV modeling tools that do not allow multiple albedo inputs.

3.4 Measurand and Instrument Selection

In the previous sections of this chapter, several different options to measure solar radiation were presented. It was made clear that different radiation components can be measured and that different solar energy technologies require different measurements. The requirements also depend on the project's phase and size.

A general recommendation about which kinds of measurements are desirable depending on a project's phase and size has been given in the Preface, and is discussed in more detail in Chapter 11. In this section, the discussion is only about projects for which measurements are actually required. In that situation, the first important question is whether a radiometric station does exist nearby and would provide usable measured data over a long enough period. If several nearby solar plants or measurement stations are available, new measurements (and thus the installation of a new station) might not be necessary, thus saving substantial expenditures. According to IEC TC 62862-1-2 (IEC TS62862-1 2017), a separation distance of 10 km can be considered safe for accurate extrapolation. There are special circumstances, however, under which a shorter distance would be preferable or a longer distance would be possible. For instance, from a geographical/meteorological point of view, the nature of the terrain and the required measurands are key factors to consider. On a mountainside, in particular, even a distance of 2 km might be too much for DNI, DHI, and surface albedo because they typically vary more with distance than GHI. Whether the nearby station's data can be effectively used also depends on their quality and detailed technical information, which must be available. Contractual limitations must be considered, and access to the station is desirable.

If no historical dataset exists or is satisfactory, and a large solar power plant is envisioned, a new station needs to be designed, procured, built, maintained, and its data stored and quality-controlled over a period of 1 year before a full analysis of the local solar resource can be done. All of this obviously requires a lot of planning and might slow down the project's financing and

construction itself. As a priority, the project managers and station designers will first need to select the radiation components and the instrumentation that will best support the data and uncertainty goals of the project during each specific project phase. The following subsections explain the most important aspects of the related decisions. Guidance is also provided to make an educated decision when having to choose between digital and analog sensors (Section 3.4.3)

3.4.1 Selection of Measurands

The measurand is the quantity to be measured. The measurands required for a solar project depend on the technology of interest and the project's phase and size. No measurand can be measured exactly, and each method of measurement and instrument has its associated uncertainties and biases. Therefore, it is important to know the desired accuracy for the measurements and what methods and instruments are required to achieve the goals. Most often, there is a trade-off to resolve between desired accuracy, instruments' performances and specifications, and budget limitations. The information in Table 3-5 provides guidance on the required and recommended radiation measurands for various applications. Further meteorological measurements such as wind, temperature, and soiling are discussed in Chapter 5.

Each project phase might require different types of measurements, or the same measurements but with different accuracy requirements. For conciseness, this section only distinguishes between what is required before and after the construction of the solar installation. The technology options included in the table are self-explanatory, but the accuracy cases referred to as "basic" and "enhanced" are much more complex. They refer to the accuracy of the possible yield analysis and design optimization before the plant's construction, and to the accuracy of the monitoring and forecasts during its operation. The goals to be set for the measurements and their uncertainty are influenced by many parameters, including technical, meteorological, financial, and legal boundary conditions. For instance, a large solar park will typically require higher accuracy because the investment's risk is also much higher. Adding radiometers obviously increases the instrumentation and operations budget, but this normally turns out to be a good investment: When considering the overall costs of acquiring the property, building the infrastructure, providing long-term labor for O&M, and underwriting the resources required for data processing and archiving, the additional equipment cost appears nominal in comparison. Ultimately, these equipment improvements will likely pay off by enhancing the project's credibility and reducing the associated financing costs. Better resource data can also improve the validation of system performance and help detect system problems at their early stages. More complex installations that, for example, apply newer technology options will also justify the need for higher yield accuracy and more refined performance analysis. Moreover, a project involving several different contractors might require more exhaustive monitoring measurements than a project that is built, operated, and owned by a single company, because the allocation of responsibilities for possible faults or underperformance is more important in this case.

International standards and specifications that define requirements for monitoring or performance evaluation of solar installations or the creation of representative meteorological years (IEC TS 62862-1-2 for concentrating solar thermal [CST] projects) are of great importance for the selection of the measurands. They are also particularly helpful for projects in which several companies are involved. Table 3-5 additionally mentions the standards that are most relevant for monitoring various solar technologies. To understand the table's recommendations, the different applications of the measurements before and after construction must be considered.

Table 3-5. Required and/or Recommended Measurands for Different Solar Energy Technologies (* for large installations (>50 MW); ** for a fixed-tilt PV system at high latitudes)

Project Phase/ Standards	Accuracy Case	Monofacial PV, Thermal Non-Concentrating	BPV	Concentrating Solar Technology
Before Construction of Large Solar Plants (based on IEC TS 62862-1-2)	Basic	GHI	GHI, RHI (albedo), DHI	GHI, and DNI or DHI
	Enhanced (large plants; complex atmosphere, terrain, technology)	GHI, GTI/PV matched GTI (in the plane(s) that has/have been selected as promising option(s) or tracked), DNI*, DHI*, RHI (albedo)**	GHI, DNI, DHI, RHI (albedo), GTI or PV-matched GTI (in the plane(s) that has/have been selected as promising option(s) or tracked)	DNI, GHI, DHI
Monitoring and Operation for Large and Medium Solar Plants (for PV: IEC 61724-1; for CST: IEC 62862-3-2, IEC 62862-5-2, IEC 62862-3-3; for thermal collectors: ISO 9806)	Basic	GHI GTI or PV-matched GTI	GHI GTI or PV-matched GTI RPOA (spectrally matched or broadband) or RHI (albedo)+DHI	DNI or DHI and GHI for medium plants
	Enhanced	GHI GTI PV-matched GTI DNI* DHI* RHI (albedo)**,	GHI GTI PV-matched GTI RPOA (spectrally matched or broadband) RHI (albedo) DHI DNI*	DNI GHI DHI

3.4.1.1 Measurands Recommended Before Construction of Large Solar Plants

Before the construction of large power plants, radiation measurements are used mainly to enhance the accuracy of satellite-derived long-term datasets with different site-adaptation methods (see Chapter 7, Section 7.6). Typically, only broadband GHI and/or DNI datasets are used in solar resource assessments. Only a few satellite-derived datasets include spectral data (Mueller et al. 2012; Xie and Sengupta 2018). Such data are not available for the full globe, and common current PV simulation software cannot directly make use of spectral data. Still, spectral data could be useful for the selection of the most suitable module technology in a solar power plant and for increasing the accuracy of yield estimations for some technologies. However, the fact that typically broadband long-term datasets are used strongly affects the requirements for the measurands discussed in the following subsections for the different technologies.

Monofacial Photovoltaic Plants and Non-Concentrating Solar Thermal: Basic Accuracy Case

For monofacial PV plants and non-CST systems, the basic option recommends the measurement of broadband GHI only. Long-term GHI data can be obtained after site adaptation with those on-site measurements. The conversion from GHI to GTI can be done subsequently with decomposition and transposition models (see Chapter 7, Section 7.3.2), but these add uncertainty. Measuring GTI for the anticipated tilt and orientation of the collectors, or measuring only the PV-matched irradiance would eliminate this added uncertainty, but currently this is only helpful as a supplementary measurement because long-term satellite-derived datasets typically do not provide these quantities. Moreover, specific site-adaptation methods have not been developed yet for them.

Monofacial Photovoltaic Plants and Non-Concentrating Solar Thermal: Enhanced Accuracy Case

In the enhanced accuracy case for these technologies, it is recommended to measure additional radiation variables, including GTI, as well as PV-matched GTI in the case of PV systems. Additional GTI measurements are advantageous for resource assessment because they might be used to select the best transposition (or decomposition and transposition) model for the site under scrutiny. One challenge for GTI measurements is selecting the right orientation and tilt of the GTI pyranometer before starting the measurement campaign. The optimal tilt and orientation depend on various factors: Latitude, meteorological conditions (cloudiness) at the site, shading effects, and electricity market value, among others. A preliminary estimate of the optimum tilt angle can be obtained from the global solar atlas[13] or, more elaborately, from system simulations using satellite-derived irradiance data.

GTI measurements are more accurate than modeled GTI estimates and can be used as direct input for detailed solar power plant modeling with appropriate simulation software. The PV-matched GTI measured using PV reference cells (Section 3.2.6) provides further advantages for PV modeling. PV power plant models include effects such as reflectance losses and spectral mismatches to derive the power output from broadband irradiance. Because modeling these effects adds uncertainties and systematic biases, the usage of reference cells offers an attractive alternative: If irradiance is measured under a flat glass cover, the reflectance losses do not need to be modeled; moreover, if the irradiance measurement is already weighted by the spectral response of the reference cell, then no spectral correction model is required. In other words, if the PV-matched GTI is measured, then the expected PV system output can be calculated with substantially fewer modeling steps, thus eliminating the uncertainty those would contribute. Therefore, including a tilted reference cell in a ground measurement station before the plant construction can be useful.

Adding reference cells to the instrument lineup in a resource assessment station before finalizing all details of the plant's design has possible drawbacks, however: The exact technology and design features (tracked vs. fixed, tilt and orientation angles) that will be eventually used in the power plant might not be known at that stage yet, as previously mentioned. This can be countered by deploying multiple reference cells, if necessary. Another important limiting factor is the available software used for PV yield simulations. Some do not let the user selectively

[13] Access the solar atlas at globalsolaratlas.info/map.

bypass certain model calculation steps, which would be required for optimal use of PV reference cell irradiance measurements. Prior to deploying reference cells to measure GTI, therefore, the capabilities of the simulation software must be known, or the modeling software should be chosen accordingly.

The uncertainty of PV yield calculations can also be decreased by measuring DNI and/or DHI in addition to GHI. The transposition procedure that derives GTI is significantly more accurate when measured DNI and/or DHI data are also available in addition to GHI, in particular for steep tilt angles (see Chapter 7, Section 7.3.2). Further, the additional availability of DNI data usually results in more accurate PV simulations because the impacts of incidence angle and shading affect the direct component, for the most part. A critical advantage of measuring GHI, DNI, and DHI with independent sensors is related to the quality control of the data and rapid detection of instrumental problems. Measuring the three components provides both the basis for the most rigorous data quality protocols and a certain redundancy for instrument failure, as described in Chapter 4. Depending upon the radiation component and the instruments, this advantage goes beyond what can be achieved with a redundant measurement of the same type. However, redundant measurements of the same component are also highly beneficial. Another advantage of measuring several radiation components is that it provides increased flexibility for the selection of the most appropriate solar technology option or mix. For instance, depending on the site's terrain conditions, a mixture of tracked PV and fixed-tilt PV could prove advantageous. Similarly, measuring the albedo could help evaluate the eventual bifaciality gain, optimize the design of a BPV system, and enhance the accuracy of the PV yield predictions.

The above recommendations on the measurands hold for both fixed and tracked PV systems, but in the latter case the importance of measuring DNI is greater than in the former case. Therefore, it is more likely that enhanced resource campaigns for tracked systems include DNI, and optionally DHI measurements, too. Tracked PV systems can also be influenced more by the albedo, and this is also the case for systems with large tilts (e.g., at high latitudes).

Bifacial Photovoltaics

For BPV, the measurands mentioned above for monofacial PV should be complemented by DHI and RHI data, even in the basic accuracy case, so that the albedo, RPOA, and bifacial gain can be estimated accurately.

The above discussion regarding possible additional measurands for monofacial PV systems for the enhanced accuracy case is also relevant for the bifacial systems. In the enhanced accuracy scenario, additional DNI measurements are particularly valuable for bifacial systems.

Concentrating Solar Thermal

For CST projects in general, an IEC technical specification on the creation of annual solar datasets for plant simulation (IEC TS62862-1 2017) exists, as well as best practice documents (Hirsch et al. 2017). Here, only the DNI resource is typically used for modeling the plant yield, and in principle only a pyrheliometer would be sufficient for a resource assessment campaign. However, the basic option is to measure GHI and either DHI or DNI and not a measurement station with a solar tracker and a pyrheliometer, because this is much more complex and costly to operate than the various alternative options (discussed in Section 3.2.5) that do not need a solar

tracker. The pros and cons of the tracker-based solution vs. other measurement options are discussed below in Section 3.4.2.

The enhanced accuracy case includes the separate measurement of all three components to enable the best data quality control methods. This is most important for CST projects because their capital costs are considerable, making them more difficult to finance. For better bankability, the uncertainty in the solar resource must be as low as possible, which can be achieved by measuring the three components independently and applying the most stringent quality control process. The measurement of circumsolar radiation is not included in this discussion, although it might be required, depending on the CST system; see Chapter 5 for more details.

3.4.1.2 Measurands for Monitoring and Operation for Large and Medium Solar Plants

To operate and monitor solar power plants, different measurements from the resource assessment phase are typically required.

For PV plants, IEC standard 61724-1 defines the quantities to be measured for monitoring purposes. GTI (or PV-matched GTI) and GHI measurements are required for the highest accuracy level defined in the standard. GHI is always necessary to compare the on-site measurements with satellite-based radiation datasets. For BPV systems, the rear-side irradiance (RPOA) and/or albedo (see Section 3.3.2) must also be measured. Diffuse irradiance measurements are recommended if RPOA is estimated using albedo data. The number of sensors of each type depends on the peak power of the PV system. The lower monitoring accuracy class only requires GTI measurements because the actual on-site GHI can be replaced by remote meteorological GHI or satellite-based GHI. This lower-accuracy class is typically not adequate for utility-scale PV plants, however.

For the operation of CST projects, individual standards are available for different technologies as provided in Table 3-5 (IEC 62862-3 2018; IEC 62862-5 2022; IEC TS 62862-3-3 2020). They define the instrumentation that should be used for performance testing at the power plant. These standards can also be used as the basis for general monitoring of the installations, but the requirements for operation might be less strict. DNI is required for all cases; GHI and DHI are recommended to improve the quality control process of the radiation measurements.

For flat-plate solar thermal collectors, ISO 9806 (ISO 9806 2017) requires GHI and GTI measurements for testing. Depending on the type of collector under test, longwave radiation might also have to be measured with a pyrgeometer in the collector's plane. However, ISO 9806 is about testing rather than regular monitoring. In the latter case, the measurement of GTI and GHI suffices.

3.4.2 Selection of Instruments

For instrument selection at any stage of a project, it is generally safest to adhere to the available standards where applicable. This prevents technical complications and facilitates communication and the decision process.

3.4.2.1 Instrument Selection Before the Construction of a Power Plant

For resource assessment before the construction of a power plant, there are no standards that define which instrument type should be used for a specific measurand or solar energy

technology. Hence, guidelines for the instrument selection suitable to this project phase are provided below for each measurand.

For GHI and GTI, ISO 9060 classified pyranometers are recommended, and Class A pyranometers are preferable.

For PV-matched GTI, usage of a PV reference cell or module that matches the characteristics of the envisioned PV technology is recommended. A spectroradiometer might alternatively be used. Although this is more costly and does not include the incidence angle effect of PV, it delivers more detailed spectral data so that a wide range of PV materials can be evaluated.

For guidance on the instrument selection before the plant construction for RHI and RPOA, refer to sections 3.3.1, 3.3.2 and 3.4.2.2.

If DNI or DHI measurements are needed, or if a highly accurate resource assessment is desired, the station designers must choose between a solar tracker and alternative measurement devices for DNI and DHI. If the best-achievable field measurement uncertainty is aimed for and if the required maintenance can be guaranteed, an ISO 9060:2018 Class A spectrally flat pyrheliometer in combination with ISO 9060:2018 Class A spectrally flat pyranometers for GHI and DHI on a two-axis tracker with a shading ball/disk are recommended. This is typically used for most PV projects of very large size (>100 MW installed capacity) and for many utility-scale CST projects. In many publicly available datasets and publicly funded measurement campaigns, this kind of weather station is referred to as “Tier 1” station (ESMAP 2020). However, considering that a low uncertainty in the resource assessment results is key to the successful financing of a large project, station designers must consider not only the accuracy under optimum maintenance conditions, but also under the suboptimal conditions that may occur in field measurement campaigns despite best efforts. Measuring the three radiation components with a solar tracker, a pyrheliometer, and two pyranometers induces a significant maintenance effort. Without trained personnel providing daily cleaning, visual detection, and prompt corrections in case of tracker malfunction or alignment errors, data gaps and increased uncertainties are common. Therefore, simple, less maintenance-intense instruments, such as RSIs, usually in combination with a thermopile pyranometer for GHI, can be a better option to determine the three radiation components. If the DHI or DNI measurement is only required for the calculation of RPOA, using a solar tracker can be seen as an unnecessary complication, and RSIs or other alternative DHI or DNI sensors with similar or better accuracy are recommended (see Section 3.2.5). This kind of weather station is often referred to as a “Tier 2” station.

At the onset of the resource assessment campaign, that is, when the weather station is being procured, station designers might already have to decide whether its instruments could later become part of the power plant monitoring system. This is possible inasmuch as the resource assessment station’s design follows the best practices and standards, including those for the ulterior monitoring phase. It is stressed here that the best practices and standards for monitoring or system testing somewhat differ from those intended for the initial resource assessment phase. For example, one meteorological station is usually sufficient per project site, unless the solar field has an area that justifies the assumption of varying microclimates. The resource assessment station that operated earlier might not be in the same area. The cost of completely moving that station (or just its instruments) to the monitoring location can be potentially substantial, hence

the costs and advantages vs. disadvantages of operating two distant stations rather than one should be evaluated.

From another perspective, the use of pyranometer ventilation units needs to be considered carefully. At "greenfield" resource assessment sites, they add substantial cost because they need a larger power supply, whose costs might outweigh the expected benefits. From another perspective, as mentioned earlier, redundant measurements of the same radiation component can be of interest to avoid data gaps and increase accuracy.

3.4.2.2 *Instrument Selection for Operation and Monitoring for Large and Medium Solar Plants*

For monitoring and operation purposes, specific standards exist for solar energy technologies. They provide much more information on the required instruments than those available for resource assessment applications before plant construction. As such standards are technology-specific, the recommendations for instrument selection are discussed for each of the solar technologies.

Photovoltaic Monitoring and Operation

IEC standard 61724-1 for PV monitoring defines the instrument types allowed according to different monitoring accuracy classes. For front-side POA (GTI), PV monitoring Class A systems use ISO 9060 spectrally flat Class A pyranometers or PV working reference devices per IEC 60904-2 (IEC 60904-2 2023) with calibration uncertainties below 2%. For GHI, ISO 9060 spectrally flat Class A pyranometers are required for the highest monitoring class. For Class A monitoring of the RPOA of BPV systems, less-accurate pyranometers and reference cells are allowed. Class B monitoring also allows less-accurate pyranometers or reference cells. This monitoring class can be of interest for small- or medium-sized power plants. In PV monitoring, the accuracy of yield predictions can be improved if using reference cells, as described above. Some of the PV simulation models that are used for PV monitoring or capacity testing can use the PV-matched GTI as input. Moreover, measurements with both pyranometers and reference cells can further improve the PV modeling accuracy. Note that the application of PV reference cells is in practice limited to PV-matched GTI and RPOA. They are not designed to sense GHI, and actually a few of them collect water when mounted horizontally, thus yielding large errors. If a low-cost substitute for a thermopile pyranometer is needed, a photodiode pyranometer is usually the better choice. IEC 61724-1 does not define which instruments must be used for RHI or DHI measurements. For DHI, that standard provides different examples, including trackers with shading disks or balls and RSIs. The recommendations above related to DNI or DHI measurement for solar resource assessments also apply here. Trackers should only be used if the highest accuracy is required and if the highest degree of maintenance can be sustained. In most cases, other measurement methods to derive DHI or DNI are more appropriate; sensors such as RSIs or alternatives with similar or better accuracy should be used (see Section 3.2.5). For RHI, see the recommendations in Section 3.3.2.

Concentrating Solar Thermal Monitoring and Operation

Virtually all utility-scale CST plants use ISO 9060 Class A pyrheliometers to measure DNI for monitoring and operation. This also agrees with the CST-specific recommendations from the IEC standards for system testing mentioned in Table 3-5. ISO 9806 for tests of thermal collectors

contains recommendations for various solar thermal systems, including concentrating collectors. In the latter case, the recommended instrumentation depends on the concentration ratio. For concentration ratios greater than 3, ISO 9060 Class A pyrheliometers or better should be used. For lower concentration ratios, ISO 9060 Class A pyranometers with shading rings and a GHI pyranometer can alternatively be used to calculate DNI, despite the disadvantages explained in Section 3.2.5 and the significantly higher uncertainties of such an indirect method. Other methods to derive DNI without using a solar tracker are considered sufficient for CST, particularly for smaller installations. This does not contradict the CST-specific IEC standards nor ISO 9806, as these are for testing and might be too strict for general operation and monitoring. Compared to non-concentrating collectors, CST technologies depend more directly on continuous radiation measurements because of the control procedures of the installation (e.g., heat transfer fluid mass flows). Thus, monitoring DNI accurately is of interest even for small-scale installations, for which the data acquisition and maintenance costs contribute relatively more to the overall costs. At present, there is no consensus regarding the required number of DNI radiometers per CST plant. Typically, one to five DNI radiometers are used for utility-scale systems in practice.

Monitoring and Operation of Non-Concentrating Solar Thermal Collectors

For testing non-CST collectors, ISO 9806 mandates ISO 9060 Class A pyranometers for both GTI and GHI measurements. That standard addresses test procedures rather than monitoring per se; for the latter, the requirements might be less strict compared to the tests covered by the standard so that pyranometers of a lower class can be sufficient depending on the installed power.

3.4.3 Selection of Instrument Output Type or Interface

Until recently, nearly all radiometers provided a small, internally generated voltage or current as output signal. Many models are now available with an optional digital interface or with only a digital interface. A digital interface contains electronics to perform the analog-to-digital conversion and a microprocessor to manage the communication with the data logger. This leads to various internal and external aspects to consider when choosing such an instrument.

Internally, the dedicated analog-to-digital converter can in principle be optimized and better matched to the detector signal than a generic external data logger. Further, the microprocessor makes it possible to apply calibration factors and carry out more sophisticated corrections—for example, to reduce temperature dependency, improve linearity, or compensate for thermal lag (i.e., reduce response time). On the other hand, the active electronic components generate a small amount of heat, which changes the thermal balance of the sensor. In some thermopile instruments, this may lead to the need for more temperature correction internally. If the energy consumption is more than ≈1 watt, it might have the beneficial side effect of reducing dew or frost formation, as has been observed on some digital reference cells. Finally, the presence of the microprocessor is key to the implementation of new internal features at only a small incremental cost, such as sensors for instrument tilt, air pressure, or internal humidity, which can be very useful for maintenance purposes.

To which extent all the above factors influence the final accuracy of the irradiance measurement varies by make, model, and user, as usual. Both digital and analog pyranometers and pyrheliometers are subject to the same accuracy classes defined in ISO 9060. Therefore, an

analog Class A instrument and its digital version can be expected to achieve the same Class A level of measurement accuracy. However, a survey of manufacturer specifications for digital instruments suggests that the digital versions of some of their best instruments can actually outperform the analog version.

The external factors that can help select between analog and digital instruments concern usability more than measurement accuracy. Mechanically, the connectors and cables are often similar to or the same as the analog versions, but length constraints might differ. All manufacturers have adopted the same communications standard, RS-485, which permits two-way serial communication (alternating send/receive) using two wires. Contrarily to analog interfaces, however, multiple digital instruments can be connected to the same two wires. This allows a cluster of sensors on a sun tracker or a weather tower to be connected together and to use a single cable leading to the data logger. Of course, the logger must also have an RS-485 interface, but one such interface can serve for multiple instruments. The information exchange on this physical connection almost always uses the Modbus protocol. With that in place, the instrument measures continually and stores the data (e.g., irradiance or temperature) in specific memory locations (registers), whereas the logger is programmed to periodically query those values and store them in a log file—together with any analog measurements it might be taking. Because the digital instrument's calibration factor is stored in the instrument, this no longer needs to be manually entered in the logger program or updated when the instrument is replaced, thereby eliminating a potential source of error. However, it is always worth double-checking that the information stored on the sensor matches the calibration certificate in case of manufacturer/calibration facility error.

Despite the widespread adoption of the RS-485 and Modbus standards for radiometers, there are differences in small but very essential details, such as the default and supported communication speeds (baud rate), default instrument address, or register numbers. Usually, a new instrument must be connected to a computer so that a manufacturer-specific software program can be used to configure the communication settings. Then the logger is programmed with the manufacturer-specific register numbers. The complexity of the setup task grows with the number of different sensors, sensor types, and manufacturers involved. Further, manufacturers continue to develop and improve their instrument software (firmware) and configuration programs, so the setup task details are bound to evolve over time.

Despite the substantial differences noted above, the way by which these external factors might affect the choice of radiometer output type depends largely on the technical context. If the planned or existing infrastructure includes digital networks, such as in large PV power plants, then digital is the likely choice. Conversely, if the planned or existing infrastructure includes other analog instruments and compatible data loggers, then analog is probably more appropriate. There is one specific application, however, for which analog sensors are currently still the only option: for high-speed or precisely synchronized measurements every 10 ms or less. This is technically not impossible to achieve with digital electronics, but the available products are not designed with this high-speed capability.

3.5 Measurement Station Design Considerations

To collect useful solar resource data, the successful design and implementation of a solar resource measurement station or a network of stations require careful consideration of the

elements discussed in this section. The measurement stations also often include additional meteorological instrumentation, such as anemometers, wind vanes, thermometers, or hygrometers. These measurements are described in Chapter 5. The general recommendations—such as station security and data logging—described in this section also apply to these instruments. Many aspects discussed in this section are also addressed in the CIMO guide (WMO 2018) and the World Bank's Energy Sector Management Assistance Program (ESMAP) Terms of Reference for Solar and Wind Measurement Campaigns (ESMAP 2020). These guides contain some guidance on equipment design, documentation, reporting, etc. The ESMAP document distinguishes between the Tier 1 and Tier 2 weather stations, referring mainly to stations including a solar tracker with measurements of DNI, DHI, and GHI (Tier 1), and stations where only two components are measured (Tier 2). This nomenclature is also used in the appendix of this chapter, which contains checklists for the various tasks to be performed from site selection to installation, as well as exemplary plans and photos of different types of stations.

3.5.1 Location

The primary purpose of setting up a solar resource measurement station before the construction of a solar power plant is to collect data that will ultimately be used by an analyst to accurately characterize the solar irradiance and relevant meteorological parameters at that specific location. Ideally, the instruments would be within the targeted analysis area. In some cases, however, separation distances might be tolerated depending on the complexities of local climate and terrain variations (Gueymard and Wilcox 2011). Less variability in terrain and climate generally translates into less variability in the solar resource over larger spatial scales. These effects should be well understood before determining the final location of a measurement station (see Chapter 6 for additional details on spatial variability and Chapter 11 for more discussion of the effect of distance between the station and plant site). The proximity to the target area must be weighed against operational factors, such as the availability of power, communications, maintenance staff, security of the station against theft/vandalism/animals, and access for maintenance, as discussed in this chapter. Considerations should also include the possible effects of local sources of pollution or dust—for example, traffic on a nearby dirt road that could impact the measurements.

Local solar radiation measurements are required for medium or large power plants (see Chapter 11). Further, measurements can be helpful for other solar energy purposes, such as testing power plant components or for PV power forecasting for many small PV systems in the vicinity of the measurement location. In power plants and for component or system tests, the position of the station must be such that the measurements reflect the conditions of the power system as accurately as possible. For large power plants, this means several distributed stations can be required. For PV systems, IEC 61724-1:2021 defines the number and accuracy class of the required radiometers within the PV power plant, depending on the system's peak power.

When measurement stations are constructed in metropolitan areas, industrial areas, or near electrical substations or solar power plants, consideration should be given to possible sources of radio-frequency signals and electromagnetic interference that could impart unwanted noise in sensors or cables. For example, the same flat roof on a tall building that could provide an attractive unobstructed site for solar measurements could also soon become the ideal location for radio or television broadcast towers or other antennas. Such sites should be investigated for interference with the irradiance sensors and monitoring station. See Section 3.5.4 for additional information regarding proper shielding and grounding.

Instrument placement is also an important consideration. If nearby objects—such as trees or buildings—shade the instruments for some period during the day, the resulting measurement will not truly represent the available solar resource in a nearby unshaded part of the site. Distant objects—especially mountains—could be legitimate obstructions because the shadows they cast are likely to produce an influence beyond the instruments' location. However, this shading effect must be documented and considered, as the station location might not be representative for the whole solar field or the satellite pixel. Conversely, nearby objects can potentially reflect solar radiation onto the instruments, resulting in measurements that do not represent the conditions for the power plant. Such cases could include a nearby wall, window, or other highly reflective object. The best practice is to locate instruments far from any objects in view of the instrument's detector. The recommendations from WMO (2018) for radiation apply, if not otherwise stated.

The easiest way to determine the quality of solar access is to scan the horizon for a full 360° of azimuth and note the elevation of any objects protruding into the sky above the local horizon. Look for buildings, trees, antennas, power poles, and even power lines. Most locations will have some obstructions, but whether they will be significant in the context of the necessary measurements must be determined. Camera-based devices can be used to assess any obstructions, including far shading from mountains, trees, etc., and the assessment can be easily documented and quantified, such as seasonal shade effects. Generally, pyranometers have an insignificant sensitivity to sky blockage within approximately 5° of elevation above the horizon. Pyrheliometers, however, are more sensitive because objects can completely block DNI, depending on the daily path of the sun throughout the year. The duration and amount of daily blockage are factors related to the object's width and height above the horizon. On an annual basis, the number of blockage days depends on where along the horizon the object lies. To be a concern, the object must be in the area of the sun near sunrise or sunset, the time and azimuth of which vary throughout the year. For most of the horizon, objects blocking the sky will not be a factor because the sun rises in a limited angular range in the east and sets likewise in the west during sunset (e.g., at 40° N latitude, sunrise occurs approximately 60° from true north at the summer solstice and 120° from true north at the winter solstice). The farther north in latitude (or south in the southern hemisphere) the site is located, however, the greater the angular range of these sunrise and sunset areas are of interest. Sun path charts as generated by appropriate tools[14] provide the solar positions throughout the year. A solar horizon map, or even a sketch of obstructions by elevation and azimuth, can help determine the areas where horizon objects will affect the measurement (Figure 3-30). Such maps can be created with digital cameras and software. Several commercial products using curved mirrors and apps for smartphones exist. In addition, modern cell phones can take a 360° panorama picture, which can be very useful in understanding the obstructions on the horizon.

[14] One such tool, from the University of Oregon Solar Radiation Monitoring Laboratory, can be accessed at solardata.uoregon.edu/SunChartProgram.php.

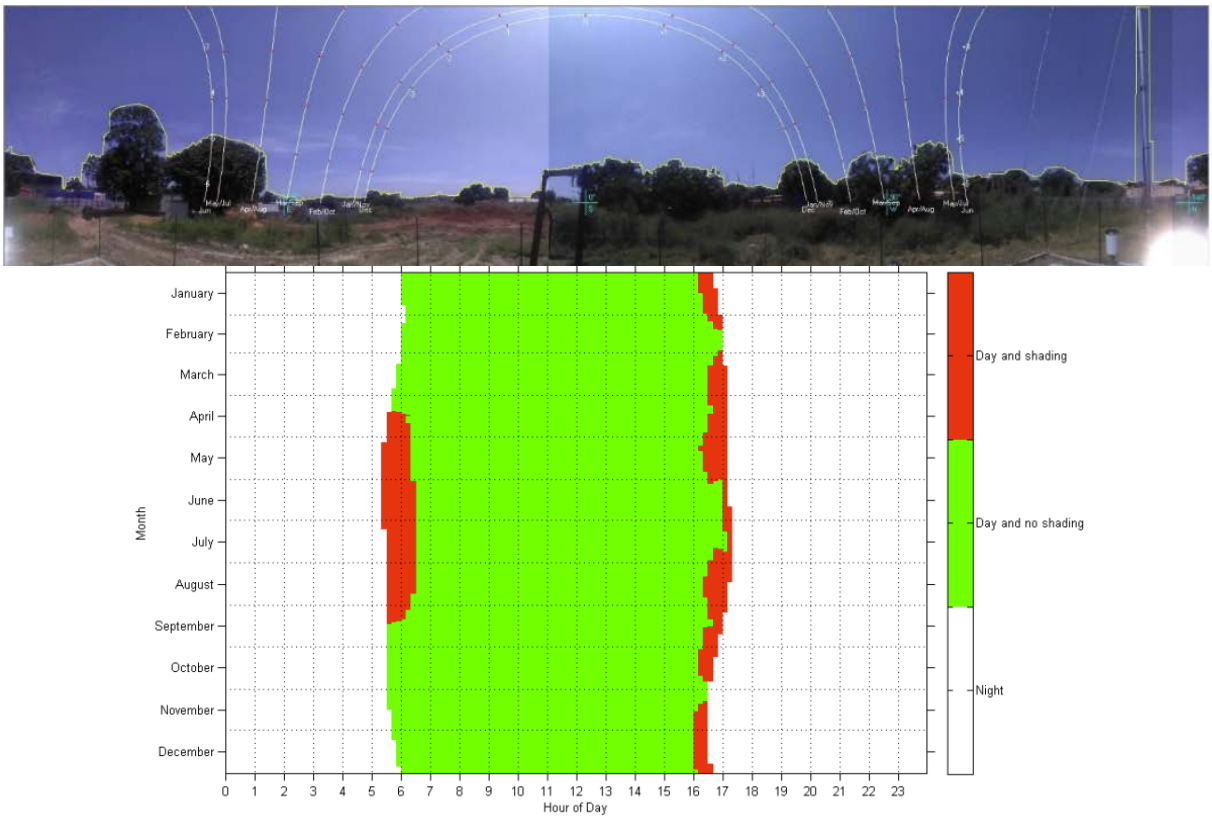

Figure 3-30. Example shading analysis: horizon line from the perspective of a tracker-mounted pyranometer and sun path throughout the year (up) and resulting shading plot (bottom).

Image from CSP Services GmbH

Considerations for locating a station should also include a variety of environmental and other factors, such as wildlife habitats, migratory paths, drainage, antiquities or archeological areas, unexploded ordnance (UXO) threats in areas of previous armed conflict, and nearby industrial/mining/agricultural activities. Refer to WMO (2018) for further general guidance. A very important factor is the availability of communication infrastructure (mobile phone network or landline internet). Its non-presence may result in significant additional costs for satellite communication solutions.

Generally, site selection is often a trade-off between desirable site features and what is actually achievable in reality. For example, a safe site with nearby presence of maintenance personnel, but with some amount of sensor shading is often preferable over a non-shaded site in which measurements are prone to interruption by theft or vandalism.

In any case, the site selection should be carefully documented and explained in the station documentation, such as in the installation report. An example for a site selection checklist can be found in Appendix A.2 of this chapter.

3.5.2 Station Security and Accessibility

Measurement stations can cost tens of thousands or even hundreds of thousands of dollars. Although the measurement equipment is typically not the target of thieves seeking property for resale, the common PV modules and batteries used for the station's power supply are subject to

theft and should be protected. Vandalism might be even more likely than theft. The less visible and accessible the station is to the public, the less likely it will be the target of theft or vandalism. For example, instruments mounted on a secured rooftop are less likely to attract unwanted attention than those unprotected beside a highway. Lack of visibility is the best defense against vandalism.

Security fences should be used if people or animals are likely to intrude. Within a fenced solar power plant, no additional fences are required. Fencing should be at least 1.8 m tall, preferably with barbed wire and fitted with locking gates in high-profile areas where intrusion attempts are likely. Less elaborate fences might suffice in areas that are generally secure and where only the curious need to be discouraged from meddling with the equipment. In remote venues with few human hazards, cattle fence paneling (approximately 1.2 m tall) might be advisable if large animals roam the area. The fencing should be sturdy enough to withstand the weight of a large animal that might rub against the compound or otherwise be pushed or fall against the fence. It might not be possible to keep smaller animals out of the station compound, and precautions should be taken to ensure that the equipment, cabling, and supports can withstand encounters with these animals. Rodents, birds, and other wildlife could move through the wires or jump over or burrow under fences. Signal cabling between modules or sensors at or near ground level is prone to gnawing by rodents and should be run through a protective conduit or buried. Any buried cable should be either specified for use underground or run through conduits approved for underground use. Underground utilities and other objects should be investigated before postholes are dug or anchors are sunk.

If fences are used, they must be considered a potential obstacle that could shade the instruments and the albedo measurement area or reflect radiation to the instruments. All radiometers except RHI pyranometers should be positioned at least above the line between the horizon and the fence (including barbed wire), if only by a few millimeters, to prevent any shading of the sensor. In any case, they should be under an elevation of 3° as seen from the sensor, corresponding to Horizon Class 1 for all radiometers at all latitudes according to WMO (2018). An optical measurement plane for the station should be established such that the solar sensors are above all other equipment and infrastructure. This assumes that the pyranometer is mounted in a horizontal position and that the pyrheliometer is installed on a solar tracker. Tilted pyranometers should have an unobstructed view of the ground and sky in front of them. For albedo measurements, fences cause measurement errors if the area under the downward-facing pyranometer is shaded (see Section 3.3.2 for details). This must be considered for the station design. The recommendations from WMO (2018) concerning obstacles should be followed. Deviations between WMO (2018) and the actual station design are acceptable if these deviations affect not only the measurement station but also the solar energy system that is analyzed using the measurements. If nearby towers are unavoidable (e.g., wind mast of the weather station), the station should be positioned between the tower and the equator (e.g., to the south of the tower in the Northern Hemisphere) to minimize shading. The radiometers should be positioned as far as possible from the tower—at least several meters—so that the tower blocks as little of the sky as possible. Between the Tropics of Cancer and Capricorn, this distance must be large enough to also avoid noon time shading when the sun's zenith angle appears to exceed 90°. Nevertheless, analog radiometer signal cables should be shorter than 50 m to avoid losses caused by line resistance. The tower should also be painted a neutral gray to minimize strong reflections that could contaminate the solar measurement. These guidelines assume that the tower is part of the

measurement station proper and that the site operator has control of the placement or modification of the tower. Without that control, the radiometers should be placed as far as possible from the tower.

Access to the equipment must also be part of a station's construction plan. Because routine maintenance is a primary factor affecting data quality, provisions must be made for reasonable, safe, and easy access to the instruments. Factors could include ease of access to cross-locked property, well-maintained all-weather roads, and roof access that could be controlled by other departments. Safety must also be a consideration. Locations that present hazardous conditions—such as rooftops without railings or that require access using unanchored ladders—must be avoided. The same applies to the position of sensors: they must be accessible any time for safe cleaning and maintenance.

3.5.3 Power Requirements

Ongoing measurements require a reliable source of electrical power to minimize system downtime from power outages. In some areas, power from the utility grid is reliable, and downtime is measured in minutes per year. In other areas, frequent and enduring power interruptions are routine. At remote sites, usually no access to the electric grid exists. Depending on the tolerance of the required analysis to missing data, precautions should be taken to ensure that gaps in the data stream from power outages do not seriously affect the results. The most common and cost-effective bridge for power outages is an uninterruptible power supply (UPS). The UPS can also filter out unwanted or harmful line voltage fluctuations that can occur for a variety of reasons. It has internal storage batteries that are used as a source of power in case of an AC power interruption. When the AC power is interrupted, internal circuitry makes an almost seamless switch from grid-connected AC power to AC provided through an inverter connected to the battery bank. When power is restored, the UPS recharges the internal battery from the AC line power. Power loss is detected quickly, as is switching to the battery, and it is measured in milliseconds or partial line cycles. Some equipment could be particularly susceptible to even millisecond-long power interruptions during switching and should be identified through trial and error to avert unexpected downtime despite use of the UPS.

The UPS is sized according to:

- Operating power: How much can the UPS continuously supply either on or off grid-connected AC power?
- Operating capacity: How long can the UPS supply power if the grid connection is interrupted?

Users should estimate the longest occurring power outage and size the UPS for the maximum load of attached devices and the maximum period of battery capacity. Batteries should be tested regularly to ensure that the device can still operate per design specifications. This is most important in hot areas (such as deserts) because batteries could overheat and become inoperative (temporarily or permanently). Internal battery test functions sometimes report errors only when batteries are near complete failure and not when performance has degraded. A timed full-power-off test should be conducted periodically to ensure that the UPS will provide backup power for the time needed to prevent measurement system failure.

At remote locations where utility power is not available, or in situations where the installation of a power line from the nearest grid access point to the weather station is more expensive than an off-grid power supply, local power generation with battery storage should be devised. Options for on-site electrical power generation include PV or small wind turbine systems (or both) combined with batteries and gasoline- or diesel-fueled generators. For typical solar measurement weather stations, combined PV+battery power supply has actually been established as a common solution that can generally be applied at most locations up to ≈45° latitude. The cost of such equipment has reduced to the point that a grid power connection with high-quality UPS is in many cases more expensive than off-grid systems, which are readily available in most countries.

At autonomous sites, the renewable energy systems should be sized to provide enough energy for the maximum continuous load and power through several days of adverse conditions (cloudy weather and/or low wind speeds). This might be demanding at sites prone to persistent surface fog, for instance. The sizing is a function of the extremes of the solar climate and should consider the longest gap during reduced generation, the shortest recharge period available after discharge, and the generation capacity and storage necessary to provide uninterrupted power for the target location. Some oversizing is necessary to accommodate the unavoidable degradation of PV panels and battery storage, and consideration should be given to ambient temperature, which affects the ability of a battery to deliver energy. Sizing calculators are available to help with this effort.[15] Mechanisms to switch off non-vital equipment that consumes electricity in case of low power or battery state of charge can also be implemented. For example, ventilation/heating units can be automatically switched off when the UPS switches to battery mode, or when battery levels drop below a certain threshold. The time period when equipment is switched off should be logged because, for instance, ventilators can affect the readings of a pyranometer. Equipment should be specified and tested for self-power-on capability in the event of a power outage. This ensures that when power is restored, the equipment will automatically resume measurements and logging without operator intervention. This is an important consideration for remote locations where considerable downtime might occur before personnel can be dispatched to restart a system.

3.5.4 Grounding and Shielding

All equipment should be protected against lightning strikes and shielded from radio-frequency interference that could damage said equipment or reduce the validity of the measurements. Several references are available that describe techniques for grounding and shielding low-voltage signal cables; see, for example, Morrison (1998). Those who design solar resource measurement systems are urged to consult these references and seek expert technical advice. If digital sensors with onboard analog-to-digital converters are used, their sensitivity to transients, surges, and ground potential rise must be considered; therefore, the power and communications lines should be isolated and surge-protected with physical isolation, surge protection devices, or other equivalent technology.

In general, the following steps should be taken when designing and constructing a measurement station:

[15] See pvwatts.nrel.gov/.

- All equipment, even systems not connected to the power grid, benefits from proper grounding.
- Use a single-point ground (e.g., a copper rod driven several feet into the ground) for all signal ground connections to prevent ground loops that can introduce noise or biases in the measurements.
- Use twisted pair shielded cables for low-voltage measurements connected as double-ended measurements at the data logger. Double-ended measurements typically require separate logger channels for + and – signal input conductors. These inputs are compared to each other; therefore, the possibilities for electrical noise introduced in the signal cable are significantly reduced. Shields should be connected to the data logger measurement ground.
- Physically isolate low-voltage sensor cables from nearby sources of electrical noise, such as power cables. Do not run signal cables in the same bundle or conduit as AC power cables. If a power cable must cross a signal cable, always position the two at right angles to each other. This case is not recommended, but this limited contact will minimize the possibility of induced voltages in the signal cable. Also, the data logger settings should be selected to avoid signal noise (the integration time of the voltage measurement adjusted to AC frequency).
- Connect metal structures such as masts and tripods to a proper electrical ground to provide an easy path to the ground in the event of a lightning strike. This will help protect sensitive instruments. Electronic equipment often has a special ground lug and associated internal protection to help protect against stray voltages from lighting strikes. These should be connected with a heavy gauge wire to ground (12 American wire gauge or larger). Metal oxide varistors, avalanche diodes, or gas tubes can be used to protect signal cables from electrical surges such as lightning. These devices must be replaced periodically to maintain effectiveness. The replacement frequency is a function of the accumulated energy dissipated by the unit. The U.S. National Electric Code recommends a ground resistance of less than 5 ohms for “sensitive” electronic equipment. If that cannot be met with one rod, multiple rods should be used and bonded together. Ground resistance should be measured with a ground resistance tester using the three-pin or four-pin method.

3.5.5 Data Loggers

Most radiometers output a voltage, current, or resistance that is measured by the data logger, which comprises a voltmeter, ammeter, and/or ohmmeter, and usually some ports for counting pulses/switch closures. The measured output value is subsequently converted to the units of the measurand through a multiplier and/or an offset determined by calibration to a recognized measurement standard.

Data loggers should be chosen to have a very small measurement uncertainty, such as 10 times smaller than the estimated measurement uncertainty associated with the radiometer. For example, a good data logger receiving a 10-mV output from a radiometer that has 1% uncertainty should have 0.1% uncertainty of reading (or full scale), corresponding to 0.010 mV, or 10 µV, at most.

The logger should also have a measurement range that can cover the signal at near full scale to best capture the resolution of the data. For example, a sensor with a full-scale output of 10 mV should be connected to a logger with a range that is at least 10 mV. A logger with a 1-V range might be able to measure 10 mV but not with the desired accuracy and resolution. Most modern data loggers have several range selections, allowing the user to optimize the match for each instrument. Because of the nature of solar radiation, radiometers (e.g., pyranometers used for GHI measurements) can sometimes produce 200% or more of clear-sky readings under certain passing cloud-enhancement conditions, and the logger range should be set to prevent over-ranging during these sky conditions. Although the absolute GHI limit that can be reached during cloud-enhancement situations is a decreasing function of the measurement time step, this can be misleading. At 1-minute resolution, a safe limit seems to be 1,800 W/m^2 at most locations, but it could reach 2,000 W/m^2 or more at a 1-second resolution with photodiode radiometers, or at exceptional locations even at 1-minute resolution (Cordero et al. 2023). Because the data logger measures near-instantaneous values regardless of its averaging or recording time step, the range should be set to accommodate the higher values described. See Gueymard (2017a; 2017b) for more details.

Some radiometers use amplifiers to increase the instrument output to a higher range to better satisfy signal range-matching requirements; however, such amplifiers will add system complexity and some uncertainty to the data with nonlinearity, noise, temperature dependence, or instability. High-quality amplifiers could minimize these effects and allow a reasonable trade-off between logger cost and data accuracy. Calibrations should be conducted for these radiometer systems by coupling the pyranometer or pyrheliometer with its uniquely associated amplifier.

The logging equipment should also have environmental specifications that are compatible with the environment in which the equipment will be used. Loggers used inside an environmentally controlled building could have less stringent environmental performance specifications than loggers mounted outside in a desert or arctic environment. Equipment enclosures can create an internal environment several degrees above ambient air temperature because of solar heating (absorption by the enclosure materials), heat generated by electronic devices mounted inside, and lack of sufficient ventilation to help purge heat.

The sampling and recording rates of the solar resource data should be determined from the desired data analysis requirements. The sampling rate refers to how often the logger samples the data in a given time interval. The recording rate is often also called the reporting rate or the time resolution and is the length of the time interval represented by one data point in the logger's output file. The data point itself is generally an integrated value of several relatively instantaneous measurements. Monthly averages or sums, daily, hourly, minute, or sub-1-minute data records can be of interest. Data loggers can generally be configured to produce output of instantaneous or integrated values at any reasonable time period consistent with the radiometer time-response characteristics. The design should consider the current requirements and, if practical, future needs for additional analyses. A high-temporal-resolution data-logging scheme can be down-sampled or integrated into longer time periods—but not the other way around. Data-logging equipment, data transfer mechanisms, and data storage can generally handle 1-minute data resolution, and this should be considered the recording rate in the data logger. A resolution of 1 minute or better is recommended to allow for accurate data quality control. Because most applications address the solar energy available over time, integrating data of sub-

minute samples within the data logger is a common method of data output regardless of the final data resolution required by the analysis. For instance, 1-second signal sampling is recommended for irradiance measurements in the Baseline Surface Radiation Network (BSRN) (McArthur 2005) so that 60 samples are averaged to the reported 1-minute data. Along with the reported 1-minute average, the standard deviation over the period is also helpful to evaluate the short-term variability of the solar signal. Before deciding on a sample rate, the data logger program execution speed should be evaluated to ensure the logger can keep pace with the specification. The output of the instantaneous samples at longer intervals is much less likely to represent the available energy and should be avoided when configuring a data logger. If the size of a measured dataset is a defining issue (e.g., limited data communications throughput), the user can determine the lowest temporal resolution necessary for the application and optimize the data collection accordingly. Alternatively, or additionally, most modern data loggers have storage expansion options (e.g., SD cards), so that data at higher temporal resolution can be stored on an expansion storage medium and be collected manually in longer intervals.

3.5.6 Data Communications

Provisions should be made for automatically and frequently transferring data from the data logger to a data processing facility. This is the basis for adequately frequent data checks and timely corrections of outages and errors. Such frequent connections also allow for automatic data logger clock corrections when a local GPS device, which is preferred, is not available. Noticeable clock corrections of more than 1 second should never be necessary. Historically, data have been captured, transferred, and processed in various ways. Today, electronics and telecommunications allow remote data collection from nearly any location. One option uses a physical connection between the logger and a computer that is used for further data analysis or that forwards the data via internet connection. To avoid a cable connection, a cellphone network can be configured to provide virtual internet links between a measurement station and the data center. Satellite uplinks and downlinks are also available for data transfers in areas that are not served by either wire- or cell-based phone service. Within the area of an observing station, wireless communications such as radio-frequency connectivity might be useful to minimize the need for long cables between radiometers and data loggers. Depending on the antennas, data can be transferred over distances of a few kilometers. Such distances can occur between the data logger and the control room in big solar power plants with several megawatts of electrical power.

To prevent data loss due to connection problems, the memory of the data logger should be selected appropriately to hold data until the connection can be restored or personnel sent to correct the problem. Memory extensions are available for many data loggers with external cards, and in-memory storage capacity of several weeks is easily attainable.

3.6 Station and Network Operations

The protocols and procedures dictating station operations play a fundamental role in the assurance of data quality. These procedures must be established prior to the start of data collection, and a process must be put into place to carry forth and document adherence to the procedures. Data quality is in large part established the moment the measurement is taken. If errors occur during the measurement, little can be done to improve fundamental quality. For example, a poorly maintained station with dirty optics or misaligned instruments will produce unreliable data with great uncertainties or systematic biases, and the magnitude of the problem is

not likely to be discernable until days or weeks later. Often, one can only guess at which approximate *a posteriori* adjustments (if any) to make.

In this context, data quality control involves a well-defined supervisory process by which station operators are confident that when a measurement is taken with unattended instruments, the instruments are in a state that produces data of known quality. This process largely encompasses the calibration, inspection, and maintenance procedures discussed in Section 3.6.2, along with log sheets and other items that document the condition of the station. It also includes a critical inspection or assessment of the data to help detect problems not evident from physical inspection of the instruments.

When designing and implementing a data quality plan, it must be kept in mind that eventually the dataset will undergo third-party scrutiny for quality. In the best scenario (and a scenario that is certainly attainable), a data analyst will feel comfortable with the quality of the dataset and will be willing to move unhindered to the analysis at hand. The plan should eliminate as much as possible any doubts and questions about how the data were collected and whether the values they contain are suitable for the intended purpose. Implementation of the best practices contained in this handbook help eliminate doubts and minimize uncertainties that might jeopardize future projects.

Specifically, the following steps should be implemented (the subsequent subsections contain additional details):

- Define exact maintenance routines and frequencies and make them available as an easily understandable manual to the on-site maintenance personnel (in their local language). At remote locations with unskilled labor for simple sensor cleaning, this can be pictograms or example photos (ideally of the particular station to avoid any confusion). Initial thorough on-site training of maintenance personnel by the installation crew is crucial.
- Perform regular on-site visits for sensor cleaning and a general visual inspection for obvious issues. These visits can be easily documented by integrating a button on the weather station that can be pressed upon sensor cleaning. An additional and more informative control measure is to have the technician take a close-up picture before and after each instrument's cleaning event, along with the time stamp. These pictures can be easily transmitted to the server and stored for further use.
- Perform frequent data inspections during the measurement period, ideally 5–7 days a week at sites subject to intense soiling. This should include a combination of automated quality control tests and visual inspection by an experienced operator, and can be supported by automated alarms and messages to the operator (e.g., power outages, strong deviation of redundant measurements). See Chapter 4 for details.
- Perform regular maintenance visits by a skilled technician. These should be done at intervals of several months and include a general check of all equipment and functionality, as well as the exchange of consumables (filters, drying silica gel) and be documented with a report on the conducted activities. Refresher training for maintenance personnel should be incorporated in the site visit, and should be mandatory if personnel have changed.
- Maintain consistent, up-to-date station documentation, including technical information (measurement site documentation, installation report, datasheets, as-built drawings,

manuals, calibration certificates, maintenance procedures, cleaning log, maintenance log, sensor exchange, data logger program with history of changes, data logger configuration, inspection of the station infrastructure).

- Ensure that sensor calibrations are always valid. Earmark the sensors for recalibrations/exchange and implement a procedure to ensure that all recalibrations/exchanges are documented and the use of current calibration factors in the data processing is warranted. For any data time stamp, the information about which sensor with which calibration factor should be traceable, and the relevant certificate should be retrievable easily. The change of calibration factor of each individual radiometer should be documented so that problematic cases with steep changes are identified.
- Perform regular reporting and data summaries with data quality review.

3.6.1 Operations Personnel

To maintain a defensible dataset that will withstand critical due diligence, qualified operations personnel must be selected based on the level of expertise required. Below is a summary of personnel at a typical station or network of stations. Depending on the size and complexity of the endeavor, more than one task may be assigned to a person.

- Operations manager: This person must have a thorough understanding of the project scope and goals, bears responsibility for adhering to best practices, and will report to the entity funding the measurement campaign.
- Information technology (IT) specialist: This position requires expertise in internet connectivity, computer configuration, cybersecurity, and other related areas. This person might be part of a corporate IT department with partial assignment to support the measurement campaign. The operations manager should make clear arrangements with this person or the IT department to ensure assistance will be available when needed.
- Electronics technician: This person must have a working familiarity with all measurement equipment deployed at the station, configuration details, interconnectivity protocols, and likely failure scenarios. This technician may have the assigned duty of commissioning a new station after construction, ensuring that all equipment is working and the installation is robust. Good electronic and mechanical troubleshooting skills are a strong advantage.
- Installation staff: This person is responsible for the proper physical construction of the station according to specifications and plans. This position often requires some physical strength as well as knowledge of mechanical fasteners, guy wire installation, mounting foundations, and ground preparation. This person should have experience with the local sourcing of supplies, such as concrete, fencing, tools, anchors, and miscellaneous hardware.
- Data quality analyst: This position requires a deep understanding of the measurement fundamentals, how they relate to each other, likely characteristics and causes of measurement failure, and the skills to effectively handle and organize large datasets.
- Equipment maintenance (cleaning) personnel: For remote installations, this part-time position is likely the most difficult fill, and without careful selection and planning, it can be a vulnerability on the path to station success. Maintenance at remote sites requires locating a qualified person nearby willing to perform duties that often necessitate a long

drive for only a few minutes of work. The qualifications for maintenance are generally nontechnical, but they require someone with the interest and disposition to reliably complete the tasks. Finding a qualified person can be particularly difficult; moreover, cultural and language barriers can further complicate communication and supervision. Attractive candidates for the position often include teachers, family members of landowners, or reliable people recommended by local businesses. In all cases, the selected person must be trained in the equipment maintenance protocols and be provided with written documentation. Documented training and remote supervision will establish their qualifications to do the job. As a rule, compensating these people for time and vehicle mileage—rather than seeking volunteers—is a necessary investment in the long run because it sets up a firm contractual commitment to perform all necessary maintenance duties. The contractual agreement may also include a mechanism of payment adjustment for insufficient cleaning and bonuses for cleaning schedule adherence. Without that formal relationship, it can become difficult to assert the need for reliable and regular attention.

3.6.2 Equipment Maintenance

Proper O&M practices are essential for acquiring accurate solar resource measurements. Several elements in a chain form a quality system. Collectively, these elements produce accurate and reliable solar resource data: station location, measurement system design, equipment installation, data acquisition, and O&M practices. Proper O&M requires long-term consistency, attention to detail, complete and transparent documentation, and a thorough appreciation for the importance of preventive and corrective maintenance of sensitive equipment.

Calibrations are performed with clean instrument optics and a carefully aligned/leveled instrument. To properly apply the calibration factor, proper cleaning and other routine maintenance is necessary. All O&M should be carefully documented with log sheets or preferably with electronic databases that contain enough information to reveal problems and solutions or to assert that the instruments were in good health when inspected. It is advisable to implement a falsification-proof documentation mechanism such as a button on the equipment that is pushed before and/or after cleaning and other maintenance work to automatically register these events in a separate data column of the logger. This serves multiple purposes: it is objective proof of the maintenance staff's presence at the site; it is a proof of maintenance visits during data scrutiny; and it helps identify the cleaning events in the data itself (looking for typical "downward spike" pattern). Time-stamped pictures taken before and after maintenance can be extremely useful to evaluate the importance of soiling and misalignment, for example. The O&M information enables an analyst to identify potentially bad data and provides important documentation to determine and defend the overall quality of the measurements.

ISO TR 9901 and ASTM G183 provide information on radiometer operation and IEC 61724-1 also contains some requirements related to the pyranometer maintenance for optimum PV monitoring. These standards agree in most aspects, but the recommended frequencies of some tasks deviate. This is due to the site dependence of the required procedures (e.g., soiling, humidity) that complicates the formulation of a single solution. Depending on the frequency and complexity of a task, different personnel can be involved in the maintenance. Experts might only be available for monthly performance of semiannual tasks.

The maintenance process includes:

- Checking the alignment/leveling of the detector. Pyrheliometers must be accurately aligned with the solar disk for accurate DNI measurements. Pyranometer detectors must be horizontal for GHI and DHI measurements and accurately tilted (or aligned with a flat-plate collector) for GTI measurements. The radiometer orientation should be checked periodically using the features described earlier in this chapter. ISO TR 9901 and ASTM G183 recommend checks every working day of the week for GHI and DNI and monthly (ISO) or semiannual (ASTM G183) checks for GTI.
- Cleaning the instrument optics. To properly measure solar irradiance, no contaminant should block or reduce the radiation falling on the detector. The outdoor environment provides many sources of such contamination, such as dust, precipitation, dew, frost, plant matter, insects, and bird droppings. The sensors should be cleaned regularly to minimize the effect of contaminants on the measurements. In many cases, this can require daily maintenance of radiometers, especially in the case of pyrheliometers. Different standards require or recommend different cleaning frequencies each weekday(ISO TR 9901, ASTM G183) or weekly (IEC 61724-1, only for pyranometers).
- Documenting obvious issues with the station. The whole measurement station should be examined each weekday for obvious issues such as condensation on window/dome/lens, damage, or wear (cables, connectors, windows, wind vane) (ISO TR 9901; ASTM G183) and proper working condition of the ventilators. Any defects should be noted and reported or corrected.
- Check and change of desiccant. The change of the desiccant is required for some instruments. The color of the desiccant indicates if it is still able to absorb humidity. Whereas ASTM G183 recommends monthly or quarterly changes, ISO TR9901 even recommends weekly control of the desiccant color.
- Control ventilator filters. Weekly checks or, in the special case of clean environments, less-frequent (e.g., monthly) checks are recommended (ISO TR 9901, ASTM G183).
- Documenting the detailed condition of the station. Monthly or semiannually detailed control of the station by an expert technician, including its sensors, loggers, and cables is recommended. During these visits the environmental conditions should also be noted (sky and weather conditions, any ground surface changes, such as vegetation removal or the presence of snow, etc.).

Maintenance frequency depends on the prevailing environmental conditions that soil the instruments. This includes dust, rain, dew, snow, birds, and insects. It also depends on instrument type. Radiometer designs based on optical diffusers as the surface separating the inside of the instrument from the environment are less susceptible to dust contamination than instruments with clear optics, such as domed pyranometers (Myers et al. 2002). This is because fine soiling particles scatter much more than they absorb solar radiation. Absorption affects instruments with clear optics and diffusers the same way. In contrast, the scattering-induced soiling effect has less impact on instruments with diffusers because the latter can transmit most of the particle-induced scattered radiation. This radiation (mostly in the forward direction) reaches the detector in nearly the same way that radiation would enter a clean diffuser. Conversely, the scattering often causes the incoming radiation to miss the detector in instruments with clear optics because the latter is some distance away from the former. This is especially relevant for pyrheliometers (Geuder and Quaschning 2006). Soiling of windowed or domed radiometers can quickly affect their reading

and increase their measurement uncertainty. This explains why thermopile radiometers must be cleaned very frequently (e.g., daily). As described earlier, using a ventilator for a pyranometer can reduce this risk of contamination; thus, it is important to consider the frequency and cost of maintenance for proper instrument specification. Although sensors with diffusers, such as RSIs, are not as prone to strong soiling effects, they still require regular cleaning (e.g., twice per month). Note that a diffuser below a clear entrance window/dome does not have an advantage compared to a thermopile below the same clear entrance window/dome.

The examples that mention daily cleaning for sensors with clear optics and cleaning twice per month for sensors with diffusers as an outer surface are useful for many sites; however, different standards require or recommend different cleaning frequencies between daily (ISO TR9901) and weekly (IEC 61724-1), as explained above. It is recommended to determine the optimal cleaning interval for each site depending on the climate or seasonal effects at similar sites or, for example, by analyzing the immediate effect of cleaning on the measurement signal. Depending on the noted period after which soiling significantly influences the measurement, the cleaning interval can be adjusted so that the degradation in sensitivity is limited to an acceptable level (e.g., <1% for high-quality stations). Each cleaning period and the state of the sensors should be documented, and the measurement values should be checked to evaluate the effect of cleaning on the recorded values.

Radiometers should be carefully cleaned at each inspection, even if soiling appears minimal. Cleaning is generally a very short procedure. A recommendation for the cleaning procedure is as follows. First, remove any loose particles from the entrance window with a soft brush or compressed air. Then clean the entrance window, dome, or diffuser with a dry cloth. If dirt remains after this step, wet a second cloth with distilled water (or methyl hydrate), and wipe the window/diffusor/dome clean. If ice sticks to the surface, try melting the ice with one's hands. Avoid using a hair dryer to melt the ice because the heat can crack the cold optics. More aggressive methods might damage the entrance windows and are therefore not recommended.

Collimators without entrance windows (as used in active cavity radiometers and at least one new commercially available low-cost pyrheliometer) greatly reduce the accumulation of dust on the sensor's entrance optics, but they could still be affected by, for example, insects or spiders that enter the collimators, causing strong signal reductions. Even a single fiber of a spiderweb can significantly reduce the signal; therefore, such collimators must be inspected frequently.

At remote sites that could be too difficult to maintain during extended periods, a higher-class windowed instrument might not be optimal, despite its potential for better measurements. The cost of maintenance for a remote site could dominate the cost of setting up and operating a station. This aspect should be anticipated when planning a measurement campaign. Often, less maintenance-intensive sensors with initially lower accuracy than windowed instruments can be a better choice, at least until the station becomes permanently serviceable on a sufficiently frequent basis.

Additional spot inspections should be conducted after significant weather events (e.g., dust storms, snowstorms, heavy rainfall, rainfall during periods with high aerosol loads, or thunderstorms). Radiometer optics might not necessarily be soiled within a 24-hour period, but the effects of soiling can be best mitigated with frequent inspection.

A general conclusion is that a conservative maintenance schedule will support the credibility of the measurement dataset and provide the analyst with a base of justification when assigning confidence intervals for the data.

3.6.3 Data Inspection

The collection of quality data cannot occur without careful and ongoing inspection of the data stream for evidence of error or malfunction. Although the maintenance procedures discussed in the previous section rely heavily on the physical appearance of the equipment to detect malfunction, some sources of error are so insidious that they cannot be revealed by simple physical observation; thus, an operations plan must include a careful inspection of the data itself for unrealistic values that might appear only with mathematical analysis. As with the inspections during equipment maintenance, inspection of data should be done with a frequency great enough to avoid prolonged error conditions that would impose a significant bias on the eventual statistical characterization of the dataset. The methods for data quality control are presented in Chapter 4.

3.6.3.1 Metadata and Record-Keeping

The interpretation and application of solar resource measurements depend greatly on the efforts to record and include metadata relevant to the observations. This includes site location; quantitative local horizon surveys with a device visualizing the solar path during the year; data acquisition system(s); input signal channel assignments; radiometer types, models, serial numbers, calibration histories, and installation schemes; and information on eventual postprocessing of the data and maintenance records. For example, online metadata are available from NREL's Solar Radiation Research Laboratory.[16] Such metadata should be included with the archiving of the measured solar resource data. Examples of issues that must be documented include damaged or misaligned sensors, maintenance works on the instruments, detection of soiled sensors and subsequent sensor cleaning, obstructed sensors, temporarily erroneous calibration constants in the program code, loose electrical connections, and data logger clock errors. These events are frequently not detected automatically or sometimes are not even detectable by automatic quality control screening tools; thus, manual on-site checks are required. The metadata should not necessarily be limited to error conditions or corrections. Information about unusual weather events, animal activity, or even significant flora blooms or vegetation die-off events might prove useful in future analyses that could benefit from knowledge of the measurement environment. Such supplementary information could convey to an auditor that the station operators were thorough in recording station details.

When deciding on a metadata archival method, some consideration should be given to the pros and cons of paper (physical) versus electronic storage. Paper, though not immune to peril, is a simple form that can be read for decades or even centuries. Electronic formats, which are invaluable for easy access and extraction for computer analyses, are too often subject to catastrophic loss through myriad electronic mishaps. Further, changes in the format of once-commonplace electronic storage schemes might also render historic metadata unreadable or inaccessible. Using both methods simultaneously solves many of these problems, but it can create new issues with the additional labor of double entry or possible inconsistencies between the two methods. A well-structured photo documentation is very useful, such as regular

[16] See www.nrel.gov/midc/srrl_bms.

photographs of sensor alignments and equipment condition. Collecting such photos is facilitated by modern communication; for instance, most people do have a smartphone (even in remote locations), or can be supplied with one at low additional cost.

Figure 3-31 shows a sample paper log that a maintenance technician is required to complete on-site during the maintenance visit. Such a log can complement the information of the recommended maintenance button or even substitute it with fully reliable personnel. The log not only provides a checklist to ensure a complete inspection but also serves as permanent documentation for the station archive. The time zone should be clearly defined and agreed upon with the maintenance technician. To avoid additional effort and possible errors by the maintenance technician, the time zone of the maintenance log is recommended to be consistent with the civil time. The civil time is the standard time in the time zone of the station, including possible adjustments for daylight saving time. It is more cumbersome for the data analyst to adjust this information to Coordinated Universal Time (UTC) or local standard time that is used in the logger, but at least this adjustment is only necessary once and not every day or each summer day. A paper log can be difficult to read when local operators are using a different script/language—in some cases local languages that virtually no one can understand or translate. Nonetheless, a well-maintained file of paper logs even in a foreign language can provide valuable evidence of careful attention to site maintenance.

SOLRMAP Maintenance Log
Rotating Shadowband Radiometer
National Renewable Energy Laboratory

Station _____ Page ____

Date (MM/DD/YYYY)	__/__/___	__/__/___	__/__/___	__/__/___	__/__/___	__/__/___	__/__/___
Time (LST HH:MM)	__:__	__:__	__:__	__:__	__:__	__:__	__:__
Technician							
Fence/security							
Tower/guys							
Anemometer Cups/propeller							
Wind Vane							
Sky/clouds							
Radiometer tripod/anchors							
Antenna							
PV Panel							
Shadowband Rotation/Motor							
Primary Sensor Condition							
Primary Sensor Level*							
Secondary Sensor Condition							
Secondary Sensor Level*							
Comments							

*Check level every other week

Bubble Level (use code and direction)
1 = Within inner circle
2 = Across inner circle
3 = Outside inner circle
4 = Touching outer edge

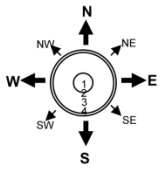

Condition Codes
√ = Clean/Okay
LD = Dry - Light Dust
HD = Dry - Heavy Dust
WS = Dry -Water Spots
DWS = Dry - Dirty Water Spots
Wet = Dew, water droplets, water sheet
Frost
Snow
Ice
BD = Bird Dropping

Circle over code = Cleaned/Corrected

Sky Conditions
Clear
Scattered
Broken
Overcast

Figure 3-31. Sample paper maintenance log sheet to be filled out by a technician on-site during a maintenance visit.

Image from NREL

Figure 3-32 shows a (partial) online log form that allows the maintenance technician to remotely access a database interface. Each item in the prescribed maintenance checklist is reported to complete the documentation for the station visit. The log sheet streamlines much of the documentation with codes and checkmarks, and it provides space for freehand comments to describe unusual conditions. For both paper and online logs, protocols must be in place to ensure that the technician is actually performing the tasks that appear in the logs. At a minimum, station management must be aware of the possibility that a dishonest technician might develop creative ways to falsify a work product. There are ways to remotely verify that the maintenance protocol is being followed. In many cases, when instruments are cleaned, an anomaly appears in the data while the sky irradiance is blocked. The analyst can look at a data plot at the logged time of the visit, and if no disruption appears, further investigation could be warranted. Some systems provide a momentary switch or button that the technician is required to push when arriving on-site. This action places a flag in the data stream verifying that the technician was on-site for the inspection. Remote video cameras can also be a valuable means to verify a proper inspection or to detect the cause of data anomalies.

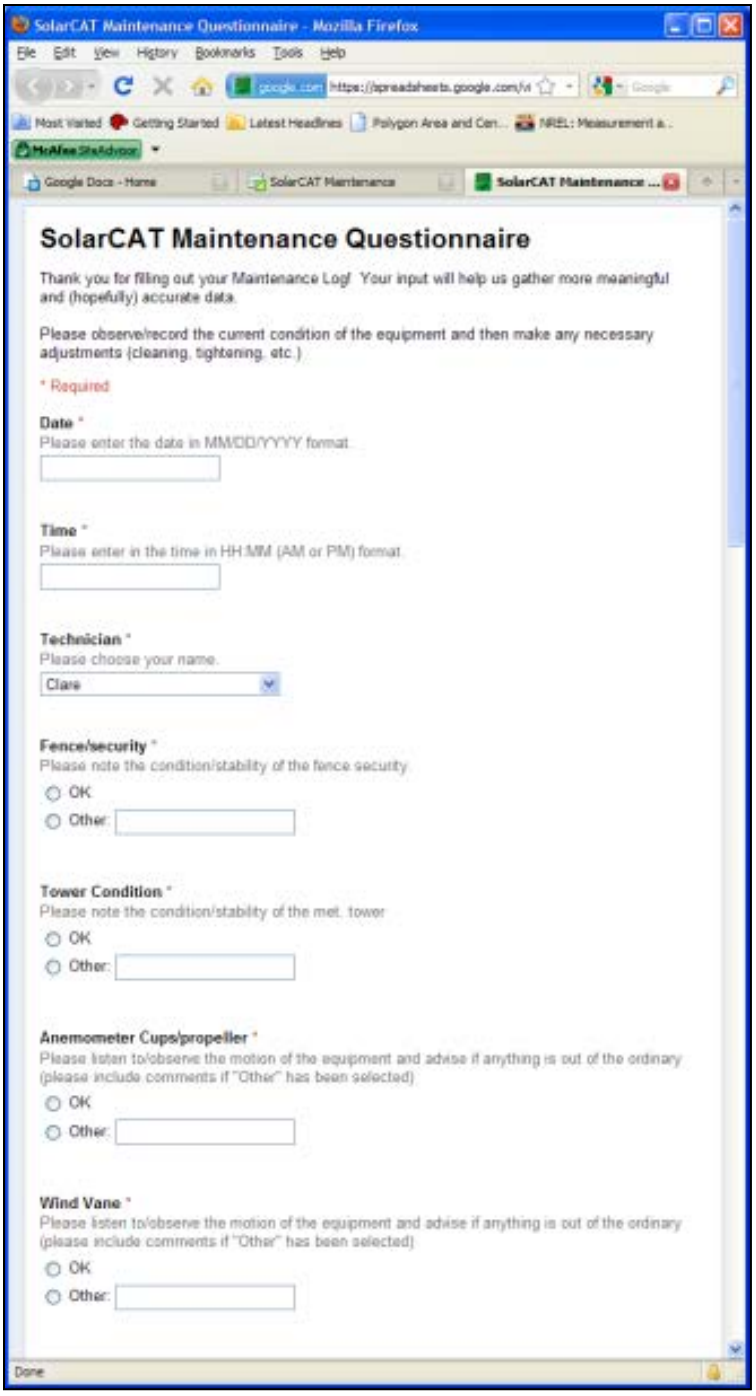

Figure 3-32. Sample online interface for documenting maintenance.

Image from NREL

Analysts—whether associated with station operations or employed in a later due-diligence process—are helped immensely by ample documentation of station O&M. The documentation, in addition to providing specific information, also indicates the extent of the maintenance protocol. This gives the analyst confidence that problems are discovered and corrected in a minimal amount of time. Further, the documents show that even at well-run stations with a few inevitable malfunctions, best practices and high-quality data govern operations.

Complete documentation includes thorough information in a dedicated metadata archive about the instruments, including manufacturer and model, serial number, calibrations (current and historical), deployment location and configuration, repairs, and inventory or storage details. Of particular importance is the record of instrument calibrations and the associated certificate, traceability, and statement of uncertainty. The calibration record is fundamental to the measurement itself and the assignment of uncertainties to the measured data. Absent a current calibration certificate, a knowledgeable analyst performing validation or due diligence on a dataset will likely reject any statement of uncertainty, rendering the measurements highly questionable.

3.6.4 Data Aggregations and Summaries

Solar irradiance measurements for renewable energy applications are becoming more common, and in some electric utility applications, they are required. These measurements are also important for applications in energy efficiency and climate research. Measurement station design includes data loggers and their configuration, as described in Section 3.5.5. Ideally, the station designers will have knowledge in advance about the form (necessary parameters, time resolution, period of record, acceptable uncertainty limits, etc.) of the data required to complete the planned analyses to satisfy the project objectives, but this is not always the case. Further, it is quite common for datasets to be accessed for uses other than their original purpose; thus, the value of a dataset could be significantly enhanced if it is in a more generic form that is easily adaptable or convertible to other more specific forms. This typically relates to the frequency of the measurements, which could range from sub-minute to monthly or even yearly. Generally, extensive documentation and metadata facilitates later adaptation to other uses than originally intended, because with complete information and well-structured data, any information subset can easily be generated.

As noted in Section 3.5.5, the time resolution of the measurements can be increased without significantly increasing the costs for data transfer and storage when compared with the overall costs of operating a station. A high time resolution enables efficient data quality control and detailed data analysis; those values can be easily converted to longer timescales. Therefore, it is recommended that the station saves data at 1-minute intervals.[17] Many commercially available data loggers are capable of sampling the instruments at 1 Hz and then calculate the average of the samples to obtain a 1-minute irradiance value in W/m² (or some other chosen time interval), as well as its standard deviation.

Aggregating solar irradiance and meteorological measurements over various timescales requires careful attention to the described measurand and its units. Irradiance data can be integrated over the time or averaged, which is in general straightforward, but the averaging or integration interval must be well defined (e.g., only positive solar elevation angles). For albedo time series and other derived parameters, simple averaging is not possible (see Section 3.3.2). Also, methods for estimating the measurement uncertainties of temporal aggregates are needed (see Chapter 10).

[17] Data recording at time intervals as short as 1 second has been needed for research applications requiring special attention to the radiometer performance specifications; see Sengupta and Andreas (2010).

References

Abreu, E.F.M., C.A. Gueymard, P. Canhoto, and M.J. Costa. 2023. "Performance Assessment of Clear-Sky Solar Irradiance Predictions Using State-of-the-Art Radiation Models and Input Atmospheric Data from Reanalysis or Ground Measurements." *Solar Energy* 252: 309–21. https://doi.org/10.1016/j.solener.2023.01.051.

Apogee. 2019. "New ISO 9060 Pyranometer Classifications." https://www.apogeeinstruments.com/content/ISO_9060_Apogee_Comparison.pdf.

Arguez, A., and R.S. Vose. 2011. "The Definition of the Standard WMO Climate Normal: The Key to Deriving Alternative Climate Normals." *Bulletin of the American Meteorological Society* 92 (6): 699–704. https://doi.org/10.1175/2010BAMS2955.1.

Asgharzadeh, A., B. Marion, C. Deline, C. Hansen, J.S. Stein, and F. Toor. 2018. "A Sensitivity Study of the Impact of Installation Parameters and System Configuration on the Performance of Bifacial PV Arrays." *IEEE Journal of Photovoltaics* 8 (3): 798–805. https://doi.org/10.1109/JPHOTOV.2018.2819676.

Asgharzadeh, A., F. Toor, B. Bourne, M.A. Anoma, A. Hoffman, C. Chaudhari, S. Bapat, et al. 2019. "A Benchmark and Validation of Bifacial PV Irradiance Models." In *2019 IEEE 46th Photovoltaic Specialists Conference (PVSC)*, 3281–87. Chicago, IL, USA: IEEE. https://doi.org/10.1109/PVSC40753.2019.8981272.

ASTM E816. 2023. "ASTM E816-15 Test Method for Calibration of Pyrheliometers by Comparison to Reference Pyrheliometers." ASTM International. https://doi.org/DOI: 10.1520/E0816-15.

ASTM E824. 2018. "ASTM E824-10R18E1 Test Method for Transfer of Calibration From Reference to Field Radiometers." ASTM International. https://doi.org/DOI: 10.1520/E0824-10R18E01.

ASTM E1125. 2020. "ASTM E1125-16 Test Method for Calibration of Primary Non-Concentrator Terrestrial Photovoltaic Reference Cells Using a Tabular Spectrum." ASTM International. https://doi.org/10.1520/E1125-16R20.

ASTM E1362. 2019. "ASTM E1362-15 Test Methods for Calibration of Non-Concentrator Photovoltaic Non-Primary Reference Cells." ASTM International. https://doi.org/10.1520/E1362-15R19.

ASTM E1918. 2023. "ASTM E1918-21 Test Method for Measuring Solar Reflectance of Horizontal and Low-Sloped Surfaces in the Field." ASTM International. https://doi.org/10.1520/E1918-21.

ASTM G167. 2023. "ASTM G167-15 Test Method for Calibration of a Pyranometer Using a Pyrheliometer." ASTM International. https://doi.org/DOI: 10.1520/G0167-15.

ASTM G183. 2023. "ASTM G183-15 Practice for Field Use of Pyranometers, Pyrheliometers and UV Radiometers." ASTM International. https://doi.org/DOI: 10.1520/G0183-15.

Augustyn, J., T. Geer, T. Stoffel, E. Kern, R. Little, F. Vignola, and R. Kessler. 2002. "Improving the Accuracy of Low Cost Measurement of Direct Normal Solar Irradiance." In *Proceedings of the Solar Conference*, 329–34. American Solar Energy Society; American Institute of Architects.

Babal, P., M. Korevaar, S. Franken, J. Mes, T. Bergmans, and K. Wilson. 2020. "Uncertainties in Irradiance Measurements of Sensors to POA $_{rear}$ of Bifacial Solar Panels." In *2020 47th IEEE Photovoltaic Specialists Conference (PVSC)*, 0959–63. Calgary, AB, Canada: IEEE. https://doi.org/10.1109/PVSC45281.2020.9301008.

Badosa, J., J. Wood, P. Blanc, C. N. Long, L. Vuilleumier, D. Demengel, and M. Haeffelin. 2014. "Solar Irradiances Measured Using SPN1 Radiometers: Uncertainties and Clues for Development." *Atmospheric Measurement Techniques* 7 (12): 4267–83. https://doi.org/10.5194/amt-7-4267-2014.

Balenzategui, J.L., F. Fabero, and J.P. Silva. 2019. "Solar Radiation Measurement and Solar Radiometers." In *Solar Resources Mapping: Fundamentals and Applications*, edited by Jesús Polo, Luis Martín-Pomares, and Antonio Sanfilippo, 15–69. Springer International Publishing. https://doi.org/10.1007/978-3-319-97484-2_2.

Balenzategui, J.L., M. Molero, J.P. Silva, F. Fabero, J. Cuenca, E. Mejuto, and J. De Lucas. 2022. "Uncertainty in the Calibration Transfer of Solar Irradiance Scale: From Absolute Cavity Radiometers to Standard Pyrheliometers." *Solar* 2 (2): 158–85. https://doi.org/10.3390/solar2020010.

Berrian, D., and J. Libal. 2020. "A Comparison of Ray Tracing and View Factor Simulations of Locally Resolved Rear Irradiance with the Experimental Values." *Progress in Photovoltaics: Research and Applications* 28 (6): 609–20. https://doi.org/10.1002/pip.3261.

Blakesley, J. C., G. Koutsourakis, S. Douglas, J. K. L. Holder, J. Torry, F. A. Mukadam, A. Schmid, and R. S. J. Abrams. 2020. "Effective Spectral Albedo from Satellite Data for Bifacial Gain Calculations of PV Systems." In *Proceedings of the 38th European Photovoltaic Solar Energy Conference and Exhibition* https://doi.org/10.4229/EUPVSEC20202020-5CO.9.3.

Blum, N.B., S. Wilbert, B. Nouri, J. Lezaca, D. Huckebrink, A. Kazantzidis, D. Heinemann, L. F. Zarzalejo, M.J. Jiménez, and R. Pitz-Paal. 2022. "Measurement of Diffuse and Plane of Array Irradiance by a Combination of a Pyranometer and an All-Sky Imager." *Solar Energy* 232: 232–47. https://doi.org/10.1016/j.solener.2021.11.064.

Blum, N., F. Maas, J. Stührenberg, R. Broda, P. Matteschk, M. Meinel, B. Nouri, et al. 2023. "A Benchmark of Simple Diffuse and Direct Irradiance Measurement Systems." *Presented at the 40th European Photovoltaic Solar Energy Conference and Exhibition*. Lisbon, Portugal.

Blum, N., and S. Wilbert. 2023. "Effect of Erroneous Albedo Data on Yield Estimation of Bifacial PV Systems." DLR workshop.

Braid, J.L., J.S. Stein, B.H. King, C. Raupp, J. Mallineni, J. Robinson, and S. Knapp. 2022. "Effective Irradiance Monitoring Using Reference Modules." In *2022 IEEE 49th Photovoltaics*

Specialists Conference (PVSC), 1073–78. Philadelphia, PA, USA: IEEE. https://doi.org/10.1109/PVSC48317.2022.9938851.

Chudinzow, D., J. Haas, G. Díaz-Ferrán, S. Moreno-Leiva, and L. Eltrop. 2019. "Simulating the Energy Yield of a Bifacial Photovoltaic Power Plant." *Solar Energy* 183: 812–22. https://doi.org/10.1016/j.solener.2019.03.071.

Cordero, R.R., S. Feron, A. Damiani, E. Sepúlveda, J. Jorquera, A. Redondas, G. Seckmeyer, J. Carrasco, P. Rowe, and Z. Ouyang. 2023. "Surface Solar Extremes in the Most Irradiated Region on Earth, Altiplano." *Bulletin of the American Meteorological Society* 104 (6): E1206–21. https://doi.org/10.1175/BAMS-D-22-0215.1.

Deline, C., S. Ayala Pelaez, S. MacAlpine, and C. Olalla. 2020. "Estimating and Parameterizing Mismatch Power Loss in Bifacial Photovoltaic Systems." *Progress in Photovoltaics: Research and Applications* 28 (7): 691–703. https://doi.org/10.1002/pip.3259.

Deline, C., S. MacAlpine, B. Marion, F. Toor, A. Asgharzadeh, and J.S. Stein. 2017. "Assessment of Bifacial Photovoltaic Module Power Rating Methodologies—Inside and Out." *IEEE Journal of Photovoltaics* 7 (2): 575–80. https://doi.org/10.1109/JPHOTOV.2017.2650565.

Dittmann, S., L. Burnham, S-Y Oh, A. Benlarabi, J-H Choi, M. Ebert, B. Figgis, R. Gottschalg, K-S Kim, and T. Reindl. 2019. "Comparative Analysis of Albedo Measurements (Plane-of-Array Horizontal Satellite) at Multiple Sites Worldwide." Albuquerque, NM: Sandia National Laboratory. https://www.osti.gov/servlets/purl/1601744.

Driesse, A. 2018. "Radiometer Response Time and Irradiance Measurement Accuracy." 35th European Photovoltaic Solar Energy Conference and Exhibition, Brussels, Belgium: 1679-1683. https://doi.org/10.4229/35THEUPVSEC20182018-6DO.10.6.

Driesse, A. 2021. "PV Reference Cells for Outdoor Use: An Investigation of Calibration Factors." NREL-SR-5D00-80437. National Renewable Energy Lab. (NREL), Golden, CO (United States). https://doi.org/10.2172/1823768.

Driesse, A., P. Gotseff, and M. Sengupta. 2022. "PV Reference Cells for Outdoor Use: Comparison of First-Year Field Measurements." NREL/SR-5D00-82086. National Renewable Energy Lab. (NREL), Golden, CO (United States). https://doi.org/10.2172/1866986.

Driesse, A., A. Habte, and M. Sengupta. 2023. *The Baseline Performance Reference for Irradiance in PV System Applications.* NREL/TP-5D00-86847. Golden, CO: NREL. https://doi.org/10.2172/2000739.

Driesse, A., and J. Stein. 2017. "Site-Specific Evaluation of Errors and Uncertainty in Irradiance Measurements." Poster presented at the 33rd European Photovoltaic Solar Energy Conference, Amsterdam, The Netherlands. https://doi.org/10.13140/RG.2.2.14876.39044.

Driesse, A., W. Zaaiman, D. Riley, N. Taylor, and J.S. Stein. 2015. "Indoor and Outdoor Evaluation of Global Irradiance Sensors." 31st European Photovoltaic Solar Energy Conference, Hamburg, Germany: 14–18. https://doi.org/10.4229/EUPVSEC20152015-5CO.5.3.

Dutton, E.G., J.J. Michalsky, T. Stoffel, B.W. Forgan, J. Hickey, D.W. Nelson, T.L. Alberta, and I. Reda. 2001. "Measurement of Broadband Diffuse Solar Irradiance Using Current Commercial Instrumentation with a Correction for Thermal Offset Errors." *Journal of Atmospheric and Oceanic Technology* 18 (3): 297–314. https://doi.org/10.1175/1520-0426(2001)018<0297:MOBDSI>2.0.CO;2.

ESMAP. 2020. "Termsof Reference Solar and Wind Measurement Campaign in XXX." Energy Sector Management Assistance Program. https://documents1.worldbank.org/curated/en/398831592957111931/pdf/ESMAP-Terms-of-Reference-for-Solar-and-Wind-Measurement-Campaign.pdf.

Fehlmann, A., G. Kopp, W. Schmutz, R. Winkler, W. Finsterle, and N. Fox. 2012. "Fourth World Radiometric Reference to SI Radiometric Scale Comparison and Implications for On-Orbit Measurements of the Total Solar Irradiance." *Metrologia* 49 (2): S34. https://doi.org/10.1088/0026-1394/49/2/S34.

Finsterle, W., et al. 2011. "WMO International Pyrheliometer Comparison, IPC-XI." WMO Instruments and Observing Methods (IOM) Report No. 108, https://library.wmo.int/idurl/4/46449.

Forstinger, A., S. Wilbert, A. Driesse, N. Hanrieder, R. Affolter, S. Kumar, N. Goswami, et al. 2020. "Physically Based Correction of Systematic Errors of Rotating Shadowband Irradiometers." *Meteorologische Zeitschrift* 29 (1): 19–39. https://doi.org/10.1127/metz/2019/0972.

Forstinger, A., S. Wilbert, A. Driesse, and B. Kraas. 2022. "Uncertainty Calculation Method for Photodiode Pyranometers." *Solar RRL* 6 (5): 2100468. https://doi.org/10.1002/solr.202100468.

Fröhlich, C. 1991. "History of Solar Radiometry and the World Radiometric Reference." *Metrologia* 28 (3): 111–15. https://doi.org/10.1088/0026-1394/28/3/001.

Geuder, N., R. Affolter, B. Kraas, and S. Wilbert. 2014. "Long-Term Behavior, Accuracy and Drift of LI-200 Pyranometers as Radiation Sensors in Rotating Shadowband Irradiometers (RSI)." *Energy Procedia* 49: 2330–39. https://doi.org/10.1016/j.egypro.2014.03.247.

Geuder, N., and V. Quaschning. 2006. "Soiling of Irradiation Sensors and Methods for Soiling Correction." *Solar Energy* 80 (11): 1402–9. https://doi.org/10.1016/j.solener.2006.06.001.

Geuder, N., R. Affolter, O. Goebel, B. Dahleh, M. Al Khawaja, S. Wilbert, B. Pape, and B. Pulvermueller. 2016. "Validation of Direct Beam Irradiance Measurements From Rotating Shadowband Irradiometers in a Region With Different Atmospheric Conditions." *Journal of Solar Energy Engineering* 138 (5): 051007. https://doi.org/10.1115/1.4034070.

Geuder, N., M. Hanussek, J. Haller, R. Affolter, and S. Wilbert. 2011. "Comparison of Corrections and Calibration Procedures for Rotating Shadowband Irradiance Sensors." SolarPACES Conference, Granada, Spain.

Geuder, N., B. Pulvermüller, and O. Vorbrugg. 2008. "Corrections for Rotating Shadowband Pyranometers for Solar Resource Assessment." *Optical Modeling and Measurements for Solar Energy Systems II*, edited by Benjamin K. Tsai, SPIE Conf. 70460F. San Diego, CA. https://doi.org/10.1117/12.797472.

Gostein, M., B. Marion, and B. Stueve. 2020. "Spectral Effects in Albedo and Rearside Irradiance Measurement for Bifacial Performance Estimation." 47th IEEE Photovoltaic Specialists Conference (PVSC), 0515–19. Calgary, AB, Canada: IEEE. https://doi.org/10.1109/PVSC45281.2020.9300518.

Gostein, M., S. Ayala Pelaez, C. Deline, A. Habte, C.W. Hansen, B. Marion, J. Newmiller, M. Sengupta, J.S. Stein, and I. Suez. 2021. "Measuring Irradiance for Bifacial PV Systems." 48th Photovoltaic Specialists Conference (PVSC), 0896–0903. Fort Lauderdale, FL, USA: IEEE. https://doi.org/10.1109/PVSC43889.2021.9518601.

Gostein, M., B. Stueve, R. Clark, P. Keelin, M. Grammatico, and M. Reusser. 2020. "Field Trial of Meteorological Station Using PV Reference Cells." 47th IEEE Photovoltaic Specialists Conference (PVSC), 0520–23. Calgary, AB, Canada: IEEE. https://doi.org/10.1109/PVSC45281.2020.9300799.

Gueymard, C.A. 2017a. "Cloud and Albedo Enhancement Impacts on Solar Irradiance Using High-Frequency Measurements from Thermopile and Photodiode Radiometers. Part 1: Impacts on Global Horizontal Irradiance." *Solar Energy* 153: 755–65. https://doi.org/10.1016/j.solener.2017.05.004.

———. 2017b. "Cloud and Albedo Enhancement Impacts on Solar Irradiance Using High-Frequency Measurements from Thermopile and Photodiode Radiometers. Part 2: Performance of Separation and Transposition Models for Global Tilted Irradiance." *Solar Energy* 153: 766–79. https://doi.org/10.1016/j.solener.2017.04.068.

Gueymard, C.A., V. Lara-Fanego, M. Sengupta, and A. Habte. 2021. "Surface Albedo Spatial Variability in North America: Gridded Data vs. Local Measurements." *Solar Energy* 227: 655–73. https://doi.org/10.1016/j.solener.2021.05.012.

Gueymard, C.A., and D.R. Myers. 2009. "Evaluation of Conventional and High-Performance Routine Solar Radiation Measurements for Improved Solar Resource, Climatological Trends, and Radiative Modeling." *Solar Energy* 83 (2): 171–85. https://doi.org/10.1016/j.solener.2008.07.015.

Gueymard, C.A., and J.A. Ruiz-Arias. 2015. "Validation of Direct Normal Irradiance Predictions under Arid Conditions: A Review of Radiative Models and Their Turbidity-Dependent Performance." *Renewable and Sustainable Energy Reviews* 45: 379–96. https://doi.org/10.1016/j.rser.2015.01.065.

Gueymard, C.A, and S.M Wilcox. 2011. "Assessment of Spatial and Temporal Variability in the US Solar Resource from Radiometric Measurements and Predictions from Models Using Ground-Based or Satellite Data." *Solar Energy* 85 (5): 1068–84. https://doi.org/10.1016/j.solener.2011.02.030.

Habte, A., and W. Beuttell. 2022. *Solar Radiometer Instrumentation Evaluation: Cooperative Research and Development (Final Report, CRADA Number CRD-16-00619).* NREL/TP-5D00-81853. National Renewable Energy Laboratory, Golden, CO; EKO Instruments USA Inc., San Jose, CA (United States). https://doi.org/10.2172/1841135.

Habte, A.M., M. Sengupta, Y. Xie, M.R. Dooraghi, I.M. Reda, A. Driesse, C.A. Gueymard, S. Wilbert, and F. Vignola. 2018. *Developing a Framework for Reference Cell Standards for PV Resource Applications.* NREL/TP-5D00-72599. National Renewable Energy Laboratory, Golden, CO. https://doi.org/10.2172/1487333.

Habte, A., M. Sengupta, A. Andreas, S. Wilcox, and T. Stoffel. 2016. "Intercomparison of 51 Radiometers for Determining Global Horizontal Irradiance and Direct Normal Irradiance Measurements." *Solar Energy* 133: 372–93. https://doi.org/10.1016/j.solener.2016.03.065.

Habte, A., M. Sengupta, I. Reda, A. Andreas, and J. Konings. 2014. *Calibration and Measurement Uncertainty Estimation of Radiometric Data.* NREL/CP-5D00-62214. National Renewable Energy Laboratory, Golden, CO.

Hansen, C.W., R. Gooding, N. Guay, D.M. Riley, J. Kallickal, D. Ellibee, A. Asgharzadeh, B. Marion, F. Toor, and J.S. Stein. 2017. "A Detailed Model of Rear-Side Irradiance for Bifacial PV Modules." 44th Photovoltaic Specialist Conference (PVSC), 1543–48. IEEE. https:doi.org/10.1109/PVSC.2017.8366707.

Harrison, L., J. Michalsky, and J. Berndt. 1994. "Automated Multifilter Rotating Shadow-Band Radiometer: An Instrument for Optical Depth and Radiation Measurements." *Applied Optics* 33 (22): 5118. https://doi.org/10.1364/AO.33.005118.

Hirsch, T., J. Dersch, T. Fluri, G. Barberena, S. Giuliano, F. Hustig, R. Meyer, M. Seitz, and E. Yildiz. 2017. "SolarPACES Guideline for Bankable STE Yield Assessment." http://www.solarpaces.org/wp-content/uploads/SolarPACES_Guideline_for_Bankable_STE_Yield_Assessment_-_Version_2017.pdf.

IEC 60891. 2021. "IEC 60891:2021 Photovoltaic Devices - Procedures for Temperature and Irradiance Corrections to Measured I-V Characteristics." https://webstore.iec.ch/publication/61766.

IEC 60904-2. 2023. "IEC 60904-2:2023 Photovoltaic Devices - Part 2: Requirements for Photovoltaic Reference Devices." https://webstore.iec.ch/publication/68536.

IEC 60904-3. 2019. "IEC 60904-3:2019 Photovoltaic Devices - Part 3: Measurement Principles for Terrestrial Photovoltaic (PV) Solar Devices with Reference Spectral Irradiance Data." https://webstore.iec.ch/publication/61084.

IEC 60904-4. 2019. "IEC 60904-4:2019 Photovoltaic Devices - Part 4: Photovoltaic Reference Devices - Procedures for Establishing Calibration Traceability." https://webstore.iec.ch/publication/31500.

IEC 61215-1. 2021. “IEC 61215-1:2021 Terrestrial Photovoltaic (PV) Modules - Design Qualification and Type Approval - Part 1: Test Requirements.”

IEC 61724-1. 2021. “IEC 61724-1:2021 Photovoltaic System Performance - Part 1: Monitoring.”

IEC 62862-3. 2018. “IEC 62862-3-2:2018 Solar Thermal Electric Plants - Part 3-2: Systems and Components - General Requirements and Test Methods for Large-Size Parabolic-Trough Collectors.”

IEC 62862-5. 2022. “IEC 62862-5-2:2022 Solar Thermal Electric Plants - Part 5-2: Systems and Components - General Requirements and Test Methods for Large-Size Linear Fresnel Collectors.”

IEC TS 62862-3-3. 2020. “IEC TS 62862-3-3:2020 Solar Thermal Electric Plants - Part 3-3: Systems and Components - General Requirements and Test Methods for Solar Receivers.”

IEC TS62862-1. 2017. “IEC TS62862-1-2:2017 Solar Thermal Electric Plants - Part 1-2: General - Creation of Annual Solar Radiation Dataset for Solar Thermal Electric (STE) Plant Simulation.”

Ineichen, P., and R. Perez. 2002. “A New Airmass Independent Formulation for the Linke Turbidity Coefficient.” *Solar Energy* 73 (3): 151–57. https://doi.org/10.1016/S0038-092X(02)00045-2.

Iqbal, M. 2012. *An Introduction to Solar Radiation*. Elsevier. https://doi.org/10.1016/B978-0-12-373750-2.50002-1.

ISO 9059. 1990. “ISO 9059:1990 Solar Energy — Calibration of Field Pyrheliometers by Comparison to a Reference Pyrheliometer.”

ISO 9060. 1990. “ISO 9060:1990 Solar Energy — Specification and Classification of Instruments for Measuring Hemispherical Solar and Direct Solar Radiation.”

———. 2018. “ISO 9060:2018 Solar Energy — Specification and Classification of Instruments for Measuring Hemispherical Solar and Direct Solar Radiation.” https://www.iso.org/obp/ui/en/#iso:std:iso:9060:ed-2:v1:en.

ISO 9806. 2017. “ISO 9806:2017 Solar Energy — Solar Thermal Collectors — Test Methods.”

ISO 9846. 1993. “ISO 9846:1993 Solar Energy — Calibration of a Pyranometer Using a Pyrheliometer.”

ISO 9847. 2023. “ISO 9847:2023 Solar Energy — Calibration of Pyranometers by Comparison to a Reference Pyranometer.”

ISO/TR 9901. 2021. “ISO/TR 9901:2021 Solar Energy — Pyranometers — Recommended Practice for Use.” https://www.iso.org/standard/81937.html.

Janssen, G., R. Gali, K. de Groot, A. J. Carr, B. B. Van Aken, and I. G. Romijin. 2017. "Impact of Inhomogenous Irradiance at the Rear of Bifacial Panels on Modelled Energy Yield." 33rd European Photovoltaic Solar Energy Conf. and Exhibition, Amsterdam, The Netherlands. https://doi.org/10.4229/EUPVSEC20172017-5BV.4.31.

Kazantzidis, A., P. Tzoumanikas, A.F. Bais, S. Fotopoulos, and G. Economou. 2012. "Cloud Detection and Classification with the Use of Whole-Sky Ground-Based Images." *Atmospheric Research* 113: 80–88. https://doi.org/10.1016/j.atmosres.2012.05.005.

Kazantzidis, A., P. Tzoumanikas, E. Nikitidou, V. Salamalikis, S. Wilbert, and C. Prahl. 2017. "Application of Simple All-Sky Imagers for the Estimation of Aerosol Optical Depth." In *AIP Conf. Proceedings*, 140012. Abu Dhabi, United Arab Emirates. https://doi.org/10.1063/1.4984520.

Kenny, R.P., E. Garcia Menendez, J. Lopez-Garcia, and B. Haile. 2018. "Characterizing the Operating Conditions of Bifacial Modules." In *AIP Conference Proceedings* 020014. Lausanne, Switzerland. https://doi.org/10.1063/1.5049253.

King, D.L., and D.R. Myers. 1997. "Silicon-Photodiode Pyranometers: Operational Characteristics, Historical Experiences, and New Calibration Procedures." 26th IEEE Photovoltaic Specialists Conference: 1285–88. Anaheim, CA, USA: IEEE. https://doi.org/10.1109/PVSC.1997.654323.

Kipp and Zonen. 2017. "Instruction Manual for the SHP1 Smart Pyrheliometer of Kipp & Zonen." https://www.kippzonen.com/Download/596/Manual-Smart-Pyrheliometer-SHP1-English.

Korevaar, M., P. Babal, S. van Nieuwkerk, K. Wilson, and J. Mes. 2020. "Simulation and Validation of Bifacial Irradiance Sensor Mounting Position." 37th European Solar Energy Conference (EUPVSEC), Lisbon, Portugal: 7–11. https://doi.org/10.4229/EUPVSEC20202020-5BO.6.6.

Kreinin, L., N. Bordin, A. Karsenty, A. Drori, D. Grobgeld, and N. Eisenberg. 2010. "PV Module Power Gain Due to Bifacial Design. Preliminary Experimental and Simulation Data." 35th IEEE Photovoltaic Specialists Conference: 002171–75. Honolulu, HI, USA: IEEE. https://doi.org/10.1109/PVSC.2010.5615874.

Kurtz, B., and J. Kleissl. 2017. "Measuring Diffuse, Direct, and Global Irradiance Using a Sky Imager." *Solar Energy* 141: 311–22. https://doi.org/10.1016/j.solener.2016.11.032.

Lara-Fanego, V., C.A. Gueymard, T. Cebecauer, and M. Suri. 2022. "Effectiveness of Short Ground-Based Measurement Campaigns of Surface Albedo." 8th World Conference on Photovoltaic Energy Conversion: 999–1003. https://doi.org/10.4229/WCPEC-82022-4BO.16.4.

Lara-Fanego, V., J.A. Ruiz-Arias, A. Skoczek, C.A. Gueymard, T. Cebecauer, and M. Suri. 2022. "Annual Energy Production Uncertainty of Bifacial PV Plants Caused by Inaccuracies in Albedo Data: Case Studies Using SAM." 49th Photovoltaics Specialists Conference (PVSC), Philadelphia, PA, IEEE. https://doi.org/10.1109/PVSC48317.2022.9938944.

Lezaca, J., R. Meyer, and D. Heinemann. 2018. “Study of an Extended Correction Algorithm for Rotating Shadowband Irradiometers (RSI) Based on Simultaneous Thermal GHI Measurements.” In *AIP Conf. Proceedings*, 190009. Santiago, Chile. https://doi.org/10.1063/1.5067194.

LI-COR. 2001. “Calibration Procedures for LI-COR Spectroradiometers, Radiation Sensors & Lamps.” Application Note #109. https://licor.app.boxenterprise.net/s/e3kud5scodpe9jeerypj (last accessed 22.5.24)

Löf, G.O.G., J.A. Duffie, and C.O. Smith. 1966. “World Distribution of Solar Radiation.” *Solar Energy* 10 (1): 27–37. https://doi.org/10.1016/0038-092X(66)90069-7.

Maxwell, E.L., S.M. Wilcox, C. Cornwall, S.H. Alawaji, B. Marion, M. bin Mahfoodh, and A. Al-Amoudi. 1999. *Progress Report for Annex II--Assessment of Solar Radiation Resources in Saudi Arabia 1993-1997*. NREL/TP-560-25374, National Renewable Energy Laboratory, Golden, CO. https://doi.org/10.2172/14391.

McArthur, L. J. B. 2005. “Baseline Surface Radiation Network (BSRN) – Operation Manual Version 2.1.” World Climate Research Programme. https://epic.awi.de/id/eprint/45991/1/McArthur.pdf.

McIntosh, K.R., M.D. Abbott, B.A. Sudbury, and J. Meydbray. 2019. “Mismatch Loss in Bifacial Modules Due to Nonuniform Illumination in 1-D Tracking Systems.” *IEEE Journal of Photovoltaics* 9 (6): 1504–12. https://doi.org/10.1109/JPHOTOV.2019.2937217.

Merodio, P., F. Martínez-Moreno, R. Moretón, and E. Lorenzo. 2023. “Albedo Measurements and Energy Yield Estimation Uncertainty for Bifacial Photovoltaic Systems.” *Progress in Photovoltaics: Research and Applications* 31 (11): 1130–43. https://doi.org/10.1002/pip.3728.

Michalsky, J., E. Dutton, M. Rubes, D. Nelson, T. Stoffel, M. Wesley, M. Splitt, and J. DeLuisi. 1999. “Optimal Measurement of Surface Shortwave Irradiance Using Current Instrumentation.” *Journal of Atmospheric and Oceanic Technology* 16 (1): 55–69. https://doi.org/10.1175/1520-0426(1999)016<0055:OMOSSI>2.0.CO;2.

Michalsky, J., E.G. Dutton, D. Nelson, J. Wendell, S. Wilcox, A. Andreas, P. Gotseff, et al. 2011. “An Extensive Comparison of Commercial Pyrheliometers under a Wide Range of Routine Observing Conditions.” *Journal of Atmospheric and Oceanic Technology* 28 (6): 752–66. https://doi.org/10.1175/2010JTECHA1518.1.

Michalsky, J.J., M. Kutchenreiter, and C.N. Long. 2017. “Significant Improvements in Pyranometer Nighttime Offsets Using High-Flow DC Ventilation.” *Journal of Atmospheric and Oceanic Technology* 34 (6): 1323–32. https://doi.org/10.1175/JTECH-D-16-0224.1.

Monokroussos, C., Q. Gao, X.Y. Zhang, E. Lee, Y. Wang, C. Zou, L. Rimmelspacher, J. Bonilla Castro, M. Schweiger, and W. Herrmann. 2020. “Rear-side Spectral Irradiance at 1 Sun and Application to Bifacial Module Power Rating.” *Progress in Photovoltaics: Research and Applications* 28 (8): 755–66. https://doi.org/10.1002/pip.3268.

Morrison, R. 1998. *Grounding and Shielding Techniques*. New York: John Wiley and Sons.

Mouhib, E., P.M. Rodrigo, L. Micheli, E.F. Fernández, and F. Almonacid. 2022. "Quantifying the Rear and Front Long-Term Spectral Impact on Bifacial Photovoltaic Modules." *Solar Energy* 247: 202–13. https://doi.org/10.1016/j.solener.2022.10.035.

Mueller, R., T. Behrendt, A. Hammer, and A. Kemper. 2012. "A New Algorithm for the Satellite-Based Retrieval of Solar Surface Irradiance in Spectral Bands." *Remote Sensing* 4 (3): 622–47. https://doi.org/10.3390/rs4030622.

Myers, D. R., and S. M. Wilcox. 2009. *Relative Accuracy of 1-Minute and Daily Total Solar Radiation Data for 12 Global and 4 Direct Beam Solar Radiometers*. NREL/CP-550-45374. National Renewable Energy Laboratory, Golden, CO. https://www.nrel.gov/docs/fy09osti/45374.pdf.

Myers, D.R., S.M. Wilcox, W.F. Marion, N.M. Al-Abbadi, M. Mahfoodh, and Z. Al-Otaibi. 2002. *Final Report for Annex II--Assessment of Solar Radiation Resources In Saudi Arabia, 1998-2000*. NREL/TP-560-31546. National Renewable Energy Laboratory, Golden, CO. https://www.osti.gov/servlets/purl/15000263.

Nollas, F.M., G.A. Salazar, and C.A. Gueymard. 2023. "Quality Control Procedure for 1-Minute Pyranometric Measurements of Global and Shadowband-Based Diffuse Solar Irradiance." *Renewable Energy* 202: 40–55. https://doi.org/10.1016/j.renene.2022.11.056.

NREL. 2022. "Broadband Outdoor Radiometer Calibration Shortwave BORCAL-SW 2022-02." National Renewable Energy Laboratory, Golden, CO. https://aim.nrel.gov/Calibrations/BORCAL/SRRL/report/2022-02_NREL-SRRL-BMS.pdf.

Osterwald, C. R., S. Anevsky, K. Bücher, A. K. Barua, P. Chaudhuri, J. Dubard, K. Emery, et al. 1999. "The World Photovoltaic Scale: An International Reference Cell Calibration Program." *Progress in Photovoltaics: Research and Applications* 7 (4): 287–97. https://doi.org/10.1002/(SICI)1099-159X(199907/08)7:4<287::AID-PIP259>3.0.CO;2-I.

Painter, H. E. 1981. "The Performance of a Campbell-Stokes Sunshine Recorder Compared with a Simultaneous Record of the Normal Incidence Irradiance." *Meteorological Magazine* 110 (1305): 102–109.

Pape, B., J. Batlles, N. Geuder, R. Zurita Pinero, F. Adan, and B. Pulvermüller. 2009. "Soiling Impact and Correction Formulas in Solar Measurements for CSP Projects." 15th SolarPACES International Symposium, Berlin, Germany.

Patel, M. Tahir, M. Ryyan Khan, Xingshu Sun, and Muhammad A. Alam. 2019. "A Worldwide Cost-Based Design and Optimization of Tilted Bifacial Solar Farms." *Applied Energy* 247: 467–79. https://doi.org/10.1016/j.apenergy.2019.03.150.

Pelaez, S.A., C. Deline, P. Greenberg, J.S. Stein, and R.K. Kostuk. 2019. "Model and Validation of Single-Axis Tracking With Bifacial PV." *IEEE Journal of Photovoltaics* 9 (3): 715–21. https://doi.org/10.1109/JPHOTOV.2019.2892872.

Pelaez, S.A., C. Deline, S.M. MacAlpine, B. Marion, J.S. Stein, and R.K. Kostuk. 2019. "Comparison of Bifacial Solar Irradiance Model Predictions With Field Validation." *IEEE Journal of Photovoltaics* 9 (1): 82–88. https://doi.org/10.1109/JPHOTOV.2018.2877000.

Pelaez, S.A., C. Deline, B. Marion, B. Sekulic, J. Parker, B. McDanold, and J.S. Stein. 2020. "Field-Array Benchmark of Commercial Bifacial PV Technologies with Publicly Available Data." 47th IEEE Photovoltaic Specialists Conference (PVSC): 1757–59. Calgary, AB, Canada: IEEE. https://doi.org/10.1109/PVSC45281.2020.9300379.

Pelaez, S.A., C. Deline, J.S. Stein, B. Marion, K. Anderson, and M. Muller. 2019. "Effect of Torque-Tube Parameters on Rear-Irradiance and Rear-Shading Loss for Bifacial PV Performance on Single-Axis Tracking Systems." 46th Photovoltaic Specialists Conference (PVSC): 1–6. Chicago, IL, USA: IEEE. https://doi.org/10.1109/PVSC40753.2019.9198975.

Plag, F., I. Kröger, S. Riechelmann, and S. Winter. 2018. "Multidimensional Model to Correct PV Device Performance Measurements Taken under Diffuse Irradiation to Reference Conditions." *Solar Energy* 174: 431–44. https://doi.org/10.1016/j.solener.2018.08.072.

Pó, M.. 2023. "Solar Irradiance beyond a Shadow of a Doubt." Power and Energy Solutions. https://pes.eu.com/wp-content/uploads/2023/05/PES-S-2-23-EKO.pdf.

Ramtvedt, E.N., and E. Næsset. 2023. "A Simple Slope Correction of Horizontally Measured Albedo in Sloping Terrain." *Agricultural and Forest Meteorology* 339: 109547. https://doi.org/10.1016/j.agrformet.2023.109547.

Reda, I. 1996. *Calibration of a Solar Absolute Cavity Radiometer with Traceability to the World Radiometric Reference*. NREL/TP-463-20619. National Renewable Energy Laboratory, Golden, CO. https://www.nrel.gov/docs/legosti/fy96/20619.pdf.

Reda, I., T. Stoffel, and D. Myers. 2003. "A Method to Calibrate a Solar Pyranometer for Measuring Reference Diffuse Irradiance." *Solar Energy* 74 (2): 103–12. https://doi.org/10.1016/S0038-092X(03)00124-5.

Riedel-Lyngskær, N., and N. Andersen. 2024. "Strategies for Rear Irradiance Monitoring in Tracked Bifacial Systems." Presented at the 2023 PV Performance Modeling Workshop, Salt Lake City, Utah. *Solar Energy* (submitted).

Riedel-Lyngskær, N., D. Berrian, D. Alvarez Mira, A. Aguilar Protti, P. Behrensdorff Poulsen, J. Libal, and J. Vedde. 2020. "Validation of Bifacial Photovoltaic Simulation Software against Monitoring Data from Large-Scale Single-Axis Trackers and Fixed Tilt Systems in Denmark." *Applied Sciences* 10 (23): 8487. https://doi.org/10.3390/app10238487.

Riedel-Lyngskær, N., M. Petit, D. Berrian, P.B. Poulsen, J. Libal, and M.L. Jakobsen. 2020. "A Spatial Irradiance Map Measured on the Rear Side of a Utility-Scale Horizontal Single Axis Tracker with Validation Using Open Source Tools." 47th IEEE Photovoltaic Specialists Conference (PVSC): 1026–32. https://doi.org/10.1109/PVSC45281.2020.9300608.

Riedel-Lyngskær, N., M. Ribaconka, M. Pó, A. Thorseth, S. Thorsteinsson, C. Dam-Hansen, and M.L. Jakobsen. 2022. "The Effect of Spectral Albedo in Bifacial Photovoltaic Performance." *Solar Energy* 231: 921–35. https://doi.org/10.1016/j.solener.2021.12.023.

Riedel-Lyngskar, N., M. Bartholomaus, J. Vedde, P. Behrensdorff Poulsen, and S. Spataru. 2022. "Measuring Irradiance With Bifacial Reference Panels." *IEEE Journal of Photovoltaics* 12 (6): 1324–33. https://doi.org/10.1109/JPHOTOV.2022.3201468.

Rossa, C., F. Martínez-Moreno, and E. Lorenzo. 2021. "Experimental Observations in Mismatch Losses in Monofacial and Bifacial PV Generators." *Progress in Photovoltaics: Research and Applications* 29 (12): 1223–35. https://doi.org/10.1002/pip.3447.

Sanchez, G., M. L. Cancillo, and A. Serrano. 2016. "An Intercomparison of the Thermal Offset for Different Pyranometers." *Journal of Geophysical Research: Atmospheres* 121 (13): 7901–12. https://doi.org/10.1002/2016JD024815.

Sanchez, G., A. Serrano, and M. L. Cancillo. 2017. "Effect of Mechanical Ventilation on the Thermal Offset of Pyranometers during Cloud-Free Summer Conditions." *Journal of Atmospheric and Oceanic Technology* 34 (5): 1155–73. https://doi.org/10.1175/JTECH-D-16-0163.1.

Sengupta, M., and A. Andreas. 2010. "Oahu Solar Measurement Grid (1-Year Archive): 1-Second Solar Irradiance; Oahu, Hawaii (Data)." https://doi.org/10.5439/1052451.

Stanhill, G. 1998. "Estimation of Direct Solar Beam Irradiance from Measurements of the Duration of Bright Sunshine." *International Journal of Climatology* 18 (3): 347–54. https://doi.org/10.1002/(SICI)1097-0088(19980315)18:3<347::AID-JOC239>3.0.CO;2-O.

Sun, X., M.R. Khan, C. Deline, and M.A. Alam. 2018. "Optimization and Performance of Bifacial Solar Modules: A Global Perspective." *Applied Energy* 212: 1601–10. https://doi.org/10.1016/j.apenergy.2017.12.041.

Viel, L. 2006. "Silicon Solar Radiation Sensor Type SOZ-03." NES Sensors GmbH. http://ctsteknik.dk/upload_dir/shop/soz-03datasheetuk-898892.pdf.

Vignola, F. 2006. "Removing Systematic Errors from Rotating Shadowband Pyranometer Data." In *Proc. of the 35th ASES Annual Conference,* Denver, CO.

Vignola, F., C.N. Long, and I. Reda. 2009. "Testing a Model of IR Radiative Losses." In *Optical Modeling and Measurements for Solar Energy Systems III*, edited by Benjamin K. Tsai, SPIE Conf. 741003. San Diego, CA. https://doi.org/10.1117/12.826325.

Vignola, F., J. Michalsky, and T.L. Stoffel. 2020. *Solar and Infrared Radiation Measurements*. Second edition. Boca Raton: CRC Press, Taylor & Francis Group.

Vignola, F., J. Peterson, R. Kessler, M. Dooraghi, M. Sengupta, and F. Mavromatakis. 2018. "Evaluation of Photodiode-Based Pyranometers and Reference Solar Cells on a Two-Axis

Tracking System." 7th World Conference on Photovoltaic Energy Conversion (WCPEC): 2376–81. Waikoloa Village, HI: IEEE. https://doi.org/10.1109/PVSC.2018.8547299.

Vignola, F., J. Peterson, R. Kessler, S. Snider, P. Gotseff, M. Sengupta, A. Habte, A. Andreas, and F. Mavromatakis. 2022. "Reference Cell Performance and Modeling on a One-Axis Tracking Surface." 49th Photovoltaics Specialists Conference (PVSC): 0146–53. Philadelphia, PA, USA: IEEE. https://doi.org/10.1109/PVSC48317.2022.9938920.

Vignola, F., J. Peterson, F. Mavromatakis, S. Wilbert, A. Forstinger, M. Dooraghi, and M. Sengupta. 2019. "Removing Biases from Rotating Shadowband Radiometers." In *AIP Conf. Proceedings*, 190017. Casablanca, Morocco. https://doi.org/10.1063/1.5117714.

Vignola, F., J. Peterson, S. Wilbert, P. Blanc, N. Geuder, and C. Kern. 2017. "New Methodology for Adjusting Rotating Shadowband Irradiometer Measurements." In *AIP Conf. Proceedings*, 140021. Abu Dhabi, United Arab Emirates. https://doi.org/10.1063/1.4984529.

Vuilleumier, L., C. Félix, F. Vignola, P. Blanc, J. Badosa, A. Kazantzidis, and B. Calpini. 2017. "Performance Evaluation of Radiation Sensors for the Solar Energy Sector." *Meteorologische Zeitschrift*. https://doi.org/10.1127/metz/2017/0836.

Walter, B., R. Winkler, F. Graber, W. Finsterle, N. Fox, V. Li, and W. Schmutz. 2017. "Direct Solar Irradiance Measurements with a Cryogenic Solar Absolute Radiometer." *AIP Conference Proceedings* 1810 (1): 080007. https://doi.org/10.1063/1.4975538.

Wang, D., S. Liang, T. He, Y. Yu, C. Schaaf, and Z. Wang. 2015. "Estimating Daily Mean Land Surface Albedo from MODIS Data: Estimating Daily Mean Albedo from MODIS." *Journal of Geophysical Research: Atmospheres* 120 (10): 4825–41. https://doi.org/10.1002/2015JD023178.

Wilbert, S., N. Geuder, M. Schwandt, B. Kraas, W. Jessen, R. Meyer, B. Nouri, A. Forstinger and F. Vignola. 2023. "Best Practices for Solar Irradiance Measurements with Rotating Shadowband Irradiometers." https://elib.dlr.de/198919/1/RSI_BestPractices_v2.pdf.

Wilbert, S., W. Jessen, A. Forstinger, A. Driesse, F. Vignola, M. Sengupta, A. Habte, L. Zarzalejo, and A. Marzo. 2019. "Application of the Clear Sky Spectral Error for Radiometer Classification in ISO 9060." In *Proceedings of the ISES Solar World Congress 2019*, 1–11. Santiago, Chile: International Solar Energy Society. https://doi.org/10.18086/swc.2019.44.08.

Wilbert, S., S. Kleindiek, B. Nouri, N. Geuder, A. Habte, M. Schwandt, and F. Vignola. 2016. "Uncertainty of Rotating Shadowband Irradiometers and Si-Pyranometers Including the Spectral Irradiance Error." In *AIP Conf. Proceedings*, 150009. Cape Town, South Africa. https://doi.org/10.1063/1.4949241.

Wilcox, S.M., and D.R. Myers. 2008. *Evaluation of Radiometers in Full-Time Use at the National Renewable Energy Laboratory Solar Radiation Research Laboratory*. NREL/TP-550-44627. National Renewable Energy Laboratory, Golden, CO. https://doi.org/10.2172/946331.

WMO. 2018. "Guide to Instruments and Methods of Observation." *World Meteorological Organization WMO*. https://library.wmo.int/index.php.

Xie, Y., and M. Sengupta. 2018. "A Fast All-Sky Radiation Model for Solar Applications with Narrowband Irradiances on Tilted Surfaces (FARMS-NIT): Part I. The Clear-Sky Model." *Solar Energy* 174: 691–702. https://doi.org/10.1016/j.solener.2018.09.056.

Zhao, C., J. Xiao, Y. Yu, and J-N Jaubert. 2021. "Accurate Shading Factor and Mismatch Loss Analysis of Bifacial HSAT Systems through Ray-Tracing Modeling." *Solar Energy Advances* 1: 100004. https://doi.org/10.1016/j.seja.2021.100004.

Ziar, H., F. Fatih Sönmez, O. Isabella, and M. Zeman. 2019. "A Comprehensive Albedo Model for Solar Energy Applications: Geometric Spectral Albedo." *Applied Energy* 255: 113867. https://doi.org/10.1016/j.apenergy.2019.113867.

Appendix. Design Examples and Checklists, From Site Selection to Installation

A-1. Examples of Meteorological Sensor Configurations and Station Layouts

Figures 3A-1–Figure 3A-7 show plans of exemplary layouts for Tier-1 and Tier-2 stations, partly including albedo measurements. The examples also illustrate the following selected design considerations:

- Easy access to the sensors that need to be cleaned regularly without additional equipment (no ladders) must be considered.
- When installing near the equator (within the tropics), sun elevation and azimuth must be considered with special attention when designing the station layout to avoid shading in the irradiance sensors. Over the course of the year, objects cast shadings in all directions, (e.g., the wind mast needs to be far enough away from the irradiance sensors so that its top does not shade the sensors when the sun is in the north/south sky quadrant [for stations in the Northern/Southern Hemisphere, respectively]).
- A station's optical reference plane should be defined at the level of the actual radiometer sensors; anything above that will be in the view of the sensors. Regular checks must ensure that no other nearby instrument, equipment, or support will intrude above that plane and adversely affect the measurements. Some unavoidable allowances must be made for certain equipment, such as a shading-ball assembly. More distant items, such as a wind tower, must also be tolerated. All other items, such as equipment boxes, hand railings, fencing, proximate meteorological instruments, conduits, cabling, etc., should be positioned below the measurement plane. This means that the measurement plane must be planned for a position above all other necessary equipment at the site and the radiometer supports designed accordingly.

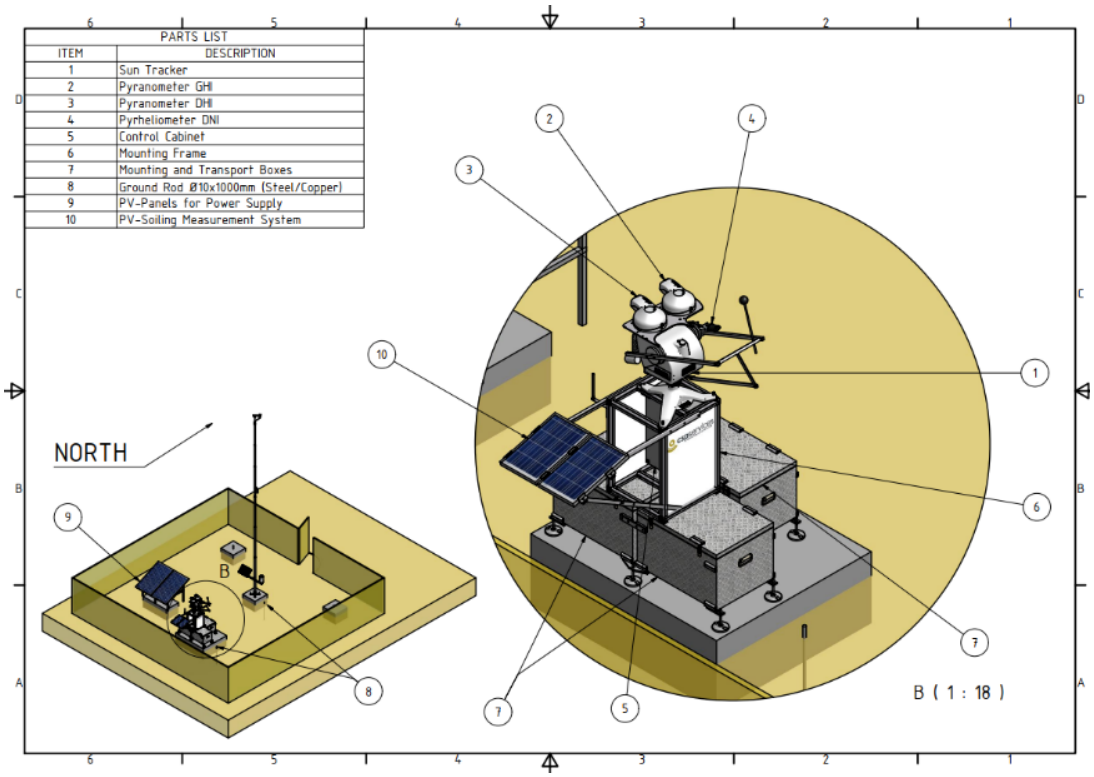

Figure 3A-1. Exemplary station design for a station in the Northern Hemisphere, with close-up of the sun tracker.

Image from CSP Services

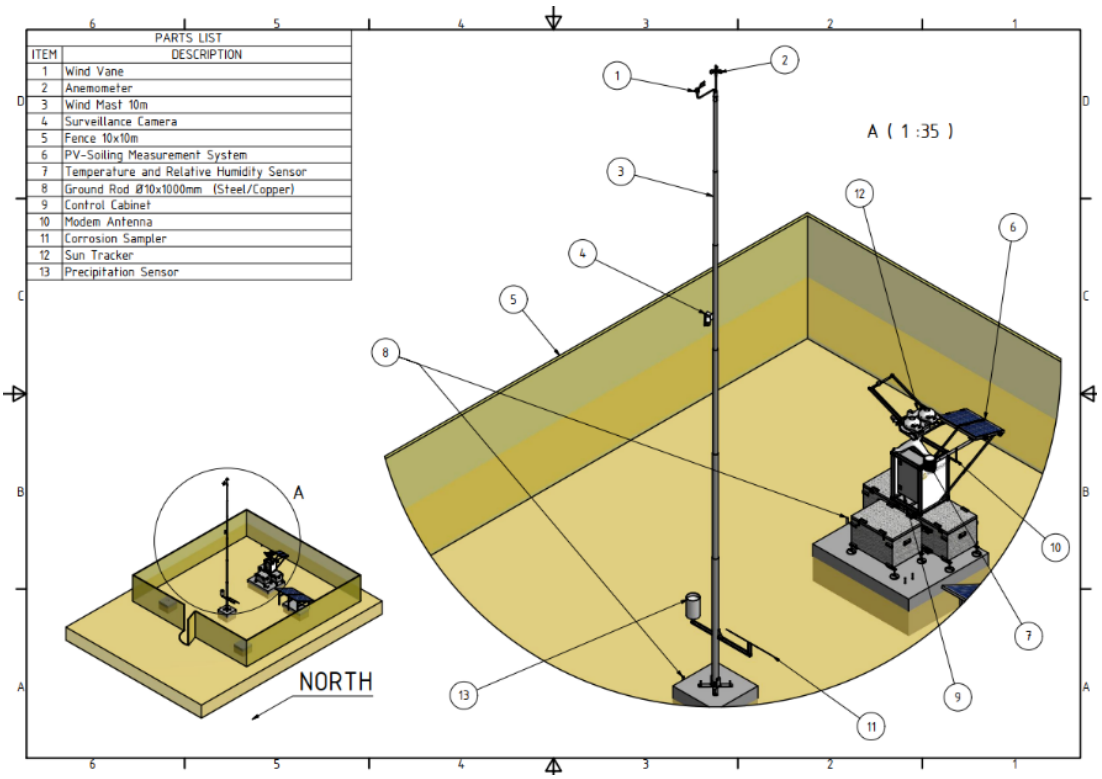

Figure 3A-2. Exemplary station design for a station in the Northern Hemisphere, with close-up of the wind mast.

Image from CSP Services

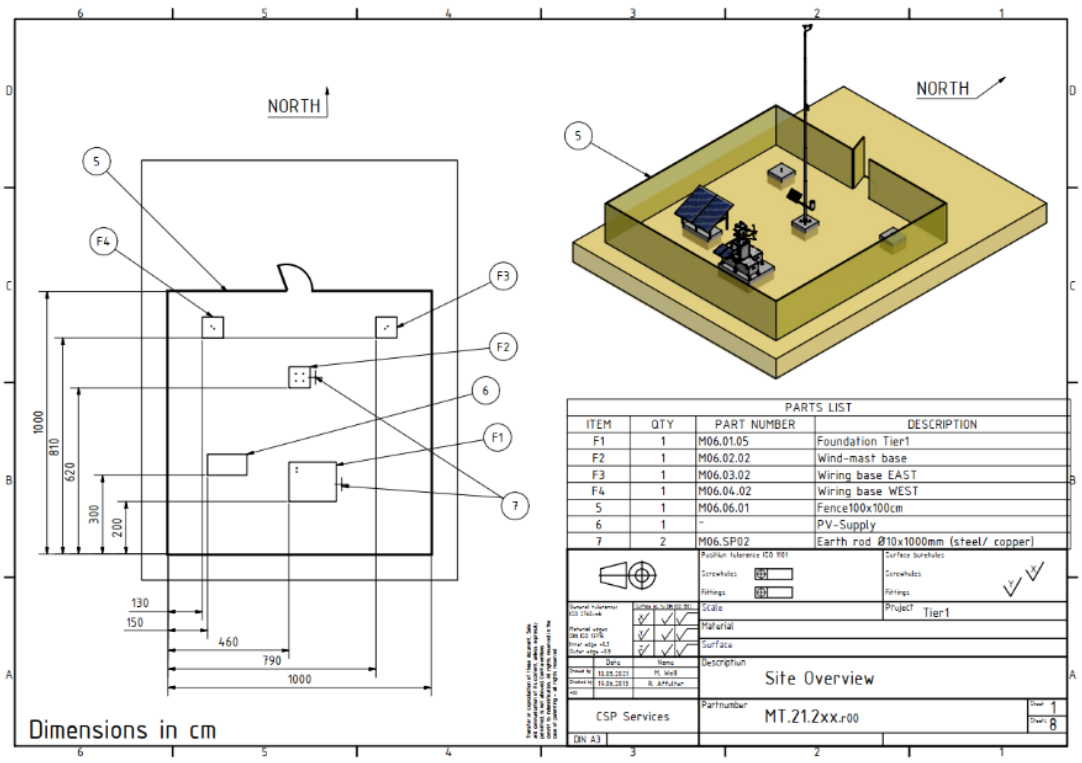

Figure 3A-3. Exemplary station design for a station in the Northern Hemisphere: general layout.

Image from CSP Services

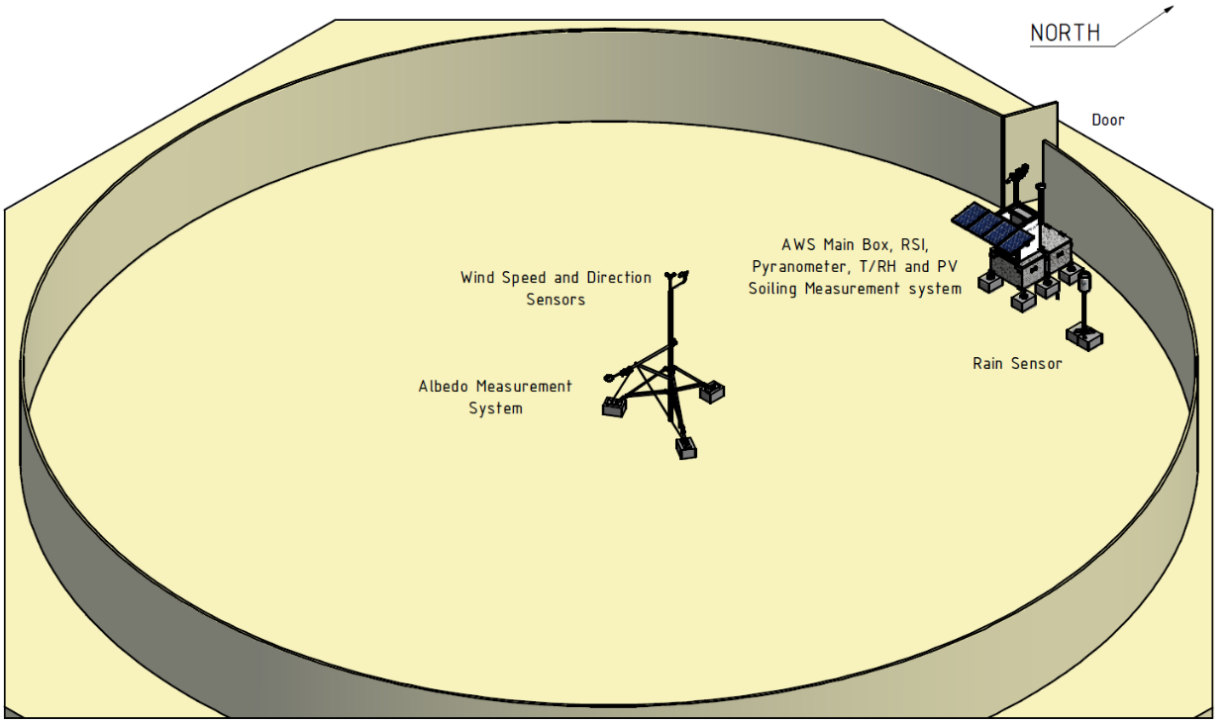

Figure 3A-4. Example station design for a Tier-2 station in the Northern Hemisphere with an albedometer (RHI pyranometer at 1.5-m height).

Image from CSP Services

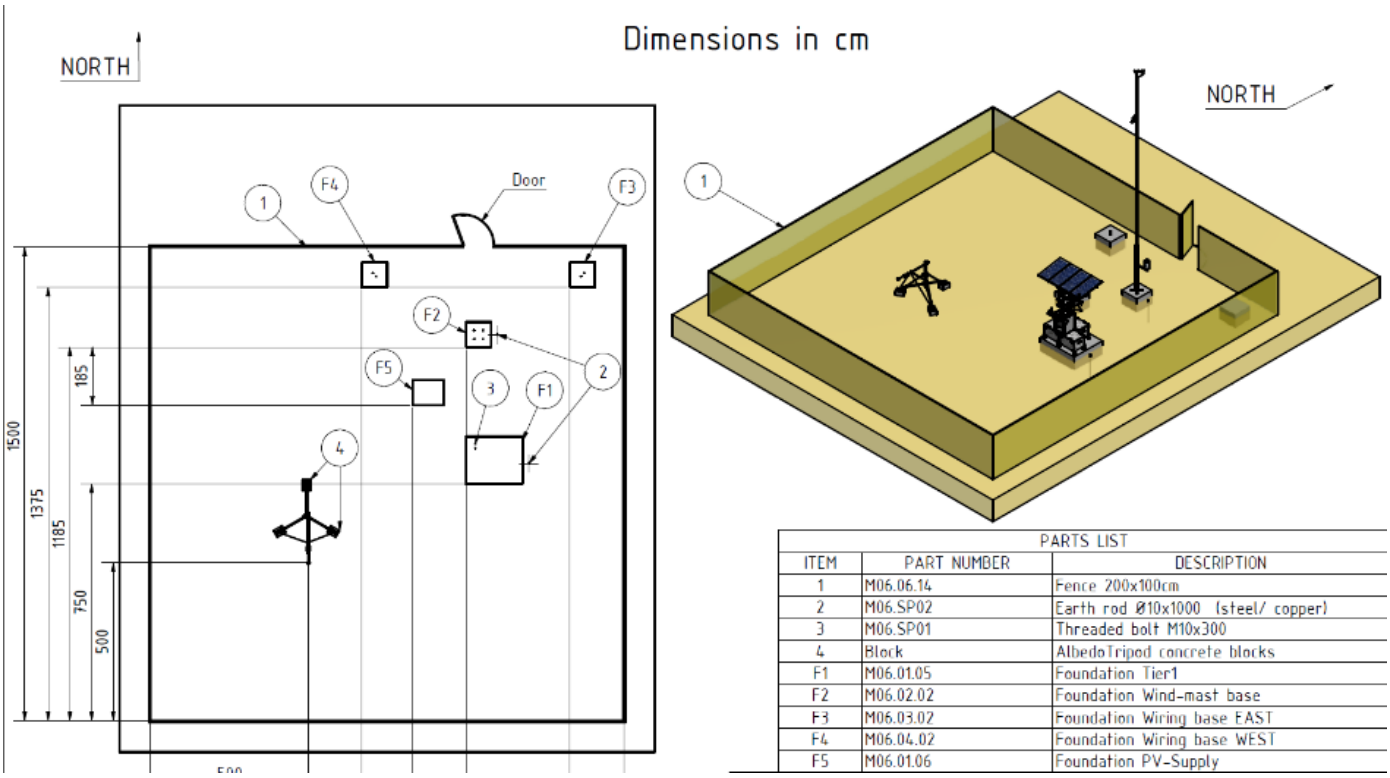

Figure 3A-5. Exemplary station design for a Tier-2 station in the Northern Hemisphere with an albedometer (RHI pyranometer at 1.5-m height).

Image from CSP Services

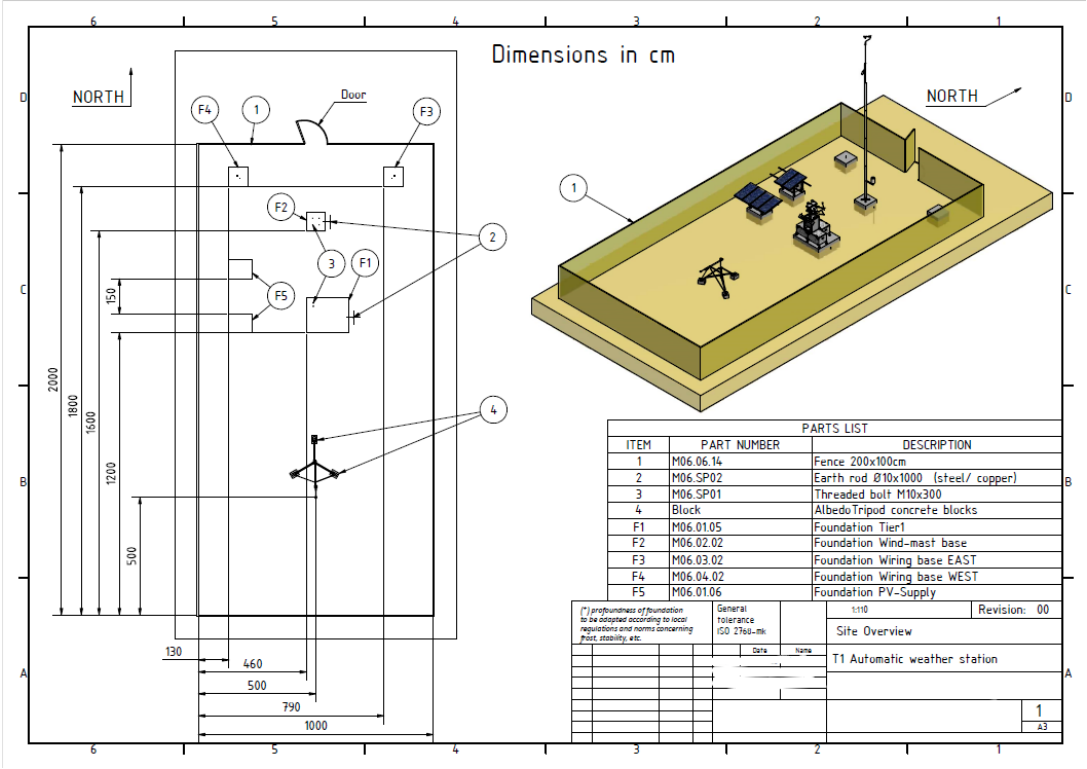

Figure 3A-6. Exemplary station design for a Tier-1 station in the Northern Hemisphere with an albedometer (RHI pyranometer at 1.5-m height).

Image from CSP Services

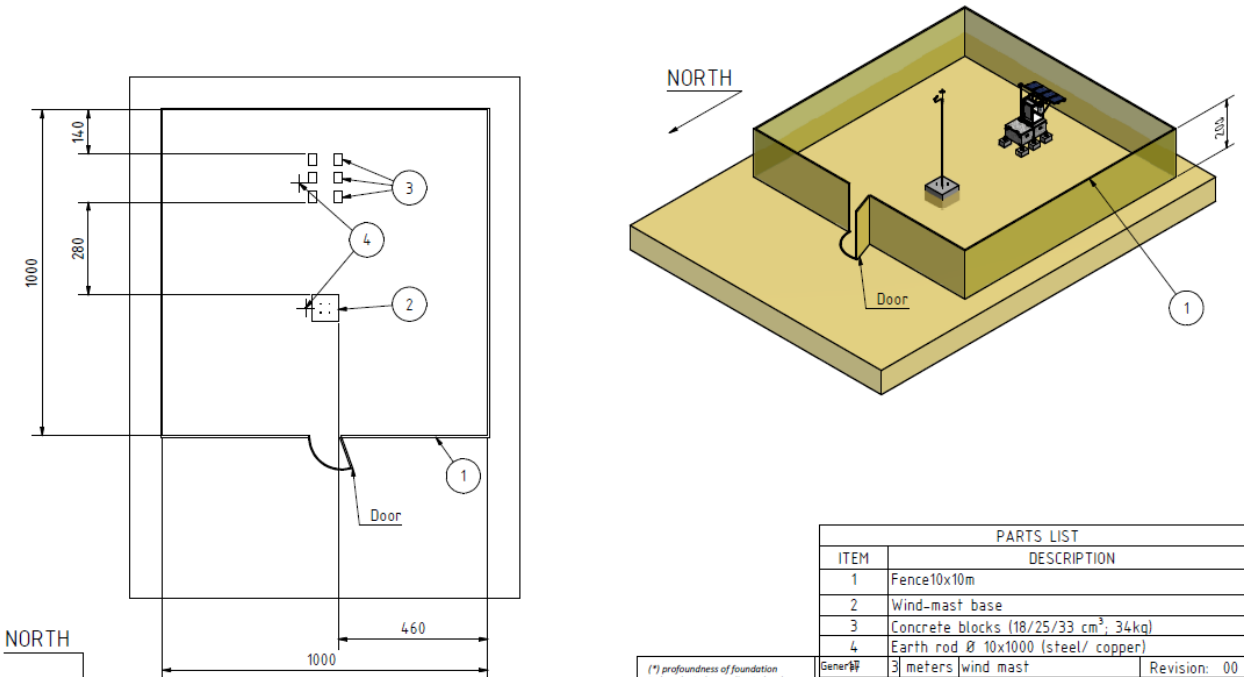

Figure 3A-7. Exemplary station design for a Tier-2 station in the Northern Hemisphere with a 3-m wind mast.

Image from CSP Services

A-2. Site Selection Checklist Examples

Table 3A-1. Site Selection Checklist

Key Information				
Date of site visit				
Site visit performed by		Name and title: Position: Telephone: Email:		
Location, site name (Country, city, street address, or description of location)				
Coordinates and altitude		°N: °S: m above sea level:		
Name of site owner				
Client representative (if present)		Name and title: Position: Telephone: Email:		
Interview partner (local contact)		Name and title: Position: Telephone: Email:		
Dimensions	Minimum area available	Minimum area requirement for weather stations (typically 10 × 10 m², may be larger with albedo measurement or other specific measurements)		
Nearby objects, shading	Unobstructed horizon	Is the horizon free of nearby objects such as trees or buildings that could shade the instruments or affect the other measurements (e.g., wind speed)?		
Surface installation	Firm natural ground	Firm ground suitable to enable secure locking of the equipment on the ground (anchors or foundations). Note the type of ground: naturally grown soil or artificially (manmade) filled soil, bedrock, loose soil or sand, grass cover, gravel.		
	Horizontally leveled	Is the site approximately (visual judgement) horizontally leveled and flat?		

Key Information				
	Excavation for foundations possible	Is it possible and permitted to lay 4–5 small foundations, each approximately 1 × 1 m² and 0.3 m deep?		
	Fencing of the site possible	Is it possible and permitted to fence the compound? Note if the location is already fenced (take photos).		
	No drifting sand, landslide	Is there danger of drifting sand or landslides/rockfalls?		
	No flooding possible	Might the terrain be flooded during heavy rainfalls?		
Rooftop installation	Easy access to rooftop installation	- Authorization from building owner to access building on weekends, holidays, or after hours. - Interior or exterior stairs with adequate safety railings OR adequate wall area for permanent and sturdy ladder installation with approved safety features. - Adequate interior or exterior routes for transporting equipment crates for station assembly (note minimum height and width along route).		
	Suitable roof substrate	Strong roof underlayment adequate to bear, without damage, the weight of: - Equipment and personnel. - Heavy anchors to secure the installation OR adequate material for drilling anchor points. Approximate weight should be determined prior to site investigations.		
	Power and grounding	- Available conduits to building interior for power or cabling if necessary. - Available electrical ground for noise suppression and lighting protection (e.g., a nearby water pipe or access to run wire across the roof and down a wall to an area suitable for a grounding rod).		
	Security	Lockable rooftop door or gate to limit access by unauthorized people from building interior or building perimeter		
Surroundings	Industrial areas or power plants	Check whether any industrial production site or power plant is located within a few kilometers, which may cause emissions of smoke, vapor, dust or other aerosols/particles. Note		

Key Information				
		any visible industry with notable emissions; ask local staff to confirm.		
	Sources of smoke or vapor	Check whether any source of smoke or water vapor columns is located in the environment. Note also if seasonal fires (natural or not) can be expected.		
	Quarry or mine	Check if quarries or mines in the environments may be causing pollution by lifting dust		
	Main road, dirt road, tracks	Check presence of nearby roads (less than 100 m away) and indicate type (paved/unpaved, main traffic or seldom used)		
	Settlements, towns, city			
	Agricultural area	Agricultural activities, main crops, use of fire to clear fields, dust lifted by machinery, animal feeding, slaughterhouse, breeding farm		
	Swamp, lake, river, ocean	Large water bodies like rivers or lakes		
	Sand dunes	Presence of sand dunes within a few kilometers		
	Animal population	Animal population in the area that might have an impact on the measurements (monkeys, birds, termites, insects like bees, wasps, etc.); ask the local staff about animal migration in the region. In what period do nomads pass through the region and with what animals?		
	Reflections or light sources in the vicinity	Check whether any reflecting surfaces like mirrors, glazing, shiny metal surfaces, PV panels, etc., or artificial light sources are in the vicinity that might cause reflections or radiation on the measurement equipment (take photos)		
	Vegetation presence	Note whether vegetation can influence the measurements due to growth or seasonal changes (take photos)		
	Future adverse development	Inquire about potential future development that could impact horizon view, impose construction traffic, or force moving the station		
	Other	Any other observations with potential impact on the measurements. In case		

Key Information				
		of doubt about an influence, please annotate the observation.		
Mobile phone network coverage	2G, 3G, 4G, 5G network available	Check for mobile phone networks by searching manually for network providers. Note signal strength for each provider available.		
Accessibility	Accessible by car	Check whether the site is easily reachable by car for installation/maintenance. Note any road conditions, including seasonal weather, which might require use of four-wheel-drive or high-clearance vehicles.		
Land use rights	Permit available	Check/ask if the land use permits are given from the landowner and who must be contacted		
Maintenance	Maintenance staff available	Check/ask/estimate the availability of local maintenance staff (on-site maintenance team)		
Security	Measures against theft or vandalism required	Check/ask/estimate the risk of theft or vandalism. Check/ask if a safety guard or similar is required or available to watch the equipment. Note if measures are already taken (existing fence or safety guards present).		
	UXO	Is the site in an area affected by previous/current armed conflict, and is there a potential risk from UXO?		
Photographic documentation	Overview photos taken	Photos that show the overall site and surroundings		Time when photos were taken:
	Panoramic photos	Panoramic image showing the horizon over a full 360°		
	360° photo series	Photo series showing the horizon over a full 360°		
	Marker for north and south direction visible in the photos	In the notes, add the kind of marker that was used (e.g., “North: red bag”; “South: flag”; “blue safety jacket”).		

A-3. Site Preparation Procedure

For this task, a handheld GPS system is needed to ensure the correct alignment of the foundations. Figure 3A-8 and Figure 3A-9 show photos of a station before the installation of the measurement equipment.

Figure 3A-8. Fence picture examples.

Photos by CSP Services

Figure 3A-9. Built foundations with threaded bolts.

Photo by CSP Services

A-4. Example Installation Checklist

Table 3A-2. Example Installation Checklist

Component	Work Item	Checked		Comments
		Yes	No	
North-south line	The station's north-south line established and clearly marked prior to construction.			
Foundations, fence	Foundations correctly prepared	X		
	Threaded bolts correctly prepared	X		
	Fence correctly prepared	X		
	Project signs attached	X		
Support structure with control box	PV mounting supports adjusted	X		
	Horizontally leveled	X		
Wiring, cables	Visual examination	X		
	Fuses okay	X		
	All sensors connected	X		
	All cables orderly fixed	X		
Solar tracker	Shading assembly installed	X		
	Horizontal leveling	X		
	East/west alignment completed	X		
Radiometers	Sensors installed	X		
	Operability of each sensor	X		
	Correct leveling	X		
Barometric pressure sensor	Sensor installed	X		
	Pressure exchange vent	X		Installed inside main control cabinet
Precipitation sensor	Sensor installed and leveled	X		
	Operability of sensor	X		
Temperature and humidity sensor	Sensor fixed to frame	X		
Wind tower, wind speed and direction sensors	Mast extended	X		Extended to length of 10 m
	Guy wires safely attached and tense	X		
	Grounding cable connected	X		To metal rod driven into ground
	Wind sensors installed	X		

Component	Work Item	Checked		Comments
		Yes	No	
	North orientation of wind direction sensor	X		
	Cable fixed to sensors, tower, and box	X		
	Operability of sensors	X		
PV soiling measurement system	Mounting structure leveled and aligned to south	X		
	PV panels installed	X		
	Tilt angle adjusted	X		8° from horizontal
	Module temp. sensors installed	X		
	Operability of system	X		
	Panels cleaned	X		
LTE router	SIM card inserted	X		Data connection to server established
	Server connection	X		Connection to server confirmed
Data logger	Operation system installed	X		Version: CR1000X Std.05.00
	Correct sensor constants in program	X		Compared against photographs of installed sensors
	Correct coordinates in program	X		Obtained from GPS
	Data logger program installed	X		Program name: ExampleStation_str_Enc.CR1X
	Data logger clock correct Correct security code entered (if used)	X		Local standard time, no daylight saving Time: e.g., UTC +0

A-5. Exemplary Final Operational Checklist

Table 3A-3. Exemplary Final Operational Checklist

Data Checkout:				
Instrument	**Signal Name**	**Instantaneous Reading w/ Units**	**Reasonable?**	**Varying Regularly?**
Primary pyranometer	Global Raw			
Secondary pyranometer	Secondary_Irradiance			
Barometric pressure (wait 15 minutes)	Press			
Air temperature	AirTemp_C			
Relative humidity	RH			
Wind speed	WS_ms			
Wind direction	WDir			
Rain gauge	Rain_mm			
Battery voltage	Batt_Volt			
Logger panel temperature	Panel_Temp_C			
…				

A-6. Exemplary Photographic Documentation Checklist

Table 3A-4. Exemplary Photographic Documentation Checklist

Needed Picture	Received
Fence and foundation with north reference	
Station and wind mast foundations	
Wind mast preparations/setup	
Wind mast foundations, ground cable fixed to ground bolt, protective tube for wind mast cables	
Wind direction sensor north mark aligned with mounting cantilever and north direction	
Wind sensors installed on wind mast	
Wind mast erected; wind direction sensor oriented to north	
Serial number of all pyranometers	
Serial number of pyrheliometer (if available)	
Leveling of all pyranometers	
Tracker leveling (if available)	
Serial number of tracker (if available)	
Installed tracker (if available)	
Shading assembly alignment (shadow on pyranometer) (if available)	
Pyrheliometer alignment (if available)	
Sun sensor serial number (if available)	
Rain sensor picture	
Rain sensor serial number	
Rain sensor leveling	
Temperature, relative humidity sensor picture	
Temperature, relative humidity sensor serial number	
Control box interior	
LTE router	
Antenna	
Power supply PV system	
Mounting structure, solar tracker, sensors, and control box from four sides	
Final station installation as seen from all sides including fence	
Locked gate (if applicable)	

4 Data Quality Assessment and Control

Adam R. Jensen,[1] Yves-Marie Saint-Drenan,[2] Christian A. Gueymard,[3] Philippe Blanc,[2] Steve Wilcox,[4] and Anton Driesse[5]

[1] *Technical University of Denmark (DTU), Denmark*
[2] *MINES Paris PSL, France*
[3] *Solar Consulting Services, USA*
[4] *Solar Resource Solutions, LLC, USA*
[5] *PV Performance Labs, Germany*

Executive Summary

The quality of solar irradiance measurements depends on several factors, including instrument characteristics, maintenance practices, and location. Even for high-quality stations adhering to accepted best practices, erroneous measurements are inevitable when measuring solar irradiance long term, such as errors due to soiling, snow, or instrument misalignments. Thus, assessing the data quality and, subsequently, flagging suspicious or erroneous measurements is crucial for applications requiring solar irradiance data with the lowest estimated uncertainty. This is becoming increasingly important as the accuracy of modeled irradiance data is approaching that of measured irradiance. This chapter provides an introduction to quality assessment and control concepts, as well as an overview of methods for different time scales—namely, instantaneous, daily, and long-term measurements. Additionally, many specific elements of quality assessment and control procedures are discussed, covering measurements from tilted radiometers, photodiodes, spectral sensors, and photovoltaic reference cells. This chapter concludes with an introduction to the data quality cycle concept and a summary of future development needs.

4.1 Introduction

All measurements are subject to errors. In particular, due to the challenging nature of making solar irradiance measurements, they are more prone to errors than other meteorological quantities, such as temperature, humidity, or wind speed (Journée and Bertrand 2011). Considering the inherent difficulties in measuring solar irradiance, it is crucial that in-depth quality control (QC) procedures are applied to ensure that the sources of errors are quickly mitigated to minimize the influence on data quality. Additionally, post-measurement data quality assessment should be conducted to eventually obtain a high-quality dataset with a low amount of erroneous data. Data assessment and QC serve two main purposes, namely, flagging suspicious or erroneous data with the aim of enhancing the quality of the dataset and using this information to provide feedback to station operators, allowing for corrective QC actions to be taken. Within the solar resource community, there is no strict definition of quality assessment or QC, and thus these terms have often been used interchangeably. In this handbook, the term "quality control" is normally indicative of procedures that are used regularly by station operators with the aim of improving data collection through corrective actions. Compared to this QC definition, the term "data quality assessment" rather describes the post-measurement evaluation of a dataset, often relying on the process of flagging periods of potentially erroneous data to eventually obtain a high-quality dataset. Whereas in this chapter the QC acronym is predominantly used, most of the procedures described here are applicable to both QC and quality assessment.

Removing potentially erroneous data is becoming increasingly important as the accuracy of modeled data approaches that of high-quality measurements under clear-sky conditions

(Gueymard 2012) and as measured data are frequently used to assess the quality of satellite-based irradiance estimates. In particular, using flawed measurement data for the task of benchmarking satellite-derived irradiance might lead to incorrect conclusions. For instance, Urraca et al. (2017) revealed a change in annual bias of up to 25 W/m^2 in satellite-based irradiance data depending on whether the reference measurements had undergone quality assessment. This emphasizes the need for stringent procedures to ensure the highest possible quality of ground measurements to undertake sensible validation or benchmarking of modeled datasets (Forstinger et al. 2021). Whereas many data providers perform detailed QC and assessments of the collected data, this is not the general case; even if they do, the applied procedures might either be inadequate or not done systematically. Thus, users are strongly urged to always conduct some level of independent quality assessment of the data and available metadata.

QC procedures of broadband irradiance measurements made with thermopile radiometers are discussed in Sections 4.2 to 4.4. These three sections present QC methods according to time scale; namely, Section 4.2 covers QC of instantaneous irradiance data, Section 4.3 covers daily irradiance data, and Section 4.4 covers QC methods for long-term irradiance data. A brief introduction to related QC concepts is given in Section 4.5, including QC of measurements from photodiode-based radiometers, photovoltaic reference cells, and spectral sensors. The concept of a data quality cycle is presented in Section 4.6. An outlook is presented in Section 4.7 with recommendations for future research.

4.1.1 Data Flagging

Different QC tests or procedures can be applied to data from different sensors, depending on the nature of their measurement type (global horizontal irradiance [GHI], direct normal irradiance [DNI], diffuse horizontal irradiance [DHI], etc.). For each QC test, each data point can be flagged depending on the test conditions. The corresponding flag is often set to 1 (True) when the test detects an issue and 0 (False) if not. Some flagging schemes combine multiple flags into an overall flag, for example, a descriptive value from 0 to 99 (e.g., Maxwell et al. [1993]), depending on which tests failed and to what extent. One ideal flagging method would use such a "super flag" as a proxy for the individual uncertainty of each data point, which is highly desirable. A flag with a low number would translate into a low uncertainty, etc. In any case, the numerical value of all flags should give practical information about the applicability of each QC test and the confidence that can be given to its results.

Some QC tests involve only data from one sensor (e.g., limit tests), whereas other tests involve comparisons of collocated and concomitant data from different sensors. In the latter case, the QC tests flag the data as suspicious without necessarily indicating which measurement is in error. Employing a third sensor can help automatically determine which sensor is in error and reset the flags of the unaffected sensor. For this reason, redundant collocated sensors are recommended and can provide a valuable QC tool.

If measurements are intended for a broad range of users, the guidelines or best practice rules below should be applied to maintain the integrity of the data while providing a useful assessment of data quality.

- No data point should be changed or discarded in the original data files.

- Corrected data should be provided separately (e.g., with clearly erroneous data removed or corrected for time stamp errors).
- Modified data should also be provided separately with proper flagging and/or documentation (e.g., with offset corrections applied or gaps filled).
- Information on the data quality should be provided, allowing end users to make informed decisions about which data points are safe to use for their application.
- Original data files should be archived separately to serve as backup if necessary.
- Available metadata, including calibration and maintenance records, should be made available upon request.

4.1.2 Station's Tier System

The majority of recent QC tests have been developed for research-grade stations that measure GHI, DHI, and DNI separately at 1-minute resolution, often referred to as "Tier-1" stations. This is the ideal case, as each component can be evaluated by deriving it from the two other components (Forstinger et al. 2021). Although such stations can produce the most accurate solar irradiance measurements, they require expensive solar trackers to align the pyrheliometer with the sun and continuously shade the diffuse radiometer with a shading ball.

Consequently, solar resource assessment campaigns, which are of a temporary nature by design, often do not feature such setups but rather measure only GHI and DHI by use of either one pyranometer for each component (using a shadowband to obtain DHI) or a dedicated instrument (such as an SPN1 or rotating shadowband irradiometer [RSI]; see Chapter 3) to obtain DHI and/or DNI without a tracker. This two-component arrangement is usually referred to as a "Tier-2" station. It is important to note that, for such stations, many of the QC tests discussed in the following sections cannot be applied, and the QC procedure is weakened. Specific QC procedures for stations that measure diffuse irradiance using a shadowband are provided by Nollas et al. (2023), although a large fraction of the procedure is also applicable to Tier-1 stations.

Finally, there are many stations that only measure GHI or global tilted irradiance (GTI). Because of the lack of measurement redundancy and the need to derive DHI and DNI from models, this represents the worst-case scenario in terms of the effectiveness of QC procedures. This simple case is normally referred to as a "Tier-3" station. Many national meteorological institutes feature networks of automatic weather stations that may qualify as Tier-3 stations, which tend to receive very little maintenance due to the large number of stations and/or budget or personnel constraints.

4.1.3 Sensor Redundancy

Employing redundant sensors can be helpful when assessing data quality and is recommended for near-real-time QC. Particularly, for Tier-2 or Tier-3 stations that only feature a single sensor, it is difficult to detect possible degradation over time, except by comparing the results of two successive calibration events. Redundant sensors are also useful for Tier-1 stations, where redundant measurements can be used to determine which measurement is in error (e.g., when indeterminant comparison tests flag multiple measurements). At Tier-3 stations measuring GHI only, redundancy is useful to avoid data breaks and estimate the confidence that can be placed into the data time series. Nevertheless, both instruments could be affected by the same issue

(e.g., prolonged soiling caused by snow, frost, or dust), which would temporarily eliminate the redundancy advantage.

4.2 Automated Tests of Instantaneous Irradiance Data

Basic checks of irradiance measurements can be made retrospectively for individual data points. Some of these checks can be used in near-real time by software without human supervision; these tests are often referred to as "automatic tests." The aim of these tests is to flag data points that appear suspicious or are truly erroneous based on automated comparisons with physical limits, redundant measurements, consistency with the closure equation, or other appropriate tests.

It is important to stress that automatic QC and assessment procedures are insufficient on their own and should be employed in conjunction with visual data inspection by an expert (Forstinger et al. 2021). This additional visual inspection is important because automatic tests are unable to detect all types of potential problems and are generally less effective during periods with low solar irradiance or low solar elevation periods (i.e., periods with high measurement uncertainty). In contrast, a trained person can easily detect anomalous features in color plots or other visualizations. Additionally, automatic checks do not usually provide information on the type of error or ways to correct suspect data. For example, it is common that the time zone is specified incorrectly, thus causing systematic errors in solar position; this, in turn, results in good measurement data being flagged as incorrect by automatic tests, although the error is easily correctable if detected.

Further, irradiance limits are often empirically developed based on data from a few stations only, and thus might be somewhat site-dependent. To be applicable to the majority of situations in practice, this section only discusses limits that are applicable to a large variety of climates. Users should be advised that more restrictive tests might be suitable for their specific location. Additionally, because of increased measurement uncertainty, most tests are not applicable to irradiance measurements below 50 W/m^2 (Long and Shi 2008) or when the solar elevation is below 2° (Journée and Bertrand 2011).

4.2.1 Time Resolution

Temporal resolution has a significant influence on the plausibility of irradiance measurements (Long and Shi 2008). Generally, the longer the data's averaging time, the narrower the testing limits can be. For instance, the maximum possible irradiance is lower for data with 15-minute resolution than for data with 1-minute resolution. This is due in part because the short-term variability is averaged out over longer time steps (e.g., differences in sensor time response) and because of the occurrence of cloud enhancement events, which are noticeable in 1-minute data but not detectable at averaging times of 15 minutes or longer (Schade et al. 2007). During cloud enhancement events, GHI can significantly exceed the clear-sky estimate or even the extraterrestrial value. As noted by Nollas et al. (2023), it is important that these values are not filtered out. Nevertheless, longer averaging times tend to be less effective from a QC perspective because a mixture of good and bad data could then exist and would not be detectable. Hence, shorter time steps (e.g., 1-minute) are typically preferred for QC procedures.

During the last decades, the general recommendation has been to log irradiance data at 1-minute resolution, and as a consequence, most recent QC tests have been developed for 1-minute data.

Unless otherwise noted, the tests described in the following sections are suitable for that resolution. In any case, it is important to select suitable test limits according to the time resolution. Noticeably, Espinar et al. (2011a) provide range limits for multiple time resolutions, ranging from 1-minute to monthly data; similarly, Journée and Bertrand (2011) provide limits for 10-minute data. Some QC tests can also be applied to the same dataset at different temporal aggregation levels. For example, Tregenza et al. (1994) evaluated 10-minute average data even though the data was available at 1-minute resolution. Comparing 1-minute data and 10-minute or 15-minute averaged data can also be useful for detecting cloud enhancement events.

4.2.2 Limit Tests

The most widely used QC checks are the Baseline Surface Radiation Network (BSRN) Global Network-recommended QC tests from Long and Dutton (2002). These checks consist of various limits and comparison tests and were later updated and published in Long and Shi (2006) and (2008). The BSRN limit tests are summarized in Table 4-1 and specify two sets of upper and lower limits for the three irradiance components.

The first set of BSRN limits is denoted "physically possible limits," that is, irradiance values that can never be exceeded. The second set corresponds to "extremely rare limits," which are stricter than the physically possible limits but might flag a very small fraction of correct data. The choice of which set of limits to use depends on the application, that is, the stricter extremely rare limits are recommended for high-accuracy applications. The limit checks are applicable to all sky conditions, including nighttime, so there are no domain restrictions. The negative lower limit values are necessary to account for negative nighttime thermal offsets caused by longwave radiation cooling, which varies depending on instrument type (see Section 3.2.1). It is emphasized that the limits described in Table 4-1 apply to 1-minute measurements obtained with thermopile radiometers with a time constant of a few seconds. For faster instruments (e.g., photodiode sensors) or for measurements recorded at higher frequency (e.g., 1 second), cloud enhancement situations can result in valid GHI data far exceeding the assumed "upper limit," according to newer data obtained with various collocated instruments (Gueymard 2017a). Moreover, considering that some even more extreme cloud enhancement situations have been recently recorded over exceptional areas (Cordero et al. 2023), it is likely that these limits will have to be revised into a more comprehensive framework. Similarly, it is stressed that the limit values for GHI and DHI in Table 4-1 assume either that the concerned pyranometers are nearly offset-free or, if not, that an appropriate offset correction has been applied to all their data (daytime and nighttime) before applying the tests (Long and Shi 2008). Many models of thermopile pyranometers have an offset larger than 4 W/m^2, and thus would not pass the test without preliminary correction. The ideal way to correct the offset is exemplified in (Gueymard and Myers 2009), but involves the concurrent measurement of net longwave irradiance. Because this type of measurement only exists at rare research-class stations, an alternate method must be followed in practice. To that effect, the simple method explained by Nollas et al. (2023) is recommended.

Table 4-1. BSRN Limit Checks

Source: Long and Shi (2008). Limits are in W/m^2.

Component	Physically Possible		Extremely Rare	
	Lower Limit	Upper Limit	Lower Limit	Upper Limit
GHI	-4	$1.5 \cdot ETR \cdot \cos^{1.2} Z + 100$	-2	$1.2 \cdot ETR \cdot \cos^{1.2} Z + 50$
DHI	-4	$0.95 \cdot ETR \cdot \cos^{1.2} Z + 50$	-2	$0.75 \cdot ETR \cdot \cos^{1.2} Z + 30$
DNI	-4	ETR	-2	$0.95 \cdot ETR \cdot \cos^{0.2} Z + 10$

Further, Nollas et al. (2023) developed an empirical lower limit for GHI and DHI, which corresponds to heavily overcast or thunderstorm conditions. The empirical equation is provided in Eq. 4-1 and is only a function of the solar zenith angle, Z, up to 90°. Given the very low minimum irradiance at high zenith angles, the limit should only be applied to irradiance data that has been corrected for thermal offsets.

$$\mathrm{GHI}_{\min} = \mathrm{DHI}_{\min} = (6.5331 - 0.065502\,Z + 1.8312 \cdot 10^{-4}\,Z^2)/(1 + 0.01113\,Z) \tag{4-1}$$

Long and Shi (2008) also propose a lower limit for DHI, corresponding to the ideal scenario of an aerosol-free and cloud-free atmosphere for which scattering is only due to interaction with air molecules (Rayleigh scattering). This limit is known as the "Rayleigh limit" (RL) and can be expressed as:

$$R_L = \cos Z\,(209.3 + 0.046725P - 708.3\cos Z + 1128.7\cos^2 Z - 911.2\cos^3 Z + 287.85\cos^4 Z) \tag{4-2}$$

where P is the surface pressure in millibars or hPa. During non-overcast periods (DNI>10 W/m^2), the noticeably higher Rayleigh limit is recommended (though this requires an estimate of DNI). Notably, Nollas et al. modified the DHI limit from R_L to R_L–1 to compensate for any possible inaccuracy. The GHI and DHI limit conditions and domain restrictions are presented in Table 4-2.

Table 4-2. GHI and DHI Lower Limits

Source: Nollas et al. (2023). Note that usage of $\mathrm{GHI}_{\min}$/$\mathrm{DHI}_{\min}$ requires that an appropriate thermal offset correction is applied to thermopile instruments.

Test	Passing Condition	Domain
GHI Lower Limit	$\mathrm{GHI} > \mathrm{GHI}_{\min}$	$Z < 90°$
DHI Lower Limit (cloudy)	$\mathrm{DHI} > \mathrm{DHI}_{\min}$	$\mathrm{DNI} < 10\ \mathrm{W/m^2}$ $Z < 90°$
DHI Lower Limit (cloudless)	$\mathrm{DHI} > R_L - 1$	$\mathrm{DNI} \geq 10\ \mathrm{W/m^2}$ $\mathrm{GHI} > 50\ \mathrm{W/m^2}$ $Z < 90°$ $K_t < 0.8$

4.2.3 Comparison Tests

The second type of tests consists of comparison tests, based on comparisons between multiple irradiance measurements and the physical relationships that connect them. One drawback of these tests, however, is that they are non-definitive: if a test fails, it does not provide information about which of the involved irradiance components is potentially in error.

The BSRN comparison tests are shown in Table 4-3. The closure test is based on the closure equation (Eq. 2-2 in Section 2.5) and compares the measured GHI to the calculated GHI derived from DNI and DHI. The strength of the closure tests results from this comparison between the same quantity from two independent sources, which constitutes a particularly useful type of redundancy.

Table 4-6. BSRN Comparison Tests

Source: Long and Shi (2008). Irradiance values are in W/m^2.

Test	Passing Criteria	Domain
Closure (low zenith)	$\left\lvert \frac{\text{GHI}}{(\text{DHI} + \text{DNI}\ \cos Z)} - 1 \right\rvert < 0.08$	$(\text{DHI} + \text{DNI}\ \cos Z) > 50$ $Z < 75°$
Closure (high zenith)	$\left\lvert \frac{\text{GHI}}{(\text{DHI} + \text{DNI}\ \cos Z)} - 1 \right\rvert < 0.15$	$(\text{DHI} + \text{DNI}\ \cos Z) > 50$ $75° < Z < 93°$
Diffuse Ratio (low zenith)	$K < 1.05$	$Z < 75°$ & $\text{GHI} > 50$
Diffuse Ratio (high zenith)	$K < 1.10$	$75° < Z < 93°$ & $\text{GHI} > 50$

The second BSRN comparison test asserts the diffuse fraction $K = \text{DHI}/\text{GHI}$. Theoretically, the upper limit for the diffuse fraction is 1, that is, diffuse irradiance can never exceed global irradiance. However, in practice, during cloudy periods when the diffuse and global irradiance are physically identical, K may exceed 1 because of measurement uncertainties, particularly at high zenith angles and/or low irradiance conditions. For this reason, the upper limit for the diffuse fraction in Table 4-3 is allowed to be slightly greater than 1. An upper limit of 1.1 was first proposed by de Miguel et al. (2001), whereas the BSRN limits use two different values depending on zenith angle. The BSRN diffuse fraction limit is higher at high solar zenith angles to account for the higher measurement uncertainties of the two pyranometers.

Recently, Nollas et al. (2023) argued that the static diffuse fraction limits just discussed are too simplistic. Instead, they propose defining the upper limits based on an uncertainty-dependent approach, thus calculating the limits explicitly rather than relying on empirical estimations. The drawback of this method is that it requires knowledge of the instruments used and their uncertainties, although the authors provide uncertainty values for two of the most commonly used pyranometers.

4.2.4 Normalized Irradiance Tests

It is often helpful to normalize irradiance values by the extraterrestrial irradiance, as this removes most of the values' intraday dependence on the solar zenith angle. Similar to Eq. 2-2, the closure

equation can be represented in the normalized *K*-space by dividing the individual terms by extraterrestrial radiation (ETR):

$$K_t = K_n + K_d \qquad (4\text{-}3)$$

where K_t is the clearness index (or total transmittance), and K_n and K_d are the direct and diffuse transmittance, respectively. Based on that *K*-space closure equation, Maxwell et al. (1993) reasoned that K_n should never exceed K_t because diffuse irradiance cannot be negative. The authors also defined a test for the normalized closure equation similar to the BSRN closure test, although this is less widely used.

Multiple upper limit values have been proposed for K_t. For example, Journée and Bertrand (2011), for 10-minute data, and Geuder et al. (2015), for 1-minute data, both used a value of 1.0, whereas Forstinger et al. (2021) used a value of 1.35. In contrast, Nollas et al. (2023) argued that these limits were too restrictive, resulting in incorrect flagging of cloud enhancement events, and instead suggested a limit of 1.4 for 1-minute data measured with thermopile radiometers.

Table 4-7. Overview of Recommended *K*-Tests

Site altitude is in m.

Test	Passing Criteria	Domain
K_t Upper Limit (Nollas et al. 2023)	$K_t < 1.4$	$Z < 90°$
(Maxwell et al. 1993; Forstinger et al. 2021)		$K_n > 0$ $K_t > 0$
K_n Upper Limit (Gueymard and Ruiz-Arias 2016)	$K_n < \frac{(1100 + 0.03\ altitude)}{ETR}$	$\mathrm{GHI} > 50\ \mathrm{W/m^2}$ $K_n > 0$
K_d Upper Limit (Perez-Astudillo et al. 2018; Nollas et al. 2023)	$K_d < 0.6$	$Z < 90°$

Similarly, several upper limits have been proposed for the diffuse transmittance, K_d. Journée and Bertrand (2011) used an upper limit of 1 (assuming diffuse irradiance can equal the extraterrestrial irradiance), Tregenza et al. (1994) used a value of 0.8, and Perez-Astudillo et al. (2018) used an even more restrictive limit of 0.6. The limit of 0.6 was verified by comparison to 1-minute experimental data by Nollas et al. (2023) and is thus the recommended limit. The test criteria and conditions are shown in Table 4-4. Maxwell et al. (1993) used paired values of a maximum K_t for each K_n in a dataset to determine a more plausible upper limit for K_d. One argument against applying a threshold limit on K_d is that it might be overly restrictive at high solar zenith angles and in any case very similar to the extremely rare BSRN limit. This specific topic would thus require further verification.

4.2.5 Tracker and Shadowband Misalignment Tests

At research-grade stations, measurements of diffuse and direct irradiance are normally done with a shaded pyranometer and a pyrheliometer mounted on a single solar tracker. Even slight misalignment of the solar tracker will cause incorrect measurements of both irradiance quantities and needs to be detected. One method is to assess the relationship between the diffuse fraction (K) and K_t. Specifically, during quasi-clear-sky conditions, there is limited scattering, and consequently, K should be low, while K_t should be high. Thus, if both K and K_t are high, the tracker must not be shading the diffuse instrument correctly, as these are mutually exclusive conditions. Long and Shi (2008) developed a test for this condition, defining near-clear-sky conditions as periods when the ratio of the clear-sky index (ratio of GHI to clear-sky GHI) exceeds 0.85 and $K < 0.85$. Geuder et al. (2015) proposed a similar (albeit more restrictive) test, which relied on K_t instead of the clear-sky index, as presented in Table 4-5. Perez-Astudillo et al. (2018) proposed an even stricter test based on the same method, although this test might flag too many good data points.

Additional tracker or RSI shadowband misalignment tests were proposed by Geuder et al. (2015) and Forstinger et al. (2021). For those calculations, Forstinger et al. (2021) used the following approximations: $\mathrm{GHI}_{\mathrm{clear}} = 0.8 \cdot \mathrm{ETR}\ \cos Z$ and $\mathrm{DNI}_{\mathrm{clear}} = 0.688 \cdot \mathrm{ETR}$, where ETR is the extraterrestrial radiation, as defined in Section 2.3.

For DHI measurements obtained from a thermopile pyranometer with an adjustable shadowband attachment, tests are more elaborate. These shadowbands require manual adjustment for changing solar declination every 2 to 3 days to maintain appropriate sun shading of the pyranometer detector. When this adjustment is not done in due time, the misaligned shadowband will cover less and less of the diffuse radiometer over time, so some fraction of the direct irradiance will reach the sensor. To detect such instances, Nollas et al. (2023) developed a method that compares the measured K with values from empirical diffuse fraction models. Specifically, the method flags any measurement for which the absolute difference between the measured and estimated diffuse fraction exceeds a certain threshold. That threshold is defined as 0.1 for clear-sky periods and 0.35 otherwise. The test is valid for Z<80°.

Table 4-8. Tracker or RSI Shadowband Misalignment Tests

Irradiance input values are in W/m².

Test's Author	Passing Criteria	Domain
Long and Shi (2008)	$K < 0.85$	$\mathrm{GHI}/\mathrm{GHI}_{\mathrm{clear}} > 0.85$ $\mathrm{DHI} > 50\ \mathrm{W/m^2}$
Forstinger et al. (2021)	$\frac{(\mathrm{GHI}_{\mathrm{clear}} - \mathrm{GHI})}{(\mathrm{GHI}_{\mathrm{clear}} + \mathrm{GHI})} > 0.2$ OR $\frac{(\mathrm{DNI}_{\mathrm{clear}} - \mathrm{DNI})}{(\mathrm{DNI}_{\mathrm{clear}} + \mathrm{DNI})} < 0.95$	$Z < 85°$
Geuder et al. (2015)	$K \leq 0.96$	$K_t > 0.6$

4.2.6 Step Change Rates

Another method for detecting implausible irradiance data is to assess the rate of change between two consecutive measurements. The step change can be calculated as the absolute value of the measured irradiance at the current time step minus the value of the measured irradiance at the previous time step. For GHI, Espinar et al. (2011b) suggest a step change limit of 1000 W/m^2 for 1-minute data, whereas Shafer et al. (2000) recommend a limit of 800 W/m^2 for 5-minute data. Similarly, Lorenz et al. (2022) also suggest using a 1000 W/m^2 threshold for 1-minute tilted irradiance (GTI) measurements. Journée and Bertrand (2011) proposed other limits for 10-minute measurements and $Z \leq 88°$. Specifically, their proposed maximum acceptable rate limits are 0.75, 0.65, and 0.35 for K_t, K_n, and K_d, respectively. The maximum limits represent what can be expected under actual weather conditions and usual instrument responsivity. Higher change rates are typically indicative of data logger or instrument malfunction.

4.2.7 Station-Specific Limits

The above QC tests and limits were developed to cover a wide range of climates and latitudes and thus might not always be stringent enough. Stricter limits can be advantageously developed for individual sites or small areas based on long-term data. For this reason, Long and Shi (2008) proposed several configurable climatological limits to complement the BSRN limit checks in Table 4-1. These configurable limits were implemented into the QCRad Fortran software (Long and Shi, 2006). The advantage of configurable limits is that they can be tailored to the conditions of a specific site, whereas the drawback is that a minimum of 1 or 2 years of historical data is typically necessary to determine them.

Configurable limits are also central to the SERI-QC software developed by the National Renewable Energy Laboratory (NREL) (Maxwell et al. 1993). SERI-QC relies on empirical envelopes in K_n-K_t space, within which a preponderance of data points are expected to lie. Measurements outside this envelope are assigned a two-digit flag, indicating the magnitude and direction of such departures. In the SERI-QC software, different envelopes must be defined for each month and for three bins of solar zenith angle. While the method's usefulness is recognized, it has seen limited usage outside of NREL. This is likely about to change, however, because the method is being expanded to estimate measurement uncertainty (Wilcox et al. 2023; 2022), and its C language code is being converted to Python for user friendliness, flexibility, and wider public adoption.

In parallel, Younes et al. (2005) developed an expectancy envelope in K-K_t space and provided a statistical method for constructing the upper and lower limits by fitting a second-degree polynomial based on hourly irradiance data. Journée and Bertrand (2011) extended that method to accept 10-minute data and eliminated the need for manual inputs. Recently, Nollas et al. (2023) further extended the method to make it suitable for 1-min data (conducive to significantly higher variability) by combining two different sets of envelopes, developed statistically, to help cover a large variety of climatic and altitudinal situations. This suggests that, although K-space envelopes can result in stricter QC tests, they are not necessarily applicable to all stations without further empirical adjustments.

4.2.8 Horizon Shading

Solar irradiance monitoring stations should ideally be sited at locations that do not have significant obstructions of the horizon, such as those resulting from nearby hills, mountains, or structures. The general recommendation is to choose a site where horizon-blocking is less than 5° in all directions, although this is not always possible. In any case, it is recommended to flag all irradiance measurements for which the sunup positions are below the effective horizon line. When the sun is blocked by an obstacle on the ideal horizon, DNI is 0, and GHI = DHI, within instrumental error. Even though these measurements are perfectly correct from a solar assessment standpoint because they reflect the actual local conditions, it is generally undesirable to use such measurements for validation of radiation models or satellite-derived datasets.

The local horizon profile can be measured using a survey compass and inclinometer, although such information is often not available. Fortunately, estimates of the local horizon profile can be retrieved freely from multiple online services. For example, the Photovoltaic Geographical Information System (PVGIS) offers users the option of downloading a local horizon profile, either using their website or an application programming interface (API) (JRC 2023). The PVGIS API has been incorporated into pvlib (Holmgren et al. 2018) and can be accessed as shown in Figure 4-1 (for a test site at 45° north latitude and 9° east longitude).

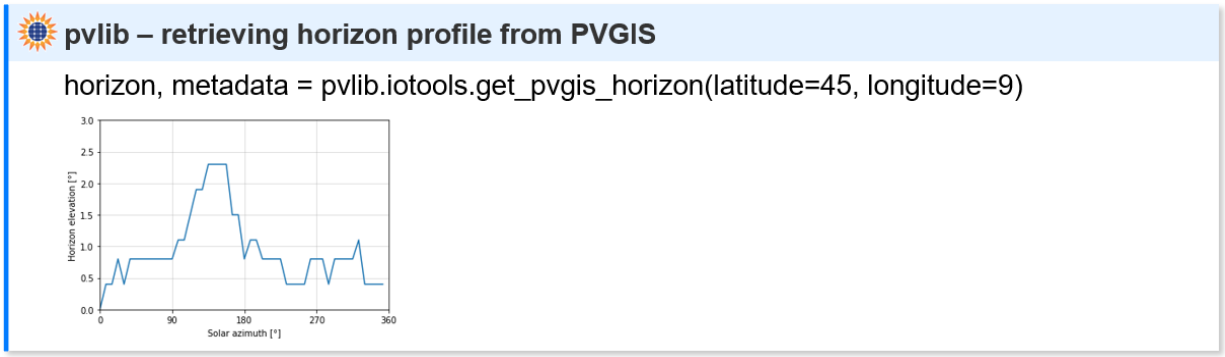

Figure 4-1. Example of retrieving the local horizon profile from PVGIS using pvlib python

MINES Paris offers a similar web processing service (WPS),[18] which computes the local horizon profile from a geolocation (latitude, longitude, altitude) and ground offset (e.g., the height of an instrument above ground). The service relies on data from a digital elevation model (DEM), either the Shuttle Radar Topography Mission (SRTM) at 90-m resolution or the 30-m ASTER dataset (Gschwind et al. 2020). The calculated horizon line has an azimuthal resolution of 1° and is available for the coverage area of the SRTM dataset, i.e., at latitudes comprised between 56°S and 60°N. The service can be accessed using HTTP requests, which must be formatted correctly.[19] Two examples of horizon shading are given in Figure 4-2. In these plots, the colored scatter points correspond to the maximal value of K_n as a function of the solar azimuth and elevation angles. The light gray areas are orientations for which DNI≈0, corresponding to

[18] Access at http://geocatalog.webservice-energy.org/geonetwork/srv/eng/main.home.

[19] The specific format of the command is described in this example: http://toolbox.1.webservice-energy.org/service/wps?service=WPS&request=Execute&identifier=compute_horizon_srtm&version=1.0.0&DataInputs=latitude=43.79;longitude=6.22;altitude=-999;ground_offset=2&RawDataOutput=result.

shading situations. The red curve is the horizon line calculated with the aforementioned WPS tool.

The top panel of Figure 4-2 corresponds to measurements made at the Carpentras BSRN station between 2015 and 2018 There is a good match between the gray area and the SRTM-based horizon, showing the accuracy of the latter's calculation. As a contrasting example, measurements from the Oak Ridge National Laboratory (ORNL) station[20] between 2015 and 2019 are displayed in the bottom panel of Figure 4-2. In this case, there are significant differences between the gray area and the SRTM-based horizon line. The shape of the gray area clearly suggests that the shadows are caused by buildings and trees surrounding the station. This demonstrates the limitation of the SRTM-based horizon line because it does not consider objects such as trees or buildings, which contribute to near-shading. In this case, a high-resolution DEM (from image stereography or LiDAR data) would be a better option (Mira et al. 2022). Alternatively, a data-driven approach such as the one proposed by Lorenz et al. (2022) would be useful to infer the horizon line from measurements. Finally, a simple photographic method is exemplified in Section 3.5.1.

[20] Access at https://midcdmz.nrel.gov/apps/sitehome.pl?site=ORNL.

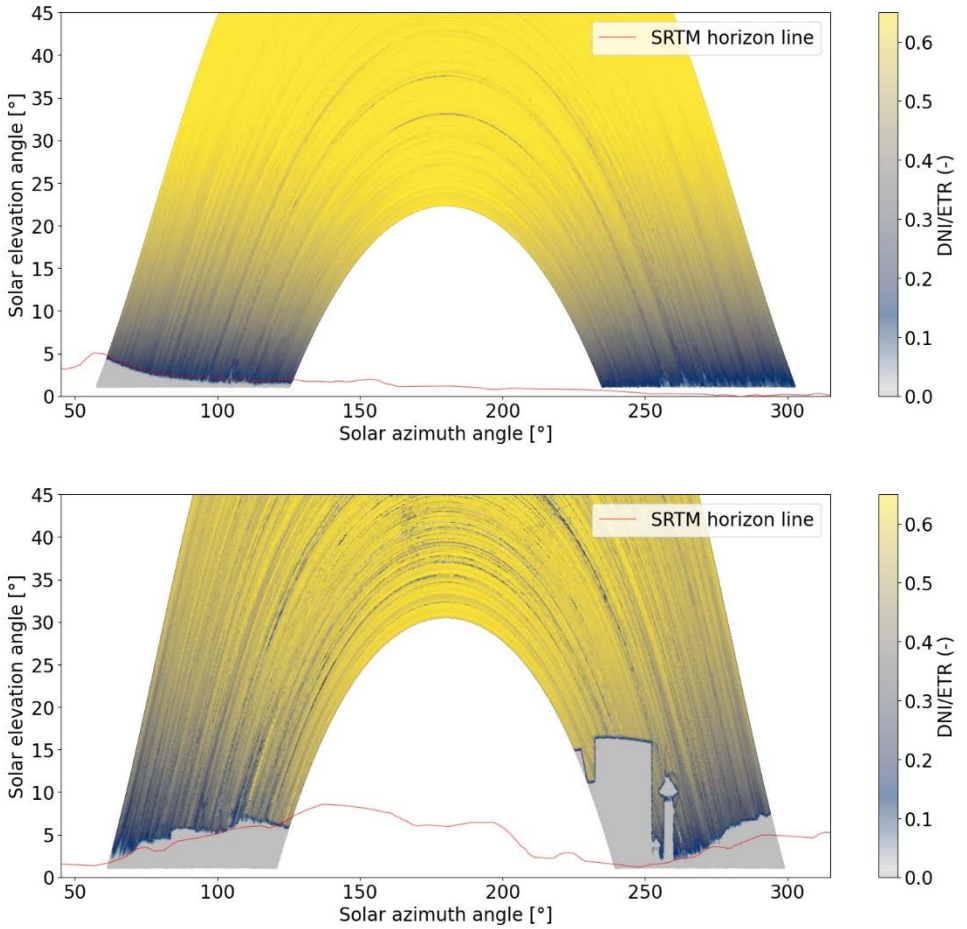

Figure 4-2. Representation of maximal values of the ratio K_n (referred to as "DNI/ETR" in the color-code scale) as a function of sun position for two sample stations (top: Carpentras BSRN, 2015–2018, bottom: ORNL, 2015–2019). Gray areas correspond to directions affected by shading (DNI≈0), and red lines represent the horizon line calculated with SRTM data.

Image by Yves-Marie Saint-Drenan

4.2.9 Tests for Tier-3 Stations

The previous sections focused on Tier-1 and Tier-2 stations, where at least two irradiance components are determined independently. There are far more stations in the world where only one component is measured. Such Tier-3 stations measure GHI or GTI with either a thermopile pyranometer or a photodiode sensor. A similar situation exists at stations measuring the ground albedo, obtained as the ratio between reflected horizontal irradiance (RHI) and GHI, the quality of which needs to be assessed separately.

To assess the quality of GHI measurements, not much can be done besides the physical limits described in Table 4-1, taking into account that fast sensors or measurements obtained at different intervals than one-minute might require limit adjustments. Because of this scarcity of QC tests for GHI-only situations, it might be tempting to compare such measurements to "high-performance" satellite-derived irradiance data. With this approach, the latter product now becomes the reference to test the validity of measurements—the opposite of the normal situation. There is some evidence that this "inverse" method can indeed detect periods during which an

instrument with poor maintenance would have been heavily soiled (e.g., during a few days), resulting in a strongly biased signal (Urraca et al. 2017; 2019; 2020). Whether this approach can be useful in detecting other typical QC issues remains to be investigated.

4.2.10 Tilted Irradiance

In recent years, the rapid development of utility-scale solar power plants has increased the need for local measurements of GTI, either on a fixed tilt or in tracking mode. The quality of GTI data is of prominent importance in solar energy utilization. Two issues have hindered efforts toward improving the quality of such data so far: (1) GTI sensors are normally calibrated in the horizontal position, either indoors or outdoors, which can introduce systematic errors when they are actually used in a tilted position, particularly if under different climate conditions than at the calibration site; and (2) all QC procedures published so far have mainly focused on the three basic components, excluding GTI.

Noticeably, Lorenz et al. (2022) developed modified limit checks for tilted irradiance similar to those from BSRN. These authors also implemented an additional flag if a step change larger than 1000 W/m^2 is encountered between two consecutive time steps, similar to what was proposed for GHI by Espinar et al. (2011a). Further, Tregenza et al. (1994) proposed QC tests of tilted irradiance by comparing to the modeled tilted irradiance calculated with the Perez et al. (1990) transposition model. Specifically, measurements that deviated more than 200–250 W/m^2 from the modeled estimate were flagged. Lorenz et al. (2022) took a similar approach and used an absolute deviation of 200 W/m^2, but also specified additional checks in case tilted irradiance measurements were available for multiple orientations.

To illustrate the various problems that might arise when dealing with GTI data, a 2-year time series of 1-minute data has been assembled, using recent measurements recorded at NREL's Solar Radiation Research Laboratory in Golden, Colorado[21] (latitude: 39.742°N, longitude: 105.18°W, elevation: 1829 m). That station is unique in the world for its installation that includes a wide variety of radiometers with remarkable redundancy, its advanced calibration methods, the detailed logging of all known instrumental issues, and for the meticulous care that each instrument receives in terms of maintenance. In particular, each instrument is checked and cleaned each *working* day (The emphasis is important here because no cleaning occurs during weekends or holidays; thus, periods of up to 3 consecutive days can occur without cleaning.) The example below shows comparisons between collocated instruments that sense the same radiometric quantity, have been calibrated the same way using NREL's advanced methods, and have received the same care. Overall, such comparisons can be understood as the best-case scenario that would seldom, if ever, occur in practice.

Measurements on an equator-facing latitude tilt (e.g., 40° at Golden) are of critical importance in the context of solar power plants using fixed-tilt panels or collectors. For this case study, such GTI measurements made with two photodiode sensors (SP-Lite 2 and LI-200R) are compared to those of a high-quality reference thermopile pyranometer (CMP22), and their difference is plotted against zenith angle in Figure 4-3. Four features are readily apparent here: (1) There are many outliers; (2) the photodiode readings have systematic bias, mostly in the case of the SP-

[21] See https://midcdmz.nrel.gov/apps/sitehome.pl?site=BMS.

Lite2; (3) the difference (in absolute value) abruptly increases for $Z > 80°$; and (4) there is a curious difference pattern for Z between about 70° and 85°. Point (1) can be mostly attributed to issues caused by snow or ice accumulation (particularly during weekends) on the sensors or to differential effects of albedo enhancement (Gueymard 2017b). Point (2) is critical because even small biases of just a few percentage points in the annual resource can have ruinous consequences in the operation of solar power plants, such as during the performance guarantee verification procedure. Point (3) is in large part the consequence of the interaction between the respective cosine errors of the instruments, but also reflects the fact that relative errors are typically larger when the irradiance is low. Point (4) is probably the result of either (i) some intricate snow/ice reflection or shading process; or (ii) some structure around the sensors either casting a shadow or reflecting differentially on them. The latter circumstances can also occur anywhere and thus need to be detected through appropriate QC tests. These results, obtained under near-ideal conditions, illustrate the difficulties associated with the development of a robust QC methodology for field GTI measurements, especially when only a single radiometer exists locally.

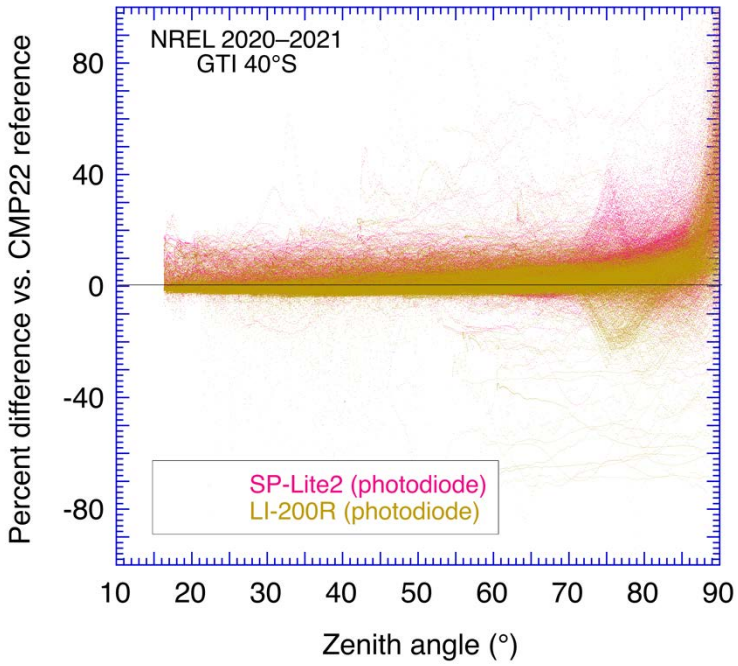

Figure 4-3. Percentage difference vs. solar zenith angle between two photodiode sensors against a reference CMP22 pyranometer for 1-minute GTI on a 40° tilt at NREL's Solar Radiation Research Laboratory 2020–2021

Image by C.A. Gueymard

In parallel, the measurement of surface albedo has become more prevalent with the rapid market penetration of bifacial photovoltaic (PV) systems. At NREL, two specimens of the same instrument's make and model are used to sense the upwelling (RHI) and downwelling (GHI) fluxes. The albedo, ρ, is simply the ratio of those two quantities. Here, obviously, unphysical values (i.e., $\rho \leq 0$ or $\rho \geq 1$) have been removed for clarity. Such values are typically obtained when the GHI sensor is completely obstructed by snow or under very low-sun conditions, respectively. Measurements from a CMP11 reference thermopile assembly are compared here with those from a lower-performance CM3 thermopile pyranometer and an LI-200 photodiode.

The results in Figure 4-4 show that the CM3 albedometer tends to overestimate the albedo by a few percentage points up to $Z \approx 80°$, but this might not be a real problem in practice. Conversely, the LI-200 readings are highly biased with considerable dispersion. This is attributed to the limited and non-uniform spectral response of the photodiode detector. The latter interacts in a complex way with the specific spectral albedo of the surface, which changes over time depending on weather and season (green vs. dry grass, snow, ice, water, etc.), as discussed in Section 3.3.1. From this plot, it is obvious that a photodiode-based albedometer should not be used to characterize the *broadband* albedo, as needed in various solar or non-solar applications. Nevertheless, it can also be argued that this specific type of measurement is spectrally more representative of the reflected radiation that a bifacial PV system would receive from the ground. In that sense, a photodiode-based albedometer is arguably more adapted to PV applications, although this remains to be demonstrated in practice (see also Section 3.3.1). In any case, the question is still how to assess the quality of albedo measurements made with either type of detector.

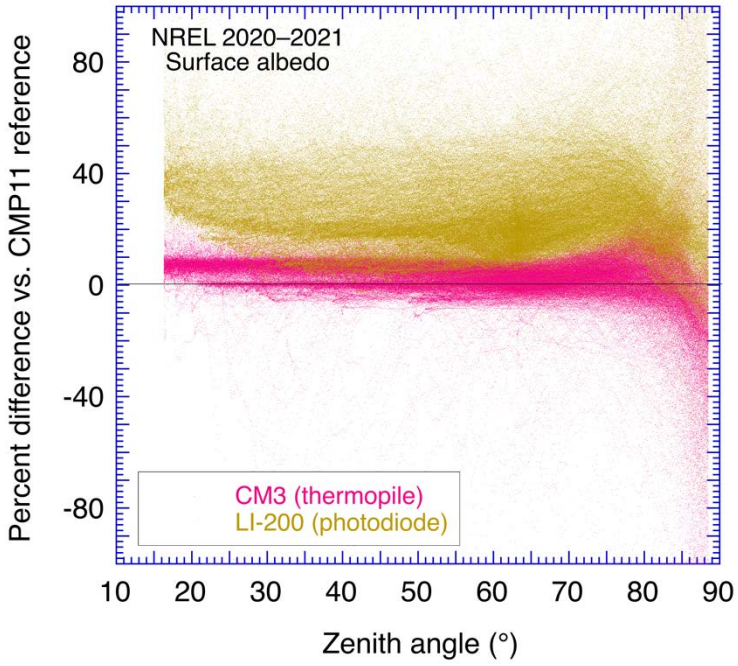

Figure 4-4. Percentage difference vs. solar zenith angle between two sets of identical radiometers against a reference CMP11 pyranometer combo for 1-minute surface albedo at NREL's Solar Radiation Research Laboratory 2020–2021

Image by C.A. Gueymard

4.2.11 Software

Several software solutions can help assess the quality of solar irradiance measurements, ranging from Python packages to stand-alone desktop applications. Within the Python package ecosystem, three noteworthy projects exist: pvanalytics, libinsitu, and pybsrnqc. All of the aforementioned packages contain a range of automatic checks for instantaneous irradiance data and are open source (i.e., free to use). The packages can be easily installed from the Python Packaging Index (PyPI) and, given that they are community-developed projects, allow for the quick addition of newly developed procedures. Their features are described below.

- pvanalytics is an affiliated package of pvlib that provides functions for quality control, filtering, and feature labeling for PV power and irradiance data. Specifically, for solar irradiance QC, functionality includes the detection of data shifts, stuck values, and nighttime periods, as well as automatic limit and comparison checks.[22]
- libinsitu includes tools to transform solar irradiance measurements in various formats to NetCDF files compliant with the Climate and Forecast conventions. It also provides tools to retrieve and manipulate those NetCDF files. In addition to supporting many of the automatic checks described in this chapter, libinsitu provides visualization capabilities important for QC and a function generating the multiplot summarizing all important QC tests (see Section 4.2).[23]
- pybsrnqc is a Python package dedicated to deriving and employing site-specific quality checks based on the BSRN QC method discussed above.[24]

As mentioned previously, work is also ongoing to convert the SERI-QC software into an open-source Python package.

Lastly, the commercial software Solargis Analyst is worth mentioning. The software is a stand-alone desktop application that allows users to visualize and perform quality assessments of solar irradiance data without programming skills.

4.3 Daily Visual Inspection of Irradiation Data

In the previous section, precise methods of data inspection were described in the context of a single set of measurements taken at a single point in time. The methods presented there are a fundamental first-pass regimen to assess quality, but by expanding the temporal view of the data, a trained analyst can almost always gain greater insight into problematic factors not apparent in the context of a single measurement. This is partly because:

- Measurements at a single point in time can mask problems if random and opposing errors cancel each other.
- Subtle problems may not seem significant until they occur in aggregate, indicating a systematic error.
- Errors caused by rapidly changing conditions can be detected at a short time scale but might not carry through to other temporally proximate measurements (e.g., they can be dismissed as fleeting behavior of instruments).
- Some types of subtle errors cannot be detected by current automatic checks, such as calibration issues and cosine response errors.

Similar to the transition from immediate data inspection to a daily regimen, a similar transition can be made to an even broader scale (monthly or yearly), as described in Section 4.4. The subsections below describe the value and necessity of a *daily* data inspection routine as part of the data quality cycle described in Section 4.6.

[22] The documentation is available at https://pvanalytics.readthedocs.io, and the source code is hosted on GitHub: https://github.com/pvlib/pvanalytics.
[23] A detailed description and usage examples of the Python library can be found at: https://libinsitu.readthedocs.io, and the source code is available on GitLab: https://git.sophia.mines-paristech.fr/oie/libinsitu.
[24] The documentation and source code are available on GitHub: https://github.com/LE2P/pybsrnqc.

4.3.1 Daily Visualization Routine

To expedite and facilitate the visualization of data, as much of the process as possible should be automated. Particularly, the more streamlined the process is, the more likely it is to be performed. With training and experience, a qualified data analyst can then inspect the daily data in detail from dozens of stations within an hour or two.

The following steps should be carried out on a daily basis to ensure a high quality of measurements and catch potential errors as quickly as possible.

Step 1: Confirm the station is operational. Determine that measurement data from all sensors are present. If data are missing, investigate these likely causes: communication errors, data logger failure, sensor malfunction, power failure at the station, or failure of automated data preprocessing.

Step 2: Inspect data visualizations. Data are most easily viewed when presented in context with other related measurements. Figure 4-5 shows GHI, DNI, and DHI measurements from an RSI. The experienced analyst can easily determine sky conditions throughout the day under examination and identify any anomalies. For example, Figure 4-5 shows a typical clear day profile, although with a conspicuous disruption in the measurements. In this case, the investigation revealed that a cleaning event occurred at approximately 10:30 and momentarily blocked the sun, causing a sharp reduction in the instrument's output.

Further inspection of Figure 4-5 shows a discontinuity in the profile from before the cleaning to after when the measurement was markedly higher. Maintenance logs revealed that a dust storm passed through the area the night before, depositing an unusual amount of dust on the sensor. The effect of cleaning is clearly evident in this plot.

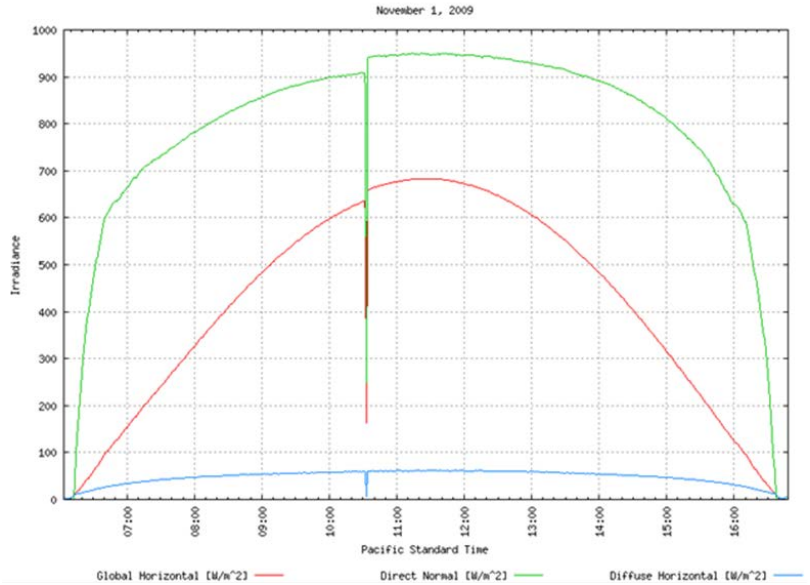

Figure 4-5. Cleaning effect on an RSI using a photodiode sensor with diffusing optics. After cleaning (indicated by the sudden irradiance drop), DHI appears not significantly different, while DNI increases by ≈5%.

Image by NREL

During automated quality checks of measurements at a single time stamp (Section 4.2), it is most likely that only the disturbance from the cleaning event itself would have been flagged, but not the data before the cleaning. This can occur because the RSI uses only one sensor, and any soiling will affect all three components with similar attenuation. Hence, when the procedure in Section 4.2 is applied, the relationships among measurements can appear normal, although at an attenuated level. It is stressed here that soiling is a quasi-constant issue at dusty or polluted sites. Excessive flagging of data periods apparently affected by soiling would lead to exaggerated loss of data. It is preferable to attribute a higher uncertainty to such affected data and to correct them appropriately (e.g., by applying a linear correction between two successive cleaning events).

The scenario evident in Figure 4-5 clearly underscores the need for visual data inspection in the context of a day. Without this process, the measurements affected by dust at this station could possibly have remained undiscovered.

Step 3: View the data in the context of other measurements. Because many radiometric stations include instruments for other meteorological quantities, the opportunity exists to put the solar data in yet a broader context. The automated inspection preparation software should include daily plots and summaries of those meteorological parameters. At such a station, the analyst can view all plots simultaneously, as shown in Figure 4-6.

Figure 4-6. Graphical interface showing colocated measurements from a monitoring station

Image by GroundWork Renewables

The plots can show the analyst evidence of changing weather conditions and how various measurements are affected. As in the case of Figure 4-6, it is very beneficial that the analyst is provided with an interactive graphical interface. This allows for quickly investigating potential erroneous measurements in a different context, e.g., looking at trends in the measurement over longer time periods or comparing two sensors.

Step 4: Examination of the maintenance logs. Station logs recorded by the station personnel should be brought up for continuous viewing during the data inspection. The logs should ideally include photos (e.g., bubble level before and after leveling, and station surroundings). This provides an easy reference for data comparison with the observations also logged by the station personnel at the time of the visit.

The time of the cleaning event is an easy and effective check on several aspects of the data. The time can be verified in the data plots by the presence of a brief discontinuity in the solar irradiance values, as shown in Figure 4-5 (an exception being for DNI under overcast skies). Discrepancies in time stamps should be investigated in the context of these possible problems: (1) The station clock is incorrect; (2) the maintenance personnel are not accurate in their log-keeping; or (3) if a verification dip in irradiance is not apparent, the station personnel might not be accomplishing their duties as assigned. For an overview of maintenance procedures, see Section 3.6.

4.4 Long-Term Irradiation Data

After the implementation of the different procedures presented in the previous sections, a large share of faulty measurements should have been successfully identified. However, some faulty measurements might pass the automatic tests or might not be detectable on a short-term time scale, so further post-measurement quality assessment is recommended. Undetected faults might, for example, include time shifts, shadows, or calibration issues. In such cases, analyzing a long-term dataset can help spot some measurement problems that have not been detected by usual QC

procedures. More generally, as discussed below, a long-term data analysis is recommended because it provides insight into the source of errors responsible for any data quality flag.

To show the advantages of the long-term analysis of solar radiation measurements, detailed inspection of the closure equation (Eq. 2-2) as a function of time is represented in Figure 4-7. In this plot, the ratio between measured GHI and calculated GHI derived from measurements of diffuse and direct normal components is represented as a function of time (only values for a solar zenith angle less than 75° are displayed). The color represents the local density of the scatter points. As a reminder, the closure equation is evaluated using the three component tests proposed by Long and Shi (2008) (Table 4-3). The acceptable limits are represented by the two red dashed and dashed-dotted lines in Figure 4-7. The light gray dashed line represents the optimal unity value for the ratio.

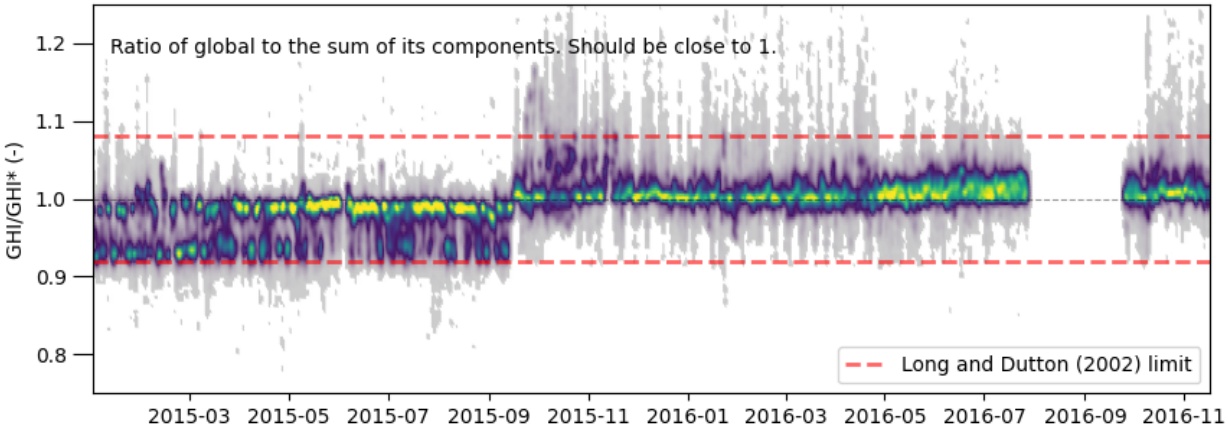

Figure 4-7. Ratio between measured GHI and calculated GHI from the diffuse and direct components as a function of time for instances when GHI is greater than 50 W/m² and SZA is less than 75°. Calculated GHI is denoted as GHI*.

Data source: BSRN Chesapeake Light station, 2015–2016

Two different regimes can be observed in Figure 4-7. After 2015-09, the ratio is distributed around 1, as expected from a high-quality measurement system. Before that date, however, the ratio is biased, with a mean value slightly greater than 0.9. The transition between the two regimes is very sudden and corresponds most probably to either a change of one or more instruments or their calibration. It is also interesting to note that most of the biased values in the earlier period are within the tolerance of the Long and Shi (2008) test (red dashed lines), so these values would not have been identified without the visual analysis of long-term data. Interpreting this data analysis also points to the importance of recording the station's operations and maintenance activities.

It is possible to apply the same methodology to the global and diffuse components by selecting only instances when the measured DNI is low. An example is given in Figure 4-8, where the global-to-diffuse irradiance ratio is represented as a function of time for instances when DNI is lower than 1 W/m^2. As the direct component is almost equal to zero, the diffuse component and the global horizontal irradiance should be equal. The same features from Figure 4-7 can be

observed in Figure 4-8. This brings the conclusion that the assumed calibration issue affects the global or diffuse instruments and not the pyrheliometer.

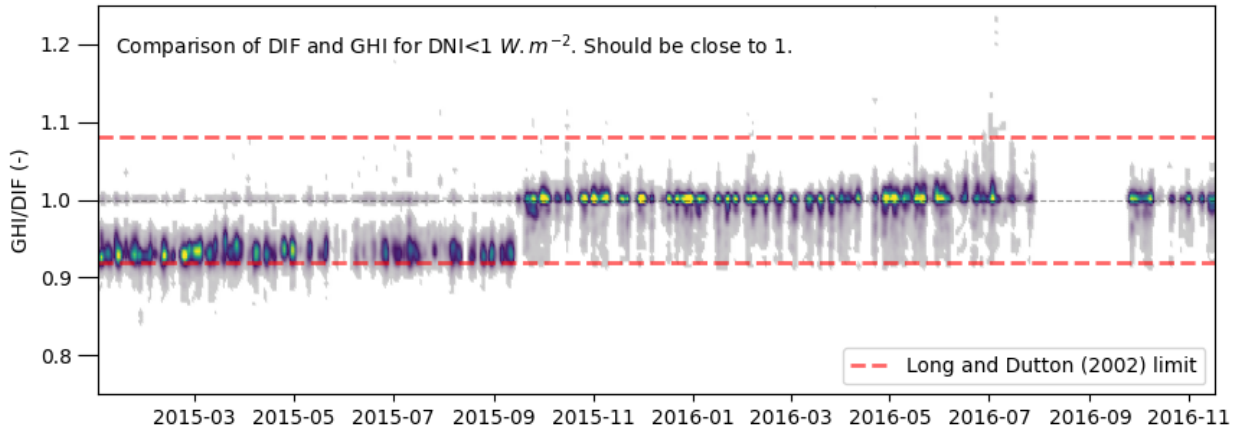

Figure 4-8. Ratio between measured GHI and DHI denoted in the figure as (DIF) as a function of time for instances when DNI is less than 1 W/m^2, GHI is greater than 50 W/m^2 and SZA is less than 75°.

Data source: BSRN station Chesapeake Light, 2015–2016

The last example illustrates the importance of comparing different analyses to infer the origin of an error. This principle has been applied to all QC tests in the collage of plots displayed in Figure 4-9. The left column of the multiplot includes different visualizations of the measurements (time series and two-dimensional date-time-of-day heatmap), as well as the closure analysis described above. The two middle columns are visual representations of standard tests, including those proposed by Long and Dutton (2002), Long and Shi (2008), and Maxwell et al. (1993), where the gray dashed lines illustrate the threshold of the different tests. The right column includes the metadata of the station, statistical distributions of the three components, and horizontality and shadow analyses.[25]

[25] A detailed description of these plots is not provided for the sake of conciseness, but refer to https://assessingsolar.org and https://git.sophia.mines-paristech.fr/oie/libinsitu for further information; the code for generating these plots is also available at https://github.com/AssessingSolar/solar_multiplot.

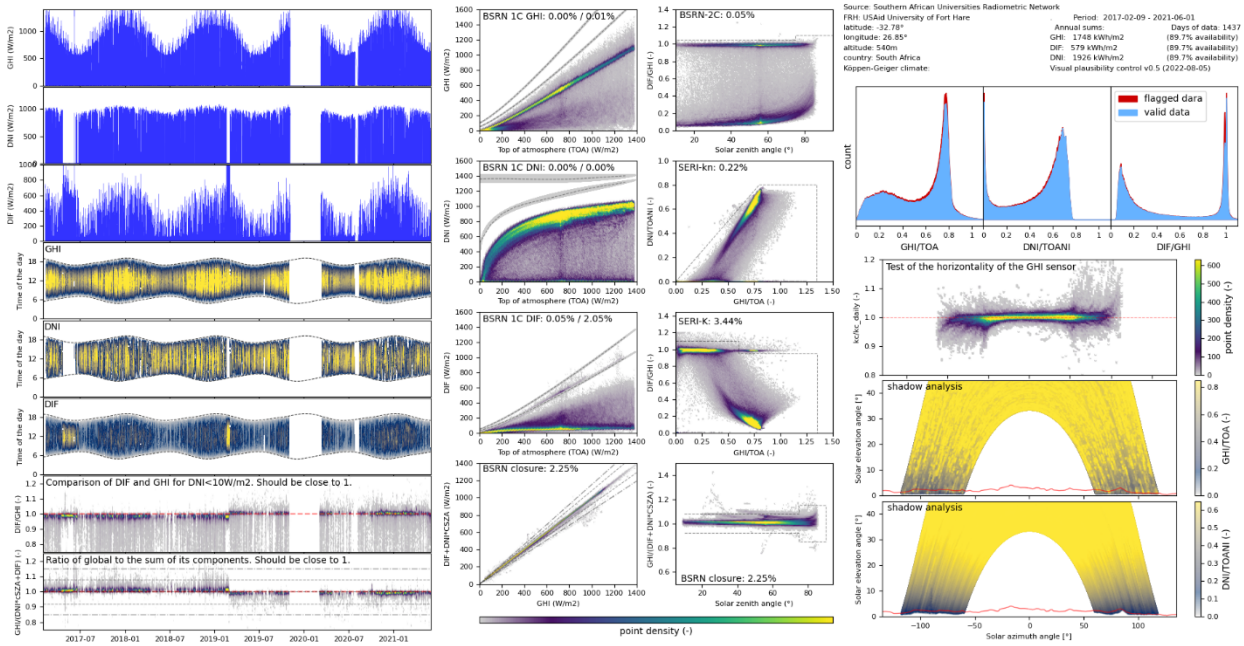

Figure 4-9. Example of a multiplot tailored for a single dashboard on a large screen, representing the visual support of different QC tests. The gray dashed lines correspond to the different tests.

Data source: SAURAN's University of Fort Hare station, 2017–2021

The data displayed in Figure 4-9 originates from a different station than that illustrated in Figure 4-7 and Figure 4-8. The two lower plots of the left panel clearly indicate that this station is also affected by a calibration problem. In addition, some abnormally high diffuse radiation values are visible in the third and fifth plots of the left panel, as well as in other plots involving this component. These high DHI values are caused by a misalignment of the shading ball. Further examples of typical errors and how to diagnose them using the long-term visualization tool illustrated in Figure 4-9 are currently under preparation and will be described on a dedicated website as part of the International Energy Agency (IEA) PVPS Task 16 activities.[26]

4.5 Methods for Other Types of Instruments

Most QC algorithms and procedures have been dedicated to broadband measurements of GHI, DHI, and DNI. However, with the growth of PV systems, spectrally selective and spectrally resolved measurements are even more widespread. This section discusses how QC procedures must be modified for such measurements and summarizes the currently available methods on this topic.

4.5.1 Photodiode Pyranometers

Photodiode pyranometers are low-cost alternatives to thermopile instruments, and, as such, they are expected to have greater measurement uncertainties. Although in principle the types of tests discussed above are all applicable, the thresholds for those tests must pass a larger range of values to accommodate expected systematic errors, especially spectral and directional errors, or to take into account their faster response. In some situations, two different thresholds might be needed: one that flags values if the systematic error grows too large, and the other to flag likely

[26] See https://assessingsolar.org.

anomalous measurements. These devices inherently respond extremely fast to changes in irradiance (µsec compared to 1–30 seconds for thermopile-based radiometers); therefore, tests for step changes may also need to be relaxed.

The body, entrance optics (diffuser), and bubble level of photodiode pyranometers are often physically smaller than their thermopile counterparts. This can make it more difficult to level these instruments, or in the case of GTI measurements, to align them to the desired tilt and orientation. Therefore, it is especially important to check the data for systematic errors due to misalignment.

Calibration of photodiode pyranometers is also challenging due to their non-uniform spectral response. The spectrum of the light source for indoor, and composition of the atmosphere at the time of outdoor calibration, is not always representative of the conditions of routine measurements. Spectral response is therefore a major contributor to the measurement uncertainty of these instruments (Reda 2011).

Finally, because they are low-cost devices, it is perhaps more likely to find that redundant devices are deployed. These can be compared directly to each other with much smaller tolerance thresholds to detect anomalies, and if the duplicate instruments are independently mounted and aligned, this comparison can also identify misalignments.

4.5.2 Photovoltaic Reference Cells

QC tests for solar irradiance measurements made with PV reference cells are much less discussed than those for radiometers designed for broadband irradiance, presumably because these measurements are usually a means to an end (for example, to evaluate the performance of PV modules) rather than an end goal (Vignola et al. 2022). Limit tests similar to those for GHI, and especially GTI, can certainly be used, but thresholds must be adjusted based on the performance specifications and estimated measurement uncertainties of the devices.

When PV reference cells are deployed together with PV modules or systems—as they frequently are—a form of redundancy is inherently present. For example, one can use the reference cell output to simulate the PV module or system power and compare with the measured power using suitable thresholds. Nevertheless, having additional reference cells and/or additional module output measurements improves the ability to distinguish between normal deviations and abnormal conditions.

For a single reference cell, or for a more objective/independent assessment, the maximum expected output can be calculated using broadband clear-sky irradiance estimates as input. Essentially, this is similar to the first steps in a PV system simulation: transposing DNI and DHI to GTI, subtracting reflection losses, and making a spectral mismatch adjustment. This clear-sky reference cell output value can then be used to set a tighter upper threshold on the range of expected values for tests.

4.5.3 Spectral Data

Hoyer-Klick et al. (2008) developed a method for calculating upper and lower limits for spectral irradiance measurements. The limits were determined by simulating a “very clear atmosphere with low extinction conditions.” Similarly, lower limits for spectral measurements can be

determined by simulating a "turbid atmosphere with large extinction conditions." The method uses the SMARTS clear-sky spectral model (Gueymard 2001; 2019) for the spectral simulations. Another approach, also based on SMARTS, was followed by (Marzo et al. 2021). This method includes automatic comparative tests, threshold tests, and various visual inspections.

4.6 Data Quality Cycle

A successful QC process requires elements of near-real-time data acquisition, quality assessment, and operations feedback. As shown in Figure 4-10, information flows from data acquisition to quality assessment, where various procedures are applied to determine post-measurement data quality. The results of the quality assessment phase are analyzed and formed into feedback that goes back to the data acquisition module. Data acquisition is thoroughly covered in Chapter 3.

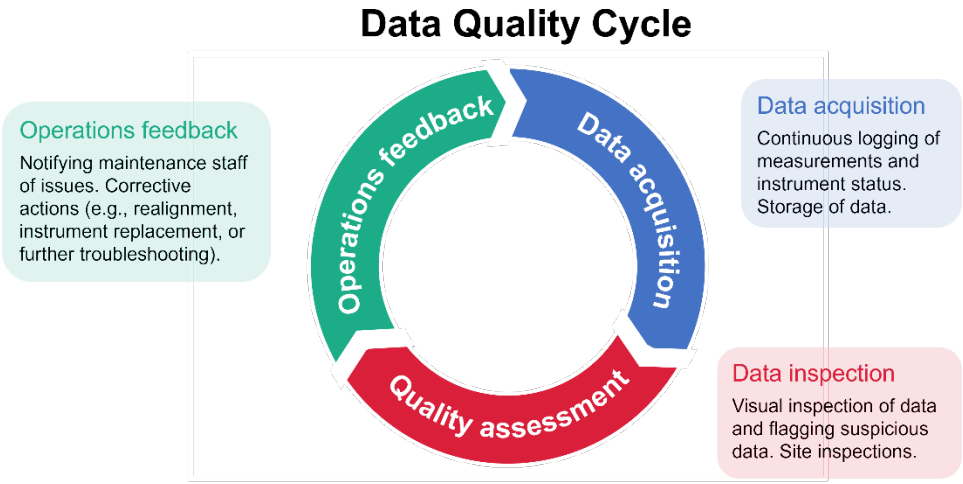

Figure 4-10. Illustration of the data quality cycle

Image by Adam R. Jensen, DTU

The activities in the data quality cycle shown in Figure 4-10 can take several forms. For example, quality assessment could be the daily site inspection, and the operations feedback could be a simple procedure that corrects the equipment issues (e.g., instrument realignment). Alternatively, the post-measurement quality assessment could be a daily summary of data quality flags, and the analysis would then provide a determination of a specific instrument problem that is transmitted back to maintenance personnel, instructing them to correct deficiencies (e.g., sensor leveling) or to further troubleshoot problems. The faster the cycle runs, the sooner problems will be detected and corrected. This reduces the amount of erroneous data collected during failure modes. Conversely, if the site is inspected infrequently, an easily correctable error, such as an instrument misalignment, can result in a large portion of the dataset being contaminated with substandard measurements. More than one data quality cycle can—and likely will—run at any time, each with a different period and emphasis—for example, daily inspection, weekly quality reports, and annual data review. For larger networks, it is often helpful to have both on-site personnel to handle maintenance and address problems and a central facility that runs in-depth QC of the data and reports data issues. The data quality cycle is critically important to the success of a measurement program, and thus it should be well-defined and funded to maintain consistent data quality over time.

4.6.1 Operations Feedback

The final component of the data quality cycle (Figure 4-10) consists of operation's feedback after the quality assessment. Intuitively, the discovery of any error requires corrective action. Even though this can be a simple text message or phone call to the station's maintenance personnel, a more formal procedure should take place to document the problem being addressed, the corrective plan, who was assigned the work, and its final resolution. The documentation need not be exhaustive but rather can contain pertinent details that will allow a future reader to reconstruct the circumstances, particularly when evidence of data errors remains in the archive. Notably, adding photo documentation can be particularly helpful.

The type of error condition encountered will dictate the type of response and feedback. When corrective action is necessary, a positive approach to the situation can help maintain a productive work environment. It can be important to reassert the technician's capabilities and training and that the project managers have confidence in their abilities. When the corrective action is complete, the station's personnel should report back the results of their activities, the cause of the problem, and if any downtime occurred at the station. This discussion shows that non-technical issues (such as human relationships) also contribute to the implementation of the data quality cycle, and ultimately to the success of any solar radiation measurement campaign—particularly in challenging environments.

4.6.2 Logging Quality Control Results

All findings during quality inspection procedures should be logged for the station's permanent records. It is useful to create a special flag accounting for issues detected during the daily inspection or from the long-term data inspection. This "manual" inspection flag defaults to False, that is, no errors, and if a potential error is detected, the flag is changed to True for the corresponding period. If possible, a note should be added stating the type of problem (physical sensor issue or measurement error), the likely cause of the error, and what corrective actions have been taken.

With this paradigm, the station record will include documentation of all positive conditions at the station, along with the occasional negative findings. It is important to document that all inspections have been made and to affirm conditions at a well-run station. This assumes the data inspection is being performed by trusted personnel who will not bypass any steps in the process.

The procedure just described is essential for resource assessment stations because of the financial issues at stake. The personnel supporting such a station and the analyst controlling and/or utilizing the data are bound to remain in close contact, which is an essential part of the process. The QC procedure is similar in the case of permanent stations designed to provide high-quality irradiance data over the long term (e.g., in the context of institutional research-class or meteorological networks). The difficulty here, however, is that the typical end user (e.g., a scientist not affiliated with the institution) does not usually have access to all data quality documentation and, therefore, might not be able to exploit the data at its fullest unless the data portal also allows public access to data quality statements.

4.7 Outlook

Automated and visual quality control and assessment methods are of utmost importance for downstream data processing, as well as upstream (e.g., maintenance and retrospective corrective measures related to measurements, sensors, installation, and maintenance procedures). However, the development and related expert consensus for these procedures mostly pertain to pyranometric reference instruments from scientific/academic institutions in meteorological, atmospheric, and solar energy research domains.

It is imperative that development continues to extend these procedures and expert consensus to solar energy-related measurements in the realms of industry and participatory sciences. These measurements could be derived from reference cells, photodiodes, PV modules, etc. With the unprecedented growth of PV systems worldwide, the quality of solar radiation measurements and their energy derivatives is already crucial for numerous industrial applications, such as maintenance monitoring for improved efficiency and forecasting for better integration into power grids. Data quality is also vital because these rapidly expanding sources of data are and will be increasingly utilized by research institutions in addition to those provided by the scientific networks of reference.

In this new context of industry and participatory sciences, measurement instruments vary significantly in terms of manufacturing sources, quality, and nature, compared to those used in scientific networks. For example, the temporal resolutions of these instruments often differ from the conventional 1-minute interval of reference instruments. Moreover, the orientations of these instruments often deviate from horizontal or normal incidence, with sometimes no precise information. Their metadata and maintenance procedures are likewise of widely varying quality or even nonexistent.

Whereas some of the QC methods described in this chapter can be readily adapted to these new diverse in-situ measurement sources, research and development efforts are still in progress to improve the existing methods. Moreover, expert discussions are necessary to establish effective means of qualifying such data and achieving broad consensus on their adoption and usage.

Emerging research avenues seek to address these new requirements, such as methods involving machine learning, applied notably to anomaly detection. These methods can integrate other simultaneous and collocated data sources, such as those from satellites or numerical weather prediction or reanalysis models. To support these data-driven developments, it is crucial to create a database that collects these new data as comprehensively as possible, thus extending the very important initiative undertaken by Task 16 of the IEA PVPS program (Forstinger et al. 2023), which focuses on research-grade radiometric networks of reference.

Lastly, it is worth noting the close methodological relationship between these new QC methods and the currently very active research and development efforts regarding short-term solar forecasting and gap-filling techniques. Indeed, automated QC procedures can be established based on smart thresholding of deviations between the current value with the imputation from an appropriate gap-filling method or the predicted value from some forecasting method. In particular, gap-filling methods potentially offer alternative values for measurements deemed questionable based on the results of the QC procedure. Some of these methods have recently been analyzed and compared under the auspices of PVPS Task 16 (Blanc and Silva 2023).

Ultimately, the synergy between these different domains should be leveraged to accelerate the implementation of more-versatile QC methods.

References

Blanc, P., and R.A. Silva. 2023. *Framework for Benchmarking of GHI Gap-Filling Methods (No. Report IEA-PVPS T16-03:2023)*. IEA-PVPS. https://iea-pvps.org/key-topics/framework-for-benchmarking-of-ghi-gap-filling-methods/.

Cordero, R.R., S. Feron, A. Damiani, E. Sepúlveda, J. Jorquera, A. Redondas, G. Seckmeyer, J. Carrasco, P. Rowe, and Z. Ouyang. 2023. "Surface Solar Extremes in the Most Irradiated Region on Earth, Altiplano." *Bull. Am. Meteorol. Soc.* 104: E1206–E1221. https://doi.org/10.1175/BAMS-D-22-0215.1.

de Miguel, A., J. Bilbao, R. Aguiar, H. Kambezidis, and E. Negro. 2001. "Diffuse Solar Irradiation Model Evaluation in the North Mediterranean Belt Area." *Sol. Energy* 70: 143–153. https://doi.org/10.1016/S0038-092X(00)00135-3.

Espinar, B., L. Wald, P. Blanc, C. Hoyer-Klick, M. Schroedter-Homscheidt, and T. Wanderer. 2011a. "Report on the Harmonization and Qualification of Meteorological Data: Project ENDORSE—Energy Downstream Service: Providing Energy Components for GMES—Grant agreement no. 262892." Accessed November 11, 2014.

Espinar, B., L. Wald, P. Blanc, C. Hoyer-Klick, M. Schroedter-Homscheidt, and T. Wanderer. 2011b. "Project ENDORSE—Excerpt of the Report on the Harmonization and Qualification of Meteorological Data—Procedures for Quality Check of Meteorological Data (No. Deliverable D3.2)." https://minesparis-psl.hal.science/hal-01493608/.

Forstinger, A., S. Wilbert, A.R. Jensen, B. Kraas, C. Fernandez-Peruchena, C.A. Gueymard, D. Ronzio, D. Yang, E. Collino, J. Polo, J. A. Ruiz-Arias, N. Hanrieder, P. Blanc, and Y.-M. Saint-Drenan. 2023. *Worldwide Benchmark of Modelled Solar Irradiance Data.* Report IEA-PVPS T16-05: 2023. IEA PVPS. https://iea-pvps.org/key-topics/worldwide-benchmark-of-modelled-solar-irradiance-data/.

Forstinger, A., S. Wilbert, B. Kraas, C. Fernández Peruchena, C.A. Gueymard, E. Collino, J.A. Ruiz-Arias, J. Polo Martinez, Y.-M. Saint-Drenan, D. Ronzio, N. Hanrieder, A.R. Jensen, and D. Yang. 2021. "Expert Quality Control of Solar Radiation Ground Datasets." *Proceedings of the ISES Solar World Congress* 2021. International Solar Energy Society. https://doi.org/10.18086/swc.2021.38.02.

Geuder, N., F. Wolfertstetter, S. Wilbert, D. Schüler, R. Affolter, B. Kraas, E. Lüpfert, and B. Espinar. 2015. "Screening and Flagging of Solar Irradiation and Ancillary Meteorological Data." *Energy Procedia 69*: 1989–1998. https://doi.org/10.1016/j.egypro.2015.03.205.

Gschwind, B., P. Blanc, and L. Menard. 2020. "SRTM-Based Horizon Profile Calculation Service." http://geocatalog.webservice-energy.org/geonetwork/srv/eng/main.home.

Gueymard, C.A. 2019. "The SMARTS Spectral Irradiance Model After 25 Years: New Developments and Validation of Reference Spectra." *Sol. Energy* 187: 233–253. https://doi.org/10.1016/j.solener.2019.05.048.

Gueymard, C.A. 2017a. "Cloud and Albedo Enhancement Impacts on Solar Irradiance Using High-Frequency Measurements From Thermopile and Photodiode Radiometers. Part 1: Impacts on Global Horizontal Irradiance." *Sol. Energy* 153: 755–765. https://doi.org/10.1016/j.solener.2017.05.004.

Gueymard, C.A. 2017b. "Cloud and Albedo Enhancement Impacts on Solar Irradiance Using High-Frequency Measurements From Thermopile and Photodiode Radiometers. Part 2: Performance of Separation and Transposition Models for Global Tilted Irradiance." *Sol. Energy* 153: 766–779. https://doi.org/10.1016/j.solener.2017.04.068.

Gueymard, C.A. 2012. "Clear-Sky Irradiance Predictions for Solar Resource Mapping and Large-Scale Applications: Improved Validation Methodology and Detailed Performance Analysis of 18 Broadband Radiative Models." *Sol. Energy* 86: 2145–2169. https://doi.org/10.1016/j.solener.2011.11.011.

Gueymard, C.A. 2001. "Parameterized Transmittance Model for Direct Beam and Circumsolar Spectral Irradiance." *Sol. Energy* 71: 325–346. https://doi.org/10.1016/S0038-092X(01)00054-8.

Gueymard, C.A., and D.R. Myers. 2009. "Evaluation of Conventional and High-Performance Routine Solar Radiation Measurements for Improved Solar Resource, Climatological Trends, and Radiative Modeling." *Sol. Energy* 83: 171–185. https://doi.org/10.1016/j.solener.2008.07.015.

Gueymard, C.A., and J.A. Ruiz-Arias. 2016. "Extensive Worldwide Validation and Climate Sensitivity Analysis of Direct Irradiance Predictions From 1-min Global Irradiance." *Sol. Energy* 128: 1–30. https://doi.org/10.1016/j.solener.2015.10.010.

Holmgren, W., C.W. Hansen, and M.A. Mikofski. 2018. "Pvlib Python: A Python Package for Modeling Solar Energy Systems." *J. Open Source Softw.* 3: 884. https://doi.org/10.21105/joss.00884.

Hoyer-Klick, C., D. Dumortier, A. Tsvetkov, J. Polo, J. Torres, C. Kurz, and P. Ineichen. 2008. "MESOR—Management and Exploitation of Solar Resource Knowledge—D 1.1.2 Existing Ground Datasets." https://www.mesor.org/docs/MESoR_D1.1.2_ExistingGroundData_v1.0.pdf.

Journée, M., and C. Bertrand. 2011. "Quality Control of Solar Radiation Data Within the RMIB Solar Measurements Network." *Sol. Energy* 85: 72–86. https://doi.org/10.1016/j.solener.2010.10.021.

JRC (European Commission—Joint Research Center). 2023. "PVGIS—Photovoltaics Geographic Information System." https://re.jrc.ec.europa.eu/pvg_tools/en/ (accessed 1.8.23).

Long, C., and E. Dutton. 2002. "BSRN Global Network Recommended QC Tests v2, Baseline Surface Radiation Network." https://bsrn.awi.de/fileadmin/user_upload/bsrn.awi.de/Publications/BSRN_recommended_QC_tests_V2.pdf.

Long, C., and Y. Shi. 2006. *The QCRad Value Added Product: Surface Radiation Measurement Quality Control Testing, Including Climatology Configurable Limits*. Atmospheric Radiat. Meas. Program Tech. Rep. https://doi.org/10.2172/1019540.

Long, C.N., and Y. Shi. 2008. "An Automated Quality Assessment and Control Algorithm for Surface Radiation Measurements." *Open Atmospheric Sci. J.* 2. https://doi.org/10.2174/1874282300802010023.

Lorenz, E., P. Guthke, A. Dittmann, N. Holland, W. Herzberg, S. Karalus, B. Müller, C. Braun, W. Heydenreich, and Y.-M. Saint-Drenan. 2022. "High Resolution Measurement Network of Global Horizontal and Tilted Solar Irradiance in Southern Germany With a New Quality Control Scheme." *Sol. Energy* 231: 593–606. https://doi.org/10.1016/j.solener.2021.11.023.

Marzo, A., J. Ballestrín, J. Alonso-Montesinos, P. Ferrada, J. Polo, G. López, and J. Barbero. 2021. "Field Quality Control of Spectral Solar Irradiance Measurements by Comparison With Broadband Measurements." *Sustainability* 13: 10585. https://doi.org/10.3390/su131910585.

Maxwell, E., S. Wilcox, and M. Rymes. 1993. *Users Manual for SERI QC Software: Assessing the Quality of Solar Radiation Data.* NREL/TP-463-5608. National Renewable Energy Laboratory, Golden, CO. https://doi.org/10.2172/10125711.

Mira, D.A., M. Bartholomaus, S. Poessl, P.B. Poulsen, and S.V. Spataru. 2022. "Comparing the Accuracy of Horizon Shade Modelling Based on Digital Surface Models Versus Fisheye Sky Imaging." 49th Photovoltaics Specialists Conference (PVSC), IEEE, Philadelphia, PA, USA: 060–065. https://doi.org/10.1109/PVSC48317.2022.9938715.

Nollas, F.M., G.A. Salazar, and C.A. Gueymard. 2023. "Quality Control Procedure for 1-Minute Pyranometric Measurements of Global and Shadowband-Based Diffuse Solar Irradiance." *Renew. Energy* 202: 40–55. https://doi.org/10.1016/j.renene.2022.11.056.

Perez, R., P. Ineichen, R. Seals, J. Michalsky, and R. Stewart. 1990. "Modeling Daylight Availability and Irradiance Components From Direct and Global Irradiance." *Sol. Energy* 44: 271–289. https://doi.org/10.1016/0038-092X(90)90055-H.

Perez-Astudillo, D., D. Bachour, and L. Martin-Pomares. 2018. "Improved Quality Control Protocols on Solar Radiation Measurements." *Sol. Energy* 169: 425–433. https://doi.org/10.1016/j.solener.2018.05.028.

Reda, I. 2011. *Method to Calculate Uncertainty Estimate of Measuring Shortwave Solar Irradiance Using Thermopile and Semiconductor Solar radiometers.* National Renewable Energy Laboratory, Golden, CO. https://doi.org/10.2172/1021250.

Schade, N.H., A. Macke, H. Sandmann, and C. Stick. 2007. "Enhanced Solar Global Irradiance During Cloudy-Sky Conditions." *Meteorol. Z.* 16: 295–303. https://doi.org/10.1127/0941-2948/2007/0206.

Shafer, M.A., C.A. Fiebrich, D.S. Arndt, S.E. Fredrickson, and T.W. Hughes. 2000. "Quality Assurance Procedures in the Oklahoma Mesonetwork." *J. Atmospheric Ocean. Technol.* 17: 474–494. https://doi.org/10.1175/1520-0426(2000)017<0474:QAPITO>2.0.CO;2.

Tregenza, P.R., R. Perez, J. Michalsky, R. Seals, B. Molineaux, and P. Ineichen. 1994. *Guide to Recommended Practice of Daylight Measurement.* CIE 108-1994. https://cie.co.at/publications/guide-recommended-practice-daylight-measurement-disk-d006.

Urraca, R., J. Antonanzas, A. Sanz-Garcia, and F.J. Martinez-de-Pison. 2019. "Analysis of Spanish Radiometric Networks with the Novel Bias-Based Quality Control (BQC) Method." *Sensors* 19: 2483. https://doi.org/10.3390/s19112483.

Urraca, R., A.M. Gracia-Amillo, T. Huld, F.J. Martinez-de-Pison, J. Trentmann, A.V. Lindfors, A. Riihelä, and A. Sanz-Garcia. 2017. "Quality Control of Global Solar Radiation Data With Satellite-Based Products." *Sol. Energy* 158: 49–62. https://doi.org/10.1016/j.solener.2017.09.032.

Urraca, R., A. Sanz-Garcia, and I. Sanz-Garcia. 2020. "BQC: A Free Web Service to Quality Control Solar Irradiance Measurements Across Europe." *Sol. Energy* 211: 1–10. https://doi.org/10.1016/j.solener.2020.09.055.

Vignola, F., J. Peterson, R. Kessler, S. Snider, P. Gotseff, M. Sengupta, and A. Habte. 2022. "Andreas, A., Mavromatakis, F., 2022. Reference Cell Performance and Modeling on a One-Axis Tracking Surface." 49th Photovoltaics Specialists Conference (PVSC), IEEE, Philadelphia, PA, USA: 0146–0153. https://doi.org/10.1109/PVSC48317.2022.9938920.

Wilcox, S., T. Stoffel, and A. Habte. 2023. "Developing the Proof of Concept for the SERI QC Flag Translation." NREL/SR-5D00-85589. National Renewable Energy Laboratory, Golden, CO. https://doi.org/10.2172/1987278.

Wilcox, S., T. Stoffel, and A. Habte. 2022. *Evaluation and Suitability of Using SERI QC Software for Estimating Measurement Uncertainty.* NREL/SR-5D00-82913. National Renewable Energy Laboratory, Golden, CO. https://doi.org/10.2172/1883560.

Younes, S., R. Claywell, and T. Muneer. 2005. "Quality Control of Solar Radiation Data: Present Status and Proposed New Approaches." *Energy* 30: 1533–1549. https://doi.org/10.1016/j.energy.2004.04.031.

5 Further Relevant Meteorological Parameters

Stefan Wilbert,[1] Christian Gueymard,[2] Aron Habte,[3] Manajit Sengupta,[3] Yu Xie,[3] Tomas Landelius,[4] Jesús Polo,[5] Vicente Lara-Fanego,[6] Frank Vignola,[7] Josh Peterson,[8] Natalie Hanrieder,[1] Anne Forstinger[9] and Birk Kraas[9]

[1] *German Aerospace Center (DLR), Germany*
[2] *Solar Consulting Services, USA*
[3] *National Renewable Energy Laboratory, USA*
[4] *Swedish Meteorological and Hydrological Institute, Sweden*
[5] *Centro de Investigaciones Energéticas, Medioambientales y Tecnológicas (CIEMAT), Spain*
[6] *Solargis, Slovakia*
[7] *University of Oregon, USA, deceased*
[8] *University of Oregon, USA*
[9] *CSP Services GmbH, Germany*

Executive Summary

Solar irradiance is the most important meteorological input parameter for solar energy, but additional meteorological quantities are required for accurate yield predictions, performance analysis, and optimal plant and grid operation and design. Different individual parameters will be needed for different technologies.

- Wind speed, wind direction, and gust
- Ambient air temperature
- Relative humidity
- Atmospheric pressure
- Precipitation type and amount (rain, snow, hail)
- Aerosols and water vapor
- Spectral irradiance
- Ultraviolet (UV) irradiance
- Circumsolar irradiance
- Attenuation between the heliostat and the receiver of solar tower plants
- Soiling of solar collectors
- Surface albedo.

These quantities might affect the design of the solar installation (e.g., wind loads) and its efficiency (e.g., temperature, soiling) or can help improve the solar radiation datasets (e.g., aerosols and water vapor).

Further parameters related to agricultural crops, such as the photosynthetically active radiation (PAR), are required for agrivoltaic projects, and the importance of some of the above variables is different for agrivoltaics because of their effects on the photovoltaic (PV) system and plant growth.

For each of these quantities, measurement methods exist, and the appropriate instruments can be added to a radiometric station. Numerical weather prediction (NWP) models provide wind, temperature, humidity, pressure, precipitation, surface albedo, and water vapor data. Satellite data can be used to determine or model surface albedo, precipitation, aerosols, water vapor, spectral irradiance, circumsolar irradiance, and atmospheric extinction between the heliostat and

the receiver on a concentrating solar thermal (CST) tower. Finally, soiling losses can be approximated based on meteorological data such as precipitation or particulate matter.

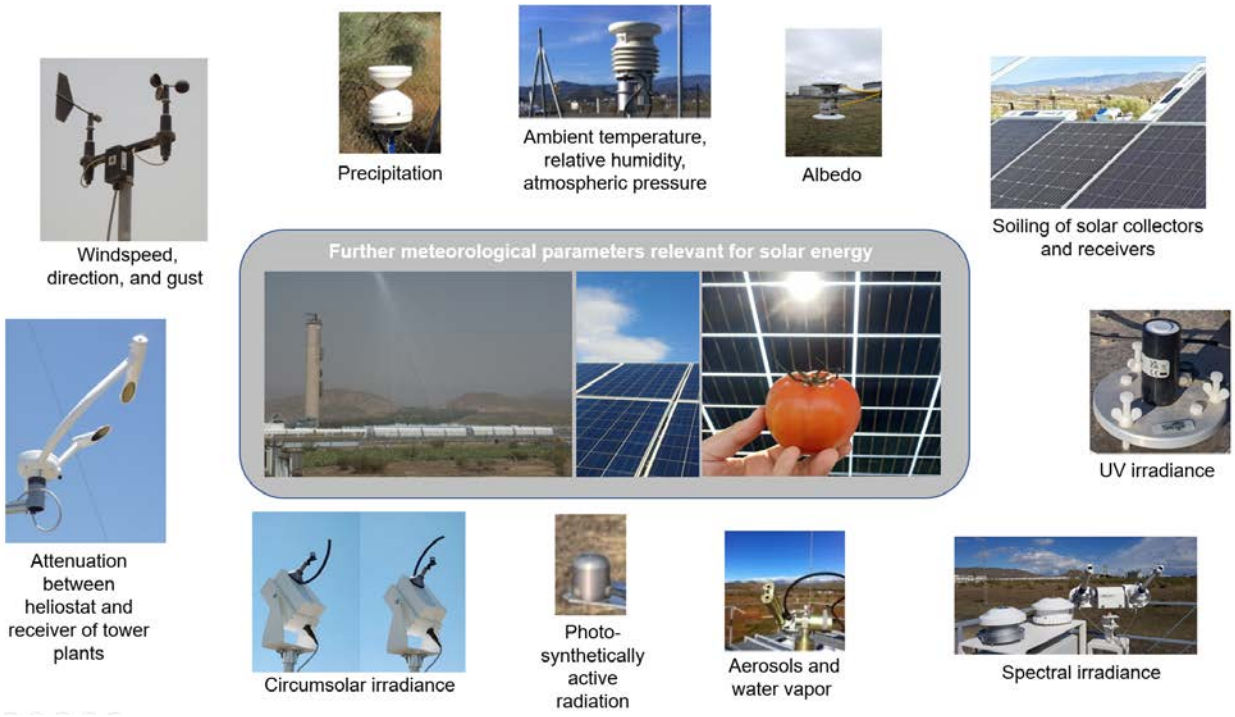

Figure ES 5-1. Exemplary measurement options for the discussed variables

Images by DLR at CIEMAT's Plataforma Solar de Almería and by University of Applied Sciences Upper Austria

5.1 Introduction

Solar radiation is the fuel of solar energy systems and the driver of their production. However, solar installations are also affected by other meteorological variables. The influence of ambient air temperature on photovoltaic (PV) efficiency is a well-known example. Recently, other parameters such as soiling have also gained interest. The following parameters are discussed in this chapter:

- Wind speed, wind direction, and gust
- Ambient air temperature
- Relative humidity
- Atmospheric pressure
- Precipitation type and amount (rain, snow, hail)
- Aerosols and water vapor
- Spectral irradiance
- Ultraviolet (UV) irradiance
- Circumsolar irradiance
- Attenuation between the heliostat and the receiver of solar tower plants
- Soiling of solar collectors
- Surface albedo.

This chapter provides definitions for these quantities, describes their effect on solar energy systems, and documents how they are measured and modeled. Moreover, some further variables required for agrivoltaics are introduced and their importance explained in that context.

Various atmospheric or meteorological quantities affect the design of solar installations (e.g., wind loads) and their efficiency (e.g., temperature, soiling), or can be used to improve the development of modeled solar radiation datasets (e.g., aerosols and water vapor). Typically, many experiments and models have been used to quantitatively understand the effect of these variables on different solar energy systems. Solar energy system models used for such purposes are described in Chapter 11, which also provides recommendations on the required or optional datasets for different project phases. Overviews of the effects of these meteorological parameters on PV systems are presented in an International Energy Agency (IEA) Photovoltaic Power Systems Programme report (Reise et al. 2018) and in Bonilla Castro et al. (2020). A discussion of the influence of different meteorological variables on concentrating solar power (CSP) can be found in Chhatbar and Meyer (2011). The IEA Solar Power and Chemical Energy Systems program has prepared a guideline for the meteorological data required for different project phases for CSP, including the proper selection and subsequent impact of key meteorological variables (Silva et al. 2021).

In practice, meteorological measurements are typically made in parallel with solar radiation measurements, as described in detail in Chapter 3. In particular, Section 3.5 of Chapter 3 provides information on how these additional instruments should be included in a solar resource assessment measurement station. Data quality control for these measurements is also required. The uncertainty of the datasets should also be known. Several radiation datasets presented in Chapter 8 include some of the variables discussed in this chapter, which reduces the required effort for data collection and merging. Additional data sources for some meteorological quantities are provided in the following sections.

5.2 Wind

Wind speed, gust, and wind direction are important for the design and performance of solar power plants and electricity grids. Wind speed and direction are often represented by the horizontal components of the wind velocity. The gust is the maximum wind speed during each time interval consistent with the measuring device performance specifications. For many applications, an interval of 3 seconds is adequate (WMO 2018).

Wind loads, and in particular wind gusts, must be considered for the design of solar collectors and overhead power transmission and distribution lines. In tracked solar collectors, high wind gusts or speeds during operation might also require moving the collectors to their stowed position to minimize wind load and avoid damage. From a different perspective, cooling effects are strongly related to wind (convection). Cooling increases the efficiency of PV, but decreases that of thermal collectors because of increased thermal losses. For some specialized applications in CSP testing (e.g., convective receiver losses), the three-dimensional wind velocities are also of interest.

Wind speed and gust can be measured using anemometers. Cup anemometers and propeller anemometers consist of a rotor whose frequency of rotation corresponds to the wind velocity. Ultrasonic anemometers measure the wind speed, gust, and direction. Many ultrasonic anemometers emit an ultrasonic signal over a constant, short distance and measure the time the signal needs to reach a detector. Using several measurement paths, the wind direction or the three-dimensional wind vector can be derived.

Mechanical sensors used to determine the wind direction are called wind vanes. The vane's position is read by, for example, a potentiometer coupled with the wind vane. Propeller anemometers often include a wind vane. Recommendations on wind measurements can be found in the *Guide to Meteorological Instruments and Methods of Observation* (WMO 2018), also known as the Commission for Instruments and Methods of Observation (CIMO) guide. In solar power applications, it is often impossible to measure the wind velocity solely by following the CIMO guide. Because wind measurements at an existing or potential solar power plant site must represent the conditions affecting the collectors, measurements might be taken much closer to obstacles (buildings, trees, etc.) than required for meteorologically representative wind measurements intended for other purposes. For resource assessment, one measurement at 3-m or 10-m height integrated with the resource assessment weather station is considered sufficient (the measurement height must be determined depending on the collectors' expected height). In existing power plants with tracked collectors, it is recommended to monitor the wind at different heights and at more than one site in the solar field. This is mainly because the wind speed in different parts of a solar field varies as a function of its geometrical coarseness. The windward side will usually experience higher wind speeds than the leeward side. Especially in power plants where wind has an influence on operation (tracked PV, CSP) it is important to know the wind load on the structures, so that wind sensors should be placed such that the highest wind speed occurring in the solar field are always recorded. Chapter 3, Section 3.5 provides information on how wind measurements should be included in a measurement station for resource assessment and yield predictions.

Ultrasonic anemometers are widely used in PV simply because most sites are unstaffed and sonic sensors do not have any moving parts, thus mitigating the need for regular scheduled maintenance that is required with mechanical sensors. Ultrasonic anemometers commonly include an embedded digital compass used to correct wind direction data; this significantly simplifies sensor installation as compared to mechanical wind directions sensors, because these require meticulous alignment to measure accurate wind direction. In contrast, mechanical anemometers typically have lower initiation thresholds than sonic sensors and can thus measure lower wind speeds, which might be a significant advantage.

In addition to measurements, modeled wind data are available based on either historical time series or forecasts. Such modeled data are typically required if long-term radiation datasets are needed, typically because of the absence of long-term ground measurements from a nearby site. Many numerical weather prediction (NWP) models and reanalysis datasets provide wind data. Examples are the Modern-Era Retrospective analysis for Research and Applications, Version 2 (MERRA-2) from the National Aeronautics and Space Administration (NASA) (Bosilovich et al. 2016); the North American Regional Reanalysis (Mesinger et al. 2006); the Climate Forecast System Reanalysis (CFSR) from the National Centers for Environmental Prediction; and ERA5 from the European Centre for Medium-Range Weather Forecasts (see also Chapter 8, Section

8.3.1). A global, albeit limited, validation of the wind speed predicted by five reanalyses has shown that their accuracy is highly variable and might not be sufficient for demanding applications (Ramon et al. 2019). Users should always be aware that wind is highly variable on a small scale and strongly affected by obstacles, structures, and terrain features, so that wind measurements taken at, or modeled for, a specific location might differ from the conditions just a short distance away.

In general, the spatial and temporal resolution of reanalysis data is coarse compared to satellite-derived irradiance data; therefore, upscaling methods are needed to increase the spatial resolution of wind data and match it with that of the solar data. Sometimes, however, reanalysis data are readily part of solar radiation datasets. The upscaled MERRA-2 wind data, for instance, is disseminated through https://nsrdb.nrel.gov, and it is also accessible through the National Renewable Energy Laboratory's (NREL's) System Advisor Model (SAM), which is a techno-economic model (Blair et al. 2018). In the latter, wind information is a weather input. Like MERRA2, ERA5 includes east- and northward components (U and V) of wind speed, but at a finer 0.25 by 0.25° grid spatial resolution. Moreover, its sister product, ERA5-Land, provides the same information at 0.1 by 0.1° (or ≈9 km) resolution, but only over land surfaces.

5.3 Ambient Air Temperature and Relative Humidity

Ambient air temperature is an important factor for calculating the efficiency of solar power plants and the maximum load of electric power transmission lines. Although PV module temperatures are typically directly measured, ambient temperature and wind speed are commonly used to model cell temperature for performance monitoring, capacity testing, and energy assessments (Driesse et al. 2022). High temperatures reduce the efficiency of many common types of PV modules, the thermal losses of thermal collectors, and the efficiency of a thermal power plant's cooling system. Transmission lines expand when heated due to the increasing air temperature, which also increases their electrical resistance, and hence the electric losses. Temperature and temperature changes are also relevant for the selection of the appropriate materials for a power plant, considering aging processes. Air temperature is often represented by dry-bulb temperature, defined by the temperature of air when shielded from radiation, wind, and moisture.

Relative humidity is the ratio (usually reported in percentages) between the observed vapor pressure and the saturation vapor pressure with respect to water at the same temperature and pressure (WMO 2018). The saturation vapor pressure is a sole function of ambient temperature, and it can be obtained using one of many empirical formulae; see Alduchov and Eskridge (1996) and Gueymard (1993). Relative humidity has an impact on the cooling processes in thermal power plants and the efficiency of thermal receivers, depending on receiver technology, such as air receivers. It is also associated with soiling processes through the formation of dew and the accumulation of particles on solar collectors and solar radiation sensor optics. Moreover, similarly to temperature, relative humidity influences aging processes.

Thermometers and hygrometers are used to measure dry-bulb temperature and relative humidity, respectively. Currently, temperature-dependent resistors, or bandgap sensors, are used in the construction of thermometers. Capacitance or resistance changes in the sensor material directly correspond to changes in humidity, thus providing the basis for measurement. Often, combined sensors (hygro-thermometers) are used and placed in a multiplate naturally ventilated radiation

shield to minimize solar heating-related temperature bias and protect the sensor from rain and snow. Aspirated solar radiation shields can alternatively be used to further reduce radiative errors in air temperature measurements at stations that are installed on a highly reflective surface or that commonly experience wind speeds less than 3–4 m/s (Huwald et al. 2009).

Higher accuracy of temperature and relative humidity can be reached with more sophisticated measurement methods, but this is usually not required in solar energy applications. Recommendations on temperature and relative humidity measurements can be found in the CIMO guide (WMO 2018).

The prediction of temperature and relative humidity is included in the output of many NWP or reanalysis models. Because of the coarse resolution of such data, upscaling is typically necessary to match satellite-based radiation data. To that end, an elevation correction of temperature and humidity needs to be applied. As an example, the upscaling method used in the production of the National Solar Radiation Database (NSRDB) is presented below. According to Hemond and Fechner (2015), the correction for temperature uses a lapse rate of 6.5°C per kilometer:

$$Air\_temperature = Coarse\_pixel\_air\_temperature + E \bullet \left(\frac{6.5}{1000}\right) \tag{5-1}$$

where E is the location's elevation (in meters) relative to the upscaled grid.

To upscale the relative humidity data, a multistep procedure has been devised for the NSRDB: the specific humidity is interpolated using a combination of nearest-neighbor temporal interpolation and second-degree inverse-distance weighting. Additional steps are taken to estimate relative humidity from the interpolated specific humidity. The saturation vapor pressure in Pa is calculated using a method described in Tetens (1930):

$$Saturation\_vapor\_pressure = 610.79 \bullet \exp\left(\frac{Air\_temperature}{Air\_temperature + 238.3} \bullet 17.2694\right) \tag{5-2}$$

where air temperature is in °C. Then the mixing ratio (w), which is the mass of water vapor per mass of dry air, is calculated using a method described by DeCaria[27]:

$$w = \frac{h}{(1-h)} \tag{5-3}$$

where h is the specific humidity 2 meters above ground level in kg kg^{-1}. The next step is to estimate the saturation mixing ratio (ws) using a method described by DeCaria[28] and the National Weather Service[29]:

$$ws = \frac{621.97 \bullet \left(\frac{Saturation\_vapor\_pressure}{1000}\right)}{Surface\_pressure - \left(\frac{Saturation\_vapor\_pressure}{1000}\right)}. \tag{5-4}$$

[27] See http://snowball.millersville.edu/~adecaria/ESCI241/esci241_lesson06_humidity.pdf.
[28] See http://snowball.millersville.edu/~adecaria/ESCI241/esci241_lesson06_humidity.pdf.
[29] See https://www.weather.gov/media/epz/wxcalc/mixingRatio.pdf.

The surface pressure is also obtained from MERRA-2 and the corresponding upscaling scheme, as discussed in Section 5.4, Eq. 5-6. Finally, relative humidity is calculated from[30]:

$$\mathrm{RH} = \frac{w}{ws}. \tag{5-5}$$

In general, it is advised to interpolate dew point and ambient temperatures separately and then calculate relative humidity at the place of interest.

5.4 Atmospheric Pressure

Atmospheric pressure has a direct effect on cooling processes in thermal plants and CSP receiver technologies, particularly on the power block efficiency. Pressure variations influence the aging processes of components with sealed volumes; however, pressure data are also used for intermediate calculations in solar resource assessments, such as the calculation of solar position, atmospheric transmittance, dew point, or relative humidity.

The atmospheric pressure on a given surface is defined as the force per unit area resulting from the weight of the atmosphere aloft (WMO 2018). Atmospheric pressure can be measured with mercury barometers, aneroid barometers, hypsometers, or electronic barometers. For solar energy applications, electronic barometers are of the most interest. Such barometers use piezoelectric materials, an aneroid capsule that changes its form or position depending on pressure, or a resonator whose mode of vibration depends on pressure. The displacement of the aneroid capsule can be detected using capacity or resistance changes. The recommendations for pressure measurements by the CIMO guide (WMO 2018) can be used in solar energy applications.

As mentioned in the previous section, surface pressure can be obtained from NWP and reanalysis data such as MERRA-2. Pressure data might also need to be upscaled. For example, to upscale the surface pressure and relative humidity data in the NSRDB, a combination of linear temporal interpolation and second-degree inverse-distance weighting is used. An elevation correction is carried out using the method described in McIntosh (1978) with elevation E in m and pressures in mbar:

$$Surface\_pressure = Coarse\_pixel\_surface\_pressure + \left[1013.25 \bullet \left\{1 - \left(1 - \frac{E}{44307.69231}\right)^{5.25328}\right\}\right]. \tag{5-6}$$

5.5 Precipitation

Precipitation (rain, hail, or snow) is another relevant quantity in solar energy applications. Because of the possible strong effects of precipitation, not only historical data and measurements, but also forecasts, are of interest. In the form of rain, precipitation can wash dirty collectors, but it can also cause efficiency loss resulting from droplets on exposed optical surfaces, especially in concentrating technologies. Rain-induced cooling effects tend to increase the efficiency of PV modules, but it reduces that of thermal plants. Moreover, precipitation can strongly influence aging processes. Large hail with diameter of more than about 4 cm (Rand et

[30] See https://www.weather.gov/media/epz/wxcalc/mixingRatio.pdf.

al. 2020) can damage solar collectors and other plant components. For this reason, hail data are important for site risk assessment and system design. Measurements and forecasts of hail events allow to stow trackers when needed. If water enters the insulation material of hot pipes, a prolonged efficiency loss occurs until the wet insulation is replaced. The effect of rain on transmission lines is less important because its cooling effect and the weight increase mostly compensate each other. Ice loads on transmission lines can be of critical importance, however, and have even resulted in catastrophic failures in the recent past, such as during the January 1998 North American ice storm (Phillips 2002).

The presence of snow can have either positive or negative effects on solar energy production. Snow in the vicinity of a PV installation or flat-plate thermal collectors could increase production because of the higher surface albedo and increased reflected irradiance (Andrews et al. 2013; Burnham et al. 2019). In some cases, this increase in reflected irradiance can combine with cloud enhancement situations and lead to substantial spikes in incident irradiance (Gueymard 2017). In turn, these spikes can have negative impacts on the normal operation of PV plants (do Nascimento et al. 2019; Järvelä et al. 2020). On the other hand, it is more likely that accumulated snow on collectors will lead to yield reductions, increased wear and tear, and even pose a danger because of the increased load on the supporting structure and snow sliding down onto underlying areas (Andenæs et al. 2018). In concentrating systems, no irradiance gains can exist because only direct radiation is used.

Rain is often measured with tipping bucket rain gauges. The raindrops are collected by a horizontal aperture of known small area, and the droplets fall on a lever. When the droplets trickle onto the lever, a signal is produced when the weight of the droplets causes the lever to move or "tip." Such rain gauges can measure only liquid precipitation. In areas where snow is common, heated systems must be considered, in which the aperture is heated and melts frozen precipitation almost immediately. In parallel to the common mechanical tipping buckets, optical pluviometers also exist. The lever can be replaced by a laser and an appropriate sensor to detect the droplets. Another optical measurement method for all types of precipitation uses an open measurement volume, which directly detects the falling raindrops or snowflakes in the air with an optical scattering method. A light source emits light, and a sensor detects the scattered light under a specific scattering angle. The number of pulses detected by the sensor corresponds to the number of particles, and the pulsing pattern helps determine the size of the droplets and distinguish between snow, rain, and other forms of precipitation. A haptic rain sensor detects and quantifies rain intensity and accumulation using vibration signals. The CIMO guide (WMO 2018) contains recommendations for precipitation measurements that are also of interest in solar applications. Precipitation data can also be obtained from NWP or reanalysis predictions, which is of great interest for the operation and design of solar energy systems despite the lower accuracy compared to measurements (De Leeuw et al. 2015; Zhao et al. 2021).

In relation to precipitation, it is of practical importance to know how long raindrops, and even more so, snow, can remain on the surface of solar collectors; thus, data about snow cover is of interest. Examples of global snow cover products include those from the Interactive Multisensor Snow and Ice Mapping System (produced by the U.S. National Ice Center), the Microwave Integrated Retrieval System, the National Oceanic and Atmospheric Administration's Microwave Surface and Precipitation Products System, and the JAXA Satellite Monitoring for Environmental Studies (produced by the Japan Aerospace Exploration Agency). Products with a

European focus are available from the CryoLand Copernicus Service. Some global snow products have been intercompared recently (Chiu et al. 2020). Other options are reanalysis data (e.g., ERA5, ERA5-Land, Copernicus Atmosphere Monitoring Service [CAMS], or MERRA-2) and databases with snow depth information from in situ measurements, such as the European Climate Assessment and Dataset project.[31] More detailed data regarding snow conditions might be also available from the national weather service of each country.

When designing installations for snowy regions, precautions should be followed to optimize the solar system's performance—see Andenæs et al. (2018) for architectural considerations. Obstructions to the sliding path of snow is the system characteristic that has the most notable effect (Pawluk et al. 2019). In particular, it is recommended to use frameless PV modules and to ensure that there is enough clearance between them and the underlying surface so that snow can slide off easily (Bogenrieder et al. 2018; Riley et al. 2019). It is good to increase the tilt angle to facilitate this process and to arrange the panels in landscape-oriented layouts to prevent the bypass diodes from becoming ineffective during periods of partial shading (Heidari et al. 2015). The possible benefit of mechanically removing snow accumulations depends on location or climate. In high-latitude regions characterized by long cloudy winters, snow clearing does not seem to be beneficial (Stridh 2012), but it might be of value in sunnier regions where the potential winter production is higher (Heidari et al. 2015). Other clearing methods like applying surface coatings or using electrostatic forces or thermal absorbers are promising, but further research and development is needed to prove their value (Pawluk et al. 2019). In Jahn et al. (2022), a suggested limit for snow accumulation on panels is 0.7 m. It is also noted that in Sweden the installer recommendation is to not actively remove snow from modules because the guarantee often becomes void if the modules are serviced mechanically.

How much loss can be expected because of snow? Existing studies based on a limited number of sites have reported annual production losses ranging from 0–25% and monthly losses as high as 100% (Andrews et al. 2013; Becker et al. 2008; Sugiura et al. 2003; Townsend and Powers 2011). In their review article Pawluk et al. (2019) found that annual losses caused by snow coverage are less than 10% in most climates. Many models have been developed to estimate the snow loss as a function of weather and installation characteristics, such as Lorenz et al. (2012) Marion et al. (2013), and Townsend and Powers (2011). Such results are site-specific, so little is known about their general validity; therefore, it is difficult to predict the potential impact of snow on the performance of future projects. Because of a lack of general snow-loss models, the major PV modeling software products on the market do not support such calculations beyond a simple scaling, such as in PVWatts® (Dobos 2014). Ryberg and Freeman (2015), however, incorporated the snow model from Marion et al. (2013) into NREL's SAM. In a 30-year simulation using NSRDB data for 239 locations across the United States, the modeled snow loss varied from 0–4% in areas with only occasional snow to 15–25% in areas with abundant snow. These limited results can be considered today's best practice for snow-loss modeling. They are also in line with the results from a Canadian study presented in a recent report on soiling losses (Schill et al. 2022).

[31] See https://www.ecad.eu/.

5.6 Aerosols and Water Vapor

Some solar energy applications can benefit from the knowledge of spectral aerosol optical depth (AOD), single-scattering albedo, asymmetry factor, scattering phase functions, and total column water vapor. The latter is often referred to as precipitable water (PW) or integrated water vapor (IWV). These variables can be used to simulate clear-sky broadband or spectral irradiance, as explained further in the following sections, and could aid in understanding the spatiotemporal variability of the radiation field. Precise knowledge of these variables at any site or instant can be used to improve modeled solar radiation datasets and to conduct site adaptations. For solar tower power plants, these variables are also helpful to model the slant-path radiation attenuation between the heliostats and the receiver.

Figure 5-1. AERONET sun photometric station at CIEMAT's Plataforma Solar de Almería

Photo from DLR

Sun photometers are typically used to determine these variables, although spectroradiometers have been used occasionally to this purpose as well (Cachorro et al. 2009). One type of sun photometer measures spectral direct normal irradiance (DNI(λ)) and the spectral sky radiance at several wavelengths (Figure 5-1). Simpler sun photometers sense only the spectral DNI. Both instruments consist of one or more photodetectors positioned behind different spectral filters and a collimator system. Additional polarization filters are optionally used. Solid-state sensors, such as photodiodes, are used for signal detection. For sun photometers that measure only spectral DNI, a sun tracker is required. For sky radiance measurements, more elaborate pointing systems are used.

Because these aerosol properties are highly wavelength-dependent, it is necessary to make measurements at more than a single wavelength. Sun photometers are primarily used to monitor aerosol properties, but they normally have a dedicated channel (near 940 nm) to also determine PW.

The direct-sun irradiance measurements are used to derive basic information on aerosols. First, the total atmospheric optical depth (TOD) is calculated at the measurement wavelengths using the spectral DNI measurements, the extraterrestrial spectral irradiance at the top of the atmosphere ETR(λ), and the airmass, m.

$$\mathrm{TOD}(\lambda) = \frac{1}{m} \ln\left(\frac{\mathrm{ETR}(\lambda)}{\mathrm{DNI}(\lambda)}\right) \quad (5\text{-}7)$$

The AOD at these wavelengths is then determined by subtracting the optical depths of all other atmospheric constituents, such as molecules, water vapor, ozone, or nitrogen dioxide. Most optical depths are obtained from separate sources (e.g., satellite retrievals or atmospheric models), whereas the water vapor optical depth is derived from the collocated PW measurement. The Ångström exponent, α_{Ang}, can then be derived and used to calculate the AOD at different wavelengths. Ångström's law is described in Eq. 5-8 as a function of wavelength λ and reference wavelength λ_0 = 1 μm:

$$\mathrm{AOD}(\lambda) = \mathrm{AOD}(\lambda_0)\left(\frac{\lambda_0}{\lambda}\right)^{\alpha_{Ang}} \quad (5\text{-}8)$$

To determine α_{Ang}, the spectral AOD for at least two wavelengths must be known. In a separate step, the direct-sun measurements can be combined with the concomitant sky radiance measurements to derive the aerosol single-scattering albedo, asymmetry factor, aerosol phase function, and other parameters using inversion algorithms (NASA 2006).

The two main sun photometer networks in the world are the Aerosol Robotic Network (AERONET)[32] and SKYNET.[33] These networks are important for solar resource assessment because of the relatively large number of available observing stations and the applied quality assurance and calibration methods (Giles et al. 2019).

The proper determination of aerosol properties (most importantly, AOD) and water vapor can be done only if the solar disk is not obscured by clouds; therefore, cloud-detection algorithms are used to post-process the raw data and generate usable data. With AERONET, for example, the spectral DNI measurements are taken in direct-sun triplets. In a triplet, three series of measurements are made in rapid succession. In each series, all different filters are used. Cloud episodes can be detected by comparing the total optical depth derived from the spectral data of the three series to each other and to defined limits (Giles et al. 2019; Smirnov et al. 2000). This cloud-screening process relies on the higher temporal variability and higher value of cloud optical depth compared to AOD.

Data from measurement networks are available in different levels of quality control. In addition to cloud screening, the quality-control procedures involve various other criteria. With AERONET, for instance, the best data quality (Level 2) includes manual outlier rejection and correction for the change of the calibration constants before and after a measurement period of approximately 1 year (Holben et al. 2006). Unfortunately, this regular calibration process, as well as other experimental difficulties that might arise in the field, result in data breaks of various duration (sometimes of many months) at all stations. Despite this important issue, the instrument's calibration is of central importance for overall data accuracy. When available, the highest-quality data should be used.

[32] See http://aeronet.gsfc.nasa.gov/new_web/index.html.
[33] See https://www.skynet-isdc.org/.

In practice, it is rare that ground measurements of aerosols and water vapor are available for the site or period under scrutiny; thus, it is generally necessary to rely on other sources of data. Aerosol data can be retrieved from spaceborne observations, such as those sensed by the Moderate Resolution Imaging Spectroradiometer (MODIS) instrument on board the Terra and Aqua satellites (Bright and Gueymard 2019; Wei et al. 2019). Another source of data is provided by reanalysis models, such as CAMS or MERRA-2 (Gueymard and Yang 2020; Kosmopoulos et al. 2018). Similarly, water vapor information can be retrieved from satellite sensors like the Global Ozone Monitoring Experiment–2 (GOME-2), the Scanning Imaging Absorption Spectrometer for Atmospheric Cartography (SCIAMACHY), and MODIS spaceborne instruments (Beirle et al. 2018; Bright et al. 2018), or from reanalysis models (Mishra 2020). Although AOD and PW are derived mostly from polar-orbiting satellites, several retrievals are developed with geostationary satellites too (Kaufman et al. 2002). This trend has accelerated in the last few years because of the launch of more-advanced sensors on board such satellites, such as Himawari-8 (Fu et al. 2023b), the Geostationary Operational Environmental Satellite (GOES) (Fu et al. 2023a), or Meteosat (Ceamanos et al., 2023). For both aerosol and water vapor, more details about the available sources of data and their accuracy are provided by Gueymard (2019a).

For most solar energy projects, aerosol and water vapor data are required only for radiation modeling (i.e., as an intermediate step). No strict recommendation is given to systematically collect such modeled or measured data; however, aerosol and water vapor data can help answer questions related to the quality of model-derived irradiance data, especially DNI data. Moreover, such data are linked to the solar spectrum, which is of interest in PV applications (see Section 5.7). Further, aerosol data are related to soiling, circumsolar radiation, and beam attenuation between the heliostats and the receiver in solar tower power plants, as discussed in Sections 5.9 to 5.11.

5.7 Spectral Irradiance

Most sections in this handbook relate to the solar resource in terms of broadband shortwave fluxes, that is, solar irradiance in the spectral range of about 280–4000 nm. Considering the rapid deployment of new solar technologies and the diversification of their physical principles, spectral solar irradiance data and models are sometimes necessary to address specific aspects of the solar resource in PV, photobiological, and photochemical processes. Hence, the demand for spectral information has considerably increased in recent decades, at least at the level of high-end research and experimentation. New investigations show that neglecting spectral and angular details can lead to significant deviations in PV power modeling (Lindsay et al. 2020).

As with broadband irradiance, the need for spectral irradiance data can be fulfilled with either measurements or models. As mentioned in Chapter 2, Section 2.5.6, a few reference clear-sky spectra have also been standardized for a potentially large number of applications—most importantly PV. Because cloudy conditions are connected to irradiance that is normally lower, highly variable, and extremely difficult to characterize, no equivalent cloudy-sky reference standard spectrum exists.

For solar PV applications, reference spectra are particularly useful to, for example: (1) obtain a performance rating following the industry's best practices, such as standard test conditions, which prescribe a reference spectrum (Emery et al. 2013; Institute for Energy 2010); (2) determine PV spectral mismatch factors when the actual spectral conditions differ from the

reference spectrum defined by ASTM G173-03 (ASTM G173 2020) or the International Electrotechnical Commission (IEC) 60904-3 (Braga et al. 2019; Mambrini et al. 2015; Müllejans et al. 2005; Myers and Gueymard 2004); or (3) evaluate how well solar simulators agree with a reference spectrum, according to, for example, IEC 60904-9 (Bliss et al. 2010; Meng et al. 2011; Sarwar et al. 2014). One issue with reference spectra is that they are developed for specific atmospheric conditions and geometric configurations (Gueymard et al. 2002) and thus might not correspond to observable natural conditions at all locations of interest or during some periods of the year. To ease this, subordinate standard spectra have been proposed (Jessen et al. 2018). These spectra are referenced in ISO standard 9060:2018 (ISO 9060 2018) to evaluate spectral mismatch factors or spectral errors in radiometers.

Under natural conditions, the solar spectrum continuously varies in both magnitude and relative distribution. It is mostly affected by solar zenith angle (SZA) (and thus by air mass) and a few variable atmospheric constituents, most importantly AOD and PW. An increase in air mass or AOD modifies the shape of both direct and global spectra in a way referred to as "red shift" because short wavelengths are attenuated more than longer ones, whereas an increase in PW does the opposite and results in a "blue shift."

Obtaining accurate outdoor solar spectra for experimental PV research or for the validation of solar radiation models requires high-quality measurements obtained with carefully maintained spectroradiometers. Different types of instruments exist, depending on their detection method: (1) scanning monochromators, (2) charge-coupled device (CCD) arrays, and (3) diode arrays. In the field, CCD-array (solid-state) instruments are preferable because they are faster, lighter, more compact, and more reliable than scanning (optomechanical) instruments. The latter are normally more accurate and are typically considered laboratory instruments for indoor measurements. Like broadband radiometers, field spectroradiometers can be deployed for unattended operation because their casing is weatherproof. They can be mounted on a sun tracker and equipped with an appropriate collimating tube to sense the direct normal spectrum. If mounted horizontally or on a tilt, they sense the global horizontal or global tilted spectrum, respectively. Examples of such mounting options are shown in Figure 5-2. This figure displays a group of three instruments because they cover different spectral bands: one has a silicon-based detector and covers the typical spectral range from approximately 350–1100 nm, another covers the UV (300–400 nm), and the last covers near-infrared in the range of 900–1700 nm. The combination makes it possible to sense the spectrum in an extended range—approximately 300–1700 nm—which might be necessary to investigate some advanced solar cells, for instance.

Figure 5-2. (Left) Three field spectroradiometers mounted on a solar tracker to sense the direct normal spectrum. (Right) The same three spectroradiometers mounted horizontally to sense the global horizontal spectrum.

Photos by NREL (left) and Christian Gueymard (right)

Figure 5-3 displays the direct normal spectra observed (at regular intervals) by a field spectroradiometer during a clear summer morning at NREL's Solar Radiation Research Laboratory in Golden, Colorado, at an elevation of 1829 m. When comparing spectra observed under contrasting sun positions (high sun versus low sun), the red shift mentioned earlier clearly appears. Two strong atmospheric absorption bands—caused by oxygen (near 760 nm) and water vapor (near 940 nm)—are also clearly visible.

Considering the significant costs associated with the deployment, calibration, and maintenance of spectroradiometers, only a few solar laboratories in the world can continuously operate such instruments for long periods. In most cases, the spectral databases collected are considered proprietary and can be difficult to obtain. A few exceptions exist, such as the public domain databases offered by NREL.[34]

[34] See https://midcdmz.nrel.gov/apps/spectra.pl?BMS.

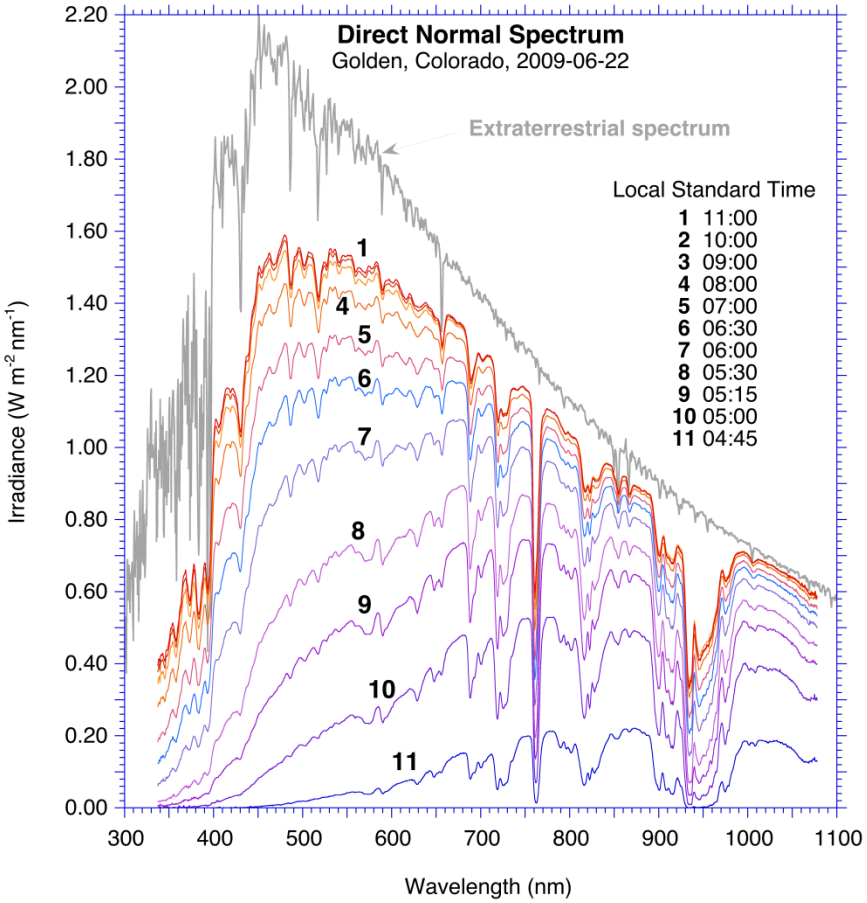

Figure 5-3. Series of DNI spectra measured during a clear summer morning by a field spectroradiometer mounted on a sun tracker at NREL. The extraterrestrial spectrum is also indicated to emphasize some important atmospheric absorption bands.

Image by C. Gueymard, based on NREL data

Because easily accessible measured data is rare, it is more convenient to depend on radiative models and obtain the solar spectrum at any location and any instant. One early spectral model used in solar engineering was SPECTRAL2 (Bird 1984). The Python library pvlib (Holmgren et al. 2018) has a subroutine that implements the SPECTRAL2 model. The SPECTRAL2 model's limited resolution, capabilities, and performance prompted the development of the Simple Model of the Atmospheric Radiative Transfer of Sunshine (SMARTS) model (Gueymard 2001; 1995), which has been thoroughly validated (Gueymard 2019b; 2008). It has been used to develop the current reference spectra mentioned in Chapter 2, Section 2.5.6. To operate a spectral radiation model such as SMARTS, precise information about atmospheric constituents such as AOD and PW is necessary, but this is essentially the same information as would be needed to obtain only broadband clear-sky irradiances with a simpler radiation model. The most accessible sources of data, particularly regarding aerosols, are discussed in detail by Gueymard (2019). Figure 5-4 compares the direct normal spectrum predicted by SMARTS for an airmass of ≈1.5 to measurements obtained with two collocated spectroradiometers at NREL's radiometric station in Golden, Colorado.

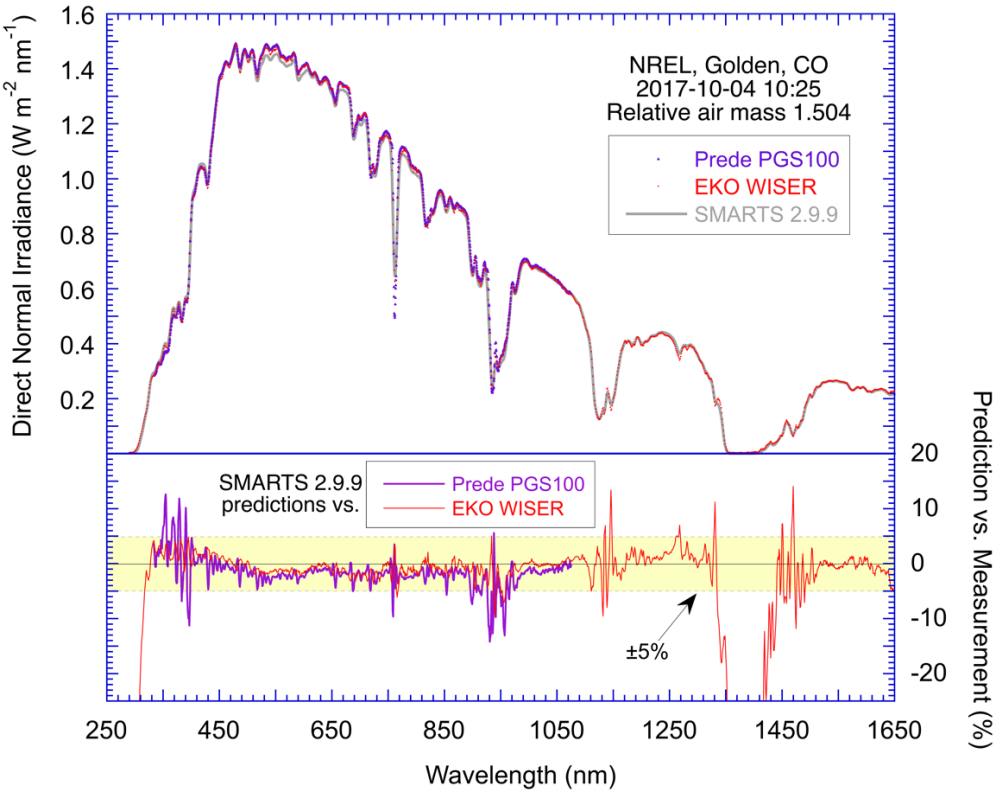

Figure 5-4. Direct normal spectrum at airmass ≈1.5 measured with two spectroradiometers at NREL's radiometric station in Golden compared with predictions from the SMARTS model (top panel). Percentage difference between the SMARTS predictions and the two separate measurement streams (bottom panel).

Image by C. Gueymard, based on NREL data

Many spectral radiation models, such as SMARTS, are limited to the prediction of clear-sky spectra. Modeling the spectral radiation under all-sky conditions is a challenge because of the need to balance the computational burden and errors attributed to the resolution of the spectral bands. As a result, high-spectral-resolution models designed to solve spectral radiation based on fundamental physics—such as the line-by-line model (Clough et al. 2005)—are often time-consuming in computing the absorption coefficients of the molecular species in the atmosphere. Adding to the complexity of the radiative transfer calculations is the cloud scattering involving highly complex interactions between clouds, the over- and underlying atmosphere, and land surface. An efficient solution—implemented in the TMYSPEC model (Myers 2012)—is to empirically develop regressions that link numerically between long-term observations of broadband and spectral solar radiation. More rigorous models based on the solution of the radiative transfer equation precompute cloud extinction, reflection, and emission for possible cloud conditions and incident and outgoing solar directions and then integrate the results with the clear-sky solution (Minnis et al. 2011). The computational efficiency of those models can be substantially improved when the precomputations are parameterized by plain functions of cloud optical and microphysical properties (Xie et al. 2016). On the other hand, the models can be extended to cover the computation of spectral irradiance—for example, the Fast All-sky Radiation Model for Solar applications with Narrowband Irradiances on Tilted surfaces (FARMS-NIT) (Xie et al. 2019; Xie and Sengupta 2018) precomputed a cloud lookup table using the 32-stream DIScrete Ordinates Radiative Transfer (DISORT) model (Stamnes et al.

1988) and the parameterization of cloud optical properties developed by Baum et al. (2011) and Hu and Stamnes (1993). The cloud bidirectional reflectance distribution function (BRDF) and bidirectional transmittance distribution function (BTDF) are stored in a lookup table containing data for 2002 wavelengths within the spectral range from 0.28–4.0 μm. Surface radiances in the spectral bands are analytically solved from the radiative transfer equation for five independent photon paths using the optical thickness of the clear-sky atmosphere provided by SMARTS and the cloud BRDF and BTDF.

Spectral data are typically required only for "high-end" solar energy applications. For thermal collectors using current technology, spectral information does not need to be collected for each individual project, and the application of standard spectra suffices. For large PV plants, however, the site-specific spectral effects should be considered to increase accuracy. This can be done best if spectral data are available. Because of the high costs of spectral measurements, the state of the art is to introduce the spectral effects via modeling approaches, such as applying satellite-derived spectra to calculate spectral mismatch factors or spectral derate factors for use in PV simulation models (Pelland and Gueymard 2022). This procedure is generally empirical and can be improved, so related research is required. Additionally, spectral irradiance data are useful in related solar technology developments, and they are also relevant as an intermediate product to understand specific effects, such as soiling, beam attenuation near the ground, or measurement error of various radiometers.

5.8 Ultraviolet Irradiance

Although UV constitutes only a small portion of the solar spectrum, the high energy of the photons contained at wavelengths less than 400 nm can cause degradation of materials, such as those used in the construction of PV modules. More generally, UV irradiance information can be useful in many research and development applications, such as PV and CSP material degradation, service life prediction, monitoring lamps in accelerated weathering chambers, aging tests in solar simulators, and climate-related research using predictions from appropriate models or actual data from weather stations; therefore, high-quality measured and modeled UV databases are often required for various locations with differing climatic conditions. Such data sources typically provide accurate inputs for these applications.

The UV spectral ranges of interest are defined in various standards and publications. ASTM G113-16 (ASTM G113 2022) defines UV irradiance for natural weathering applications as the amount of electromagnetic radiation greater than 295 nm and less than the visible electromagnetic radiation. According to ASTM G177 (ASTM G177 2020), the total UV is defined from 280–400 nm, and it is subdivided into UV-A (320–400 nm) and UV-B (280–320 nm). The World Health Organization (WHO 2016), however, defines these ranges slightly differently, using 315–400 nm for UV-A and 280–315 nm for UV-B. Other definitions can be found in the literature or in the specifications for UV radiometers. In weathering and durability studies, for instance, radiant UV doses are reported from 295–400 nm or 295–385 nm (Habte et al. 2019).

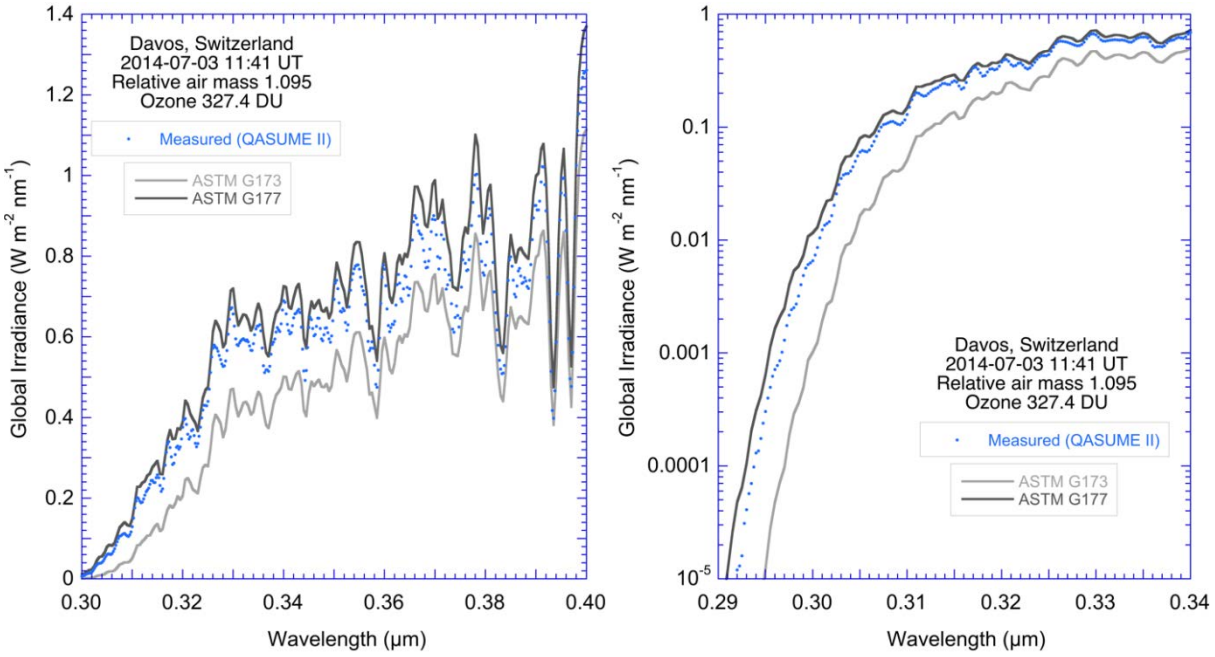

Figure 5-5. UV global spectrum measured with a QASUME II spectroradiometer at the PMOD/WRC laboratory (elevation 1589 m) under high-sun conditions compared with standards ASTM G173 (low UV) and G177 (high UV) in (left) linear scale and (right) logarithmic scale.

Image by C. Gueymard, based on PMOD-WRC data

The varying definitions that currently exist may introduce confusion, especially because the UV irradiance magnitude is highly dependent on wavelength. This is shown in Figure 5-5, where actual measurements of spectral global horizontal irradiance (GHI) conducted at the Physikalisch-Meteorologisches Observatorium Davos/World Radiation Center (PMOD/WRC) with a QASUME II spectroradiometer are compared with the reference global tilted irradiance spectra promulgated in standards ASTM G173 (for moderate air mass, AM1.5) and G177 (for low air mass, AM1.05). As shown, at less than approximately 0.33 μm, the irradiance magnitude varies considerably for only small incremental changes in wavelength, clearly indicating the need for an excellent wavelength calibration of UV radiometers. A consensus on the range of UV irradiances applicable for solar energy conversion technologies is desirable, but such a consensus has not yet been reached.

Some information disseminated by WHO about the UV irradiance distribution is valuable because of its relevance to solar energy applications. In particular, clean snow reflects up to ≈80% of UV, and more than ≈90% of UV irradiance can be transmitted through thin clouds. Further, WHO emphasizes the relationship between site elevation and UV irradiance, stating an increase of 4% in UV irradiance for a 300-m increase in altitude. Additionally, most of the daily UV dose is said to be received during a 4-hour period centered on local solar noon.

As stated in Hülsen and Gröbner (2007), spectroradiometers are the best instruments for measuring UV irradiance, but they are expensive and require high maintenance. High-end instruments, called double monochromators, are less sensitive to stray-light issues than simpler instruments based on CCD technology, and they are necessary to sense the UV accurately at less than ≈320 nm, but they are also extremely delicate and expensive; therefore, in most cases, only

broadband UV radiometers are used in applications that do not demand spectral information. All UV radiometers can be calibrated so that they are traceable to one of the existing National Metrological Institutes through a calibrated reference lamp. Further, some institutions, such as the World Meteorological Organization (WMO), help maintain traceability through a commonly accepted calibration methodology and through regular intercomparisons using standard reference spectroradiometers maintained and operated by the PMOD/WRC. In general, an annual calibration interval is recommended because UV radiometers are susceptible to atmospheric constituent changes, degradation and stability issues, and other uncertainties (Webb et al. 2006).

Many types of broadband UV radiometers exist, as described in Hülsen et al. (2020). There are also multiwavelength narrowband filter radiometers that measure solar irradiance at a few wavelengths in the UV spectrum, but they require an intricate absolute calibration process that involves model simulations (Kerr and Fioletov 2008).

Measuring UV is difficult because such measurements are prone to high measurement uncertainty, resulting from factors such as stray-light contamination, calibration error, or directional response deviation. On the other hand, measured and/or modeled GHI data of fairly low uncertainty is relatively abundant for many locations. Many studies have attempted to parameterize the global UV irradiance (UV-B and/or UV-A)—for example, by considering the empirical relationship between global UV irradiance and other readily available quantities, such as GHI (Fioletov et al. 1997; Habte et al. 2019; McArthur et al. 1999; Schwander 2002). A standard practice to estimate UV in two different bands from GHI has been recently promulgated in ASTM G222 (ASTM G222 2021). Some studies have used radiative transfer models (Evans 1998; Koepke 2009; Madronich and Flocke 1997; Mayer and Kylling 2005; Ricchiazzi and Gautier 1998), while others have used satellite instruments, such as the Ozone Monitoring Instrument (OMI), to estimate surface UV irradiance (Herman et al. 1999; Krotkov et al. 1998; Levelt et al. 2006; Peeters et al. 1998; Tanskanen et al. 2006).

5.9 Soiling

Soiling occurs when airborne particles, such as dust or pollutants, or nearly opaque obstructions, such as bird droppings or leaves, settle on and adhere to the surface of solar energy systems. The accumulation of particulate matter is the result of a multifactorial phenomenon that arises from the interplay of various elements and processes operating across different spatial and time scales. Soiling can greatly reduce the efficiency of solar collectors (Shaik et al. 2023). In the case of PV systems or non-concentrating thermal collectors, this is caused by the reduction of light transmitted through the collector's front glass cover. For concentrating collectors, soiling may reduce both the specular reflectance of the mirrors and the transmittance of receiver envelope tubes or transparent covers. On the other hand, beyond its effect on energy production, soiling is one of the most relevant factors for reducing the performance of radiometers. For any solar radiation measurement station, an appropriate sensor cleaning schedule is of utmost importance for obtaining reliable data (see Chapter 3, Section 3.6.2).

The action of various atmospheric agents, like temperature, wind, or relative humidity, modulates the sequence of soiling depending on the physical and chemical properties of the different particle species present, such as their size distribution, density, or composition (Bergin et al. 2017; Ilse et al. 2018; Micheli et al. 2019; Micheli and Muller 2017). However, as part of the complexity of this phenomenon, not all variables involved always act the same way. An

important example is that of precipitation, which can cause either the deposition of airborne particles (a process known as wet deposition) or their removal. Nonetheless, it should be noted that the literature in this field has not been able to propose a clear threshold of daily rain accumulation above which the natural cleaning process caused by rainfall takes place (Pelland et al. 2018). Thus, soiling has a global dimension, with a heterogeneous distribution in space and time and, in general, it depends on local ambient conditions, time of year, and characteristics of each solar system. Given the complexity of the soiling process and its effects on energy production, it is difficult to model, and it is difficult even to measure its effects accurately. Therefore, the potential losses caused by soiling are one of the most intricate sources of uncertainty to estimate in solar projects (Muller and Rashed 2023). Nonetheless, the economic losses caused by this issue worldwide are estimated at several billion dollars per year (Ilse et al. 2019). Therefore, it is essential for the solar industry to better understand the soiling process and its impacts on solar systems because it is unavoidable. Moreover, soiling produces significant direct losses and contributes to the degradation of solar components. Soiling effects can be mitigated by different methods, generally classified into preventive and corrective measures (Schill et al. 2022). The costs of soiling mitigation being substantial, mitigation measures must be designed appropriately for each individual case to achieve an optimum cost-benefit ratio. Reviews of actual soiling effects on solar power plants can be found in (Ilse et al. 2019; Maghami et al. 2016; Sarver et al. 2013). For PV technology most particularly, the comprehensive review in the IEA PVPS Task 13 report of (Schill et al. 2022) is recommended.

Usually, soiling is quantified in terms of what is commonly known as the soiling ratio (SR), or "cleanliness." The soiling ratio is defined as the ratio of the solar plant's output power under soiling conditions to the power under clean condition generated by the same component under identical operation conditions (Schill et al. 2022). The soiling loss (SL) is simply the complement of the soiling ratio, SL = 1–SR. The soiling ratio is 1 when the component is completely clean (SL = 0) and 0 when solar energy cannot reach the receiver because of extreme soiling (SL = 1). Figure 5-6 displays a time series of daily averages of observed soiling ratios evaluated at a PV plant over 2 years, along with the rain events and their daily accumulation. Another widely used quantity is the soiling rate, which describes the rate of change of cleanliness over time. In the case of flat-plate panels, soiling rates are approximately 10 times less than in the case of reflectors of concentrating systems for the same conditions, because the forward-scattered light still contributes to the PV or flat-plate collector yield (Bellmann et al. 2020), while largely missing the receiver in a concentrating system.

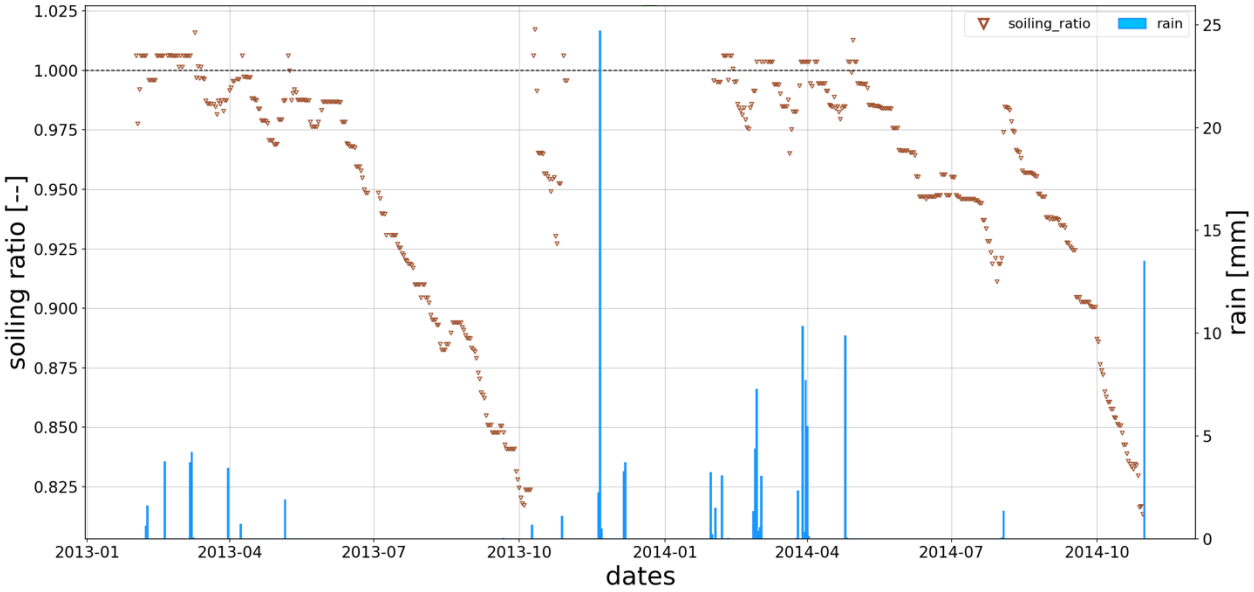

Figure 5-6. Average daily soiling ratio and daily accumulated precipitation observed at a PV plant, 2013–2014

Image by SolarGIS

The cleanliness can be measured using different techniques. For PV, two methods, both based on the use of a pair of clean and soiled PV devices (constituted of identical reference modules or PV cells), are defined in detail in IEC 61724-1, Annex C. As described there, a method for monitoring soiling losses at low equipment cost consists of measuring the short-circuit current of the reference soiled PV device and comparing it to that of its clean counterpart. The soiling ratio can then be estimated, assuming that the power output is proportional to the short-circuit current, which is appropriate for low soiling inhomogeneity over the module's surface (Dunn et al. 2013). Care should be taken when making soiling measurements using reference cells because soiling is often not uniform, particularly near the edges of the reference device. Because reference cells have a proportionally larger edge-to-area ratio than a PV module, the soiling ratio might then not be accurate. A measurement using the short-circuit current of a pair of PV modules can be inaccurate if the module's surface is not homogeneously soiled (Gostein et al. 2015). In such cases of heterogeneous soiling (e.g., along the edges or sides of the modules), the use of the short-circuit current method might underestimate the actual impact of soiling on the actual power output. In that configuration, either the current-voltage curves of both a clean and a soiled module must be analyzed for an accurate estimation of the soiling ratio, or the power outputs from both modules obtained with maximum power point trackers must be compared. Care must be taken if only a single module or cell is used for the estimation of the cleanliness by comparing its performance before and after cleaning, because the external conditions might have changed in the meantime. Moreover, the module or cell temperature can be affected by the cleaning process itself.

A practical recommendation for short-circuit-based measurements is to avoid the soiled module accumulating too much soiling, as this will more likely lead to an inhomogeneous soiling distribution, with increased soiling near the bottom. Moreover, because of the changed surface properties (roughness, humidity, etc.), too-high soiling losses might also lead to other unwanted effects, such as saturation or different particle adhesion properties.

Proper installation and maintenance of any soiling measurement system are critical for preventing a too-low signal-to-noise ratio in the measurement of soiling ratios and rates. In particular, the regular cleaning of the clean reference glass sheet or reference module/cell is of great importance. Automatic cleaning of the reference device is complex, whereas manual cleaning is time-consuming. Soiling ratio calculations should be performed immediately after the clean module is cleaned (Peterson et al. 2022). Several days after the clean module is cleaned, its cleanliness should be already called into question, because during that time several days' worth of soiling has been accumulated. In field measurements, a perfectly clean state is often unattainable because of practical limitations (lack of clean water, inappropriate/unclean wiping material, inappropriate detergents, unfavorable weather conditions during cleaning, etc.), and thus residual soiling of the clean reference device might remain even after cleaning. This can largely be overcome by determining a calibration value for the clean device immediately after each cleaning, which is then used only until the next cleaning event.

When installing a soiling measurement system based on a dual reference device (clean vs. soiled), extreme care must be taken to ensure that its two components are in the same plane. Non-coplanar devices receive different amounts of light at any given time. This modifies the comparison of the two devices and masks the desired effects of soiling. Upon installation, it is also advised to observe the soiling ratio over the course of a clear day to ensure that the soiling ratio does not change, at least for incidence angles below ≈50°. If well-designed and implemented, soiling measurements with the clean-and-soiled-device method can reach a low measurement uncertainty of ≈1% or better (Dunn et al. 2013; Peterson et al. 2022).

A shortcoming of the soiling measurement system described above is the need for frequent cleaning of the reference PV device. Soiling sensors with PV device pairs and automatic cleaning systems for the clean PV device are offered commercially, but their reliability has not been fully proven, and any imperfect cleaning can strongly affect their accuracy. Therefore, sensors requiring less maintenance without such automatic cleaning systems have been developed. One such method that can be applied to either PV or CSP uses a photodiode behind a glass sheet and a detector that senses the scattered radiation; see, for example, (Korevaar et al. 2017) for PV systems. Soiling on the glass sheet increases the detector signal that can be converted into a transmittance or reflectance reduction. Another optical approach is based on taking images of particles on a glass sample with reference marks from within an enclosure (Gostein et al. 2018). If the sun is used as the light source, soiling attenuates the incoming radiation, and the reduction of the image brightness by each particle can be translated into a soiling loss. To further increase accuracy, this system also uses LEDs placed next to the camera that illuminate the dust particles at night. The images' brightness increases due to dust particles on the glass surface and is used to correct the soiling loss measured, using the sun as a light source. Nevertheless, these two indirect measurement methods of soiling loss have shown lower accuracy compared to well-maintained soiling sensors with pairs of PV devices (Morley et al. 2020). Other methods are currently under development—for example, using a lamp that periodically illuminates a PV reference cell (Campos et al. 2022; Muller et al. 2021). The lamps are protected against soiling so that the change of the lamp-induced reference cell signal can be used to determine the PV soiling.

For CSP mirrors, one option to measure the soiling loss is to use handheld reflectometers and regularly measure the reflectance of working mirrors or sample mirrors. Transmissometers can

be used to monitor soiling effects on CSP entrance windows. These measurements are time-consuming and expensive; therefore, automatic methods have been developed for reflectance (Heimsath et al. 2019; Wolfertstetter et al. 2014) and transmittance (Wolfertstetter et al. 2020b), respectively.

Further, methods based on the analysis of digital pictures of soiled collectors are under development. These may potentially be applied to surveillance cameras overseeing large parts of a solar field or to airborne observations with unmanned air vehicles (Winkel et al. 2022; Wolfertstetter et al. 2020a). Other image-based methods use highly resolved microscopic images and detect individual particles on the surface, but such methods are subject to significant uncertainty, that is, caused by variable results depending on image analysis software or the specific methodology employed by various operators (Smestad et al. 2023).

Figure 5-7. Several cleanliness measurement options for PV and CSP

Photo by DLR

Some of the aforementioned measurement options are shown in Figure 5-7. For fixed-tilt and tracked reference cells, the orientation of the soiling sensors is crucial and should be as close as possible to that of the plant itself. Further, the test material must be similar—or ideally identical—to that in the power plant; therefore, the photo shows two different types of reference cells.

Effects related to the incidence angle, for example, can cause the soiling rate to change strongly throughout the day. Even if the component is not cleaned, positive soiling rates (increase of

cleanliness) occur, at least momentarily, if the time resolution is too high; therefore, soiling rates are reported most frequently at a daily resolution. To properly determine the soiling rate, it is important to compare data points collected under similar conditions. For instance, the cleanliness measured at noon under clear-sky conditions should not be compared to that of the next days if measured under cloudy conditions or at a different sun elevation. Soiling rate analysis techniques are discussed in Peterson et al. (2022).

Several systems are commercially available for the measurement of cleanliness and soiling rate. Soiling measurements are recommended during the site selection process, especially if no soiling data are available from nearby sites, and continue to be desirable during plant operation. Depending on the soiling levels at a PV plant and the peak power of a PV plant, for instance, IEC 61724-1 defines a certain number of required soiling measurements.

Soiling rate results are not widely available in the public domain, and only a few datasets are available from data portals.[35]

Modeling the soiling phenomenon is a potential way to greatly reduce the costs associated with measuring soiling data. One approach analyzes the solar power production data to derive the soiling losses; see, for example, Brenner et al. (2023) and Micheli et al. (2022). A challenge for these approaches is to separate the soiling effect from other losses and from the yield modeling uncertainty. The other soiling modeling approach is based on meteorological data and allows the user to rapidly provide both long-term historical and forecasting datasets at any site. Soiling models are mainly based on particle concentration and precipitation, though other meteorological data are also required in general. Existing models (Coello and Boyle 2019; Kimber et al. 2006; Micheli and Muller 2017; Picotti et al. 2018; Wolfertstetter et al. 2019) are currently further enhanced and adapted to create soiling maps and soiling forecasts based on atmospheric dust transportation models (Micheli et al. 2019). Schill et al. (2022) presents an exhaustive review of different existing soiling models for PV applications. The models are classified into four categories, namely: linear regression models, semi-physical models, artificial intelligence models, and geospatial models. Some of those models have been also evaluated in independent research works (Bessa et al. 2022; Polo et al. 2021). In general, the performance of the different models differs significantly. In fact, many are adjusted according to the particular conditions of a specific location. Further, only few evaluation studies have a global coverage, as well as very few comparative studies between models and sites (Pelland et al. 2018). A fundamental reason for the lack of this type of study is the notable scarcity of publicly available measurements that can be used as reference.

All of this contributes to the difficulty in estimating the soiling model's uncertainty, which is challenging to isolate from the other sources of uncertainty that are attached to the cleaning events, the observational data, and the input data (For instance, the latter are usually associated with huge spatial and temporal averages compared to the scales of the soiling phenomenon.) This makes the estimation of soiling losses one of the most difficult sources of uncertainty to consider in solar projects. As such, there is room for improvement in this field of knowledge. However,

[35] See https://www.nrel.gov/pv/soiling.html or https://energydata.info/ (which includes recent stations in West Africa, e.g., https://energydata.info/dataset/benin-solar-radiation-measurement-data).

modeled soiling data can be obtained from various groups, including several companies that offer data commercially.

5.10 Circumsolar Radiation

As discussed in Chapter 2, Section 2.5.2, circumsolar radiation is the scattered radiation received from the angular region close to the sun. Most of the circumsolar radiation is included in DNI measurements from pyrheliometers with a 5º field of view, but typically only a smaller part of the measurement can be used by focusing collectors; therefore, information on circumsolar radiation is important for CSP plant yield assessments and the design of any type of concentrating power plant. High circumsolar radiation contributions to DNI can reduce the efficiency by 10% or more compared to the efficiency for low circumsolar radiation contributions, even for DNIs greater than 200 W/m². Using typical estimates of the average circumsolar radiation conditions can lead to errors of several percentage points in the long-term plant yield (e.g., approximately 2% for an exemplary tower plant in the United Arab Emirates [Wilbert 2014]).

Different techniques are available to measure circumsolar radiation. For instance, a method based on two commercial instruments: a camera-based "sun and aureole measurement system" and a sun photometer (Gueymard 2010; Wilbert et al. 2013). Another camera-based method is also used in Schrott et al. (2014). A different system uses two pyrheliometers with contrasting acceptance angles (Wilbert et al. 2013). Alternatively, and much more simply, circumsolar radiation can be measured with unmodified rotating shadowband irradiometers (RSIs) by analyzing the irradiance signal collected during the rotation of the shadowband (Wilbert et al. 2018).

Only camera-based systems can measure the sunshape. This quantity (not to be confused with the shape of the sun disk itself) is defined as the normalized radially averaged radiance profile as a function of the angular distance from the apparent sun center. The other radiometric systems can derive the circumsolar contribution to DNI, which can in turn be used to estimate the sunshape. Because of the high costs, maintenance and calibration constraints, and analysis difficulties, so far, the existing camera-based systems have been limited to high-end scientific studies. In contrast, RSI- and pyrheliometer-based methods are already commercially available.

Circumsolar radiation measurements are available for several sites (Bendt and Rabl 1980; Noring et al. 1991; Wilbert 2014; Wilbert and Guillot 2013). For nearby plant projects, or for projects in a similar climate, such measurements might be sufficient for plant yield calculations. For other regions and climates, measurement campaigns are recommended for site assessment, CSP technology selection, acceptance testing, or optimization of plant operation.

An alternative to costly in situ measurements is modeling, though obtaining long-term information on circumsolar radiation to help the development of a power plant project at an early stage might require substantial modeling effort. Reinhardt et al. (2014) presented a model for the influence of thin ice clouds (cirrus), which considerably increase the circumsolar contribution. The effect of aerosols can also be modeled (Eissa et al. 2018). More recent work using specialized radiative models to evaluate the difference between the true and apparent DNI can be found in Räisänen and Lindfors (2019), Sun et al. (2020), and Xie et al. (2020). Abreu et al. (2023) also recently presented a model to evaluate the circumsolar contribution for various view

angles and its effect on CSP systems. In any case, so far, modeled circumsolar data are not routinely available for site assessment, which means that each developer must use one of these models and obtain the appropriate input data, which can be cumbersome. More research is necessary before the circumsolar contribution can be easily determined by analysts at any location and any instant in solar resource assessments.

5.11 Beam Attenuation Between Heliostats and Receivers in Tower Power Plants

Among all CSP technologies, tower power plants present a specific challenge because atmospheric constituents tend to attenuate the radiation beams along their path from the heliostats to the solar receiver on the tower. This attenuation might significantly impact the efficiency of this technology (Figure 5-8). During clear days, the optical losses over a 1-km slant range can be less than approximately 5%. Under hazy, humid conditions, however, more than 50% can be lost; thus, attenuation data must be available for the plant design, plant yield analysis, and plant operation. Under extreme conditions, high extinction levels could prevent towers from being an economically feasible technology option.

Figure 5-8. (Left) CIEMAT's CESA 1 solar tower on a clear day and (right) on a hazy day

Photos by DLR

Beam attenuation along a slant path can be evaluated with scatterometers or transmissiometers (Hanrieder et al. 2015). Camera-based methods also exist (Ballestrín et al. 2018), and at least three such options are commercially available. Hanrieder et al. (2020; 2016) and Sengupta and Wagner (2012) presented models to derive the attenuation based on only conventional DNI measurements. Polo et al. (2017; 2016) estimated the attenuation based on aerosol data. Mishra et al. (2020) assessed the sensitivity of three existing attenuation models for different atmospheric conditions and evaluated the feasibility of using satellite data as additional inputs. The methodology of retrieving atmospheric extinction based on aerosol information has been recently extended to the estimation of world extinction maps (Salmon et al. 2022). A main difficulty for modeling and measuring extinction resides in the estimation of the vertical profile of the aerosol concentration.

Hanrieder et al. (2017) presented an overview of measurement, modeling methods, and the effect of attenuation on CSP plants. A sensitivity analysis of the potential impact of the extinction in CSP tower plants production has been modeled with SAM for different climatic and boundary conditions (Polo et al. 2017; 2016).

For prefeasibility and feasibility studies, the existing attenuation models should be applied to obtain a first estimate of the extinction levels at the site(s) of interest. The extinction varies over time, depending on aerosol and humidity conditions; thus, the frequency of situations of high turbidity and/or high humidity becomes a relevant factor. Under clear conditions, the existing models can provide sufficient accuracy. Under hazy conditions with insufficient local atmospheric data on aerosols or humidity, the uncertainties can be quite high. In that case, measurements are recommended for reasonable plant yield estimates. For acceptance tests and plant operation, particularly at sites that are frequently impacted by hazy conditions, measurements are recommended.

5.12 Surface Albedo

The surface albedo is a measure of the relative amount of incident energy that is reflected upward by the surface (i.e., the ratio of the reflected irradiance to the total incident irradiance). Properly characterizing the surface albedo is especially important in applications that benefit from surface reflections, most importantly when collectors are mounted vertically or when using bifacial PV panels. The latter are precisely designed to exploit the irradiance that reaches their rear side—mostly in the form of ground reflection. Albedo has been defined in Chapter 2, Section 2.5.5.1, and its measurements have been discussed in Chapter 3, Section 3.3.2.

In addition to ground-based measurements, albedo information is also generated using either satellite data or reanalysis models, as discussed in a review of available albedo datasets (Gueymard et al. 2019). Among satellite sources, MODIS has received considerable attention; its albedo products (which include spectral and directional information) are used extensively in a variety of disciplines. One difficulty for the future is that the two MODIS instruments have now reached their end of life, with no immediate replacement.

In reanalysis models, albedo is obtained as a spatiotemporal quantity using NWP methodologies that combine various sources of meteorological information, such as satellite observations, surface measurements, and radiative transfer models. Satellite and reanalysis albedo data are of great interest because of their spatial and temporal continuity, long-period historical data, and global reach. However, they have a low spatial resolution (several hundred meters to tens of km), which can be problematic particularly for such a spatially variable quantity (Gueymard et al. 2021). For this reason, they may not only deviate significantly from the average value but also describe an erroneous spatiotemporal distribution. Figure 5-9 shows an example of the strong underestimation of the albedo estimated by the MERRA-2 reanalysis for a ground station in Denmark close to a fjord. The MERRA-2 estimate is less than half the ground measurement. This is a consequence of the coarse resolution of the MERRA-2 grid (≈50 km by 60 km), which largely affects the albedo for the station's pixel because of the low albedo of sea water. According to Lara-Fanego et al. (2022b), a 10% error in ground albedo can result in deviations of up to 2.5% in the estimated annual energy production of a generic bifacial PV plant.

A small set of eight sources of gridded global albedo data (Table 5-1), seven of which are publicly available, was compared to 29 ground stations in Lara-Fanego et al. (2022a). In this comparison, the worst results were found in winter, because snow might not accumulate evenly over the surface area. The comparison showed that sources with a coarser resolution, like ERA5 or MERRA-2, are typically less accurate. A notable exception to this finding was the Satellite

Application Facility on Climate Monitoring (CMSAF) database, which has a 25-km resolution. Remarkably, MODIS-based observations reached the lowest deviations in the comparison.

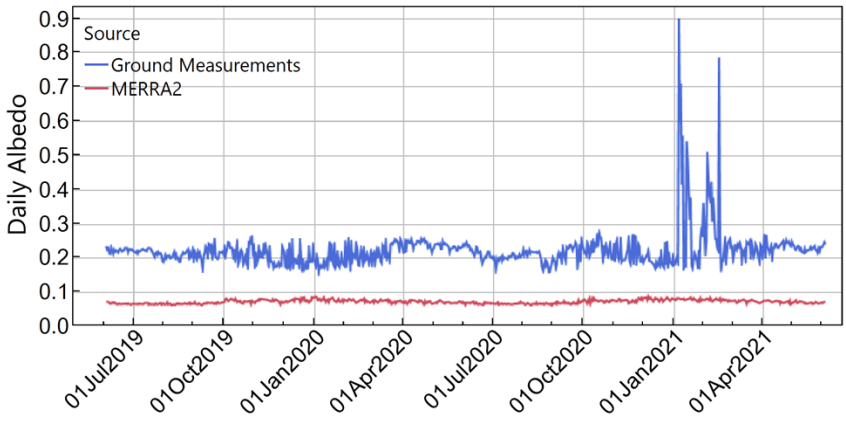

Figure 5-9. Time series of measured albedo at a ground station in Denmark modeled with MERRA-2. The latter's pixel that includes the station also includes a large fraction of sea water, which explains the low and roughly constant albedo.

Image by SolarGIS

Table 5-1. Selected Albedo Datasets Evaluated in Lara-Fanego et al. (2022a)

All datasets are in the public domain except SGClim, commercially available from Solargis.

Dataset Name	Source	Time Resolution	Spatial Resolution [km]
CMSAF	Satellite, CLARA-A2-SAL	5 d	25
GLASS	Satellite, AVHRR	8 d	5.6
MCD43A3	Satellite, MODIS	1 d	5.6
Mines ParisTech	Satellite, MODIS	Monthly mean (2004–2011)	≈5.6
NSRDB	Satellite, MODIS	1 d	4
SGClim	Satellite, MODIS, and Solargis method	Monthly mean (2006–2015)	1
ERA5	ECMWF, reanalysis	1 h	≈30
MERRA2	NASA, reanalysis	1 h	≈55

5.13 Other Parameters Relevant for Agrivoltaics

The increasing competition for land resulting from population growth and associated rising demands for food and energy is one main barrier for large-scale PV development, because of PV's large land requirements. Agrivoltaic systems integrate crop production and PV power generation, and thus offer a potential solution to the land-saving problem. For this technology, the resource assessments must address the additional radiation parameters required for the crops and the effects of PV shading on crop production. A shading analysis is necessary to establish a correlation between growth indicators, crop quality, and PV system characteristics (e.g., the PV cover ratio). Important factors related to crop growth are the altered microclimate parameters and

the installation's impacts on irrigation, water conservation, and economic viability. In agriculture, various meteorological metrics are used to optimize the operation of agricultural crops and equipment. Compared to other PV systems, the importance of some of the previously described parameters is enhanced in the case of agrivoltaics.

What follows is a presentation of the different variables specific to agrivoltaics and specific measurands. Measurement guidelines for these quantities, including meteorological station classes and instrumentation, are summarized in the *Guide to Agricultural Meteorological Practices* (WMO 2012). Remote sensing and geographic information system (GIS) applications for agrometeorology, as well as forecasting requirements, are included in the guidelines.

Temperature strongly affects the crop growth rate depending on plant type and development stage (Moragues and McMaster 2012). Usually, a minimum, maximum, and optimum temperature for each crop type is known. Between the minimum and optimum temperatures, the specific crop increases its growth rate. In contrast, temperatures higher than the optimum lower the plant growth rate, whereas at temperatures above the maximum, no crop growth is possible. The optimum temperature is usually higher during the vegetative development than during the reproductive period of the crop (Hatfield et al. 2011). In some agrivoltaic experiments, a lower mean air temperature was observed below the PV modules because of the additional shade compared to reference conditions without PV modules. On the other hand, the temperature also strongly depends on the height of the mounted modules and the corresponding airflow below the modules and ultimately the resulting prevented convection. Therefore, in the case of low-mounted modules and low wind speeds, the average air temperature as well as humidity below the PV modules might increase. In general, however, air temperature around agrivoltaic installations is significantly lower than with stand-alone PV systems because of the presence of crops (Mamun et al. 2022).

Relative humidity affects the evaporation and transpiration of the crops and thus has an impact on growth and water requirements. For instance, dry conditions imply an increase in crop transpiration, so that the cell growth might slow down if dry conditions persist. If plant transpiration increases, a potential mineral deficiency of the crops results from decreased nutrient transport (Nederhoff 2009). Relative humidity also influences the health of the crops: a high relative humidity induces a decrease in transpiration and increases the risk for fungal diseases (Cadenas Tortosa et al. 2003).

Wind speed, wind direction, and wind loads play an important role in agrivoltaic installations. Larger agrivoltaic systems can change the wind speed profile. In several studies, plant growth under PV panels was significantly impacted by wind speed, regardless of the height of the ground clearance. On the other hand, crop growth under PV systems can cause differences in wind direction. Wind speed also affects plant evaporation and can increase water demand. In addition, strong winds can cause damage to plants (Mamun et al. 2022) .

Agricultural maintenance work can negatively impact the PV power output, increasing the soiling of the PV surface and decreasing the transmittance of the top glass cover (Ketzer et al. 2020; Sekiyama and Nagashima 2019). On the other hand, vegetation below solar collectors might also decrease dust deposition in comparison to a bare soil surface.

The amount and distribution of precipitation has a major impact on plant growth and yields, so that its distribution over time and area is usually measured. Especially for agrivoltaic systems, rainwater harvesting with electricity production might enable a self-watering and self-powering approach (Santra et al. 2020). The angle of incidence of rainfall is also a key factor (Elamri et al. 2018; Elamri et al. 2018; Weselek et al. 2019). Overflow during heavy rainfall can lead to soil erosion and the formation of gullies. This problem occurs mainly in the early development phase, when the soil is not covered, or is barely covered, by vegetation. In addition, the type of precipitation is a crucial factor for agrivoltaic systems. For example, hail events can damage not only the PV system but also the corresponding crop, although the crop can be protected from hail by the overarching modules.

Figure 5-10. Various instruments for agrivoltaic applications. Foreground, from left to right: PAR spectrometer, pyranometer, six UV and PAR sensors. Background: wind mast with pyranometer, relative humidity and wind sensors.

Photo by DLR

To characterize the solar resource, the common GHI is used not only for PV modeling but also for analyzing plant growth and yield, and thus needs to be measured or estimated. However, for photosynthesis and optimal crop growth, solar irradiance in the wavelength 400–700-nm range—the photosynthetically active radiation (PAR)—is most relevant. This spectral range can be absorbed mainly by plant pigments chlorophyll a and b and carotenoids (La Notte et al. 2020). Specific PAR radiometers, also called quantum sensors, are available for these measurements. They are typically photodiode-based sensors with flat quantum response in the PAR wavelength interval. Moreover, PAR spectroradiometers are available for wavelength resolved radiation measurements in the PAR range, mostly for research purposes (Figure 5-10).

The photosynthetic photon flux density (PPFD) indicates the number of active photons per second incident on a unit surface in the PAR range and is expressed in µmol/(m^2·s). This quantum PAR quantity should not be confused with the radiometric PAR, which is the solar irradiance limited to 400–700 nm, expressed in W/m^2. The conversion between the quantum and radiometric PAR units depends on atmospheric conditions and thus relies on experimental data.

For the global PAR, Dye (2004) obtained a conversion factor varying between 4.23 and 4.68 µmol/J, with a mean value of 4.56 µmol/J, which is close to the conventional fixed value of 4.57 µmol/J obtained originally by McCree (1972). In parallel, calculations with the SMARTS model (which can estimate both spectral PPFD and radiometric PAR under cloudless skies) show that this unit conversion is also a function of SZA, and peaks for SZA around 70–80°, depending on atmospheric conditions. For the diffuse PAR, a fixed conversion factor of 4.24 µmol/J was proposed by McCree (1972). Experimental all-sky results (Dye 2004), as well as SMARTS clear-sky simulations, indicate that the conversion factor for diffuse radiation is actually much more variable than for global radiation.

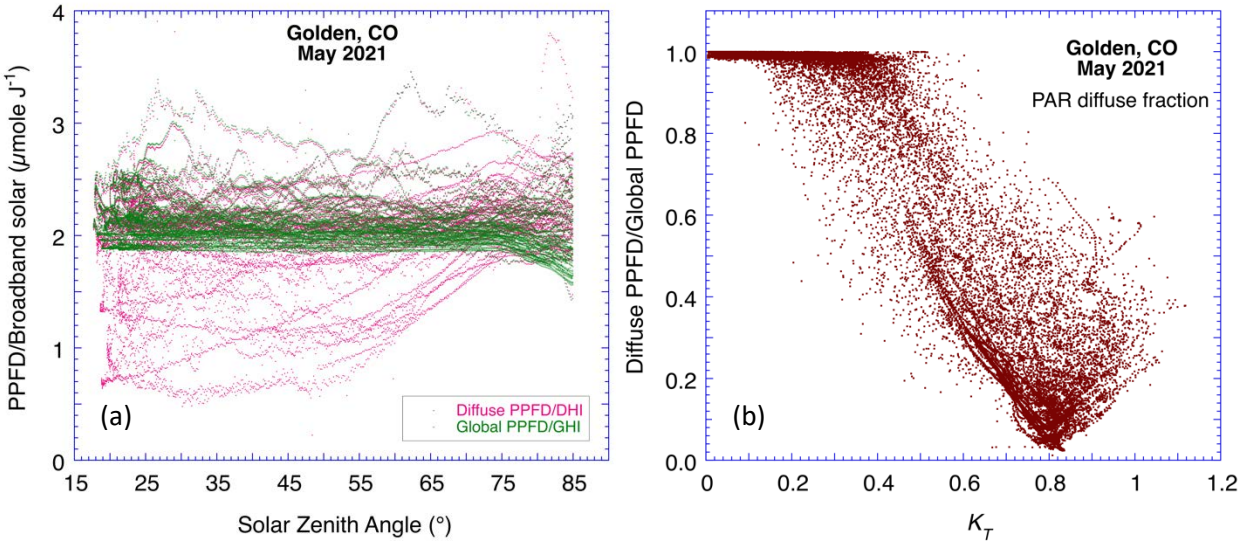

Figure 5-11. (a) Ratios of PPFD (diffuse and global) normalized by their broadband counterparts (DHI and GHI, respectively) as a function of SZA, as measured during 1 month at the NREL station in Golden, Colorado. (b) PPFD diffuse ratio as a function of clearness index based on the same 1-minute data.

Image by C. Gueymard, based on NREL data

As PAR measurement stations are scarce, quantum or radiometric global PAR data are usually derived from GHI measurements or from satellite observations. This is generally achieved using empirical models (see a review in [Gardea et al. 2021]), typically assuming a linear relationship between GHI and PAR. Based on one month of measured 1-min data obtained at NREL's Solar Radiation Research Laboratory in Golden, Colorado (latitude: 39.742°N, longitude: 105.18°W, elevation: 1829 m), Figure 5-11a indeed shows that the ratio between global PPFD and GHI is relatively constant, with most values around 2 µmol/J. For the diffuse PPFD, however, its ratio with DHI is much more variable, depending on SZA and atmospheric conditions, making its prediction much more difficult. Figure 5-11b, however, shows that the PPFD diffuse fraction has a relationship with the clearness index, K_t, that closely resembles that of the broadband diffuse fraction, DHI/GHI, as discussed further in Chapter 7, Section 7.3.1. Therefore, the separation models mentioned there should provide reasonable estimates of the diffuse PPFD from its global counterpart.

Many plants have a strong preference for diffuse light because it can reach its lower parts much more effectively than direct light. Hence, a quantification of the natural diffuse PAR fraction is

of importance. A serious difficulty is that measurements of the PAR components (diffuse or direct) are extremely rare. Thus, the empirical method just mentioned above is currently the best way to obtain estimates of the diffuse PPFD.

To improve the light distribution under the PV system at plant level, agrivoltaic systems might include PV modules that are distributed in a checkerboard pattern (Figure 5-12) or special PV modules with transparent spaces between the cells. Raytracing simulations are considered the best way to evaluate the global and diffuse PPFD at various plant levels for complex designs (Vindel et al. 2018). Recently, however, new computer graphics techniques have been developed to obtain visual and quantitative results in a fraction of the considerable computer time required by raytracing (El Boujdaini et al. 2023).

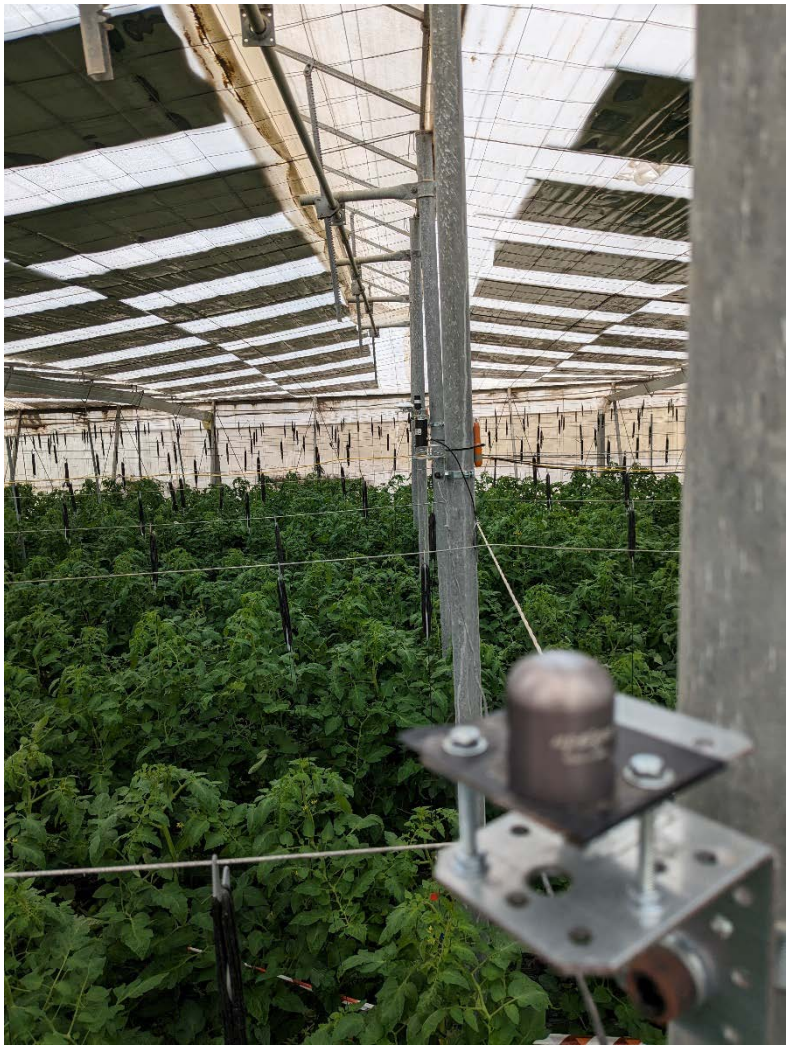

Figure 5-12. Example of agrivoltaic experiment in a greenhouse of Fundación UAL-Anecoop in Spain

Photo by DLR

The daily light integral (DLI) is the PAR irradiation integrated over a day, expressed in mol/(m^2·day). Plants can be roughly divided into high-light, medium-light, and low-light demanding crops. Different thresholds for the corresponding optimal and sufficient DLI levels

for each plant species can be found in the literature; see, for example, Cossu et al. (2020). Light quality for optimal plant growth refers to quantities affecting the photoreceptors that control photomorphogenesis. Whereas the blue and red parts of the solar spectrum are mainly used for photosynthesis (because the chlorophyll can absorb the most radiation in that spectral range), the green part of the spectrum penetrates further into the leaves and canopy, because chlorophyll absorbs less in the green area. Light quality for plant growth is therefore usually indicated by the red/far-red ratio (R/FR, also R:FR) and/or the blue/far-red ratio. Very low R/FR ratios can cause the "shade avoidance syndrome," in which plants try to compensate by stem elongation (Franklin 2008; Xu et al. 2021). R/FR ratios are of interest but are not required for all agrivoltaic projects. These ratios can be measured with spectroradiometers.

Potential evapotranspiration is defined as the amount of water that evaporates from the soil-air interface and from plants when the soil is at field capacity. Actual evapotranspiration is defined as the evaporation at the soil-air interface, plus the transpiration of plants, under the existing conditions of soil moisture. Measurement and modeling (Almorox et al. 2015) of evaporation from the soil, and of transpiration from vegetation, remains of great importance in agricultural meteorology and therefore also in agrivoltaics (WMO 2012).

The daily average soil temperature beneath PV systems has been found to decrease significantly following their installation, as compared with full-sun exposure (Marrou et al. 2013). The dynamic radiation heat transfer process affects the evaporation rate of the soil and thus the soil temperature (Roy and Ghosh 2017). Soil moisture affects root growth and plant water requirements; consequently, a change in soil moisture resulting from agrivoltaic installation has been detected (Mamun et al. 2022). A drastic soil moisture increase can result from the rain runoff from the PV panels, causing uneven water circulation at the lower panel edge compared to the sheltered area (Elamri et al. 2018). This does not occur in the case of vertical panels, however.

Different soil nutrients are crucial for plant growth. The right level of phosphorus, iron, calcium, or even nitrate (nitrogen) in the soil is essential for good soil quality.

In controlled agrivoltaic systems like greenhouses, the carbon dioxide (CO_2) concentration is a relevant factor for optimizing crop growth (Sánchez-Guerrero et al. 2005) because the photosynthetic activity is a direct function (Valera et al. 2016). Moreover, the CO_2 concentration usually drops with time, which can be avoided by CO_2 enrichment (Valera et al. 2016). Therefore, such measurements might be of interest.

References

Abreu, E.F.M., P. Canhoto, and M.J. Costa. 2023. "Prediction of Circumsolar Irradiance and Its Impact on CSP Systems under Clear Skies." *Energies* 16: 7950. https://doi.org/10.3390/en16247950.

Alduchov, O.A., and R.E. Eskridge. 1996. "Improved Magnus Form Approximation of Saturation Vapor Pressure." *J. Appl. Meteorol.* 35: 601–609. https://doi.org/10.1175/1520-0450(1996)035<0601:IMFAOS>2.0.CO;2.

Almorox, J., V.H. Quej, and P. Martí. 2015. "Global performance ranking of temperature-based approaches for evapotranspiration estimation considering Köppen climate classes." *J. Hydrol.* 528: 514–522. https://doi.org/10.1016/j.jhydrol.2015.06.057.

Andenæs, E., B.P. Jelle, K. Ramlo, T. Kolås, J. Selj, and S.E. Foss. 2018. "The influence of snow and ice coverage on the energy generation from photovoltaic solar cells." *Sol. Energy* 159: 318–328. https://doi.org/10.1016/j.solener.2017.10.078.

Andrews, R.W., A. Pollard, and J.M. Pearce. 2013. "The effects of snowfall on solar photovoltaic performance." *Sol. Energy* 92: 84–97. https://doi.org/10.1016/j.solener.2013.02.014.

ASTM G113. 2022. "ASTM G113-16 Terminology Relating to Natural and Artificial Weathering Tests of Nonmetallic Materials." ASTM International. https://doi.org/10.1520/G0113-16.

ASTM G173. 2020. "ASTM G173-3 Tables for Reference Solar Spectral Irradiances: Direct Normal and Hemispherical on 37° Tilted Surface." ASTM International. https://doi.org/10.1520/G0173-03R20.

ASTM G177. 2020. "ASTM G177-03 Tables for Reference Solar Ultraviolet Spectral Distributions: Hemispherical on 37° Tilted Surface." https://doi.org/10.1520/G0177-03R20.

ASTM G222. 2021. "ASTM G222-21 Standard Practice for Estimation of UV Irradiance Received by Field-Exposed Products as a Function of Location." https://doi.org/10.1520/G0222-21.

Ballestrín, J., R. Monterreal, M.E. Carra, J. Fernández-Reche, J. Polo, R. Enrique, J. Rodríguez, M. Casanova, F.J. Barbero, J. Alonso-Montesinos, G. López, J.L. Bosch, F.J. Batlles, and A. Marzo. 2018. "Solar extinction measurement system based on digital cameras. Application to solar tower plants." *Renew. Energy* 125: 648–654. https://doi.org/10.1016/j.renene.2018.03.004.

Baum, B.A., P. Yang, A.J. Heymsfield, C.G. Schmitt, Y. Xie, A. Bansemer, Y-X. Hu, and Z. Zhang. 2011. "Improvements in Shortwave Bulk Scattering and Absorption Models for the Remote Sensing of Ice Clouds." *J. Appl. Meteorol. Climatol*. 50: 1037–1056. https://doi.org/10.1175/2010JAMC2608.1.

Becker, G., B. Schiebelsberger, W. Weber, J. Schumacher, M. Zehner, G. Wotruba, and C. Vodermayer. 2008. "Energy Yields of PV Systems - Comparison of Simulation and Reality." In

Proceedings of the 23rd European Photovoltaic Solar Energy Conference and Exhibition. https://doi.org/10.4229/23RDEUPVSEC2008-4BV.1.57.

Beirle, S., J. Lampel, Y. Wang, K. Mies, S. Dörner, M. Grossi, D. Loyola, A. Dehn, A. Danielczok, M. Schröder, and T. Wagner. 2018. "The ESA GOME-Evolution "Climate" water vapor product: a homogenized time series of H2O columns from GOME, SCIAMACHY, and GOME-2." *Earth Syst. Sci. Data* 10: 449–468. https://doi.org/10.5194/essd-10-449-2018.

Bellmann, P., F. Wolfertstetter, R. Conceição, and H.G. Silva. 2020. "Comparative modeling of optical soiling losses for CSP and PV energy systems." *Sol. Energy* 197: 229–237. https://doi.org/10.1016/j.solener.2019.12.045.

Bendt, P., and A. Rabl. 1980. *Effect of circumsolar radiation on performance of focusing collectors.* NASA STIRecon Tech. Rep. N 80, 31916.

Bergin, M.H., C. Ghoroi, D. Dixit, J.J. Schauer, and D.T. Shindell. 2017. "Large Reductions in Solar Energy Production Due to Dust and Particulate Air Pollution." *Environ. Sci. Technol. Lett.* 4: 339–344. https://doi.org/10.1021/acs.estlett.7b00197.

Bessa, J.G., L. Micheli, J. Montes-Romero, F. Almonacid, and E.F. Fernández. 2022. "Estimation of Photovoltaic Soiling Using Environmental Parameters: A Comparative Analysis of Existing Models." *Adv. Sustain. Syst.* 6: 2100335. https://doi.org/10.1002/adsu.202100335.

Bird, R.E. 1984. "A simple, solar spectral model for direct-normal and diffuse horizontal irradiance." *Sol. Energy* 32: 461–471. https://doi.org/10.1016/0038-092X(84)90260-3.

Blair, N., DiOrio, N., Freeman, J.M., P. Gilman, S. Janzou, T. Neises, and M. Wagner. 2018. *System Advisor Model (SAM) general description (version 2017.9.5).* NREL/TP-6A20-70414. National Renewable Energy Lab., Golden, CO (United States). https://www.nrel.gov/docs/fy18osti/70414.pdf.

Bliss, M., T.R. Betts, and R. Gottschalg. 2010. "Indoor measurement of photovoltaic device characteristics at varying irradiance, temperature and spectrum for energy rating." *Meas. Sci. Technol.* 21: 115701. https://doi.org/10.1088/0957-0233/21/11/115701.

Bogenrieder, J., C. Camus, M. Hüttner, P. Offermann, J. Hauch, and C.J. Brabec. 2018. "Technology-dependent analysis of the snow melting and sliding behavior on photovoltaic modules." *J. Renew. Sustain. Energy* 10: 021005. https://doi.org/10.1063/1.5001556.

Bonilla Castro, J., M. Schweiger, D. Moser, T. Tanahashi, B.H. King, G. Friesen, L. Haitao, R. French, L.S. Bruckman, and B. Müller. 2020. *Climatic rating of photovoltaic modules: Different technologies for various operating conditions.* Report IEA-PVPS T13-20:2020. https://iea-pvps.org/wp-content/uploads/2021/02/Report-IEA-PVPS-T13-20_2020-Climatic-Rating-of-PV-Modules.pdf.

Bosilovich, M.G., R. Lucchesi, and M. Suarez. 2016. *MERRA-2: File specification*. https://ntrs.nasa.gov/api/citations/20150019760/downloads/20150019760.pdf.

Braga, M., L.R. do Nascimento, and R. Rüther. 2019. "Spectral modeling and spectral impacts on the performance of mc-Si and new generation CdTe photovoltaics in warm and sunny climates." *Sol. Energy* 188: 976–988. https://doi.org/10.1016/j.solener.2019.06.073.

Brenner, A., J. Kahn, T. Hirsch, M. Röger, and R. Pitz-Paal. 2023. "Soiling determination for parabolic trough collectors based on operational data analysis and machine learning." *Sol. Energy* 259: 257–276. https://doi.org/10.1016/j.solener.2023.05.008.

Bright, J.M., and C.A. Gueymard. 2019. "Climate-specific and global validation of MODIS Aqua and Terra aerosol optical depth at 452 AERONET stations." *Sol. Energy* 183: 594–605. https://doi.org/10.1016/j.solener.2019.03.043.

Bright, J.M., C.A. Gueymard, S. Killinger, D. Lingfors, X. Sun, P. Wang, and N.A. Engerer. 2018. "Climatic and Global Validation of Daily MODIS Precipitable Water Data at AERONET Sites for Clear-sky Irradiance Modelling." in: Proceedings of EuroSun 2018, Rapperswil, Switzerland: 1–12. https://doi.org/10.18086/eurosun2018.09.07.

Burnham, L., D. Riley, B. Walker, and J.M. Pearce. 2019. "Performance of bifacial photovoltaic modules on a dual-axis tracker in a high-latitude, high-albedo environment." In: 2019 IEEE 46th Photovoltaic Specialists Conference (PVSC). IEEE: 1320–1327. https://doi.org/10.1109/PVSC40753.2019.8980964.

Cachorro, V.E., A. Berjón, C. Toledano, S. Mogo, N. Prats, A.M. De Frutos, J.M. Vilaplana, M. Sorribas, B.A. De La Morena, J. Gröbner, and N. Laulainen. 2009. "Detailed Aerosol Optical Depth Intercomparison between Brewer and Li-Cor 1800 Spectroradiometers and a Cimel Sun Photometer." *J. Atmospheric Ocean. Technol.* 26: 1558–1571. https://doi.org/10.1175/2009JTECHA1217.1.

Cadenas Tortosa, F., J. Gonzalez, and M. Hernandez. 2003. *El cultivo protegido del tomate, in: Técnicas de producción en cultivos protegidos*. Instituto Cajamar, Almería, Spain. ISBN 84-95531-16-X: 481–537.

Campos, L., S. Wilbert, J. Carballo, J. Meyer Zu Köcker, F. Wolfertstetter, J. La Casa, E. Borg, K. Schmidt, L.F. Zarzalejo, A. Fernández-García, F.N. Santos, and G. García. 2022. "Autonomous measurement system for photovoltaic and radiometer soiling losses." *Prog. Photovolt. Res. Appl.* pip.3650. https://doi.org/10.1002/pip.3650.

Ceamanos, X., B. Six, S. Moparthy, D. Carrer, A. Georgeot, J. Gasteiger, J. Riedi, J-L Attié, A. Lyapustin, and I. Katsev. 2023. "Instantaneous aerosol and surface retrieval using satellites in geostationary orbit (iAERUS-GEO) – Estimation of 15-min AOD from MSG/SEVIRI and evaluation with reference data (preprint)." *Aerosols/Remote Sensing/Data Processing and Information Retrieval*. https://doi.org/10.5194/amt-2023-1.

Chhatbar, K., and R. Meyer. 2011. *The influence of meteorological parameters on the energy yield of solar thermal plants.* SolarPACES conference, Granada, Spain. https://epic.awi.de/id/eprint/24776/1/Chh2011a.pdf.

Chiu, J., S. Paredes-Mesa, T. Lakhankar, P. Romanov, N. Krakauer, R. Khanbilvardi, and R. Ferraro. 2020. "Intercomparison and Validation of MIRS, MSPPS, and IMS Snow Cover Products." *Adv. Meteorol.* 2020: 1–10. https://doi.org/10.1155/2020/4532478.

Clough, S.A., M.W. Shephard, E.J. Mlawer, J.S. Delamere, M.J. Iacono, K. Cady-Pereira, S. Boukabara, and P.D. Brown. 2005. "Atmospheric radiative transfer modeling: a summary of the AER codes." *J. Quant. Spectrosc. Radiat. Transf.* 91: 233–244. https://doi.org/10.1016/j.jqsrt.2004.05.058.

Coello, M., and L. Boyle. 2019. "Simple Model for Predicting Time Series Soiling of Photovoltaic Panels." *IEEE J. Photovolt.* 9: 1382–1387. https://doi.org/10.1109/JPHOTOV.2019.2919628.

Cossu, M., A. Yano, S. Solinas, P.A. Deligios, M.T. Tiloca, A. Cossu, and L. Ledda. 2020. "Agricultural sustainability estimation of the European photovoltaic greenhouses." *Eur. J. Agron.* 118: 126074. https://doi.org/10.1016/j.eja.2020.126074.

De Leeuw, J., J. Methven, and M. Blackburn. 2015. "Evaluation of ERA-Interim reanalysis precipitation products using England and Wales observations." *Q. J. R. Meteorol. Soc*. 141: 798–806. https://doi.org/10.1002/qj.2395.

do Nascimento, L.R., T. de Souza Viana, R.A. Campos, and R. Rüther. 2019. "Extreme solar overirradiance events: Occurrence and impacts on utility-scale photovoltaic power plants in Brazil." *Sol. Energy* 186: 370–381. https://doi.org/10.1016/j.solener.2019.05.008.

Dobos, A.P. 2014. *PVWatts version 5 manual.* NREL/TP-6A20-62641. National Renewable Energy Lab., Golden, CO. https://doi.org/10.2172/1158421.

Driesse, A., M. Theristis, and J.S. Stein. 2022. "PV Module Operating Temperature Model Equivalence and Parameter Translation." In: IEEE 49th Photovoltaics Specialists Conference (PVSC), Philadelphia, PA: 0172–0177. https://doi.org/10.1109/PVSC48317.2022.9938895.

Dunn, L., B. Littmann, J.R. Caron, and M. Gostein. 2013. "PV module soiling measurement uncertainty analysis." In: IEEE 39th Photovoltaic Specialists Conference (PVSC), Tampa, FL: 0658–0663. https://doi.org/10.1109/PVSC.2013.6744236.

Dye, D.G. 2004. "Spectral composition and quanta-to-energy ratio of diffuse photosynthetically active radiation under diverse cloud conditions." *J. Geophys. Res. Atmospheres* 109: D10203. https://doi.org/10.1029/2003JD004251.

Eissa, Y., P. Blanc, H. Ghedira, A. Oumbe, and L. Wald. 2018. "A fast and simple model to estimate the contribution of the circumsolar irradiance to measured broadband beam irradiance under cloud-free conditions in desert environment." *Sol. Energy* 163: 497–509. https://doi.org/10.1016/j.solener.2018.02.015.

El Boujdaini, I., R. Bruhwyler, P. Rajan, J.R. Bueno, B. Sarr, J. Leloux, F. Lebeau, and C.A. Gueymard. 2023. "3D Modelling of Light-Sharing Agrivoltaic Systems for Orchards, Vineyards

and Berries." In: 40th European Photovoltaic Solar Energy Conference and Exhibition, Lisbon, Portugal. https://doi.org/10.4229/EUPVSEC2023/4DO.2.3.

Elamri, Y., B. Cheviron, J-M. Lopez, C. Dejean, and G. Belaud. 2018. "Water budget and crop modelling for agrivoltaic systems: Application to irrigated lettuces." *Agric. Water Manag.* 208: 440–453. https://doi.org/10.1016/j.agwat.2018.07.001.

Elamri, Yassin, B. Cheviron, A. Mange, C. Dejean, F. Liron, and G. Belaud. 2018. "Rain concentration and sheltering effect of solar panels on cultivated plots." *Hydrol. Earth Syst. Sci*. 22: 1285–1298. https://doi.org/10.5194/hess-22-1285-2018.

Emery, K., A. Anderberg, M. Campanelli, P. Ciszek, C. Mack, T. Moriarty, C. Osterwald, L. Ottoson, S. Rummel, and R. Williams. 2013. "Rating photovoltaics." In: IEEE 39th Photovoltaic Specialists Conference (PVSC), Tampa, FL: 0001–0006. https://doi.org/10.1109/PVSC.2013.6744086.

European Commission. Joint Research Centre. Institute for Energy. 2010. Guidelines for PV power measurement in industry. Publications Office, LU. http://repository.supsi.ch/id/eprint/9717.

Evans, K.F. 1998. "The Spherical Harmonics Discrete Ordinate Method for Three-Dimensional Atmospheric Radiative Transfer." *J. Atmospheric Sci.* 55: 429–446. https://doi.org/10.1175/1520-0469(1998)055<0429:TSHDOM>2.0.CO;2.

Fioletov, V.E., J.B. Kerr, D.I. Wardle. 1997. "The relationship between total ozone and spectral UV irradiance from Brewer observations and its use for derivation of total ozone from UV measurements." *Geophys. Res. Lett.* 24: 2997–3000. https://doi.org/10.1029/97GL53153.

Franklin, K.A. 2008. "Shade avoidance." *New Phytol.* 179: 930–944. https://doi.org/10.1111/j.1469-8137.2008.02507.x.

Fu, D., C.A. Gueymard, and X. Xia. 2023a. "Validation of the improved GOES-16 aerosol optical depth product over North America." *Atmos. Environ*. 298: 119642. https://doi.org/10.1016/j.atmosenv.2023.119642.

Fu, D., C.A. Gueymard, D. Yang, Y. Zheng, X. Xia, and J. Bian. 2023b. "Improving aerosol optical depth retrievals from Himawari-8 with ensemble learning enhancement: Validation over Asia." *Atmospheric Res.* 284: 106624. https://doi.org/10.1016/j.atmosres.2023.106624.

Gardea, M.M.A.N., L.F.C. Martínez, M.A. Morales, G.T. Schiaffino, and D.P.S. Peimbert. 2021. "Modeling photosynthetically active radiation: A review." *Atmósfera* 34: 357–370. https://doi.org/10.20937/ATM.52737.

Giles, D.M., A. Sinyuk, M.G. Sorokin, J.S. Schafer, A. Smirnov, I. Slutsker, T.F. Eck, B.N. Holben, J.R. Lewis, J.R. Campbell, E.J. Welton, S.V. Korkin, and A.I. Lyapustin. 2019. "Advancements in the Aerosol Robotic Network (AERONET) Version 3 database – automated near-real-time quality control algorithm with improved cloud screening for Sun photometer

aerosol optical depth (AOD) measurements." *Atmospheric Meas. Tech.* 12: 169–209. https://doi.org/10.5194/amt-12-169-2019.

Gostein, M., T. Duster, and C. Thuman. 2015. "Accurately measuring PV soiling losses with soiling station employing module power measurements." In: IEEE 42nd Photovoltaic Specialist Conference (PVSC), New Orleans, LA: 1–4. https://doi.org/10.1109/PVSC.2015.7355993.

Gostein, M., S. Faullin, K. Miller, J. Schneider, and B. Stueve. 2018. "Mars Soiling Sensor™." In: IEEE 7th World Conference on Photovoltaic Energy Conversion (WCPEC), Waikoloa Village, HI: 3417–3420. https://doi.org/10.1109/PVSC.2018.8547767.

Gueymard, C.A. 2019a. "Clear-Sky Radiation Models and Aerosol Effects." In: Polo, J., Martín-Pomares, L., Sanfilippo, A. (Eds.), *Solar Resources Mapping, Green Energy and Technology*. Springer International Publishing, pp. 137–182. https://doi.org/10.1007/978-3-319-97484-2_5.

Gueymard, C.A. 2019b. "The SMARTS spectral irradiance model after 25 years: New developments and validation of reference spectra." *Sol. Energy* 187: 233–253. https://doi.org/10.1016/j.solener.2019.05.048.

Gueymard, C.A. 2017. "Cloud and albedo enhancement impacts on solar irradiance using high-frequency measurements from thermopile and photodiode radiometers. Part 1: Impacts on global horizontal irradiance." *Sol. Energy* 153: 755–765. https://doi.org/10.1016/j.solener.2017.05.004.

Gueymard, C.A. 2010. "Spectral Circumsolar Radiation Contribution To CPV." *AIP Conf. Proc*. 1277: 316–319. https://doi.org/10.1063/1.3509220.

Gueymard, C.A. 2008. "Prediction and validation of cloudless shortwave solar spectra incident on horizontal, tilted, or tracking surfaces." *Sol. Energy* 82: 260–271. https://doi.org/10.1016/j.solener.2007.04.007.

Gueymard, C.A. 2001. "Parameterized transmittance model for direct beam and circumsolar spectral irradiance." *Sol. Energy* 71: 325–346. https://doi.org/10.1016/S0038-092X(01)00054-8.

Gueymard, C.A.1995. *SMARTS2, A Simple Model of The Atmospheric Radiative Transfer of Sunshine.* FSEC-PF-270-95. Florida Solar Energy Center, Cocoa, FL. http://publications.energyresearch.ucf.edu/wp-content/uploads/2018/06/FSEC-PF-270-95.pdf.

Gueymard, C.A. 1993. "Assessment of the Accuracy and Computing Speed of Simplified Saturation Vapor Equations Using a New Reference Dataset." *J. Appl. Meteorol.* 32: 1294–1300. https://doi.org/10.1175/1520-0450(1993)032<1294:AOTAAC>2.0.CO;2.

Gueymard, C.A., V. Lara-Fanego, M. Sengupta, and A. Habte. 2021. "Surface albedo spatial variability in North America: Gridded data vs. local measurements." *Sol. Energy* 227: 655–673. https://doi.org/10.1016/j.solener.2021.05.012.

Gueymard, C.A., V. Lara-Fanego, M. Sengupta, and Y. Xie. 2019. "Surface albedo and reflectance: Review of definitions, angular and spectral effects, and intercomparison of major

data sources in support of advanced solar irradiance modeling over the Americas." *Sol. Energy* 182: 194–212. https://doi.org/10.1016/j.solener.2019.02.040.

Gueymard, C.A., D. Myers, and K. Emery. 2002. "Proposed reference irradiance spectra for solar energy systems testing." *Sol. Energy* 73: 443–467. https://doi.org/10.1016/S0038-092X(03)00005-7.

Gueymard, C.A., and D. Yang. 2020. "Worldwide validation of CAMS and MERRA-2 reanalysis aerosol optical depth products using 15 years of AERONET observations." *Atmos. Environ*. 225: 117216. https://doi.org/10.1016/j.atmosenv.2019.117216.

Habte, A., M. Sengupta, C.A. Gueymard, R. Narasappa, O. Rosseler, and D.M. Burns. 2019. "Estimating Ultraviolet Radiation From Global Horizontal Irradiance." *IEEE J. Photovolt.* 9: 139–146. https://doi.org/10.1109/JPHOTOV.2018.2871780.

Hanrieder, N., A. Ghennioui, S. Wilbert, M. Sengupta, and L.F. Zarzalejo. 2020. "AATTENUATION—The Atmospheric Attenuation Model for CSP Tower Plants: A Look-Up Table for Operational Implementation." *Energies* 13: 5248. https://doi.org/10.3390/en13205248.

Hanrieder, N., M. Sengupta, Y. Xie, S. Wilbert, and R. Pitz-Paal. 2016. "Modeling beam attenuation in solar tower plants using common DNI measurements." *Sol. Energy* 129: 244–255. https://doi.org/10.1016/j.solener.2016.01.051.

Hanrieder, N., S. Wilbert, D. Mancera-Guevara, R. Buck, S. Giuliano, and R. Pitz-Paal. 2017. "Atmospheric extinction in solar tower plants – A review." *Sol. Energy* 152: 193–207. https://doi.org/10.1016/j.solener.2017.01.013.

Hanrieder, N., S. Wilbert, R. Pitz-Paal, C. Emde, J. Gasteiger, B. Mayer, and J. Polo. 2015. "Atmospheric extinction in solar tower plants: absorption and broadband correction for MOR measurements." *Atmospheric Meas. Tech.* 8: 3467–3480. https://doi.org/10.5194/amt-8-3467-2015.

Hatfield, J.L., K.J. Boote, B.A. Kimball, L.H. Ziska, R.C. Izaurralde, D. Ort, A.M. Thomson, and D. Wolfe. 2011. "Climate Impacts on Agriculture: Implications for Crop Production." *Agron. J.* 103: 351–370. https://doi.org/10.2134/agronj2010.0303.

Heidari, N., J. Gwamuri, T. Townsend, and J.M. Pearce. 2015. "Impact of Snow and Ground Interference on Photovoltaic Electric System Performance." *IEEE J. Photovolt.* 5: 1680–1685. https://doi.org/10.1109/JPHOTOV.2015.2466448.

Heimsath, A., T. Schmidt, S. Rohani, L. Haack, R. Meyer, J. Steinmetz, and P. Nitz. 2019. "Monitoring of soiling with the AVUS instrument – Technical and economic assessment." SOLARPACES 2018: International Conference on Concentrating Solar Power and Chemical Energy Systems, Casablanca, Morocco, p. 190007. https://doi.org/10.1063/1.5117704.

Hemond, H.F., and E.J. Fechner. 2015. "Chapter 4-The Atmosphere." *Chem. Fate Transp. Environ*: 311–454.

Herman, J.R., N. Krotkov, E. Celarier, D. Larko, and G. Labow. 1999. "Distribution of UV radiation at the Earth's surface from TOMS-measured UV-backscattered radiances." *J. Geophys. Res. Atmospheres* 104: 12059–12076. https://doi.org/10.1029/1999JD900062.

Holben, B.N., T.F. Eck, I. Slutsker, A. Smirnov, A. Sinyuk, J. Schafer, D. Giles, and O. Dubovik. 2006. "Aeronet's Version 2.0 quality assurance criteria." In: Tsay, S.-C., Nakajima, T., Singh, R.P., Sridharan, R. (Eds.). Presented at the Asia-Pacific Remote Sensing Symposium, Goa, India, SPIE Conf. 6408. https://doi.org/10.1117/12.706524.

Holmgren, W., W. Hansen, and A. Mikofski. 2018. "pvlib python: a python package for modeling solar energy systems." *J. Open Source Softw*. 3: 884. https://doi.org/10.21105/joss.00884.

Hu, Y.X., and K. Stamnes. 1993. "An Accurate Parameterization of the Radiative Properties of Water Clouds Suitable for Use in Climate Models." *J. Clim*. 6: 728–742. https://doi.org/10.1175/1520-0442(1993)006<0728:AAPOTR>2.0.CO;2.

Hülsen, G., and J. Gröbner. 2007. "Characterization and calibration of ultraviolet broadband radiometers measuring erythemally weighted irradiance." *Appl. Opt.* 46: 5877. https://doi.org/10.1364/AO.46.005877.

Hülsen, G., J. Gröbner, A. Bais, M. Blumthaler, H. Diémoz, D. Bolsée, A. Diaz, I. Fountoulakis, E. Naranen, J. Schreder, F. Stefania, and J. Manuel Vilaplana Guerrero. 2020. "Second solar ultraviolet radiometer comparison campaign UVC-II." *Metrologia* 57: 035001. https://doi.org/10.1088/1681-7575/ab74e5.

Huwald, H., C.W. Higgins, M. Boldi, E. Bou-Zeid, M. Lehning, and M.B. Parlange. 2009. "Albedo effect on radiative errors in air temperature measurements." *Water Resour. Res.* 45: 2008WR007600. https://doi.org/10.1029/2008WR007600.

Ilse, K., L. Micheli, B.W. Figgis, K. Lange, D. Daßler, H. Hanifi, F. Wolfertstetter, V. Naumann, C. Hagendorf, R. Gottschalg, and J. Bagdahn. 2019. "Techno-Economic Assessment of Soiling Losses and Mitigation Strategies for Solar Power Generation." *Joule* 3: 2303–2321. https://doi.org/10.1016/j.joule.2019.08.019.

Ilse, K.K., B.W. Figgis, V. Naumann, C. Hagendorf, and J. Bagdahn. 2018. "Fundamentals of soiling processes on photovoltaic modules." *Renew. Sustain. Energy Rev*. 98: 239–254. https://doi.org/10.1016/j.rser.2018.09.015.

ISO 9060. 2018. "ISO 9060:2018 Solar energy—Specification and classification of instruments for measuring hemispherical solar and direct solar radiation."

Jahn, U., B. Herteleer, C. Tjengdrawira, and I. Tsanakas. 2022. *Guidelines for Operation and Maintenance of Photovoltaic Power Plants in Different Climates*. Report IEA-PVPS T13-25:2022. https://iea-pvps.org/wp-content/uploads/2022/11/IEA-PVPS-Report-T13-25-2022-OandM-Guidelines.pdf.

Järvelä, M., K. Lappalainen, and S. Valkealahti. 2020. "Characteristics of the cloud enhancement phenomenon and PV power plants." *Sol. Energy* 196: 137–145. https://doi.org/10.1016/j.solener.2019.11.090.

Jessen, W., S. Wilbert, C.A. Gueymard, J. Polo, Z. Bian, A. Driesse, A. Habte, A. Marzo, P.R. Armstrong, F. Vignola, and L. Ramírez. 2018. "Proposal and evaluation of subordinate standard solar irradiance spectra for applications in solar energy systems." *Solar Energy* 168: 30–43. https://doi.org/10.1016/j.solener.2018.03.043.

Kaufman, Y.J., D. Tanré, and O. Boucher. 2002. "A satellite view of aerosols in the climate system." *Nature* 419: 215–223. https://doi.org/10.1038/nature01091.

Kerr, J.B., and V.E. Fioletov. 2008. "Surface ultraviolet radiation." *Atmosphere-Ocean* 46: 159–184. https://doi.org/10.3137/ao.460108.

Ketzer, D., P. Schlyter, N. Weinberger, and C. Rösch. 2020. "Driving and restraining forces for the implementation of the Agrophotovoltaics system technology – A system dynamics analysis." *J. Environ. Manage.* 270: 110864. https://doi.org/10.1016/j.jenvman.2020.110864.

Kimber, A., L. Mitchell, S. Nogradi, and H. Wenger. 2006. "The Effect of Soiling on Large Grid-Connected Photovoltaic Systems in California and the Southwest Region of the United States." In: 2006 IEEE 4th World Conference on Photovoltaic Energy Conference. Presented at the 2006 IEEE 4th World Conference on Photovoltaic Energy Conference, IEEE, Waikoloa, HI, pp. 2391–2395. https://doi.org/10.1109/WCPEC.2006.279690.

Koepke, P. 2009. "Radiative models for the evaluation of the UV radiation at the ground." *Radiat. Prot. Dosimetry* 137: 188–192. https://doi.org/10.1093/rpd/ncp211.

Korevaar, M., J. Mes, P. Nepal, G. Snijders, and X. Van Mechelen. 2017. "Novel Soiling Detection System for Solar Panels." 33rd Eur. Photovolt. Sol. Energy Conf. Exhib. 2349-2351 3 pages, 5416 kb. https://doi.org/10.4229/EUPVSEC20172017-6BV.2.11.

Kosmopoulos, P., S. Kazadzis, H. El-Askary, M. Taylor, A. Gkikas, E. Proestakis, C. Kontoes, and M. El-Khayat. 2018. "Earth-Observation-Based Estimation and Forecasting of Particulate Matter Impact on Solar Energy in Egypt." *Remote Sens.* 10: 1870. https://doi.org/10.3390/rs10121870.

Krotkov, N.A., P.K. Bhartia, J.R. Herman, V. Fioletov, and J. Kerr. 1998. "Satellite estimation of spectral surface UV irradiance in the presence of tropospheric aerosols: 1. Cloud-free case." *J. Geophys. Res. Atmospheres* 103: 8779–8793. https://doi.org/10.1029/98JD00233.

La Notte, L., L. Giordano, E. Calabrò, R. Bedini, G. Colla, G. Puglisi, and A. Reale. 2020. "Hybrid and organic photovoltaics for greenhouse applications." *Appl. Energy* 278: 115582. https://doi.org/10.1016/j.apenergy.2020.115582.

Lara-Fanego, V., C.A. Gueymard, J.A. Ruiz-Arias, T. Cebecauer, and J. Betak. 2022a. "Extensive Evaluation and Uncertainty Estimation of Albedo Data Sources." IEEE 49th

Photovoltaics Specialists Conference (PVSC), Philadelphia, PA: 0945–0947. https://doi.org/10.1109/PVSC48317.2022.9938504.

Lara-Fanego, V., J.A. Ruiz-Arias, A. Skoczek, C.A. Gueymard, T. Cebecauer, and M. Suri. 2022b. "Annual Energy Production Uncertainty of Bifacial PV Plants Caused by Inaccuracies in Albedo Data: Case Studies Using SAM." IEEE 49th Photovoltaics Specialists Conference (PVSC), Philadelphia, PA. https://doi.org/10.1109/PVSC48317.2022.9938944.

Levelt, P.F., E. Hilsenrath, G.W. Leppelmeier, G.H.J. van den Oord, P.K. Bartia, J. Tamminen, J.F. de Haan, and J.P. Veefkind. 2006. "Science objectives of the ozone monitoring instrument." *IEEE Trans. Geosci. Remote Sens.* 44: 1199–1208. https://doi.org/10.1109/TGRS.2006.872336.

Lindsay, N., Q. Libois, J. Badosa, A. Migan-Dubois, and V. Bourdin. 2020. "Errors in PV power modelling due to the lack of spectral and angular details of solar irradiance inputs." *Sol. Energy* 197: 266–278. https://doi.org/10.1016/j.solener.2019.12.042.

Lorenz, E., D. Heinemann, and C. Kurz. 2012. "Local and regional photovoltaic power prediction for large scale grid integration: Assessment of a new algorithm for snow detection: Assessment of a new algorithm for snow detection." *Prog. Photovolt. Res. Appl.* 20: 760–769. https://doi.org/10.1002/pip.1224.

Madronich, S., and S. Flocke. 1997. "Theoretical Estimation of Biologically Effective UV Radiation at the Earth's Surface," in: Zerefos, C.S., Bais, A.F. (Eds.), *Solar Ultraviolet Radiation.* Springer Berlin Heidelberg, Berlin, Heidelberg, pp. 23–48. https://doi.org/10.1007/978-3-662-03375-3_3.

Maghami, M.R., H. Hizam, C. Gomes, M.A. Radzi, M.I. Rezadad, and S. Hajighorbani. 2016. "Power loss due to soiling on solar panel: A review." *Renew. Sustain. Energy Rev*. 59: 1307–1316. https://doi.org/10.1016/j.rser.2016.01.044.

Mambrini, T., A.M. Dubois, C. Longeaud, J. Badosa, M. Haeffelin, L. Prieur, and V. Radivoniuk. 2015. "Photovoltaic yield: correction method for the mismatch between the solar spectrum and the reference ASTMG AM1.5G spectrum." *EPJ Photovolt.* 6: 60701. https://doi.org/10.1051/epjpv/2014011.

Mamun, M.A.A., P. Dargusch, D. Wadley, N.A. Zulkarnain, and A.A. Aziz. 2022. "A review of research on agrivoltaic systems." *Renew. Sustain. Energy Rev*. 161: 112351. https://doi.org/10.1016/j.rser.2022.112351.

Marion, B., R. Schaefer, H. Caine, and G. Sanchez. 2013. "Measured and modeled photovoltaic system energy losses from snow for Colorado and Wisconsin locations." *Sol. Energy* 97: 112–121. https://doi.org/10.1016/j.solener.2013.07.029.

Marrou, H., L. Guilioni, L. Dufour, C. Dupraz, and J. Wery. 2013. "Microclimate under agrivoltaic systems: Is crop growth rate affected in the partial shade of solar panels?" *Agric. For. Meteorol.* 177: 117–132. https://doi.org/10.1016/j.agrformet.2013.04.012.

Mayer, B., and A. Kylling. 2005. "Technical note: The libRadtran software package for radiative transfer calculations - description and examples of use." *Atmospheric Chem. Phys.* 5: 1855–1877. https://doi.org/10.5194/acp-5-1855-2005.

McArthur, L.J.B., V.E. Fioletov, J.B. Kerr, C.T. McElroy, and D.L.Wardle. 1999. "Derivation of UV-A irradiance from pyranometer measurements." *J. Geophys. Res. Atmospheres* 104: 30139–30151. https://doi.org/10.1029/1999JD900808.

McCree, K.J. 1972. "Test of current definitions of photosynthetically active radiation against leaf photosynthesis data." *Agric. Meteorol.* 10: 443–453. https://doi.org/10.1016/0002-1571(72)90045-3.

McIntosh, D.H. 1977. *Atmospheric science: An introductory survey.* Academic Press (New York).

Meng, Q., Y. Wang, and L. Zhang. 2011. "Irradiance characteristics and optimization design of a large-scale solar simulator." *Sol. Energy* 85: 1758–1767. https://doi.org/10.1016/j.solener.2011.04.014.

Mesinger, F., G. DiMego, E. Kalnay, K. Mitchell, P.C. Shafran, W. Ebisuzaki, D. Jović, J. Woollen, E. Rogers, E.H. Berbery, M.B. Ek, Y. Fan, R. Grumbine, W. Higgins, H. Li, Y. Lin, G. Manikin, D. Parrish, and W. Shi. 2006. "North American Regional Reanalysis." *Bull. Am. Meteorol. Soc.* 87: 343–360. https://doi.org/10.1175/BAMS-87-3-343.

Micheli, L., M.G. Deceglie, M. Muller. 2019. "Mapping Photovoltaic Soiling Using Spatial Interpolation Techniques." *IEEE J. Photovolt.* 9: 272–277. https://doi.org/10.1109/JPHOTOV.2018.2872548.

Micheli, L., E.F. Fernández, A. Fernández-Solas, J.G. Bessa, F. Almonacid. 2022. "Analysis and mitigation of nonuniform soiling distribution on utility-scale photovoltaic systems." *Prog. Photovolt. Res. Appl.* 30: 211–228. https://doi.org/10.1002/pip.3477.

Micheli, L., and M. Muller. 2017. "An investigation of the key parameters for predicting PV soiling losses." *Prog. Photovolt. Res. Appl.* 25: 291–307. https://doi.org/10.1002/pip.2860.

Minnis, P., S. Sun-Mack, D.F. Young, P.W. Heck, D.P. Garber, Y. Chen, D. Spangenberg, R.F. Arduini, Q.Z. Trepte, W.L. Smith, J.K. Ayers, S.C. Gibson, W.F. Miller, C. Hong, V. Chakrapani, Y. Takano, et al. 2011. "CERES Edition-2 Cloud Property Retrievals Using TRMM VIRS and Terra and Aqua MODIS Data—Part I: Algorithms." *IEEE Trans. Geosci. Remote Sens*. 49: 4374–4400. https://doi.org/10.1109/TGRS.2011.2144601.

Mishra, A.K. 2020. "Variability of integrated precipitable water over India in a warming climate." *Meteorol. Appl.* 27. https://doi.org/10.1002/met.1869.

Mishra, B.R., N. Hanrieder, A. Modi, and S.B. Kedare. 2020. "Comparison of three models to estimate the slant path atmospheric attenuation in central receiver solar thermal plants under Indian climatic conditions." *Sol. Energy* 211: 1042–1052. https://doi.org/10.1016/j.solener.2020.10.049.

Moragues, M., and G.S. McMaster. 2012. “Crop Development Related to Temperature and Photoperiod,” in: Meyers, R.A. (Ed.), *Encyclopedia of Sustainability Science and Technology*. Springer New York, New York, NY, pp. 2540–2558. https://doi.org/10.1007/978-1-4419-0851-3_384.

Morley, K., J. Robinson, J. Chard, J. Peterson. 2020. “In-situ comparison of five soiling measurement systems.” Presented at the PVPMC Webinar on Solar Resource Assessment. https://pvpmc.sandia.gov/download/4811/?tmstv=1722826421.

Müllejans, H., A. Ioannides, R. Kenny, W. Zaaiman, H.A. Ossenbrink, and E. Dunlop. 2005. “Spectral mismatch in calibration of photovoltaic reference devices by global sunlight method.” *Meas. Sci. Technol.* 16: 1250–1254. https://doi.org/10.1088/0957-0233/16/6/002.

Muller, M., L. Micheli, A.F. Solas, M. Gostein, J. Robinson, K. Morely, M. Dooraghi, Y.A. Alghamdi, Z.A. Almutairi, F. Almonacid, and E.F. Fernandez. 2021. “An in-depth field validation of “DUSST”: A novel low-maintenance soiling measurement device.” *Prog. Photovolt. Res. Appl.* 29: 953–967. https://doi.org/10.1002/pip.3415.

Muller, M., and F. Rashed. 2023. “Considering the Variability of Soiling in Long-Term PV Performance Forecasting.” *IEEE J. Photovolt.* 13: 825–829. https://doi.org/10.1109/JPHOTOV.2023.3300369.

Myers, D.R. 2012. “Direct beam and hemispherical terrestrial solar spectral distributions derived from broadband hourly solar radiation data.” *Sol. Energy* 86: 2771–2782. https://doi.org/10.1016/j.solener.2012.06.014.

Myers, D.R., and C.A. Gueymard. 2004. “Description and availability of the SMARTS spectral model for photovoltaic applications,” in: Kafafi, Z.H., Lane, P.A. (Eds.), SPIE Organic Photovoltaics Conf. 5520, Denver, CO, p. 56. https://doi.org/10.1117/12.555943.

NASA. AERONET Inversion Products. https://aeronet.gsfc.nasa.gov/new_web/draw_map_display_inv_v3.html.

Nederhoff, E. 2009. “Air Humidity, Stomata and Transpiration.” *Pract. Hydroponics Greenh.* 109: 37–42.

Noring, J.E., D.F. Grether, and A.J. Hunt. 1991. *Circumsolar Radiation Data: The Lawrence Berkeley Laboratory Reduced Data Base, Final Subcontract Report*. NREL/TP-262-4429. National Renewable Energy Laboratory. Golden, CO. https://doi.org/10.2172/6125786.

Pawluk, R.E., Y. Chen, Y. She. 2019. “Photovoltaic electricity generation loss due to snow – A literature review on influence factors, estimation, and mitigation.” *Renew. Sustain. Energy Rev.* 107: 171–182. https://doi.org/10.1016/j.rser.2018.12.031.

Peeters, P., J-F Müller, P.C. Simon, E. Celarier, and J. Herman. 1998. Estimation of UV flux at the Earth’s surface using GOME data. Royal Belgian Institute for Space Aeronomy. https://orfeo.belnet.be/handle/internal/5396.

Pelland, S., and C.A. Gueymard. 2022. "Validation of Photovoltaic Spectral Effects Derived From Satellite-Based Solar Irradiance Products." *IEEE J. Photovolt.* 12: 1361–1368. https://doi.org/10.1109/JPHOTOV.2022.3216501.

Pelland, S., P. Pawar, A. Veeramani, W. Gustafson, and L.L.A. Etringer. 2018. "Testing Global Models of Photovoltaic Soiling Ratios Against Field Test Data Worldwide." IEEE 7th World Conference on Photovoltaic Energy Conversion (WCPEC), Waikoloa Village, HI, pp. 3442–3446. https://doi.org/10.1109/PVSC.2018.8548204.

Peterson, J., J. Chard, and J. Robinson. 2022. "Extraction of Prevailing Soiling Rates from Soiling Measurement Data." IEEE 49th Photovoltaics Specialists Conference (PVSC), Philadelphia, PA, USA, pp. 0684–0691. https://doi.org/10.1109/PVSC48317.2022.9938838.

Phillips, D. 2002. "A Closer Look at a Rare Situation. 1998 Ice Storm." Meteorological Service of Canada.

Picotti, G., P. Borghesani, M.E. Cholette, and G. Manzolini. 2018. "Soiling of solar collectors – Modelling approaches for airborne dust and its interactions with surfaces." *Renew. Sustain. Energy Rev.* 81: 2343–2357. https://doi.org/10.1016/j.rser.2017.06.043.

Polo, J., J. Ballestrín, J. Alonso-Montesinos, G. López-Rodriguez, J. Barbero, E. Carra, J. Fernández-Reche, J.L. Bosch, and F.J. Batlles. 2017. "Analysis of solar tower plant performance influenced by atmospheric attenuation at different temporal resolutions related to aerosol optical depth." *Sol. Energy* 157: 803–810. https://doi.org/10.1016/j.solener.2017.09.003.

Polo, J., J. Ballestrín, and E. Carra. 2016. "Sensitivity study for modelling atmospheric attenuation of solar radiation with radiative transfer models and the impact in solar tower plant production." *Sol. Energy* 134: 219–227. https://doi.org/10.1016/j.solener.2016.04.050.

Polo, J., N. Martín-Chivelet, C. Sanz-Saiz, J. Alonso-Montesinos, G. López, M. Alonso-Abella, F.J. Battles, A. Marzo, and N. Hanrieder. 2021. "Modeling soiling losses for rooftop PV systems in suburban areas with nearby forest in Madrid." *Renew. Energy* 178: 420–428. https://doi.org/10.1016/j.renene.2021.06.085.

Räisänen, P., and A.V. Lindfors. 2019. "On the Computation of Apparent Direct Solar Radiation." *J. Atmospheric Sci.* 76: 2761–2780. https://doi.org/10.1175/JAS-D-19-0030.1.

Ramon, J., L. Lledó, V. Torralba, A. Soret, and F.J. Doblas-Reyes. 2019. "What global reanalysis best represents near-surface winds?" *Q. J. R. Meteorol. Soc.* 145: 3236–3251. https://doi.org/10.1002/qj.3616.

Rand, J., C. Thompson, M. Reed, A. Hendricks, A. Cooper, and P. Donley. 2020. "Hail Damage – A 2019 Case Study and Lab Trials." Presented at the NREL Photovoltaic Reliability Workshop. https://coreenergyworks.com/wp-content/uploads/2021/06/COREEnergyWorks-NREL-PVRW-white-paper-20200529-1.pdf.

Reinhardt, B., R. Buras, L. Bugliaro, S. Wilbert, and B. Mayer. 2014. "Determination of circumsolar radiation from Meteosat Second Generation." *Atmos. Meas. Tech.* 7: 823–838. https://doi.org/10.5194/amt-7-823-2014.

Reise, C., B. Müller, D. Moser, G. Belluardo, and P. Ingenhoven. 2018. *Uncertainties in PV System Yield Predictions and Assessments.* Report IEA PVPS T13-12: 2018. https://iea-pvps.org/wp-content/uploads/2020/01/Uncertainties_in_PV_System_Yield_Predictions_and_Assessments_by_Task_13.pdf.

Ricchiazzi, P., and C. Gautier. 1998. "Investigation of the effect of surface heterogeneity and topography on the radiation environment of Palmer Station, Antarctica, with a hybrid 3-D radiative transfer model." *J. Geophys. Res. Atmospheres* 103: 6161–6176. https://doi.org/10.1029/97JD03629.

Riley, D., L. Burnham, B. Walker, and J.M. Pearce. 2019. "Differences in Snow Shedding in Photovoltaic Systems with Framed and Frameless Modules," in: 2019 IEEE 46th Photovoltaic Specialists Conference (PVSC). IEEE 46th Photovoltaic Specialists Conference (PVSC), Chicago, IL, USA, pp. 0558–0561. https://doi.org/10.1109/PVSC40753.2019.8981389.

Roy, S., and B. Ghosh. 2017. "Land utilization performance of ground mounted photovoltaic power plants: A case study." *Renew. Energy* 114: 1238–1246. https://doi.org/10.1016/j.renene.2017.07.116.

Ryberg, D.S., and J. Freeman. 2015. *Integration, validation, and application of a PV snow coverage model in SAM.* NREL/TP-6A20-68705. National Renewable Energy Laboratory, Golden, CO. https://doi.org/10.2172/1374128.

Salmon, A., A. Marzo, J. Polo, J. Ballestrín, E. Carra, and J. Alonso-Montesinos. 2022. "World map of low-layer atmospheric extinction values for solar power tower plants projects." *Renew. Energy* 201: 876–888. https://doi.org/10.1016/j.renene.2022.11.003.

Sánchez-Guerrero, M.C., P. Lorenzo, E. Medrano, N. Castilla, T. Soriano, and A. Baille. 2005. "Effect of variable CO2 enrichment on greenhouse production in mild winter climates." *Agric. For. Meteorol*. 132: 244–252. https://doi.org/10.1016/j.agrformet.2005.07.014.

Santra, P., R.K. Singh, H.M. Meena, R.N. Kumawat, D. Mishra, D. Machiwal, D. Dayal, D. Jain, O.P. Yadav. 2020. "Agri-Voltaic System for Crop Production and Electricity Generation from a Single Land Unit," in: Singh, S., Ramadesigan, V. (Eds.), Advances in Energy Research, Vol. 1. Springer, Singapore, pp. 45–56. https://doi.org/10.1007/978-981-15-2666-4_6.

Sarver, T., A. Al-Qaraghuli, and L.L. Kazmerski. 2013. "A comprehensive review of the impact of dust on the use of solar energy: History, investigations, results, literature, and mitigation approaches." *Renew. Sustain. Energy Rev*. 22: 698–733. https://doi.org/10.1016/j.rser.2012.12.065.

Sarwar, J., G. Georgakis, R. LaChance, and N. Ozalp. 2014. "Description and characterization of an adjustable flux solar simulator for solar thermal, thermochemical and photovoltaic applications." *Sol. Energy* 100: 179–194. https://doi.org/10.1016/j.solener.2013.12.008.

Schill, C., A. Anderson, C. Baldus-Jeursen, L. Burnham, and L. Micheli. 2022. *Soiling Losses – Impact on the Performance of Photovoltaic Power Plants*. Report IEA-PVPS T13-21:2022. https://iea-pvps.org/wp-content/uploads/2023/01/IEA-PVPS-T13-21-2022-REPORT-Soiling-Losses-PV-Plants.pdf.

Schrott, S., T. Schmidt, T. Hornung, and P. Nitz. 2014. "Scientific system for high-resolution measurement of the circumsolar radiation." Presented at the 3rd International Conference on Theoretical and Applied Physics 2013, Malang, East Java, Indonesia, pp. 88–91. https://doi.org/10.1063/1.4897035.

Schwander, H. 2002. "Modification of spectral UV irradiance by clouds." *J. Geophys. Res.* 107: 4296. https://doi.org/10.1029/2001JD001297.

Sekiyama, T., and A. Nagashima. 2019. "Solar Sharing for Both Food and Clean Energy Production: Performance of Agrivoltaic Systems for Corn, A Typical Shade-Intolerant Crop." *Environments* 6: 65. https://doi.org/10.3390/environments6060065.

Sengupta, M., and M. Wagner. 2012. *Atmospheric attenuation in central receiver systems from DNI measurements.* NREL/CP-5500-54760. National Renewable Energy Laboratory, Golden, CO.

Shaik, S., P. Vigneshwaran, A. Roy, K.J. Kontoleon, D. Mazzeo, E. Cuce, C.A. Saleel, M. Alwetaishi, S.A. Khan, A.E. Gürel, and Ü. Ağbulut. 2023. "Experimental analysis on the impacts of soil deposition and bird droppings on the thermal performance of photovoltaic panels." *Case Stud. Therm. Eng.* 48: 103128. https://doi.org/10.1016/j.csite.2023.103128.

Silva, M., L. Ramirez, F. Vignola, M. Sengupta, K.P. Nielsen, M. Schroedter-Homscheidt, M. Blanco, R. Meyer, M. Larrañeta, C. Fernandez-Peruchena, and S. Moreno. 2021. *Solar radiation products for the end-users - final report.* SolarPACES report. https://www.solarpaces.org/wp-content/uploads/SunUpReport_210419-V2-web.pdf.

Smestad, G.P., C. Anderson, M.E. Cholette, P. Fuke, A.A. Hachicha, A. Kottantharayil, K. Ilse, M. Karim, M.Z. Khan, H. Merkle, D.C. Miller, J.M. Newkirk, G. Picotti, F. Wiesinger, G. Willers, and L. Micheli. 2023. "Variability and associated uncertainty in image analysis for soiling characterization in solar energy systems." *Sol. Energy Mater. Sol. Cells* 259: 112437. https://doi.org/10.1016/j.solmat.2023.112437.

Smirnov, A., B.N. Holben, T.F. Eck, O. Dubovik, and I. Slutsker. 2000. "Cloud-Screening and Quality Control Algorithms for the AERONET Database." *Remote Sens. Environ.* 73: 337–349. https://doi.org/10.1016/S0034-4257(00)00109-7.

Stamnes, K., S-C. Tsay, W. Wiscombe, and K. Jayaweera. 1988. "Numerically stable algorithm for discrete-ordinate-method radiative transfer in multiple scattering and emitting layered media." *Appl. Opt.* 27: 2502. https://doi.org/10.1364/AO.27.002502.

Stridh, B. 2012. “Evaluation of economical benefit of cleaning of soiling and snow in PV plants at three European locations.” 38th IEEE Photovoltaic Specialists Conference, Austin, TX, USA, pp. 001448–001451. https://doi.org/10.1109/PVSC.2012.6317869.

Sugiura, T., T. Yamada, H. Nakamura, M. Umeya, K. Sakuta, and K. Kurokawa. 2003. “Measurements, analyses and evaluation of residential PV systems by Japanese monitoring program.” *Solar Energy Materials and Solar Cells* 75: 767–779. https://doi.org/10.1016/S0927-0248(02)00132-0.

Sun, Z., Jiangnan Li, G. Shi, J. Manners, and Jiandong Li. 2020. “Fast scheme for determination of direct normal irradiance. Part II: Parameterization of circumsolar radiation.” *Sol. Energy* 199: 256–267. https://doi.org/10.1016/j.solener.2020.02.029.

Tanskanen, A., N.A. Krotkov, J.R. Herman, and A. Arola. 2006. “Surface ultraviolet irradiance from OMI.” *IEEE Trans. Geosci. Remote Sens.* 44: 1267–1271. https://doi.org/10.1109/TGRS.2005.862203.

Tetens, O. 1930. “Uber einige meteorologische Begriffe.” *Z Geophys* 6: 297–309.

Townsend, T., and L. Powers. 2011. “Photovoltaics and snow: An update from two winters of measurements in the SIERRA.” IEEE 37th Photovoltaic Specialists Conference (PVSC), Seattle, WA, USA, pp. 003231–003236. https://doi.org/10.1109/PVSC.2011.6186627.

Valera, D.L., L.J. Belmonte, F.D. Molina, and A. López. 2016. “Greenhouse agriculture in Almería: A comprehensive techno-economic analysis.” Cajamar Caja Rural Almería, Spain 408.

Vindel, J., R. Valenzuela, A. Navarro, L. Zarzalejo, A. Paz-Gallardo, J. Souto, R. Méndez-Gómez, D. Cartelle, and J. Casares. 2018. “Modeling Photosynthetically Active Radiation from Satellite-Derived Estimations over Mainland Spain.” *Remote Sens*. 10: 849. https://doi.org/10.3390/rs10060849.

Webb, A., J. Gröbner, and M. Blumthaler. 2006. A practical guide to operating broadband instruments measuring erythemally weighted irradiance. EUR-OP. http://www-med-physik.vu-wien.ac.at/uv/cost726/COST726_Dateien/TrainingSchool/materials/publications/GuideBB_COST726.pdf.

Wei, J., Z. Li, Y. Peng, and L. Sun. 2019. “MODIS Collection 6.1 aerosol optical depth products over land and ocean: validation and comparison.” *Atmos. Environ*. 201: 428–440. https://doi.org/10.1016/j.atmosenv.2018.12.004.

Weselek, A., A. Ehmann, S. Zikeli, I. Lewandowski, S. Schindele, and P. Högy. 2019. “Agrophotovoltaic systems: applications, challenges, and opportunities. A review.” *Agron. Sustain. Dev.* 39: 35. https://doi.org/10.1007/s13593-019-0581-3.

WHO. 2016. “Radiation: Ultraviolet (UV) radiation.” https://www.who.int/news-room/questions-and-answers/item/radiation-ultraviolet-(uv).

Wilbert, S. 2014. *Determination of Circumsolar Radiation and its Effect on Concentrating Solar Power*. PhD Thesis, Rheinisch-Westfälischen Technischen Hochschule Aachen. https://publications.rwth-aachen.de/record/444996/files/5171.pdf.

Wilbert, S., and E. Guillot. 2013. "Database with frequencies of circumsolar ratio (CSR) occurrence at different sites and correlations of CSR with DNI and DHI data." Almería. DLR CNRS.

Wilbert, Stefan, R. Pitz-Paal, and J. Jaus. 2013. "Comparison of measurement techniques for the determination of circumsolar irradiance." *AIP Conference Proc.* 1556: 162–167. https://doi.org/10.1063/1.4822222.

Wilbert, S., B. Reinhardt, J. DeVore, M. Röger, R. Pitz-Paal, C.A. Gueymard, and R. Buras. 2013. "Measurement of Solar Radiance Profiles With the Sun and Aureole Measurement System." *J. Sol. Energy Eng.* 135: 041002. https://doi.org/10.1115/1.4024244.

Wilbert, S., M. Röger, J. Csambor, M. Breitbach, F. Klinger, B. Nouri, N. Hanrieder, F. Wolfertstetter, D. Schüler, S. Shaswattam, et al. 2018. "Sunshape measurements with conventional rotating shadowband irradiometers." *AIP Conference Proc.* 2033: 190016. https://doi.org/10.1063/1.5067201.

Winkel, P., F. Wolfertstetter, S. Wilbert, M. Röger, J. Krauth, N. Algner, L. Zarzalejo, D. Martinez, J. Polo, and C. Alonso. 2022. Zell-aufgelöste Bestimmung der Verschmutzung von PV Modulen mit bildgebenden Verfahren. PV Symposium 2022.

WMO. 2012. *Guide to Agricultural Meteorological Practices (GAMP)* (No. ISBN 978-92-63-10134-1).

WMO. 2018. *Guide to instruments and methods of observation.* World Meteorol. Organ. WMO.

Wolfertstetter, F., R. Fonk, C. Prahl, M. Röger, S. Wilbert, and J. Fernández-Reche. 2020a. "Airborne soiling measurements of entire solar fields with Qfly." *AIP Conference Proc.* 2303: 100008. https://doi.org/10.1063/5.0028968.

Wolfertstetter, F., S. Wilbert, P. Bellmann, S.G. Rodriguez, T.R. Navarro, L. Keller, and A. Fernandez-Garcia. 2020b. "T-TraCS – An automated method to measure soiling losses at parabolic trough receiver tubes." *AIP Conference Proc.* 2303: 210006. https://doi.org/10.1063/5.0029685.

Wolfertstetter, F., K. Pottler, N. Geuder, R. Affolter, A.A. Merrouni, A. Mezrhab, and R. Pitz-Paal. 2014. "Monitoring of Mirror and Sensor Soiling with TraCS for Improved Quality of Ground based Irradiance Measurements." *Energy Procedia* 49: 2422–2432. https://doi.org/10.1016/j.egypro.2014.03.257.

Wolfertstetter, F., S. Wilbert, F. Terhag, N. Hanrieder, A. Fernandez-García, C. Sansom, P. King, L. Zarzalejo, and A. Ghennioui. 2019. "Modelling the soiling rate: Dependencies on meteorological parameters." *AIP Conference Proc*. 2126: 190018. https://doi.org/10.1063/1.5117715.

Xie, Y., and M. Sengupta. 2018. "A Fast All-sky Radiation Model for Solar applications with Narrowband Irradiances on Tilted surfaces (FARMS-NIT): Part I. The clear-sky model." *Sol. Energy* 174: 691–702. https://doi.org/10.1016/j.solener.2018.09.056.

Xie, Y., M. Sengupta, and J. Dudhia. 2016. "A Fast All-sky Radiation Model for Solar applications (FARMS): Algorithm and performance evaluation." *Sol. Energy* 135: 435–445. https://doi.org/10.1016/j.solener.2016.06.003.

Xie, Y., M. Sengupta, Y. Liu, H. Long, Q. Min, W. Liu, and A. Habte. 2020. "A Physics-Based DNI Model Assessing All-Sky Circumsolar Radiation." *iScience* 23: 100893. https://doi.org/10.1016/j.isci.2020.100893.

Xie, Y., M. Sengupta, and C. Wang. 2019. "A Fast All-sky Radiation Model for Solar applications with Narrowband Irradiances on Tilted surfaces (FARMS-NIT): Part II. The cloudy-sky model." *Sol. Energy* 188: 799–812. https://doi.org/10.1016/j.solener.2019.06.058.

Xu, H., P. Chen, and Y. Tao. 2021. "Understanding the Shade Tolerance Responses Through Hints From Phytochrome A-Mediated Negative Feedback Regulation in Shade Avoiding Plants." *Front. Plant Sci.* 12: 813092. https://doi.org/10.3389/fpls.2021.813092.

Zhao, P., Q.J. Wang, W. Wu, and Q. Yang. 2021. "Which precipitation forecasts to use? Deterministic versus coarser-resolution ensemble NWP models." *Q. J. R. Meteorol. Soc.* 147: 900–913. https://doi.org/10.1002/qj.3952.

6 Solar Resource Variability

Christian Gueymard,[1] Kristian Pagh Nielsen,[2] Miguel Larrañeta,[3] Aron Habte,[4] and Richard Perez[5]

[1] *Solar Consulting Services, USA*
[2] *Danish Meteorological Institute, Copenhagen, Denmark*
[3] *Universidad de Sevilla, Spain*
[4] *National Renewable Energy Laboratory, USA*
[5] *University at Albany, The State University of New York, USA*
Note: Stephen Wilcox contributed to previous versions of this chapter.

Executive Summary

Although the solar resource is relatively abundant on a global scale, it is also variable over time and space. This inherent variability is the root cause of the difficulty of harnessing the solar resource efficiently and using some form of storage (or other techniques) to flatten the peaks and valleys of the power production and ultimately make production closer to the power demand curve.

This chapter examines the most important causes of variability, in addition to the unavoidable natural variations caused by the Sun-Earth geometry (e.g., day/night alternation and seasons). The discussion is conducted in terms of atmospheric processes and weather or climatic patterns at various temporal scales, from the very short term to multidecadal. These include impacts on the cloud and aerosol regimes. Although the focus is mainly on temporal variability, some information is also provided about spatial variability.

Aside from the main results of the literature, some simple statistical tools commonly used to quantify variability are explained and concrete examples are given in this chapter. The discussion extends to the critical topics of quantifying solar resource trends and how their current estimates should be extrapolated to evaluate the future solar resource, as the latter is needed for the proper design and financing of major solar power plants.

6.1 Introduction and Background

As discussed in previous chapters, the solar resource is inherently variable, which makes solar energy utilization challenging in practice. To improve this situation, the variability in the solar resource must be evaluated by various means in terms of both time and space. The temporal variability, discussed in Section 6.2, is probably the most important aspect because of its direct connection with various sources of uncertainty in solar resource assessments, and to the whole topic of solar forecasting, which is discussed further in Chapter 9. In comparison, the spatial variability has received less attention in the literature, as overviewed in Section 6.3.

In general terms, variability characterizes the relative or absolute change experienced by a variable during a specific period (temporal variability) or over a specific area (spatial variability). It is often expressed either as the coefficient of variation (COV) for variables having a normal distribution (Calif and Soubdhan 2016) or as the variance for any other known statistical distribution, or even as the interquartile range when the distribution is unknown. COV is obtained by dividing the standard deviation by the mean of the population or sample. Variance measures how far each number in a dataset is from the mean and is the square of the standard

deviation. The interquartile range characterizes the spread of the middle half of a distribution, between the 25th and 75th percentiles.

Temporal variability can be analyzed at various timescales (Bengulescu et al. 2018). Similarly, spatial variability is also a function of spatial scale. These quantitative aspects are detailed in Section 6.4. Finally, Sections 6.5 and 6.6 discuss other aspects of temporal variability, namely the practical importance of obtaining synthetic data at high temporal resolution and the impact of variability on solar energy production, respectively.

In addition to its temporal and spatial aspects, the variability in the solar resource is also dependent on the irradiance component under scrutiny. It is typically different for direct normal irradiance (DNI), global horizontal irradiance (GHI), and global tilted irradiance (GTI) because the direct component varies much more than the diffuse component at all temporal or spatial scales. As a result, the term "variability" must be specified precisely as it relates to both the analyzed period (e.g., yearly variability of daily GHI, long-term variability of DNI) and a given geographic area (e.g., spatial variability of DNI over an area of 50 by 50 km), thus resulting in the necessity of a detailed definition (e.g., spatial variability of daily GTI over an area of 4 by 4 km).

6.2 Temporal Variability

Solar radiation is variable at widely different timescales, from quasi-instantaneous to multidecadal. This variability is caused by weather influences at scales up to ≈10 years and climatic or other influences at longer timescales. More details on the causes of variability at different scales are given in the following subsection.

6.2.1 Very Short Timescale

Over periods of ≈1 second to ≈1 hour, the main cause of variability is the passage of clouds and, thus, the alternance of sunny and cloudy periods. A typical situation is that of scattered cumulus clouds with a blue-sky background. The passage of each cloud obscuring the sun's disc generates a ramp, alternatively up and down. When the sun's disc is completely obscured by a thick cloud, direct normal irradiance (DNI) reduces to 0, whereas the diffuse radiation field does not change much, so global horizontal irradiance (GHI) becomes small but not 0. The ramping process is sharp and strongly affects the immediate photovoltaic (PV) output locally (Kreuwel et al. 2020; Lappalainen and Valkealahti 2017; Lave et al. 2015), but is typically attenuated when considering a large area because of the spatial smoothing and aggregation effects (Ellis et al. 2021; Hoff and Perez 2012). An extreme case of ramping involves multiple cloud layers or complex sun-cloud geometries that result in the cloud enhancement phenomenon (sometimes referred to as "overirradiance"), during which GHI can reach extremely high values (even exceeding their extraterrestrial counterpart by a substantial margin) over a period of up to a few minutes (Cordero et al. 2023; Gueymard 2017). The sudden change in GHI and its large excursion in magnitude make it difficult to obtain accurate measurements, depending in large part on the time constant of the radiometer (Gueymard 2017; Martins et al. 2022). These occurrences have been found relatively frequently under a variety of climates (do Nascimento et al. 2019; Inman et al. 2016; Kreuwel et al. 2020; Yordanov et al. 2015) and have potentially significant impacts on the design, operation, and safety of PV inverters (Allen and Hobbs 2022; Burger and Rüther 2006; Chen et al. 2013; Luoma et al. 2012). Just like with the ramping

phenomenon, cloud enhancement events are smoothed out when considering their average effect over a large area (Järvelä et al. 2020).

6.2.2 Intra-Daily Timescale

During daylight periods, solar irradiance is determined in large part by the sun geometry, the position of which can be calculated accurately, including in the distant future. For typical solar applications, it is thus possible to estimate the variation in the top-of-atmosphere irradiance with a high degree of precision. Using appropriate radiation models and high-quality atmospheric inputs (see Chapter 7), it is also possible to estimate the clear-sky surface irradiance with reasonable accuracy at various temporal and spatial timescales. Apart from sun geometry, which only induces smooth and predictable variations in surface irradiance, rapid changes in atmospheric constituents are the other relevant source of solar irradiance variability at intra-daily or longer timescales. Obviously, temporal variations in cloudiness represent the main cause of that variability, which is difficult to resolve with models. Additionally, abrupt variations in irradiance can be caused by the passage of thick smoke or dust clouds, but these are relatively infrequent events, although some specific regions can be more prone to such events. In general, sun geometry combines with the characteristics of the local cloud field at any instant to determine the solar irradiance variability.

6.2.3 Monthly and Seasonal Timescales

In addition to the expected progressive variations in sun geometry, weather and climatological patterns typically affect the solar resource on a monthly basis. For instance, in temperate climates, summer is typically less cloudy than winter, while the opposite can be true over semitropical areas. Moreover, close to the equator, the alternance of dry and wet periods is driven by the annual variation between south and north of the Intertropical Convergence Zone (ITCZ), which results in large spatiotemporal variations in the radiation field (Marie-Joseph et al. 2013; Vindel et al. 2020). Over the tropical Indian Ocean and Pacific regions, an approximately periodic variation pattern, referred to as the Madden-Julian Oscillation (Madden and Julian 1971), also moves from west to east every 30–60 days. In regions around the North Atlantic Ocean, the variability patterns on monthly and subseasonal timescales are of a chaotic nature, and are, at present, unpredictable.

6.2.4 Interannual Timescale

At timescales longer than about a year, various weather and/or climate patterns interact and typically have a chaotic impact on atmospheric conditions and ultimately on the surface irradiance and the solar resource. Various cycles have been detected and studied for decades, as the next subsections discuss in reasonable detail. Nevertheless, it is always difficult to predict how these cycles will continue to interact during the next few decades. As mentioned in Chapter 2, the ≈11-year sun cycle also has direct impact on all forms of solar irradiance, but its magnitude is typically much lower than the uncertainty of usual radiometric measurements. This impact can be neglected in practice.

6.2.4.1 Cloudiness Variability

Some years might be cloudier than others because of natural variations in weather- or climate-induced phenomena, yielding interannual variations in the solar resource. These are important to consider because they ultimately determine the variations in the annual production of any solar

power plant, which ultimately determines its yield—a key performance indicator. The two major climate components of interannual variability are the El Niño-Southern Oscillation (ENSO) and the North Atlantic Oscillation (NAO). Both directly affect cloudiness, and thus the solar resource, with significant spatial and seasonal underpinnings (Bloomfield et al. 2022; Correia et al. 2020; Laguarda et al. 2020; McFarlane et al. 2013; Murari et al. 2020; Pozo-Vazquez et al. 2011). ENSO is characterized by the succession of warmer (El Niño) and colder (La Niña) periods of ocean temperatures over the equatorial Pacific (Figure 6-1). Each period typically lasts 1–4 years, but La Niña periods are typically longer than El Niño's. The El Niño years tend to bring more moisture to various land areas (particularly over North and Central America), and therefore more cloudiness and precipitation, whereas Australia can be affected by drier weather. As a result, it has been shown that, for instance, the response of DNI to the ENSO intensity in the southwestern United States is detectable, and ultimately impacts the operation and power production of concentrating solar power (CSP) systems (Mohammadi and Goudarzi 2018). The strength of the ENSO cycle is characterized by the Oceanic Niño Index (ONI),[36] which represents the 3-month running mean of sea surface temperature anomalies in the ENSO region (5ºN–5ºS, 120º–170ºW), based on 30-year base periods updated every 5 years. A time series of ONI during the last three decades appears in Figure 6-2.

ENSO is also related to the Madden-Julian Oscillation. Because of this direct link, and of ENSO's larger scale, it is more predictable. For instance, when ENSO goes into a strong positive phase during a specific year, it often remains in this so-called El Niño phase the following year.

[36] See https://origin.cpc.ncep.noaa.gov/products/analysis_monitoring/ensostuff/ONI_v5.php.

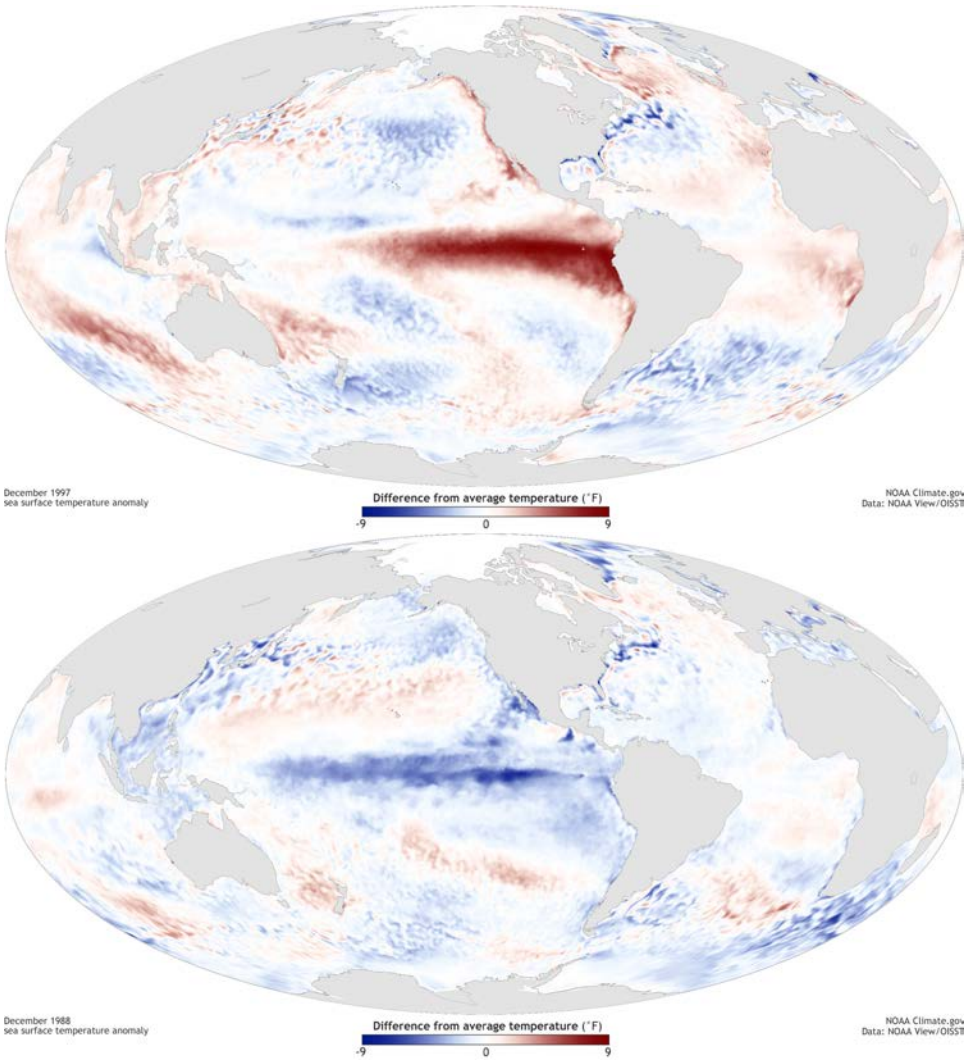

Figure 6-1. Temperature anomaly over the oceans in Dec. 1997 during an El Niño period (top) and in Dec. 1988 during a La Niña period (bottom)

Image from NOAA

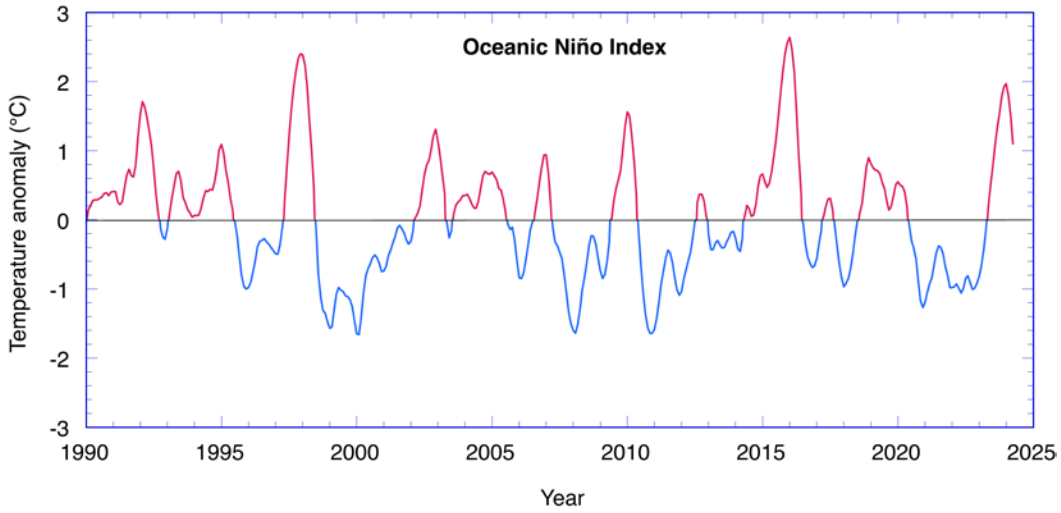

Figure 6-2. Time series of ONI since 1990.

The red and blue curves indicate El Niño and La Niña periods, respectively.

Image by C. Gueymard from NCEP-NOAA data

NAO is a climatic pattern whose empirical discovery dates back several centuries ago. Whereas ENSO is essentially a cycle that is powered by the warm temperatures of the Pacific Ocean, NAO affects climate variability throughout the Arctic and northern Atlantic, affecting a large part of Europe, up to coastal regions of Siberia. NAO's amplitude peaks during winter because of the strong activity in the atmosphere, typically resulting in substantial cloudiness during that season, particularly from December through March. Like with ENSO, an NAO index exists, but has various flavors depending on the source and season used for the data (Hurrell et al. 2003). The connection between the NAO index and GHI has been studied over various areas, including the British Isles (Colantuono et al. 2014; Correia et al. 2020), the Mediterranean (Pozo-Vazquez et al. 2011), and Europe (Chiacchio and Wild 2010). Although ENSO and NAO are two different mechanisms that follow different cycles, their interaction can lead to remarkable anomalies, depending on the intensity of their respective phases (King et al. 2023; Mu et al. 2022; Wu and Zhang 2015).

In addition to ENSO and NAO, two somewhat lesser-known cycles are the Pacific Decadal Oscillation (PDO) and the Atlantic Multidecadal Oscillation (AMO), whose impacts on cloudiness have been investigated by (Schwartz et al. 2014) and (Brown et al. 2016; Mann et al. 1995), respectively. Recently, however, the underlying mechanism behind the AMO cycle has been scrutinized again, with the conclusion that it might not exist as an actual cycle per se, but could be the result of volcanic forcing (Mann et al. 2021). Current research in climate science attempts to separate the various effects (on cloudiness and the irradiance incident at the surface, most importantly) induced by internal climate variability from those induced by climate forcing signals (Chtirkova et al. 2022; Folini et al. 2017; Lehner and Deser 2023).

6.2.4.2 Impacts of Volcanic Aerosols

Debris from volcanic eruptions affect the solar resource over large areas (at the country, continental, or global scale) and have radiative effects that can last up to a few years, depending on the eruption's strength and location. The main impact of volcanic aerosols on the solar resource arises when significant amounts of sulfur dioxide (SO_2) gas are ejected into the stably

stratified stratosphere. Smaller volcanic eruptions do not reach the stratosphere, and thus they have only short-lived, local effects. SO_2 reacts with water vapor and is converted into droplets of sulfuric acid that scatter solar irradiance very efficiently. These particles increase the total aerosol optical depth (AOD) and affect DNI more than GHI. The AOD of the droplets decreases exponentially with a decay time of approximately 1 year (Crowley and Unterman 2013; Robock 2000). Overall, the droplets can stay in suspension for several years after an eruption. For instance, El Chichón (1982) and Pinatubo (1991) impacted the solar resource globally for up to ≈3 years. Figure 6-3 shows a time series of the stratospheric AOD at 550 nm induced by various volcanic eruptions since 1850.

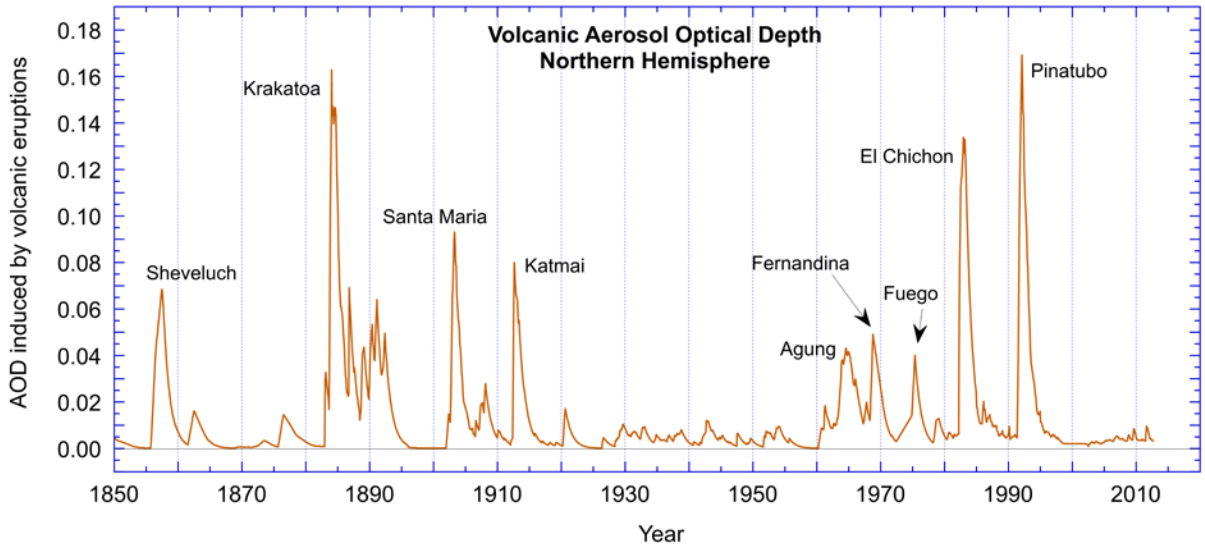

Figure 6-3 Estimated stratospheric AOD at 550 nm of volcanic aerosols over the Northern Hemisphere induced by eruptions, 1850–2012

Image by C. Gueymard, based on National Aeronautics and Space Administration Goddard Institute for Space Studies data

Once they have reached the stratosphere, volcanic aerosols spread relatively rapidly (for instance, both the El Chichón and Pinatubo aerosol clouds circled the globe in 3 weeks), meaning their impacts can be felt over a large part of the planet, with some regional variations in intensity. This intensity can be quantified by the atmospheric transmission factor (ATF), introduced by (Ellis and Pueschel 1971). The ATF is routinely calculated from the DNI measurements that have been continuously carried out at the Mauna Loa observatory (MLO, located on the big island of Hawaii) since 1958. The daily ATF has been studied by (Dutton et al. 1985) using this definition:

$$\mathrm{ATF} = \frac{1}{3}\sum_{m=3}^{m=5}\frac{E_{bn}(m)}{E_{bn}(m-1)} \qquad (6\text{-}1)$$

where $E_{bn}(m)$ is the measured DNI at airmass m. Because of this definition, ATF is not a function of m, contrary to the direct transmittance, K_n, discussed in other chapters. Just like K_n, however, ATF is found to be a direct inverse function of AOD (the higher the AOD, the lower the ATF), making it strongly sensitive to variations in volcanic aerosols. The monthly evolution of ATF at Mauna Loa appears in Figure 6-4, based on National Oceanic and Atmospheric

Administration (NOAA) measurements, clearly showing the strong impact from El Chichón and Pinatubo. Interestingly, El Chichón had a measurably stronger attenuation effect than Pinatubo at MLO, though Figure 6-3 suggests otherwise, since Pinatubo's AOD peaked higher. This is possibly because the data behind the latter figure are only estimates for the whole Northern Hemisphere, whereas Figure 6-4 is based on precise data for a single site at low latitude. In contrast to the significant effects of major eruptions, the natural background ATF is only affected by very small seasonal or long-term variability. This is because MLO is an isolated high-elevation site with no significant local sources of aerosols and only rare or small impacts from transoceanic dust or pollution plumes.

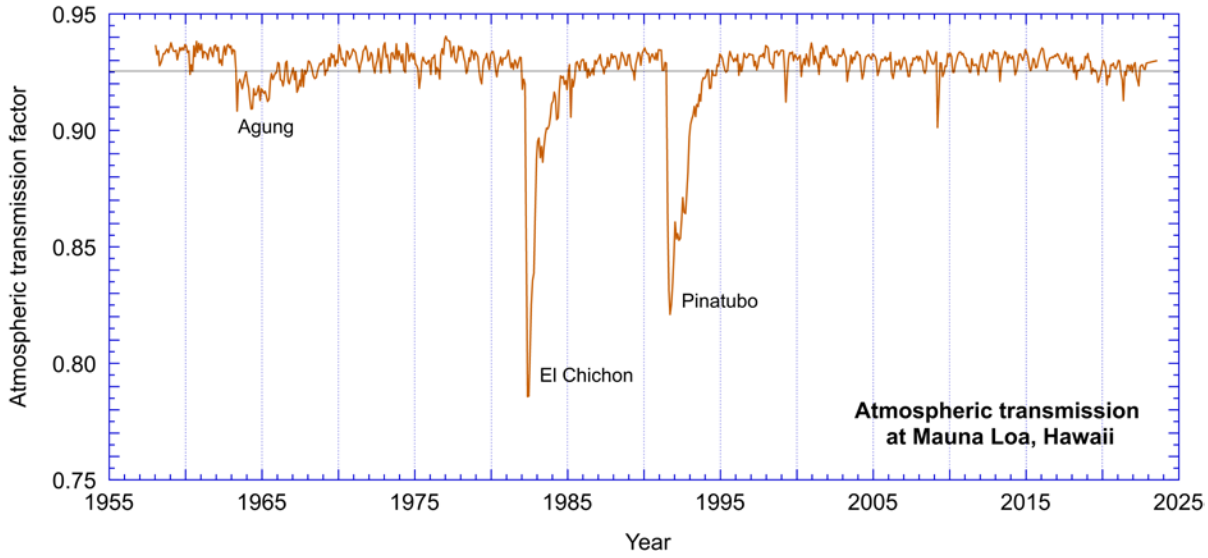

Figure 6-4. ATF at Mauna Loa, Hawaii, as impacted by large volcanic eruptions

The thin horizontal line indicates the long-term average (0.925).

Image by C. Gueymard, based on NOAA data

Most solar resource datasets do not extend far enough into the past to cover any large volcanic event. One exception is the National Solar Radiation Database (NSRDB) (Wilcox et al. 2007), whose data can be used to estimate the effect this eruption had on the solar resource (Vignola et al. 2013). The reduction in DNI reached up to ≈20% at midlatitude sites in the Northern Hemisphere a few months after the eruption, which in turn had an even larger negative impact on the electricity production of CSP plants (Michalsky et al. 1994).

The risk of major volcanic eruptions with a worldwide effect has been estimated from analysis of ice core samples from the thickest parts of the Antarctic and Greenland ice sheets. Ice rarely or never melts there, so the accumulated snow is covered and compressed into layers of ice over time. These layers can be counted like tree rings and analyzed chemically—including the amount of sulfuric acid that has been deposited from year to year. The mass of sulfuric acid deposited depends linearly on the sulfuric acid mass load in the atmosphere. Analyzing layers 2,000 years back in time, it has been found that the likelihood of volcanic eruptions causing high concentrations of sulfuric acid causing a global average AOD of 0.1 or higher is 16.5% per decade. Similarly, for AODs of 0.2 of higher, the likelihood is 8% per decade (Sigl et al. 2015). For comparison, these authors estimated that the Pinatubo eruption had a maximum global average AOD of 0.18.

Way before irradiance or aerosol measurements began, the Tambora eruption of 1815 injected a mass of sulfuric acid into the stratosphere that was estimated to be more than four times that of Pinatubo. For such cases, the paleoclimatic studies suggest that the linear relationship between the mass load of stratospheric sulfate and its AOD does not apply anymore. Thus, the AOD for Tambora has been estimated to be only 0.45. More generally, the relationship between the stratospheric AOD from eruptions larger than Pinatubo and the corresponding stratospheric mass load of sulfuric acid is estimated to follow a two-thirds power law.

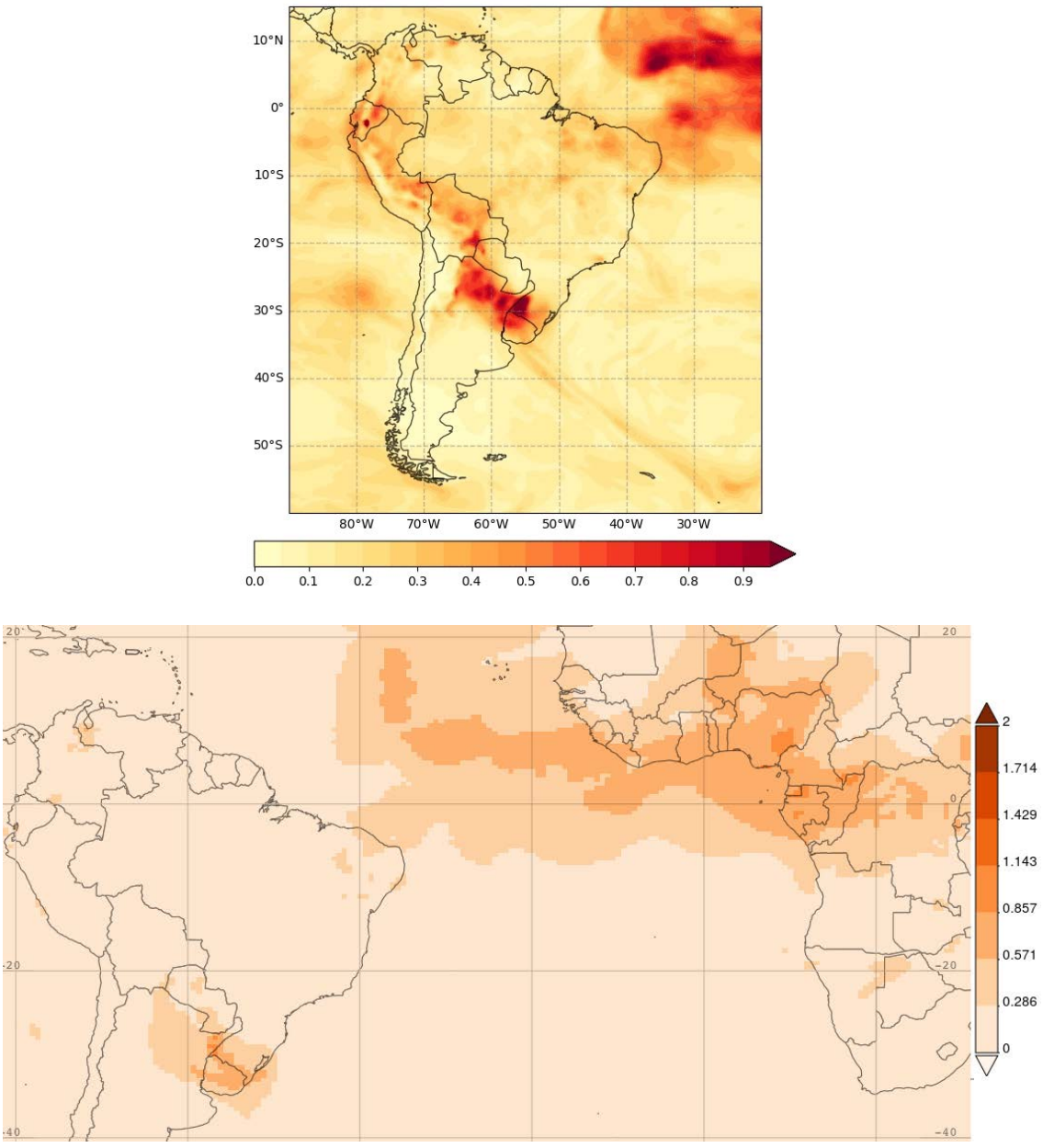

Figure 6-5. Total AOD on Feb. 12, 2022, over South America, as predicted by CAMS (top) and over South America and western Africa by MERRA-2 (bottom)

Images by ECMWF-Copernicus and NASA

6.2.4.3 Impacts of Smoke Aerosols

Wildfires occur in many regions of the globe, although tropical regions are typically more prone to them. These events release smoke plumes that can travel vast distances (Lee et al. 2005; Rahim et al. 2017; Rogers and Bowman 2001), as can be visualized in Figure 6-5 for an exemplary case on a day when wildfires occurred in both South America and western Africa. Here, the total AOD (mostly smoke) is predicted by two different reanalyses, the Copernicus Atmosphere Monitoring Service (CAMS) from the European Centre for Medium-Range Weather Forecasts (ECMWF) and NASA's Modern-Era Retrospective analysis for Research and Applications, Version 2 (MERRA-2), which both assimilate aerosol observations from various satellites to improve the modeled predictions. Along the smoke plumes' path, solar radiation is significantly attenuated because their AOD is large (often >1), which can directly impact the solar resource and thus solar production during many days (Casagrande et al. 2021; Herman-Czezuch et al. 2022; Isaza et al. 2023; Liu et al. 2014; Nobre et al. 2016; Perry and Troccoli 2015; Rosário et al. 2013), in addition to their detrimental effect on air quality. During the past decades, various studies have identified trends in wildfires, but they do not always agree on the trend sign (either positive or negative), depending on region and objective quantity being analyzed (e.g., number of fires, particle emissions, or burned areas); see, for example, (Andela et al. 2017; Dennison et al. 2014; Doerr and Santín 2016; Fan et al. 2023). It is thus difficult to have a clear picture at continental or global scale.

6.2.4.4 Impacts of Dust Aerosols

Similar to the impacts of wildfires, dust storms frequently occur over many deserts or arid areas and emit considerable quantities of dust aerosols. Just like smoke clouds, dust clouds can reach altitudes of a few kilometers above the ground and can be transported over long distances (Aldhaif et al. 2020; Husar et al. 2001), adding dust AODs that are frequently more than 1.0—and can even exceed 5.0 in the source regions—along the way (Bencherif et al. 2022; Gkikas et al. 2019; Gueymard et al. 2017; Logothetis et al. 2021; Xia et al. 2021). For instance, Europe and the Mediterranean basin are often impacted by severe dust intrusions from the Sahara (Cuevas-Agulló et al. 2024). Additionally, once deposited at ground level, this dust becomes a major source of soiling for all types of solar collectors (Fountoukis et al. 2018; Javed et al. 2021); see also Chapter 5. The impacts of dust clouds on the temporary depletion of the incident irradiance and the resulting decrease in solar production are well documented (Al-Rasheedi et al. 2020; Cañadillas-Ramallo et al. 2022; Dabou et al. 2016; Rieger et al. 2017). Estimates of the historical trends in dust storm frequency and strength depend on many factors and do vary depending on region and method of analysis (Alizadeh-Choobari et al. 2016; An et al. 2018; Guo et al. 2018; Logothetis et al. 2021; Ravi Kumar et al. 2019; Shaheen et al. 2023; Shi et al. 2020; Sun et al. 2020; Wang et al. 2017; Xi 2021).

Considering the direct impacts of dust clouds on the immediate loss of production by solar collectors and their substantial soiling, which might require a rapid cleaning to avoid further losses, an interesting resource is the ensemble forecast of dust AOD and dust surface concentrations available from the Sand and Dust Storm Warning Advisory and Assessment System (SDS-WAS) of the World Meteorological Organization (WMO). This system relies on a few regional centers to prepare publicly accessible forecasts of dust AOD: the Northern Africa-

Middle East-Europe (NA-ME-E) Regional Center,[37] the Asia Regional Center,[38] and the Pan-American Regional Center.[39] An example of visualization offered by the NA-ME-E Regional Center is shown in Figure 6-6 for both dust AOD and dust surface concentration, obtained from an ensemble currently counting nine different models. For each quantity and forecast issued every 6 hours with a forecast horizon of 72 hours, four maps provide the median, mean, standard deviation, and range at 0.5 by 0.5° resolution. For conciseness, only the mean of each quantity obtained by a single ensemble forecast is shown in Figure 6-6.

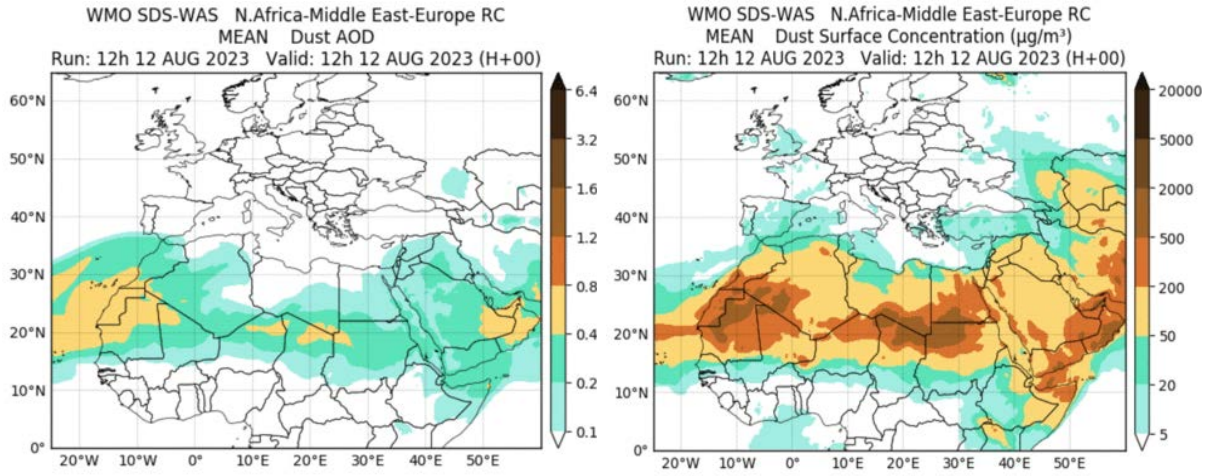

Figure 6-6. Forecasts of mean dust AOD and mean dust surface concentration issued on Feb. 12, 2022

Image by SDS-WAS NA-ME-E Regional Center

6.2.4.5 Impacts of Pollution Aerosols

Pollution aerosols are typically concentrated over large urban and industrial areas, but they can be transported far away, just like other types of aerosols (Chin et al. 2007). Highly polluted areas, such as megacities, are characterized by AODs typically above 0.5, and even above 1.0 in the worst cases (Guo et al. 2021; Li 2020; Papachristopoulou et al. 2022). The effects of pollution aerosols on the solar resource have been studied for various conditions and radiation components, including spectral irradiance (Ye et al. 2021). In turn, a lower incident irradiance results in significant production losses for solar systems located in urban areas (Li et al. 2017; Zhou et al. 2021; Zhang et al. 2020). Conversely, some studies have attempted to quantify the technical and societal benefits that hypothetical clean-air policy measures could have on solar energy production (Ghosh et al. 2022; Zhang et al. 2023). Interestingly, the positive impacts of China's clean-air action plan (implemented in 2013) on lowering AOD and improving PV production have been documented (Shi et al. 2021; Zhang et al. 2023). More generally, country-wide air quality measures have been found to improve the trend in surface irradiance, referred to as brightening, as discussed further in Section 6.2.5.2.

[37] See https://sds-was.aemet.es/forecast-products/dust-forecasts/ensemble-forecast.
[38] See http://www.asdf-bj.net/.
[39] See http://sds-was.cimh.edu.bb/.

6.2.5 Multidecadal Timescale and Long-Term Trends

Multidecadal trends must be considered to properly carry out the solar resource assessment of large solar projects, which must be viable many years into the future. An accurate solar resource assessment with the lowest possible bias and uncertainty is critical because this ultimately conditions design, financing, and long-term viability. The next subsections provide background information about the link between the long-term irradiance variability at a specific site and the evaluation of its solar resource.

6.2.5.1 Drivers of the Future Solar Resource

Solar power plants are expected to last many decades. At the financing stage, costs and revenue projections must be as accurate as possible over a period of typically 15–20 years. Over such a period, climatic trends can affect the solar resource. Thus, research abounds on the topic of evaluating trends in the radiative climate of past decades (Dutton et al. 2006; Sanchez-Lorenzo et al. 2015; Wang et al. 2020; Jiang et al. 2023; Müller et al. 2014; Stamatis et al. 2023) and predicting its future (Gil et al. 2019; Ruosteenoja et al. 2019; Soares et al. 2019), either globally or over various regions. In particular, the impacts on the future climate of various particle emission scenarios and radiative forcing assumptions are typically studied by running various climate models, including those from the Coupled Model Intercomparison Project Phase 5 (CMIP5) or Phase 6 (CMIP6). Because wildly different scenarios regarding the main drivers—most particularly aerosol and gaseous emissions—are still considered possible, these impacts also vary largely, and the future radiative climate is still uncertain. Among the numerous variables these models attempt to predict, the incident irradiance, cloud fraction, and temperature are key elements for evaluating the solar resource of the future and its impact on solar systems (Gaetani et al. 2014; Gutiérrez et al. 2020; He et al. 2023; Kozarcanin et al. 2019; Wild et al. 2015; Zhao et al. 2020; Zou et al. 2019). Moreover, indirect effects of the generally rising temperatures can be expected to result in an increase in wildfires, at least over those regions that become drier (Sarangi et al. 2023; Turco et al. 2018; Wang et al. 2023). In turn, those fires create extended smoke plumes that decrease the solar resource, as discussed in Section 6.2.4.3.

A similar situation can be expected for plumes caused by dust storms, albeit with opposite trends depending on region: potentially more emissions from North Africa or the Middle East vs. less emissions from Asia (Zhao et al. 2023). In parallel, long-term trends in pollutant emissions are one major cause for the so-called dimming and brightening phenomena (i.e., decreasing or increasing trend in irradiation, respectively), which are strongly dependent on the evolution of air quality measures at country or continental level (Antuña-Marrero et al. 2019; Cusworth et al. 2017; Hatzianastassiou et al. 2020; Manara et al. 2016; Tanaka et al. 2016; Wild et al. 2021; Yang et al. 2019). These phenomena are further discussed in Section 6.2.5.2. Aerosols also cause indirect effects because they create the necessary conditions for clouds to develop. At present, the effects of sulfate aerosols (mostly caused by pollution) on cloud cover, cloud lifetime, and cloud transmittance are believed to dominate these indirect phenomena (IPCC 2023). The net effect is that more sulfate pollution causes less solar irradiance, and vice versa, reduced sulfate pollution causes more solar irradiance.

Interestingly, the future climate might have differing impacts on the short-term irradiance variability, depending on climatic region. In the case of Australia, for example, the use of regional climate model projections under a high-emissions scenario resulted in a slight increase

in the solar resource with more frequent clear periods, and thus a decrease in short-term variability (Poddar et al. 2023). More investigations of this kind would be needed to obtain a complete picture at global scale.

Finally, the incident irradiance is also affected by stratospheric aerosols. These are normally in too low concentrations to affect the resource, but volcanic activity can change this situation in a dramatic and unpredictable way, as discussed further in Section 6.2.4.2. A related source of concern comes from the experiments in geoengineering that have started to be undertaken, whereby various kinds of particles are injected into the stratosphere. These intend to purposefully decrease the solar flux to mitigate the impacts of climate change (*Climate Intervention* 2015; Kravitz et al. 2015; Richter et al. 2022; Weisenstein et al. 2015). It is currently not clear whether or when these experiments will increase in scope. If they are generalized, they could seriously impact the global solar energy production. This appears paradoxical, as the latter is viewed as a way to combat climate change by displacing carbon-emitting power plants.

6.2.5.2 Dimming and Brightening

The dimming and brightening phenomena are highly relevant to the solar community because of their direct impact on many calculations in the practice of solar resource assessments (Müller et al. 2014; Wild et al. 2015). In general, the solar resource is primarily (but far from completely) characterized by a single number, which is the average irradiation (GHI, GTI, or DNI, depending on the type of solar system) over a long-term period. The discussion that follows underlines two issues that many solar analysts face in their daily work.

The first practical issue is selecting the most-appropriate duration for the reference long-term period. To that effect, it is useful to analyze some long-term records of measured GHI that originate from many stations in the world. Such records (at monthly and annual temporal resolution) can be obtained from the Global Energy Balance Archive (GEBA) database[40] (Wild et al. 2017). The annual GHI anomaly (i.e., the percentage of difference between the mean GHI of any year and the site's long-term mean) for the two stations having the longest GEBA records appears in Figure 6-7. Over their respective measurement periods, the interannual variability appears significant. Moreover, the linear trends are slightly positive, thus indicating a barely perceptible brightening effect. The upward trend is, however, much steeper since the mid-1980s at those two sites. Shorter records appear in Figure 6-8 for six other stations of interest because of their differing overall trends, from negative to neutral to positive.

[40] See http://www.geba.ethz.ch.

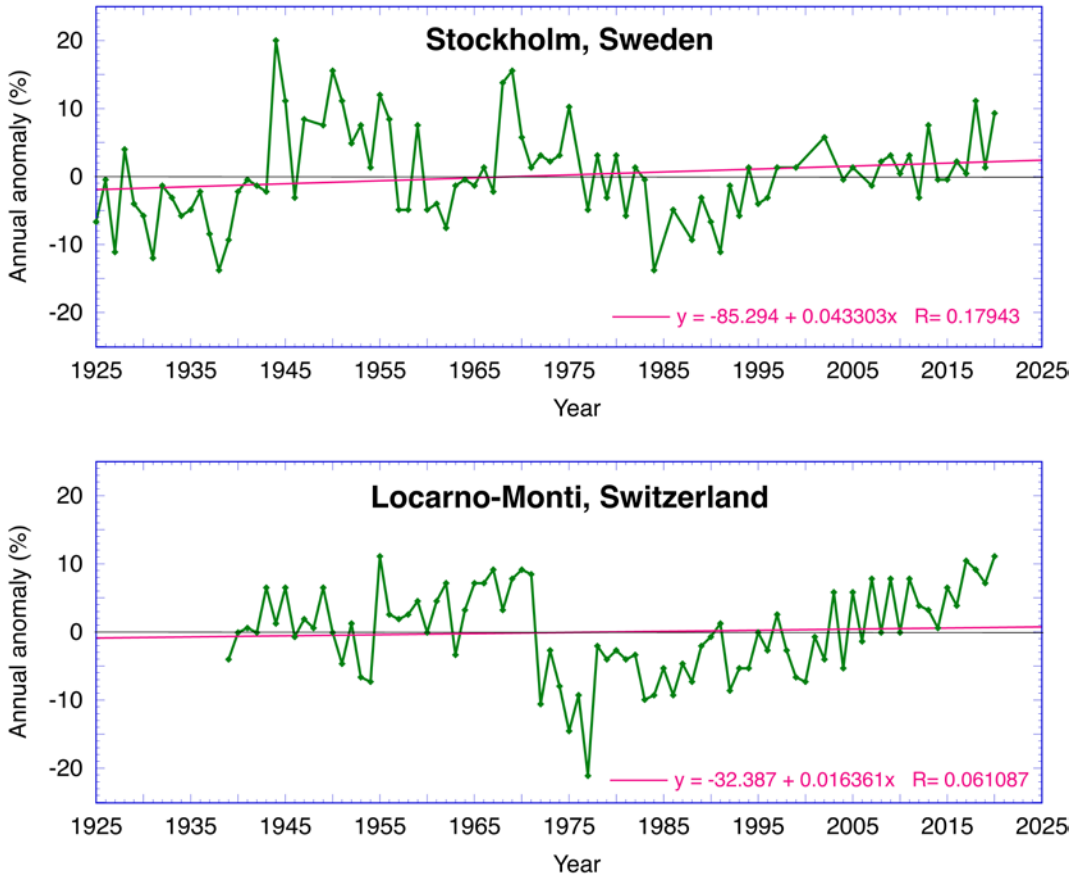

Figure 6-7. Mean annual anomaly (relative to the long-term mean) and linear trend of GHI measured at Stockholm, Sweden, and Locarno-Monti, Switzerland

Image by C. Gueymard, based on data from GEBA

The comparison of these different types of trends during the last decades, and even during the last few years, clearly indicates that the strength and sign of GHI trends vary significantly over time and space (This is also more the case for GTI, and even a lot more the case for DNI because the latter and, to a lesser extent, GTI, are much more sensitive than GHI to the effects of cloudiness and aerosols.). Thus, this first issue cannot be addressed easily. Depending on region, it might be better to use the last 10, 15, or 20 years to obtain a meaningful solar resource. It could even be tempting to use only the last 5 years, but then some critical information about the interannual variability would be lost. This first issue is particularly important over areas where strong trends have occurred during the last 10–20 years, like brightening over parts of Europe, as thoroughly discussed with regard to the yield of monitored PV installations in Germany and Spain (Müller et al. 2015).

The second practical issue is properly extrapolating the satellite-derived data already off-hand into the future, assuming the current solar resource is accurately determined from an appropriate time series of that data source and that it is of high quality. No extrapolation is obviously necessary if there is no reason to suspect that a positive or negative trend will occur during the next one or two decades. The information in Sections 6.2.4 and 6.2.5.1, however, suggests that, depending on region, some past trends are likely to continue or, conversely, to be reversed in the near future. These two practical issues cannot be resolved satisfactorily with current knowledge

and thus must be treated as additional sources of uncertainty regarding the actual solar resource during the solar project's lifetime, as discussed in Chapter 10.

6.2.5.3 Reliability of Historical Measurements

Some of the interannual fluctuations shown in Figure 6-7 and Figure 6-8 appear unrealistically large, which suggests that the time series might not be homogenous. For instance, many changes of instrument type or make and model must have taken place because the first "modern" pyranometers started to be deployed at meteorological stations in the early 1960s. Moreover, the methods of calibration, maintenance, cleaning, recording, data processing, and data-gap filling have changed over time, sometimes drastically (e.g., moving from voltmeters to strip-chart recorders to mechanical integrators to digital dataloggers). When considering only the type and specification of modern instruments, various collocated thermopile pyranometers might generate mean annual GHI results with sizeable differences, even if all instruments are calibrated and maintained the same way (Gueymard and Myers 2009).

Considering the limited availability of long-term time series of GHI and DNI data based on consistent, decades-long, high-quality measurements, it is tempting to use the modeled data provided by one of two prominent reanalyses, namely the ECMWF ReAnalysis v5 (ERA5) from ECMWF and MERRA-2 from NASA. Their features are further discussed in Chapter 7. ERA5 evaluates the hourly global horizontal and direct horizontal irradiations since 1940 for both clear-sky and all-sky conditions. One important caveat in the present context, however, is that the underlying calculations are based on an aerosol climatology (i.e., long-term monthly averages). Hence, the calculated irradiations cannot properly detect any dimming or brightening trend that would be caused directly by aerosols. It can thus be anticipated that any apparent GHI trend in the ERA5 predictions is caused solely by changes in cloud regime and is only partially representative of the actual trend that would be detected when using high-quality measurement time series. In contrast, MERRA-2's hourly predictions of the clear-sky and all-sky GHI are based on coincident aerosol predictions since 1980—so, to the extent that these aerosol predictions are unbiased, it can be anticipated that the aerosol-induced trends are better reproduced by MERRA-2 than by ERA5. MERRA-2's caveat, however, is that its GHI modeling suffers from systematic errors caused by its usage of an incorrect sun position algorithm that ignores the equation of time, as mentioned in (Gueymard 2022; Salazar et al. 2020). This induces an often-substantial daily variable error in GHI, depending on month and location. For these reasons, any trend possibly detected in ERA5 or MERRA-2 GHI datasets might not be realistic.

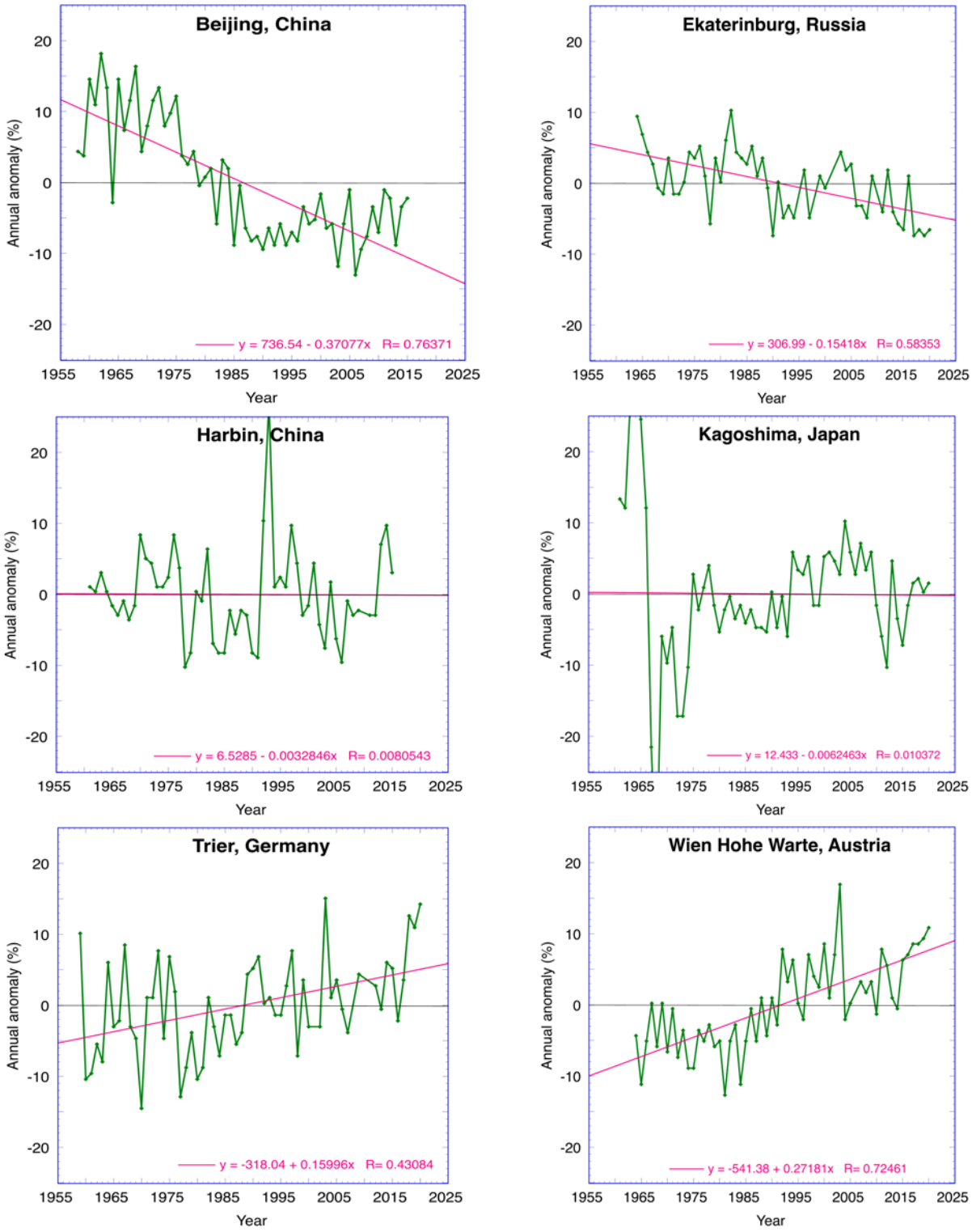

Figure 6-8. Mean annual anomaly (relative to the long-term mean) and linear trend of GHI measured at six stations

Image by C. Gueymard, based on data from GEBA

6.3 Spatial Variability

At any given instant, the solar resource might vary substantially between nearby locations. The main underlying reason for this is the ever-changing cloud field. At daily or monthly time frames, however, these effects compensate each other, so that other causes of spatial inhomogeneity can be detected. At those timescales, various factors can contribute to create relatively significant changes in incident irradiance over short distances. These are typically of an orographic nature, such as elevation, terrain complexity, urbanization, or presence of large water bodies. In turn, these factors directly affect the aerosol and water vapor columns, and can also modify the cloud regime by inducing, for example, local frequent fog. These local or regional effects tend to introduce uncertainty when attempting to extrapolate solar resource data, sometimes over short distances. Remarkably, such small-scale variability effects have been demonstrated experimentally using dense radiometric networks (Madhavan et al. 2016; Perez-Astudillo and Bachour 2015; Sun et al. 2022).

A study conducted by the Management and Exploitation of Solar Resource Knowledge (MESoR) project in Europe (Beyer et al. 2009) provided insights into the spatial distribution of irradiance variability by cross-comparing five different data sources. Inherent differences were found between databases based on in situ (ground) measurement interpolations and those based on satellite observations as well as in the methods used to process such data. The databases relying on the interpolation of ground observations were sensitive to the quality and completeness of ground measurements and to the density of the measurement network. Terrain effects (e.g., shadowing by surrounding terrain) played a role in solar radiation modeling over hilly and mountainous regions. The spatial resolution of the input data and the selected digital elevation model were identified as factors with direct impact on the accuracy of the estimates. Finally, to compare modeled data properly, particularly under clear-sky conditions, it is important to consider how each model deals with cloud identification and AOD characterization (Ruiz-Arias et al. 2016). This is particularly important for DNI because of its higher sensitivity to AOD than GHI (Gueymard 2012; Ruiz-Arias et al. 2019).

The quality and spatial detail of satellite-derived or numerical databases are determined by the specific input data used in the models. As can be expected, the main parameters describe the cloud properties and the optical transparency of the atmosphere in relation to aerosols and water vapor (Ruiz-Arias et al. 2016). Regarding DNI more specifically, AOD is the most important variable under clear-sky conditions (Gueymard 2019, 2003) (see also Chapters 3 and 7). (Cebecauer et al. 2011) provide a comprehensive and qualitative review of the different factors (including terrain) affecting the accuracy of DNI modeling. Overall, the literature on spatial variability is much less complete than that on temporal variability. Nevertheless, other aspects of spatial variability are described next, as well as some examples of results.

6.4 Evaluation of the Variability of the Solar Resource

Variability is a wide-ranging term that can characterize the solar resource in many ways, either from a spatial or temporal perspective. In the latter case, all temporal scales can be considered, depending on context, from subsecond to multiyear scales. Temporal variability, if well characterized for a climate region, can be useful to determining the suitability of a short-term dataset to produce valid long-term statistics. For instance, the term can be applied to the interannual

variability of the resource. Figure 6-9 shows the interannual variability in monthly DNI in Daggett, California, in terms of monthly average daily total irradiation.

As mentioned above, the long-term dispersion of the solar resource is often characterized by COV, which is the unitless ratio between the standard deviation and mean (Calif and Soubdhan 2016; Gueymard and Wilcox 2011; Habte et al. 2020):

$$\sigma_t = \sqrt{\left[\frac{1}{n}\sum_{i=1}^{i=n}\left(Yr_{irr_n} - \overline{Yr_{irr}}\right)^2\right]} \tag{6-2}$$

$$\text{COV} = \frac{\sigma_t}{\overline{Yr_{irr}}}. \tag{6-3}$$

where σ_t is the standard deviation, Yr_{irr_n} is the annual irradiance of the individual n years, and $\overline{Yr_{irr}}$ is the mean of irradiance of all years.

Long-term oscillations in GHI and DNI are also important because of the succession of periods known as "dimming" and "brightening" that affect both climate change and the extrapolation of the historical solar resource into the future, as discussed in Section 6.2.5.2. It is important to consider these sources of variability in the context of solar performance forecasting.

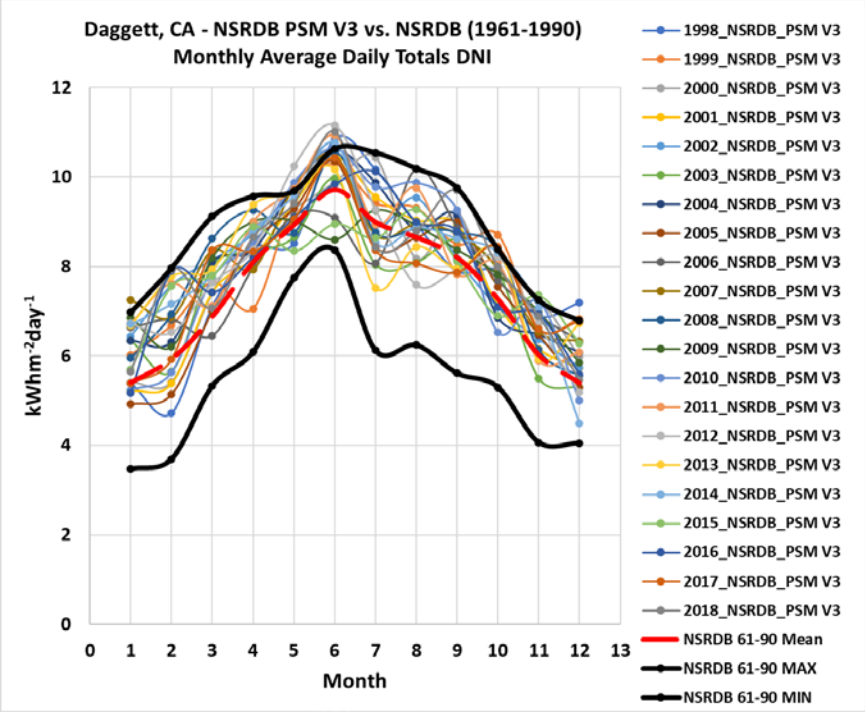

Figure 6-9. Example of direct-beam monthly average daily total (kWh/m^2) illustrating interannual and seasonal variability from 1961–2018 in Daggett, California

Image by NREL

The term variability is also used to describe the spatial variability of the resource in a climatological context. Spatial variability can help determine the applicability of a particular dataset for a nearby location, possibly saving the need for additional measurements. In this case,

variability characterizes microclimatic features and regional resource gradients. An example is provided in Figure 6-10, which shows the climatological GHI resource distribution over the Island of Oahu, Hawaii. Similarly, Figure 6-11 shows the spatial variability of DNI and GTI over 50-by-50-km areas throughout the United States in terms of COV (Gueymard and Wilcox 2011).[41]

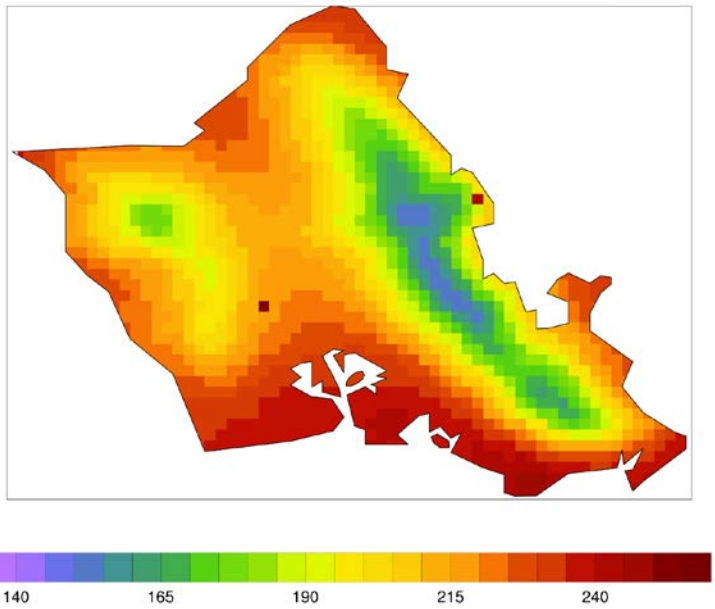

Figure 6-10. Example of microclimatic spatial variability for the Island of Oahu

The 1-km resolution map displays mean hourly GHI in W/m^2.

Image from SolarAnywhere V3.0 (2015)

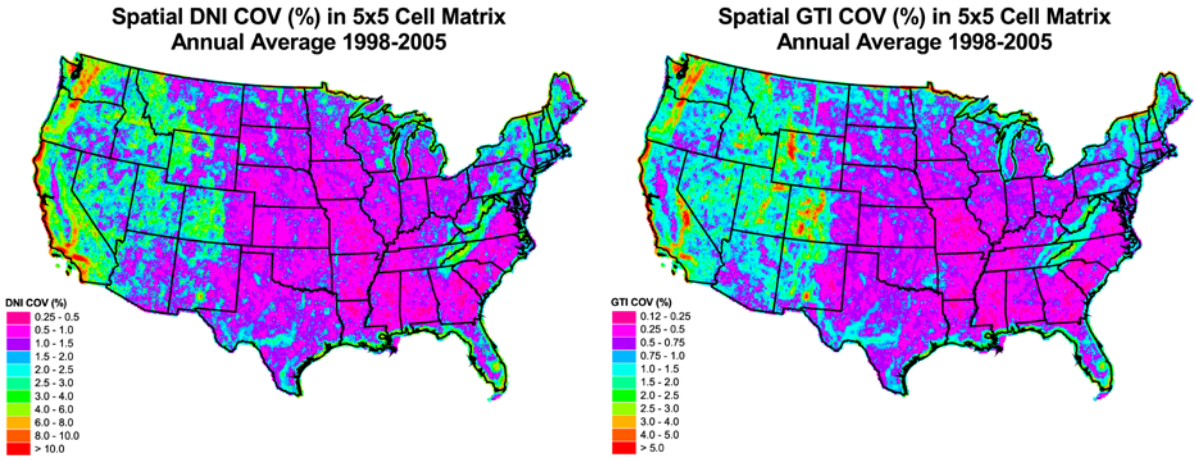

Figure 6-11. Spatial variability in (left) DNI and (right) GTI over the continental United States in percentage of COV

Images from NREL

[41] Such spatial and temporal variability maps are available at https://www.nrel.gov/grid/solar-resource/variability.html.

From a resource assessment perspective, the term variability is associated with the time/space impact of weather and the cycle of days and seasons on the output of solar systems. This output can vary from zero to full power and is outside the control of plant operators. Understanding the solar resource's variability is key to optimally integrating the power output of solar electric systems into electric grids. This is discussed further in Section 6.6 and Chapter 11.

Space/time variability has two causes: one cause is fully predictable and is the result of the apparent seasonal and daily motion of the sun in the sky and the Sun-Earth distance; and the other cause results from the motion of clouds and, to a lesser extent, of aerosols in relation to weather systems. It is useful to first consider the temporal and spatial scales involved and how they impact the available solar resource.

6.4.1 Temporal Scale

Beginning with an intuitive example (Figure 6-12), a single location on a partly cloudy day will experience a high degree of temporal variability because of changes in the sun's position and the motion of clouds; however, the solar energy accumulated during several days at that same location exhibits less variability. Variability in GHI becomes small as the temporal integration increases to 1 year and more, but that in DNI or even GTI can still be significant (Gueymard and Wilcox 2011). In addition, investigating intra-seasonal variability can provide insightful information. In some areas, for example, summers might exhibit less variability than winters if there are typically only a few cloudy days in summer and not-too-dissimilar numbers of cloudy and sunny days in winter. Adding or subtracting a sunny day during the summer does not significantly affect the monthly average in this case, contrary to what can happen in winter. In many temperate areas, on the other hand, low variability caused by consistently cloudy conditions is typical in winter, whereas a succession of clear and cloudy days is typical in summer (high variability).

Figure 6-13 shows a representation of interannual variability over the Americas, demonstrating some geographic dependence because of microclimate or long-term climatic fluctuations. Studies of GHI and DNI distributions in the United States show that GHI's interannual variability typically ranges from 2–6% in terms of COV, whereas the variability of DNI is between 5% and 15%, about twice as much (Gueymard and Wilcox 2011; Habte et al. 2020). A single year can deviate much more from the long-term average. (Gueymard and Wilcox 2009) analyzed the long-term data from four stations with continuous high-quality measurements spanning more than ≈25 years to examine how many individual years would be required to converge to the long-term mean and whether the interannual irradiance variability changes significantly from one site to another. Sorting the data from the most exceptional years (largest anomalies) to the most typical years (smallest anomalies), the results showed that, first, there is much lower interannual variability in GHI than in DNI. In the examined stations in the United States, GHI is almost always within ±5% of the true long-term mean after only 1 year of measurements (Figure 6-14). The situation is quite different for DNI. After only 1 year of measurements, the study showed that the estimate of the average DNI is no better than ±10–20% of the true long-term mean. Note, however, that the worst years were associated with strong volcanic activity, which significantly impacts DNI (see Section 6.2.4.2).

Another interesting question is whether it is likely that good years with high irradiation occur in groups or are independent from the previous year's irradiation. (Tomson et al. 2008) showed that the mean annual GHI in any year is virtually independent from that of the previous year.

6.4.2 Spatial Scale

Increasing the solar generation footprint from a single location to a region, and even to a continent, considerably reduces intermittency. Increasing this footprint to the entire planet eliminates intermittency almost entirely (Figure 6-15). This spatial integration effect is often referred to as the (geographic) "smoothing effect," which is discussed next.

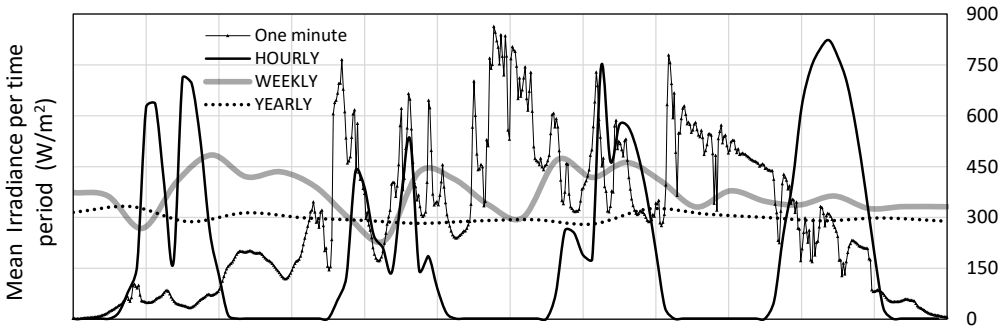

Figure 6-12. Variability of global irradiance time series at a North American location shown as a function of integration time

The plot includes 1 day of 1-minute data, 4 days of hourly data, 26 weeks of weekly data, and 16 years of yearly integrated data.

Image from Perez et al. (2016)

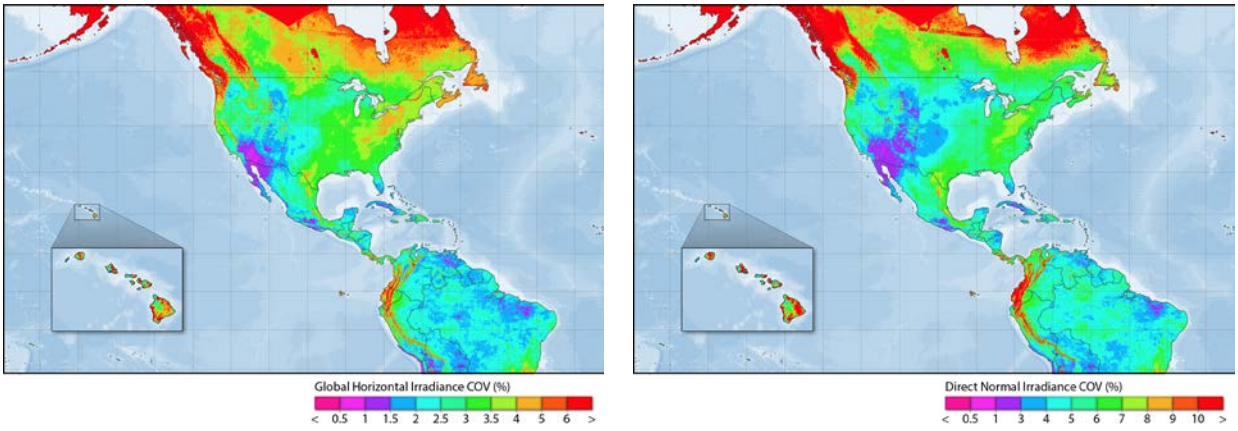

Figure 6-13. Interannual variability in (left) GHI and (right) DNI using the 1998–2017 NSRDB data expressed in percentage of COV

Images from NREL

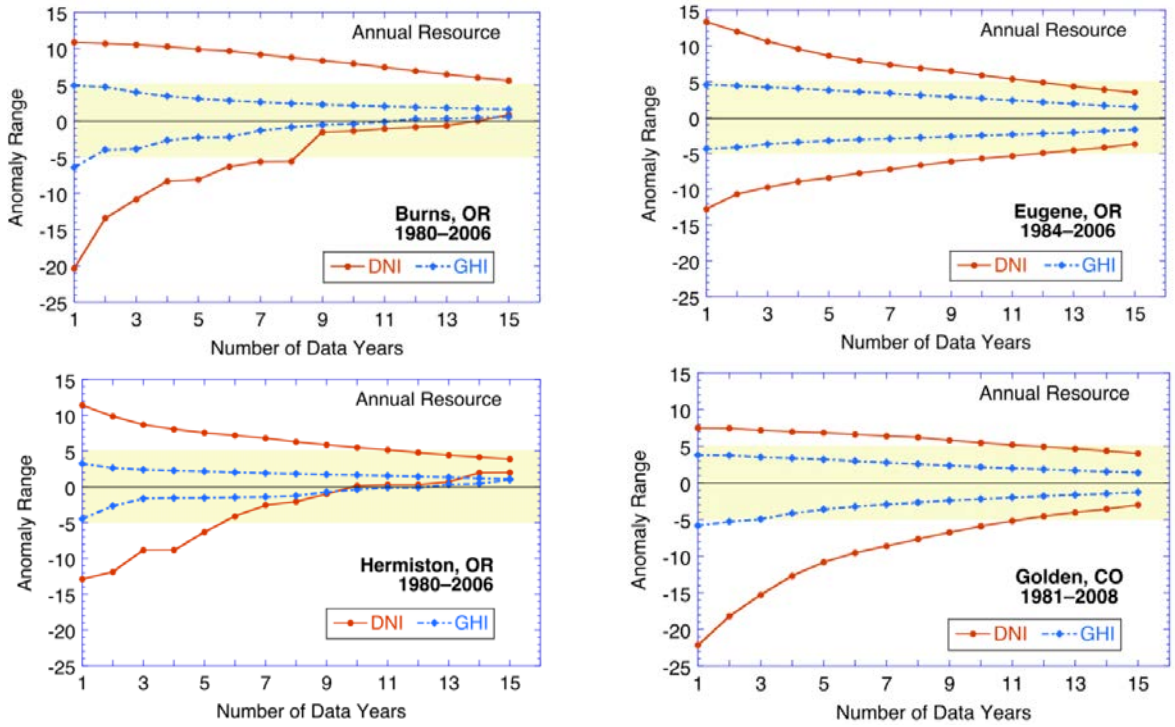

Figure 6-14. Number of years to stabilize DNI and GHI in (clockwise from upper left) Burns, Oregon; Eugene, Oregon; Hermiston, Oregon; and Golden, Colorado

Specific sorting (along the x-axis) from the most exceptional years (largest anomalies) to the most typical years (smallest anomalies).

Images from (Gueymard and Wilcox 2009)

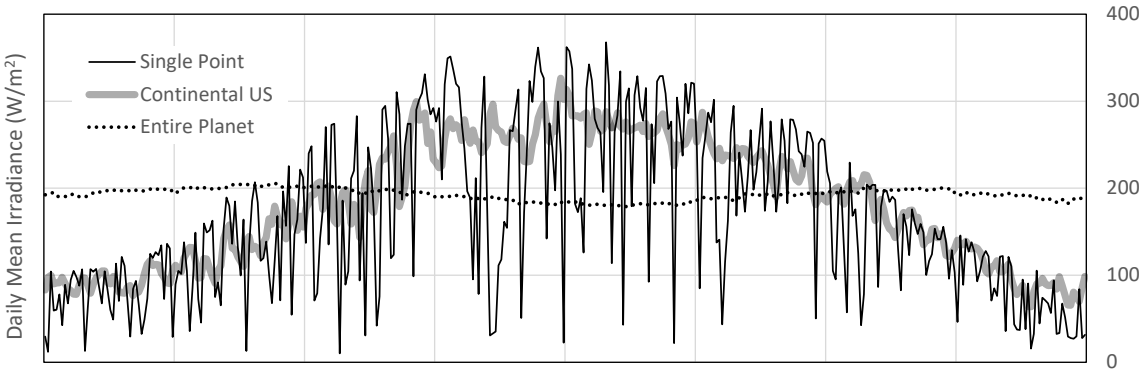

Figure 6-15. Variability of daily global irradiance time series over 1 year as a function of the considered footprint

Image from Perez et al. (2016)

6.4.3 Variability Impacts

Both the temporal variability and the spatial variability are specific to a site (or area) and period. Temporal variability could change seasonally, as mentioned. The two types of variability directly affect solar resource analyses for various reasons, including:

- Measured datasets often contain data gaps due to instrument failure or various problems, such as dew or snow on instruments. (A recent Task-16 report was dedicated to this topic: (Blanc and Silva 2023).) To avoid any discontinuity in the time series, analysts are typically tempted to use some form of temporal interpolation to fill the gaps. This is convenient but can significantly increase the overall uncertainty. The magnitude of the overall uncertainty depends on the time period, the method used to fill the gaps, and the data used for these tasks (Roesch et al. 2011a, 2011b). Moreover, replacing extended data breaks with climatological average values tends to underestimate the actual temporal variability. When calculating monthly averages in particular, it is possible to avoid the gap filling step altogether if an appropriate statistical method is used (Roesch et al. 2011a, 2011b). The method is intricate but has been successfully demonstrated in the case of 1-minute radiation data from a Baseline Surface Radiation Network (BSRN) station, for instance (Salazar et al. 2020).
- If no on-site measurements exist at the project's site but some exist at one or more nearby sites some distance away, analysts are tempted to extrapolate or average the data from those alternate sites. Depending on the distance and spatial variability over that region, this might introduce significant errors.

Interannual and long-term variability (decadal oscillations) must be considered to correctly project the measurements or modeled data of the past into the future for design and bankability purposes. These considerations explain why an evaluation of variability is an important step for accurate solar resource assessment at any location of interest. Further, the expected variability in the very near future (minutes to days) is also essential information for the correct operation and profitability of existing solar power plants. This can be estimated with appropriate solar forecasts (see Chapter 9).

Various studies have analyzed the spatial or temporal variability of the solar resource at the country or continental scale (e.g., (Badosa et al. 2013; Castillejo-Cuberos and Escobar 2020; Davy and Troccoli 2012; Gueymard and Wilcox 2011; Habte et al. 2020; Lohmann et al. 2006; Perez-Astudillo and Bachour 2015). A general finding is that the spatiotemporal variability of DNI is larger than that of GHI for any given location. Because GTI is normally richer in direct irradiance than GHI, it can also be said that the variability in GTI is larger than that in GHI.

From an application perspective, the solar resource variability translates into power production variability, which could impact the stability of electric grids or the economics of the facility. One important question that has received specific attention is: How much is the temporal variability at one power plant site correlated with that of another site some distance away? This is discussed further in Section 6.6 and Chapter 11.

Predicting the behavior of existing or future solar systems assumes that the temporal and spatial irradiance variability can be adequately characterized with measurements and/or modeled data. It is easy to take care of the deterministic variability caused by location, date, and time of day. What matters most is the variability (temporal or spatial) in weather and climate.

With some knowledge about the interannual irradiance variability at a specific site, users can, in principle, select a particular experimental period to adequately characterize the solar resource. Ideally, such on-site measurement campaigns should last many years; however, in most cases,

practical reasons limit them to 1 year or less, which increases the uncertainty in the long-term estimates. Likewise, with knowledge of the spatial variability over the area around a measurement station, users can evaluate the applicability of those measurements to a location some distance away using the appropriate extrapolation or interpolation methods. Knowledge of variability then becomes valuable when deciding how long to make measurements at a particular location and whether the characteristics of the solar resource at that location can be extrapolated to other nearby locations.

With such variability maps or statistics, users can better understand the extent of measurements required to best characterize the solar resource for a particular application. In areas with low interannual variability, a shorter measurement period could suffice. In areas with low spatial variability, a measurement station could represent the solar resource at nearby locations (e.g., within 10–50 km), avoiding the need for additional measurements. An analyst can use this information to build better confidence in a dataset as being sufficient for an analysis and can use these data to understand the consistency of future solar power plant performance and how that relates to the economic viability of a particular location.

One remaining question is whether solar resource data of past decades can represent that of the future. To that end, the long-term trends in GHI and DNI must be investigated in relation to dimming and brightening climate cycles (Müller et al. 2014; Pfeifroth et al. 2018) because of their impact on the yield predictions of solar installations (Müller et al. 2015); see Section 6.2.5.2 for details.

Some statistics that are commonly used to describe the temporal variability of irradiance components assume that their distribution is Gaussian, which is a typical assumption (Cebecauer and Suri 2015). (Fernández-Peruchena et al. 2016) tested that assumption in annual GHI and in DNI time series. Regarding GHI, results from two normality tests indicated that the Gaussian assumption could not be rejected at all 10 tested locations. In the case of DNI, five tests were applied to the annual DNI series for evaluating the Weibull goodness of fit at six locations, and the results suggested that such a distribution is more appropriate than a Gaussian distribution. Considering these results, the temporal variability requires further analysis to clarify whether annual, monthly, or seasonal solar radiation values can be properly assumed: (1) as independent; (2) as only random samples of the same population; or, conversely, (3) as representative of different probabilistic models having, for example, a stationary behavior.

As mentioned in Chapter 8, typical meteorological years (TMYs) eliminate all interannual variability by design. Nevertheless, they can be used, at least on a monthly-mean basis, to investigate the spatial variability of the solar resource wherever gridded TMY databases are available (Habte et al. 2014).

6.5 Temporal Variability and Resolution

Based on the information presented previously, it is clear that temporal variability is a direct function of the temporal resolution of data time series: The higher the resolution, the higher variability can be expected. In many cases, it is necessary to simulate the energy flows of a solar system at high resolution (e.g., at 1-minute time steps or better) to investigate the effects of short-term variability on the system, whereas the available solar radiation dataset is at coarser (e.g., hourly) resolution. Most generally, the use of high-resolution solar data is crucial for

accurate performance modeling of solar power plants, particularly in the case of nonlinear systems. Modeling at hourly resolution can result in unrealistic representations of the performance of CSP (Meybodi et al. 2017) or PV (Villoz et al. 2022) systems. For instance, (Hirsch et al. 2010) demonstrated that, when simulating the dynamic behavior of oil-based parabolic trough plants, the energy produced could be inaccurately estimated when using time steps larger than 30 minutes, compared to the reference 1-minute time step. Therefore, it is usually necessary to use finer time resolutions, such as subhourly or even minute-level data, to better capture the variability and dynamics of solar radiation and its impact on system performance. One approach to resolving this kind of temporal mismatch is to use synthetic datasets at high resolution.

The primary objective behind the development of synthetic datasets is to provide solar irradiance data in situations where ground-measured data are unavailable or where the global gridded irradiance data have insufficient spatial or temporal resolution (Bright 2021). The choice of the most suitable model for synthetic generation depends on the desired time resolution of the dataset. Autoregressive models have been found to be effective for monthly and daily synthetic generation (Boland 2008). This process involves adding a seasonal component to a stochastic and autoregressive component.

For intra-daily synthetic solar data, the process generally involves downscaling, in which the output data has a higher resolution than the input data. Downscaling can be achieved using simple (Ngoko et al. 2014) or multiple (Bright et al. 2015) Markov chains, bootstrapping methods (Grantham et al. 2018; Polo et al. 2011), and nondimensional daily profiles (Fernández-Peruchena et al. 2015; Larrañeta et al. 2018). Regardless of the approach, all such models aim to replicate the inherent variability of solar radiation based on historical data.

6.6 Variability of Solar Energy Production

From an application perspective, solar resource variability translates into power production variability, which could impact the stability of electric grids or the economics of the facility. In this respect, two key questions are: (1) How should the temporal variability in the solar resource at the site of a future project be taken into account at the design stage? and (2) How long should the historical time series be when used to evaluate the solar resource and its variability at any site?

The practical importance of correctly dealing with the consequences of the solar resource's temporal variability is particularly evident at the design stage because of the ingrained reliance of designers on single-year (e.g., TMY) data files, whereas only multiyear time series can convey the necessary information about interannual variability. A quantification of the unwanted consequences on project costs and financing for simply using short-term averages of solar resource data and ignoring temporal interdependencies at the design stage now exists (Bothwell and Hobbs 2023). The practical aspects of this important topic are further elaborated in Chapter 11.

For more details on the characterization of the effects on PV production of the solar resource's spatiotemporal variability, the reader is referred to a report from PVPS Task 14 (Remund et al. 2015).

References

Aldhaif, A.M., D.H. Lopez, H. Dadashazar, and A. Sorooshian. 2020. "Sources, frequency, and chemical nature of dust events impacting the United States East Coast." *Atmos. Environ. 231*, 117456. https://doi.org/10.1016/j.atmosenv.2020.117456.

Alizadeh-Choobari, O., P. Ghafarian, and E. Owlad. 2016. "Temporal variations in the frequency and concentration of dust events over Iran based on surface observations." *Int. J. Climatol*. 36, 2050–2062. https://doi.org/10.1002/joc.4479.

Allen, J.O., and W.B. Hobbs. 2022. "The effect of short-term inverter saturation on modeled hourly PV output using minute DC power measurements." *J. Renew. Sustain. Energy* 14, 063503. https://doi.org/10.1063/5.0130265.

Al-Rasheedi, M., C.A. Gueymard, M. Al-Khayat, A. Ismail, J.A. Lee, H. Al-Duaj. 2020. "Performance evaluation of a utility-scale dual-technology photovoltaic power plant at the Shagaya Renewable Energy Park in Kuwait." *Renew. Sustain. Energy Rev.* 133, 110139. https://doi.org/10.1016/j.rser.2020.110139.

An, L., H. Che, M. Xue, T. Zhang, H. Wang, Y. Wang, C. Zhou, H. Zhao, K. Gui, Y. Zheng, T. Sun, Y. Liang, E. Sun, H. Zhang, and X. Zhang. 2018. "Temporal and spatial variations in sand and dust storm events in East Asia from 2007 to 2016: Relationships with surface conditions and climate change." *Sci. Total Environ.* 633, 452–462. https://doi.org/10.1016/j.scitotenv.2018.03.068.

Andela, N., D.C. Morton, L. Giglio, Y. Chen, G.R. van der Werf, P.S. Kasibhatla, R.S. DeFries, G.J. Collatz, S. Hantson, S. Kloster, et al. 2017. "A human-driven decline in global burned area." *Science* 356, 1356–1362. https://doi.org/10.1126/science.aal4108.

Antuña-Marrero, J.C., F. García, R. Estevan, B. Barja, and A. Sánchez-Lorenzo. 2019. "Simultaneous dimming and brightening under all and clear sky at Camagüey, Cuba (1981–2010)." *J. Atmospheric Sol.-Terr. Phys*. 190, 45–53. https://doi.org/10.1016/j.jastp.2019.05.004.

Badosa, J., M. Haeffelin, and H. Chepfer. 2013. "Scales of spatial and temporal variation of solar irradiance on Reunion tropical island." *Sol. Energy* 88, 42–56. https://doi.org/10.1016/j.solener.2012.11.007.

Bencherif, H., A. Bounhir, N. Bègue, T. Millet, Z. Benkhaldoun, K. Lamy, T. Portafaix, and F. Gadouali. 2022. "Aerosol Distributions and Sahara Dust Transport in Southern Morocco, from Ground-Based and Satellite Observations." *Remote Sens.* 14, 2454. https://doi.org/10.3390/rs14102454.

Bengulescu, M., P. Blanc, and L. Wald. 2018. "On the intrinsic timescales of temporal variability in measurements of the surface solar radiation." *Nonlinear Process. Geophys.* 25, 19–37. https://doi.org/10.5194/npg-25-19-2018.

Beyer, H.G., J. Polo Martinez, M. Suri, J.L. Torres, E. Lorenz, S. Müller, C. Hoyer-Klick, and P. Ineichen. 2009. *Report on Benchmarking of Radiation Products* (No. D1.1.3, Contract No. 038665).

Blanc, P., and R.A. Silva. 2023. *Framework for Benchmarking of GHI Gap-Filling Methods.* Report IEA-PVPS T16-03:2023. https://iea-pvps.org/wp-content/uploads/2023/06/Report-IEA-PVPS-T16-03-2023-Framework-for-benchmarking-of-GHI-gap-filling-methods-1.pdf.

Bloomfield, H.C., C.M. Wainwright, and N. Mitchell. 2022. "Characterizing the variability and meteorological drivers of wind power and solar power generation over Africa." *Meteorol. Appl.* 29, e2093. https://doi.org/10.1002/met.2093.

Boland, J. 2008. "Time Series Modelling of Solar Radiation." In: Badescu, V. (Ed.), *Modeling Solar Radiation at the Earth's Surface.* Springer Berlin Heidelberg, Berlin, Heidelberg, pp. 283–312. https://doi.org/10.1007/978-3-540-77455-6_11.

Bothwell, C.D., and B.F. Hobbs. 2023. "How Sampling and Averaging Historical Solar and Wind Data Can Distort Resource Adequacy." *IEEE Trans. Sustain. Energy* 14, 1337–1345. https://doi.org/10.1109/TSTE.2022.3156869.

Bright, J.M. 2021. "Introduction To Synthetic Solar Irradiance." In: Bright, J.M. (Ed.), *Synthetic Solar Irradiance: Modeling Solar Data*. AIP Publishing.

Bright, J.M., C.J. Smith, P.G. Taylor, and R. Crook. 2015. "Stochastic generation of synthetic minutely irradiance time series derived from mean hourly weather observation data." *Sol. Energy* 115, 229–242. https://doi.org/10.1016/j.solener.2015.02.032.

Brown, P.T., M.S. Lozier, R. Zhang, and W. Li. 2016. "The necessity of cloud feedback for a basin-scale Atlantic Multidecadal Oscillation." *Geophys. Res. Lett.* 43, 3955–3963. https://doi.org/10.1002/2016GL068303.

Burger, B., and R. Rüther. 2006. "Inverter sizing of grid-connected photovoltaic systems in the light of local solar resource distribution characteristics and temperature." *Sol. Energy* 80, 32–45. https://doi.org/10.1016/j.solener.2005.08.012.

Calif, R., and T. Soubdhan. 2016. "On the use of the coefficient of variation to measure spatial and temporal correlation of global solar radiation." *Renew. Energy* 88, 192–199. https://doi.org/10.1016/j.renene.2015.10.049.

Cañadillas-Ramallo, D., A. Moutaoikil, L.E. Shephard, and R. Guerrero-Lemus. 2022. "The influence of extreme dust events in the current and future 100% renewable power scenarios in Tenerife." *Renew. Energy* 184, 948–959. https://doi.org/10.1016/j.renene.2021.12.013.

Casagrande, M.S.G., F.R. Martins, N.E. Rosário, F.J.L. Lima, A.R. Gonçalves, R.S. Costa, M. Zarzur, M.P. Pes, and E.B. Pereira. 2021. "Numerical Assessment of Downward Incoming Solar Irradiance in Smoke Influenced Regions—A Case Study in Brazilian Amazon and Cerrado." *Remote Sens.* 13, 4527. https://doi.org/10.3390/rs13224527.

Castillejo-Cuberos, A., and R. Escobar. 2020. "Understanding solar resource variability: An in-depth analysis, using Chile as a case of study." *Renew. Sustain. Energy Rev.* 120, 109664. https://doi.org/10.1016/j.rser.2019.109664.

Cebecauer, T., and M. Suri. 2015. "Typical Meteorological Year Data: SolarGIS Approach." *Energy Procedia* 69, 1958–1969. https://doi.org/10.1016/j.egypro.2015.03.195.

Cebecauer, T., M. Šúri, and C.A. Gueymard. 2011. "Uncertainty sources in satellite-derived direct normal irradiance: how can prediction accuracy be improved globally." In: Proceedings of the SolarPACES 2011 Conference. Granada, Spain, pp. 20–23.

Chen, S., P. Li, D. Brady, and B. Lehman. 2013. "Determining the optimum grid-connected photovoltaic inverter size." *Sol. Energy* 87, 96–116. https://doi.org/10.1016/j.solener.2012.09.012.

Chiacchio, M., and M. Wild. 2010. "Influence of NAO and clouds on long-term seasonal variations of surface solar radiation." In *Europe. J. Geophys. Res. Atmospheres* 115. https://doi.org/10.1029/2009JD012182.

Chin, M., T. Diehl, P. Ginoux, and W. Malm. 2007. "Intercontinental transport of pollution and dust aerosols: implications for regional air quality." *Atmospheric Chem. Phys*. 7, 5501–5517. https://doi.org/10.5194/acp-7-5501-2007.

Chtirkova, B., D. Folini, L.F. Correa, and M. Wild. 2022. "Internal Variability of All-Sky and Clear-Sky Surface Solar Radiation on Decadal Timescales." *J. Geophys. Res. Atmospheres* 127, e2021JD036332. https://doi.org/10.1029/2021JD036332.

Climate Intervention: Reflecting Sunlight to Cool Earth. 2015. National Academies Press, Washington, D.C. https://doi.org/10.17226/18988.

Colantuono, G., Y. Wang, E. Hanna, and R. Erdélyi. 2014. "Signature of the North Atlantic Oscillation on British solar radiation availability and PV potential: The winter zonal seesaw." *Sol. Energy* 107, 210–219. https://doi.org/10.1016/j.solener.2014.05.045.

Cordero, R.R., S. Feron, A. Damiani, E. Sepúlveda, J. Jorquera, A. Redondas, G. Seckmeyer, J. Carrasco, P. Rowe, and Z. Ouyang. 2023. "Surface Solar Extremes in the Most Irradiated Region on Earth, Altiplano." *Bull. Am. Meteorol. Soc.* 1. https://doi.org/10.1175/BAMS-D-22-0215.1.

Correia, J.M., F. McDermott, C. Sweeney, E. Doddy, and S. Griffin. 2020. "An investigation of the regional correlation gradients between Euro-Atlantic atmospheric teleconnections and winter solar short wave radiation in northwest Europe." *Meteorol. Appl*. 27, e1892. https://doi.org/10.1002/met.1892.

Crowley, T.J., and M.B. Unterman. 2013. "Technical details concerning development of a 1200 yr proxy index for global volcanism." *Earth Syst. Sci. Data* 5, 187–197. https://doi.org/10.5194/essd-5-187-2013.

Cuevas-Agulló, E., D. Barriopedro, R.D. García, S. Alonso-Pérez, J.J. González-Alemán, E. Werner, D. Suárez, J.J. Bustos, G. García-Castrillo, O. García, A. Barreto, and S. Basart. 2024. "Sharp increase of Saharan dust intrusions over the western Euro-Mediterranean in February-March 2020–2022 and associated atmospheric circulation." *Atmos. Chem. Phys.* 24, 4083–4104. https://doi.org/10.5194/acp-24-4083-2024.

Cusworth, D.H., L.J. Mickley, E.M. Leibensperger, and M.J. Iacono. 2017. "Aerosol trends as a potential driver of regional climate in the central United States: evidence from observations." *Atmos. Chem. Phys*. 17, 13559–13572. https://doi.org/10.5194/acp-17-13559-2017.

Dabou, R., F. Bouchafaa, A.H. Arab, A. Bouraiou, M.D. Draou, A. Neçaibia, A., and M. Mostefaoui. 2016. "Monitoring and performance analysis of grid connected photovoltaic under different climatic conditions in south Algeria." *Energy Convers. Manag.* 130, 200–206. https://doi.org/10.1016/j.enconman.2016.10.058.

Davy, R.J., and A. Troccoli. 2012. "Interannual variability of solar energy generation in Australia." *Sol. Energy* 86, 3554–3560. https://doi.org/10.1016/j.solener.2011.12.004.

Dennison, P.E., S.C. Brewer, J.D. Arnold, and M.A. Moritz. 2014. "Large wildfire trends in the western United States, 1984–2011." *Geophys. Res. Lett.* 41, 2928–2933. https://doi.org/10.1002/2014GL059576.

do Nascimento, L.R., T. de Souza Viana, R.A. Campos, and R. Rüther. 2019. "Extreme solar overirradiance events: Occurrence and impacts on utility-scale photovoltaic power plants in Brazil." *Sol. Energy* 186, 370–381. https://doi.org/10.1016/j.solener.2019.05.008.

Doerr, S.H., and C. Santín. 2016. "Global trends in wildfire and its impacts: perceptions versus realities in a changing world." *Philos. Trans. R. Soc. B Biol. Sci.* 371, 20150345. https://doi.org/10.1098/rstb.2015.0345.

Dutton, E.G., J.J. Deluisi, and P. Arne. 1985. "Interpretation of Mauna Loa atmospheric transmission relative to aerosols, using photometric precipitable water amounts." *J. Atmospheric Chem*. 3, 53–68. https://doi.org/10.1007/BF00049368.

Dutton, E.G., D.W. Nelson, R.S. Stone, D. Longenecker, G. Carbaugh, J.M. Harris, and J. Wendell. 2006. "Decadal variations in surface solar irradiance as observed in a globally remote network." *J. Geophys. Res. Atmospheres* 111. https://doi.org/10.1029/2005JD006901.

Ellis, B.E., N. Pearre, and L. Swan. 2021. "Power ramp rates and variability of individual and aggregate photovoltaic systems using measured production data at the municipal scale." *Sol. Energy* 220, 363–370. https://doi.org/10.1016/j.solener.2021.03.042.

Ellis, H.T., and R.F. Pueschel. 1971. "Solar Radiation: Absence of Air Pollution Trends at Mauna Loa." *Science* 172, 845–846. https://doi.org/10.1126/science.172.3985.845.

Fan, H., X. Yang, C. Zhao, Y. Yang, and Z. Shen. 2023. "Spatiotemporal variation characteristics of global fires and their emissions." *Atmos. Chem. Phys*. 23, 7781–7798. https://doi.org/10.5194/acp-23-7781-2023.

Fernández-Peruchena, C.M., M. Blanco, M. Gastón, and A. Bernardos. 2015. "Increasing the temporal resolution of direct normal solar irradiance series in different climatic zones." *Sol. Energy* 115, 255–263. https://doi.org/10.1016/j.solener.2015.02.017.

Fernández-Peruchena, C.M., L. Ramírez, L., M.A. Silva-Pérez, V. Lara, D. Bermejo, M. Gastón, S. Moreno-Tejera, J. Pulgar, J. Liria, S. Macías, R. Gonzalez, A. Bernardos, et al. 2016. "A statistical characterization of the long-term solar resource: Towards risk assessment for solar power projects." *Sol. Energy* 123, 29–39. https://doi.org/10.1016/j.solener.2015.10.051.

Folini, D., T.N. Dallafior, M.Z. Hakuba, and M. Wild. 2017. "Trends of surface solar radiation in unforced CMIP5 simulations." *J. Geophys. Res. Atmospheres* 122, 469–484. https://doi.org/10.1002/2016JD025869.

Fountoukis, C., B. Figgis, L. Ackermann, and M.A. Ayoub. 2018. "Effects of atmospheric dust deposition on solar PV energy production in a desert environment." *Sol. Energy* 164, 94–100. https://doi.org/10.1016/j.solener.2018.02.010.

Gaetani, M., T. Huld, E. Vignati, F. Monforti-Ferrario, A. Dosio, and F. Raes. 2014. "The near future availability of photovoltaic energy in Europe and Africa in climate-aerosol modeling experiments." *Renew. Sustain. Energy Rev.* 38, 706–716. https://doi.org/10.1016/j.rser.2014.07.041.

Ghosh, S., S. Dey, D. Ganguly, S.B. Roy, and K. Bali. 2022. "Cleaner air would enhance India's annual solar energy production by 6–28 TWh." *Environ. Res. Lett.* 17, 054007. https://doi.org/10.1088/1748-9326/ac5d9a.

Gil, V., M.A. Gaertner, C. Gutierrez, and T. Losada. 2019. "Impact of climate change on solar irradiation and variability over the Iberian Peninsula using regional climate models." *Int. J. Climatol.* 39, 1733–1747. https://doi.org/10.1002/joc.5916.

Gkikas, A., T.M. Giannaros, V. Kotroni, and K. Lagouvardos. 2019. "Assessing the radiative impacts of an extreme desert dust outbreak and the potential improvements on short-term weather forecasts: The case of February 2015." *Atmospheric Res.* 226, 152–170. https://doi.org/10.1016/j.atmosres.2019.04.020.

Grantham, A.P., P.J. Pudney, and J.W. Boland. 2018. "Generating synthetic sequences of global horizontal irradiation." *Sol. Energy* 162, 500–509. https://doi.org/10.1016/j.solener.2018.01.044.

Gueymard, C., and S. Wilcox. 2009. "Spatial and temporal variability in the solar resource: Assessing the value of short-term measurements at potential solar power plant sites." in: ASES National Solar Conference. Buffalo, New York.

Gueymard, C.A. 2022. "Solar Radiation Resource: Measurement, Modeling, and Methods. In: Letcher, T.M. (Ed.), *Comprehensive Renewable Energy (Second Edition).* Elsevier, Oxford, pp. 176–212. https://doi.org/10.1016/B978-0-12-819727-1.00101-1.

Gueymard, C.A. 2019. "Clear-Sky Radiation Models and Aerosol Effects." In: Polo, J., Martín-Pomares, L., Sanfilippo, A. (Eds.), *Solar Resources Mapping, Green Energy and Technology.* Springer International Publishing, pp. 137–182. https://doi.org/10.1007/978-3-319-97484-2_5.

Gueymard, C.A. 2017. "Cloud and albedo enhancement impacts on solar irradiance using high-frequency measurements from thermopile and photodiode radiometers. Part 1: Impacts on global horizontal irradiance." *Sol. Energy* 153, 755–765. https://doi.org/10.1016/j.solener.2017.05.004.

Gueymard, C.A. 2012. "Temporal variability in direct and global irradiance at various time scales as affected by aerosols." *Sol. Energy* 86, 3544–3553.

Gueymard, C.A. 2003. "Direct solar transmittance and irradiance predictions with broadband models. Part I: detailed theoretical performance assessment." *Sol. Energy* 74, 355–379. https://doi.org/10.1016/S0038-092X(03)00195-6.

Gueymard, C.A., M. Al-Rasheedi, A. Ismail, and T. Hussain. 2017. "Long-Term Variability of Aerosol Optical Depth, Dust Episodes, and Direct Normal Irradiance over Kuwait for CSP Applications." In: Proceedings of the ISES Solar World Congress. Abu Dhabi, United Arab Emirates. https://doi.org/doi:10.18086/swc.2017.04.04.

Gueymard, C.A., and D.R. Myers. 2009. "Evaluation of conventional and high-performance routine solar radiation measurements for improved solar resource, climatological trends, and radiative modeling." *Sol. Energy* 83, 171–185. https://doi.org/10.1016/j.solener.2008.07.015.

Gueymard, C.A., and S.M. Wilcox. 2011. "Assessment of spatial and temporal variability in the US solar resource from radiometric measurements and predictions from models using ground-based or satellite data." *Sol. Energy* 85, 1068–1084. https://doi.org/10.1016/j.solener.2011.02.030.

Guo, L., B. Fan, F. Zhang, Z. Jin, and H. Lin. 2018. "The Clustering of Severe Dust Storm Occurrence in China From 1958 to 2007." *J. Geophys. Res. Atmospheres* 123, 8035–8046. https://doi.org/10.1029/2018JD029042.

Guo, Y., P. Crippa, A. Thota, and S.C. Pryor. 2021. "Extreme Aerosol Events Over Eastern North America: 1. Characterizing and Simulating Historical Events." *J. Geophys. Res. Atmospheres* 126, e2020JD033758. https://doi.org/10.1029/2020JD033758.

Gutiérrez, C., S. Somot, P. Nabat, M. Mallet, L. Corre, E. Meijgaard, O. van, Perpiñán, O., and M.A. Gaertner. 2020. "Future evolution of surface solar radiation and photovoltaic potential in Europe: investigating the role of aerosols." *Environ. Res. Lett.* 15, 034035. https://doi.org/10.1088/1748-9326/ab6666.

Habte, A., A. Lopez, M. Sengupta, and S. Wilcox. 2014. *Temporal and Spatial Comparison of Gridded TMY, TDY, and TGY Datasets*. NREL/TP-5D00-60886. National Renewable Energy Laboratory. Golden, CO. https://doi.org/10.2172/1126297.

Habte, A., M. Sengupta, C.A. Gueymard, A. Golnas, and Y. Xie. 2020. "Long-term spatial and temporal solar resource variability over America using the NSRDB version 3 (1998–2017)." *Renew. Sustain. Energy Rev.* 134, 110285. https://doi.org/10.1016/j.rser.2020.110285.

Hatzianastassiou, N., E. Ioannidis, M-B Korras-Carraca, M. Gavrouzou, C.D. Papadimas, C. Matsoukas, N. Benas, A. Fotiadi, M. Wild, and I. Vardavas. 2020. "Global Dimming and Brightening Features during the First Decade of the 21st Century." *Atmosphere* 11, 308. https://doi.org/10.3390/atmos11030308.

He, J., L. Hong, C. Shao, and W. Tang. 2023. "Global evaluation of simulated surface shortwave radiation in CMIP6 models." *Atmospheric Res.* 292, 106896. https://doi.org/10.1016/j.atmosres.2023.106896.

Herman-Czezuch, A., A.Z. Mekeng, S. Meilinger, J. Barry, and N. Kimiaie. 2022. "Impact of aerosols on photovoltaic energy production using a spectrally resolved model chain: Case study of southern West Africa." *Renew. Energy* 194, 321–333. https://doi.org/10.1016/j.renene.2022.04.166.

Hirsch, T., H. Schenk, N. Schmidt, and R. Meyer. 2010. "Dynamics of oil-based parabolic trough plants - impact of transient behaviour on energy yields." In: Proceedings of the SolarPACES 2010 Conference. SolarPACES, Perpignan, France.

Hoff, T.E., and R. Perez. 2012. "Modeling PV fleet output variability." *Sol. Energy* 86, 2177–2189. https://doi.org/10.1016/j.solener.2011.11.005.

Hurrell, J.W., Y. Kushnir, G. Ottersen, and M. Visbeck. 2003. "An Overview of the North Atlantic Oscillation." In: *The North Atlantic Oscillation: Climatic Significance and Environmental Impact. American Geophysical Union (AGU)*, pp. 1–35. https://doi.org/10.1029/134GM01.

Husar, R.B., D.M. Tratt, B.A. Schichtel, S.R. Falke, F. Li, D. Jaffe, S. Gassó, T. Gill, N.S. Laulainen, F. Lu, M.C. Reheis, Y. Chun. 2001. "Asian dust events of April 1998." *J. Geophys. Res. Atmospheres* 106, 18317–18330. https://doi.org/10.1029/2000JD900788.

Inman, R.H., Y. Chu, and C.F.M. Coimbra. 2016. "Cloud enhancement of global horizontal irradiance in California and Hawaii." *Sol. Energy* 130, 128–138. https://doi.org/10.1016/j.solener.2016.02.011.

IPCC (Intergovernmental Panel on Climate Change). 2023. *AR6 Synthesis Report: Climate Change 2023.* Intergovernmental Panel on Climate Change.

Isaza, A., M. Kay, J.P. Evans, A. Prasad, and S. Bremner. 2023. "Air quality impacts on rooftop photovoltaic energy production during the 2019–2020 Australian bushfires season." *Sol. Energy* 257, 240–248. https://doi.org/10.1016/j.solener.2023.04.014.

Järvelä, M., K. Lappalainen, and S. Valkealahti. 2020. "Characteristics of the cloud enhancement phenomenon and PV power plants." *Sol. Energy* 196, 137–145. https://doi.org/10.1016/j.solener.2019.11.090.

Javed, W., B. Guo, B. Figgis, and B. Aïssa. 2021. "Dust potency in the context of solar photovoltaic (PV) soiling loss." *Sol. Energy* 220, 1040–1052. https://doi.org/10.1016/j.solener.2021.04.015.

Jiang, H., N. Lu, L. Yao, J. Qin, and T. Liu. 2023. "Impact of climate changes on the stability of solar energy: Evidence from observations and reanalysis." *Renew. Energy* 208, 726–736. https://doi.org/10.1016/j.renene.2023.03.114.

King, M.P., N. Keenlyside, C. Li. 2023. "ENSO teleconnections in terms of non-NAO and NAO atmospheric variability." *Clim. Dyn*. https://doi.org/10.1007/s00382-023-06697-8.

Kozarcanin, S., H. Liu, and G.B. Andresen. 2019. "21st Century Climate Change Impacts on Key Properties of a Large-Scale Renewable-Based Electricity System." *Joule* 3, 992–1005. https://doi.org/10.1016/j.joule.2019.02.001.

Kravitz, B., A. Robock, S. Tilmes, O. Boucher, J.M. English, P.J. Irvine, A. Jones, M.G. Lawrence, M. MacCracken, H. Muri, and J.C. Moore. 2015. "The Geoengineering Model Intercomparison Project Phase 6 (GeoMIP6): simulation design and preliminary results." *Geosci. Model Dev.* 8, 3379–3392. https://doi.org/10.5194/gmd-8-3379-2015.

Kreuwel, F.P.M., W.H. Knap, L.R. Visser, W.G.J.H.M. van Sark, J. Vilà-Guerau de Arellano, and C.C. van Heerwaarden. 2020. "Analysis of high frequency photovoltaic solar energy fluctuations." *Sol. Energy* 206, 381–389. https://doi.org/10.1016/j.solener.2020.05.093.

Laguarda, A., R. Alonso-Suárez, and R. Terra. 2020. "Solar irradiation regionalization in Uruguay: Understanding the interannual variability and its relation to El Niño climatic phenomena." *Renew. Energy* 158, 444–452. https://doi.org/10.1016/j.renene.2020.05.083.

Lappalainen, K., and S. Valkealahti. 2017. "Effects of PV array layout, electrical configuration and geographic orientation on mismatch losses caused by moving clouds." *Sol. Energy* 144, 548–555. https://doi.org/10.1016/j.solener.2017.01.066.

Larrañeta, M., C. Fernandez-Peruchena, M.A. Silva-Pérez, and I. Lillo-Bravo. 2018. "Methodology to synthetically downscale DNI time series from 1-h to 1-min temporal resolution with geographic flexibility." *Sol. Energy* 162, 573–584. https://doi.org/10.1016/j.solener.2018.01.064.

Lave, M., M.J. Reno, and R.J. Broderick. 2015. "Characterizing local high-frequency solar variability and its impact to distribution studies." *Sol. Energy* 118, 327–337. https://doi.org/10.1016/j.solener.2015.05.028.

Lee, K.H., J.E. Kim, Y.J. Kim, J. Kim, and W. von Hoyningen-Huene. 2005. "Impact of the smoke aerosol from Russian forest fires on the atmospheric environment over Korea during May 2003." *Atmos. Environ.* 39, 85–99. https://doi.org/10.1016/j.atmosenv.2004.09.032.

Lehner, F., and C. Deser. 2023. "Origin, importance, and predictive limits of internal climate variability." *Environ. Res. Clim.* 2, 023001. https://doi.org/10.1088/2752-5295/accf30.

Li, J. 2020. “Pollution Trends in China from 2000 to 2017: A Multi-Sensor View from Space.” *Remote Sens.* 12, 208. https://doi.org/10.3390/rs12020208.

Li, X., F. Wagner, W. Peng, J. Yang, and D.L. Mauzerall. 2017. “Reduction of solar photovoltaic resources due to air pollution in China.” *Proc. Natl. Acad. Sci.* 114, 11867–11872. https://doi.org/10.1073/pnas.1711462114.

Liu, H., A.M. Nobre, D. Yang, J.Y. Ye, F.R. Martins, R. Rüther, T. Reindl, A.G. Aberle, and I.M. Peters. 2014. “The Impact of Haze on Performance Ratio and Short-Circuit Current of PV Systems in Singapore.” *IEEE J. Photovolt.* 4, 1585–1592. https://doi.org/10.1109/JPHOTOV.2014.2346429.

Logothetis, S.-A., V. Salamalikis, A. Gkikas, S. Kazadzis, V. Amiridis, and A. Kazantzidis. 2021. “15-year variability of desert dust optical depth on global and regional scales.” *Atmos. Chem. Phys.* 21, 16499–16529. https://doi.org/10.5194/acp-21-16499-2021.

Lohmann, S., C. Schillings, B. Mayer, and R. Meyer. 2006. “Long-term variability of solar direct and global radiation derived from ISCCP data and comparison with reanalysis data.” *Sol. Energy* 80, 1390–1401. https://doi.org/10.1016/j.solener.2006.03.004.

Luoma, J., J. Kleissl, and K. Murray. 2012. “Optimal inverter sizing considering cloud enhancement.” *Sol. Energy* 86, 421–429. https://doi.org/10.1016/j.solener.2011.10.012.

Madden, R.A., and P.R. Julian. 1971. “Detection of a 40–50 Day Oscillation in the Zonal Wind in the Tropical Pacific.” *J. Atmospheric Sci.* 28, 702–708. https://doi.org/10.1175/1520-0469(1971)028<0702:DOADOI>2.0.CO;2.

Madhavan, B.L., J. Kalisch, and A. Macke. 2016. “Shortwave surface radiation network for observing small-scale cloud inhomogeneity fields.” *Atmospheric Meas. Tech.* 9, 1153–1166. https://doi.org/10.5194/amt-9-1153-2016.

Manara, V., M. Brunetti, A. Celozzi, M. Maugeri, A. Sanchez-Lorenzo, and M. Wild. 2016. “Detection of dimming/brightening in Italy from homogenized all-sky and clear-sky surface solar radiation records and underlying causes (1959 & 2013).” *Atmos. Chem. Phys*. 16, 11145–11161. https://doi.org/10.5194/acp-16-11145-2016.

Mann, M.E., J. Park, and R.S. Bradley. 1995. “Global interdecadal and century-scale climate oscillations during the past five centuries.” *Nature* 378, 266–270. https://doi.org/10.1038/378266a0.

Mann, M.E., B.A. Steinman, D.J. Brouillette, and S.K. Miller. 2021. “Multidecadal climate oscillations during the past millennium driven by volcanic forcing.” *Science* 371, 1014–1019. https://doi.org/10.1126/science.abc5810.

Marie-Joseph, I., L. Linguet, M-L Gobinddass, and L. Wald. 2013. “On the applicability of the Heliosat-2 method to assess surface solar irradiance in the Intertropical Convergence Zone, French Guiana.” *Int. J. Remote Sens*. 34, 3012–3027. https://doi.org/10.1080/01431161.2012.756598.

Martins, G.L., S.L. Mantelli, and R. Rüther. 2022. "Evaluating the performance of radiometers for solar overirradiance events." *Sol. Energy* 231, 47–56. https://doi.org/10.1016/j.solener.2021.11.050.

McFarlane, S.A., C.N. Long, and J. Flaherty. 2013. "A Climatology of Surface Cloud Radiative Effects at the ARM Tropical Western Pacific Sites." *J. Appl. Meteorol. Climatol.* 52, 996–1013. https://doi.org/10.1175/JAMC-D-12-0189.1.

Meybodi, M.A., L. Ramirez Santigosa, and A.C. Beath. 2017. "A study on the impact of time resolution in solar data on the performance modelling of CSP plants." *Renew. Energy* 109, 551–563. https://doi.org/10.1016/j.renene.2017.03.024.

Michalsky, J.J., R. Perez, R. Seals, and P. Ineichen. 1994. "Degradation of solar concentrator performance in the aftermath of Mount Pinatubo." *Sol. Energy* 52, 205–213. https://doi.org/10.1016/0038-092x(94)90070-1.

Mohammadi, K., and N. Goudarzi. 2018. "Association of direct normal irradiance with El Niño Southern Oscillation and its consequence on concentrated solar power production in the US Southwest." *Appl. Energy* 212, 1126–1137. https://doi.org/10.1016/j.apenergy.2017.12.102.

Mu, B., J. Li, S. Yuan, and X. Luo. 2022. "The NAO Variability Prediction and Forecasting with Multiple Time Scales Driven by ENSO Using Machine Learning Approaches." *Comput. Intell. Neurosci.* 2022, e6141966. https://doi.org/10.1155/2022/6141966.

Müller, B., L. Hardt, A. Armbruster, K. Kiefer, and C. Reise. 2015. "Yield predictions for photovoltaic power plants: empirical validation, recent advances and remaining uncertainties." *Prog. Photovolt. Res. Appl.* 24, 570–583. https://doi.org/10.1002/pip.2616.

Müller, B., M. Wild, A. Driesse, and K. Behrens. 2014. "Rethinking solar resource assessments in the context of global dimming and brightening." *Sol. Energy* 99, 272–282. https://doi.org/10.1016/j.solener.2013.11.013.

Murari, T.B., A.S.N. Filho, M.A. Moret, S. Pitombo, and A.A.B. Santos. 2020. "Self-Affine Analysis of ENSO in Solar Radiation." *Energies* 13, 4816. https://doi.org/10.3390/en13184816.

Ngoko, B.O., H. Sugihara, and T. Funaki. 2014. "Synthetic generation of high temporal resolution solar radiation data using Markov models." *Sol. Energy* 103, 160–170. https://doi.org/10.1016/j.solener.2014.02.026.

Nobre, A.M., S. Karthik, H. Liu, D. Yang, F.R. Martins, E.B. Pereira, R. Rüther, T. Reindl, and I.M. Peters. 2016. "On the impact of haze on the yield of photovoltaic systems in Singapore. Renew." *Energy* 89, 389–400. https://doi.org/10.1016/j.renene.2015.11.079.

Papachristopoulou, K., I-P Raptis, A. Gkikas, I. Fountoulakis, A. Masoom, and S. Kazadzis. 2022. "Aerosol optical depth regime over megacities of the world." *Atmos. Chem. Phys.* 22, 15703–15727. https://doi.org/10.5194/acp-22-15703-2022.

Perez, R., M. David, T. E. Hoff, M. Jamaly, S. Kivalov, J. Kleissl, P. Lauret, and M. Perez. 2016. "Spatial and Temporal Variability of Solar Energy." *Foundations and Trends in Renewable Energy* 1: 1–44. https://doi.org/10.1561/2700000006.

Perez-Astudillo, D., and D. Bachour. 2015. "Variability of measured Global Horizontal Irradiation throughout Qatar." *Sol. Energy* 119, 169–178. https://doi.org/10.1016/j.solener.2015.06.045.

Perry, M., and A. Troccoli. 2015. "Impact of a fire burn on solar irradiance and PV power." *Sol. Energy* 114, 167–173. https://doi.org/10.1016/j.solener.2015.01.005.

Pfeifroth, U., A. Sanchez-Lorenzo, V. Manara, J. Trentmann, and R. Hollmann. 2018. "Trends and Variability of Surface Solar Radiation in Europe Based on Surface- and Satellite-Based Data Records." *J. Geophys. Res. Atmospheres* 123, 1735–1754. https://doi.org/10.1002/2017jd027418.

Poddar, S., M. Kay, A. Prasad, J.P. Evans, and S. Bremner. 2023. "Changes in solar resource intermittency and reliability under Australia's future warmer climate." *Sol. Energy* 266, 112039. https://doi.org/10.1016/j.solener.2023.112039.

Polo, J., L.F. Zarzalejo, R. Marchante, A.A. Navarro. 2011. "A simple approach to the synthetic generation of solar irradiance time series with high temporal resolution." *Sol. Energy* 85, 1164–1170. https://doi.org/10.1016/j.solener.2011.03.011.

Pozo-Vazquez, D., F.J. Santos-Alamillos, V. Lara-Fanego, J.A. Ruiz-Arias, and J. Tovar-Pescador. 2011. "The Impact of the NAO on the Solar and Wind Energy Resources in the Mediterranean Area." In: Vicente-Serrano, S.M., Trigo, R.M. (Eds.), *Hydrological, Socioeconomic and Ecological Impacts of the North Atlantic Oscillation in the Mediterranean Region*, Advances in Global Change Research. Springer Netherlands, Dordrecht, pp. 213–231. https://doi.org/10.1007/978-94-007-1372-7_15.

Rahim, N.A., M.F. Mohammed, and B.M. Eid. 2017. "Assessment of effect of haze on photovoltaic systems in Malaysia due to open burning in Sumatra." *IET Renew. Power Gener*. 11, 299–304. https://doi.org/10.1049/iet-rpg.2016.0069.

Ravi Kumar, K., R. Attada, H.P. Dasari, R.K. Vellore, Y.O. Abualnaja, K. Ashok, and I. Hoteit. 2019. "On the Recent Amplification of Dust Over the Arabian Peninsula During 2002–2012." *J. Geophys. Res. Atmospheres* 124, 13220–13229. https://doi.org/10.1029/2019JD030695.

Richter, J.H., D. Visioni, D. G. MacMartin, D.A. Bailey, N. Rosenbloom, B. Dobbins, W.R. Lee, M. Tye, and J-F Lamarque. 2022. "Assessing Responses and Impacts of Solar climate intervention on the Earth system with stratospheric aerosol injection (ARISE-SAI): protocol and initial results from the first simulations." *Geosci. Model Dev.* 15, 8221–8243. https://doi.org/10.5194/gmd-15-8221-2022.

Rieger, D., A. Steiner, V. Bachmann, P. Gasch, J. Förstner, K. Deetz, B. Vogel, and H. Vogel. 2017. "Impact of the 4 April 2014 Saharan dust outbreak on the photovoltaic power generation in Germany." *Atmos. Chem. Phys.* 17, 13391–13415. https://doi.org/10.5194/acp-17-13391-2017.

Robock, A. 2000. “Volcanic eruptions and climate.” *Rev. Geophys.* 38, 191–219. https://doi.org/10.1029/1998rg000054.

Roesch, A., M. Wild, A. Ohmura, E.G. Dutton, C.N. Long, and T. Zhang. 2011a. “Assessment of BSRN radiation records for the computation of monthly means.” *Atmospheric Meas. Tech.* 4, 339–354. https://doi.org/10.5194/amt-4-339-2011.

Roesch, A., M. Wild, A. Ohmura, E.G. Dutton, C.N. Long, and T. Zhang. 2011b. “Corrigendum to “Assessment of BSRN radiation records for the computation of monthly means.” *Atmospheric Meas. Tech.* 4, 973–973. https://doi.org/10.5194/amt-4-973-2011.

Rogers, C.M., and K.P. Bowman. 2001. “Transport of smoke from the Central American fires of 1998.” *J. Geophys. Res. Atmospheres* 106, 28357–28368. https://doi.org/10.1029/2000JD000187.

Rosário, N.E., K.M. Longo, S.R. Freitas, M.A. Yamasoe, and R.M. Fonseca. 2013. “Modeling the South American regional smoke plume: aerosol optical depth variability and surface shortwave flux perturbation.” *Atmos. Chem. Phys.* 13, 2923–2938. https://doi.org/10.5194/acp-13-2923-2013.

Ruiz-Arias, J.A., C. Arbizu-Barrena, F.J. Santos-Alamillos, J. Tovar-Pescador, and D. Pozo-Vázquez. 2016. “Assessing the Surface Solar Radiation Budget in the WRF Model: A Spatiotemporal Analysis of the Bias and Its Causes.” *Mon. Weather Rev*. 144, 703–711. https://doi.org/10.1175/MWR-D-15-0262.1.

Ruiz-Arias, J.A., C.A. Gueymard, and T. Cebecauer. 2019. “Direct normal irradiance modeling: Evaluating the impact on accuracy of worldwide gridded aerosol databases.” *AIP Conference Proc*. 2126: 190013. https://doi.org/10.1063/1.5117710.

Ruosteenoja, K., P. Räisänen, S. Devraj, S.S. Garud, and A.V. Lindfors. 2019. “Future Changes in Incident Surface Solar Radiation and Contributing Factors in India in CMIP5 Climate Model Simulations.” *J. Appl. Meteorol. Climatol.* 58, 19–35. https://doi.org/10.1175/JAMC-D-18-0013.1.

Salazar, G., C.A. Gueymard, J.B. Galdino, O. Vilela, N. de C., Fraidenraich. 2020. “Solar irradiance time series derived from high-quality measurements, satellite-based models, and reanalyses at a near-equatorial site in Brazil.” *Renew. Sustain. Energy Rev.* 117, 109478. https://doi.org/10.1016/j.rser.2019.109478.

Sanchez-Lorenzo, A., M. Wild, M. Brunetti, J.A. Guijarro, M.Z. Hakuba, J. Calbó, S. Mystakidis, and B. Bartok. 2015. “Reassessment and update of long-term trends in downward surface shortwave radiation over Europe (1939–2012).” *J. Geophys. Res. Atmospheres* 120, 9555–9569. https://doi.org/10.1002/2015JD023321.

Sarangi, C., Y. Qian, L.R. Leung, Y. Zhang, Y. Zou, and Y. Wang. 2023. “Projected increases in wildfires may challenge regulatory curtailment of $PM_{2.5}$ over the eastern US by 2050.” *Atmos. Chem. Phys*. 23, 1769–1783. https://doi.org/10.5194/acp-23-1769-2023.

Schwartz, R.E., A. Gershunov, S.F. Iacobellis, and D.R. Cayan. 2014. "North American west coast summer low cloudiness: Broadscale variability associated with sea surface temperature." *Geophys. Res. Lett.* 41, 3307–3314. https://doi.org/10.1002/2014GL059825.

Shaheen, A., R. Wu, R. Yousefi, F. Wang, Q. Ge, D.G. Kaskaoutis, J. Wang, P. Alpert, and I. Munawar. 2023. "Spatio-temporal changes of spring-summer dust AOD over the Eastern Mediterranean and the Middle East: Reversal of dust trends and associated meteorological effects." *Atmospheric Res.* 281, 106509. https://doi.org/10.1016/j.atmosres.2022.106509.

Shi, H., J. Zhang, B. Zhao, X. Xia, B. Hu, H. Chen, J. Wei, M. Liu, Y. Bian, D. Fu, Y. Gu, and K-N Liou. 2021. "Surface Brightening in Eastern and Central China Since the Implementation of the Clean Air Action in 2013: Causes and Implications." *Geophys. Res. Lett.* 48, e2020GL091105. https://doi.org/10.1029/2020GL091105.

Shi, L., J. Zhang, F. Yao, D. Zhang, and H. Guo. 2020. "Temporal variation of dust emissions in dust sources over Central Asia in recent decades and the climate linkages." *Atmos. Environ.* 222, 117176. https://doi.org/10.1016/j.atmosenv.2019.117176.

Sigl, M., M. Winstrup, J.R. McConnell, K.C. Welten, G. Plunkett, F. Ludlow, U. Büntgen, M. Caffee, N. Chellman, D. Dahl-Jensen, and H. Fischer, et al. 2015. "Timing and climate forcing of volcanic eruptions for the past 2,500 years." *Nature* 523, 543–549. https://doi.org/10.1038/nature14565.

Soares, P.M.M., M.C. Brito, and J.A.M. Careto. 2019. "Persistence of the high solar potential in Africa in a changing climate." *Environ. Res. Lett.* 14, 124036. https://doi.org/DOI:10.1088/1748-9326/ab51a1.

Stamatis, M., N. Hatzianastassiou, M-B Korras-Carraca, C. Matsoukas, M. Wild, and I. Vardavas. 2023. "An Assessment of Global Dimming and Brightening during 1984–2018 Using the FORTH Radiative Transfer Model and ISCCP Satellite and MERRA-2 Reanalysis Data." *Atmosphere* 14, 1258. https://doi.org/10.3390/atmos14081258.

Sun, H., X. Liu, and A. Wang. 2020. "Seasonal and interannual variations of atmospheric dust aerosols in mid and low latitudes of Asia – A comparative study." *Atmospheric Res*. 244, 105036. https://doi.org/10.1016/j.atmosres.2020.105036.

Sun, X., D. Yang, C.A. Gueymard, J.M. Bright, and P. Wang. 2022. "Effects of spatial scale of atmospheric reanalysis data on clear-sky surface radiation modeling in tropical climates: A case study for Singapore." *Sol. Energy* 241, 525–537. https://doi.org/10.1016/j.solener.2022.06.001.

Tanaka, K., A. Ohmura, D. Folini, M. Wild, and N. Ohkawara. 2016. "Is global dimming and brightening in Japan limited to urban areas?" *Atmos. Chem. Phys.* 16, 13969–14001. https://doi.org/10.5194/acp-16-13969-2016.

Tomson, T., V. Russak, and A. Kallis. 2008. "Dynamic Behavior of Solar Radiation." In: *Modeling Solar Radiation at the Earth's Surface*. Springer, Berlin, Heidelberg, pp. 257–281. https://doi.org/10.1007/978-3-540-77455-6_10.

Turco, M., J.J. Rosa-Cánovas, J. Bedia, S. Jerez, J.P. Montávez, M.C. Llasat, and A. Provenzale. 2018. "Exacerbated fires in Mediterranean Europe due to anthropogenic warming projected with non-stationary climate-fire models." *Nat. Commun*. 9, 3821. https://doi.org/10.1038/s41467-018-06358-z.

Vignola, F.E., A.C. McMahan, and C.N. Grover. 2013. "Bankable Solar-Radiation Datasets, in: Kleissl, J. (Ed.), Solar Energy Forecasting and Resource Assessment." Elsevier, pp. 97–131. https://doi.org/10.1016/b978-0-12-397177-7.00005-x.

Villoz, A., B. Wittmer, A. Mermoud, M. Oliosi, and A. Bridel-Bertomeu. 2022. "A Model Correcting the Effect of Subhourly Irradiance Fluctuations on Overload Clipping Losses in Hourly Simulations." In: Proceedings of the 8th World Conference on Photovoltaic Energy Conversion. WCPEC, Milan, Italy, pp. 1151–1156. https://doi.org/10.4229/WCPEC-82022-4EO.2.2.

Vindel, J.M., R.X. Valenzuela, A.A. Navarro, and J. Polo. 2020. "Temporal and spatial variability analysis of the solar radiation in a region affected by the intertropical convergence zone." *Meteorol. Appl.* 27, e1824. https://doi.org/10.1002/met.1824.

Wang, R., B. Liu, H. Li, X. Zou, J. Wang, W. Liu, H. Cheng, L. Kang, and C. Zhang. 2017. "Variation of strong dust storm events in Northern China during 1978–2007." *Atmospheric Res.* 183, 166–172. https://doi.org/10.1016/j.atmosres.2016.09.002.

Wang, S.S.-C., L.R. Leung, and Y. Qian. 2023. "Projection of Future Fire Emissions Over the Contiguous US Using Explainable Artificial Intelligence and CMIP6 Models." *J. Geophys. Res. Atmospheres* 128, e2023JD039154. https://doi.org/10.1029/2023JD039154.

Wang, Y., S. Yang, A. Sanchez-Lorenzo, W. Yuan, and M. Wild. 2020. "A Revisit of Direct and Diffuse Solar Radiation in China Based on Homogeneous Surface Observations: Climatology, Trends, and Their Probable Causes." *J. Geophys. Res. Atmospheres* 125, e2020JD032634. https://doi.org/10.1029/2020JD032634.

Weisenstein, D.K., D.W. Keith, and J.A. Dykema. 2015. "Solar geoengineering using solid aerosol in the stratosphere." *Atmos. Chem. Phys.* 15, 11835–11859. https://doi.org/10.5194/acp-15-11835-2015.

Wilcox, S., M. Anderberg, R. George, W. Marion, D. Myers, D. Renné, N. Lott, T. Whitehurst, W. Beckman, C.A. Gueymard, R. Perez, P. Stackhouse, and F. Vignola. 2007. "Completing production of the updated National Solar radiation Database for the United States." In: Proceedings of the Solar 2007 Conf. ASES, Cleveland, Ohio.

Wild, M., D. Folini, F. Henschel, N. Fischer, and B. Müller. 2015. "Projections of long-term changes in solar radiation based on CMIP5 climate models and their influence on energy yields of photovoltaic systems." *Sol. Energy* 116, 12–24. https://doi.org/10.1016/j.solener.2015.03.039.

Wild, M., A. Ohmura, C. Schär, G. Müller, D. Folini, M. Schwarz, M.Z. Hakuba, and A. Sanchez-Lorenzo. 2017. "The Global Energy Balance Archive (GEBA) version 2017: a database

for worldwide measured surface energy fluxes." *Earth Syst. Sci. Data* 9, 601–613. https://doi.org/10.5194/essd-9-601-2017.

Wild, M., S. Wacker, S. Yang, and A. Sanchez-Lorenzo. 2021. "Evidence for Clear-Sky Dimming and Brightening in Central Europe." *Geophys. Res. Lett.* 48, e2020GL092216. https://doi.org/10.1029/2020GL092216.

Wu, Z., and P. Zhang. 2015. "Interdecadal variability of the mega-ENSO–NAO synchronization in winter." *Clim. Dyn.* 45, 1117–1128. https://doi.org/10.1007/s00382-014-2361-8.

Xi, X. 2021. "Revisiting the Recent Dust Trends and Climate Drivers Using Horizontal Visibility and Present Weather Observations." *J. Geophys. Res. Atmospheres* 126, e2021JD034687. https://doi.org/10.1029/2021JD034687.

Xia, X., H. Che, H. Shi, H. Chen, X. Zhang, P. Wang, P. Goloub, and B. Holben. 2021. "Advances in sunphotometer-measured aerosol optical properties and related topics in China: Impetus and perspectives." *Atmospheric Res.* 249, 105286. https://doi.org/10.1016/j.atmosres.2020.105286.

Yang, S., X.L. Wang, and M. Wild. 2019. "Causes of Dimming and Brightening in China Inferred from Homogenized Daily Clear-Sky and All-Sky in situ Surface Solar Radiation Records (1958–2016)." *J. Clim*. 32, 5901–5913. https://doi.org/10.1175/JCLI-D-18-0666.1.

Ye, S., P. Xue, W. Fang, Q. Dai, J. Peng, Y. Sun, J. Xie, and J. Liu. 2021. "Quantitative effects of PM concentrations on spectral distribution of global normal irradiance." *Sol. Energy* 220, 1099–1108. https://doi.org/10.1016/j.solener.2020.08.070.

Yordanov, G.H., T.O. Saetre, and O-M Midtgård. 2015. "Extreme overirradiance events in Norway: 1.6 suns measured close to 60°N." *Sol. Energy* 115, 68–73. https://doi.org/10.1016/j.solener.2015.02.020.

Zhang, L., Y. Zhang, X. Yi, Y. Yang, M. Zhao, and J. Zhou. 2020. "Seasonal variations of the impact of urban aerosol pollution on distributed solar photovoltaic generation of nine megacities in China." *Urban Clim.* 34, 100723. https://doi.org/10.1016/j.uclim.2020.100723.

Zhang, Y., W. Qin, L. Wang, C. Yang, X. Su, and J. Wu. 2023. "Enhancement of Photovoltaic Power Potential in China from 2010 to 2020: The Contribution of Air Pollution Control Policies." *Remote Sens*. 15, 228. https://doi.org/10.3390/rs15010228.

Zhao, X., G. Huang, C. Lu, X. Zhou, and Y. Li. 2020. "Impacts of climate change on photovoltaic energy potential: A case study of China." *Appl. Energy* 280, 115888. https://doi.org/10.1016/j.apenergy.2020.115888.

Zhao, Y., X. Yue, Y. Cao, J. Zhu, C. Tian, H. Zhou, Y. Chen, Y. Hu, W. Fu, and X. Zhao. 2023. "Multi-model ensemble projection of the global dust cycle by the end of 21st century using the Coupled Model Intercomparison Project version 6 data." *Atmos. Chem. Phys.* 23, 7823–7838. https://doi.org/10.5194/acp-23-7823-2023.

Zhou, Z., A. Lin, L. Wang, W. Qin, L. Zhao, S. Sun, Y. Zhong, L. He, and F. Chen. 2021. "Estimation of the losses in potential concentrated solar thermal power electricity production due to air pollution in China." *Sci. Total Environ*. 784, 147214. https://doi.org/10.1016/j.scitotenv.2021.147214.

Zou, L., L. Wang, J. Li, Y. Lu, W. Gong, and Y. Niu. 2019. "Global surface solar radiation and photovoltaic power from Coupled Model Intercomparison Project Phase 5 climate models." *J. Clean. Prod*. 224, 304–324. https://doi.org/10.1016/j.jclepro.2019.03.268.

7 Modeling Solar Radiation: Current Practices

Manajit Sengupta,[1] Yu Xie,[1] Christian Gueymard,[2] and Hadrien Verbois[3]
[1] *National Renewable Energy Laboratory, USA*
[2] *Solar Consulting Services, USA*
[3] *MINES Paristech, France*

Executive Summary

Radiative transfer modeling has existed for over a century and has primarily been used in meteorological applications. With the advent of solar energy, modeling requirements have changed significantly over the years. Satellite-based applications required fast modeling techniques, while direct normal irradiance (DNI) and global tilted irradiance (GTI) became important quantities. Satellite-based solar energy estimates have been developed over the years and are still being actively improved as next-generation meteorological satellites are deployed. Merging satellite estimates and ground observations have become important as the solar energy modeling world responds to the need for unbiased estimates of higher accuracy. Numerical weather prediction (NWP) models have also evolved over the years to fulfill the needs of solar energy forecasting.

This chapter provides a brief overview of solar radiation modeling methods, specifically emphasizing satellite-based models. Since the 1980s, the technology of operational meteorological satellites and models to estimate surface radiation from these satellites have improved in their resolution and accuracy. With the launch of the Geostationary Operational Environmental Satellite (GOES)-R series, Meteosat Third Generation (MTG_I1), the FengYun (FY)4 series, Himawari-9, and GEO-KOMPSAT-2A (GK-2A) geostationary satellites, the world is now covered at temporal resolutions of 15 minutes or better and spatial resolutions of ≈1 km, except at high latitudes. Improvements in computational capabilities have also contributed to improving the scientific community's ability to use increasingly sophisticated models capable of handling large volumes of satellite and ancillary datasets and that ultimately deliver products of increasing resolution and accuracy. Additional discussions include more recent efforts to use machine learning (ML)-based methods to estimate solar radiation.

Site-adaptation models have been used to improve local assessments of solar radiation. These models generally use short-term ground-based solar measurements to adjust long-term satellite-based solar radiation datasets. This chapter contains a summary of site-adaptation practices.

This chapter also contains a short introduction to NWP modeling because improvements in that area can contribute to better irradiance estimates around the globe.

7.1 Introduction

High-quality solar resource assessment accelerates the deployment of solar technologies by making a positive impact on decision-making and minimizing uncertainty in investment choices. Global horizontal irradiance (GHI), GTI, and/or DNI are quantities of interest for solar resource assessment and characterization at a particular location. Surface-based measurements of DNI and GHI can be made only on a relatively sparse network, given the high operational and maintenance costs. GTI measurements are even less common in radiometric networks. Nevertheless, observations from ground networks have been used in conjunction with models to

generate surface solar radiation maps (Qin et al. 2020). An alternative approach involves leveraging information from geostationary satellites to estimate GHI and DNI at the Earth's surface (Beyer et al. 1996; Cano et al. 1986; Cebecauer and Suri 2010; Diabaté et al. 1987; Perez et al. 2002; Pinker and Laszlo 1992; Qu et al. 2017; Rigollier et al. 2004). Because different geostationary satellites cover distinct longitudes worldwide, solar radiation data can be obtained for the entire globe (at least between latitudes from approximately -60° to +60°) at temporal and spatial resolutions representative of a particular satellite. A compilation of satellite-derived data based on observations from polar orbiters offers good spatial coverage for regions located at higher northern or southern latitudes, but typically at a lower spatiotemporal resolution (Karlsson et al. 2017a; 2017b; Kato et al. 2018).

Solar radiation models relying solely on ground-measured input parameters were used in the past when satellite or weather-model-derived databases were not available. Examples of such models are briefly mentioned in this chapter for historic reasons. One notable model type is based on data from the Campbell-Stokes sunshine duration recorder. This model derives the monthly-mean GHI by fitting a regression equation to the number of sunshine hours measured by the sunshine recorder's burn marks when direct solar irradiance exceeds an assumed threshold value of 120 W/m^2. The regression coefficients are calculated using existing GHI measurements at specific locations. The exact method to calculate GHI using sunshine recorder information is empirical and therefore specific to each geographic area. Moreover, the meteorological services of some countries, such as the United States or Canada, have discontinued the measurement of sunshine duration due to its limited quality, lack of standardization, and variation among countries.

In the absence of surface radiation measurements, estimates of surface radiation can be made using routine meteorological ground measurements and human observations of cloud cover in a radiative transfer model (Marion and Wilcox 1994). For instance, the METeorological-STATistical (METSTAT) model (Maxwell 1998) used information about cloud cover, water vapor, ozone, and aerosol optical depth (AOD) to develop empirical correlations to compute atmospheric transmittance extinction during both clear- and cloudy-sky conditions. That model was used to create earlier versions of the U.S. National Solar Radiation Database (NSRDB) (1991–2005) (e.g., [George et al. 2008]). Similar developments have been carried out in Europe with successive versions of the European Solar Radiation Atlas (Page et al. 2001).

Long-term GHI data can also be obtained from various NWP models, either through operational weather forecasts or their derived reanalysis mode for historical time series. Examples of reanalysis data include the European Center for Medium-Range Weather Forecasting (ECMWF) Reanalysis version 5 (ERA5) (Hersbach et al. 2020; Trolliet et al. 2018) and the Modern Era Retrospective analysis for Research and Applications, Version 2 (MERRA-2) from the National Aeronautics and Space Administration (NASA) (Collow et al. 2023; Trolliet et al. 2018) . Weather forecasts such as those from the ECMWF's Integrated Forecasting System (IFS) and the National Oceanic and Atmospheric Administration's (NOAA's) Global Forecast System (GFS) can also provide estimates of GHI. Such estimates, however, are typically not as accurate as those derived from satellite-based models, and thus often require careful bias corrections (Boilley and Wald 2015; Urraca et al. 2018).

This chapter contains an introduction to satellite-based models, information about currently operational models that provide surface radiation data for current or recent periods, and a summary of radiative transfer models used in the operational models. A short discussion on NWP-based solar radiation data is also included. The uncertainty in modeled irradiance predictions and solar-based resource assessments is further elaborated upon in Chapter 10.

7.2 Radiative Transfer Models

To evaluate the solar irradiance incident at the planetary surface, various types of calculation methods have been proposed. As a general rule, simple empirical models should be avoided because of their limited spatial representativeness. Nevertheless, such models are still necessary to separate GHI into its direct and diffuse components (Section 7.3.1) and to estimate GTI (Section 7.3.2). In general, though, the surface predictions of GHI (at least) based on satellite imagery or made by NWP models are based on one or more radiative transfer models. The all-sky calculations are typically made in two steps: a clear-sky model is used first to evaluate the ideal clear-sky irradiance components, and then a cloud model is activated (if necessary) to alter those ideal results and reflect realistic conditions. Radiative transfer models are normally of a spectral nature for physical reasons, but broadband or multiband simplifications also exist, which are used more widely in solar applications because they are faster. Sections 7.2.1 and 7.2.2 provide details on clear-sky models and cloudy-sky models, respectively.

7.2.1 Clear-Sky Radiative Transfer Models

The Bird clear-sky model (Bird and Hulstrom 1981) is a broadband algorithm that produces estimates of clear-sky direct beam, hemispherical diffuse, and total hemispherical solar radiation on a horizontal surface. It uses a parameterization based on radiative transfer computations and that comprises simple algebraic expressions. The model results are expected to exhibit agreement within ±10% when compared to detailed high-resolution spectral or broadband physics-based radiative transfer models. The Bird clear-sky model can be used at resolutions of 1 minute or better and can duly accept inputs at that frequency, if available. In the absence of high-temporal-resolution input parameters, however, climatological or annual average values can be used as suitable alternatives. The Bird clear-sky model also forms the foundation for the clear-sky component of METSTAT, albeit with minor modifications (Maxwell 1998). The performance of both models has been assessed rigorously and compared to other algorithms (Badescu et al. 2012; Gueymard 2012a; 2004a; 2004b; 2003a; 2003b; Gueymard and Myers 2008; Gueymard and Ruiz-Arias 2015).

The European Solar Radiation Atlas (ESRA) model is another example of a clear-sky model (Rigollier et al. 2000). Used in the Heliosat-2 model that estimates GHI from satellites, this model computes DNI, GHI, and DHI using Rayleigh optical depth, elevation, and the Linke turbidity factor as its inputs. The performance of the model has been evaluated at various locations (Badescu et al. 2012; Gueymard 2012a; Gueymard and Myers 2008; Gueymard and Ruiz-Arias 2015).

The Solar Irradiance Scheme (SOLIS) model (Mueller et al. 2004) is a relatively simple clear-sky model that can calculate DNI, GHI, and DHI over the relatively narrow spectral bandwidth of various spaceborne radiometer channels, based on an approximation to the Lambert-Beer relation for computing DNI:

$$I = I_0 \, e^{(-M*\tau)} \quad (7\text{-}1)$$

where:

- τ is the atmospheric optical depth at a specific wavelength.
- M is the optical air mass.
- I_0 is the top-of-atmosphere (TOA) spectral direct irradiance.
- I is the spectral DNI at the surface.

This equation is modified to account for slant paths and adapted for global and diffuse radiation. The modified Lambert-Beer relation (Mueller et al. 2004) is:

$$I(\text{SZA}) = I_0 \cdot \exp(-\tau_c / \cos^c(\text{SZA})) \quad (7\text{-}2)$$

where:

- I(SZA) is one of the irradiance components GHI, DNI, or DHI.
- c is an empirical exponent that depends on the radiation component DNI, DHI, or GHI.
- τ_c is the vertical broadband optical depth of the atmosphere for the radiation component of interest.
- SZA is the solar zenith angle.

The Beer-Lambert equation is a simple relationship to evaluate DNI based only on the impact of atmospheric attenuation. On the other hand, DHI and GHI contain energy that is scattered by the atmosphere. The empirical exponent c is thus used as an adjustment to compute either GHI or DHI using the modified Beer-Lambert approach represented by Eq. 7-2. Ineichen (2008) further developed the "simplified SOLIS" (broadband) version of that clear-sky model by obtaining parameterizations (for a limited range of atmospheric conditions) to replace radiative transfer model runs, thereby increasing the speed of the model and its functionality in most solar applications.

The McClear model is a clear-sky broadband model that implements a fully physical approach, replacing the empirical relations or simpler models used before, such as ESRA. It exploits the recent results on aerosol properties and total column content in water vapor and ozone produced by the European Copernicus Atmosphere Monitoring Service (CAMS) project. It is based on lookup tables precomputed with the radiative transfer model libRadtran (Gschwind et al. 2019). The model is not operable by individuals, but its outputs are offered as a free web-based service to registered users.[42] McClear irradiance predictions were compared to 1-minute measurements conducted under clear-sky conditions at several Baseline Surface Radiation Network (BSRN) stations representative of various climates (Lefèvre et al. 2013). The correlation coefficients range from 0.95–0.99 and from 0.86–0.99 for GHI and DNI, respectively. The bias ranges from 14–25 W/m² and 49–33 W/m², respectively. The root mean-square errors range from 20 W/m² (3% of the mean observed irradiance) to 36 W/m² (5%) and from 33 W/m² (5%) to 64 W/m² (10%), respectively.

[42] See https://www.soda-pro.com/web-services/radiation/cams-mcclear.

Reference Evaluation of Solar Transmittance v2 (REST2) is a high-performance model that utilizes transmittance parameterizations across two distinct spectral bands separated at 0.7 μm. The model's development and its benchmarking are described by Gueymard (2008b). REST2 has been thoroughly validated and compared to other irradiance models under varied atmospheric conditions, including scenarios with extremely high aerosol loads (Antonanzas-Torres et al. 2016; Engerer and Mills 2015; Gueymard 2014; 2012a; Gueymard and Ruiz-Arias 2015; Sengupta and Gotseff 2013; Zhong and Kleissl 2015). The model is used in solar-related applications, including the benchmarking of the radiative output of the Weather Research and Forecasting (WRF) model (Ruiz-Arias et al., 2012), the operational derivation of surface irradiance components using Moderate Resolution Imaging Spectroradiometer (MODIS) satellite observations (Chen et al. 2014), the improvement in GHI to DNI separation modeling (Vindel et al. 2013), and the development of future climate scenarios (Fatichi et al. 2011). REST2 is integrated into the algorithms used by some commercial providers to derive satellite-based irradiance data. Similarly, it is also integrated into the Fast All-sky Radiation Model for Solar applications (FARMS) suite of algorithms (Xie et al. 2016) that produces the current version of the National Renewable Energy Laboratory's (NREL's) NSRDB (1998–2022, with annual updates), as discussed further in the following subsections.

7.2.2 Cloudy-Sky Radiative Transfer Models

Radiative transfer models can simulate atmospheric radiation under all-sky conditions and have been used in a broad range of applications, such as satellite remote sensing and climate studies. Compared to other applications, solar energy has unique requirements from radiative transfer models and thus has prerequisites in the model design. For instance, the study of solar energy demands more-efficient simulations of solar irradiance than the conventional models used in weather or climate studies, such as the Rapid Radiation Transfer Model (RRTM) or its simplified two-stream version specially tailored for general circulation models (RRTMG). To provide a new option for efficiently computing solar radiation, NREL developed FARMS (Xie et al. 2016) using cloud transmittances and reflectances for direct and diffuse radiation computed by RRTM with the 16-stream discrete-ordinates radiative transfer method. To reduce the computing burden, the cloud transmittances and reflectances are parameterized as functions of SZA, cloud thermodynamic phase, optical thickness, and particle size. The all-sky GHI, DHI, and DNI are ultimately computed by coupling the cloud transmittances and reflectances with surface albedo and a fast clear-sky radiation model (REST2, discussed above) to account for atmospheric absorption and scattering.

To evaluate the accuracy and efficiency of FARMS, GHI was simulated using the cloud microphysical and optical properties retrieved from GOES data during 2009–2012 with both FARMS and RRTMG and compared to measurements taken at the Southern Great Plains site of the U.S. Department of Energy's Atmospheric Radiation Measurement Climate Research Facility. Results indicate that FARMS achieves comparable or superior accuracy compared to the two-stream approach; however, FARMS is approximately 1000 times more efficient and faster because it does not explicitly solve the radiative transfer equation for each individual cloud condition. Note that FARMS, as well as the conventional radiative transfer models developed for weather and climate studies, outputs only broadband irradiance over horizontal surfaces. Recently, FARMS expanded its capabilities to incorporate tilted surfaces and spectral distributions (Xie et al. 2019; Xie and Sengupta 2018). The model's spectral expansion follows the same principle of separation between the clear atmosphere and the cloud layer as in the

broadband version of FARMS but replaces the REST2 clear-sky predictions with those from the SMARTS spectral model, described in Gueymard (2022; 2001).

The CAMS radiation service[43] uses a physical retrieval of cloud parameters and the fast parameterized radiative transfer method called Heliosat-4 (Qu et al. 2017). The new Heliosat-4 method computes GHI, DNI, and DHI under all-sky conditions as a broadband aggregation of spectrally resolved internal computations. It is a highly efficient yet accurate physical model that mimics a full radiative transfer model, and it is well suited for geostationary satellite retrievals. The foundation of Heliosat-4 is based on the work conducted by Oumbe et al. (2014), which proved that the surface solar irradiance can be approximated by the product of the irradiance under cloudless conditions and a modification index depending solely on cloud properties and ground albedo. This is why Heliosat-4 contains two precomputed lookup-table-based models: the McClear model (Gschwind et al. 2019; Lefèvre et al. 2013) for clear-sky conditions, discussed above, and the McCloud model for cloudy conditions. Like with McClear, the McCloud database was developed using the libRadtran radiative transfer model (Mayer and Kylling 2005). The main input to the McCloud part of Heliosat-4 is the cloud optical depth (COD). With Meteosat Second Generation (MSG) satellite observations, cloud properties are derived at a 15-minute temporal resolution using an adapted Advanced Very High Resolution Radiometer (AVHRR) Processing scheme Over cLouds, Land, and Ocean (APOLLO) retrieval scheme. Schroedter-Homscheidt et al. (2021) have written a concise summary of this topic.

7.3 Other Irradiance Models for Solar Energy Applications

7.3.1 Estimating the Direct and Diffuse Components From Global Horizontal Irradiance

During clear and partly cloudy conditions, the diffuse irradiance incident on a horizontal surface, DHI, is often a relatively small part (<30%) of GHI. In contrast, during dense overcast conditions, GHI and DHI should be identical. In situations in which there are no simultaneous DHI or DNI measurements and alternate determinations are unavailable—for example, from physical-based satellite-based models—DNI and DHI must be estimated from GHI data. Many models based on empirical correlations between GHI and either DHI or DNI hourly data have been developed over the years (Erbs et al. 1982; Liu and Jordan 1960; Maxwell 1987; Perez et al. 1990). More recently, Engerer (2015), Aler et al. (2017), Yang and Gueymard (2020), Starke et al. (2021), Yang et al. (2024), and Ruiz-Arias and Gueymard (2024), among others, extended this empirical methodology to obtain DNI and DHI at 1-minute resolution. These algorithms use correlations between the global clearness index, K_t = GHI/[ETR cos(SZA)], and the diffuse fraction, K = DHI/GHI, the diffuse clearness index (i.e., the diffuse transmittance), K_d = DHI/[ETR cos(SZA)], or the direct clearness index (direct transmittance), K_n = DNI/ETR. These separation models are derived empirically, using measurements from a variable number of stations. There are reviews of the substantial literature on this topic (e.g., Gueymard [2008a], Gueymard and Ruiz-Arias [2016], Tapakis et al. [2016], and Tan et al. [2023]). Analysts should note that certain hourly separation models, including the most popular ones, might not perform correctly when applied to subhourly data (Gueymard and Ruiz-Arias 2016).

[43] See https://www.soda-pro.com/web-services/radiation/cams-radiation-service.

7.3.2 Estimating Irradiance on a Tilted Surface (Transposition Models)

Solar conversion systems, such as flat-plate collectors or non-concentrating photovoltaics (PV), are typically inclined toward the equator to optimize their solar resource. Estimating or modeling the irradiance incident upon them is essential to predicting their performance and yield. This irradiance incident on the plane of array (POA) is commonly referred to as GTI, or POA irradiance. GTI can be measured directly by pyranometers that are tilted in the same manner as the collector plane. Modeling GTI mainly requires data of the three main components on the horizontal surface (GHI, DNI, and DHI). GTI can be estimated as the sum of the incident beam, incident sky diffuse, and incident ground-reflected irradiances on the tilted surface. The incident beam contribution involves a straightforward geometric transformation of DNI, requiring only the angle of incidence of DNI on the tilted plane (see Chapter 2). The ground-reflected contribution is generally small for tilts less than 45°, unless the ground is covered with snow. A simple estimation is possible but requires several assumptions: the foreground is assumed infinite, horizontal, and of isotropic reflectance. In practice, however, the reflected irradiance incident on collectors or the front panel of PV modules located behind the front row would be overestimated with this approach. In recent years, the rapid uptake of bifacial PV technology has brought the calculation of reflected irradiance to the forefront because it is the main resource for the backside of PV modules. That calculation is complex because of the number of variables involved, including the directional and spectral properties of the reflectance for each type of surface and the shading caused by the supporting structure. No simple model is currently available to provide accurate results in all possible cases and geometries.

In general, the main difficulty is the computation of the sky diffuse irradiance, which has been studied by many authors with different approaches, ranging from the simplest isotropic model to more elaborate and complex formulations (Gueymard 1987; 2008a; Kambezidis et al. 1994; Khalil and Shaffie 2013; Liu and Jordan 1960; Loutzenhiser et al. 2007; Muneer and Saluja 1985; Olmo et al. 1999; Padovan and Del Col 2010; Wattan and Janjai 2016; Xie and Sengupta 2016). See also the review of these models in Yang (2016). Among the various models available, the Perez model (Perez et al. 1990; 1988; 1987) has gained widespread usage and has been validated at a variety of stations. It is the result of a thorough analysis of the isotropic diffuse, circumsolar, and horizon brightening irradiances computed by using empirically derived parameters. The Perez model works well with hourly data, but it might generate erroneous values with subhourly data under extreme conditions when $K_t > 1$ (i.e., cloud-enhancement events) (Gueymard 2017). A modified version of the Perez model has been proposed recently (Driesse et al. 2024) to remove any temporal discontinuity in its predictions.

7.4 Introduction to Satellite-Based Models

The goal of satellite-based irradiance models is to use observed information on TOA upwelling radiances, atmospheric properties, and surface albedos to derive GHI and DNI at the surface of the Earth. During the last decades, satellite-based retrievals of GHI have been used, for example, for climate studies (Justus et al. 1986). Renné et al. (1999) provide a comprehensive overview of these methods, which were originally classified into subjective, empirical/statistical, empirical/physical, and physical methods (Myers 2013; Pinker et al. 1995; Schmetz 1989). The empirical/statistical methods are based on developing relationships between satellite- and ground-based observations; the empirical/physical and theoretical methods estimate surface radiation directly from satellite information using retrieval schemes to determine the atmospheric

properties important to radiative transfer. Most empirical/statistical and empirical/physical models are now considered semiempirical because they involve the development of intermediate relationships either to relate satellite observations with surface radiation measurements or to convert satellite observations directly to solar radiation estimates. A schematic flowchart is shown in Figure 7-1. Empirical and semiempirical methods generally produce only GHI and require additional models (see Section 7.3.1) to estimate DNI from GHI. Physical models, on the other hand, generally follow a two-step process that derives cloud optical properties using the satellite radiances in the first step and computes both GHI and DNI using these cloud properties in a radiative transfer model in the second step, as described in Figure 7-2.

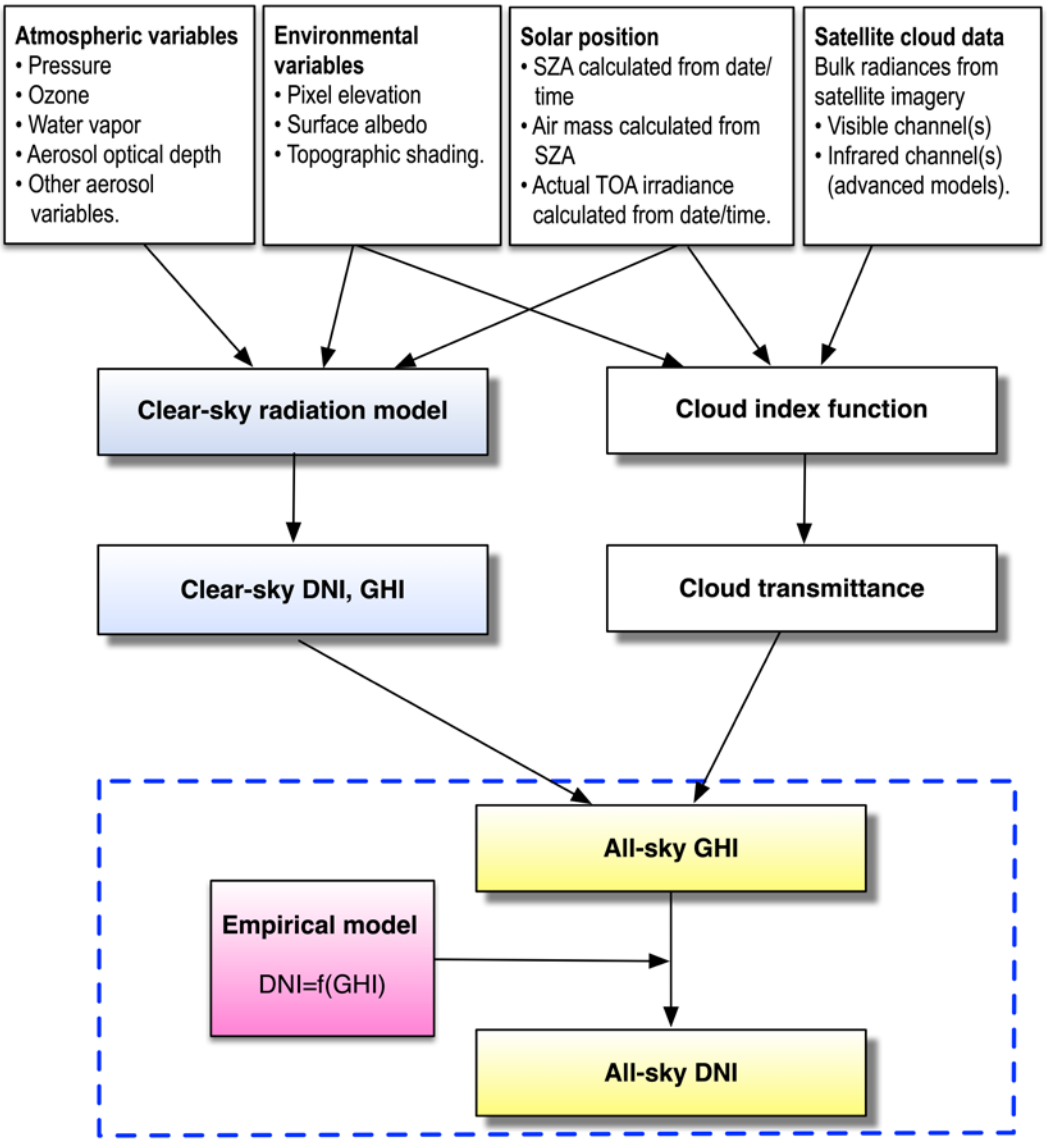

Figure 7-1. Schematic flowchart describing the different modeling parts of semiempirical satellite models (SZA: Solar zenith angle; TOA: Top of atmosphere)

Image by C. Gueymard

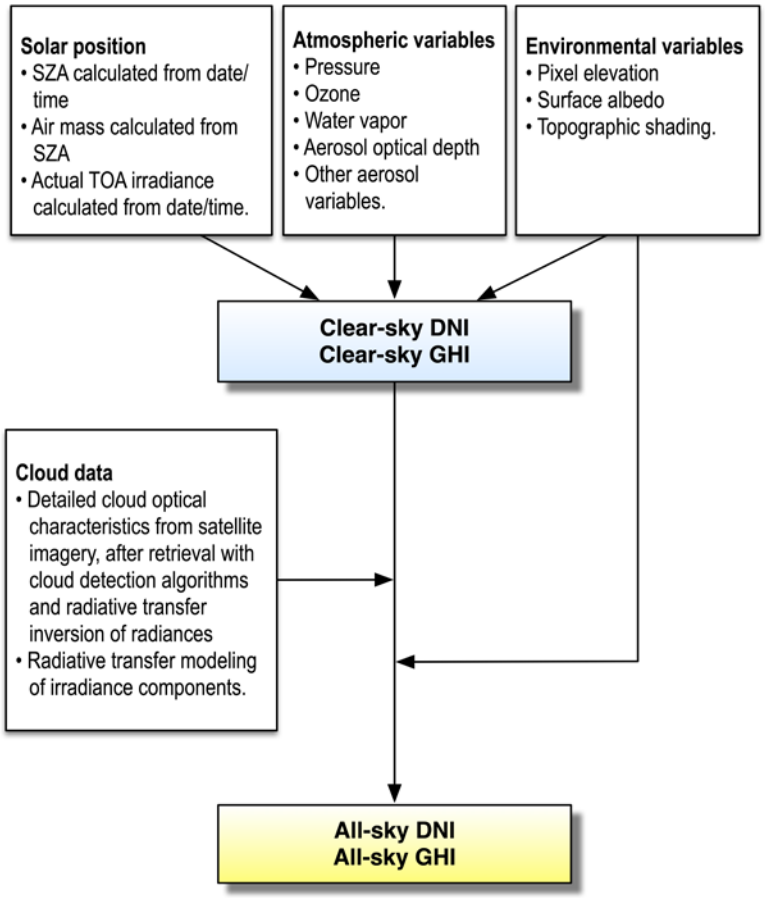

Figure 7-2. Schematic flowchart describing the different modeling parts of physical satellite models (SZA: Solar zenith angle; TOA: Top of atmosphere)

Image by C. Gueymard

7.4.1 Geostationary Meteorological Satellites

Geostationary satellites positioned above the equator and synchronized with the Earth's rotation provide continuous coverage within their field of view. Observations are usable up to latitudes 60°N and 60°S only because of the Earth's curvature, as shown in Figure 7.3. A number of satellites are required for global coverage, as depicted in that figure. Below, the various satellites that are currently operational around the world are introduced. These satellites have been deployed by various countries or groups of countries.

GOES is designed to cover North and South America. Two satellites of the most recent GOES-R series (GOES-East/GOES-16 and GOES-West/GOES-17) operate concurrently and provide full-disk coverage of North and South America every 10–15 minutes and of the Northern Hemisphere part of that domain every 5 minutes. The Advanced Baseline Imager (ABI) sensor on the current GOES satellites makes radiance observations in 16 wavelength bands, or spectral regions (Table 7-1) (Schmit et al. 2018; 2005). GOES-16 and -17 became operational in 2018 and 2019, respectively. The wavelengths in Table 7-1 are representative of the latest generation of GOES satellites. The previous version of the GOES-East and GOES-West series provided data for only

five channels (one visible, four infrared) every 30 minutes for the Northern Hemisphere and every 3 hours at full disk.

Table 7-1. GOES-16 and GOES-17 ABI Bands

ABI Band	Central Wavelength (μm)	Type	Spatial Resolution at Nadir (km)
1	0.47	Visible	1
2	0.64	Visible	0.5
3	0.86	Near-infrared	1
4	1.37	Near-infrared	2
5	1.6	Infrared	1
6	2.2	Infrared	2
7	3.9	Infrared	2
8	6.2	Infrared	2
9	6.9	Infrared	2
10	7.3	Infrared	2
11	8.4	Infrared	2
12	9.6	Infrared	2
13	10.3	Infrared	2
14	11.2	Infrared	2
15	12.3	Infrared	2
16	13.3	Infrared	2

The Meteosat series of satellites, owned by the European Organisation for the Exploitation of Meteorological Satellites (EUMETSAT), offer coverage over Europe, Africa, Middle East, the Indian Ocean, and western Asia. The visible and infrared imager on the Meteosat First Generation (MFG) satellites (up to Meteosat-7) had three visible channels, water vapor (6.2 μm), and infrared. The visible and infrared channels both produced imagery at 5-km nadir resolution. Moreover, there were two channels with 2.5-km resolution, presented in an interleaved format. Imagery had a repetition frequency of 30 minutes. The Spinning Enhanced Visible and InfraRed Imager (SEVIRI) on the MSG satellites (Meteosat-8 onward) provides satellite imagery every 15 minutes at a nominal 3-km resolution for 11 channels (Schmetz et al. 2002). The twelfth channel, a high-resolution visible channel, has a nadir resolution of 1 km. EUMETSAT operates two satellites simultaneously to cover Europe and Africa. These coverages are generally referred to as “prime coverage” and Indian Ocean Data Coverage (IODC). EUMETSAT recently launched a Meteosat Third Generation (MTG) satellite, MTG-I1. The Flexible Combined Imager (FCI) onboard MTG replaces the SEVIRI instrument and contains 16 channels covering the visible, near-infrared, and infrared parts of the spectrum. Meteosat-9 (IODC), Meteosat-10, and Meteosat-11 remain the operational satellites for EUMETSAT, while MTG-I1 still undergoes various tests.

The Himawari series of satellites are third-generation satellites comparable to GOES-16 and MTG. The Himawari series provides coverage over East Asia and the Western Pacific region. Himawari-8 was launched in October 2014 and harbors the Advanced Himawari Imager (AHI), which has characteristics similar to the ABI (Bessho et al. 2016). Of the 16 bands, the visible and

near-infrared bands sense at 0.5-km or 1-km resolution, whereas the infrared bands sense at 2-km resolution. A full-disk image is produced every 10 minutes, and the sectors are generated every 2.5 minutes. Himawari-8 replaced the Multifunctional Transport Satellite series of satellites, which had been in operation since 2005. Himawari-9 was launched in 2017 and was transitioned to full operation in December 2022, at which point Himawari-8 was placed on standby.

The FengYun (FY-4) is the second-generation of meteorological weather satellites first launched by the Chinese Meteorological Administration (CMA) in 2016. The 14-channel Advanced Geostationary Radiation Imager (AGRI) provides high-resolution images in the visible and infrared. The FY-4A and FY-4B are the currently operational satellites, providing data every 15 minutes at a 4-km resolution covering China, Southeast Asia, and Australia. Using FY-4A imagery, a combination of the Heliosat-2 semiempirical method and regional adaptation has been used to derive GHI at subkilometer resolution over China (Huang et al. 2023).

The Korean Meteorological Administration launched the GEO-KOMPSAT-2A (GK-2A) in 2018, which became operational in 2019. The Advanced Meteorological Imager (AMI) onboard GK-2A has 16 channels comparable to ABI and AHI. This satellite is located at 128.2ºE and covers India, Southeast Asia, Korea, China, and Australia. Data is collected every 10 minutes for the full disk. The spatial resolution is 1 km for the visible and 2 km for the infrared channels.

The Indian National Satellite-3DR (INSAT-3DR) is the latest in the INSAT series and has been in service since 2016. INSAT-3DR is located at 74ºE and collects data from the Imager instrument in 6 channels covering the visible and infrared regions. Data is available every half-hour at a spatial resolution of 1–4 km and covers India and Southeast Asia.

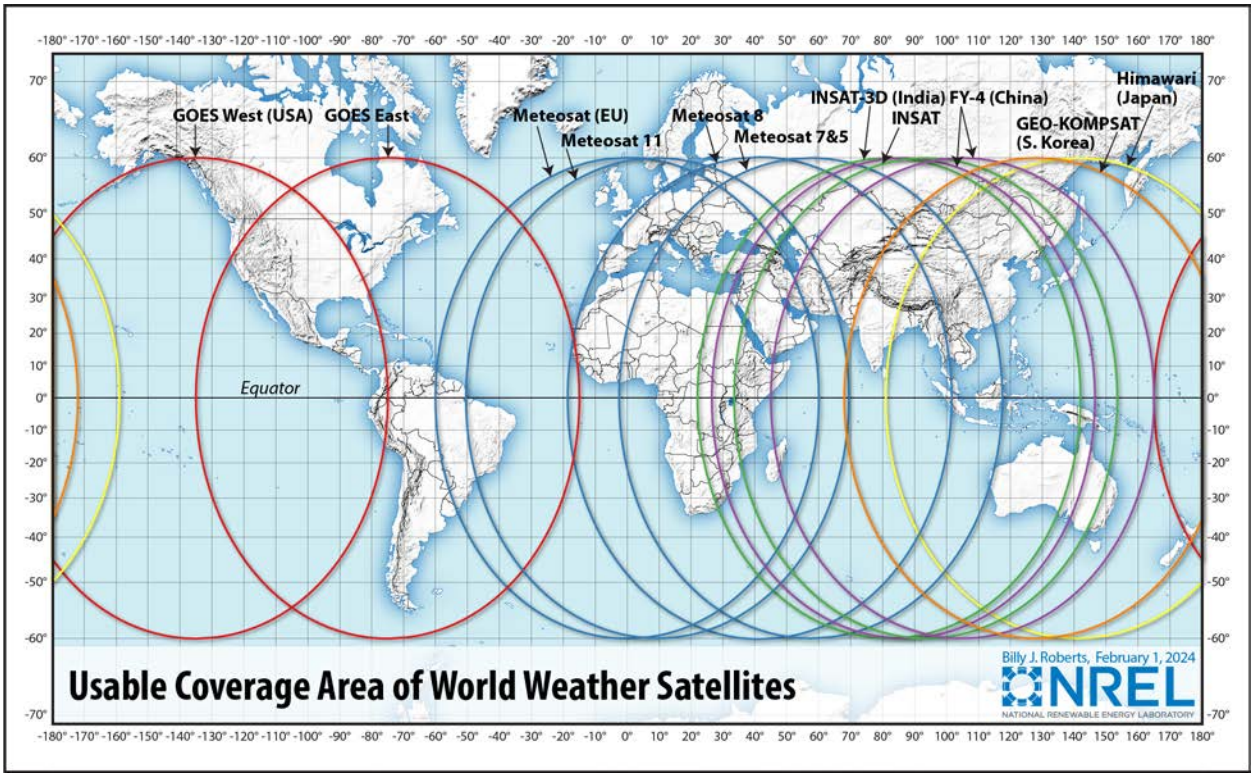

Figure 7-3. Location of the current geostationary satellites providing coverage around the globe

Image by Billy Roberts, NREL

7.4.2 Polar-Orbiting Satellites

Polar-orbiting satellites are used to continuously sense the Earth and retrieve cloud properties and solar radiation at the surface, among many other features. One widely used instrument for this purpose is the AVHRR, which is mounted on the NOAA series of polar-orbiting platforms. Other examples are MODIS, the Multi-angle Imaging SpectroRadiometer (MISR), and the Clouds and the Earth's Radiant Energy System (CERES) instruments on NASA's Aqua and Terra satellites. Aqua and Terra (launched in 2002 and 1999, respectively) have already far exceeded their design life. Terra began drifting in early 2020 and was repositioned to a lower orbit a few months later. The end of their lives is fast approaching, but there are currently no specific plans to replace them.

The Joint Polar Satellite System (JPSS) series of satellites is expected to replace the legacy NOAA polar satellites. The first satellite in the JPSS series was launched in 2011 and is called the Suomi National Polar-Orbiting Partnership. The second satellite, NOAA-20, was launched in 2017, and the third satellite, NOAA-21, became operational in November 2023. This next-generation series of satellites features a suite of instruments, including the Visible Infrared Imaging Radiometer Suite, Cross-track Infrared Sounder, Advance Technology Microwave Sounder, Ozone Mapping and Profiler Suite, and CERES.

Although polar orbiters provide global coverage, their temporal coverage is limited due to their orbital characteristics, resulting in one single coverage instant per specific location and per day at lower latitudes. At higher latitudes, a combination of many polar-orbiting satellite-based

products is recommended to achieve a sufficient temporal resolution while also benefiting from better spatial resolution.

7.4.3 Deep Space Satellite

The Deep Space Climate Observatory (DSCOVR) spacecraft was launched in 2015 and is located at the Lagrange L1 point ≈1.5 million km from Earth, which gives DSCOVR a unique vantage point to monitor the Earth atmosphere—and even, occasionally, the far side of the Moon (Figure 7-4). The Earth Polychromatic Imaging Camera (EPIC) instrument onboard DSCOVR takes full Earth pictures (including polar regions) at ≈10-km resolution every 2 hours, which makes its refresh rate intermediate between that of geosynchronous satellites and polar orbiters. Information on ozone, aerosols, clouds, and various other atmospheric constituents is retrieved operationally from the EPIC imagery. NOAA has not developed an operational EPIC-derived irradiance product, unfortunately, except for the photosynthetically active radiation (PAR) component, which is limited to the 400–700-nm waveband. Nevertheless, an empirical model has been developed to derive GHI and its direct and diffuse components on an hourly basis (Hao et al. 2020). A recent validation, however, showed various issues with this methodology and that its GHI results were not up to par with reanalysis products (Yang et al. 2022).

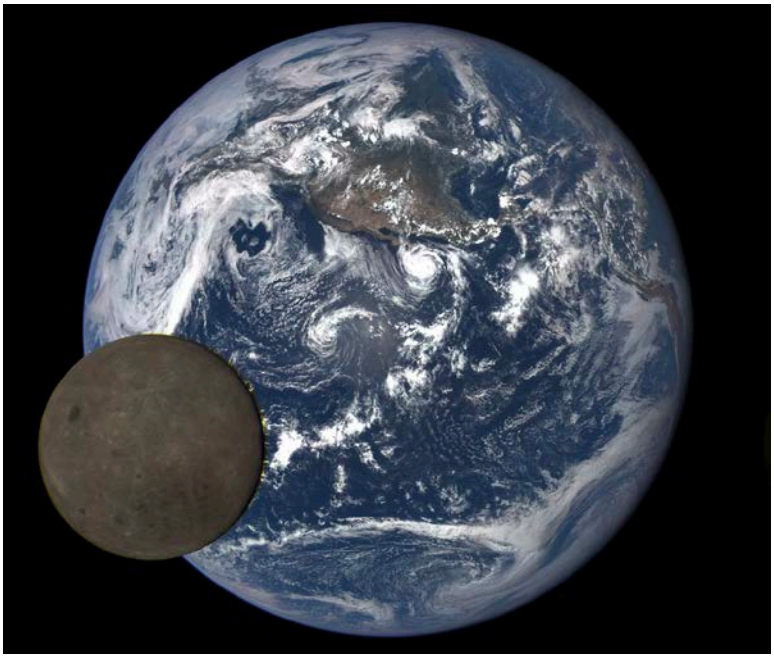

Figure 7-4. View of Earth and far side of the Moon from the EPIC instrument onboard DSCOVR at Lagrange Point L1 on July 16, 2015

Image from NASA/NOAA

7.4.4 Satellite-Based Empirical and Semiempirical Methods

Satellite-based semiempirical methods consider a pseudo-linear correlation between the atmospheric transmittance and the radiance sensed by the satellite. These models belong to the semiempirical category due to their hybrid approach to retrieving surface radiation from satellite observations, in which the normalized satellite-observed reflectance is related to GHI at the surface. Cloud-cover indices that use visible satellite imagery are first created with budget equations between TOA and surface radiation. Those indices are then used to modify the clear-

sky GHI and estimate GHI at the ground consistent with the cloud scene. DNI can then be derived from GHI and the clear-sky DNI using one of the empirical methods discussed in Section 7.3.1.

The semiempirical approach was originally designed to create regression relationships between what is simultaneously observed by a satellite and ground-based instruments (Cano et al. 1986; Hay 1978; Justus et al. 1986; Tarpley 1979). The Heliosat method, which was initially developed by Cano et al. (1986), has been regularly updated and modified. A more recent implementation relies on the atmospheric transmittance properties of water vapor and aerosols to provide solar radiation estimates under clear-sky conditions rather than through direct empirical relationships with ground data. In what follows, the focus is on satellite-based methods in the public domain, but other models are proprietary and used by commercial data providers (see Chapter 8). Evaluating the comparative performance of these models under realistic situations requires elaborate studies. This has been addressed in a separate report from Photovoltaic Power Systems (PVPS) Task 16.[44]

The original Heliosat method evaluates the clearness index, K_t, or the ratio of the radiative flux at the Earth's surface and the radiative flux at the TOA (which is known), using the relationship:

$$K_t = a\, n + b \tag{7-3}$$

where a and b are the slope and intercept of the assumed linear relation, and n is the so-called cloud index defined as:

$$n = [\rho - \rho_g] \,/\, [\rho_{cloud} - \rho_g] \tag{7-4}$$

where ρ, ρ_{cloud}, and ρ_g are the satellite-based reflectance observations of the current scene, of the brightest clouds, and of the ground, respectively. The cloud index is close to 0 when the observed reflectance is close to the ground reflectance (i.e., when the sky is clear). It can be negative if the sky is very clear, in which case ρ is smaller than ρ_g. The cloud index increases as clouds appear and can be greater than 1 for clouds that are optically very thick.

The parameters a and b in Eq. 7-3 can be derived empirically by comparison with coincident ground measurements, or they can rather be determined from the physical principles of atmospheric transmittance, which include not only the cloud index but also the influence of aerosols, water vapor, and trace gases. Diabaté et al. (1987) observed that three sets of such quantities for the morning, noon, and afternoon were needed for Europe. The Heliosat method (just like all cloud-index-based methods) requires the determination of cloud-free and extremely high cloud reflectivity instances to establish bounds to Eq. 7-3. Espinar et al. (2009) and Lefèvre et al. (2007) found that a relative error in the ground albedo caused by errors in reflectivity of cloud-free pixels leads to a relative error of the same magnitude in GHI under clear-sky conditions. This corresponds to an error of ≈10% in GHI under clear skies. Under cloudy conditions, the GHI bias, which is caused by an uncertainty in the limit for the albedo of the brightest clouds, increases as COD increases, and can reach ≈60% (Espinar et al. 2009; Lefèvre et al. 2007).

[44] See https://iea-pvps.org/key-topics/worldwide-benchmark-of-modelled-solar-irradiance-data/.

Beyer et al. (1996) developed an enhanced version of the original Heliosat method called Heliosat-1. One major enhancement was the adoption of the clear-sky index, K_c (the ratio of the actual GHI to the GHI under ideal clear conditions), instead of the clearness index, K_t. This resulted in the relationship $K_c = 1 - n$, which simplified the method. Additional work was done to remove the dependence of the satellite-measured radiance in the visible channel based on the sun-to-satellite geometry, thereby leading to a more spatially homogeneous cloud index. In addition, the determination of ground albedo and cloud albedo was improved by Beyer et al. (1996). Rigollier et al. (2004) developed Heliosat-2, which further enhanced Heliosat-1 by removing parameters that needed to be tuned and replacing them with either constants or values that can be computed automatically during the process. The HelioClim-3 and Solar Energy Mining (SOLEMI) databases, produced by MINES ParisTech and Deutsches Zentrum für Luft- und Raumfahrt (DLR), respectively, use Heliosat-2. The Heliosat-3 version was designed collaboratively by the University of Oldenburg, MINES ParisTech, and DLR, among others, and it uses the SOLIS clear-sky model, which approximates radiative transfer equations for fast implementation (Mueller et al. 2004), as described in Section 7.2.1. Centro de Investigaciones Energéticas, Medioambientales y Tecnológicas (CIEMAT) and its spin-off, IrSoLaV, performed remarkable modifications on the Heliosat-3 scheme. This resulted in a different model, which includes a clear-sky detection algorithm, different possible clear-sky models with atmospheric component datasets as input, and a dynamic model for estimating the ground albedo as a function of the scattering angle (Polo et al. 2013; 2012).

Hay (1978) developed a regression model that relates the atmospheric transmittance to the ratio of incoming to outgoing radiation at the TOA. By utilizing this relationship, the model enables the estimation of GHI. In this method, the coefficients of the regression model change significantly based on location, and they need to be trained with surface observations (Nunez 1990) to produce accurate results. The Tarpley (1979) method also used the well-known relation between surface radiation, TOA radiation (both upwelling and downwelling) and atmospheric transmittance to create three separate regression equations. The regression equations were classified based on sky conditions labeled as clear, partly cloudy, and cloudy, and they were used accordingly.

Models such as those developed by Perez et al. (2002), Rigollier et al. (2004), and Cebecauer and Suri (2010) evolved from Cano et al. (1986) and included refinements to address albedo issues (particularly when the surface is covered by snow) and the effects of sun-satellite geometry. Some of these models have since been modified to include the simplified SOLIS model (Ineichen 2008), and are used to estimate GHI first and then DNI after component separation (Section 7.3.1).

7.4.5 Satellite-Based Physical Models

Physical models generally use radiative transfer theory to directly estimate surface radiation based on first principles using cloud properties, water vapor, AOD, ozone, and surface albedo as inputs. The radiative transfer models can be classified as either broadband or spectral, depending on whether the radiative transfer calculations involve a single broadband calculation or multiple calculations in different wavelength bands.

The broadband method proposed by Gautier et al. (1980) used thresholds depending on multiple days of satellite pixel measurements to determine clear and cloudy skies. Separate clear-sky and

cloudy-sky models were then used to evaluate the surface DNI and GHI. The clear-sky model initially included water vapor and Rayleigh scattering but progressively added ozone (Diak and Gautier 1983) and aerosols (Gautier and Frouin 1984). Assuming that attenuation caused by the atmosphere does not vary from clear to cloudy conditions, Dedieu et al. (1987) created a method that combines the impacts of clouds and the atmosphere. This method uses a time series of images to determine clear-sky periods for computing surface albedo. Darnell et al. (1988) created a parameterized model to calculate surface radiation using a product of the TOA irradiance, atmospheric transmittance, and cloud transmittance. Developed with data from polar-orbiting satellites, this model used collocated surface and satellite measurements to create relationships between cloud transmittance and planetary albedo.

Möser and Raschke (1983) created a model based on the premise that GHI is related to fractional cloud cover. This model, applied to Meteosat data, enabled the estimation of solar radiation over Europe (Möser and Raschke 1984). The fractional sky cover was determined to be a function of satellite measurements in the visible channel. Radiative transfer modeling (Kerschgens et al. 1978) was employed to determine the clear- and overcast-sky boundaries. Stuhlmann et al. (1990) have since enhanced the model to include elevation dependence and additional constituents as well as multiple reflections in the all-sky model.

An important spectral model developed by Pinker and Ewing (1985) divided the solar spectrum into 12 intervals and applied the Delta-Eddington approximation for radiative transfer (Joseph et al. 1976) to a three-layer atmosphere. The primary input to the model is the COD, which can be provided from various sources. This model was enhanced by Pinker and Laszlo (1992) and used in conjunction with cloud information from the International Satellite Cloud Climatology Project (ISCCP) (Schiffer and Rossow 1983). Another physical method involves the use of satellite information from multiple channels to derive cloud properties (Stowe et al. 1999) and then evaluate DNI and GHI using the cloud properties in a radiative transfer model. This method was originally developed using the polar satellite data from the AVHRR instrument onboard NOAA satellites, and the processing system was called Clouds from AVHRR Extended System (CLAVR-x) (Heidinger 2003; Pavolonis et al. 2005). The method was later modified and enhanced to use cloud properties from the GOES satellites. In 2013, CLAVR-x was updated again to support the generation of higher spatial resolution output for the NOAA National Centers for Environmental Prediction weather forecast models and incorporated many algorithm improvements from the GOES-R Algorithm Working Group effort. The cloud information produced from the CLAVR-x type of algorithms can be input to a radiative transfer model, such as FARMS (Xie et al. 2016), to calculate GHI and DNI, as has been done for the development of the most recent versions of NREL's gridded NSRDB (1998–2022).

The Cloud Physical Properties (CPP) retrieval algorithms were developed at EUMETSAT's Satellite Application Facility on Climate Monitoring (CMSAF)[45] as well as other European or national (The Netherlands) projects (Benas et al. 2017; Karlsson et al. 2017a; 2017b; Roebeling et al. 2006; Stengel et al. 2014). The retrieved basic variables are cloud mask, cloud-top height, cloud thermodynamic phase, COD, particle effective radius, and water path. GHI, DNI, and DHI are then derived, as well as precipitation. The CPP algorithm first identifies cloudy and cloud-

[45] See http://www.soda-pro.com/documents/10157/326332/CAMS72_2015SC3_D72.1.3.1_2018_UserGuide_v1_201812.pdf.

contaminated pixels using a series of thresholds and spatial coherence tests imposed on the measured visible and infrared radiances (Roebeling et al. 2006). Depending on the results of these tests, the sky can be classified as clear, partly cloudy, or overcast. Subsequently, cloud optical properties (COD and effective radius) are retrieved by matching the observed reflectances at visible (0.6 μm) and near-infrared (1.6 μm) wavelengths to the simulated reflectances of homogeneous clouds comprising either liquid or ice particles. The thermodynamic phase (liquid or ice) is determined as part of this procedure using a cloud-top temperature estimate as additional input. Building on the retrieval of cloud physical properties, the Surface Insolation under Clear and Cloudy Skies (SICCS) algorithm was developed to model GHI, DNI, and DHI using broadband radiative transfer simulations (Deneke et al. 2008; Greuell et al. 2013). The cloud properties are the main input for cloudy and partly cloudy pixels. Information about atmospheric aerosols from the Monitoring Atmospheric Composition and Climate (MACC) is used for cloud-free scenes. Other inputs for the CPP and SICCS algorithms include surface elevation from the 2-minute gridded global relief Earth TOPOgraphy (ETOPO2v2-2006)[46] database, monthly varying integrated atmospheric water vapor from the ECMWF ERA5 reanalysis, and 8-day varying surface albedo derived from MODIS data.

Another cloud retrieval scheme, called APOLLO, was developed by Kriebel et al. (2003; 1989) for the AVHRR instrument. APOLLO has been adapted for use with data obtained from the SEVIRI instrument on the MSG satellite. APOLLO-derived cloud products, including COD and cloud type, can be used in a radiative transfer model such as Heliosat-4 (Oumbe 2009; Qu et al. 2017), made operational by the Copernicus service.[47]

The ISCCP (Schiffer and Rossow 1983) was established in 1982 as part of the World Climate Research Programme. The ISCCP cloud products include COD, cloud-top temperature, cloud particle size, and other cloud properties that could be used to derive surface radiation.

Physical models are computationally more intensive than empirical and semiempirical models. Nevertheless, they offer distinct advantages by: (a) providing the capability to compute GHI, DNI, and DHI without using empirical decomposition models; and (b) leveraging additional channels from new satellites like MTG or GOES-16 to improve cloud property retrieval.

7.4.6 Machine Learning-Based Models

Several studies have explored the possibility of bypassing physical or empirical satellite retrieval methods altogether and directly inferring a statistical relationship between the satellite images and the ground irradiance. (Jiang et al. 2019) implemented a convolutional neural network to process images of the Multi-functional Transport Satellite (MTSAT) and produce a map of solar surface irradiance over China. Hao et al. (2019) applied a Random Forest to the EPIC images to estimate solar surface irradiance globally. The ability of these methods to generalize in space has, nonetheless, been challenged by Yang et al. (2022), who were not able to reproduce some of the published conclusions (see Section 7.4.3.). Verbois et al. (2023) proposed an explanation for these seemingly conflicting results. They showed that the performance of ML-based satellite

[46] See https://www.ncei.noaa.gov/products/etopo-global-relief-model.
[47] See http://www.copernicus-atmosphere.eu.

retrieval models is strongly dependent on the choice of the training set and that it can be challenging to ensure that an ML model will generalize to any unseen location.

More sensible uses of ML are also being envisaged in the form of hybrid or physically informed models. Buster et al. (2022; 2021) developed a physically aware architecture, dubbed Physics Guided Neural Network (PHYGNN), to estimate cloud properties from GOES images based on a mixed loss function. It significantly outperforms the Physical Solar Model (PSM) (the underlying model used to develop the NSRDB -see Sec 7.3.5) with 2.16 and 3.95 overall percentage point improvement for GHI and DNI, respectively. Li et al. (2022) took a different approach and used transfer learning to incorporate physical information into a neural network. They first trained their network with simulated radiative transfer data and then fine-tuned its weight on real-world observations.

7.5 Numerical Weather Prediction-Based Solar Radiation Estimates

NWP models, run in either reanalysis mode or when providing weather forecasts, can provide GHI estimates for long periods of time. The accuracy of such estimates is known to be less than those provided by satellite-based models. Significant improvements, however, can be obtained by improving both the model physics and the assimilation of various observations. Some commonly available models and datasets are described in the following sections. Note that this is not a complete and comprehensive list. The goal is only to provide the user with initial information related to this potential source of data.

7.5.1 Reanalysis Models

ERA5 is a global atmospheric reanalysis that provides data starting in 1940. This dataset is produced from the ECMWF's data assimilation system used in their forecast model, IFS. This system uses four-dimensional variational analysis and provides analysis data with TOA and both GHI and beam horizontal irradiance (BHI) (all-sky and clear-sky) at hourly time resolution on an approximate 0.25° by 0.25° grid. More information can be found on the Copernicus ERA5 website.[48] In parallel, ERA5-Land provides hourly irradiance data on a ≈9-km grid since 1950, but only for the all-sky GHI over land areas.

NASA's MERRA-2 is another global atmospheric reanalysis dataset that provides data starting in 1980 and comprises TOA and GHI (all-sky and clear-sky). It includes additional datasets from those assimilated into the original MERRA dataset. The spatial resolution is 0.5° by 0.625°, and the temporal resolution is hourly.[49]

Finally, the Climate Forecast System Reanalysis from NOAA provides reanalysis data from 1979. The all-sky GHI data are available hourly at a 0.5° resolution.[50]

7.5.2 Forecast Models

Various national meteorological agencies run operational weather forecasts both regionally and globally. Some data from these operational models might be available from archives. Some of the most popular examples of global datasets are from the ECMWF's IFS runs and from

[48] See https://cds.climate.copernicus.eu/cdsapp#!/dataset/reanalysis-era5-single-levels?tab=overview/.
[49] See https://gmao.gsfc.nasa.gov/reanalysis/MERRA-2/.
[50] See https://www.ncei.noaa.gov/products/weather-climate-models.

NOAA's GFS runs. There are various regional model runs by national meteorological agencies that produce forecasts for individual countries and regions. Because many datasets now exist, this type of data is mentioned without pointing to specific sources. See Chapter 9, Section 9.4.2 for additional information and some examples of such datasets.

Solar forecasting requires improved forecasting of clouds, which is generally a weakness in many NWP models, so there have been significant recent efforts to improve cloud and radiation modeling, especially within the WRF mesoscale model. This led to the development of the WRF-Solar model (Jimenez et al. 2016), which includes significant improvements in cloud modeling as well as the capability to compute surface radiation using FARMS.

7.6 Site Adaptation: Merging Measured and Modeled Data

A major goal of solar resource assessments is to provide high-quality data for evaluating the financial viability of solar power plant projects (Moser et al. 2020). This essentially implies that accurate data over long time periods are available for conducting these studies. Normally, satellite-derived data time series fulfill the requirement for long-term data; however, they could be hampered by inherent biases and uncertainties stemming from the following factors:

- The information content, quality, and spatial and temporal resolution of the raw satellite data
- The approximations made by the models converting satellite observations into surface solar radiation estimates
- The uncertainty in ancillary information needed by these models
- The uncertainty added by the empirical methods used to separate the direct and diffuse components
- The uncertainty added by the empirical methods used to transpose components onto tilted surfaces.

In some cases, such as at high latitudes, modeled irradiance estimates cannot be derived from geostationary satellite sensors data, so that estimates from either polar orbiters or reanalysis data must be used, which are of comparatively lower accuracy.

As part of a resource assessment study for a new large solar power plant (e.g., >10 MW), ground-based solar measurements are conducted for a short period of time (nominally approximately 1 year) and used to validate the values estimated from satellite-based measurement. The main goal is to mitigate uncertainties and biases present in the modeled datasets. This process has been given various names, including "site adaptation," which is used here for simplification. A review paper by Polo et al. (2016) provides a summary of the methods that were current at that time. Some methods in the public domain have been benchmarked (Polo et al. 2020) within the International Energy Agency's Photovoltaic Power Systems Program Task 16. Since then, more methods have been introduced; see, for example, Han and Vohnicky (2022); Narvaez et al. (2021); Pereira et al. (2022); Tahir et al. (2021); Yang and Gueymard (2021); Kazantzidis et al. (2020); Fernández-Peruchena et al. (2020); Yang (2020); Muñoz-Salcedo et al. (2022); and Dhata et al. (2022).

Note, however, that the ground-based irradiance data must be high quality to ensure the effectiveness of the adjustment methods and identify any degradation of the modeled time series.

High-quality ground measurements can be achieved only by using well-calibrated, high-quality instruments that have been deployed at well-chosen locations using optimal installation methods and regular maintenance, per the best practices described in other sections (Chapter 3, in particular).

Site-adaptation methods can be classified into two broad categories. The first consists of physical methods that attempt to reduce the uncertainty and bias in the data by improving the clear-sky model inputs, such as AOD. The second approach develops statistical correction schemes directly comparing the satellite-based irradiance estimates with "unbiased" ground observations and uses those functions to correct the satellite-based radiation estimates.

7.6.1 Physical Methods

Because the highest uncertainty in satellite models is in DNI, the primary goal is to reduce errors in DNI by improving the quantification of AOD. Methods such as those proposed by Gueymard (2012a; 2012b) demonstrate how accurate AOD data obtained from ground sunphotometric measurements can improve DNI. Nevertheless, the scarcity of such high-quality AOD observations implies that other sources should be considered. Possible sources of AOD with global coverage include retrievals from the MODIS and MISR satellites and data assimilation output from ECMWF's CAMS or NASA's MERRA-2 data (Gueymard and Yang 2020). CAMS and MERRA-2 are the preferred sources to obtain gridded irradiance predictions on a global scale because they have no data gaps, contrary to satellite observations. Their spatial resolution is limited, however, 0.5° by 0.625° for MERRA-2, for example, which typically induces difficulties over complex mountainous terrain in particular. For that reason, specific methods have been developed by Gueymard and Thevenard (2009) and Ruiz-Arias et al. (2013); Ruiz-Arias et al. (2013) to correct biases and uncertainties in the satellite- or model-based AOD data using ground observations. These adjusted AOD datasets have been shown to improve the satellite-based solar radiation estimates at various locations.

7.6.2 Statistical Methods

Various statistical methods have been developed to identify and remove biases in long-term satellite-based datasets using short-term ground irradiance measurements. The techniques used depend on the data available and, largely, on the context in which they are employed. These bias correction methods range from linear methods (Cebecauer and Suri 2010; Harmsen et al. 2014; Polo et al. 2015; Vindel et al. 2013) to various nonlinear methods, including feature transformation (Schumann et al. 2011), polynomial-based corrections (Mieslinger et al. 2014), model output statistics corrections (Bender et al. 2011; Gueymard et al. 2012), measure-correlate-predict corrections (Thuman et al. 2012), probabilistic postprocessing (Yang and Gueymard 2021), Gaussian process (Cornejo-Bueno et al. 2019), and Fourier-decomposition-based corrections (Vernay et al. 2013). Other statistical methods include regional fusion methods of ground observations with satellite-based data and improvements to the irradiance cumulative distribution function (Blanc et al. 2012; Cebecauer and Suri 2012).

For a-posteriori corrections, that is, when the corrections are done on past data, quantile mapping is a popular approach. It adjusts the distribution of the satellite-derived estimations so that all its quantiles are identical to those of the ground measurements. Quantile mapping thereby corrects the bias of the satellite-derived estimations as well as higher-order moments. It can be further improved using kernel density estimate (Yezeguelian et al. 2021).

In the case such corrections need to be done in real time, they are usually required to be unbiased but also temporally accurate. Quantile mapping is then not appropriate, and models akin to Model Output Statistics (MOS) are necessary. MOS models were primarily introduced for NWP postprocessing (Glahn and Lowry 1972); these models aim to establish a statistical relationship between a set of outputs of a model (the predictors) and a target. In the case of site adaptation, the target is the surface solar irradiance or a normalized variable, such as the clear-sky index or the clearness index. The choice of predictors varies among the methods. Simpler models use a single predictor, usually with a relatively simple regression model: Aguiar et al. (2019) combined a linear regression with k-mean clustering, and Vernay et al. (2013) used a simple linear correction in the Fourier domain.

Larger predictor sets can be used to allow a condition-dependent correction, typically, multiple components of GHI, solar geometry information, basic weather data, and spatiotemporal context. The relationships between these predictors and the target (the measured GHI) are complex, and nonlinear algorithms are preferred: neural networks (Şahin et al. 2014) and support vector machines (Tiba et al. 2019) have already been successfully implemented. For applications at high latitudes, a comparison of seven ML methods has been carried out to obtain site adaptations of the Swedish Meteorological and Hydrological Institute's (SMHI) STRÅNG mesoscale solar radiation model[51] (Zainali et al. 2023). Although all methods were able to significantly improve the modeled GHI, no universal ML method could be identified because of the spatiotemporal heterogeneity in model performance over Sweden.

In recent years, more advanced regression models have been utilized to produce long-term satellite-based datasets on a regional scale—sometimes called global or regional adaptation techniques (Polo et al. 2015). Unlike the conventional site adaptation technique, which focuses on a single location, regional adaptation aims to improve satellite-derived irradiance estimations over large areas. The statistical models used must therefore generalize the correction learned for specific training measurement stations to new locations. (Ruiz-Arias et al. 2015) used an optimal interpolation technique applied to NWP-derived gridded estimates of GHI and DNI at 10-km resolution over Spain. Davy et al. (2016) proposed to combine generalized additive models and distance-weighted interpolation to correct and merge satellite data with a numerical weather model and produce high-quality solar surface irradiance estimations over Australia. Babar et al. (2020) proposed to use a random forest for the same purpose in Scandinavia; the interpolation was not done explicitly but delegated to the random forest, which takes the latitude and longitude as additional predictors. Similarly, Verbois et al. (2023) developed a regional postprocessing model based solely on gradient boosting, which leveraged a dense network of measurement stations to improve the Helioclim-3 database over France, without the need for an explicit interpolation.

7.7 Conclusions

Whereas ground-based solar measurements are deemed the most accurate source of data and will always form the basis of ground truth, the sparse nature of their availability is not expected to change in the foreseeable future. Therefore, modeled solar radiation forms an important part of solar resource assessment and forecasting, as it provides the capability to generate time series of GHI, DNI, and DHI for long periods of time at high spatial and temporal resolution with global

[51] See https://strang.smhi.se/.

coverage. Additionally, models will always be used to transform solar radiation information to meet specific needs of solar generation projects. There have been explosive recent advancements in weather satellite technologies, and solar resource accuracy and resolution have significantly improved in the last few years. Additional advancements are still expected in both satellite technologies as the need to cater to solar generation in newer environments (e.g., bifacial PV, agrivoltaics, and floating PV) will require additional modeling advances. Future editions of the handbook and specifically this chapter are expected to cover those advances.

References

Aguiar, L.M., J. Polo, J.M. Vindel, and A. Oliver. 2019. "Analysis of satellite derived solar irradiance in islands with site adaptation techniques for improving the uncertainty." *Renew. Energy* 135, 98–107. https://doi.org/10.1016/j.renene.2018.11.099.

Aler, R., I.M. Galván, J.A. Ruiz-Arias, and C.A. Gueymard. 2017. "Improving the separation of direct and diffuse solar radiation components using machine learning by gradient boosting." *Sol. Energy* 150, 558–569. https://doi.org/10.1016/j.solener.2017.05.018.

Antonanzas-Torres, F., J. Antonanzas, R. Urraca, M. Alia-Martinez, and F.J. Martinez-de-Pison. 2016. "Impact of atmospheric components on solar clear-sky models at different elevation: Case study Canary Islands." *Energy Convers. Manag*. 109, 122–129. https://doi.org/10.1016/j.enconman.2015.11.067.

Babar, B., L.T. Luppino, T. Boström, and S.N. Anfinsen. 2020. "Random forest regression for improved mapping of solar irradiance at high latitudes." *Sol. Energy* 198, 81–92. https://doi.org/10.1016/j.solener.2020.01.034.

Badescu, V., C.A. Gueymard, S. Cheval, C. Oprea, M. Baciu, A. Dumitrescu, F. Iacobescu, I. Milos, and C. Rada. 2012. "Computing global and diffuse solar hourly irradiation on clear sky. Review and testing of 54 models." *Renew. Sustain. Energy Rev*. 16, 1636–1656. https://doi.org/10.1016/j.rser.2011.12.010.

Benas, N., S. Finkensieper, M. Stengel, G-J van Zadelhoff, T. Hanschmann, R. Hollmann, and J.F. Meirink. 2017. "The MSG-SEVIRI-based cloud property data record CLAAS-2." *Earth Syst. Sci. Data* 9, 415–434. https://doi.org/10.5194/essd-9-415-2017.

Bender, G., F. Davidson, F. Eichelberger, and C.A. Gueymard. 2011. "The Road to Bankability: Improving Assessments for More Accurate Financial Planning." In: Proceedings of Solar 2011 Conference of American Solar Energy Society. Presented at the Solar 2011, American Solar Energy Society, Raleigh, NC.

Bessho, K., K. Date, M. Hayashi, A. Ikeda, T. Imai, H. Inoue, Y. Kumagai, T. Miyakawa, H. Murata, and T. Ohno, et al. 2016. "An Introduction to Himawari-8/9 – Japan's New-Generation Geostationary Meteorological Satellites." *J. Meteorol. Soc. Jpn.* Ser II 94, 151–183. https://doi.org/10.2151/jmsj.2016-009.

Beyer, H.G., C. Costanzo, and D. Heinemann. 1996. "Modifications of the Heliosat procedure for irradiance estimates from satellite images." *Sol. Energy* 56, 207–212. https://doi.org/10.1016/0038-092X(95)00092-6.

Bird, R.E., and R.L. Hulstrom. 1981. *Simplified clear sky model for direct and diffuse insolation on horizontal surfaces.* https://doi.org/10.2172/6510849.

Blanc, P., A. Boilley, N. Killius, P. Massip, and L. Schroedter-Homscheidt. 2012. *Methods for Data Fusion*. Report of the Project ENDORSE, 7th Framework Programme, Europe.

Boilley, A., and L. Wald. 2015. "Comparison between meteorological re-analyses from ERA-Interim and MERRA and measurements of daily solar irradiation at surface." *Renew. Energy* 75, 135–143. https://doi.org/10.1016/j.renene.2014.09.042.

Bosilovich, M.G., R. Lucchesi, and M. Suarez. 2016. "MERRA-2: File specification." https://ntrs.nasa.gov/api/citations/20150019760/downloads/20150019760.pdf.

Buster, G., M. Bannister, A. Habte, D. Hettinger, G. Maclaurin, M. Rossol, M. Sengupta, and Y. Xie. 2021. "Physics-Guided Machine Learning for Prediction of Cloud Properties in Satellite-Derived Solar Data." IEEE 48th Photovoltaic Specialists Conference (PVSC), Fort Lauderdale, FL, pp. 0335–0338. https://doi.org/10.1109/PVSC43889.2021.9519065.

Buster, G., M. Bannister, A. Habte, D. Hettinger, G. Maclaurin, M. Rossol, M. Sengupta, and Y. Xie. 2022. "Physics-guided machine learning for improved accuracy of the National Solar Radiation Database." *Sol. Energy* 232, 483–492. https://doi.org/10.1016/j.solener.2022.01.004.

Cano, D., J.M. Monget, M. Albuisson, H. Guillard, N. Regas, and L. Wald. 1986. "A method for the determination of the global solar radiation from meteorological satellite data." *Sol. Energy* 37, 31–39. https://doi.org/10.1016/0038-092X(86)90104-0.

Cebecauer, T., and M. Suri. 2010. "Accuracy Improvements of Satellite-Derived Solar Resource Based on GEMS Re-Analysis Aerosols." In: Proceedings of SolarPACES 2010 Conference, Perpignan, France.

Cebecauer, T., and M. Suri. 2012. "Correction of Satellite-Derived DNI Time Series Using Locally-Resolved Aerosol Data." In: Proceedings of SolarPACES 2012 Conference, Marrakesh, Morocco.

Chen, M., Q. Zhuang, and Y. He. 2014. "An Efficient Method of Estimating Downward Solar Radiation Based on the MODIS Observations for the Use of Land Surface Modeling." *Remote Sens.* 6, 7136–7157. https://doi.org/10.3390/rs6087136.

Collow, A., N. Thomas, M. Bosilovich, A. Dezfuli, and R. Lucchesi. 2023. File Specification for MERRA-2 Climate Statistics Products. GMAO Office Note No. 19 (Version 1.3), 17 pp. http://gmao.gsfc.nasa.gov/pubs/office_notes.

Cornejo-Bueno, L., C. Casanova-Mateo, J. Sanz-Justo, and S. Salcedo-Sanz. 2019. "Machine learning regressors for solar radiation estimation from satellite data." *Sol. Energy* 183, 768–775. https://doi.org/10.1016/j.solener.2019.03.079.

Darnell, W.L., W.F. Staylor, S.K. Gupta, and F.M. Denn. 1988. "Estimation of Surface Insolation Using Sun-Synchronous Satellite Data." *J. Clim.* 1, 820–835. https://doi.org/10.1175/1520-0442(1988)001<0820:EOSIUS>2.0.CO;2.

Davy, R.J., J.R. Huang, and A. Troccoli. 2016. "Improving the accuracy of hourly satellite-derived solar irradiance by combining with dynamically downscaled estimates using generalised additive models." *Sol. Energy* 135, 854–863. https://doi.org/10.1016/j.solener.2016.06.052.

Dedieu, G., P.Y. Deschamps, and Y.H. Kerr. 1987. "Satellite Estimation of Solar Irradiance at the Surface of the Earth and of Surface Albedo Using a Physical Model Applied to Meteosat Data." *J. Appl. Meteorol. Climatol.* 26, 79–87. https://doi.org/10.1175/1520-0450(1987)026<0079:SEOSIA>2.0.CO;2.

Deneke, H.M., A.J. Feijt, and R.A. Roebeling. 2008. "Estimating surface solar irradiance from METEOSAT SEVIRI-derived cloud properties." *Remote Sens. Environ.* 112, 3131–3141. https://doi.org/10.1016/j.rse.2008.03.012.

Dhata, E.F., C.K. Kim, H-G Kim, B. Kim, and M. Oh. 2022. "Site-Adaptation for Correcting Satellite-Derived Solar Irradiance: Performance Comparison between Various Regressive and Distribution Mapping Techniques for Application in Daejeon, South Korea." *Energies* 15, 9010. https://doi.org/10.3390/en15239010.

Diabaté, L., H. Demarcq, N. Michaud-Regas, and L. Wald. 1987. "Estimating Incident Solar Radiation at the Surface from Images of the Earth Transmitted by Geostationary Satellites: the Heliosat Project." *Int. J. Sol. Energy* 5, 261–278. https://doi.org/10.1080/01425918708914425.

Diak, G.R., and C. Gautier. 1983. "Improvements to a Simple Physical Model for Estimating Insolation from GOES Data." *J. Clim. Appl. Meteorol.* 22, 505–508.

Driesse, A., A.R. Jensen, and R. Perez. 2024. "A continuous form of the Perez diffuse sky model for forward and reverse transposition." *Sol. Energy* 267, 112093. https://doi.org/10.1016/j.solener.2023.112093.

Engerer, N.A. 2015. "Minute resolution estimates of the diffuse fraction of global irradiance for southeastern Australia." *Sol. Energy* 116, 215–237. https://doi.org/10.1016/j.solener.2015.04.012.

Engerer, N.A., and F.P. Mills. 2015. "Validating nine clear sky radiation models in Australia." *Sol. Energy* 120, 9–24. https://doi.org/10.1016/j.solener.2015.06.044.

Erbs, D.G., S.A. Klein, and J.A. Duffie. 1982. "Estimation of the diffuse radiation fraction for hourly, daily and monthly-average global radiation." *Sol. Energy* 28, 293–302. https://doi.org/10.1016/0038-092X(82)90302-4.

Espinar, B., L. Ramírez, A. Drews, H.G. Beyer, L.F. Zarzalejo, J. Polo, and L. Martín. 2009. Analysis of different comparison parameters applied to solar radiation data from satellite and German radiometric stations." *Sol. Energy* 83, 118–125. https://doi.org/10.1016/j.solener.2008.07.009.

Fatichi, S., V.Y. Ivanov, and E. Caporali. 2011. "Simulation of future climate scenarios with a weather generator." *Adv. Water Resour.* 34, 448–467. https://doi.org/10.1016/j.advwatres.2010.12.013.

Fernández-Peruchena, C.M., J. Polo, L. Martín, and L. Mazorra. 2020. "Site-Adaptation of Modeled Solar Radiation Data: The SiteAdapt Procedure." *Remote Sens*. 12, 2127. https://doi.org/10.3390/rs12132127.

Gautier, C., G. Diak, and S. Masse. 1980. "A Simple Physical Model to Estimate Incident Solar Radiation at the Surface from GOES Satellite Data." *J. Appl. Meteorol. Climatol.* 19, 1005–1012. https://doi.org/10.1175/1520-0450(1980)019<1005:ASPMTE>2.0.CO;2.

Gautier, C., and R. Frouin. 1984. "Satellite-Derived Ocean Surface Radiation Fluxes, in: Proceedings of the Workshop on Advances in Remote Sensing Retrieval Methods." Presented at the Workshop on Advances in Remote Sensing Retrieval Methods, Williamsburg, Virginia.

George, R., S. Wilcox, and M. Anderberg. 2008. "National Solar Radiation Database (NSRDB) - 10 km Gridded Hourly Solar Database." Presented at the Solar Resource Assessment Workshop, National Renewable Energy Laboratory. https://www.osti.gov/biblio/921216.

Glahn, H.R., and D.A. Lowry. 1972. "The Use of Model Output Statistics (MOS) in Objective Weather Forecasting." *J. Appl. Meteorol*. 11, 1203–1211. https://doi.org/10.1175/1520-0450(1972)011<1203:TUOMOS>2.0.CO;2.

Greuell, W., J.F. Meirink, and P. Wang. 2013. "Retrieval and validation of global, direct, and diffuse irradiance derived from SEVIRI satellite observations." *J. Geophys. Res. Atmospheres* 118, 2340–2361. https://doi.org/10.1002/jgrd.50194.

Gschwind, B., L. Wald, P. Blanc, M. Lefèvre, M. Schroedter-Homscheidt, and A. Arola. 2019. "Improving the McClear model estimating the downwelling solar radiation at ground level in cloud-free conditions – McClear-v3." *Meteorol. Z.* 28, 147–163. https://doi.org/10.1127/metz/2019/0946.

Gueymard, C. 1987. "An anisotropic solar irradiance model for tilted surfaces and its comparison with selected engineering algorithms." *Sol. Energy* 38, 367–386. https://doi.org/10.1016/0038-092X(87)90009-0.

Gueymard, C.A. 2022. "Corrigendum to "The SMARTS spectral irradiance model after 25 years: New developments and validation of reference spectra." *Sol. Energy* 187 (2019) 233–253]. *Sol. Energy* 236, 906–907. https://doi.org/10.1016/j.solener.2022.02.046.

Gueymard, C.A. 2017. "Cloud and albedo enhancement impacts on solar irradiance using high-frequency measurements from thermopile and photodiode radiometers. Part 2: Performance of separation and transposition models for global tilted irradiance." *Sol. Energy* 153, 766–779. https://doi.org/10.1016/j.solener.2017.04.068.

Gueymard, C.A. 2014. "A review of validation methodologies and statistical performance indicators for modeled solar radiation data: Towards a better bankability of solar projects." *Renew. Sustain. Energy Rev*. 39, 1024–1034. http://dx.doi.org/10.1016/j.rser.2014.07.117.

Gueymard, C.A. 2012a. "Clear-sky irradiance predictions for solar resource mapping and large-scale applications: Improved validation methodology and detailed performance analysis of 18 broadband radiative models." *Sol. Energy* 86, 2145–2169. https://doi.org/10.1016/j.solener.2011.11.011.

Gueymard, C.A. 2012b. “Temporal variability in direct and global irradiance at various time scales as affected by aerosols.” *Sol. Energy* 86, 3544-3553. https://doi.org/10.1016/j.solener.2012.01.013.

Gueymard, C.A. 2008a. “From global horizontal to global tilted irradiance: how accurate are solar energy engineering predictions in practice?” In: Solar 2008 Conference, San Diego CA. American Solar Energy Society.

Gueymard, C.A. 2008b. “REST2: High-performance solar radiation model for cloudless-sky irradiance, illuminance, and photosynthetically active radiation – Validation with a benchmark dataset.” *Sol. Energy* 82, 272–285. https://doi.org/10.1016/j.solener.2007.04.008.

Gueymard, C.A. 2004a. “Corrigendum to “Direct solar transmittance and irradiance predictions with broadband models. Part I: detailed theoretical performance assessment.” [*Solar Energy* 74 (2003) 355–379]. *Sol. Energy* 76, 513. https://doi.org/10.1016/j.solener.2003.11.002.

Gueymard, C.A. 2004b. “Corrigendum to “Direct solar transmittance and irradiance predictions with broadband models. Part II: validation with high-quality measurements.” [*Solar Energy* 74 (2003) 381–395]. *Sol. Energy* 76, 515. https://doi.org/10.1016/j.solener.2003.11.003.

Gueymard, C.A. 2003a. “Direct solar transmittance and irradiance predictions with broadband models. Part I: detailed theoretical performance assessment.” *Sol. Energy* 74, 355–379. https://doi.org/10.1016/S0038-092X(03)00195-6.

Gueymard, C.A. 2003b. “Direct solar transmittance and irradiance predictions with broadband models. Part II: validation with high-quality measurements.” *Sol. Energy* 74, 381–395. https://doi.org/10.1016/S0038-092X(03)00196-8.

Gueymard, C.A. 2001. “Parameterized transmittance model for direct beam and circumsolar spectral irradiance.” *Sol. Energy* 71, 325–346. https://doi.org/10.1016/S0038-092X(01)00054-8.

Gueymard, C.A., W. Gustafson, A. Etringer, and P. Storck. 2012. “Evaluation of procedures to improve solar resource assessments: Optimum use of short-term data from a local weather station to correct bias in long-term satellite derived solar radiation time series.” In Proceedings of the World Renewable Energy Forum, Denver, CO, USA, 13–17 May 2012.

Gueymard, C.A., and D.R. Myers. 2008. “Validation and Ranking Methodologies for Solar Radiation Models.” In: Badescu, V. (Ed.), *Modeling Solar Radiation at the Earth’s Surface.* Springer.

Gueymard, C.A., and J.A. Ruiz-Arias. 2016. “Extensive worldwide validation and climate sensitivity analysis of direct irradiance predictions from 1-min global irradiance.” *Sol. Energy* 128, 1–30. https://doi.org/10.1016/j.solener.2015.10.010.

Gueymard, C.A., and J.A. Ruiz-Arias. 2015. “Validation of direct normal irradiance predictions under arid conditions: A review of radiative models and their turbidity-dependent performance.” *Renew. Sustain. Energy Rev*. 45, 379–396. https://doi.org/10.1016/j.rser.2015.01.065.

Gueymard, C.A., and D. Thevenard. 2009. "Monthly average clear-sky broadband irradiance database for worldwide solar heat gain and building cooling load calculations." *Sol. Energy* 83, 1998–2018. https://doi.org/10.1016/j.solener.2009.07.011.

Gueymard, C.A., and D. Yang. 2020. "Worldwide validation of CAMS and MERRA-2 reanalysis aerosol optical depth products using 15 years of AERONET observations." *Atmos. Environ.* 225, 117216. https://doi.org/10.1016/j.atmosenv.2019.117216.

Han, J.-Y., and P. Vohnicky. 2022. "An optimized approach for mapping solar irradiance in a mid-low latitude region based on a site-adaptation technique using Himawari-8 satellite imageries." *Renew. Energy* 187, 603–617. https://doi.org/10.1016/j.renene.2022.01.027.

Hao, D., G.R. Asrar, Y. Zeng, Q. Zhu, J. Wen, Q. Xiao, and M. Chen. 2020. "DSCOVR/EPIC-derived global hourly and daily downward shortwave and photosynthetically active radiation data at 0.1° × 0.1° resolution." *Earth Syst. Sci. Data* 12, 2209–2221. https://doi.org/10.5194/essd-12-2209-2020.

Hao, D., G.R. Asrar, Y. Zeng, Q. Zhu, J. Wen, Q. Xiao, and M. Chen. 2019. "Estimating hourly land surface downward shortwave and photosynthetically active radiation from DSCOVR/EPIC observations." *Remote Sens. Environ*. 232, 111320. https://doi.org/10.1016/j.rse.2019.111320.

Harmsen, E.W., P.T. Cruz, and J.R. Mecikalski. 2014. "Calibration of selected pyranometers and satellite derived solar radiation in Puerto Rico." *Int. J. Renew. Energy Technol*. 5, 43–54. https://doi.org/10.1504/IJRET.2014.059660.

Hay, J. 1978. "A satellite-based methodology for determining solar irradiance at the ocean surface during GATE." *Bull Amer Meteor Sci* 59, 1549.

Heidinger, A.K. 2003. "Rapid Daytime Estimation of Cloud Properties over a Large Area from Radiance Distributions." *J. Atmospheric Ocean. Technol*. 20, 1237–1250. https://doi.org/10.1175/1520-0426(2003)020<1237:RDEOCP>2.0.CO;2.

Hersbach, H., B. Bell, P. Berrisford, S. Hirahara, A. Horányi, J. Muñoz-Sabater, J. Nicolas, C. Peubey, R. Radu, D. Schepers, and A. Simmons, et al. 2020. "The ERA5 global reanalysis." *Q. J. R. Meteorol. Soc.* 146, 1999–2049. https://doi.org/10.1002/qj.3803.

Huang, C., H. Shi, D. Yang, L. Gao, P. Zhang, D. Fu, X. Xia, Q. Chen, Y. Yuan, M. Liu, B. Hu, K. Lin, and X. Li. 2023. "Retrieval of sub-kilometer resolution solar irradiance from Fengyun-4A satellite using a region-adapted Heliosat-2 method." *Sol. Energy* 264, 112038. https://doi.org/10.1016/j.solener.2023.112038.

Ineichen, P. 2008. "A broadband simplified version of the Solis clear sky model." *Sol. Energy* 82, 758–762. https://doi.org/10.1016/j.solener.2008.02.009.

Jiang, H., N. Lu, J. Qin, W. Tang, and L. Yao. 2019. "A deep learning algorithm to estimate hourly global solar radiation from geostationary satellite data." *Renew. Sustain. Energy Rev.* 114, 109327. https://doi.org/10.1016/j.rser.2019.109327.

Jimenez, P.A., J.P. Hacker, J. Dudhia, S.E. Haupt, J.A. Ruiz-Arias, C.A. Gueymard, G. Thompson, T. Eidhammer, and A. Deng. 2016. "WRF-Solar: Description and Clear-Sky Assessment of an Augmented NWP Model for Solar Power Prediction." *Bull. Am. Meteorol. Soc.* 97, 1249–1264. https://doi.org/10.1175/BAMS-D-14-00279.1.

Joseph, J.H., W.J. Wiscombe, and J.A. Weinman. 1976. "The Delta-Eddington Approximation for Radiative Flux Transfer." *J. Atmospheric Sci.* 33, 2452–2459. https://doi.org/10.1175/1520-0469(1976)033<2452:TDEAFR>2.0.CO;2.

Justus, C.G., M.V. Paris, and J.D. Tarpley. 1986. "Satellite-measured insolation in the United States, Mexico, and South America." *Remote Sens. Environ*. 20, 57–83. https://doi.org/10.1016/0034-4257(86)90014-3.

Kambezidis, H.D., B.E. Psiloglou, and C. Gueymard. 1994. "Measurements and models for total solar irradiance on inclined surface in Athens, Greece." *Sol. Energy* 53, 177–185. https://doi.org/10.1016/0038-092X(94)90479-0.

Karlsson, K.-G., K. Anttila, J. Trentmann, M. Stengel, J. Fokke Meirink, A. Devasthale, T. Hanschmann, S. Kothe, and E. Jääskeläinen. 2017a. "CLARA-A2: the second edition of the CM SAF cloud and radiation data record from 34 years of global AVHRR data." *Atmos. Chem. Phys.* 17, 5809–5828. https://doi.org/10.5194/acp-17-5809-2017.

Karlsson, Karl-Göran, K. Anttila, J. Trentmann, M. Stengel, J.F. Meirink, A. Devasthale, T. Hanschmann, S. Kothe, and E. Jääskeläinen. 2017b. *CLARA-A2: CM SAF cLoud, Albedo and surface RAdiation dataset from AVHRR data - Edition 2*. https://doi.org/10.5676/EUM_SAF_CM/CLARA_AVHRR/V002.

Kato, S., F.G. Rose, D.A. Rutan, T.J. Thorsen, N.G Loeb, D.R. Doelling, X. Huang, W.L. Smith, W. Su, and S-H Ham. 2018. "Surface Irradiances of Edition 4.0 Clouds and the Earth's Radiant Energy System (CERES) Energy Balanced and Filled (EBAF) Data Product." *J. Clim*. 31, 4501–4527. https://doi.org/10.1175/JCLI-D-17-0523.1.

Kazantzidis, A., V. Salamalikis, S-A Logothetis, and I. Vamvakas. 2020. "Aerosol classification and bias-adjustment of global horizontal irradiance for middle East-North Africa region." *AIP Conf. Proc*. 2303, 180002. https://doi.org/10.1063/5.0028544.

Kerschgens, M., U. Pilz, and E. Raschke. 1978. "A modified two-stream approximation for computations of the solar radiation budget in a cloudy atmosphere." *Tellus* 30, 429–435. https://doi.org/10.3402/tellusa.v30i5.10386.

Khalil, S.A., and A.M. Shaffie. 2013. "A comparative study of total, direct and diffuse solar irradiance by using different models on horizontal and inclined surfaces for Cairo, Egypt." *Renew. Sustain. Energy Rev*. 27, 853–863. https://doi.org/10.1016/j.rser.2013.06.038.

Kriebel, K.T., G. Gesell, M. Ka¨stner, and H. Mannstein. 2003. "The cloud analysis tool APOLLO: Improvements and validations." *Int. J. Remote Sens.* 24, 2389–2408. https://doi.org/10.1080/01431160210163065.

Kriebel, K.T., R.W. Saunders, and G. Gesell. 1989. "Optical Properties of Clouds Derived from Fully Cloudy AVHRR Pixels." *Beitr. Phys. Atmosph*. 62 (3): 165–171.

Lefèvre, M., A. Oumbe, P. Blanc, B. Espinar, B. Gschwind, Z. Qu, L. Wald, M. Schroedter-Homscheidt, C. Hoyer-Klick, and A. Arola, et al. 2013. "McClear: a new model estimating downwelling solar radiation at ground level in clear-sky conditions." *Atmospheric Meas. Tech.* 6, 2403–2418. https://doi.org/10.5194/amt-6-2403-2013.

Lefèvre, M., L. Wald, and L. Diabaté. 2007. "Using reduced datasets ISCCP-B2 from the Meteosat satellites to assess surface solar irradiance." *Sol. Energy* 81, 240–253. https://doi.org/10.1016/j.solener.2006.03.008.

Li, R., D. Wang, S. Liang, A. Jia, and Z. Wang. 2022. "Estimating global downward shortwave radiation from VIIRS data using a transfer-learning neural network." *Remote Sens. Environ.* 274, 112999. https://doi.org/10.1016/j.rse.2022.112999.

Liu, B.Y.H., and R.C. Jordan. 1960. "The interrelationship and characteristic distribution of direct, diffuse and total solar radiation." *Sol. Energy* 4, 1–19. https://doi.org/10.1016/0038-092X(60)90062-1.

Loutzenhiser, P.G., H. Manz, C. Felsmann, P.A. Strachan, T. Frank, and G.M. Maxwell. 2007. "Empirical validation of models to compute solar irradiance on inclined surfaces for building energy simulation." *Sol. Energy* 81, 254–267. https://doi.org/10.1016/j.solener.2006.03.009.

Marion, W., and S. Wilcox. 1994. *Solar radiation data manual for flat-plate and concentrating collectors.* NREL/TP-463-5607. National Renewable Energy Laboratory. Golden, CO. https://doi.org/10.2172/10169141.

Maxwell, E.L. 1998. "METSTAT—The solar radiation model used in the production of the National Solar Radiation Data Base (NSRDB)." *Sol. Energy* 62, 263–279. https://doi.org/10.1016/S0038-092X(98)00003-6.

Maxwell, E.L. 1987. *A quasi-physical model for converting hourly global horizontal to direct normal insolation.* SERI/TR-215-3087. National Renewable Energy Laboratory. Golden, CO. https://www.nrel.gov/docs/legosti/old/3087.pdf.

Mayer, B., and A. Kylling. 2005. "Technical note: The libRadtran software package for radiative transfer calculations - description and examples of use." *Atmos. Chem. Phys*. 5, 1855–1877. https://doi.org/10.5194/acp-5-1855-2005.

Mieslinger, T., F. Ament, K. Chhatbar, and R. Meyer. 2014. "A New Method for Fusion of Measured and Model-derived Solar Radiation Time-series." *Energy Procedia* 48, 1617–1626. https://doi.org/10.1016/j.egypro.2014.02.182.

Moser, D., S. Lindig, M. Herz, B. Müller, I. Horvath, A. Schils, S. Ramesh, M. Green, J. Vedde, D. Barnard, B. Herteleer, and J.A. Tsanakas, et al. 2020. "Benchmarking Yield Assessment Exercise in Different Climates within an International Collaboration Framework." In: 37th

European Photovoltaic Solar Energy Conference and Exhibition: 1317-1323. https://doi.org/10.4229/EUPVSEC20202020-5CO.10.3.

Möser, W., and E. Raschke. 1984. "Incident Solar Radiation over Europe Estimated from METEOSAT Data." *J. Appl. Meteorol. Climatol.* 23, 166–170. https://doi.org/10.1175/1520-0450(1984)023<0166:ISROEE>2.0.CO;2.

Möser, W. and E. Raschke. 1983. "Mapping of global radiation and cloudiness from Meteosat image data - Theory and ground truth comparisons." *Meteorol. Rundsch*. 36, 33–41.

Mueller, R.W., K.F. Dagestad, P. Ineichen, M. Schroedter-Homscheidt, S. Cros, D. Dumortier, R. Kuhlemann, J.A. Olseth, G. Piernavieja, C. Reise, L. Wald, and D. Heinemann. 2004. "Rethinking satellite-based solar irradiance modelling: The SOLIS clear-sky module." *Remote Sens. Environ.* 91, 160–174. https://doi.org/10.1016/j.rse.2004.02.009.

Muneer, T., and G.S. Saluja. 1985. "A brief review of models for computing solar radiation on inclined surfaces." *Energy Convers. Manag*. 25, 443–458. https://doi.org/10.1016/0196-8904(85)90009-3.

Muñoz-Salcedo, M., F. Peci-López, and F. Táboas. 2022. "An Empirical Correction Model for Remote Sensing Data of Global Horizontal Irradiance in High-Cloudiness-Index Locations." *Remote Sens.* 14, 5496. https://doi.org/10.3390/rs14215496.

Myers, D.R. 2013. "Solar radiation: Practical modeling for renewable energy applications." CRC Press. https://doi.org/10.1201/b13898.

Narvaez, G., L.F. Giraldo, M. Bressan, and A. Pantoja. 2021. "Machine learning for site-adaptation and solar radiation forecasting." *Renew. Energy* 167, 333–342. https://doi.org/10.1016/j.renene.2020.11.089.

Nunez, M. 1990. "Solar energy statistics for Australian capital regions." *Sol. Energy* 44, 343–354. https://doi.org/10.1016/0038-092X(90)90138-3.

Olmo, F.J., J. Vida, I. Foyo, Y. Castro-Diez, and L. Alados-Arboledas. 1999. "Prediction of global irradiance on inclined surfaces from horizontal global irradiance." *Energy* 24, 689–704. https://doi.org/10.1016/S0360-5442(99)00025-0.

Oumbe, A. 2009. *Exploitation Des Nouvelles Capacités D'observation De La Terre Pour Evaluer Le Rayonnement Solaire Incident Au Sol (Assessment of Solar Surface Radiation Using New Earth Observation Capabilities)*. Ph.D. thesis, École Nationale Supérieure des Mines de Paris, Paris, France. https://pastel.hal.science/pastel-00005759v1/file/these_oumbe.pdf.

Oumbe, A., Z. Qu, P. Blanc, M. Lefèvre, L. Wald, and S. Cros. 2014. "Decoupling the effects of clear atmosphere and clouds to simplify calculations of the broadband solar irradiance at ground level." *Geosci. Model Dev*. 7, 1661–1669. https://doi.org/10.5194/gmd-7-1661-2014.

Padovan, A., and D. Del Col. 2010. "Measurement and modeling of solar irradiance components on horizontal and tilted planes." *Sol. Energy* 84, 2068–2084. https://doi.org/10.1016/j.solener.2010.09.009.

Page, J., M. Albuisson, and L. Wald. 2001. "The European Solar Radiation Atlas: a valuable digital tool." *Sol. Energy* 71, 81–83. https://doi.org/10.1016/S0038-092X(00)00157-2.

Pavolonis, M.J., A.K. Heidinger, and T. Uttal. 2005. "Daytime Global Cloud Typing from AVHRR and VIIRS: Algorithm Description, Validation, and Comparisons." *J. Appl. Meteorol.* 44, 804–826. https://doi.org/10.1175/JAM2236.1.

Pereira, S., E.F.M. Abreu, M. Iakunin, A. Cavaco, R. Salgado, and P. Canhoto. 2022. "Method for solar resource assessment using numerical weather prediction and artificial neural network models based on typical meteorological data: Application to the south of Portugal." *Sol. Energy* 236, 225–238. https://doi.org/10.1016/j.solener.2022.03.003.

Perez, R., P. Ineichen, K. Moore, M. Kmiecik, C. Chain, R. George, and F. Vignola. 2002. "A new operational model for satellite-derived irradiances: description and validation." *Sol. Energy* 73, 307–317. https://doi.org/10.1016/S0038-092X(02)00122-6.

Perez, R., P. Ineichen, R. Seals, J. Michalsky, and R. Stewart. 1990. "Modeling daylight availability and irradiance components from direct and global irradiance." *Sol. Energy* 44, 271–289. https://doi.org/10.1016/0038-092X(90)90055-H.

Perez, R., R. Seals, P. Ineichen, R. Stewart, and D. Menicucci. 1987. "A new simplified version of the perez diffuse irradiance model for tilted surfaces." *Sol. Energy* 39, 221–231. https://doi.org/10.1016/S0038-092X(87)80031-2.

Perez, R., R. Stewart, R. Seals, and T. Guertin. 1988. *The Development and Verification of the Perez Diffuse Radiation Model.* SAND88-7030. Sandia National Lab., Albuquerque, NM. https://doi.org/10.2172/7024029.

Pinker, R.T., and J.A. Ewing. 1985. "Modeling Surface Solar Radiation: Model Formulation and Validation." *J. Appl. Meteorol. Climatol.* 24, 389–401. https://doi.org/10.1175/1520-0450(1985)024<0389:MSSRMF>2.0.CO;2.

Pinker, R.T., R. Frouin, and Z. Li. 1995. "A review of satellite methods to derive surface shortwave irradiance." *Remote Sens. Environ*. 51, 108–124. https://doi.org/10.1016/0034-4257(94)00069-Y.

Pinker, R.T., and I. Laszlo. 1992. "Modeling Surface Solar Irradiance for Satellite Applications on a Global Scale." *J. Appl. Meteorol. Climatol*. 31, 194–211. https://doi.org/10.1175/1520-0450(1992)031<0194:MSSIFS>2.0.CO;2.

Polo, J., C. Fernández-Peruchena, V. Salamalikis, L. Mazorra-Aguiar, M. Turpin, L. Martín-Pomares, A. Kazantzidis, P. Blanc, and J. Remund. 2020. "Benchmarking on improvement and site-adaptation techniques for modeled solar radiation datasets." *Sol. Energy* 201, 469–479. https://doi.org/10.1016/j.solener.2020.03.040.

Polo, J., L. Martín, and M. Cony. 2012. "Revision of ground albedo estimation in Heliosat scheme for deriving solar radiation from SEVIRI HRV channel of Meteosat satellite." *Sol. Energy* 86, 275–282. https://doi.org/10.1016/j.solener.2011.09.030.

Polo, J., L. Martín, and J.M. Vindel. 2015. "Correcting satellite derived DNI with systematic and seasonal deviations: Application to India." *Renew. Energy* 80, 238–243. https://doi.org/10.1016/j.renene.2015.02.031.

Polo, J., J.M. Vindel, and L. Martín. 2013. "Angular dependence of the albedo estimated in models for solar radiation derived from geostationary satellites." *Sol. Energy* 93, 256–266. http://dx.doi.org/10.1016/j.solener.2013.04.019.

Polo, J., S. Wilbert, J.A. Ruiz-Arias, R. Meyer, C.A. Gueymard, M. Súri, L. Martín, T. Mieslinger, P. Blanc, I. Grant, J. Boland, et al. 2016. "Preliminary survey on site-adaptation techniques for satellite-derived and reanalysis solar radiation datasets." *Sol. Energy* 132, 25–37. https://doi.org/10.1016/j.solener.2016.03.001.

Qin, W, L. Wang, C.A. Gueymard, M. Bilal, A. Lin, J. Wei, M. Zhang, and X. Yang. 2020. "Constructing a gridded direct normal irradiance dataset in China during 1981–2014." *Renew. Sustain. Energy Rev*. 131, 110004. https://doi.org/10.1016/j.rser.2020.110004.

Qu, Z., A. Oumbe, P. Blanc, B. Espinar, G. Gesell, B. Gschwind, L. Klüser, M. Lefèvre, L. Saboret, M. Schroedter-Homscheidt, and L. Wald. 2017. "Fast radiative transfer parameterisation for assessing the surface solar irradiance: The Heliosat-4 method." *Meteorol. Z.* 26, 33–57. https://doi.org/10.1127/metz/2016/0781.

Renné, D., R. Perez, A. Zelenka, C.H. Whitlock, and R.C. DiPasquale. 1999. "Use of Weather and Climate Research Satellites for Estimating Solar Resources." In: Advances in Solar Energy: An Annual Review of Research and Development. American Solar Energy Society, Boulder, CO.

Rigollier, C., O. Bauer, and L. Wald. 2000. "On the clear sky model of the ESRA — European Solar Radiation Atlas — with respect to the Heliosat method." *Sol. Energy* 68, 33–48. https://doi.org/10.1016/S0038-092X(99)00055-9.

Rigollier, C., M. Lefèvre, and L. Wald. 2004. "The method Heliosat-2 for deriving shortwave solar radiation from satellite images." *Sol. Energy* 77, 159–169. https://doi.org/10.1016/j.solener.2004.04.017.

Roebeling, R.A., A.J. Feijt, and P. Stammes. 2006. "Cloud property retrievals for climate monitoring: Implications of differences between Spinning Enhanced Visible and Infrared Imager (SEVIRI) on METEOSAT-8 and Advanced Very High Resolution Radiometer (AVHRR) on NOAA-17." *J. Geophys. Res. Atmospheres* 111. https://doi.org/10.1029/2005JD006990.

Ruiz-Arias, J. A., J. Dudhia, C.A. Gueymard, and D. Pozo-Vázquez. 2013. "Assessment of the Level-3 MODIS daily aerosol optical depth in the context of surface solar radiation and numerical weather modeling." *Atmos. Chem. Phys.* 13, 675–692. https://doi.org/10.5194/acp-13-675-2013.

Ruiz-Arias, José A., J. Dudhia, F.J. Santos-Alamillos, and D. Pozo-Vázquez. 2013. "Surface clear-sky shortwave radiative closure intercomparisons in the Weather Research and Forecasting model." *J. Geophys. Res. Atmospheres* 118, 9901–9913. https://doi.org/10.1002/jgrd.50778.

Ruiz-Arias, J.A., and C.A. Gueymard. 2024. "GISPLIT: High-performance global solar irradiance component-separation model dynamically constrained by 1-min sky conditions." *Sol. Energy* 269, 112363. https://doi.org/10.1016/j.solener.2024.112363.

Ruiz-Arias, J.A., C.A. Gueymard, J. Dudhia, and D. Pozo-Vázquez. 2012. "Improvement of the Weather Research and Forecasting (WRF) model for solar resource assessment and forecasts under clear skies." Presented at the World Renewable Energy Forum, Denver, CO.

Ruiz-Arias, J.A., S. Quesada-Ruiz, E.F. Fernández, and C.A. Gueymard. 2015. "Optimal combination of gridded and ground-observed solar radiation data for regional solar resource assessment." *Sol. Energy* 112, 411–424. https://doi.org/10.1016/j.solener.2014.12.011.

Şahin, M., Y. Kaya, M. Uyar, and S. Yildirim. 2014. "Application of extreme learning machine for estimating solar radiation from satellite data." *Int. J. Energy Res*. https://doi.org/10.1002/er.3030.

Schiffer, R.A., and W.B. Rossow. 1983. "The International Satellite Cloud Climatology Project (ISCCP): The First Project of the World Climate Research Programme." *Bull. Am. Meteorol. Soc.* 64, 779–784. https://doi.org/10.1175/1520-0477-64.7.779.

Schmetz, J. 1989. "Towards a surface radiation climatology: Retrieval of downward irradiances from satellites." *Atmospheric Res.* 23, 287–321. https://doi.org/10.1016/0169-8095(89)90023-9.

Schmetz, J., P. Pili, S. Tjemkes, D. Just, J. Kerkmann, S. Rota, and A. Ratier. 2002. "An Introduction to Meteosat Second Generation (MSG)." *Bull. Am. Meteorol. Soc.* 83, 977–992. https://doi.org/10.1175/1520-0477(2002)083<0977:AITMSG>2.3.CO;2.

Schmit, T.J., M.M. Gunshor, W.P. Menzel, J.J. Gurka, J. Li, and A.S. Bachmeier. 2005. "Introducing the Next-Generation Advanced Baseline Imager on GOES-R." *Bull. Am. Meteorol. Soc*. 86, 1079–1096. https://doi.org/10.1175/BAMS-86-8-1079.

Schmit, T.J., S.S. Lindstrom, J.J. Gerth, and M.M. Gunshor. 2018. "Applications of the 16 Spectral Bands on the Advanced Baseline Imager (ABI)." *J. Operational Meteor.* 6, 33–46. https://doi.org/10.15191/nwajom.2018.0604.

Schroedter-Homscheidt, Marion, Faiza Azam, Jethro Betcke, C. Hoyer-Klick, M. Lefèvre, Y-M Saint-Drenan, E. Wey, and L. Saboret. 2021. *User Guide to the CAMS Radiation Service (CRS).* Report. CAMS2_73_2021SC1_D3.2.1_2021_UserGuide_v1. Copernicus. https://atmosphere.copernicus.eu/sites/default/files/2020-03/CAMS72_2018SC1_D72.4.3.1_2019_UserGuide_v1.1.pdf.

Schumann, K., H.G. Beyer, K. Chhatbar, and R. Meyer. 2011. "Improving satellite-derived solar resource analysis with parallel ground-based measurements." Presented at the Solar World Congress, ISES, Kassel, Germany. https://doi.org/doi:10.18086/swc.2011.24.28.

Sengupta, M., and P. Gotseff. 2013. "Evaluation of Clear Sky Models for Satellite-Based Irradiance Estimates." NREL/TP-5D00-60735. National Renewable Energy Laboratory, Golden, CO. https://doi.org/10.2172/1118101.

Starke, A.R., L.F.L. Lemos, C.M. Barni, R.D. Machado, J.M. Cardemil, J. Boland, and S. Colle. 2021. "Assessing one-minute diffuse fraction models based on worldwide climate features." *Renew. Energy* 177, 700–714. https://doi.org/10.1016/j.renene.2021.05.108.

Stengel, M., A. Kniffka, J.F. Meirink, M. Lockhoff, J. Tan, and R. Hollmann. 2014. "CLAAS: the CM SAF cloud property dataset using SEVIRI." *Atmos. Chem. Phys.* 14, 4297–4311. https://doi.org/10.5194/acp-14-4297-2014.

Stowe, L.L., P.A. Davis, and E.P. McClain. 1999. "Scientific Basis and Initial Evaluation of the CLAVR-1 Global Clear/Cloud Classification Algorithm for the Advanced Very High Resolution Radiometer." *J. Atmospheric Ocean. Technol.* 16, 656–681. https://doi.org/10.1175/1520-0426(1999)016<0656:SBAIEO>2.0.CO;2.

Stuhlmann, R., M. Rieland, and E. Paschke. 1990. "An Improvement of the IGMK Model to Derive Total and Diffuse Solar Radiation at the Surface from Satellite Data." *J. Appl. Meteorol. Climatol.* 29, 586–603. https://doi.org/10.1175/1520-0450(1990)029<0586:AIOTIM>2.0.CO;2.

Tahir, Z. ul R., M. Amjad, M. Asim, M. Azhar, M. Farooq, M.J. Ali, S.U. Ahmad, G.M. Amjad, and A. Hussain. 2021. "Improving the accuracy of solar radiation estimation from reanalysis datasets using surface measurements." *Sustain. Energy Technol. Assess.* 47, 101485. https://doi.org/10.1016/j.seta.2021.101485.

Tan, Y., Q. Wang, and Z. Zhang. 2023. "Algorithms for separating diffuse and beam irradiance from data over the East Asia-Pacific region: A multi-temporal-scale evaluation based on minute-level ground observations." *Sol. Energy* 252, 218–233. https://doi.org/10.1016/j.solener.2023.01.061.

Tapakis, R., S. Michaelides, and A.G. Charalambides. 2016. "Computations of diffuse fraction of global irradiance: Part 1 – Analytical modelling." *Sol. Energy* 139, 711–722. https://doi.org/10.1016/j.solener.2014.10.005.

Tarpley, J.D. 1979. "Estimating Incident Solar Radiation at the Surface from Geostationary Satellite Data." *J. Appl. Meteorol. Climatol.* 18, 1172–1181. https://doi.org/10.1175/1520-0450(1979)018<1172:EISRAT>2.0.CO;2.

Thuman, C., M. Schnitzer, and P. Johnson. 2012. "Quantifying the accuracy of the use of Measure–Correlate–Predict methodology for long-term solar resource estimates." Proc. American Solar Energy Soc. Annual Conf., Denver, CO.

Tiba, C., L.F. Souza, and M.H. Filho. 2019. "Methods for Site-Adaptation of Satellite-Based DNI Time Series: Application to Brazilian Northeast." In: Solar World Congress, ISES, Santiago, Chile. https://doi.org/doi:10.18086/swc.2019.45.11.

Trolliet, M., J.P. Walawender, B. Bourlès, A. Boilley, J. Trentmann, P. Blanc, M. Lefèvre, and L. Wald. 2018. "Downwelling surface solar irradiance in the tropical Atlantic Ocean: a comparison of re-analyses and satellite-derived datasets to PIRATA measurements." *Ocean Sci*. 14, 1021–1056. https://doi.org/10.5194/os-14-1021-2018.

Urraca, R., T. Huld, A. Gracia-Amillo, F.J. Martinez-de-Pison, F. Kaspar, and A. Sanz-Garcia. 2018. "Evaluation of global horizontal irradiance estimates from ERA5 and COSMO-REA6 reanalyses using ground and satellite-based data." *Sol. Energy* 164, 339–354. https://doi.org/10.1016/j.solener.2018.02.059.

Verbois, H., Y-M Saint-Drenan, V. Becquet, B. Gschwind, and P. Blanc. 2023. "Retrieval of surface solar irradiance from satellite imagery using machine learning: pitfalls and perspectives." *Atmospheric Meas. Tech*. 16, 4165–4181. https://doi.org/10.5194/amt-16-4165-2023.

Verbois, Hadrien, Y-M Saint-Drenan, Q. Libois, Y. Michel, M. Cassas, L. Dubus, and P. Blanc. 2023. "Improvement of satellite-derived surface solar irradiance estimations using spatio-temporal extrapolation with statistical learning." *Sol. Energy* 258, 175–193. https://doi.org/10.1016/j.solener.2023.04.037.

Vernay, C., P. Blanc, and S. Pitaval. 2013. "Characterizing measurements campaigns for an innovative calibration approach of the global horizontal irradiation estimated by HelioClim-3." *Renew. Energy* 57, 339–347. https://doi.org/10.1016/j.renene.2013.01.049.

Vindel, J.M., J. Polo, and F. Antonanzas-Torres. 2013. "Improving daily output of global to direct solar irradiance models with ground measurements." *J. Renew. Sustain. Energy* 5, 063123. https://doi.org/10.1063/1.4850515.

Wattan, R., and S. Janjai. 2016. "An investigation of the performance of 14 models for estimating hourly diffuse irradiation on inclined surfaces at tropical sites." *Renew. Energy* 93, 667–674. https://doi.org/10.1016/j.renene.2016.02.076.

Xie, Y., and M. Sengupta. 2016. "Performance Analysis of Transposition Models Simulating Solar Radiation on Inclined Surfaces." In: European PV Solar Conference and Exhibition, Munich, Germany June 20–24. https://doi.org/10.4229/EUPVSEC20162016-5CV.3.21.

Xie, Y., and M. Sengupta. 2018. "A Fast All-sky Radiation Model for Solar applications with Narrowband Irradiances on Tilted surfaces (FARMS-NIT): Part I. The clear-sky model." *Sol. Energy* 174, 691–702. https://doi.org/10.1016/j.solener.2018.09.056.

Xie, Y., M. Sengupta, and J. Dudhia. 2016. "A Fast All-sky Radiation Model for Solar applications (FARMS): Algorithm and performance evaluation." *Sol. Energy* 135, 435–445. https://doi.org/10.1016/j.solener.2016.06.003.

Xie, Y., M. Sengupta, and C. Wang. 2019. "A Fast All-sky Radiation Model for Solar applications with Narrowband Irradiances on Tilted surfaces (FARMS-NIT): Part II. The cloudy-sky model." *Sol. Energy* 188, 799–812. https://doi.org/10.1016/j.solener.2019.06.058.

Yang, D. 2020. “Ensemble model output statistics as a probabilistic site-adaptation tool for solar irradiance: A revisit.” *J. Renew. Sustain. Energy* 12, 036101. https://doi.org/10.1063/5.0010003.

Yang, D. 2016. “Solar radiation on inclined surfaces: Corrections and benchmarks.” *Sol. Energy* 136, 288–302. https://doi.org/10.1016/j.solener.2016.06.062.

Yang, D., Y. Gu, M.J. Mayer, C.A. Gueymard, W. Wang, J. Kleissl, M. Li, Y. Chu, and J.M. Bright. 2024. “Regime-dependent 1-min irradiance separation model with climatology clustering.” *Renew. Sustain. Energy Rev.* 189, 113992. https://doi.org/10.1016/j.rser.2023.113992.

Yang, D., and C.A. Gueymard. 2021. “Probabilistic post-processing of gridded atmospheric variables and its application to site adaptation of shortwave solar radiation.” *Sol. Energy* 225, 427–443. https://doi.org/10.1016/j.solener.2021.05.050.

Yang, D., and C.A. Gueymard. 2020. “Ensemble model output statistics for the separation of direct and diffuse components from 1-min global irradiance.” *Sol. Energy* 208, 591–603. https://doi.org/10.1016/j.solener.2020.05.082.

Yang, X., J.M. Bright, C.A. Gueymard, B. Acord, and P. Wang. 2022. “Worldwide validation of an Earth Polychromatic Imaging Camera (EPIC) derived radiation product and comparison with recent reanalyses.” *Sol. Energy* 243, 421–430. https://doi.org/10.1016/j.solener.2022.08.013.

Yezeguelian, L., C. Vernay, T. Carrière, and P. Blanc. 2021. “Characterizing The Convergence And Robustness Of The Kernel Density Mapping Method For Site-Adaptation Of Global Horizontal Irradiation In Western Europe.” In: 38th European Photovoltaic Solar Energy-Conference and Exhibition. https://doi.org/10.4229/EUPVSEC20212021-5BO.6.3.

Zainali, S., D. Yang, T. Landelius, and P.E. Campana. 2023. “Site adaptation with machine learning for a Northern Europe gridded global solar irradiance product.” *Energy AI* 100331. https://doi.org/10.1016/j.egyai.2023.100331.

Zhong, X., and J. Kleissl. 2015. “Clear sky irradiances using REST2 and MODIS.” *Sol. Energy* 116, 144–164. https://doi.org/10.1016/j.solener.2015.03.046.

8 Solar Resource Models and Data

Manajit Sengupta,[1] Aron Habte,[1] Christian Gueymard,[2] and Adam R. Jensen[3]
[1] *National Renewable Energy Laboratory, USA*
[2] *Solar Consulting Services, USA*
[3] *Technical University of Denmark, Denmark*

Executive Summary

This chapter summarizes commonly used models and data sources. The goal is to describe all the sources of information that can be expected to be available at any one location. Nevertheless, the lists of models and data should not be treated as exhaustive because new databases regularly appear. In parallel, existing databases are typically regularly updated, so their details might change. Additionally, users should use their judgement to decide on the most appropriate models and data for their purpose. Table 8-2 provides information about various all-sky and clear-sky broadband models, spectral models, decomposition models, and transposition models. The data sources presented in this chapter are from ground-based measurements, satellite-based calculations, and numerical weather predictions.

8.1 Introduction

Understanding the long-term spatial and temporal variability of the available solar resources is fundamental to any assessment of solar energy potential. Information derived from historical solar resource data can be used to make energy policy decisions, to select optimum energy conversion technologies, to design systems for specific locations, and to operate and maintain installed solar energy conversion systems. Historical solar resource data can be the result of *in situ* measurement programs, satellite remote-sensing methods, or meteorological model outputs. As described in the previous chapters, each type of data has different information content and applicability.

This chapter summarizes the voluminous information available about the many solar models that are publicly available as well as historical solar resource data available around the world. Additional details about the solar models include their inputs and outputs. Similarly, the inventory of representative sources of solar radiation data includes the main characteristics associated with each of them (e.g., period of record, temporal and spatial resolutions, available data elements, and estimated uncertainties). Some datasets discussed in this chapter are commercial and might not be freely available. Additionally, some historical datasets that were listed in previous editions are not retained in this version because direct links to download them are no longer available. Please refer to previous versions of this handbook for references to historical archives with no known direct source of download.

The authors and other participants in the International Energy Agency's (IEA's) Photovoltaic Power Systems Programme (PVPS) Task 16 have made every effort to include and describe models and data products that are as useful, robust, and representative as possible; however, the responsibility for correctly applying these models and data resides with the user. A thorough understanding of the models and data sources, how they are created, and their limitations remains vital to the proper application of the models and resource data to analyses and subsequent decision making. This chapter presents discussions and examples of the use of several of these

datasets for solar energy applications. Users are encouraged to read the pertinent sections of this chapter before applying solar resource and meteorological data.

Measured solar irradiance data can provide detailed temporal information for a specific site. Because solar radiation measurement stations are challenging to operate and because the collected data are not used for routine weather forecasts, their density is low, and they typically have limited data collection records. Some examples of relatively long records of solar radiation data in the United States are the National Oceanic and Atmospheric Administration's (NOAA's) Surface Radiation Budget Network (SURFRAD) and SOLRAD networks, the University of Oregon network, stations from the U.S. Department of Energy's (DOE's) Atmospheric Radiation Measurement (ARM) program, and the National Renewable Energy Laboratory (NREL). There are now more than 3,000 ground stations measuring solar irradiance in some form and with a wide range of data quality in the United States alone. These stations are operated by several interests producing data for varied applications (including agriculture). Links to most of these stations are not presented here because there is limited confidence in the data quality. For other parts of the world, users are encouraged to refer to the Baseline Surface Radiation Network (BSRN) network[52] for high-quality data (Driemel et al. 2018). Table 8-1 provides more details on the sources of the measured or partly measured databases. (The meteorological services of various countries might operate many radiometric stations, so Table 8-1 should not be considered exhaustive. Also, some national services do not release their data in the public domain.) An increasing number of photovoltaic (PV) and concentrating solar power installations now collect high-quality solar radiation data, but those datasets are usually not publicly available, so they are not listed in this chapter.

Satellite-based observations and mesoscale meteorological models address the needs for understanding the spatial variability of solar radiation resources throughout a range of distances. Present state-of-the-art models provide estimates for global horizontal irradiance (GHI) and direct normal irradiance (DNI) at spatial resolutions of 10 km or less for the United States and other parts of the world—e.g., see the European Organisation for the Exploitation of Meteorological Satellites (EUMETSTAT) Satellite Application Facility on Climate Monitoring (CM SAF), the National Solar Radiation Database (NSRDB), Meteonorm, the Photovoltaic Geographical Information System (PVGIS), SolarAnywhere, Solcast, and Solargis in Table 8-1). Numerical weather prediction models can be used to produce long-term meteorological information when they are used in reanalysis mode. The reanalysis models described in Chapter 7 have spatially coarser resolutions and have higher uncertainty in estimating solar radiation than satellite models or ground measurements. Nevertheless, reanalysis datasets such as ERA5, which is the fifth-generation atmospheric reanalysis of the global climate from the European Center for Medium-Range Weather Forecasts (ECMWF),[53] or the National Aeronautics and Space Administration's (NASA's) Modern-Era Retrospective analysis for Research and Applications, Version 2 (MERRA-2)[54] are useful sources of data because they are available globally and for periods longer than 30 years. The rapidly growing needs for more accurate solar resource

[52] See https://bsrn.awi.de.
[53] See http://climate.copernicus.eu/products/climate-reanalysis.
[54] See https://gmao.gsfc.nasa.gov/reanalysis/MERRA-2/.

information at shorter temporal and smaller spatial scales require the user to fully appreciate the characteristics of all available data, especially those from historical sources.

8.2 Solar Resource Data Characteristics

Characterizing the available solar resources for solar energy applications is important for all aspects of realizing the full potential of this utility-scale energy source. Energy policy decisions, engineering designs, and system deployment considerations require an accurate understanding of the relevant historical solar resource data, the ability to assess the accuracy of current solar measurement and modeling techniques, and forecasts of the levels of solar irradiance for various temporal and spatial scales.

Measured solar irradiance data can provide information about the temporal variability at a specific site. Today, 1-minute (or shorter) digital recordings are available from fast-response silicon photodiodes and improved thermopile-type pyranometers and pyrheliometers that are deployed in regional measurement networks to provide solar energy resource data for a variety of applications.

Modeled solar resource data derived from available surface meteorological observations and satellite measurements provide estimates of solar resource potential for locations lacking actual measurements. These modeling methods address the needs for improved spatial resolutions of the resource data. In the United States, the first national effort to model solar resources in the 1970s advanced the understanding of solar radiation distributions based on the then-available historical measurements at 26 locations to an additional 222 meteorological observing stations with detailed records of hourly cloud amounts and other relevant data (SOLMET/ERSATZ[55]). Today, satellite-based observations of clouds are used to model subhourly surface solar fluxes with a 2-km spatial resolution over North America and part of South America (Sengupta et al. 2018). Similar efforts are conducted over other parts of the world.

8.3 Solar Resource Data Long-Term and Typical Meteorological Datasets

Understanding the time frame, or period of record, associated with solar resource data and related meteorological information is important for conducting useful analyses. These weather-driven variables have fluctuations that can range from seconds to years and longer. Long-term data can be representative of the climate if the period of record is at least 30 years. By convention, according to the 1933 International Meteorological Conference in Warsaw, the meteorological community has deemed that a 30-year interval is sufficient to reflect longer-term climatic trends and filter the short-term interannual fluctuations and anomalies. Climate "normals" are recomputed each decade to address temperature, pressure, precipitation, and other surface meteorological variables. Note that the term *normal* is not equivalent to "average" and has a specific meaning in the meteorological and climatological community—namely, *normal* refers to the 30-year average of an observed parameter that is updated every 10 years (Arguez and Vose 2011); thus, the averaging period shifts every 10 years.

[55] See https://nsrdb.nrel.gov/data-sets/archives.

Often, solar power plant project developers require "typical" meteorological information related to a potential plant site for prefeasibility studies. The most common type of typical meteorological year (TMY) dataset provides designers and other users with a small-size annual dataset that holds 8,760 hourly meteorological values that typify conditions at a specific location throughout a longer period, such as the 30-year climatic normal. Different types of TMYs exist, including TMYs at subhourly temporal resolution. Twelve typical meteorological months (TMMs) selected based on their similarity of individual cumulative frequency distributions for selected data elements comprise the TMY dataset. The longer-term distributions are determined for that month using data from the full period of record. The TMMs are then concatenated, essentially without modification, to form a single year with a serially complete data record. The resulting TMY dataset contains measured and/or modeled time series of solar radiation and surface meteorological data, though some hourly records might contain filled or interpolated data for periods when original observations are missing from the data archive. Further, many methods are used to develop TMMs, as reviewed in Nielsen et al. (2017) and García, de Blas, and Torres (2020). In particular, new developments include a climate-based ensemble empirical mode decomposition (Fan 2022), the generation of TMYs at high temporal resolution (Ernst and Gooday 2019), the preparation of TMYs specifically tailored for PV applications focusing on either broadband irradiance (Sengupta and Habte 2019) or spectral irradiance (Polo et al. 2020), and even customized TMYs (Sengupta, Habte, and Freeman 2019).

Note that TMY datasets were primarily developed for use in building design and were later adopted by solar designers and others for modeling renewable energy conversion systems. Therefore, by their nature of construction, TMY datasets provide only an artificial year brought about by the concatenation of "median" months. TMY data are not designed to provide meteorological extremes, although they contain natural diurnal and seasonal variations. A TMY dataset should *not* be used to predict weather or solar resources for a particular period of time, nor is it an appropriate basis for evaluating real-time energy production, detailed power plant design, or the probability of energy yield exceedances. Also, TMY data are not suited for designing systems and their components to meet the worst-case weather conditions.

8.4 Solar Resource Data Key Considerations

Applying solar and meteorological data from different sources requires attention to these key considerations:

- **Period of record.** Influenced by many factors, solar resource data vary yearly, seasonally, monthly, weekly, daily, and on timescales down to 1 second (see Chapter 6). In contrast, the 30-year averaging period involved in the production of climate normals (introduced in Section 8.3) is updated (shifted) every 10 years. For instance, the current climate normals span the period from 1991–2020, but eventually the 2001–2030 normals will become available from meteorological services around the world. The normal for one period will not likely be the same as a normal for previous or successive periods. Another popular approach is to determine a TMY dataset from a statistical analysis of multiyear data and eventually derive a single year of data that is deemed representative of a longer-term record. Comparative analyses must account for any natural differences that result from the periods when the data were acquired.

- **Temporal resolution.** Solar resource data can range from annually averaged daily irradiation, typically used for mapping resource distributions, to 1-second samples of irradiance for operational time-series analyses. Other considerations depend on the data type.
- **Units.** The unit of irradiance is W m^{-2}. The most common unit of irradiation, or integrated power, is kWh m^{-2}. The actual Système International unit for irradiation, J m^{-2}, is rarely used anymore. The conversion is 1 kWh m^{-2} = 3.6 MJ m^{-2}. Note that daily average irradiation data produced by or for climatologists are most often incorrectly reported with a unit of W m^{-2}. Here, a daily irradiation of 1 W m^{-2} means an average irradiance of 1 W m^{-2} over 24 hours, or 24 Wh m^{-2}. Unfortunately, this can create confusion. A daily irradiation should be expressed in kWh m^{-2}, not kWh m^{-2} day^{-1}, even though this is a frequent mistake.
- **Spatial coverage.** The area represented by the data can range from a single station, to a sample geographic region, to a global (world) perspective.
- **Spatial resolution.** Ground-based measurements are site specific. Current satellite remote-sensing estimates are representative of areas typically spanning 3 km by 3 km to 10 km by 10 km. The "pixel" size of reanalysis data is significantly larger, at least 30 km by 30 km with current products.
- **Data elements and sources of the data.** The usefulness of solar resource data might depend on the available data elements (e.g., DNI or GHI) and whether the data were measured, modeled, or produced from a combination of measurements and models.
- **Time stamp.** There are three possible time references: Local Apparent Time (LAT, also known as Apparent Solar Time or True Solar Time), Local Standard Time (LST), and Universal Time (UT). The former is rarely used anymore. Global databases tend to use UT, but there is no general rule. Moreover, for comparative purposes, it is also important to consider what each time stamp specifically refers to. Depending on the database, it can be the start, the midpoint, or the end of the time period (for subdaily data). In climatology, the latter is standard. For more details, see Polo et al. (2019).
- **Availability.** Data are distributed in the public domain, for purchase, or by license.

8.5 Solar Resource Data Resolution

Spatial resolution and temporal resolution are two key characteristics of any solar irradiance dataset. These characteristics depend on the source of data under scrutiny, and thus they need to be qualified in an appropriate context, as discussed in the following:

- Ground-based irradiance measurements have the finest spatial resolution (point source) and a temporal resolution that can be high (1 min or better) if used directly without modification, or coarser if aggregated into hourly, daily, monthly, or annual averages. Contrary to all the other sources of data mentioned here, ground-based measurements represent an *average* between two consecutive time stamps.
- Predictions from clear-sky radiation models normally have a point-source spatial resolution and the same temporal resolution as their time interval. This is the case *only* if their key atmospheric input data (aerosols and water vapor) are derived "instantaneously" from a collocated instrument (in practice, a sunphotometer). In the more frequent case that such inputs are obtained from gridded data generated by, e.g., a reanalysis model, the actual spatiotemporal resolution of the predictions reflects theirs, even if interpolation is

used to refine the inputs. This case is exemplified by the Copernicus Atmosphere Monitoring Service (CAMS) McClear Service (see Table 8-2).

- For numerical weather prediction models, the spatial resolution is that of their grid at the surface, and the temporal resolution is determined by the frequency of their output (e.g., hourly).
- With satellite-derived irradiance data, the situation is more complex. Under cloudless or quasi-cloudless conditions, the spatiotemporal resolution is determined by the clear-sky model, per the discussion here. For instance, this can be 0.5° by 0.625° hourly in the case of MERRA-2 inputs or 0.75° by 0.75° 3-hourly with CAMS inputs. Spatiotemporal interpolation is normally used to refine the inputs to match the desired irradiance grid size, but this does not fundamentally improve the actual resolution. Under cloudy conditions, the temporal resolution is typically determined by that of the imagery snapshots, and the spatial resolution is also that of the satellite sensor (or a multiple of it). Caution is necessary, however, because the spatial resolution is always indicated by a nominal value, which refers to the sensor's nadir view. For example, many irradiance products that are derived from Meteosat's Second Generation satellite have a quoted spatial resolution of 3 km. Depending on the site under scrutiny, the resolution varies between 3 and approximately 12 km (Figure 8-1).

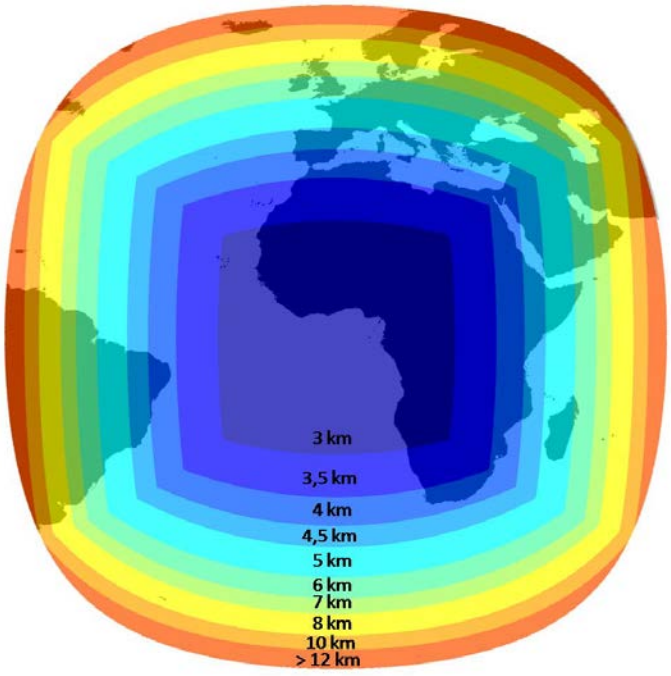

Figure 8-1. Actual spatial resolution of the imagery from the primary Meteosat Second Generation satellite

Image from MINES ParisTech

Table 8-1. Selected Solar Radiation Models

Model	Description	Inputs	Outputs	Source/Website
All-Sky Models				
Fast All-sky Radiation Model for Solar applications (FARMS)	Prediction of solar irradiance	Cloud type (ice or water), COD, cloud effective radius, surface pressure, PWV, AOD, surface albedo	GHI, DNI, and DHI	https://github.com/NREL/farms https://doi.org/10.1016/j.solener.2016.06.003
libRadtran	Calculation of solar and thermal radiation in the atmosphere	Various relevant atmospheric data	Spectral radiance, broadband irradiance (GHI, DNI, DHI)	http://libradtran.org
Clear-Sky Models				
Bird Simple Spectral Model (SPECTRL2)	Estimation of terrestrial spectra of irradiance	Zenith angle, albedo, air mass, PWV, ozone, etc.	Spectral irradiance for wavelengths from 300 nm–4,000 nm	https://pvlib-python.readthedocs.io/en/stable/reference/generated/pvlib.spectrum.spectrl2.html
Bird Clear Sky Solar Model	Estimation of clear-sky irradiance	Zenith angle, air mass, AOD (380 nm and 500 nm), PWV, ozone, albedo	Clear-sky GHI, DNI, and DHI	https://pvlib-python.readthedocs.io/en/stable/reference/generated/pvlib.clearsky.bird.html
REST2	Prediction of clear-sky irradiance, illuminance, and PAR	Various atmospheric data	Clear-sky GHI, DNI, and DHI, as well as illuminance and PAR components	https://solarconsultingservices.com/rest2.php
Simple Model of the Atmospheric Radiative Transfer of Sunshine (SMARTS)	Estimation of clear-sky spectral irradiances	Various atmospheric data	Clear-sky spectral and broadband irradiances for various collector geometries	https://nrel.gov/grid/solar-resource/smarts.html https://solarconsultingservices.com/smarts.php
McClear (web service)	Estimation of clear-sky broadband irradiances	Location and period (See Table 8-2.)	Clear-sky GHI, DNI, and DHI	https://www.soda-pro.com/web-services/radiation/cams-mcclear

Model	Description	Inputs	Outputs	Source/Website
Ineichen and Perez clear-sky model	Estimation of clear-sky broadband irradiances	Zenith angle, air mass, Linke turbidity	Clear-sky GHI, DNI, and DHI	Ineichen and Perez (2002)
Simplified Solis	Estimation of clear-sky broadband irradiances	Zenith angle, AOD (700 nm), PWV	Clear-sky GHI, DNI, and DHI	https://pvlib-python.readthedocs.io/en/stable/reference/generated/pvlib.clearsky.simplified_solis.html
European Solar Radiation Atlas (ESRA) clear-sky model	Estimation of clear-sky broadband irradiances	Solar constant, Zenith angle, location's altitude, Linke turbidity at air mass = 2	Clear-sky GHI, DNI, and DHI	https://www.oie.minesparis.psl.eu/Valorisation/Outils/Clear-Sky-Library/
Haurwitz	Estimation of clear-sky global irradiance	Zenith angle	Clear-sky GHI	https://pvlib-python.readthedocs.io/en/stable/reference/generated/pvlib.clearsky.haurwitz.html
Reno and Hansen clear-sky detection model	Detection of clear-sky periods from GHI measurements	Measured and clear-sky GHI	Boolean array of whether or not the given time is clear	https://pvlib-python.readthedocs.io/en/stable/reference/generated/pvlib.clearsky.detect_clearsky.html
Decomposition Models				
DISC	Estimates DNI from GHI	GHI, zenith angle	DNI	https://pvlib-python.readthedocs.io/en/stable/reference/generated/pvlib.irradiance.disc.html
DIRINT	Estimates DNI from GHI (modification of DISC model)	GHI, zenith angle	DNI	https://pvlib-python.readthedocs.io/en/stable/reference/generated/pvlib.irradiance.dirint.html
DIRINDEX	Estimates DNI from GHI (modification of DIRINT model)	GHI, clear-sky GHI and DNI, zenith angle	DNI	https://pvlib-python.readthedocs.io/en/stable/reference/generated/pvlib.irradiance.dirindex.html
Erbs	Estimates DHI from GHI	GHI, zenith angle	DHI	https://pvlib-python.readthedocs.io/en/stable/reference/generated/pvlib.irradiance.erbs.html
GISPLIT	Estimates DNI and DHI from GHI	GHI, clear-sky GHI and DNI, zenith angle	DNI, DHI	https://github.com/jararias/gisplit
Boland	Estimates DHI from GHI	GHI, zenith angle	DHI	https://pvlib-python.readthedocs.io/en/stable/reference/generated/pvlib.irradiance.boland.html

Model	Description	Inputs	Outputs	Source/Website
GTI DIRINT	Estimates GHI from GTI (reverse transposition)	Measured GTI, solar position, surface orientation	GHI, DNI, DHI	https://pvlib-python.readthedocs.io/en/stable/reference/generated/pvlib.irradiance.gti_dirint.html
Transposition Models				
Perez transposition model	Estimates in-plane sky diffuse irradiance	Surface orientation, solar position, DNI, DHI	GTI	https://pvlib-python.readthedocs.io/en/stable/reference/generated/pvlib.irradiance.perez.html
Hay-Davies transposition model	Estimates in-plane sky diffuse irradiance	Surface orientation, solar position, DNI, DHI	GTI	https://pvlib-python.readthedocs.io/en/stable/reference/generated/pvlib.irradiance.haydavies.html

Table 8-2. Inventory of Solar Resource Data Sources

Presented in Alphabetical Order

Database	Period of Record	Temporal Resolution	Spatial Coverage	Spatial Resolution	Data Elements and Sources	Availability
U.S. Department of Energy (DOE) Atmospheric Radiation Measurement (ARM) Program	1997–present	20-second instantaneous samples and 1-minute averages of 2-second scans	Southern Great Plains, North Slope of Alaska, and tropical western Pacific	32 (active and inactive)	GHI, DNI, DHI, downwelling longwave irradiance, upwelling longwave irradiance, and upwelling (reflected) shortwave irradiance. Measurements from the Eppley Model PSP (GHI, DHI, and upwelling shortwave irradiance), Model 8-48 (DHI after 2000), Model NIP (DNI), and Model PIR (upwelling and downwelling infrared) radiometers	DOE, ARM Climate Research Facility: http://www.arm.gov. Datasets are labeled SIRS, SKYRAD, and GNDRAD. SIRS data form the Billings and E13 locations are also submitted to the World Radiation Monitoring Center (WRMC)-Baseline Surface Radiation Network (BSRN) archives: http://www.bsrn.awi.de/.
Baseline Surface Radiation Network (BSRN)	1992–present	1 minute (3 minutes for SURFRAD stations before 2009)	Global	76 radiometric stations (51 active, 9 declared inactive, 16 closed, as of December 2023)	The number and type of measurements vary by station. Basic radiation measurements include GHI, DNI, DHI, downwelling infrared irradiance, upwelling infrared irradiance, and upwelling (reflected) shortwave irradiance. Measurements are from radiometers of various manufacturers. Synoptic meteorological observations, upper air measurements, and numerous expanded and supporting measurements are available.	The World Radiation Monitoring Center (WRMC) provides web-based and File Transfer Protocol data access: https://bsrn.awi.de/en/
Australian Bureau of Meteorology (BOM) 1-Minute Solar Data	Varies	1 minute	Australia	21 radiometric stations	GHI, DNI, DHI, DIR, longwave, and sunshine	http://www.bom.gov.au/climate/data/oneminsolar/stations.shtml

Database	Period of Record	Temporal Resolution	Spatial Coverage	Spatial Resolution	Data Elements and Sources	Availability
Copernicus Atmospheric Monitoring Service (CAMS) McClear Service	2004–present	1 minute, 15 minutes, 1 hour, 1 day, 1 month	Global	Various input data sources with different spatial resolutions are interpolated to the location of interest.	Clear-sky global, direct, direct normal, and diffuse irradiances; inputs describe atmospheric conditions (aerosols, water vapor, trace gases, surface reflectivity parameters).	http://www.soda-pro.com/web-services/radiation/cams-mcclear
CAMS Radiation Service	2004–present	1 minute, 15 minutes, 1 hour, 1 day, 1 month	Europe, Africa, Middle East, Atlantic Ocean, and eastern part of South America (-66° to 66° in both latitudes and longitudes)	Various input data sources with different spatial resolutions are interpolated to the location of interest.	All-sky GHI, DNI, DIR, DHI, and corresponding clear-sky irradiances; inputs describe atmospheric conditions (aerosols, clouds, water vapor, trace gases, surface reflectivity parameters).	http://www.soda-pro.com/web-services/radiation/cams-radiation-service
Clean Power Research—SolarAnywhere	1998–present	1 hour, 30 minutes, 15 minutes, options for high-resolution data	Continental United States, Hawaii, Canada up to 60° N, South America India, parts of the Middle East, and parts of Europe	1 km 2.5 km, 3 km 2.5 km, 1 km	GHI, DNI, wind speed, and ambient air temperature	https://www.solaranywhere.com/solutions/solaranywhere-data/
Clouds and the Earth's Radiant Energy System (CERES) SYN1deg	2000–2019	1 hour, 3 hours	Global	1° x 1°	GHI, DHI, and DIR based on physical modeling and satellite-based cloud observations	https://ceres.larc.nasa.gov/data/
EUMETSTAT's Satellite Application Facility on Climate Monitoring (CM SAF) Cloud, Albedo, and Surface Radiation Data Set From Advanced Very-	2019–2023 (CLARA-A 2) 2023–2023 (CLARA_A 3)	Daily, monthly averages	Global	0.25° x 0.25°	Cloud properties, surface albedo, and surface radiation parameters derived from the AVHRR sensor onboard polar-orbiting NOAA and MetOp satellites GHI	https://wui.cmsaf.eu/

Database	Period of Record	Temporal Resolution	Spatial Coverage	Spatial Resolution	Data Elements and Sources	Availability
High-Resolution Radiometer (AVHRR) Data, Edition 2 and 3 (CLARA-A2 and CLARA-A3)						
CM SAF Surface Solar Radiation Data Set – Heliosat (SARAH), Edition 3, Climate Data Record (CDR) and Interim Climate Data Record (ICDR)	1983–2020 (CDR) 2021–present (ICDR)	30 minutes, daily, monthly	Europe, Africa, and parts of South America	0.05°	Based on MVIRI/SEVIRI instruments onboard the Meteosat satellites; GHI, DNI, and DIR	https://wui.cmsaf.eu/
CM SAF Surface Solar Radiation Data Set - Heliosat – East (SARAH-E), Edition 1.1	1999–2016	1 hour, daily, monthly	Most parts of Asia, Africa; western part of Australia	0.05°	Based on MVIRI instruments onboard the Meteosat Indian Ocean Data Coverage (IODC) satellites GHI, DNI, and DIR	https://wui.cmsaf.eu/
Daymet	1980–2019	Daily	Continental United States	1 km	GHI, air temperature (minimum and maximum), vapor pressure, and snow water equivalent	https://daymet.ornl.gov
Deutsches Zentrum für Luft- und Raumfahrt (DLR; (German Aerospace Center) Integrated Surface Irradiance Study (ISIS)	July 1983–December 2004	3 hours	Global	280 km by 280 km	DNI and GHI from a radiative transfer model using cloud and aerosol inputs	http://www.pa.op.dlr.de/ISIS/

Database	Period of Record	Temporal Resolution	Spatial Coverage	Spatial Resolution	Data Elements and Sources	Availability
European Center for Medium-Range Weather Forecasts (ECMWF) ERA5 Reanalysis	1979–present	1 hour	Global	31 km	Clear-sky and all-sky GHI and DIR, UV irradiance, longwave irradiance, and surface albedo	https://cds.climate.copernicus.eu/cdsapp#!/dataset/reanalysis-era5-complete?tab=form
European Center for Medium-Range Weather Forecasts (ECMWF) ERA5-Land Reanalysis	1950–present	1 hour	Global (land only)	9 km	All-sky GHI, longwave irradiance, and surface albedo	https://cds.climate.copernicus.eu/cdsapp#!/dataset/reanalysis-era5-land?tab=form
European Solar Radiation Atlas (ESRA)	1981–1990	Monthly and annual average daily totals (kWh/m^2)	Europe	10 km	GHI, DNI, and DHI, sunshine duration, air temperature, precipitation, water vapor pressure, and air pressure at several stations	Les Presses MINES ParisTech: http://www.mines-paristech.fr/Ecole/Culture-scientifique/Presses-des-mines/#54. See also http://www.soda-pro.com/home.
Global Atlas (IRENA)		Monthly and annual average daily totals (kWh/m^2)			GHI, DNI, DHI, and many other variables	https://globalatlas.irena.org/workspace
Global Solar Atlas (ESMAP)	Variable start (1994–2018) depending on region, up to 2023	Annual average	Land areas, 65°N to 45°S	≈250 m	GHI, DNI, DHI, temperature, optimum tilt	https://globalsolaratlas.info/map
Green Power Labs: SolarSatData	1995–present (Americas) 2000–present (Europe) 2005–present (Asia, Australia)	30 minutes	Americas, Asia, Australia, and Europe	1–4 km	GHI, DNI, DHI, GTI, temperature, pressure, wind speed, ozone, water vapor, and total cloud fraction Irradiance time series for P10, P50, P90, and P95 exceedance probabilities	https://greenpowerlabs.com/

Database	Period of Record	Temporal Resolution	Spatial Coverage	Spatial Resolution	Data Elements and Sources	Availability
HelioClim V2–V5	2004–present	15 minutes	Europe and Africa	5 km	Hourly and daily GHI from satellite remote-sensing mode	MINES ParisTech Armines Center for Energy and Processes: http://www.soda-pro.com/home
Historically Black Colleges and Universities Solar Measurement Network	1985–1996	5 minutes	Southeastern United States: Daytona Beach, Florida; Savannah, Georgia; Itta Bena, Mississippi; Elizabeth City, North Carolina; Orangeburg, South Carolina; and Bluefield, West Virginia	Six radiometric stations	GHI, DNI (at three stations), DHI (shadowband) from measurements by Eppley Model PSP pyranometers and Model NIP pyrheliometers mounted in automatic solar trackers (LI-COR Model 2020)	NREL: https://www.nrel.gov/grid/solar-resource/hbcu.html (includes quality-assessed monthly data files, monthly summary reports, and monthly irradiance plots)
International Energy Agency (IEA) Photovoltaic Power Systems Programme (PVPS) Task-16 Reference Solar Measurements	2015–2020	1 minute	Global	Quality-controlled data from 115 world radiometric stations	GHI, DNI, and DHI	http://geocatalog.webservice-energy.org/geonetwork/srv/eng/catalog.search#/metadata/3491b1a6-e32d-4b34-9dbb-ee0affe49e36
Land Surface Analysis (LSA) Satellite Application Facility (SAF)	2004–present	15 minutes	Europe, Africa, and parts of Asia and South America (no geographic subsetting offered)	0.05° x 0.05°	GHI, diffuse fraction, albedo, snow cover, and vegetation cover	https://landsaf.ipma.pt/en/data/catalogue/

Database	Period of Record	Temporal Resolution	Spatial Coverage	Spatial Resolution	Data Elements and Sources	Availability
Meteonorm	2001–2020/ 2005–present	1-minute and 1-hour modeled data	Global	Data from 8,350 meteorological stations are interpolated using satellite data to establish weather data at any specified point. Ultimate resolution: 0.0625° x 0.0625°	Measured: monthly means of GHI, temperature, humidity, precipitation, wind speed and direction, and bright sunshine duration. Modeled typical years: 1-minute and hourly typical year radiation parameters (GHI, DNI, DHI, GTI, downwelling infrared, luminance, and UVA and UVB), precipitation, and humidity parameters (dew point, relative humidity, mixing ratio, and psychrometric temperature). Radiation data from ground measurements blended with satellite-based long-term averages. Time series based on satellite data only.	Meteotest: https://meteonorm.com/
Meteonorm time series	2010 (depending on region)–present	1-hour measured data	Global (62°S to 62°N)	0.0625° x 0.0625°	Measured time series: GHI from satellite, temperature, wind speed, humidity, precipitation, and wind speed from ERA5T and Swissmetnet	Meteotest: https://meteonorm.com/
National Aeronautics and Space Administration's (NASA's) GeoNEX	2018–2021	1 hour	Americas (Geostationary Operational Environmental Satellite [GOES-16])	0.01 x 0.01°	All-sky GHI and PAR	https://data.nas.nasa.gov/geonex/geonexdata/GOES16/GEONEX-L2/DSR-PAR/
National Aeronautics and Space Administration's (NASA's) GeoNEX	2015–2021	1 hour	Asia, Australia, and the Pacific (Himawari-8)	0.01 x 0.01°	All-sky GHI and PAR	https://data.nas.nasa.gov/geonex/geonexdata/HIMAWARI8/GEONEX-L2/DSR-PAR/
National Aeronautics and Space Administration's (NASA's) Modern-Era Retrospective Analysis for	1980–present	1 hour	Global	0.5° x 0.625°	Clear-sky and all-sky GHI, detailed information on clouds, atmospheric constituents (aerosols, water vapor, etc.), weather variables (temperature, wind, etc., and surface albedo	https://gmao.gsfc.nasa.gov/reanalysis/MERRA-2/data_access/

Database	Period of Record	Temporal Resolution	Spatial Coverage	Spatial Resolution	Data Elements and Sources	Availability
Research and Applications, Version 2 (MERRA-2)						
National Aeronautics and Space Administration's (NASA's) Prediction of Worldwide Energy Resources (POWER)	July 1983–present	Monthly and annual average daily totals and hourly (kWh/m^2)	Global	0.5° x 0.5°	GHI, DNI, and DHI from a satellite remote-sensing model. Also available: estimates of clear-sky GHI, DNI, and DHI and tilted surface irradiance, temperature, pressure, humidity, precipitation, and wind speed	https://power.larc.nasa.gov/
National Center for Environmental Protection (NCEP)/ National Center for Atmospheric Research Global Reanalysis Products	1948–present	6 hours ($W\ m^{-2}$)	Global	2.5° (nominal)	GHI and more than 80 variables, including geopotential height, temperature, relative humidity, and U and V wind components, in several coordinate systems, such as a 17-pressure-level stack on 2.5° x 2.5° grids, 28 sigma-level stacks on 192 x 94 Gaussian grids, and 11 isentropic-level stacks on a 2.5° x 2.5° grid	University Center for Atmospheric Research, Computational and Information Systems Laboratory Research Data Archive: http://rda.ucar.edu/datasets/ds090.0/.
National Oceanic and Atmospheric Administration's (NOAA's) Global Monitoring Laboratory (GML)/Earth System Research Laboratory (ESRL) Baseline Network	Varies	1 minute	Global	Five stations: Hawaii, Alaska, California, Greenland, American Samoa	GHI, DNI, DHI, downwelling infrared irradiance, upwelling infrared irradiance, and upwelling (reflected) shortwave irradiance. Photosynthetically active radiation, solar net radiation, infrared net radiation, global UVB, air temperature, relative humidity, and wind speed and direction (10-m AGL)	https://esrl.noaa.gov/gmd/dv/site/index.php?program=grad

Database	Period of Record	Temporal Resolution	Spatial Coverage	Spatial Resolution	Data Elements and Sources	Availability
National Oceanic and Atmospheric Administration's (NOAA's) SOLRAD Network	1995–present	1 minute (15 minutes before 2001)	Continental United States	Nine stations: New Mexico, North Dakota, California, Wisconsin, Tennessee, Washington, Utah, Virginia, and Florida	GHI, DNI, DHI, downwelling infrared irradiance, upwelling infrared irradiance, and upwelling (reflected) shortwave irradiance. Photosynthetically active radiation, solar net radiation, infrared net radiation, global UVB, air temperature, relative humidity, and wind speed and direction (10-m AGL)	NOAA, Earth Systems Research Laboratory, Global Monitoring Division, Boulder, Colorado: https://gml.noaa.gov/grad/solrad/index.html. Data available from: ftp://aftp.cmdl.noaa.gov/data/radiation/solrad.
National Oceanic and Atmospheric Administration's (NOAA's) Surface Radiation Budget Network (SURFRAD)	1993–present	Data are reported as 3-minute averages of 1-second samples before Jan. 1, 2009, and 1-minute averages on and after Jan. 1, 2009.	Continental United States	Seven permanent stations: Montana, Colorado, Illinois, Mississippi, Pennsylvania, Nevada, and South Dakota Four temporary stations: Arizona, Colorado, Oregon, and Vermont	GHI, DNI, DHI, downwelling infrared irradiance, upwelling infrared irradiance, and upwelling (reflected) shortwave irradiance. Photosynthetically active radiation, solar net radiation, infrared net radiation, global UVB, air temperature, relative humidity, wind speed and direction (10-m AGL), and all-sky images	NOAA, Earth Systems Research Laboratory, Global Monitoring Division, in Boulder, Colorado: https://gml.noaa.gov/grad/surfrad/sitepage.html. Data available from: ftp://aftp.cmdl.noaa.gov/data/radiation/surfrad/. SURFRAD data from permanent stations are also submitted to the BSRN archives: www.bsrn.awi.de/.
National Renewable Energy Laboratory (NREL) Solar Radiation Research Laboratory (SRRL) Measurement and Instrumentation Data Center (MIDC)	1981–present	5 minutes (beginning July 15, 1981), 1 minute (beginning Jan. 13, 1999)	Golden, Colorado	One radiometric station	GHI, DNI, DHI (from shadowband and tracking disk), global on tilted surfaces, reflected solar irradiance, UV, infrared (upwelling and downwelling), photometric and spectral radiometers, sky imagery, and surface meteorological conditions (temperature, relative humidity, barometric pressure, precipitation, snow cover, and wind speed and direction at multiple levels)	http://www.nrel.gov/midc/srrl_bms/

Database	Period of Record	Temporal Resolution	Spatial Coverage	Spatial Resolution	Data Elements and Sources	Availability
National Solar Radiation Database (NSRDB) 1961–1990	1961–1990	1 hour	United States and territories	239 stations (56 stations have some radiation measurements)	Hourly GHI, DNI, DHI, ETR, direct normal ETR, total sky cover, opaque sky cover, ceiling height, dry-bulb temperature, dew point, relative humidity, atmospheric pressure, horizontal visibility, wind speed, wind direction, present weather, AOD, total precipitable water, snow depth, and number of days since last snowfall	NREL: https://nsrdb.nrel.gov/data-sets/archives
National Solar Radiation Database (NSRDB) 1991–2005	1991–2005	1 hour	United States	10-km by 10-km grid (1998–2005)	Computed or modeled data: ETR on surfaces horizontal and normal to the sun, GHI, DNI, and DHI. Measured or observed data: total sky cover, opaque sky cover, dry-bulb temperature, dew point, relative humidity, station pressure, wind speed and direction, horizontal visibility, ceiling height, precipitable water, AOD, surface albedo, and precipitation	NSRDB: Data available from: https://www.ncei.noaa.gov/data/nsrdb-solar/ https://nsrdb.nrel.gov/data-sets/archives.
National Solar Radiation Database (NSRDB) 1991–2010	1991–2010	1 hour	United States	1,454 locations and 10-km by 10-km grid (1998–2009)	Computed or modeled data: ETR on surfaces horizontal and normal to the sun, GHI, DNI, and DHI. Measured or observed data: total sky cover, opaque sky cover, dry-bulb temperature, dew point, relative humidity, station pressure, wind speed and direction, horizontal visibility, ceiling height, precipitable water, AOD, surface albedo, and precipitation	*NSRDB User's Manual*: http://www.nrel.gov/docs/fy12osti/54824.pdf. Data available upon request from NREL.
National Solar Radiation Database (NSRDB)	1998–2022 (updated annually)	5 minutes from 2018 Half-hourly until 2017	Southern Canada, United States, and parts of South America (longitude: -25° E to -175° W, latitude: -21° S to 60° N). India 2000–2014	4 km; 2 km from 2018	GHI, DNI, DHI, clear-sky DHI, clear-sky DNI, clear-sky GHI, cloud type, dew point, surface air temperature, surface pressure, surface relative humidity, solar zenith angle, total precipitable water, wind direction, wind speed, and surface albedo	https://nsrdb.nrel.gov

Database	Period of Record	Temporal Resolution	Spatial Coverage	Spatial Resolution	Data Elements and Sources	Availability
European Organisation for the Exploitation of Meteorological Satellites (EUMETSAT) Ocean and Sea Ice Satellite Application Facility (OSI-SAF)	2011–present	1 hour	Africa, Americas, Europe, western Asia, and Atlantic high-latitude	0.05° x 0.05°	GHI and longwave infrared irradiance	https://osi-saf.eumetsat.int/products/radiative-fluxes-products
Pacific Northwest Solar Radiation Data Network	1975–present	1 minute to 1 hour, depending on station and date	Oregon, Idaho, Washington, Utah, Wyoming, and Montana	39 stations	Varies by site and date—GHI, DNI, DHI, GTI, spectral irradiance, surface meteorological data (temperature, relative humidity barometric pressure, precipitation, precipitable water vapor), and PV output	http://solardata.uoregon.edu
Photovoltaic Geographical Information System (PVGIS)	2005–2020	1 hour	Europe, Africa, and most parts of Asia and America	1-km aggregated to 3 arc-minutes (~5 km)	GHI, DNI, DHI, and GTI, based on the CM SAF, NREL, and ECMWF databases, optional terrain shadowing. Also TMY datasets	European Commission Joint Research Centre, Directorate for Energy, Transport and Climate; Energy Efficiency and Renewables Unit: https://ec.europa.eu/jrc/en/pvgis
Reuniwatt—SunSat	2004 (depending on region)–present	10/15 minutes, 1 hour	Worldwide between latitudes 60° N and 60° S	500 m–3 km, depending on location	GHI, DNI, DHI, BHI, GTI, and corresponding clear-sky irradiance, cloud index, meteorological conditions (temperature, relative humidity, wind speed, pressure, aerosol optical depth, precipitable water, total column water vapor, etc.)	https://reuniwatt.com
Southern African Universities Radiometric Network (SAURAN)	Varies	1 minute	Botswana, Namibia, and South Africa	23 radiometric stations	GHI, DNI, and DHI; meteorological data	https://sauran.ac.za/

Database	Period of Record	Temporal Resolution	Spatial Coverage	Spatial Resolution	Data Elements and Sources	Availability
Solar Energy and Meteorological Research Training Sites	1979–1983	1 minute	Fairbanks, Alaska; Atlanta, Georgia; Albany, New York; and San Antonio, Texas	Four radiometric stations	GHI, DNI, and DHI; GTI on various surfaces, infrared irradiances, UV and other spectral irradiance (varies), and surface meteorological conditions (temperature, relative humidity, pressure, visibility, wind speed, and direction at 10 m, precipitation, etc.)	NREL: https ://www.nrel.gov/grid/solar-resource/semrts.html
Solcast	2007–present	1, 5, 10, 15, or 30 minutes, and 1 hour	Global, except polar areas	1–2 km cloud index, scaled to 150 m using a digital elevation model	GHI, DNI, EBH, DIF/DHI, GTI, cloud opacity, solar zenith angle, solar azimuth angle, temperature, wind speed, wind direction, relative humidity, surface pressure, precipitable water, snow depth, dew point, albedo. Data available as time series, typical year with P50, P75, P90, P95, or Pxx exceedance probabilities, and monthly and annual averages	https://solcast.com/
Solargis	1994, 1999, 2007–present (depending on region)	15 and 30 minutes	Land area, worldwide, between latitudes 60° N and 50° S	~3 km (at the equator) downscaled to ~80 m using SRTM-3 a digital elevation model	DNI, GHI, DHI, GTI, and air temperature (2-m AGL) and others	http://solargis.info
Solar Energy Mining (SOLEMI)	1991–present	30 minutes	Europe, Africa, South America, Western Asia, and Western Australia	2.5 km	GHI, DNI	DLR: Data available upon request.
State Key Laboratory of Remote Sensing Science, Aerospace Information Research Institute, Chinese Academy of Sciences CARE	2016–2020	10 minutes	Asia-Pacific	0.05° x 0.05°	GHI, DIR PAR (global and direct components) UV-A (global and direct components) UV-B (global and direct components)	http://www.slrss.cn/care/sp/pc/

Database	Period of Record	Temporal Resolution	Spatial Coverage	Spatial Resolution	Data Elements and Sources	Availability
Typical Meteorological Year (TMY) 98–19	1998–2019	1 hour	Southern Canada, United States, and parts of South America (longitude: -25° E to -175° W, latitude: -20° S to 60° N)	4 km	GHI, DNI, DHI, cloud type, dew point, surface air temperature, surface pressure, wind direction, wind speed	https://nsrdb.nrel.gov
TMY2	One year representative of the 1961–1990 NSRDB data period	1 hour	United States and territories	239 stations representing the 1961–1990 NSRDB	Same as NSRDB 1961–1990	NREL: https://nsrdb.nrel.gov/data-sets/archives
TMY3	1991–2005	1 hour	United States and territories	1,020 locations	Computed or modeled data: ETR on surfaces horizontal and normal to the sun, GHI and illuminance, DNI and illuminance, DHI and illuminance, zenith luminance. Measured or observed data: total sky cover, opaque sky cover, dry-bulb temperature, dew point, relative humidity, station pressure, wind speed and direction, horizontal visibility, ceiling height, precipitable water, AOD, surface albedo, and precipitation	NREL: https://nsrdb.nrel.gov/data-sets/archives
Vaisala (formerly 3Tier) Solar Time Series	January 1997–present	Approx. 30-minute instantaneous and 1-hour averages	Global	2 arc-minutes (~3 km)	GHI, DNI, and DHI from model estimates based on satellite remote-sensing input data	https://www.vaisala.com/en/digital-and-data-services/renewable-energy
Western Energy Supply and Transmission (WEST) Associates Solar Monitoring Network	1976–1980	15 minutes	Arizona, California, Colorado, Nevada, New Mexico, and Wyoming	52 radiometric stations	GHI, DNI, and dry-bulb temperature measured with pyranometers (Eppley Black and White, Eppley Model PSP, and the Spectrolab Spectrosun SR75) and pyrheliometers (Eppley NIP) in automatic solar trackers	NREL: https://www.nrel.gov/grid/solar-resource/west-manual.html

Database	Period of Record	Temporal Resolution	Spatial Coverage	Spatial Resolution	Data Elements and Sources	Availability
World Meteorological Organization (WMO) World Radiation Data Center (WRDC)	1964–present	Daily totals with some 1-hour measurements at a few sites	Global	More than 1,000 radiometric stations	Primarily daily total GHI, radiation balance, and sunshine duration, but some DHI and DNI. Some hourly measurements are available from a few sites.	http://wrdc.mgo.rssi.ru

References

Arguez, A., and R. S. Vose. 2011. "The Definition of the Standard WMO Climate Normal: The Key to Deriving Alternative Climate Normals." *Bull. Am. Meteorol. Soc.* 92: 699–704. https://doi.org/10.1175/2010BAMS2955.1.

Driemel, A., J. Augustine, K. Behrens, S. Colle, C. Cox, E. Cuevas-Agulló, F. M. Denn, T. Duprat, M. Fukuda, H. Grobe, M. Haeffelin, G. Hodges, N. Hyett, O. Ijima, A. Kallis, W. Knap, V. Kustov, C. N. Long, D. Longenecker, A. Lupi, M. Maturilli, M. Mimouni, L. Ntsangwane, H. Ogihara, X. Olano, M. Olefs, M. Omori, L. Passamani, E. B. Pereira, H. Schmithüsen, S. Schumacher, R. Sieger, J. Tamlyn, R. Vogt, L. Villaume, X. Xia, A. Ohmura, and G. König-Langlo. 2018. "Baseline Surface Radiation Network (BSRN): Structure and Data Description (1992–2017)." *Earth Syst. Sci. Data* 10: 1491–1501. https://doi.org/10.5194/essd-10-1491-2018.

Ernst, M., and J. Gooday. 2019. "Methodology for Generating High Time Resolution Typical Meteorological Year Data for Accurate Photovoltaic Energy Yield Modelling." *Sol. Energy* 189: 299–306. https://doi.org/10.1016/j.solener.2019.07.069.

Fan, X. 2022. "A Method for the Generation of Typical Meteorological Year Data Using Ensemble Empirical Mode Decomposition for Different Climates of China and Performance Comparison Analysis." *Energy* 240, 122822. https://doi.org/10.1016/j.energy.2021.122822.

García, I., M. de Blas, and J. L. Torres. 2020. "Proposal and Evaluation of Typical Illuminance Year (TIY) Generation Procedures From Illuminance or Irradiance Data for Daylight Assessment in the Long Term." *Sol. Energy* 205: 496–511. https://doi.org/10.1016/j.solener.2020.05.083.

Ineichen, P., and R. Perez. 2002. "A New Airmass Independent Formulation for the Linke Turbidity Coefficient." *Sol. Energy* 73: 151–157. https://doi.org/10.1016/S0038-092X(02)00045-2.

Nielsen, K. P., F. Vignola, L. Ramírez, P. Blanc, R. Meyer, and M. Blanco. 2017. "Excerpts From the Report: 'BeyondTMY—Meteorological Data Sets for CSP/STE Performance Simulations.'" *AIP Conference Proceedings*. https://doi.org/10.1063/1.4984525.

Polo, J., L. Martín Pomares, C. A. Gueymard, J. Balenzategui, F. Fabero, and J. P. Silva Montero. 2019. "Fundamentals: Quantities, Definitions, and Units: Fundamentals and Applications." *Green Energy and Technology*: 1–14. https://doi.org/10.1007/978-3-319-97484-2_1.

Polo, J., M. Alonso-Abella, N. Martín-Chivelet, J. Alonso-Montesinos, G. López, A. Marzo, G. Nofuentes, and N. Vela-Barrionuevo. 2020. "Typical Meteorological Year Methodologies Applied to Solar Spectral Irradiance for PV Applications." *Energy* 190, 116453. https://doi.org/10.1016/j.energy.2019.116453.

Sengupta, M., A. M. Habte, and J. M. Freeman. 2019. "The Case for Custom TMY's: Examples Using the NSRDB." IEEE 46th Photovoltaic Specialists Conference (PVSC): 2287–2292. https://doi.org/10.1109/PVSC40753.2019.8980811.

Sengupta, M., and A. M. Habte. 2019. “The Impact of Plane-of-Array-Based TMYs on Solar Resource for PV Applications.” Presented at the 2019 European Photovoltaic Specialists Conference (EUPVSEC), Marseille, France, Sept. 9–13, 2019. https://www.nrel.gov/docs/fy20osti/74768.pdf.

Sengupta, M., Y. Xie, A. Lopez, A. Habte, G. Maclaurin, and J. Shelby. 2018. “The National Solar Radiation Data Base (NSRDB).” *Renew. Sustain. Energy Rev.* 89: 51–60. https://doi.org/10.1016/j.rser.2018.03.003.

9 Forecasting Solar Radiation and Photovoltaic Power

Elke Lorenz,[1] Bijan Nouri,[2] Sylvain Cros,[3] Kristian Pagh Nielsen,[4] Rafael Fritz,[5] Garrett Good,[5] Marco Pierro,[6] Guadalupe Sanchez Hernandez,[7] Philippe Lauret,[8] Mathieu David,[8] Rodrigo Amaro e Silva,[9,10] Carlos Fernandez Peruchena,[11] and Cristina Cornaro[12]

[1] *Fraunhofer Institute for Solar Energy Systems (Fraunhofer ISE), Germany*
[2] *German Aerospace Center (DLR), Institute of Solar Research, Germany*
[3] *Laboratoire de Météorologie Dynamique (LMD)/Institut Pierre-Simon Laplace (IPSL), École Polytechnique, Institut Polytechnique de Paris, Ecole normale supérieure (ENS), Université Paris Sciences & Lettres (PSL), Sorbonne Université, Centre national de la recherche Scientifique (CNRS), France*
[4] *Danish Meteorological Institute, Denmark*
[5] *Fraunhofer Institute for Energy Economics and Energy System Technology (Fraunhofer IEE), Germany*
[6] *Eurac Research, Bolzano, Italy*
[7] *Department of Physics, University of Jaen, Spain*
[8] *University of La Réunion, France*
[9] *Centre Observations, Impacts, Energie (O.I.E.), MINES Paris - PSL Research University, France*
[10] *Instituto Dom Luiz, Faculdade de Ciências, Universidade de Lisboa, Portugal*
[11] *National Renewable Energy Centre of Spain (CENER), Spain*
[12] *University of Rome Tor Vergata, Department of Enterprise Engineering, Italy*

Executive Summary

Solar power forecasting is essential for the reliable and cost-effective system integration of solar energy. It is necessary for a variety of applications that have specific requirements with respect to forecast horizon and spatiotemporal resolution, including the management of electric grids and energy management systems as well as the marketing of solar power.

Different input data and models are suitable for different forecast horizons, generally with a decreasing spatiotemporal resolution with increasing forecast horizon (see Fig. 9-1):

- Short-term irradiance forecasts up to 10–20 minutes ahead resolving irradiance ramps with a temporal resolution of minutes or even less are derived from all-sky imagers (ASIs).
- Irradiance forecasts up to several hours ahead with typical resolutions of 10–15 minutes are derived from satellite images covering large areas.
- Irradiance forecasts from several hours to days ahead essentially rely on numerical weather prediction (NWP) models, which have the capability to describe complex atmospheric dynamics, including advection as well as the formation and dissipation of clouds.

Complementing empirical and physical models, statistical and machine learning (ML) methods are widely used in solar irradiance and power forecasting. To train time-series models, the availability of irradiance and/or photovoltaic (PV) power measurements is crucial, as is proper quality control of the data. Assuming good data quality, these methods can be effectively applied to:

- Improve forecasts with empirical or physical models (postprocessing).

- Combine different input data and forecasts (model blending); here, very short-term forecasting, up to approximately 1 hour ahead, greatly benefits from the use of local online irradiance or PV power measurements as input.
- Derive PV power forecasts from meteorological forecasts.

Besides time-series forecasting, ML algorithms are increasingly used for image prediction using ASI or satellite data, e.g., to compute the optical flow in cloud motion approaches.

State-of-the-art PV power forecasting services do not rely on a single forecasting model but integrate different inputs and models. Prominent examples are intraday forecasting systems up to several hours ahead integrating online measurements, satellite-based forecasts, and NWP model forecasts or day-ahead forecasting systems combining different NWP models, both using statistical and/or ML algorithms for forecast optimization.

Besides forecasting for single PV power plants and portfolios of PV plants, the estimation and forecasting of regionally aggregated PV power is important for grid operators for marketing of PV power and grid management. Here, an additional challenge is that PV power is not measured at a sufficient resolution for most plants in many countries, and information on PV systems is incomplete. Still, because of spatial smoothing effects, forecast errors of regionally aggregated PV power as well as virtual power plants (VPPs) (normalized to their installed power) are much smaller than for single PV plants, depending on the size of the region and the set of PV plants contributing.

Forecast evaluations provide users with necessary information on forecast accuracy, assisting them in choosing between different forecasting services or assessing the risk when a forecast is used as a basis for decisions. Beyond general information on the overall accuracy of deterministic forecasts, probabilistic forecasts provide specific uncertainty information for each forecast value, depending on the weather conditions, and they allow for better risk management.

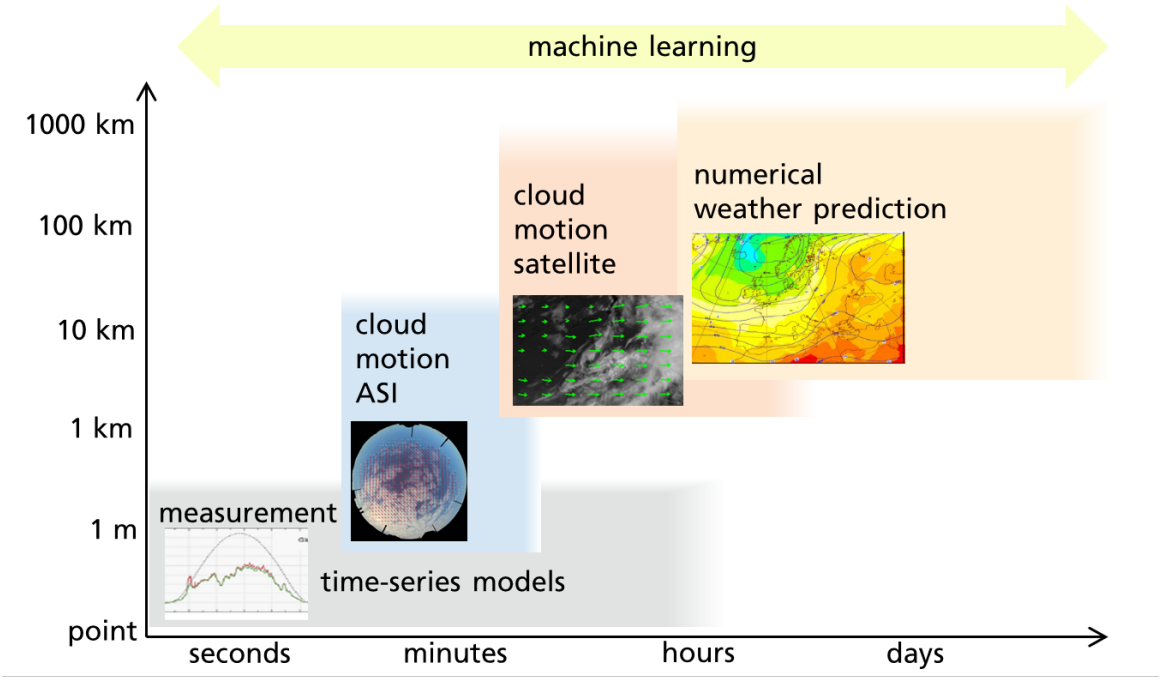

Figure 9-1. Different forecasting methods suitable for various spatial and temporal scales

Empirical and/or physical models are combined with statistical and/or ML models for forecast optimization. The spatial scales of the forecasting methods are defined by spatial resolution and spatial coverage. The temporal scales are defined by temporal resolution, update frequency, and forecast horizon.

Image by Fraunhofer ISE

9.1 Introduction

The variability of solar power generation poses a challenge for electric power systems to balance both generation and demand and to ensure the resilient operation of electric grids.

Besides the deterministic apparent course of the sun, this variability is largely determined by the inherent uncertainty of weather conditions. Therefore, forecasting plays a crucial role for power system operators in managing the electric grid, avoiding congestion, and following protocols (Bessa et al. 2014), and it is also essential for aggregators and energy traders (Pierro et al. 2017). It is one of the most cost-effective solutions to integrate variable renewable energy sources (Notton et al. 2018; Tuohy et al. 2015).

Solar forecasts are used in myriad contexts, with a variety of spatiotemporal scales, and their accuracy can have a great impact on power system performance. Various specific use cases and benefits of solar forecasting have been detailed in the literature, as described in this nonexhaustive list:

- Marketing of solar power by grid operators, plant operators, or direct marketers, reducing the need for balancing power or penalties, depending on national regulations. This is, e.g. described in Antonanzas et al. (2017) for day-ahead markets and in Kaur et al. (2016) for intraday markets. The impact of the update rate of solar forecasts (Cros, Sylvain et al. 2015) and of the presence of storage (David et al. 2021) have also been discussed.

Moreover, concentrating solar power (CSP) plants making use on direct normal irradiance (DNI) forecasts can benefit from bidding in the day-ahead (Kraas et al. 2013) and intraday (Law, Kay, and Taylor 2016) markets, potentially including the scheduling of coupled thermal storage.

- Scheduling storage systems to attenuate power fluctuations in large PV power plants (Marcos et al. 2013), particularly relevant in the presence of ramp-rate restrictions. Cirés et al. (2019) discuss how accurate forecasts reduce storage needs for this effect.
- Supporting generator scheduling of power systems, reducing the need for fossil fuels and costly fast-ramping generators (Brancucci Martinez-Anido et al. 2016), and mitigating operational imbalances (Pierro et al. 2020c). Some studies address the specificities of microgrids as well as insular and hybrid off-grid systems, e.g., (Ramahatana et al. 2022; Simoglou et al. 2014; Jamal et al. 2019).
- For CSP plants, Nouri et al. (2020) show how sky imager forecasts can increase plant efficiency and lifetime.

Solar power forecasting, including both PV and CSP, essentially relies on irradiance forecasting as a first step. Depending on the specific application and requirements regarding forecast horizon and spatiotemporal resolution, different input data and forecasting methods are customarily used. From short to long forecasting horizons (see Figure 9-1), the most important input data and solar forecasting methods are:

- **Time-series models based on local measurements:** They require on-site observations of irradiance and/or PV power, and possibly further meteorological variables that are processed using either statistical methods or artificial intelligence (AI) and ML algorithms, such as neural networks. They might provide meaningful forecasts even up to a few hours ahead under relatively stable sky conditions; however, these methods rarely perform well under variable-sky conditions, given the chaotic behavior of the cloud system and the limited information contained in point-wise observations.
- **Forecasts based on ASIs:** Using information on the local distribution of clouds, collected by one or more ground-based ASIs, the forecast skill can be enhanced relative to time-series models based on local measurements only. This information is key to the generation of solar irradiance forecasts with a temporal resolution on the order of seconds to minutes and a spatial resolution from 10–100 m covering a few square kilometers around the ASIs. The typical forecast horizon of these systems is 10–20 minutes, depending on cloud height and speed.
- **Forecasts based on data from geostationary satellites:** Forecasts up to several hours ahead benefit from wide-area observations of cloud fields. Because of their broad coverage, data from geostationary satellites are an appropriate source for these horizons. Satellite-based forecasts frequently use cloud motion vector (CMV) techniques to extrapolate cloud locations into the future. The typical spatial resolution is from 1–5 km^2 for the current generation of geostationary satellites, with forecast updates every 10–30 minutes, and the typical forecast horizon is 4–6 hours.
- **NWP:** NWP models constitute the main approach for forecast horizons more than several hours and up to several days or weeks ahead. These models predict the evolution of the atmospheric system, including the formation, advection, diffusion, and dissipation of clouds. They are based on a physical description of the dynamic processes occurring in the atmosphere by solving and parameterizing the governing system of equations, and

they depend on an observed set of initial conditions. Current global NWP models cover the Earth with a spatial resolution from approximately 0.1°–0.5° and a temporal resolution from 1–3 hours. Regional models, which are also referred to as limited area models or mesoscale models, typically have an hourly temporal resolution and a spatial resolution of a few kilometers in the covered area.

- **Postprocessing and model blending with statistical and ML models:** When historical or near-real-time on-site solar irradiance or PV yield observations are available, these described methods can be further improved by combining them with ML, resulting in hybrid methods. For NWP forecasts, model output statistic (MOS) techniques are often applied. Here too, satellite-derived irradiance might be used as a reference for model training. Further, state-of-the-art solar irradiance or PV power forecasting services do not rely on a single forecasting model but integrate different input and tools with statistical or ML algorithms, which is referred to as model blending.

Solar power forecasts can be derived based on irradiance forecasts using these different models. Converting irradiance to PV power forecasts requires PV system modeling using parametric PV simulation models and plant data, e.g., nominal power and orientation, and/or ML approaches, learning from PV power measurements.

Generally, solar irradiance and PV power forecasting approaches can be categorized into either physical and empirical models or statistical and ML approaches. Physical models (e.g., radiative transfer models, NWP models, PV module or inverter models) are based on solving basic physical equations. Empirical models are also based on physical considerations, but they do not describe all atmospheric processes in detail. Typical examples are cloud index models, parametric clear-sky models, and cloud motion approaches based on ASI or satellite data.

Statistical and ML algorithms establish the dependence of forecast values (predictands) on input variables (predictors) in a training phase by learning from historical data. Here, it is assumed that patterns in the historical datasets are repeated in the future and thus might be exploited for forecasting. These approaches include classical regression methods, such as autoregressive and autoregressive-integrated moving-average models as well as ML or AI techniques, such as artificial neural networks (ANNs), k-nearest neighbors, or support vector regression. They are widely applied for different purposes in irradiance and PV power forecasting. Coimbra and Pedro (2013) and Diagne et al. (2013) provided an overview of different statistical approaches used for solar irradiance forecasting. Voyant et al. (2017) and Sobri, Koohi-Kamali, and Rahim et al. (2018) reviewed the topic with a focus on the use of ML methods for solar radiation or power forecasting as well as for postprocessing.

For many years, statistical and ML methods were mostly used in time-series forecasting. This includes their application in pure time-series approaches aimed at forecasting solar irradiance or solar power, based solely on local measurements (i.e., time-series approaches with no exogenous input) for forecast horizons from several minutes to several hours ahead. They also play an important role in enhancing the output of physical and empirical forecast models, namely, NWP and CMV forecasts. The community of statistical modeling and AI refers to these models as statistical models with exogenous input. In contrast, meteorologists commonly use the terms statistical postprocessing or, more specifically, MOS in the context of NWP, which is the terminology adopted here.

The availability of ground truth is essential in training ML models. In irradiance and PV power forecasting, mostly irradiance and PV power measurements are used as ground truth data because they are expected to have a relatively small uncertainty compared to other options (see Chapter 10). Still, this uncertainty should not be neglected. The use of satellite-derived irradiance data is also an option, mostly used in postprocessing NWP forecasts.

With the rapid progress of research in AI (e.g., deep learning (DL) and computer vision) during the last few years, the potential offered by these methods in the field of irradiance and PV power forecasting is also growing. ML and AI algorithms are also increasingly used for image-based predictions using ASI or satellite data, e.g., to compute the optical flow for cloud motion approaches but also to directly predict future cloud conditions or irradiance from raw image data.

Besides categorizing solar forecasts by the different forecasting approaches, from a user's point of view, the following general use cases can be distinguished:

- **Forecasts for individual solar systems** are necessary for owners and operators of PV and CSP plants. In particular, day-ahead forecasts of the solar power generated by large PV plants are now mandatory in many countries (Italy, Germany, Spain, Romania, United States, Japan, China, etc.). Further, they can contribute to improved performance supervision and fault detection and to predictive maintenance and operations and maintenance planning as well as the reduction of power ramps. They are also needed by owners, operators, and providers of PV battery systems and energy management systems as an essential input for the predictive scheduling of storage and energy management.
- **Portfolio forecasts,** consisting of an ensemble of PV systems—and potentially also other generators—are frequently used in direct marketing because of their smaller relative forecast errors compared to single-site forecasts, which is due to spatial smoothing. Such portfolios are also referred to as VPPs. It is expected that they will become increasingly important also for the energy management of multilocation companies aiming toward 100% renewable energy supply or for the management of quarters and districts with a high share of solar power.
- **Forecasts of aggregated regional PV power** are needed by grid operators for the grid management and marketing of PV power, depending on national regulations and feed-in tariffs. This comes with the additional challenge that PV power is not measured at a sufficient resolution for most plants in many countries, and information on PV systems is incomplete. Still, as for portfolios, relative forecast errors of regionally aggregated PV power are much smaller than for single PV plants, depending on the size of the region and the set of PV plants contributing.

This chapter provides an overview of the basic concepts of solar irradiance and PV power forecasting by referring to examples and operational models. More complete reviews of the state of the art can be found elsewhere, including in Kleissl (2013), Yang et al. (2018), Visser et al. (2022), and, for PV applications, Antonanzas et al. (2016). The examples presented here have been investigated in the context of the International Energy Agency (IEA) Solar Heating and Cooling Programme (SHC) Task 36 and Task 46 and the Photovoltaic Power Systems Programme (PVPS) Task 16.We illustrate the forecast performance of the different models described in this chapter by showing basic forecasts scores (e.g., root mean square error (RMSE)). A more detailed discussion on forecast evaluation and uncertainty assessment is given

in Chapter 10 (Section 10.2.3). Evaluation results depend on multiple factors, including the climatological and meteorological conditions at the evaluation site and period (season and year), the forecast horizon, the temporal and spatial resolutions of the forecasts, and the forecasting model used. Therefore, both the forecast scores and the differences between the forecasting models might considerably differ depending on these factors. Here, we provide evaluation results for several examples and model benchmarks to illustrate some general findings.

The model descriptions and evaluations of the different irradiance forecasting approaches given here focus on global horizontal irradiance (GHI) and PV applications. Nevertheless, the forecasting methods also apply to DNI to a large extent. A focus on DNI forecasting can be found in Law et al. (2014) and Schroedter-Homscheidt and Wilbert (2017). Other environmental factors—including ambient temperature, air humidity, wind speed, and wind direction—have a nonnegligible impact on the final power yield of solar plants; however, this handbook focuses on the solar resource aspect, and thus the forecasting of these ancillary variables is not discussed further.

Beyond the description of different forecasting models and their performances for different spatiotemporal scales in this chapter, the "IEA Wind Recommended Practices for the Implementation of Renewable Energy Forecasting Solutions" (Möhrlen et al. 2023) focuses on decision support tools for the energy industry. These tools aim to maximize the benefit of renewable energy forecasts, including PV, in operational decision-making. Therefore, detailed guidelines and recommended practices in selecting and evaluating an appropriate forecasting solution for a given application are given.

The following sections first describe the different approaches for irradiance forecasting: time-series forecasting based on local measurements (Section 9.2), irradiance forecasting based on cloud images (ASI or satellites, Section 9.3), NWP (Section 9.4), and postprocessing and model blending with statistical and ML methods (Section 9.5). Then, Section 9.6 addresses PV power prediction for single sites, portfolios, and regionally aggregated power. Next, Section 9.7 introduces probabilistic forecasting. Finally, Section 9.8 provides a summary and recommendations for irradiance forecasting.

9.2 Time-Series Forecasting Based on Measurements

The goal of pure time-series approaches is to derive solar irradiance or power forecasts based solely on local measurements, i.e., without involving any physical modeling. They require real-time access to measurements and are suitable for forecast horizons from several minutes to several hours ahead. Section 9.2.1 introduces persistence as a baseline approach, which constitutes the simplest possible model, using only local irradiance or PV power measurements. Section 9.2.2 provides a short introduction to selected ML models, which are frequently used for applications in time-series forecasting of solar irradiance. Finally, Section 9.2.3 addresses forecasting methods based on pure time-series models and includes a discussion of their advantages and limitations.

9.2.1 Persistence

Persistence is a trivial model that simply assumes that the current situation does not change during a forecast run. Typically, persistence is based on recent on-site measurements. In solar radiation forecasting, persistence is the simplest and most widely used reference model. It is

commonly used to evaluate forecast skill (see Chapter 10, Section 10.5.1.2). It is also used in operational forecasting, e.g., as an input to hybrid forecasting approaches, requiring online measurements as a basis. Alternatively, satellite- or ASI-derived irradiance values can be used as a starting point for persistence, although in that case the forecast uncertainty for very short-term forecast horizons is higher than that for measurement-based persistence.

Several definitions of the persistence of solar irradiance exist, including *simple* persistence; *scaled* persistence, which accounts for solar geometry changes; and more advanced concepts, such as *smart* persistence. The most widely used definitions are presented next.

For day-ahead forecasting, the simplest approach is to assume that irradiance, I (GHI or DNI), persists during a period of 24 hours:

$$I_{\mathrm{per,24h}}(t) = I_{\mathrm{meas}}(t - 24\mathrm{h}). \tag{9-1}$$

A more elaborate option for GHI is to separate the clear-sky and cloudy contributions to solar radiation and to assume that only the cloud conditions persist during a forecast run; this defines the scaled persistence. Clear-sky irradiance is strongly influenced by the deterministic solar geometry and can be described with reasonable accuracy using a clear-sky radiation model (see Chapter 7, Section 7.2.1). In such a modeling approach, the persisting magnitude is the clear-sky index, K_c, calculated as the ratio between the measured GHI and a clear-sky GHI estimate, $\mathrm{GHI_{clear}}$. For forecast horizons of several hours (Δt) ahead, the scaled persistence, $\mathrm{GHI_{per,}}\ K_c$, for time t is then defined as:

$$\mathrm{GHI}_{\mathrm{per\ Kc,\Delta t}}(t) = \mathrm{GHI}_{\mathrm{clear}}(t)\ K_c(t - \Delta t). \tag{9-2}$$

For DNI, a similar approach can be used, now based on the beam clear-sky index or the Linke turbidity factor (Kuhn et al. 2017).

To make the most of persistence in a solar context, the so-called "smart persistence," $\mathrm{GHI_{per\ smart}}$, was proposed in the context of the IEA SHC Task 46. It consists of increasing the integration time that defines the current conditions commensurately to the forecast time horizon. Δt:

$$GHI_{per\ smart,\Delta t}(\mathrm{t}) = GHI_{clear}(\mathrm{t})\frac{1}{\Delta t}\int_{t-2*\Delta t}^{t-\Delta t} K_c(t')dt' \tag{9-3}$$

Or, for measurements available in a discrete time interval, Δt_{meas} :

$$GHI_{per\ smart,\Delta t}(\mathrm{t}) = GHI_{clear}(\mathrm{t})\frac{1}{N}\sum_{i=1}^{N} K_c\left(t - \Delta t\left(1 + \frac{i}{N}\right)\right), \tag{9-4}$$

with $N = \frac{\Delta t}{\Delta t_{meas}}$.

Alternatively, if long-term irradiance measurements are available, combinations of climatology and persistence can be used, as recommended by Yang et al. (2020), as an advanced reference model for forecast evaluation.

Despite its simplicity, persistence can outperform forecasts based on empirical and physical model forecasts for very short-term forecast horizons (see Section 9.3.1.3, Section 9.3.2.2, and Section 9.5.4). A further improvement for these forecast horizons can be achieved by applying statistical and ML models using online measurements as input, as described in the following sections.

9.2.2 Examples of Machine Learning Models Applied for Solar Forecasting

The use of state-of-the-art ML models is popular in both irradiance and PV power forecasting. This section describes several ML approaches that are used frequently, as discussed by Winter et al. (2019), including ANNs, extreme learning machines, gradient-boosted regression trees, and random forests. Further, auto-machine learning (AutoML) has become a hot topic in this field because of its high accuracy, deployment simplicity, and time efficiency. The ML approaches introduced here are used not only for pure time-series forecasting but also for postprocessing and model blending (Section 9.5) and partly also in image prediction (Section 9.3).

9.2.2.1 Artificial Neural Networks

ANNs constitute one of the most versatile ML methods and are known for their use in complex tasks, such as image or speech recognition (LeCun et al. 1989; Sak, Senior, and Beaufays 2014).

As described in Bishop (1995), an ANN consists of a fixed number of nodes, called units, that can take on numerical values and are arranged in several layers. The input layer contains one unit for each feature of the dataset, whereas the output layer, in the case of a single regression problem, is only one unit. The layers between the input and output layers are referred to as hidden layers. The key task is to establish a connection between the nodes by assigning to each unit in one layer the weighted sum of the previous layer's units, and to then apply a nonlinear activation function. In the case of a regression problem, a linear activation function is applied to the weighted sum of the output unit.

By training an ANN on a given set of input and output data, all its weights are adjusted to minimize an error function, typically the mean square error (MSE). This is usually done by back-propagation—an iterative process for calculating the gradient of the error function with respect to each weight (Rumelhart and McClelland 1986). At each step, the weights get updated by using a gradient descent optimization algorithm. An alternative option is the method of adaptive moment estimation, or "Adam," as described by Kingma and Ba (2014). Instead of calculating the gradient of the error function with respect to the full dataset, the weights can be updated at each step only with respect to a subset of the dataset (see Bottou (1998) and Ruder (2017)). The weights can be initialized using a common heuristic, as described by Glorot and Bengio (2010).

To make an ANN able to learn nonlinear relationships between input and output, a nonlinear activation function must be chosen. For example, the leaky rectified linear unit activation function can be used (Maas 2013).

9.2.2.2 Extreme Learning Machines

An extreme learning machine, as proposed by Huang, Zhu, and Siew (2006), is an ANN with a single hidden layer between the input and output layers. Its learning method does not rely on gradient descent. Instead, the weights between the input and hidden layers are chosen randomly. In this way, only the weights between the hidden and output layers need to be determined.

Because this is only a linear regression problem, an analytic solution exists, which can be calculated directly without an iterative optimization algorithm. Hence, training the model is considerably faster while maintaining its good performance.

9.2.2.3 Gradient-Boosted Regression Trees

Gradient-boosted regression trees are an ensemble technique using multiple classification and regression trees (CART), as introduced by Breiman et al. (2017). The CART algorithm creates binary decision trees, which means that at each new node, the data are split into two parts according to a threshold value. Starting with a root node, which, in general, contains all training data, the tree grows until some stop condition is reached. The last nodes form the tree's leaves. Each splitting leads to either another node or a leaf. The leaf contains the class to be predicted. In the case of regression, a leaf returns the mean value of the training samples it contains.

The principle of boosting is described by Friedman (2001). Starting with a single CART tree that is fit to minimize the MSE on the training data, the following trees are trained consecutively so that each new tree predicts the residual error. This residual error is proportional to the gradient of the MSE. By scaling the new tree's prediction with a step size between 0 and 1 and by adding it to the current ensemble, every new tree aims to further reduce the MSE of the ensemble's prediction.

9.2.2.4 Random Forest

A random forest is another technique based on ensembles of CARTs, as presented by Breiman (2001). The ensemble's prediction is the average over all single-tree predictions. Each tree is trained on a bootstrap dataset generated by randomly drawn samples with replacement from the original dataset (Efron 1979). Further, for each node split, only a random subset of features is considered. By randomly omitting data, the resulting trees become less correlated. This reduced correlation of single trees has been observed to reduce the model error.

9.2.2.5 Auto-Machine Learning

AutoML techniques have achieved considerable success in solving and improving any kind of problems in an ever-increasing number of disciplines, further reducing the manual workload. They are based on sequential stages of data processing, from preprocessing the data to hyperparameter tuning and model ensembles, where the use of several base ML models (ANN, random forest, or gradient boosting machines, among others) provide ensemble predictions. A successful ensemble has proven to be the multilayer stack, where the first layer has multiple base models, and whose outputs are concatenated and then fed into the next layer, which itself consists of multiple stacker models. These stackers then act as base models to an additional layer. Note that to take advantage of all available data and also to mitigate overfitting, k-fold ensemble bagging of all models at all layers of the stack is typically used.

9.2.3 Time-Series Forecasting With Statistical and Machine Learning Approaches

Intrahour or hours-ahead solar irradiance and PV power forecasting with pure time-series models use recent measurements of irradiance or PV power as a basic input, possibly complemented by measurements of other variables. Examples are the application of a coupled autoregressive and dynamic system model for forecasting solar radiation on an hourly timescale, as described by Huang et al. (2013), the comparison of ANN and classical time-series models by Reikard (2009),

and the short-term PV power prediction approach of Bacher, Madsen, and Nielsen (2009). Through their review of ML methods, Voyant et al. (2017) concluded that although ANN and autoregression-style methods still dominate statistical forecasting, other methods (e.g., support vector regression, regression tree, random forest, or gradient boosting) are increasingly being used. Although the ranking of such methods is complicated by many factors, it generally holds that a multi-model approach results in an improvement in forecasting performance (Zemouri, Bouzgou, and Gueymard 2019).

For any statistical or ML model, the selection and availability of appropriate input variables, as well as the optimized preprocessing of the data, are of critical importance for good forecast performance. Additionally, the choice of the model and of its configuration (e.g., the ANN architecture or the selection of hyperparameters in ML models) is essential. Finally, the setup of the training sample (e.g., the number of days and sites used for the training) has a noteworthy influence on forecast accuracy. In recent years, automated AutoML tools have been increasingly used for that (see Section 9.2.2.5). They are applied to optimize the ML pipeline, including the identification of the most suitable model and hyperparameters, which can be done using genetic programming.

The advantages and limits of purely statistical approaches are discussed next. High-quality measurements of the actual surface solar irradiance or PV power constitute the best possible starting point for any forecast. In comparison, the assessment of the initial irradiance conditions (i.e., the irradiance analysis) with an empirical or physical forecasting model shows considerably higher uncertainties. Any physics-based forecasting model has an inherent uncertainty, regardless of the forecast horizon, that is caused by limits in the spatial and temporal resolutions, uncertainty in input parameters, and simplifying assumptions within the model. Time-series models exploit the autocorrelation in the time series of solar irradiance, cloud cover and, possibly, other explanatory variables. For very short-term forecast horizons, forecasts based on accurate on-site measurements and statistical methods are affected by forecast errors that are typically smaller than the errors from either NWP analysis or irradiance forecasts derived from satellite or ASI images that correspond to the starting points of the respective forecast runs.

Given the inherent chaotic nature of weather phenomena, any existing autocorrelation decreases as the time lag between time-series instances increases. Hence, the performance of these models is (1) strongly determined by the underlying autocorrelation of each particular weather condition and (2) decreases as the forecast lead time increases. For longer forecast horizons, wide-area observations of clouds or irradiance (e.g., those from satellites images) or NWP model forecasts are necessary to meet forecast skill requirements.

Therefore, pure time-series approaches are typically applied to forecast horizons ranging from several minutes to a few hours ahead. Evidently, their performance compared to other methods strongly depends on the prevailing climate and weather conditions (e.g., the stability of the sky situation), the spatiotemporal resolution of the forecasts, and the models to which they are compared.

Finally, the uncertainty of the irradiance measurements used for both input and as ground truth for model training has a strong impact on the performance of time-series models. This uncertainty strongly depends on the instrument class as well as maintenance of the stations (see

Chapter 3, Chapter 4, and Chapter 10). Any statistical or ML forecasting model will adapt to the irradiance—or PV power—measurements it is trained to. This includes any possible systematic deviations in the measurements, e.g., calibration errors or soiling in case the station under scrutiny is not properly maintained. Therefore, high-quality measurements are crucial for statistical and ML models.

9.2.4 Forecasting With Machine Learning Methods and Data From Sensor Networks

As discussed, irradiance or PV power measurements from a single site can be used as the basis for time-series forecasts, but there are also forecasting methods that seek to explore spatiotemporal correlations from *in situ* solar measurements distributed in space. A review of such methods appears in Benavides Cesar et al. (2022). Bosch and Kleissl (2013) first showed that a pyranometer network was effective in detecting cloud advection. In a follow-up study, Lonij et al. (2013) did one of the earliest forecasting demonstrations, using a network of 80 distributed PV systems (considered as sensors) over an area of 2,500 km^2.Other studies sought to understand some of the nuances involved. In particular, Amaro e Silva and Brito (2017) showed that such an approach surpasses smart persistence from the seconds- to days-ahead timescale as long as the increase in forecasting horizon is met by a larger spatial coverage of the data and a coarser time resolution. Later, Amaro E Silva and Brito (2019) also found that the tilt and orientation of the sensor ensemble impact the added value of such an approach.

The main advantage of this kind of approach is its flexibility regarding the time and spatial scales. Two other benefits are also worth mentioning: The need for imagery and image processing (from satellite or ASI) is eliminated, and useful new data can be generated for use in regional studies regarding variability and upscaling approaches. Conversely, a disadvantage of this approach in solar resource applications is its dependence on potentially expensive and maintenance-intensive sensors. There are also approaches that explore PV generation data from a fleet of PV systems, but the challenge here is that such data sources mostly belong to private companies and are thus not publicly available.

9.3 Irradiance Forecasting Based on Cloud Images

Forecasting the evolution of clouds is essential in irradiance forecasting. Therefore, cloud images providing spatially extended information on clouds are suitable sources to extend forecast horizons compared to pure time-series models based on local measurements only. Two types of cloud images are used in irradiance forecasting: (1) cloud information for small areas with very high spatiotemporal resolution, obtained from ground-based ASIs, and used for very short-term forecast horizons of typically 10–20 minutes ahead; and (2) cloud information derived from geostationary satellite data, covering large areas at high temporal resolution, and suitable to forecast clouds and solar irradiance up to several hours ahead. Though covering different forecast horizons and areas, the basic steps in irradiance forecasting based on ASI and satellite imagery are similar.

At timescales from a few minutes to a few hours, horizontal advection has a strong impact on the temporal evolution of cloud patterns, with the shape of clouds often remaining quite stable. Here, the spatial scale is also extremely important because small-scale cloud structures change faster than larger structures. In these situations, techniques for detecting clouds and their motion

trajectories, referred to as CMV techniques, are used to provide valuable information for irradiance forecasting. Obviously, the performance of these forecasting methods degrades as the importance of local processes of cloud formation and dissipation, such as strong thermally driven convection, increases.

CMV-based techniques consist of the following basic steps:

- Images with cloud information are derived from ASI or satellite data.
- Assuming stable cloud structures and optical properties, the CMVs are determined by identifying matching cloud structures in consecutive cloud images.
- To predict future cloud conditions, the CMVs are applied to the latest available cloud image assuming cloud speed persistence.
- Solar irradiance forecasts are calculated from the predicted cloud structures.

For these steps, physical, empirical, or ML models can be employed, as described in more detail next, for irradiance forecasting based on either ASI (Section 9.3.1) or satellite imagery (Section 9.3.2). In addition to the CMV-based techniques, approaches to directly predict irradiance from cloud images with ML models have been developed during the last few years.

9.3.1 Forecasting Using Ground-Based All-Sky Imagers

Solar irradiance forecasts at subhourly scales with high spatiotemporal resolution can be derived from ground-based ASIs. Such imagers are installed horizontally and sense the whole sky above them (Figure 9-4, upper row). These highly resolved sky images contain information on the cloud cover that can be exploited for forecasting. At times, ASIs are also called whole-sky imagers, sky imagers, or sky cameras. (Note that a sky *imager* is not strictly identical to a sky *camera*; in all publications from IEA PVPS Task 16 participants and within this handbook, the term ASI is normally used.)

ASIs can capture sudden changes in irradiance, which are often referred to as *ramps*, at temporal scales from seconds to minutes (Figure 9-2). Cloud fields sensed from ASIs, or from an assembly of several ASIs, can be resolved with high detail, allowing the partial cloud cover over large PV installations to be modeled and forecasted. The maximum predictable horizon strongly depends on cloud conditions, and it is constrained by the cloud speed and the field of view of the ASIs. This forecast horizon typically ranges from 10–20 minutes, but it can reach more than 30 minutes in favorable cases. Considering the high resolution combined with a very fast update rate, ASI forecasts can play a valuable role in the economic operation of PV plants. Another advantage is that they can significantly reduce the overall societal costs caused by active intermittence mitigation (Wan et al. 2015).

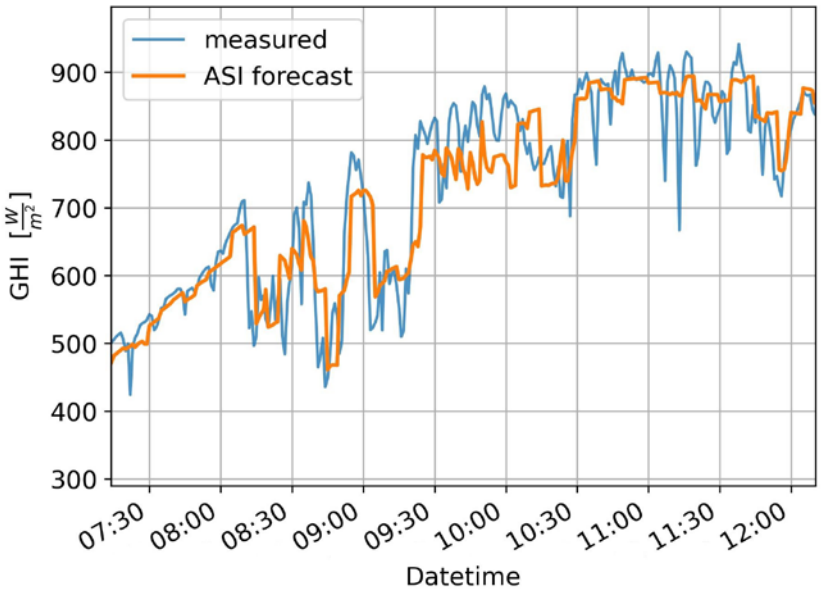

Figure 9-2. Example of minute-resolution GHI forecasts using an ASI

The forecasts with lead times up to 5 minutes ahead are updated every 5 minutes. May 9, 2021. Location: Freiburg in Germany.

Image by Fraunhofer ISE

9.3.1.1 All-Sky Imager Hardware

Currently, there is no defined standard for sky imaging hardware, camera calibration, or image processing techniques. Systems in use include commercially available, low-cost webcams or surveillance cameras, and systems developed specifically for sky imaging ,e.g., (Urquhart et al. 2015). Most systems use digital red-green-blue (RGB) cameras with fish-eye lenses and therefore sense visible radiation only, although some systems work with infrared cameras, which are more expensive. In particular, older RGB systems and some infrared cameras use a downward-looking camera that takes photos of an image of the sky that appears on a roughly spherical upward-looking mirror. This is where the term *imager* comes from. This concept—unlike the smaller lens or dome of fish-eye cameras—has the disadvantage that the *whole* mirror must be cleaned. Moreover, some older systems use sun-tracked "shadowbands" to prevent direct sunlight from reaching the camera. This can reduce lens flare-induced saturated areas in the photos, but the shadowband also covers a noticeable part of the image. Because the required tracking of the shadowband entails higher costs and can lead to system failures, shaded devices have become uncommon in recent years. In addition to the sky imager(s), an ASI forecasting system typically includes a radiometer at the sky imager location. The irradiance measurements are used as additional input to infer irradiance from ASI images and/or as ground truth for model training.

9.3.1.2 All-Sky Imager-Based Forecasting

The classical operation of ASI-based forecasts typically involves a physics-oriented chain of processing steps, e.g., (Marquez and Coimbra 2013). These physics-based or empirical solar forecasting approaches are also referred to as *indirect forecasting* (Lin, Zhang, and Wang 2023).

Nevertheless, because of the great success of ML in computer vision, recent developments show a clear trend to so-called *direct forecasting* approaches (Lin, Zhang, and Wang 2023). These direct approaches use trained models that derive the forecasts directly from the sky images , e.g.,(Chu et al. 2015). The advantages of ML in computer vision have also led to the application of ML methods as a way to improve the individual processing steps of indirect methods (e.g., cloud detection (Hasenbalg et al. 2020)). Figure 9-3 illustrates the general scheme of ASI-based forecast methods. The corresponding processing steps, along with some relevant image preprocessing procedures, are outlined in the following.

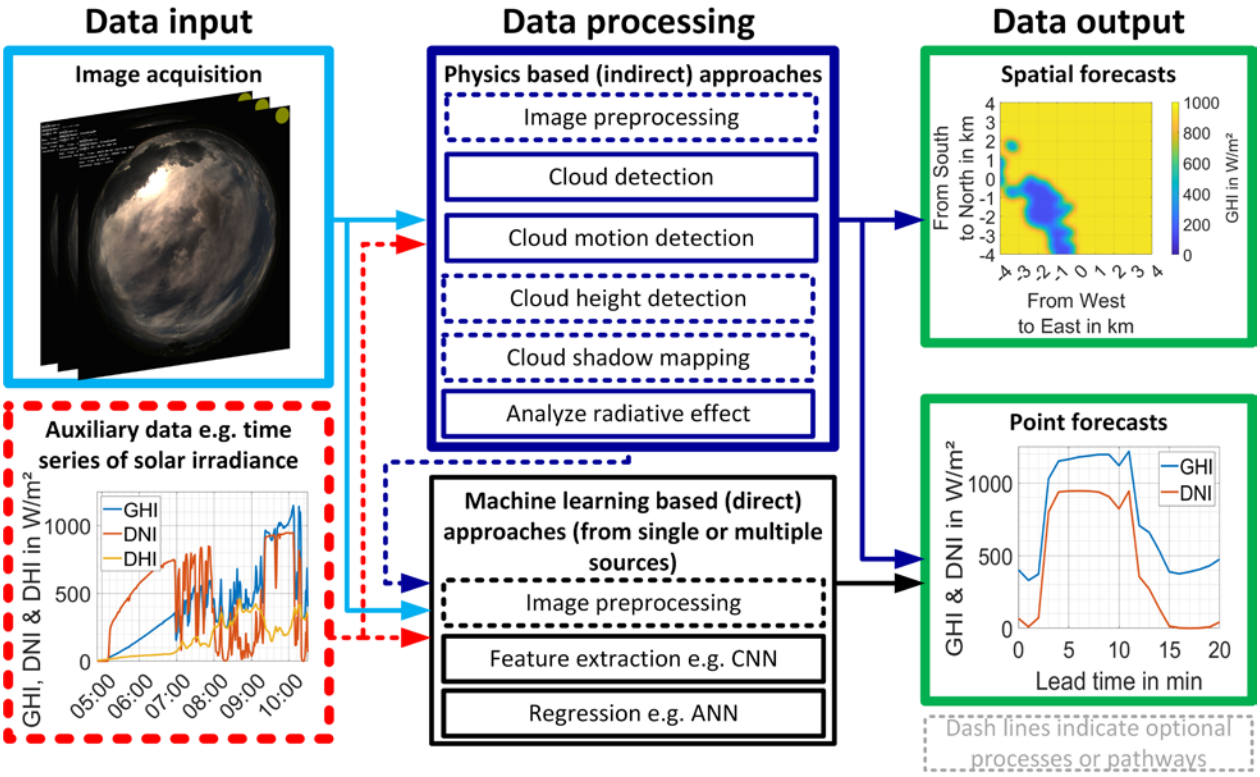

Figure 9-3. General scheme of ASI-based forecasting methods

Image by DLR Institute of Solar Research

Image preprocessing: Both direct and indirect approaches may apply different image preprocessing steps. Following are some frequently used preprocessing steps:

- Fish-eye distortion: Using fish-eye lenses leads to strong radial distortion effects that increase with greater distance from the zenith. Different processing steps might require/benefit from orthogonal projections (e.g., cloud motion detection (Marquez and Coimbra 2013) or cloud height detection (Nouri et al. 2019)). A commonly used approach for fish-eye distortion correction is described in Scaramuzza, Martinelli, and Siegwart (2006).
- Partial masking: Masking disturbing objects like shadowbands (Chow et al. 2011)
- Cropping and downscaling: An ML model's performance might increase if the training datasets are based on higher-resolution imagery; however, this also comes with increased

computational costs (Sun, Szűcs, and Brandt 2018). Cropping and downscaling sky images is therefore common practice.

- High-dynamic-range techniques: The illumination range of sky images can be very large because of the scattering effects of solar radiation (especially under complex cloudiness patterns or in the circumsolar region. High-dynamic-range techniques tackle this challenge by combining multiple images with different exposure times into a single image with dynamic illumination range (Chauvin et al. 2017).

Indirect (empirical) approaches are typically divided into the following main processing steps: (1) cloud detection, (2) cloud motion detection, (3) analysis of the radiative effect, (4) cloud height detection, and (5) cloud shadow mapping. For point forecasts at the sky imager location, information about cloud height is not required because the cloud movement can be parameterized in terms of "pixels per second"; they can be derived using steps (1), (2), and (3) only. The additional processing steps (4) and (5) are required when spatial forecasts are desired (Urquhart et al. 2012).

Cloud detection/segmentation: Three main cloud segmentation techniques are described in the literature and are summarized as follows:

1. Thresholding-based approaches exploit the different spectrally resolved scattering properties of clouds and cloudless sky by analyzing the red-to-blue ratio. Long et al. (2006) proposed a simple empirically defined fixed red-to-blue threshold. A more sophisticated adaptive thresholding, based on a database of image properties during clear-sky conditions (referred to as a "clear-sky library"), was introduced by Chow et al. (2011). An automated way to construct such a database was devised by Shaffery et al. (2020).
2. Superpixel cloud segmentation approaches evaluate multiple pixel features (brightness, color, and texture) and then group pixels into coarse regions (Shi et al. 2017). These compact and perceptually coherent regions are commonly referred to as superpixels.
3. Various ML approaches can be applied to the cloud segmentation tasks. Lately, DL-based approaches using convolutional neural networks (CNNs) have seemed to prevail (Xie et al. 2020). Various benchmarks have shown a clear advantage of DL approaches compared to classical thresholding-based approaches, e.g., ((Hasenbalg et al. 2020; Xie et al. 2020). Some samples of such a comparison are illustrated in Figure 9-4. Critiques mention the requirement of large manually segmented ground truth databases for supervised learning (Lin, Zhang, and Wang 2023); however, this demand can be significantly reduced through the use of transfer learning and pretrained weights for initialization (Fabel et al. 2022). That process involves initially employing a self-supervised approach to establish weights using an extensive unlabeled dataset, followed by a subsequent supervised approach that relies on a small labeled dataset. Ye et al. (2019) combined superpixels with a DL approach (support vector machines) for a semantic segmentation based on nine distinct cloud categories.

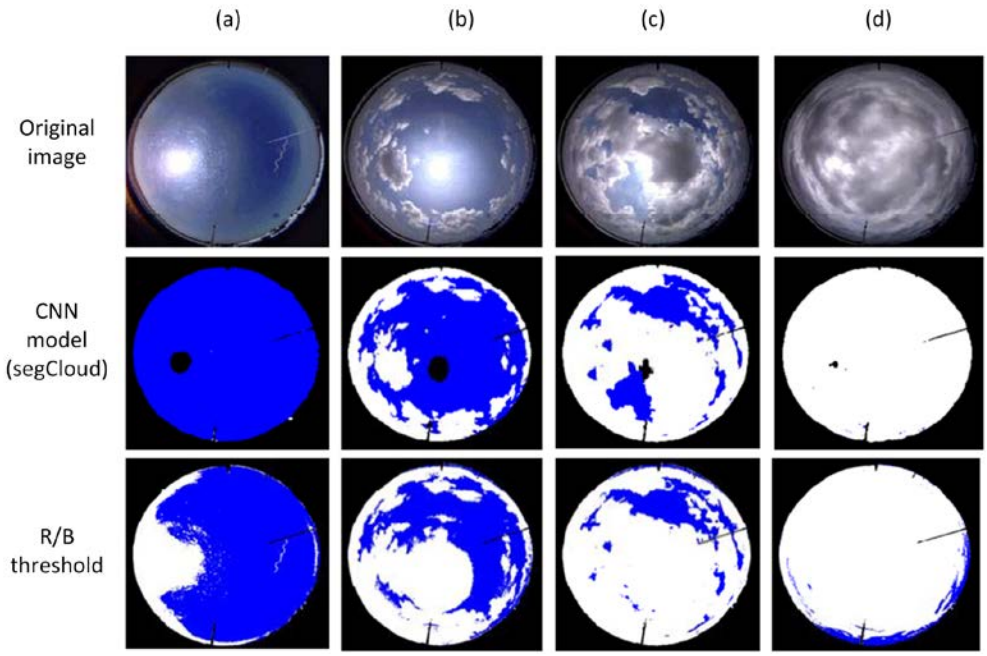

Figure 9-4. Examples of four segmentation results (columns a to d)

Clouds, sky, and the sun are colored white, blue, and black, respectively. The second row illustrates results from a CNN model, and the third row depicts results based on a red-to-blue ratio threshold.

Image by Xie et al. (2020)

Cloud motion detection: Global or multiple CMVs, up to a dense vector field having a single CMV for each pixel, can be derived from sky images. Generally, this is done via similarity maximization, optical flow, or feature tracking. similarity maximization often involves block-matching approaches (see Figure 9-5). Different subparts of consecutive image series are compared for their similarity via cross-correlation (Chauvin et al. 2016). The optical flow approaches assume that cloud motion only leads to a pixel shift at constant pixel brightness (Paragios, Chen, and Faugeras 2006), providing a way to derive dense vector fields. Overall, optical flow typically outperforms similarity maximization approaches; however, this advantage comes at the expense of increased computational costs (Peng et al. 2016). Finally, feature tracking approaches try to find and track unique feature points, such as cloud edges or corners. This method offers notable computational efficiency by prioritizing a few prominent features but is limited by the granularity of the CMVs (Su et al. 2015).

Cloud height detection: Stereoscopic cloud height measurement approaches based on multiple ASIs are described in, e.g., Nguyen and Kleissl (2014). Some of these methods are effective at deriving different cloud heights for the individual clouds seen in the sky image (Peng et al. 2015). That process is exemplified in Figure 9-5. Alternative approaches include the integration of supplementary instruments. In particular, the most accurate determination of the cloud-base height directly above the ASI instrument is currently obtained with ceilometers (Arbizu-Barrena et al. 2015); however, ceilometers are costly and limited to cloud measurements directly above the sensor, and therefore they are not ideally suited for multilayer cloud conditions. Combinations of ASIs with radiometers have also been described, but these approaches do not achieve the performance of a stereoscopic assembly with multiple ASIs (Kuhn et al. 2018).

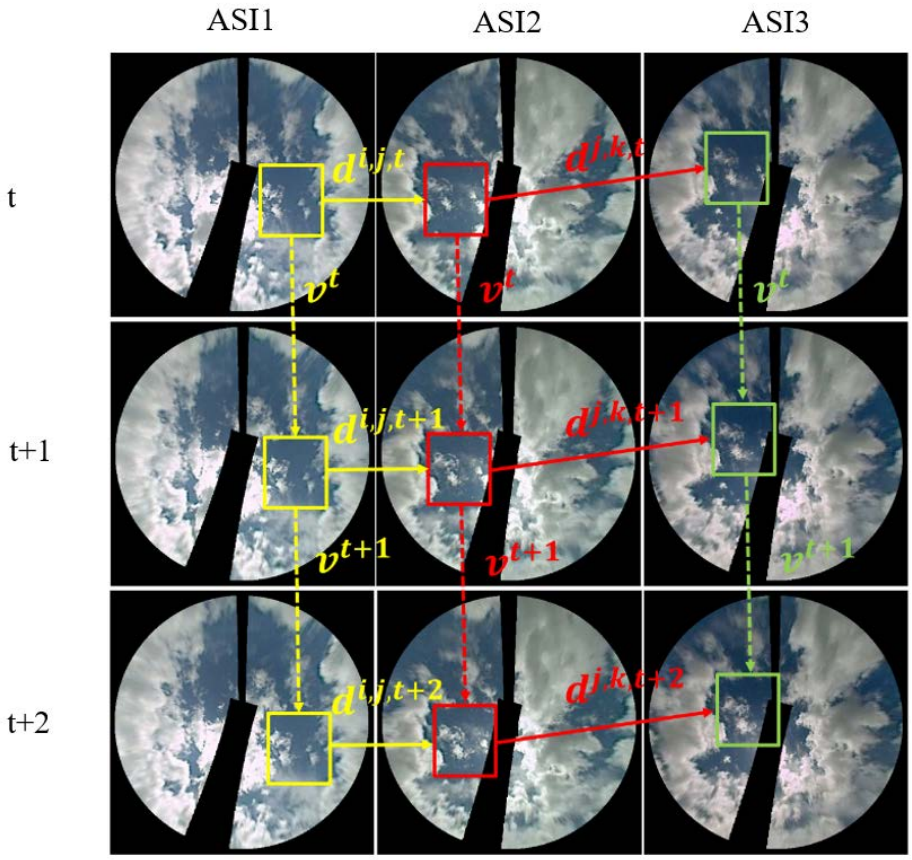

Figure 9-5. Matching cloud blocks for cloud motion and height detection from three consecutive images and three distinct ASIs

In the ASI1, ASI2, and ASI3 images, the cloud block of interest is denoted by the yellow, red, and green boxes, respectively. The detected movement of the cloud block between two consecutive frames is visually represented by a dotted arrow labeled "v." Additionally, the displacement vector between a pair of ASIs captured at the same time stamp is indicated by a solid arrow and labeled "d."

Image by Peng et al. (2015)

Cloud shadow mapping and irradiance forecasting: Cloud shadow maps at the surface are produced by projecting the forecasted cloud scenes with their assigned height using information about the position of the sun and a digital elevation model. Local irradiance or PV power measurements can be used to estimate the cloud effects on irradiance or PV power for either point or spatial forecasts. Urquhart et al. (2013) analyzed the frequency distributions of PV power normalized to clear-sky conditions to determine a clear and a cloudy mode and to assign them to shaded and unshaded cells, respectively. Schmidt et al. (2016) and Dittmann, Holland, and Lorenz (2021) used the clear-sky index derived from recent pyranometer measurements to determine the forecasted all-sky GHI. Similarly, for DNI forecasting, Blanc et al. (2017) used the beam clear-sky index determined from the last 30 minutes of pyrheliometer measurements to derive the cloud transmittance. Ghonima et al. (2012) proposed a method to differentiate thin and thick clouds for various atmospheric conditions using a clear-sky library.

Using multiple ASIs to create networks of ASIs is useful to increase the spatial coverage, the forecast horizon, and the accuracy of observations by providing a more accurate 3D reconstruction of the cloud field (Mejia et al. 2018). Moreover, the combination of several ASI-

derived intermediate results (e.g., segmentation and cloud height) can be used to improve the nowcasts (Blum et al. 2022). Exemplary results of such a network are presented in Figure 9-6.

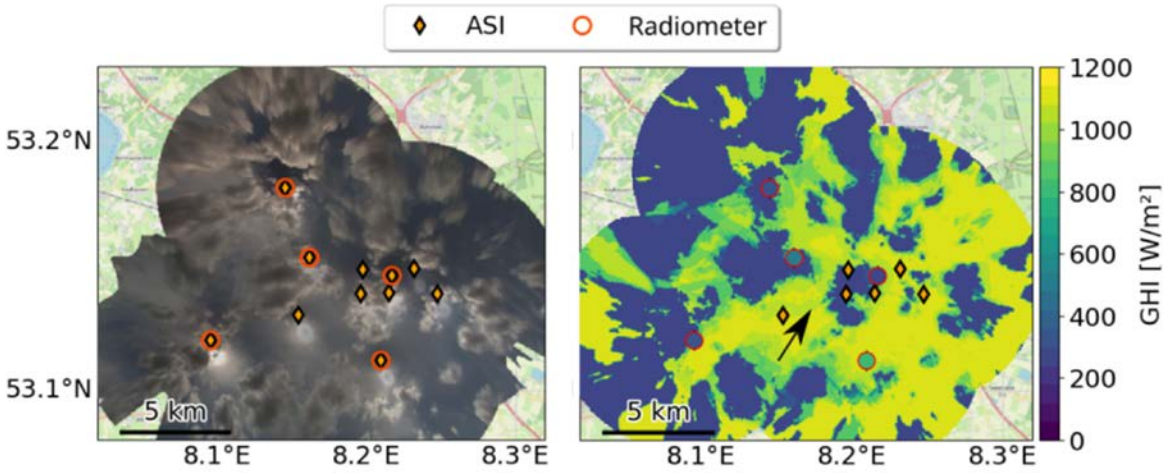

Figure 9-6. Exemplary results obtained by an ASI network

(Left) Stitched raw, undistorted, and georeferenced ASI images and (right) the GHI map derived by the ASI network.

Image by Blum et al. (2022)

Direct approaches use a supervised ML framework, which facilitates the creation of a mapping function that directly associates sky images with their corresponding solar irradiance values. The majority of approaches described in the literature rely on CNNs (Lin et al. 2023). The CNNs automatize the extraction of essential features from the input data. Once the features are extracted, they are flattened to a 1D vector and forwarded to an additional neural network, which proceeds with the regression procedure using solar irradiance as ground truth (Sun, Roth, and Black 2018). Sequential data are a valuable source of information regarding cloud motion, but its processing using traditional 2D CNN kernels is not direct. To overcome this challenge, specialized 3D CNN methods have been developed that are specifically designed to extract cloud features from a sequence of consecutive stacked sky images (Zhao et al. 2019). Another effective strategy involves the fusion of CNNs with recurrent neural networks (RNNs), known for their aptitude in handling subsequent data. Features extracted from the convolutional blocks are flattened and seamlessly passed to the RNN, employing a long short-term memory (LSTM) block for improved memory retention and sequential processing (Zhang et al. 2018). More recently, a variant was introduced called convolutional LSTM (convLSTM) , which directly accepts a sequence of sky images as input, removing the need for intermediate flattening and streamlining the processing of sequential data (Kong et al. 2020). Incorporating auxiliary data, such as solar irradiance time series, into a direct approach can enhance its predictive capabilities. One potential method involves the training of two parallel neural networks, one dedicated to processing images and the other designed for handling time-series data (see Figure 9-7). The extracted features from both networks can then be concatenated and fed into a final neural network, which performs the solar irradiance prediction (Paletta, Arbod, and Lasenby 2021). Recently, attention-based transformer architectures have been employed based on this strategy, and they appear to outperform CNNs and RNNs (Fabel et al. 2023).

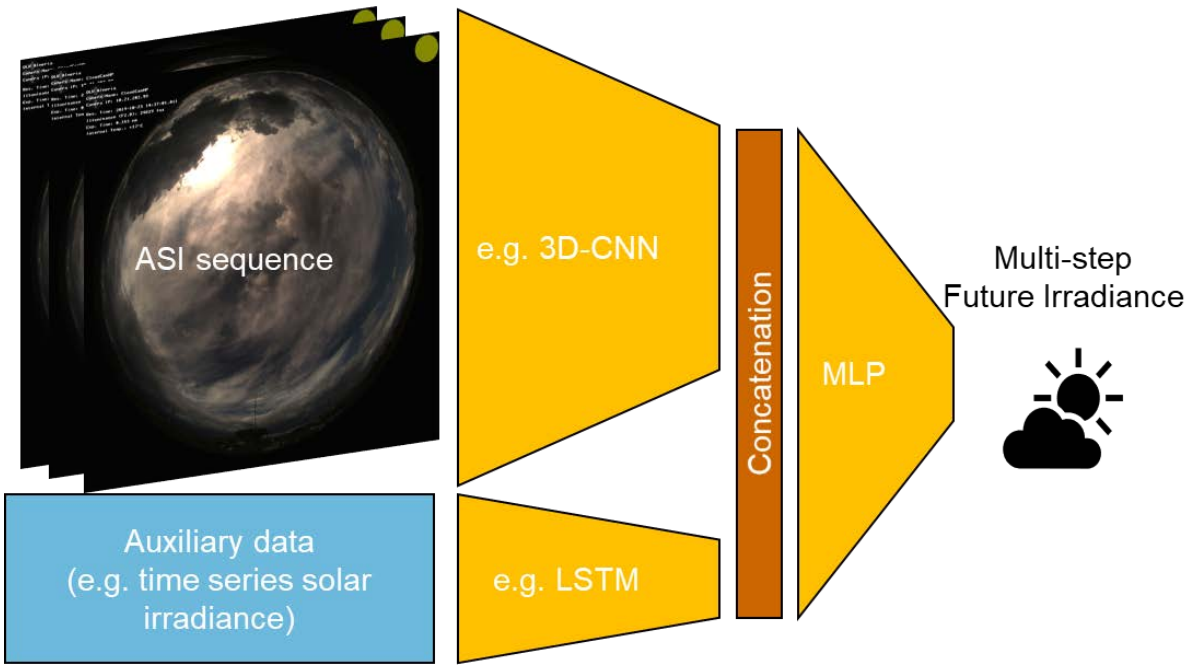

Figure 9-7. Potential general architecture of a multimodal model incorporating ASI sequences and auxiliary data

Image by DLR Institute of Solar Research

There is a noticeable trend toward adopting direct approaches in solar forecasting (Lin et al. 2023). These direct approaches consistently demonstrate impressive performance when assessed using well-established metrics such as RMSE or forecast skill; however, note that these direct approaches often exhibit characteristics similar to a "very smart persistence model," which mitigates the overall deviations. Although this characteristic often leads to lower average errors, it can potentially compromise the ability to accurately represent current conditions or accurately capture ramps (Paletta, Arbod, and Lasenby 2021). As a result, recent approaches have embraced the integration of preliminary results derived from indirect methods, such as CMVs, within the framework of direct approaches (Kamadinata, Ken, and Suwa 2019).

Regardless of direct or indirect methods, almost all ASI-based nowcasting systems provide deterministic forecasts. Recently some new approaches have been designed to provide probabilistic forecasts as well (Nouri et al. 2023; Paletta, Arbod, and Lasenby 2023).

In addition to irradiance nowcasting, ASIs have many other applications that are relevant to meteorology and solar energy. Deriving GHI and/or DNI from sky images is discussed by Dev et al. (2019), Sánchez-Segura et al. (2021), Schmidt et al. (2016), Chauvin et al. (2018), Kurtz and Kleissl (2017), and Gauchet et al. (2012). It is also possible to estimate the sky radiance distribution (Chauvin et al. 2015) and the aerosol optical depth (AOD) (Olmo et al. 2008; Kazantzidis et al. 2017).

9.3.1.3 Performance of All-Sky Imager Irradiance Forecasting: Results of a Benchmarking Exercise

To illustrate the performance of ASI-based forecasts, examples of results from the benchmarking exercise performed within the IEA PVPS Task 16 framework (Logothetis et al. 2022) are

presented next. That exercise aimed at nowcasting GHI with five ASI systems located at the Plataforma Solar de Almeria in southern Spain (Almeria). The experiment lasted 28 days during September–November 2019 and encompassed a large variety of cloud conditions. Six different cloudiness classes, including clear sky, were identified manually from the images. Various forecast lead times, ranging from 1–20 min, were considered. For each cloudiness class, the variation of the RMSE (defined in Chapter 10, Equation 10-4) over increasing forecast lead times (Figure 9-8) indicates that:

- Forecast and persistence errors, as well as differences between forecasts models, strongly depend on the cloud conditions and are smallest for cloud-free conditions.
- Forecast and persistence errors mostly increase with forecast lead time.
- ASI forecasts can outperform persistence in terms of RMSE for all cloud conditions and all lead times (ASI1 and ASI2). All investigated ASI-based models outperform persistence from several minutes onward for most cloud classes.
- Under clear-sky conditions, ASI forecasts show a similar RMSE as persistence, which is expected.

These findings agree with those from the other studies mentioned in Section 9.3.2.1. A comparison of ASI-based methods to satellite-based forecasting is discussed in Section 9.5.3.

In summary, ASI-based forecasting systems have gained popularity in the energy meteorology community because of their exceptional ability to provide very high-resolution intrahour forecasts. In recent years, ML-based direct approaches have gained ground; however, pure ML approaches have been found to have certain weaknesses (e.g., strong smoothing of predictions to minimize deviations). As a result, some of the most recent works advocate for integrating indirect physics-based approaches with direct data-driven approaches.

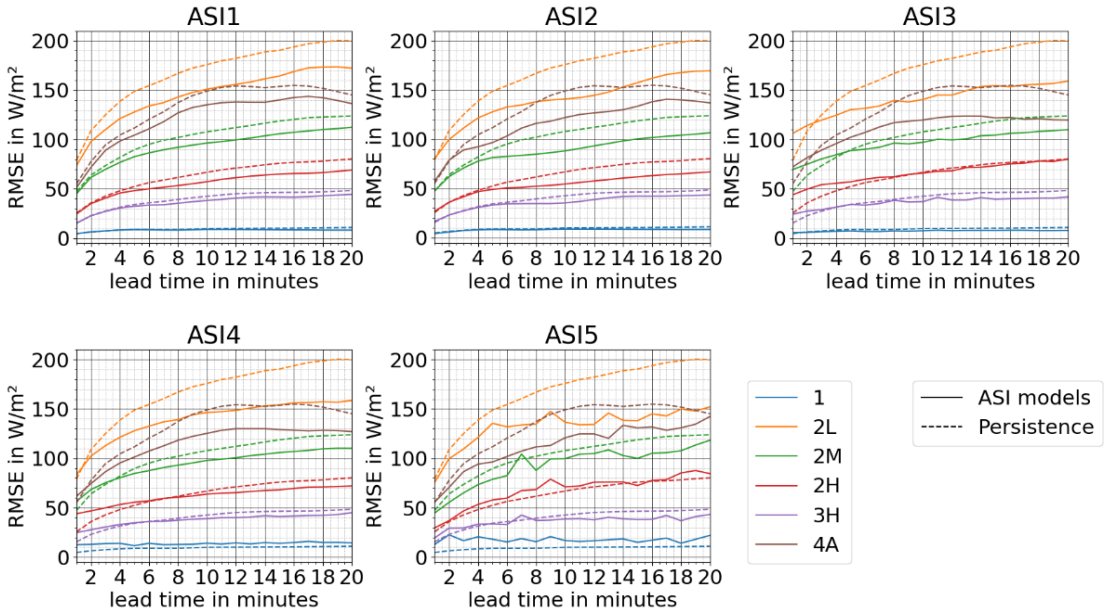

Figure 9-8. RMSE of five different ASI forecasting approaches (model, solid lines) compared to scaled persistence (PERS, dashed lines) over forecast lead times up to 20 minutes ahead for six different cloud classes as presented by Logothetis et al. (2022)

Dataset: Minute values: 28 days from September–November 2019 in southern Spain (Almeria). Cloud classes: 1: cloud-free (or almost cloud-free); 2L: scattered low clouds; 2 M: scattered multiple clouds; 2H scattered high/middle clouds; 3H: scattered high/middle clouds during half the day, cloud-free during the other half; 4A: overcast cloud conditions during half the day, scattered clouds during the other half.

Image by DLR with data from University of Patras and DLR

9.3.2 Satellite-Based Forecasts

Geostationary meteorological satellites have been operational since the late 1970s. The different geostationary meteorological satellites are now able to observe the complete Earth every 15 or 10 minutes with a spatial resolution of 1–3 km (see Chapter 7, Section 7.4.1). Each satellite observes the Earth from a different location—see Figure 9-9 for the 0º degree service (main mission) of Meteosat Second Generation (MSG) satellites. Each satellite has an onboard multichannel sensor to observe the radiance reflected by the atmosphere and clouds in an appropriate spectral range. This information can be used to assess the attenuating effects of clouds and ultimately estimate the incident radiation reaching a solar panel at any location, applying the models discussed in Chapter 7. In solar forecasting, this information is used to obtain forecasts of solar irradiance up to a few hours ahead and over large areas with a high-revisit frequency without requiring any specialized hardware and thus at low cost.

Figure 9-9. Image of the full Earth disc by MSG satellite located at 0º latitude and longitude

Image by EUMETSAT, contains EUMETSAT Meteosat data, 2023

9.3.2.1 Satellite-Based Forecasting Approaches

Satellite-based forecasting approaches include cloud motion analysis and direct ML methods, such as those employed in ASI forecasting, as discussed.

9.3.2.1.1 Satellite-Based Forecasts Using Cloud Motion Analysis

Since the late 1970s, when the first geostationary meteorological satellites became operational, cloud motion analysis has become a prominent technique to retrieve large-scale wind information for weather forecast models. Originally, this analysis was made by an operator who observed similar cloud patterns between consecutive images and manually drew the most plausible wind vectors between these patterns (Wolfgang Benesch 2007). This rather time-consuming and error-prone approach was later automated by detecting the minimal error between blocks of subsequent images and is still called "block-matching." Its first well-known application for solar energy forecasts was set by Lorenz, Hammer, and Heinemann (2004). The block-matching approach produces a CMV field that is applied on a current image to extrapolate it and to infer the future spatial distribution of clouds (see Figure 9-10).

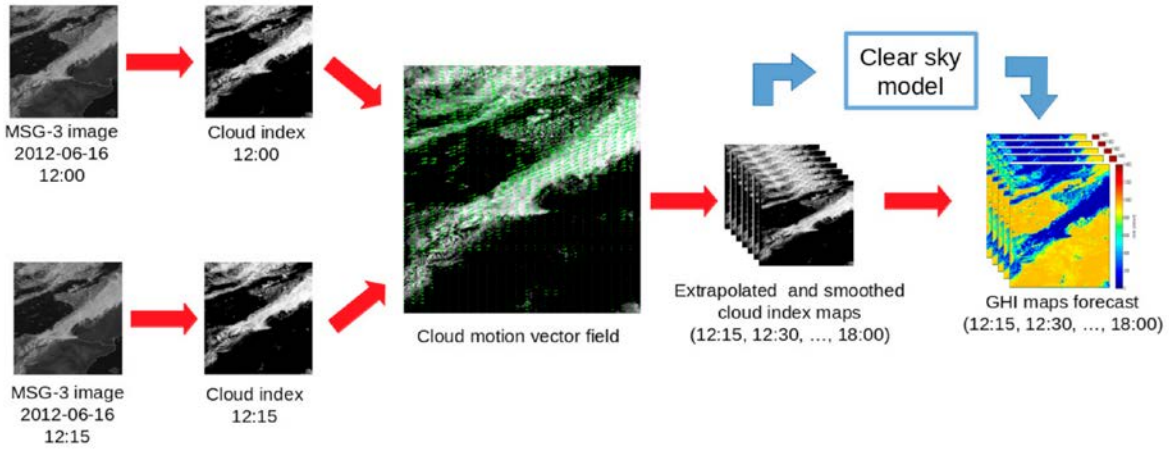

Figure 9-10. Generic process of a satellite-based forecast using CMV analysis

Image by Cros et al. (2020)

In recent decades, several methods have been designed based on these general principles; however, their differences can be established according to the method selected to resolve each main step, namely:

- The CMV field computation
- The extrapolation technique
- The satellite-derived variable to extrapolate, including the method to derive it.

These steps are further detailed in the following.

The block-matching technique has been widely used in cloud motion analysis thanks to its simplicity to ease of use (Lorenz, Hammer, and Heinemann 2004; Perez and Hoff 2013, 233–265; Kühnert, Lorenz, and Heinemann 2013, 267–297; Alonso-Montesinos and Batlles 2015; Cros et al. 2020). Its implementation requires tuning several parameters, such as vector grid resolution and sizes of the blocks to match.

9.3.2.1.1.1 Cloud Motion Vector Field Computation

The development of cloud motion analysis for ASI irradiance forecasting as well as advances in ML-based modeling have inspired researchers to also consider optical flow analysis techniques. These methods have the advantage of producing a dense CMV field (one vector per pixel) and thus propose more realistic extrapolated images than those issued from block-matching. Originating from the computer vision research area, most methods are conveniently available in precoded and well-documented libraries (Lucas and Kanade 1981; Farnebäck 2003; (Sun, Roth, and 2010); however, Bresky and Daniels (2006) noted that optical flow analysis does not provide a noticeable difference for cloud cover forecasts compared to block-matching mainly because the optical flow analysis was designed for fluid animated video (e.g., 24 images/s), whereas satellites provide 1 image every 5–10 minutes in the best case. Nevertheless, the convenient implementation of the optical flow analysis has attracted many solar energy forecasters (Cros et al. 2014; Nonnenmacher and Coimbra 2014; Sirch et al. 2017; Urbich, Bendix, and Müller 2019, Kallio-Myers et al. 2020; Kosmopoulos et al. 2020; Prasad and Kay 2021). A recent comparison of four optical flow methods and block-matching applied for CMV forecasting using

Geostationary Operational Environmental Satellite (GOES)-East satellite images for six sites in South America (Aicardi, Musé, and Alonso-Suárez 2022) shows better forecasting scores of the optical flow methods than the block-matching (see Section 9.3.2.2).

Another technique inspired from rainfall radar data processing is referred to as cloud-shape matching using contour and centroids (Wang et al. 2019). In parallel, sectoral cloud tracking (Schroedter-Homscheidt and Pulvermüller 2011) divides an image part into several parts around the sun position for direct irradiance forecast. Finally, wind vectors derived from NWP models are also used despite the associated operational constraints to obtain these additional data. This can explain why the main references on this approach in an operational context (Müller and Remund 2014; Miller et al. 2018) originate from providers of NWP forecasts.

9.3.2.1.1.2 The Extrapolation Technique

The extrapolation techniques applied to infer future images are not clearly documented in most of the aforementioned publications. Some details can be found in Cros et al. (2020), Gallucci et al. (2018), and Aicardi, Musé, and Alonso-Suárez (2022). The impact of different extrapolation approaches (called "push" and "pull," or their combination) on forecast quality is found to be small. The important aspect is to extrapolate each forecasted image in a step-by-step approach, with consideration for the possibly curved motions defined by the CMV. As a final step in the prediction of future images, smoothing filters are applied to eliminate randomly varying small-scale structures that are hardly predictable; this step can considerably reduce the forecast RMSE (Aicardi, Musé, and Alonso-Suárez 2022; Kühnert 2015; Lorenz, Hammer, and Heinemann 2004); see Chapter 10, Section 10.6.2.3.

9.3.2.1.1.3 Variable Used to Describe Cloudiness

Existing methods are also differentiated by the choice of the variable used to describe cloudiness. Many methods use a dimensionless cloud index or cloud albedo derived from the broadband visible channel of satellite sensors, e.g., using the semiempirical Heliosat method (Hammer et al. 2003; Rigollier, Lefèvre, and Wald 2004; Mueller et al. 2012). Carrière et al. (2021) rather used the clear-sky index, K_c, which is fully correlated with the cloud index. The advantage here is that K_c can be also defined as an objective physical variable. Kosmopoulos et al. (2020) experimented with the use of cloud optical depth because this variable is provided in standard physical satellite-derived products, such as the Nowcasting Satellite Application Facility (SAF-NWC)[56] or the Advanced Very-High-Resolution Radiometer (AVHRR) Processing scheme Over cLouds, Land, and Ocean (APOLLO) (Kriebel et al. 2003). Similarly, Wang et al. (2019) used cloud microphysical data from cloud physical property (CPP)-Surface Insolation under Clear and Cloudy Skies (SICCS).

9.3.2.1.2 Bidimensional Machine Learning Approach

CMV-based methods are proven to provide satisfactory results for nowcasting and have been operationally implemented around the world by different service providers using various geostationary satellites; however, their performance is known to reach a limit when cloud cover does not follow a net advection motion. Cloud appearance or disappearance caused by convective situations, cold or warm fronts passing, or coastal effects are not considered and can induce large forecast errors. To overcome this, some researchers have attempted to compensate

[56] See https://www.nwcsaf.org/.

for this lack of information by using ML approaches. Different types of ML algorithms can be applied following this principle. For instance, Licciardi et al. (2015) used neural networks (autoencoder combined with nonlinear principal component analysis). Dambreville et al. (2014) proposed an autoregression model using external variables (AR-X), where the surrounding GHI is the main input and the statistical CMV field provides external information. André et al. (2019) underlined that the autoregressive approach can be penalized by the lack of cloud motion information. Cros, Deroubaix, and Schmutz (2015) extended the AR-X approach with a dynamic CMV.

According to the aforementioned authors, such approaches can significantly improve the forecast accuracy on very short time horizons (up to approximately 2 hours). For longer time horizons, CMV seems more robust.

9.3.2.1.3 Probabilistic Forecasting

Information on the uncertainty associated with any kind of forecasting is essential for many applications. In particular, probabilistic forecasting (see Section 9.7) constitutes a concrete answer for electricity trading or microgrid management. Probabilistic forecasting is a common feature when using NWP models because they can be operated to produce ensemble forecasts. The synthesis of several forecast members is, by definition, a probabilistic result. Conversely, forecasts based on CMV are, by design, deterministic. The associated uncertainty is typically derived from metrics such as RMSE. Carrière et al. (2021) proposed adding a Gaussian distribution of the errors in the direction of each CMV to obtain a probabilistic speed and direction of cloud motion and then obtain probabilistic forecasts. Figure 9-11 shows the CMV field (top left), a probabilistic representation of the area where the clouds come from (top right), and an example of a probabilistic GHI forecast run (bottom).

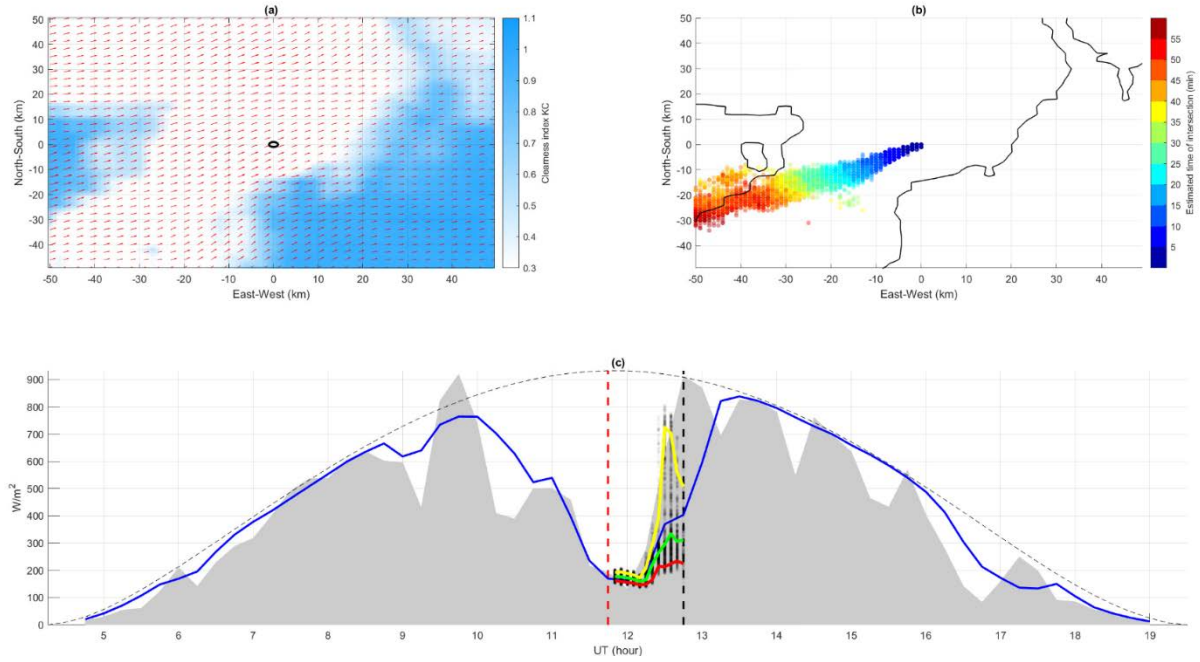

Figure 9-11. Snapshot of CMV-based probabilistic forecast

Example of the CMV-based probabilistic forecast on Carpentras, July 11, 2016, at 12:00 UT, for 1 hour ahead every 5 minutes. (a) Clear-sky index map at 12:00 UT, along with CMV (small red arrows), with a radius of 50 km around the location of interest. (b) Contour map of the clear-sky index map with 0.5 as a threshold, along with dots identifying pixels converging to the monitored perimeter of interest. The color of the dots represents the estimated time of intersection. (c) The gray area represents the reference measured GHI at a 15-minute time step. The blue line represents the corresponding estimation from satellites. The black dashed line represents the corresponding clear-sky GHI. The probabilistic forecasting issued at 12:00 UT (vertical red dashed line) up to 2 hours ahead (vertical black dashed line) is represented by the ensemble of potential converging clear-sky index, K_c, in black dots. For illustration purposes, the 10th, 50th, and 90th percentiles of this ensemble are represented by the red, green, and yellow lines, respectively.

Image by Carrière et al. (2021)

9.3.2.1.4 Satellite Data as Input to Deep Learning Forecast Techniques

Using satellite data as input to DL approaches is becoming increasingly popular in solar forecasting. Using satellite images provides several advantages:

- Data are regularly spatialized with long homogenous archives.
- GHI and/or cloud index are bounded values, limiting the risk of divergence in the training process.
- The available variables are linked by known physical relationships (PV power, GHI, cloud index, …), and thus an elaborate indexation process is not required.
- Small-scale stochastic cloud motion cannot be accurately modeled by thermodynamic equations. DL approaches might overcome this limit to some extent.

Several recent investigations have developed forecast models by applying CNNs on various cloud or GHI datasets derived from geostationary satellites.

Several recent works developed forecast models by applying various CNNs on various cloud or GHI dataset derived from geostationary satellite. Berthomier, Pradel, and Perez (2020) used the U-Net model to forecast the evolution of SAF-NWC cloud masks over the next 2 hours. Nielsen,

Iosifidis, and Karstoft (2021) developed a convLSTM architecture applied to the European Organisation for the Exploitation of Meteorological Satellites (EUMETSAT) Satellite Application Facility on Climate Monitoring (CM SAF) Surface Solar Radiation Data Set - 2 (SARAH-2) satellite-based maps to forecast the surface solar irradiance. Gallo et al. (2022) also trained a convLSTM model with ground and MSG data. Kellerhals, Leeuw, and Rodriguez Rivero (2022) applied a convGRU model on MSG-CPP data for cloud nowcasting. Similar approaches have been applied to the imagery from the Communication Ocean and Meteorological Satellite (COMS) (Ahn, Yu, and Yeom 2022) and Himawari-9 (Jiang et al. 2019) satellites.

9.3.2.2 Performance of Satellite-Based Irradiance Forecasting: Example Comparing Different Cloud Motion Vector Techniques

This section illustrates the performance of satellite-based irradiance forecasting using the CMV technique in the study by Aicardi, Musé, and Alonso-Suárez (2022) as an example. The study compares four optical flow methods and block-matching to obtain hourly GHI forecasts up to 5 hours ahead using GOES-East satellite images for six sites in Uruguay. All methods are operated with individual optimization of the parameter settings and smoothing.

For the different approaches, an analysis of the variation of RMSE with forecast lead time is illustrated in Figure 9-12 and provides results that agree with many of the other studies discussed in Section 9.3.2.1:

- Satellite-based predictions outperform persistence (even in combination with climatology) for forecast horizons from 1–5 hours ahead, with a clear advantage beyond 2 hours ahead.
- The RMSE of GHI forecasts strongly increases with the forecast horizon, as expected.

Further, the comparison shows that different optical flow forecasting methods perform very similarly and can outperform simple block-matching. A comparison of satellite-based methods with both ASI and NWP forecasting is given in Section 9.5.4.

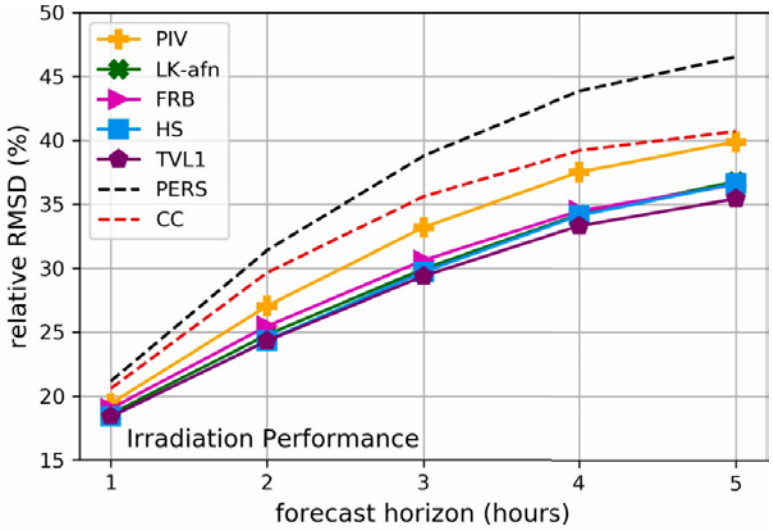

Figure 9-12. Relative RMSE of five different satellite-based CMV forecasting approaches (solid lines, PIV: block-matching; LK-afn: optical flow, Lukas Kanade; FRB: optical flow, Farnebäck; HS: optical flow, Horn and Schnuck; TVL1: optical flow with L1 norm; compared to persistence (PERS) and a model combining persistence and climatology, CC (dashed lines), over forecast lead times up to 5 hours. Dataset: Hourly values, years: 2015 and 2016, six sites in Uruguay.

Image by Aicardi et al. (2022)

In summary, satellite-based forecasting plays an important role in solar irradiance and PV power forecasting up to several hours ahead, typically with hourly or 15-minute resolutions, which is particularly important for intraday power markets. Thanks to the broad coverage of geostationary satellites, forecasts can be provided over large areas with a high-revisit frequency and without any additional hardware requirements. Whereas CMV techniques are still very popular in satellite-based irradiance forecasting, direct ML-based approaches have been increasingly used during the last few years and show promising results, similar to ASI forecasting.

9.4 Numerical Weather Prediction

NWP models are routinely operated by weather services to forecast the state of the atmosphere. Starting from initial conditions that are derived from routine Earth observations from worldwide networks of meteorological sensors, the temporal evolution of the atmosphere is simulated by solving the equations that describe the physical processes occurring in the atmosphere (Figure 9-13). Such physical modeling is the main forecasting approach for time horizons longer than approximately 5 hours ahead. A comprehensive overview of NWP modeling was given by Bauer, Thorpe, and Brunet (2015).

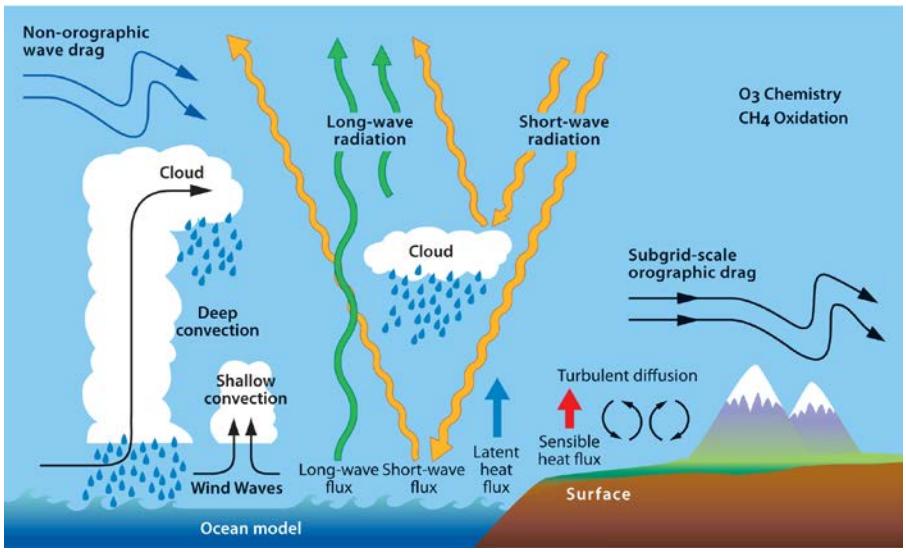

Figure 9-13. Illustration of atmospheric processes modeled in NWP

Image by ECMWF (https://www.ecmwf.int/en/research/modelling-and-prediction/atmospheric-physics), accessed on 28.04.2024; Creative Commons Attribution 4.0 International Public License

9.4.1 Basic Principles of Numerical Weather Prediction Forecasting and Challenges in Irradiance Forecasting

Global NWP models predict the future state of the atmosphere worldwide. To determine the initial state from which an NWP model is run, data assimilation techniques are applied to make efficient use of worldwide meteorological observations (Jones and Fletcher 2013). These include observations from ground-based weather stations, buoys, radiosondes, airplanes, and spaceborne sensors (i.e., satellites), see Figure 9-14.

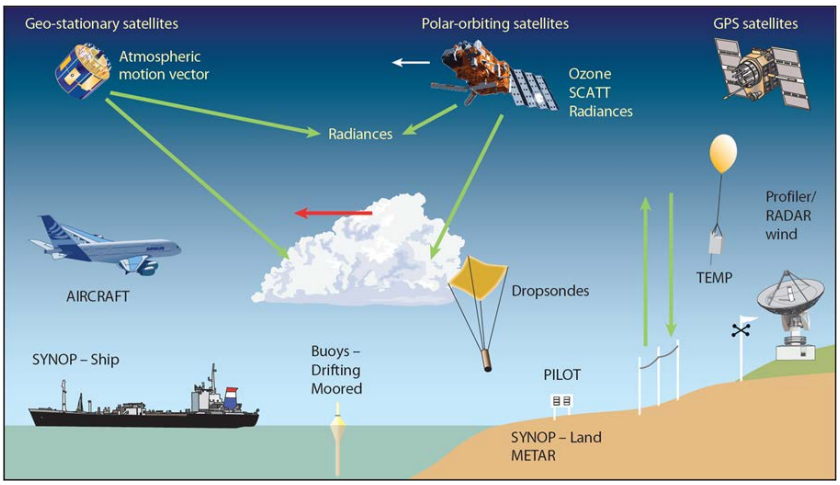

Figure 9-14. Sensors collecting meteorological observations

Image by ECMWF (https://www.ecmwf.int/en/research/data-assimilation/observations), accessed on 28.04.2024; Creative Commons Attribution 4.0 International Public License

NWP models operate by solving conservation equations for the atmosphere and the surface layers immediately below using spatial and temporal discretization. The spatiotemporal resolution of this discretization determines the computational cost of the simulation. Primarily,

the equations of momentum and energy are solved, but equations for hydrometeors, water vapor, radiative transfer, soil moisture, etc., are also needed.

In addition, many physical processes occur on spatial scales smaller than the grid size, including, most importantly, condensation, convection, turbulence, as well as scattering and absorption of shortwave and longwave radiation (see Figure 9-13). This depends on the model resolution, though. Models with a spatial resolution approaching 1 km can resolve deep convection, whereas models with a finer resolution of approximately 100 m can resolve shallow convection as well. The effect of unresolved processes on the mean flow at the model's grid size is evaluated with the so-called parameterizations of atmospheric physics. They include interactions of the land and ocean with the atmosphere, vertical and temporal development of the planetary boundary layer, cumulus triggering and cloud microphysics, as well as shortwave and longwave radiation. These physical parameterizations are key components of obtaining accurate predictions with NWP models. They bridge the small-scale and large-scale processes, and they prompt the convergence of the numerical routines that solve the physical equations.

Currently, global NWP models are run by approximately 15 national and international weather services, and their spatial resolution ranges from approximately 10 km–50 km. The temporal resolution of the global model outputs is typically 1 or 3 hours, their forecasts are normally updated every 6 or 12 hours, and they are run 10 days or longer into the future.

Regional models—also called limited area models or mesoscale models—cover only a limited area of the Earth. They take the lateral boundary conditions from a concurrent or previous global NWP model run and refine the spatial and temporal grid of the global NWP model. A typical example of successively finer grids is shown in Figure 9-15. They use initial conditions from a previous run with the same model and need several months to get slowly varying variables, such as soil water or temperatures, correct. Weather services typically operate mesoscale models with a spatial resolution ranging from 1–10 km, and they provide hourly forecasts, though higher resolutions are feasible. Compared to global models, the higher spatial resolution of mesoscale models allows for explicit modeling of small-scale atmospheric phenomena.

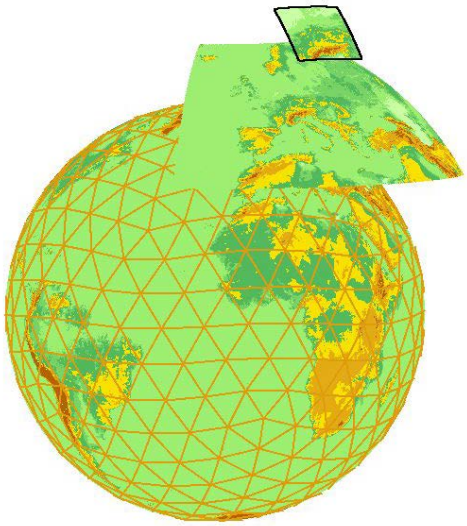

Figure 9-15. Downscaling from global to regional NWP with a higher spatial and temporal resolution

Image by Deutscher Wetterdienst DWD
(https://www.dwd.de/EN/research/weatherforecasting/num_modelling/06_nwp_emergency_response_system/num_weather_prediction_emergency_system_node.html) accessed on 28.04.2024

Clouds and their optical properties are of primary importance for irradiance forecasting. They are strongly affected by the model's initial conditions and by several processes in and around the atmospheric system. For instance, the deep soil's water concentration affects the available cloud water via evapotranspiration from plants and trees. In parallel, clouds related to weather systems at approximately 1,000 km (synoptic) scale are most accurately forecasted. This includes clouds along a warm front with consistent rising motion over a large region.

Thunderstorm clouds (cumulonimbus) appear dark gray and can block most of the solar irradiance. They can form in conditionally strongly unstable atmospheric conditions and are the most difficult to predict. They can form due to cascading outflows from other cumulonimbus clouds that are in essence of a chaotic nature. This process is inherently impossible to accurately predict in day-ahead forecasts. In practice, a region with the likely formation of such clouds is forecasted based on an ensemble of NWP models (see Section 9.7). Here, the members of the ensemble can have perturbed initial conditions, surface conditions, and physics parametrizations. The output from several NWP models can also be combined into multi-model ensembles to improve accuracy.

Fog is also often difficult to forecast. Recent work in several weather centers has focused on better representations of aerosols and cloud-aerosol microphysical interactions to improve these forecasts. Cloud-aerosol interactions have also been shown to be important for cloud ice nucleation, which can create high-level cirrus clouds. These developments are likely to improve the cloud forecasts in the coming years. Additionally, explicit aerosol forecasts in regional NWP models will improve the clear-sky irradiance forecasts compared to the previous models that mostly use fixed aerosol climatologies based on average historical conditions.

Most current NWP models offer the surface GHI as a normal output. Some models also offer direct and/or diffuse irradiance on a horizontal surface as a normal output, or even DNI forecasts. Note that if direct horizontal irradiance, noted DIR in Chapter 8, is accumulated over 1 hour by the model, its conversion to DNI can only be approximate; thus, whenever possible, it is best to obtain DNI directly. Additionally, some models provide clear-sky irradiance, which includes the effect of aerosols and other atmospheric constituents. This clear-sky irradiance is necessary to obtain the clear-sky index. Although in principle the surface irradiance output can be used directly in solar energy applications, in practice additional postprocessing is customarily applied to improve forecast accuracy (see Section 9.5).

9.4.2 Examples of Operational Numerical Weather Prediction Models

Some examples of NWP models are given and specific references are provided with respect to the application and evaluation of irradiance forecasts in the context of solar energy applications. Note that the sample of operational models and applications given here is nonexhaustive; it simply summarizes the research experience and lessons learned from research completed within the frameworks of the IEA SHC Task 36 and Task 46 (now completed) as well as the current IEA PVPS Task 16.

9.4.2.1 Global Numerical Weather Prediction Models

Many of today's operational global NWP models are listed in Table 9-1, including their current spatial resolution. Of these, this section introduces the Integrated Forecasting System (IFS) by the European Centre for Medium-Range Weather Forecasts (ECMWF), and the Global Forecast Systems (GFS) by the U.S. National Centers for Environmental Prediction (NCEP).

Table 9-1. Nonexhaustive List of Global NWP Models and the National Bureaus That Run Them

Meteorological Bureau	Country	Model (Resolution)[a]
BOM	Australia	ACCESS-G (12–17 km)
CMA	China	GRAPES-GFS (26 km)
CMC	Canada	GEM (22 km)
DWD	Germany	ICON (13 km)
JMA	Japan	GSM (20 km)
KMA	South Korea	KIM (12 km)
ECMWF	Europe[b]	IFS (9 km)
MF	France	ARPEGE (7.5-37 km)
NCEP	United States	GFS (23 km)
NCMRWF	India	NEPS-G (12 km)
RUMS	Russia	SL-AV (25 km)
UKMO	United Kingdom	UM (10 km)

[a] Some models are run with varying resolutions for different areas. For these, the range of resolutions is given.
[b] In addition to European member states and cooperating states, Morocco and Israel are cooperating states.

The ECMWF's IFS is a global model currently being operated on 137 vertical levels for high-resolution deterministic forecasts. Since the Summer of 2023, all 51 ensemble members of the IFS have been run with a horizontal grid resolution of approximately 9 km. During each model run, many resources are spent on analyzing the initial model state to be as accurate as possible and balanced. If the model state is not balanced, the model will quickly go from the analyzed state to one that significantly differs. For instance, if more water vapor is present than can be withheld in the atmosphere, this will quickly precipitate and be removed. To avoid this, the temperature needs to be adequate to contain the amount of water vapor to be assimilated in the initial state. To efficiently ingest observations and initialize each model run, the method used in the IFS is called 4-Dimensional Variational (4D-Var) data assimilation (Bonavita and Lean 2021).

IFS irradiance forecasts have been extensively evaluated for PV power forecasting (Lorenz et al. 2009; Lorenz et al. 2011). For example, their excellent performance has been shown over the United States, Canada, and Europe (Perez and Hoff 2013) and over Europe (Lorenz et al. 2016) in the benchmarking studies performed under the auspices of IEA SHC Task 36 and Task 46, respectively; see Section 9.4.3. For research purposes, IFS forecasts are available from the archive free of charge in full resolution. Additionally, a subset of IFS real-time forecasts is made available to the public free of charge.[57]

Similarly, NCEP's GFS is frequently used in PV power forecasting, in part because its forecasts are provided free of charge to any user. It is currently being operated at a spatial resolution of approximately 13 km over 64 vertical levels; however, the outputs are provided using a regular latitude/longitude grid with a relaxed resolution of 0.25º and 46 levels, with an hourly resolution up to 120 hours ahead and a 3-hour resolution up to 240 hours ahead. The model is cycled every 6 hours. Comparisons of intraday GHI forecasts of the GFS and IFS forecasts are discussed in Mathiesen and Kleissl (2011) and Perez et al. (2018); see Figure 9-20.

9.4.2.2 Regional Numerical Weather Prediction Models

Meteorological observations are shared internationally among almost 200 member countries and territories around the world. Many of these countries also run their own national regional weather models, including their own initial state data analysis, which gives an advantage to these models. For instance, the U.K. Met Office develops and runs the Unified Model (UM), which is also used in the UM core partnering countries: Australia, India, Singapore, New Zealand, and South Korea. The German Weather Service (DWD) develops and runs forecasts with the Consortium for Small-scale MOdeling (COSMO) model in collaboration with institutes from Greece, Israel, Italy, Poland, Romania, and Switzerland. In addition, they develop and run the ICOsahedral Nonhydrostatic (ICON) model in a broader consortium including the Max Planck Institute of Meteorology, COSMO, and other computing and meteorological institutes in Germany and Switzerland. Météo-France leads ACCORD (A Consortium for Convection-scale modeling Research and Development), which includes 26 national meteorological services across Europe and the Mediterranean region.

Beyond the models developed and run by national weather centers and consortia of these, the mesoscale (or regional) Weather Research and Forecasting (WRF) model (Skamarock et al.

[57] See https://www.ecmwf.int/en/forecasts/datasets/open-data.

2005) is an open-source NWP model that is widely used in energy meteorology. It was developed in the framework of a long-term collaborative effort of several institutes led by the National Center for Atmospheric Research (NCAR) in the United States. It is now a "community model," meaning that it is publicly and freely available, and it can receive contributions from all participants. The WRF model is nonhydrostatic, has multiple nesting capabilities, and offers several schemes for each different parameterization of the atmospheric physical processes. This makes the WRF model adaptable to widely different climate conditions and different applications over virtually any region of interest.

The WRF model has been extensively evaluated in the context of solar energy applications, and it was also part of the IEA SHC Task 36 NWP benchmark (Perez et al. 2013). Other studies from the last few years have evaluated the model over widely different regions, including Lara-Fanego et al. (2012) in Southern Spain; Isvoranu and Badescu (2013) in Romania; Zempila et al. (2016) in Greece; Aryaputera, Yang, and Walsh (2015) in Singapore; He, Yuan, and Yang (2016) in China; Lima et al. (2016) in Brazil; Gueymard and Jiménez (2018) in Kuwait; and Sosa-Tinoco et al. (2016) in Mexico.

An important milestone in the use of the WRF model for solar radiation applications has been the recent development of WRF-Solar, a dedicated suite of WRF model parameterizations for solar radiation forecasting (Deng et al. 2014; Ruiz-Arias, Dudhia, and Gueymard 2014; Thompson and Eidhammer 2014) within the U.S. Department of Energy's Sun4Cast project (Haupt et al. 2016). Some of these improvements, and others, have been summarized by Jiménez et al. (2016). Moreover, the Sun4Cast project has contributed to the development of the Multisensor Advection Diffusion nowCast (MADCast) system (Descombes et al. 2014), which is a particular configuration of the WRF model for the fast assimilation of satellite reflectance images. That configuration can be used to obtain a proxy field to cloud fraction that can be subsequently advected in WRF and used to compute solar radiation nowcasts. Lee et al. (2017) presented a comparative evaluation of WRF-Solar, MADCast, and satellite-based forecasts and found that WRF-Solar performed generally well at predicting GHI under challenging situations in California. Beyond MADCast, MAD-WRF (Jiménez et al. 2022) blends satellite information directly into WRF.

To extend the WRF-Solar capabilities beyond deterministic forecasts, the WRF-Solar Ensemble Prediction System (WRF-Solar EPS) has been developed. WRF-Solar EPS introduces stochastic perturbations in the most relevant variables for solar irradiance forecasts that have been identified with tangent linear models of selected parameterizations (Yang et al. 2021). The model provides a user-friendly configuration to set the characteristics of the perturbations for each variable and to select the variables to perturb. A detailed description and evaluation of WRF-Solar EPS for the United States is given in Sengupta et al. (2022); see Chapter 10, Section 10.5.2.1. The WRF model is run operationally for solar irradiance forecasting at several public and private entities.

9.4.3 Performance of NWP GHI Forecasts: Results of a Benchmarking Exercise

Results of the IEA SHC Task 36 benchmark of NWP GHI forecasts (Perez et al. 2013) are shown here to illustrate the forecast performance of NWP models up to several days ahead. Although the performance of NWP irradiance forecasts has been clearly improved since then, the general findings outlined here are still valid, as confirmed in many other studies, e.g., those given

in Section 9.4.2. A new worldwide benchmark of NWP irradiance forecasts is planned for the next phase of the IEA PVPS Task 16.

Perez et al. (2013) evaluated different NWP models for a variety of climates in the United States, Canada, and Europe. The evaluations are performed for seven sites in the United States from May 2009–April 2010; three sites in Canada from June 2009–May 2010; and 24 sites in Europe, namely, in Germany, Austria, Switzerland, and Spain, from July 2007–June 2008. The evaluated models include IFS and different implementations of the WRF model for all sites, mostly with no postprocessing.

An analysis of the RMSE variation with the forecast lead time, here grouped to entire days up to several days ahead (Figure 9-16), indicates the following:

- NWP models clearly outperform persistence from the first day onward.
- The RMSE of NWP forecasts slightly increases with increasing lead time.
- A big difference exists in the RMSE of different NWP models, which can be partly attributed to differences in their spatiotemporal resolutions (see Chapter 10, Section 10.3). The IFS forecasts show comparatively low RMSE values for all investigated areas.
- Both the absolute and relative RMSE values strongly depend on climatic conditions. The relative RMSE is typically smaller in sunny areas, as shown in the bottom plot of Figure 9-16 for Spain.

A comparison of the performance of NWP forecasts to satellite-based forecasts and persistence for intraday forecasting is given in Section 9.5.3.

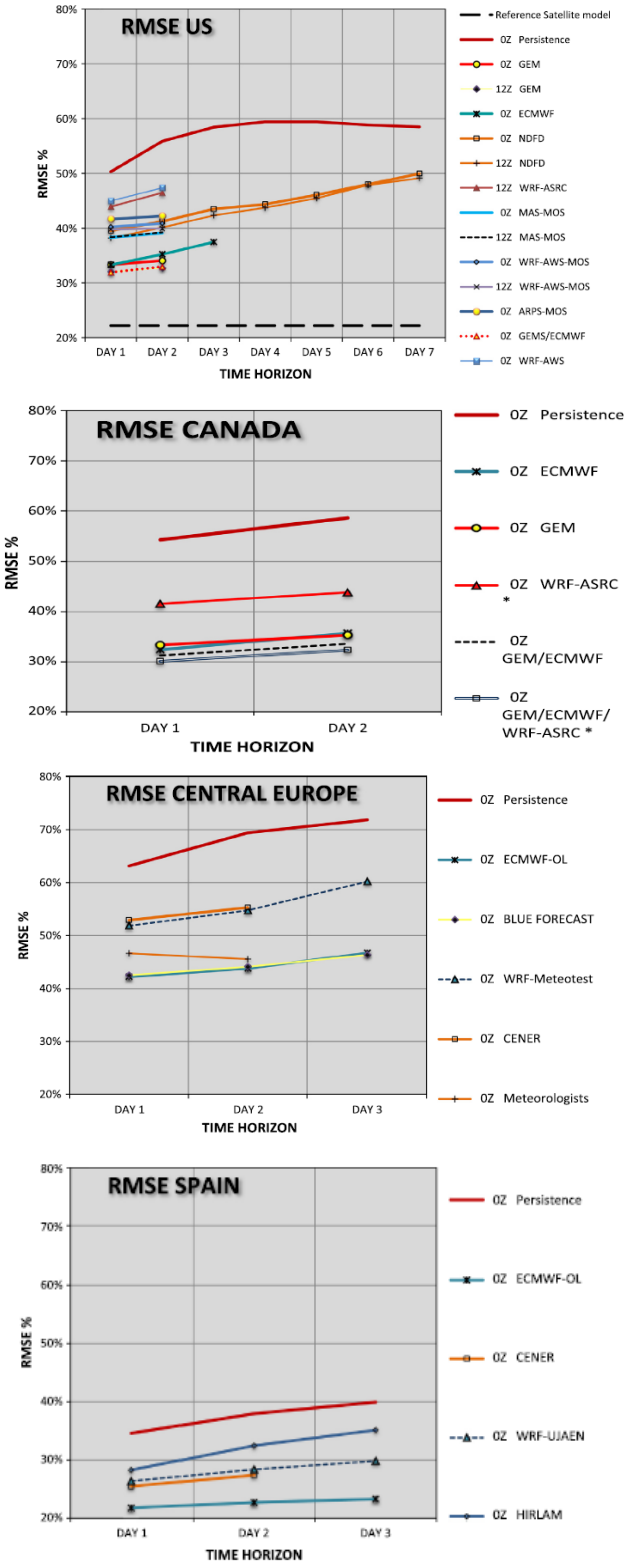

Figure 9-16. Relative RMSE of GHI forecasts for different NWP models and model combinations over forecast horizons up to 3 days

United States: composite of 7 sites (first row); Canada: composite of 3 sites (second row); Central Europe (composite of 21 sites (third row); and Spain: composite of 3 sites (last row). *Image by Perez et al. (2013)*

9.5 Postprocessing and Model Blending With Statistical and Machine Learning Methods

Postprocessing empirical or physical model outputs plays an important role in irradiance and PV power forecasting.

Particularly, various postprocessing methods are applied to:

- Reduce model errors of physical or empirical models by considering unaccounted or partially accounted local and regional effects (e.g., topography or aerosols)
- Combine the outputs of different models (model blending)
- Derive quantities that are not included in the normal model outputs
- Calibrate NWP ensemble forecasts
- Derive probabilistic forecasts from deterministic forecasts.

Currently, postprocessing is mostly performed by statistical or ML methods. These are referred to as "ML models with exogenous input" in the ML community. Nevertheless, empirical and physical models are also employed for postprocessing, especially to derive quantities that are not included in the normal model outputs. Further, a traditional method to obtain improved local forecasts from NWP model outputs is to involve the human knowledge of forecast experts. Especially in difficult forecast situations, such as fog, this alternate approach offers potential for improved irradiance forecasts.

To train ML algorithms, the availability of irradiance and/or PV power measurements is crucial (see Section 9.2). These are used as ground truth for model training. Whereas time-series models require near-real-time data as inputs, postprocessing algorithms can be trained on historic (or "offline") data. Whenever near-real-time (or "online") measurements are available, online training (which consists of regularly retraining the model with new measurements as they become available) is an option to better adapt ML models to current conditions, e.g., seasonal changes. Moreover, satellite-derived irradiance data with their high spatial resolution are a suitable reference for postprocessing NWP model forecasts.

Again, note that uncertainty and especially systematic deviations of ground truth data have a large impact on ML model performance (see Section 9.2.3). Therefore, thorough quality control is essential before using measurements as ground truth for model training. This is also the case for satellite-based irradiance estimates if they are used as ground truth.

The following sections summarize various postprocessing methods for the deterministic forecasting applications enumerated here. The application of statistical and ML models in the context of probabilistic forecasting is addressed in Section 9.7.

9.5.1 Model Output Statistics

MOS are widely used to refine the output of NWP models, primarily to account for local variations in weather and surface conditions. Already more than 50 years ago, Glahn and Lowry (1972) used measurements and/or climatology for specific locations as a basis to adapt the forecasts. Overall, MOS techniques constitute a powerful tool to adapt the results from NWP or satellite-based models to site-specific conditions (e.g., (Gueymard et al. 2012). The set of

predictors consists of various NWP outputs and might be extended by including any relevant information—for example, prior observations or climatological values.

Originally, the term *model output statistics* was associated with the use of regression equations; however, a generalization of this concept now involves other statistical or ML approaches. A bias correction of ECMWF irradiance forecasts in dependence of solar elevation and clear-sky index has been applied by Lorenz et al. (2009). Kalman filters have been proposed by Pelland, Galanis, and Kallos (2013) to improve the irradiance forecasts of the Canadian Global Environmental Multiscale (GEM) model and by Diagne et al. (2014) for WRF solar irradiance forecasts. The application of ANNs to predicted variables from a weather forecasting database has been investigated by, e.g., Marquez and Coimbra (2011). Gastón et al. (2009) used an ML algorithm to enhance the solar irradiance forecasts of the SKIRON model. Pierro et al. (2015) proposed an MOS technique to correct WRF-based GHI forecasts by coupling two intermediate MOS corrections, consisting of correlations with relative humidity and ANNs, respectively. Other powerful postprocessing approaches have been thoroughly reviewed by Yang and Van Der Meer (2021).

9.5.2 Model Blending

Combining —or "blending"—the output of different models can considerably increase the forecast accuracy. First, simple averaging is beneficial for models with similar accuracy, exploiting the fact that forecast errors of different models are usually not perfectly correlated (Lorenz et al. 2016; Perez et al. 2013). Blending methods using more advanced techniques can also account for strengths and weaknesses of the different models for certain situations, for example, by adapting the contribution of each model depending on the weather situation.

A common customer request consists of obtaining short-term forecasts as a single continuous product, even if different observation technologies are used as input. Model blending with statistical and ML approaches is applied to produce such seamless irradiance forecasts covering horizons from several minutes to several days ahead. They integrate different inputs suitable for the different forecast horizons with an optimized weighting. These inputs might include measurements, ASI- and satellite-based forecasts, as wells as NWP forecasts.

Various approaches to this aim have been proposed, mostly based on measurements and/or satellite-based predictions in combination with NWP models. For instance, a weighted average of satellite-based and NWP forecasts was investigated in Lorenz and Heinemann (2012), with the weights optimized for each forecast horizon using linear regression. Kühnert (2015) additionally integrated PV power measurements using the same approach. Bacher, Madsen, and Nielsen (2009) applied an autoregressive model for hourly solar power forecasting combining measurements and NWP forecasts. Sanfilippo et al. (2016) applied a multi-model approach to solar forecasting using supervised classification to select the best predictions from support vector regression and diverse stochastic models. Wolff et al. (2016) and Aguiar et al. (2016) combined forecasts based on support vector regression and ANNs, respectively. Yang et al. (2017) used a hierarchical scheme and minimization of the trace of the forecast error covariance matrix. Within the context of the Sun4Cast project, NCAR's DICast system (Haupt et al. 2018) has been applied to blend multiple solar radiation forecasts. This system—which has already been applied in other forecasting areas, such as transportation, agriculture, and wind energy—consists of a two-step

process: (1) a statistical bias correction process using a dynamic MOS and (2) optimization of the model blending weights for each lead time (Haupt et al. 2016).

Further, the integration of ASI-based forecasting methods to blending models were demonstrated to be valuable for short-term high-resolution forecasting. Pedro et al. (2018) and Huang et al. (2019) assessed intrahour hybrid forecasting models that combine statistical or ML methods with measurements and information extracted from sky imagery and found substantial improvements compared to simple time-series models. Recently, combinations of measurements with ASI- and satellite-based forecasts have also been investigated in López-Cuesta et al. (2023) and Straub et al. (2024, 2023).

Example evaluations of the performance of blending models are given in Section 9.5.4 and demonstrate the benefit of combining different input data over single modes performance.

9.5.3 Postprocessing to Derive Additional Quantities

Not all variables of interest in the context of solar energy forecasting (i.e., global tilted irradiance [GTI], DNI, or PV power) are always available as direct NWP outputs or as a result of CMV forecasts. Postprocessing can be applied to derive these quantities. To that aim, empirical methods are typically employed, but statistical or ML methods as well as physical models are also frequently used to derive the desired quantity from the direct output of the forecasting model.

Although GHI has now become a standard output of NWP models, this was not the case when the field of solar forecasting started to emerge. For example, Perez et al. (2007) proposed an empirical solar radiation forecast model relating sky-cover predictions from the National Digital Forecast Database to the clear-sky index to derive GHI forecasts.

The irradiance components (diffuse horizontal irradiance [DHI] and DNI) are still not provided as normal outputs by all irradiance forecasting systems. To derive them from GHI forecasts, several empirical diffuse or direct fraction models can be used, which were originally developed for application to measurements and later applied to satellite data (see Chapter 7, Section 7.3.1). These models are also being used in DNI forecasting systems that are based on a GHI forecast, as discussed e.g., in Schroedter-Homscheidt, Benedetti, and Killius (2017). For DNI forecasts, several physical postprocessing approaches have also been proposed, specifically for better consideration of aerosols. Breitkreuz et al. (2009) proposed a forecasting approach for direct and diffuse irradiance based on the combination of a chemistry transport model and an NWP model in which forecasts of AOD are directly collected from the chemistry transport model outputs. Similarly, Gueymard and Jiménez (2018) used WRF-Solar with hourly inputs of aerosol forecasts from the National Aeronautics and Space Administration's (NASA's) Goddard Earth Observing System Model 5 (GEOS-5) atmospheric analysis model. Such aerosol forecasts, together with other remote sensing data (ground albedo and ozone) and NWP parameters (water vapor and clouds) are used as input to radiation transfer calculations to derive the irradiance forecasts. A similar approach was used by Lara-Fanego et al. (2012) to derive DNI from WRF output using aerosol observations from the Moderate Resolution Imaging Spectroradiometer (MODIS) onboard the Terra satellite.

In the context of PV applications, forecasting GTI (or plane-of-array [POA] irradiance) or directly PV power is also of interest, as discussed in Section 9.6.1.

9.5.4 Performance of Blending Models: Examples for Intrahour and Intraday Forecasting

The performance of different blending models is illustrated along with a comparison of the different single-model irradiance forecasts used as input to them. The examples shown here cover high-resolution *intrahour* forecasts that integrate measurements and/or ASI and satellite-based forecasts as well as *intraday* forecasts integrating measurements, satellite-based, and NWP forecasts.

9.5.4.1 High-Resolution Intrahour Forecasting

The examples for high-resolution intrahour model blending presented here include:

- A comparison of minute-resolution ASI forecasts, satellite-based CMV forecasts, and a combination of both with lead-time-dependent weights for the DLR-operated Eye2Sky network in Northern Germany, which integrates several ASIs and irradiance measurement stations
- A comparison of ground-based persistence, ASI-based and satellite-based forecasts, as well as a combination of them using linear regression, again with lead-time-dependent weights, but for a radiometric network of eight stations in Freiburg (Southern Germany) (Straub et al. 2024).

For these comparisons, the satellite-based forecasts with their native resolution of 15 minutes are up-sampled to minute-resolution forecasts.

Analyses of the RMSE of the different minute-resolution forecast models over lead times of up to 30 minutes for the two examples (Figure 9-17 and Figure 9-18, respectively) illustrate the following:

- ASI forecasts outperform ground-based persistence from lead times of about 2 minutes onward (Figure 9-18), which agrees with the results in Section 9.3.1.3.
- Up-sampled satellite-based forecasts outperform scaled persistence from about 5 minutes onward (Figure 9-18).
- ASI forecasts outperform satellite-based forecasts up to lead times ranging from 10–20 minutes ahead, depending on whether one is using a network of ASIs or a single ASI, the quality of the models applied to derived forecasts from ASI and the satellite images as well as the climatic conditions for the evaluation site and period.
- Blending models clearly outperform single-model forecasts for all lead times.

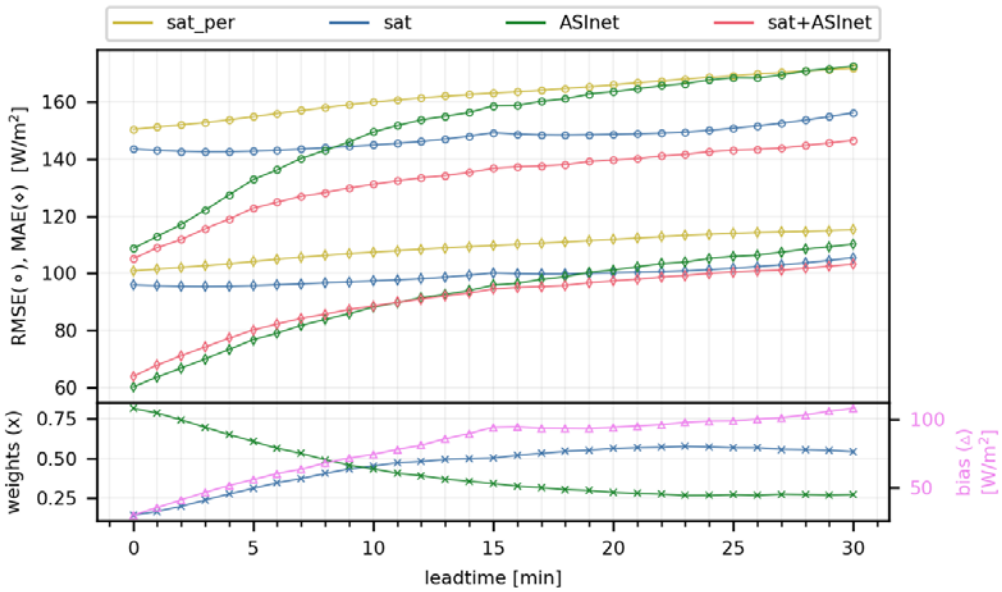

Figure 9-17. RMSE, MAE, and bias (MBE), as well as weight of the blending model of minute-resolution GHI forecasts over forecast lead times up to 30 minutes ahead for satellite-based persistence (sat_per), satellite-based forecasts (sat), forecasts derived from the Eye2Sky ASI network (ASInet), and a combination of the latter two (sat + ASInet)

Dataset: Two validation sites within the DLR Eye2Sky network, August 2020. *Image by DLR Institute of Networked Energy Systems*

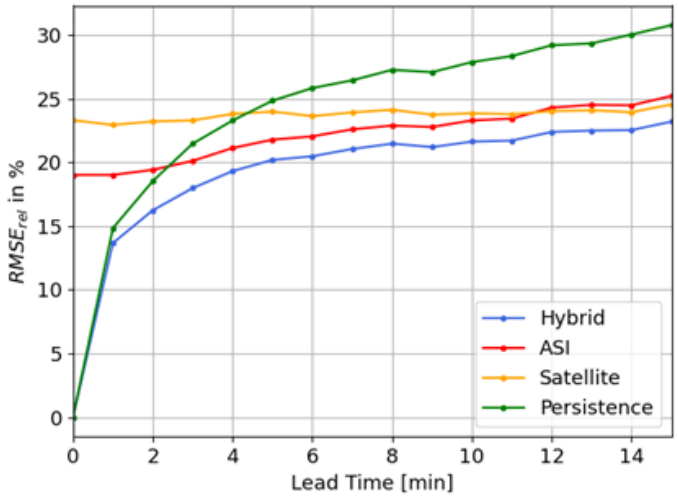

Figure 9-18. Relative RMSE of minute-resolution GHI forecasts over lead times up to 15 minutes ahead for ground-based persistence (persistence), ASI-based forecasts (ASI), satellite-based CMV forecasts (satellite), and a combination of the three (hybrid).

Dataset: Eight sites in Freiburg, May 2021–April 2022; test data: every fourth day, including only complete forecast runs for all models.

Image by Straub et al. (2024)

9.5.4.2 Intraday Forecasting

The examples for intraday forecasting with model blending presented here include:

- A comparison of smart persistence, satellite-based CMV forecasts, different NWP models, and various combination approaches, all at an hourly resolution for intraday and day-ahead forecasting, conducted at seven U.S. sites (Perez et al. 2018).
- A comparison of ground-based scaled persistence, satellite-based CMV forecasts, and IFS forecasts, and a combination those three methods using linear regression with lead-time-dependent weights for sites in Germany, all at a 15-minute resolution.

Analyses of the RMSE over forecast lead times for these examples (Figure 9-19, Figure 9-20) illustrate the following:

- Ground-based-scaled or smart persistence performs better than NWP model forecasts in the first hour or even up to 3 hours ahead, depending on the NWP model (Figure 9-19).
- The performance of the satellite-based forecasts is similar to, or slightly better than, persistence in the first hour (Figure 9-19). For more than 1 hour ahead, satellite-based forecasts clearly outperform persistence. For forecasts at a 15-minute resolution, an advantage of the satellite-based CMV forecasts over scaled persistence is found from 30 minutes onward (Figure 9-20).
- Satellite-based forecasts outperform NWP models up to lead times ranging from 2–5 hours ahead, depending on the NWP model and also on the satellite model and evaluation site and period.
- The RMSE of persistence and satellite-based CMV forecasts increases much faster with the lead time than the RMSE of NWP models.
- The performance of NWP models considerably differs for intraday as well as day-ahead forecasts (Figure 9-19; compare also Section 9.4.3).
- The blending models clearly outperform single-model forecasts for all lead times. Whereas for intraday forecasting, a combination of persistence, satellite-based forecasts, and NWP forecasts is beneficial (Figure 9-20), integrating several NWP models considerably reduces the forecast RMSE in day-ahead forecasting (Figure 9-19).
- The performance of blending models differs with training data, e.g., using site-independent or site-specific ground truth, or using either ground-measured or satellite-derived irradiance values (Figure 9-19). The evaluations show that satellite-derived irradiance data are a suitable alternative to ground measurements for model training if the latter are not available.

These findings agree with other studies, e.g., those given in Section 9.5.2.

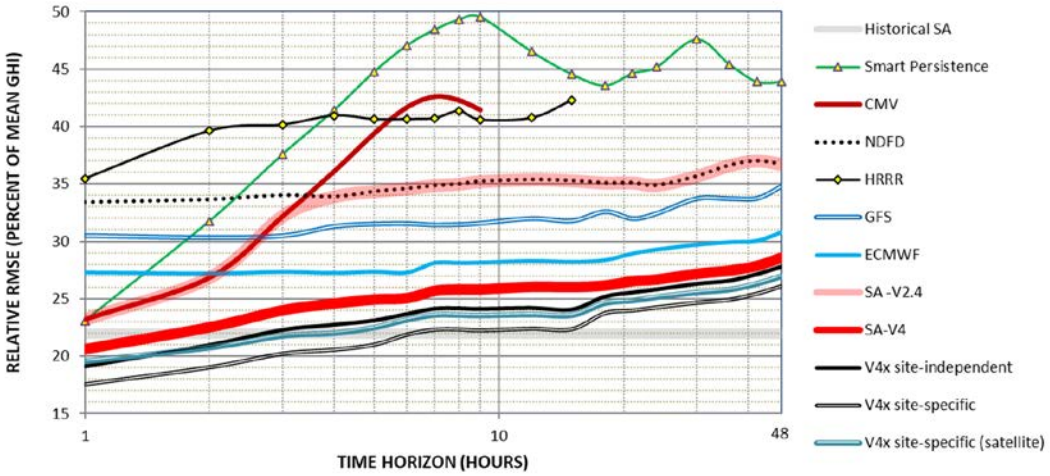

Figure 9-19. Relative RMSE of hourly GHI forecasts up to 48 hours ahead, with different approaches: ground-based smart persistence, satellite-based CMV forecasts (CMV), different NWP forecasts: NDFD, HRRR, GFD by NCEP, ECMWF IFS, and different blending models: SolarAnywhere (SA) V2.4, SA V4, V4 site independent; V4 site specific; and V4 site specific (satellite)

The RMSE of satellite-derived irradiance data (historical SolarAnywhere) is given for comparison. Data: Seven Surface Radiation Budget Network (SURFRAD) sites in the United States from July 2015–April 2016.

Image by Perez et al. (2018)

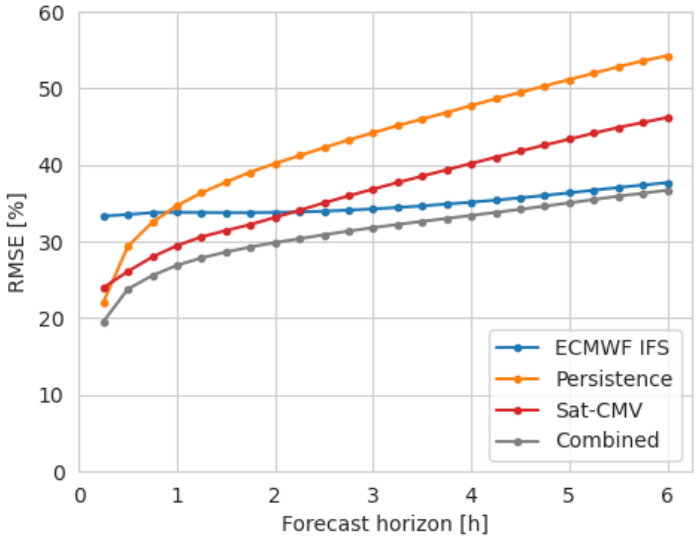

Figure 9-20. Relative RMSE (normalized to the average GHI) of 15-minute-resolution GHI forecasts over lead times up to 6 hours ahead for ground-based scaled persistence (persistence), satellite-based CMV forecasts (Sat-CMV), ECMWF IFS irradiance, and a combination of the three (combined)

Data: Eighteen sites in Germany operated by the German Weather Service during 2018.

Image by Fraunhofer ISE

9.6 PV Power Forecasting

PV power forecasts—pertaining to either a given PV plant, a portfolio of plants, or aggregated regional PV power—are important for plant operators, grid operators, and the marketing of the produced energy. They are based on irradiance predictions with the different models described in sections 9.2 through 9.5. To convert irradiance forecasts into PV power forecasts, physics-based or statistical and ML methods can be applied (Figure 9-21). Both approaches can also be combined. Complementing irradiance forecasts, near-real-time PV power measurements can be included as inputs.

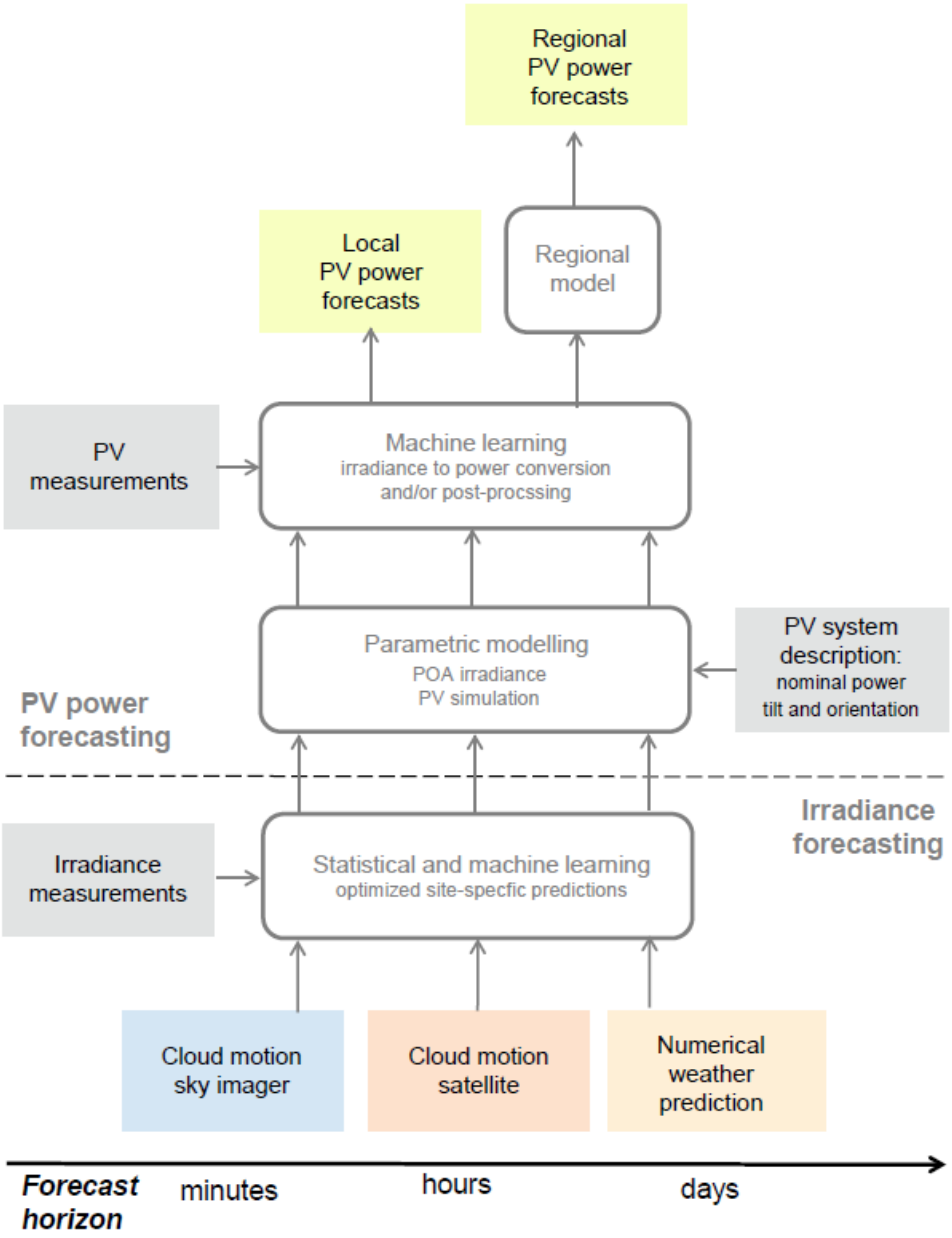

Figure 9-21. Overview of basic modeling steps in PV power prediction

Irradiance prediction: Different forecasting models for different forecast horizons (cloud motion from ASI and satellite data, NWP) and combinations with statistical and ML approaches for optimized site-specific predictions. PV power prediction: Conversion of irradiance to PV power with parametric PV simulation models and/or statistical ML approaches; regional PV power predictions require a regional model (e.g., upscaling) as a last step.

Image reproduced from Lorenz (2018)

Physics-based parametric modeling involves transposing GHI to POA irradiance and then applying a PV simulation model. For this, information on the characteristics of the PV system configuration is required in addition to the meteorological input data. The most important plant data include information on the installed capacity and module tilt and orientation. Further information on the module efficiency and inverter performance can also help to model the PV power output as a function of irradiance and temperature. For more detailed simulations,

additional information can also be used, for example, to model the local shading conditions. Alternatively, the relationship between the PV power output and irradiance forecasts and other input variables can be reverse-engineered with ML methods based on historical datasets containing measured and predicted PV power. In practice, these approaches are often combined; for instance, statistical postprocessing using measured PV power data can be applied to improve predictions with parametric simulation models.

PV power forecasting for plant operation, e.g., storage management, and direct marketing requires forecasts for single plants (Section 9.6.1). In contrast, PV power prediction for grid operators requires forecasts of the aggregated PV power generation for their grid areas or for grid nodes (i.e., regional forecasts are needed instead of single-site forecasts). These regional predictions are typically obtained by regional models, such as upscaling (Section 9.6.2). Portfolio forecasts are based on the same modeling approaches as single PV plants because they are typically generated as the sum of the forecast of the plants contributing to the portfolio. With respect to forecast performance, they benefit from regional smoothing effects, such as forecasts of regionally aggregated PV.

9.6.1 PV Power Forecasting for Single Plants

One way to forecast the production of a PV power plant is to apply a PV power simulation model to the forecast of the relevant predicting variables, primarily irradiance and ambient temperature, but possibly also other meteorological variables (e.g., (Pelland, Galanis, and Kallos 2013; Kühnert 2015)).

Here, the transposition of GHI into GTI to obtain the POA irradiance constitutes the first modeling step. Unless DNI and DHI are explicitly provided by the forecast model, this requires splitting GHI into its direct and diffuse irradiance components. For that purpose, many empirical diffuse or direct fraction models are available (see Section 9.5.3 and Chapter 7, Section 7.3.1 for discussion). Next, the direct and diffuse components are projected or "transposed" to the POA irradiance. The transposition of the direct irradiance is only geometric and thus straightforward. The transposition of the diffuse irradiance to POA requires models that ideally also account for the directional distribution of radiance over the sky, describing anisotropic effects, such as horizon brightening and circumsolar irradiance. Again, empirical models that were developed for the transposition of measured and satellite-derived irradiance data can be directly applied here. An overview of such models is given Chapter 7, Section 7.3.1.

In the next step, the POA irradiance is converted into PV power output. The available PV simulation models and tools, such as those described in more details in Chapter 11, Section 11.7, have been developed mostly in the context of long-term-yield predictions. They can also be directly applied to PV power forecasting. Deeper insight into the modeling of PV power and corresponding variables can be achieved with the tools provided by pvlib,[58] a software package for modeling PV systems (Andrews et al. 2014). Most simple PV simulation models use only the GTI on the POA as input. State-of-the-art PV simulation models consider additional influencing factors. The DC module efficiency depends on the POA irradiance and decreases with increasing temperature, which is typically considered in PV power forecasting systems. Additionally, it is secondarily affected by wind speed and direction, e.g., (Beyer et al. 2004). The angular and

[58] See https://pvlib-python.readthedocs.io/en/stable.

spectral distributions of irradiance are other influencing factors; however, these comparatively small effects are usually not included in detail in current PV power forecasting systems.

The availability of information on PV system parameters can be a problem when using such parametric models. A natural approach is to use the metadata available for the PV system—most importantly, peak power and orientation; however, this information is frequently missing or erroneous, especially for smaller PV systems, which can significantly decrease the PV power forecast quality. Information on the module and inverter specifications is less critical, hence standard values are typically used.

When historical power measurements are available for a PV plant, data-driven models tend to deliver the best results (e.g., Inman, Pedro, and Coimbra 2013; Gensler et al. 2016). Such models can reverse-engineer a lot of effects that depart from the idealized scenario by a physical model or that would require too detailed information, such as how different plant materials perform, how soiled the plant usually is, how the incident radiation is shaded or reflected by local surroundings, or how the plant has aged. Depending on how impactful these factors are at a particular site, generalized physical models might perform quite badly.

However, it is emphasized that measurement issues and plant outages can impact the performance of ML models. Failures of technical components are likely to have large impacts, but the same is true with curtailment caused by grid operation or electricity market price constraints. Proper quality control of PV power measurements and/or adapted training procedures (e.g., Saint-Drenan 2015) are therefore essential when applying ML models in PV power forecasting.

Data-driven models are used in different ways for PV power forecasts. They can be applied for the postprocessing of forecasts with PV simulation tools (e.g., Kühnert 2015). They can also be used to learn PV system parameters from historical data (e.g., Saint-Drenan 2015), or applied to directly transform predicted irradiance and other meteorological parameters into PV power forecasts.

Note that the ultimate objective of such regression or ML models is to minimize an error metric, typically the RMSE between the predictions and ground truth. These methods can only learn from the patterns that exist in the training data, which must be representative of the use case. The result tends to be smoothed, or they do not properly represent very high or low values to avoid large errors. ML can better learn specific factors about a power plant, such as when exactly it starts production at sunrise. But it might also focus the model on best predicting afternoons or summers when production values—and thus absolute errors—are larger. In any case, ML-generated results should always be visually inspected. Nevertheless, ML methods can learn both nonlinear and nonstationary relationships specific to any particular plant (Das et al. 2018; Ulbricht et al. 2013) and are prevalent when historical data is available.

It is not uncommon to train multiple models to the same plant for different weather inputs, time horizons, or seasons. Whereas a physical model uses an established relationship to derive power from irradiance, an ML method implicitly contains some kind of postprocessing to correct bias and optimize the performance between particular input and target data. Hence, different models

might be trained to calculate power from measurements, satellite-derived irradiance data, and intraday or day-ahead forecasts to eventually deliver the lowest errors possible in each use case.

9.6.2 Regional PV Estimation and Forecasting

Regional PV power estimates or forecasts aim to represent the aggregated PV output that is fed into the grid over regions that can range from a few streets feeding into a single, low-voltage substation, to a municipality, to a control zone of a distribution system operator or a transmission system operator, or even an entire country. A region could be geometrically defined, for which the allocation of which plants are in which region is clear, or it could be defined by a shared grid node, in which case detailed grid data might be needed or the selection of plants in the region might be uncertain or dynamic. A regional forecast represents an ensemble of contiguous plants in an area of interest, either geographically or within a branch of the electric grid. Thus, it tends to differ from a portfolio forecast that is used (e.g., in direct marketing).

Different approaches can estimate and forecast regional power, depending on what kind of data are available. Reference plant power measurements can be useful to estimate PV power output or to train forecasts. Weather-based models can use satellite-derived irradiance for real-time power estimation or NWP forecasts to predict future power generation. If metadata on the individual plants is available, the variation of the solar resource and plant characteristics within the region can be considered.

Data availability, however, poses a major challenge. Ideally, detailed registries of all installed plants would exist, and measurements would be available for all of them. Yet, in many countries, many solar plants (especially small ones) have been installed without any record. Existing data often belong to private companies (particularly measurements) or government institutions and often cannot be shared because of legal or privacy restrictions. Some private companies sell commercial datasets, but they are not necessarily representative, and sometimes they are aggregated to anonymize private data. Even among distribution system operators and transmission system operators, data quality and sharing can be a challenge.

Some national and international efforts are underway to create better and even public databases. At the very least, it is necessary to know how much PV capacity is installed in a region up to a given date. Organizations like the European Network of Transmission System Operators for Electricity (ENTSO-E) or the International Renewable Energy Agency (IRENA) aim to provide annual estimates of national PV generation and installed capacity. Detailed registries of data on individual plants are still needed, however. National efforts here include SOWISP in Spain (Jiménez-Garrote et al. 2023) and the market master data register (MaStR) in Germany. Methods for the automated recognition of plants based on satellite or aerial imagery are also improving, aiming to find missing installations and/or to validate information on their characteristics, e.g. (Kleebauer, Horst, and Reudenbach 2021). Nevertheless, this approach is still mostly experimental, so obtaining complete and accurate registries is still difficult in most countries.

Despite these challenges, an important aspect of regional forecasts is that the larger the region and the number of PV plants, the less the uncertainty because positive errors partly balance negative errors. Moreover, including more plants in the mix improves balancing the uncertainty of their characteristics, just as a larger region improves balancing the meteorological uncertainty of the solar resource.

9.6.2.1 Regional PV Power Without Plant Data and Measurements

In some countries, access to PV plant data and measurements is very restricted. When a provider of regional PV estimates and forecasts has no access to plant data or measurements in a region, some general approaches are still possible to evaluate the regional PV production directly from openly available meteorological information, such as satellite-derived irradiance data or NWP analyses or forecasts. If historical power estimates are available from a third party having access to more detailed data (such as from a grid operator), the strictly weather-based model can be optimized to best match the estimates with a method such as upscaling while avoiding the intermediate step of obtaining the details of the installed plants.

Perhaps the simplest and most economic approach is to treat the entire region as a VPP, whereby the solar resource in the region is averaged to a single value and the power is calculated as if originating from a single plant whose characteristics are somewhat representative of the aggregate. This method is known as *model inputs average*, and the power conversion can be made using the same methods as described in Section 9.6.1 for single PV plants (da Silva Fonseca Junior et al. 2014; Zamo et al. 2014; Pierro et al. 2020a). It is also possible to use multiple VPPs for different subregions or characteristics and to combine these into a single model (Pierro et al. 2017). It is not possible, however, to optimize a model for all the existing individual plants because there are too many degrees of freedom to train into a single regional target.

New areas of research include larger-scale ML methods, such as random forest or CNNs, as well as DL. These can be trained to a target estimate using the raw input of gridded weather data, attempting to learn the intraregional dependencies of the regional PV fleet; however, such approaches are not yet as widely researched as single-plant models. They run the risk of overtraining and are computationally expensive for large areas.

9.6.2.2 PV Plant Data

PV plant data for the power plants contributing to regional PV power feed-in is valuable information for regional estimates and forecasting. In its most basic form, plant data include the size, location, and installation date of the plants. This is used by more advanced regional methods that attempt to account for the regional variations of the installed plants as well as for the spatial variability of clouds. Plant location data normally consist of exact coordinates, but sometimes only a city or postal code is available. Depending on the spatial resolution of the reference plants or weather data, the latter might also suffice.

Additional installation information that is necessary or useful to calculate PV production but that is not always available includes, in roughly descending order of importance: the azimuthal direction and tilt of the arrays, the size of the inverter, whether the operator consumes any fraction of the power before feeding it in (with an estimate of how much they do consume on average), and whether there is storage or feed-in limits. The usefulness of some of this information depends on whether the value of interest is the overall production, the actual power feed-in, or the load to the grid.

Plant data can be collected from different sources, such as national registries, commercial datasets, and grid operators. It is more common to find data about large solar plants than small, household solar plants. For some regional PV estimation and forecasting approaches, statistical

modeling is used to account for missing or underrepresented data by using the available data from PV plants to extrapolate how common such plants are overall. Typical PV system characteristics, e.g., tilt and azimuth for different PV system sizes, were investigated in various studies, e.g., (Killinger et al. 2018). For example, the typical orientation of PV plants correlates with their size and the kind of surface on which they are installed, e.g., ground-mounted or rooftop systems. And whether a plant has storage or is designed for self-consumption can depend on its size and age, whether it is part of a household, the kind of incentives that were available at the time of installation, etc.

For regional forecasting, the differences between thousands of plants can quickly even out, although statistical differences might exist when comparing e.g., urban and rural areas. Figure 9-22 shows the distribution of array orientations in the German MaStR registry as a function of the number of plants as well as their capacity; the difference demonstrates how larger solar plans tend to be optimized, with a larger share of the systems oriented toward the equator with close to optimum tilt, whereas a larger variation in tilt as well as azimuth angles is found with smaller plants.

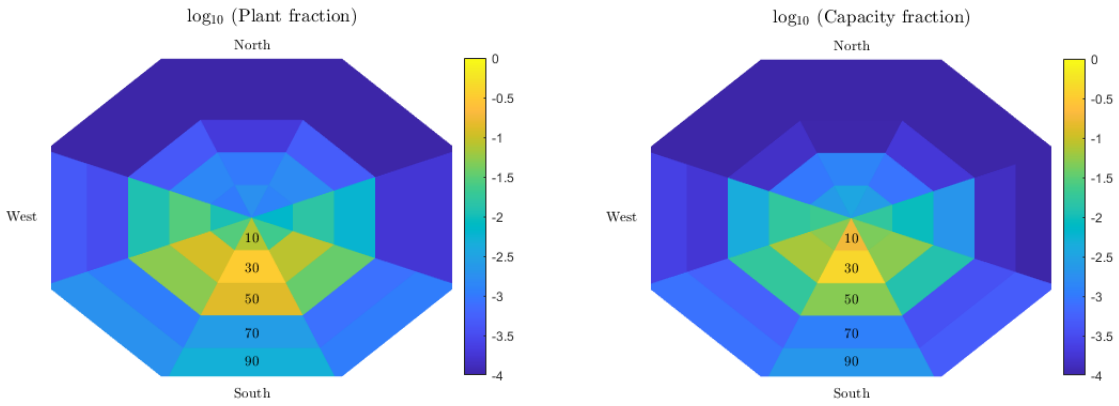

Figure 9-22. Fraction (on a log scale) of the number of plants (left) and overall capacity (right) installed for different plant geometries in Germany according to the MaStR registry as of June 2023

The angles are discretized in eight azimuth and five tilt categories. A linear scale would show essentially all plants to be somewhat southward facing, whereas the log scale better illustrates the frequency of all orientations.

Image by Fraunhofer IEE

9.6.2.3 Regional PV Power Upscaling

If the measurements of all PV power plants in a region are available, the regional production or feed-in would simply be their sum. Measurement availability, however, remains the exception. A region can contain millions of plants with only tens or at most thousands of them (typically large solar plants rather than household rooftop installations) being monitored at high temporal resolutions; however, it is possible to upscale the available power measurements to obtain a value for the entire region without any additional inputs, such as meteorological data, or physical modeling.

Note that there might be two different upscaled values: (1) a real-time estimate for markets and grid operation that is based on the available live measurements and (2) a more accurate estimate that can be calculated days or even weeks later, when all possible data have been gathered. The quality of the upscaling depends on the number and representativeness of the measurements.

The current popularity of the upscaling method stems, at least to some extent, from its large adoption in wind energy, where it is more suitable. Relatively many turbines are monitored, and they behave much more similarly to one another than do PV plants with diverse orientations. As PV installations increase, however, so should the popularity of more complex upscaling methods that account for different PV characteristics (Killinger et al. 2016).

If the reference plants in a region are both well distributed and representative, the first upscaling option is to simply scale the sum of their power measurements to the installed capacity of the entire region according to the plant data. Operationally, such an approach can also first be performed on smaller subregions or plant categories and then aggregated to different regions of interest, which considerably improves accuracy (Kühnert 2015; Lorenz et al. 2011; Saint-Drenan et al. 2016).

Another approach that uses data on PV system location relies on the spatial interpolation or extrapolation of the measurements to derive power values for the plants that are located between them (or simply to points on an installed capacity grid), as illustrated in Figure 9-23. There are many ways of doing this; see Li and Heap (2014) for a review. Inverse distance weighting is simple and robust and thus most common (Bright et al. 2018; Saint-Drenan et al. 2011), though kriging is also popular with irradiation data (Jamaly and Kleissl 2017; Yang et al. 2013).

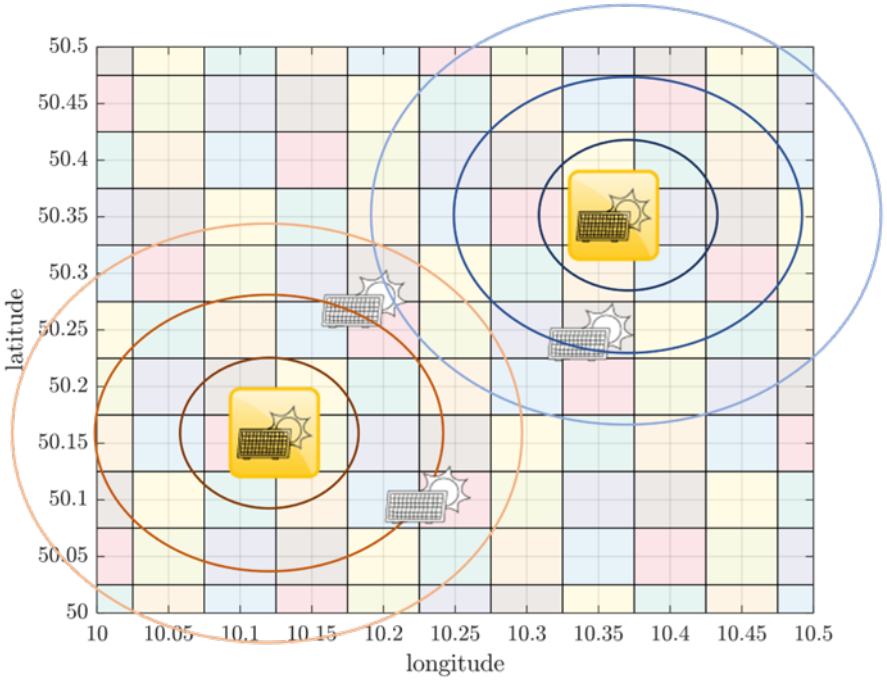

Figure 9-23. Illustration of the upscaling method based on two monitored PV plants (yellow) to also consider nonmonitored plants (black and white)

The weights for each reference plant decrease with distance. *Image by Fraunhofer IEE*

The upscaling approach used with reference measurements for regional power estimation is also popular for regional power forecasting, whereby the problem of regional forecasting is transformed into forecasting the production from every reference plant. As the reference plants have historical measurements to train on, this facilitates a data-driven approach of using, e.g., ML methods to forecast plant power from weather prediction data.

9.6.2.4 Physical Modeling of All PV Plants

Finally, all PV plants in a region can be simulated without any power measurements from meteorological data in combination with generalized physical models. Physical models can describe all known characteristics of each plant in a region and simulate their power output from appropriate local meteorological data, usually at higher spatiotemporal resolution than offered by reference plants. For computational efficiency, nearby plants with the same primary characteristics can also be grouped together.

A generalized physical model is fairly accurate and has the advantage of being able to provide results anywhere, even if a plant is not monitored. Note, however, that for any given plant, a generalized model cannot be as accurate as a model trained to actual measurements. Registry data do not include the efficiency curve of a particular inverter, how the plant might be shaded over different angles, or any other small details that a trained model might consider. In regional forecasting, it is generally sufficient to assume typical values for most plant characteristics and to statistically model or optimize the most important ones.

If the plant geometries are not known, a single POA can be used, or a distribution of tilts and orientations can be simulated at all locations and statistically weighted, e.g., (Saint-Drenan, Good, and Braun 2017). Similar statistical modeling is used by the Copernicus Climate Change Service to generate regional PV power for each region in Europe, with values for each country updated monthly and made available through the Copernicus Data Store.[59] If no local statistics on plant geometry are available, it is possible to modify the known geometry distributions from other countries according to the locally optimized tilt angle (Saint-Drenan et al. 2018). An alternative is to optimize the distribution of geometries to a power estimate. The relationship between plant tilt angles and latitude also somewhat depends on local architectural constraints. For instance, the geometry of installations made on flat roofs, which are typical in some arid climates, might be latitude-optimized as freestanding modules, whereas plants on tilted roofs are typically adapted to the roof orientation and therefore show a larger variation of geometries. In the future, moreover, diverse orientations might also be purposefully selected to better distribute the PV production throughout the day, even in the case of large installations.

Figure 9-24 shows a snapshot of a spatially resolved forecast from such a physical model based on a German plant registry using statistical modeling of the plants' orientations. The power production and feed-in are calculated everywhere according to the local cloud features and can be aggregated according to the local installed capacity. Although the figure's normalized values highlight the solar resource rather than the installed PV capacity, the self-consumption values demonstrate how the plants can have different characteristics in populated areas.

[59] See https://cds.climate.copernicus.eu.

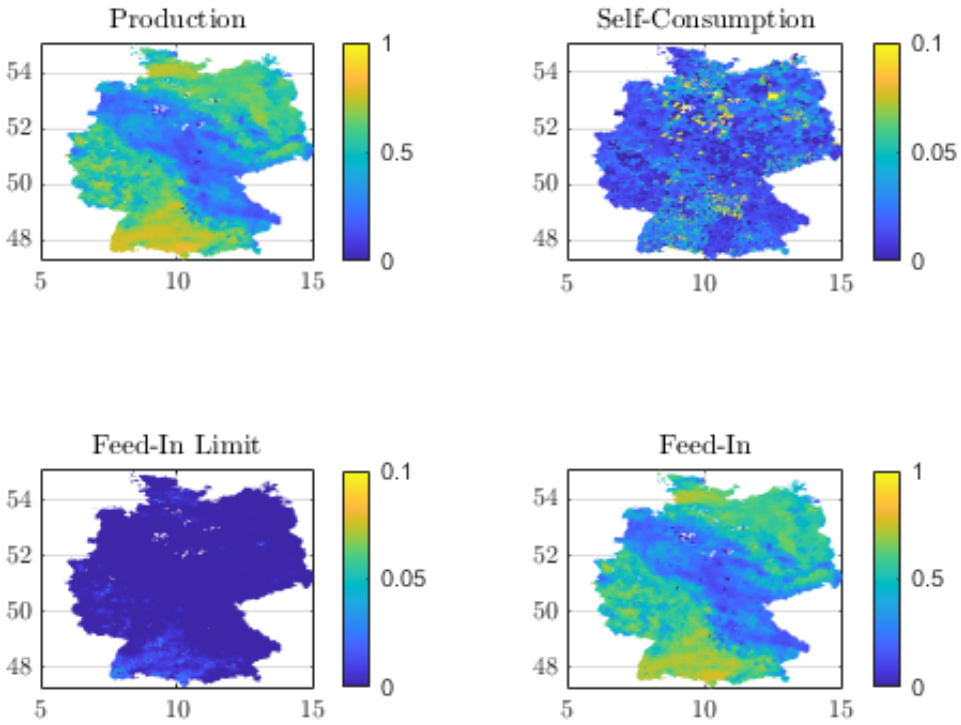

Figure 9-24. Snapshot of estimated local German PV values, normalized by installed capacity, according to real-time satellite data and a physical power model with probabilistic plant information from Fraunhofer IEE

"Feed-in limit" indicates power lost due to plants whose feed-in power is capped at, e.g., 70% of capacity.

Image by Fraunhofer IEE

9.6.2.5 PV Self-Consumption and Regional Power Feed-In

All of the energy produced by a solar power plant is not necessarily fed into the grid, which complicates the estimation and forecasting of PV power feed-in that are needed for smooth grid operation. Many small- or medium-size plants are installed on residences or commercial buildings, and such plants are now increasingly designed to allow behind-the-meter usage (i.e., self-consumption by the user), which was not necessarily the case in the past.

At any given moment, a user typically first self-consumes as much produced energy as possible, stores another fraction if battery storage exists, and feeds in the rest. The self-consumption and feed-in power might also be limited by the inverter size and any feed-in capping by the grid. The energy, S, that can be directly self-consumed at time t is:

$$S(t) = min\,(P_{AC}(t), L(t)), \qquad (9\text{-}5)$$

where P_{AC} is the current PV power generation, and L is the current system load. If the nominal power of a PV plant is small compared to typical loads, it will generally never feed in. If it is very large, then the load becomes less important; however, the load uncertainty of a particular household is typically much greater than that of the solar resource, making it very difficult to accurately forecast the feed-in power of any given plant with self-consumption. Loads are unique to every building and user because they depend on human behavior, have weekly and seasonal

cycles, and exhibit spikes when, e.g., compressors for refrigeration turn on or off. This is an interesting challenge to data-driven and upscaling forecasting strategies because most measurements are made only at the meter, making the measurements nontransferable, even between plants with otherwise identical characteristics. An advantage of physical models is that they do simulate PV generation and thus can be used to distinguish between power generation and feed-in.

If available, registry data on plant self-consumption tend to be either Boolean, i.e., whether or not a plant self-consumes at all, or (more rarely) a scalar value of how much of the production is consumed on average. The time dependency of the load or self-consumption is typically not recorded. Simple strategies to account for the general self-consumption on a plant-by-plant basis do exist in the form of either multiplication by a constant factor or subtraction of a constant load ("band method"). Standard load profiles can be used to introduce a time dependency, although these can greatly differ from any given real load because profiles are generally smooth and designed to represent an average of many users for grid resource planning. The aggregated demand over large regions is much more predictable and should make self-consumption easier to model regionally. Though this is technically a plant-by-plant problem, as self-consumption is determined by local load and generation (Eq. 9-5) and additionally local feed-in limits, battery size or maximum loading speed might also come into play. On a single-plant level, stochastic bottom-up models can be used for local consumption and PV generation, as proposed by Karalus et al. (2023).

The share of self-consumption depends on national regulations and strongly varies between countries and even between regions within a country. For areas with a low self-consumption rate, simple approaches can also be expected to yield reasonable results, on average. Figure 9-25 shows a week of satellite-based estimates of self-consumption compared to production and feed-in power in a control area in Germany Annually, this statistical model estimates that self-consumption currently amounts to approximately 3% of total production in the control zone, which is similar to the value obtained by aggregating the self-consumption averages in the plant metadata. The same model estimates that feed-in limits were rarely active and only reduced the feed-in power by approximately 0.3% annually.

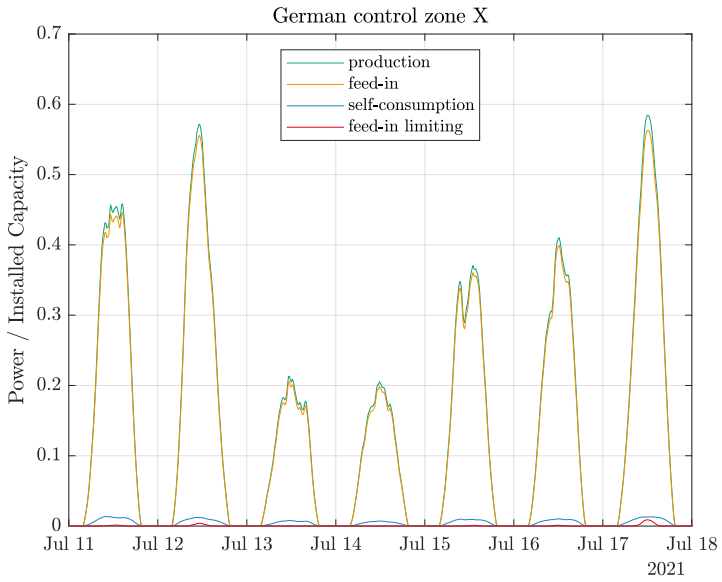

Figure 9-25. One-week time series obtained with the same physical power model and probabilistic plant information from Fraunhofer IEE shown in Figure 9-24 but now aggregated to a control zone

Image by Fraunhofer IEE

The seasonal dependence of PV self-consumption is illustrated in Figure 9-26 for another control area in Germany with an average self-consumption share of 9.5% in 2018 (Karalus et al. 2023). During summer with higher PV generation, self-consumption rates are smaller than during winter with low PV generation. The figure also shows different shares of self-consumption for different portfolios of PV-load systems, depending on PV system size and residential or commercial loads, among other factors.

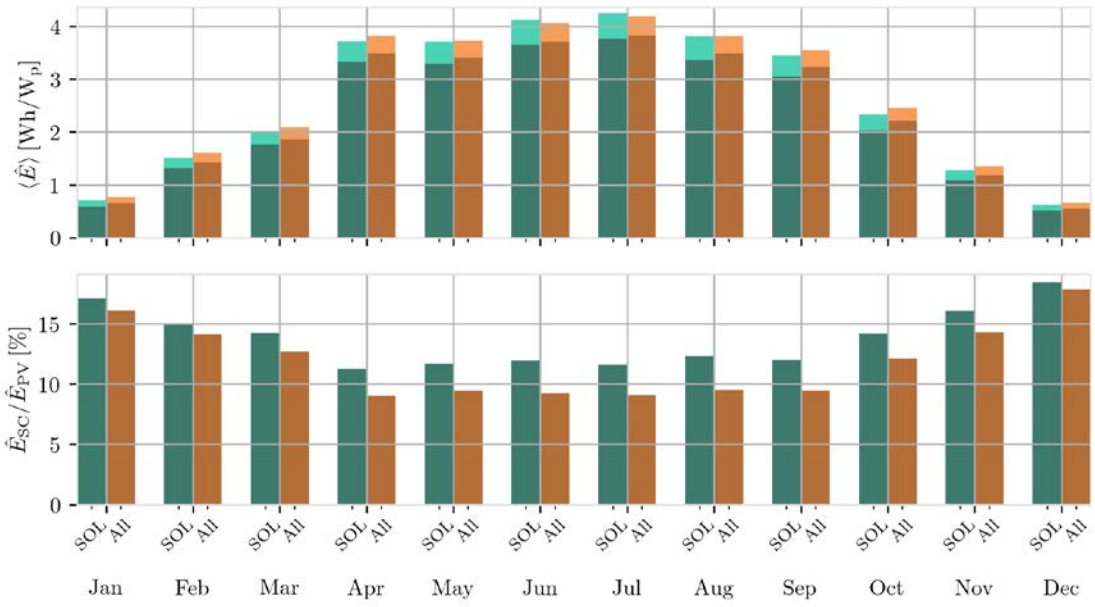

Figure 9-26. Monthly self-consumption derived with a stochastic bottom-up model for a German control area (TransnetBW) during 2018

Top: Monthly average of daily specific PV generation (normalized to the installed PV power) split into feed-in power (dark colors) and self-consumption (light colors) for a portfolio of PV systems with feed-in monitoring (SOL, green) and for all PV systems in the control area (All, orange). Bottom: Corresponding self-consumption rates per month.

Image by Karalus et al. (2023)

It must be emphasized that the share of PV self-consumption is quickly growing in many countries. In Germany, for example, the majority of new PV installations are designed for self-consumption. At the current rate of PV growth, self-consumption will soon have a first-order effect on regional PV power feed-in. It is difficult to find measurements of both production and feed-in power for plants throughout a region to validate self-consumption models because usually only feed-in power is measured, the measurements are not communicated, or the data are protected by privacy laws. In the future, behind-the-meter forecasting will play a crucial role (Erdener et al. 2022).

9.6.2.6 Regional PV Best Practices

Estimates and forecasts of regional PV production and feed-in can be made by the different methods described here, depending on which plant data, reference measurements, and/or regional estimates are available. Complementary to these basic approaches, preprocessing techniques such as calibrating and blending weather predictions to measurements are common, as are postprocessing techniques such as model output statistics or multi-models trained to good estimates. Figure 9-27 illustrates such a forecasting chain.

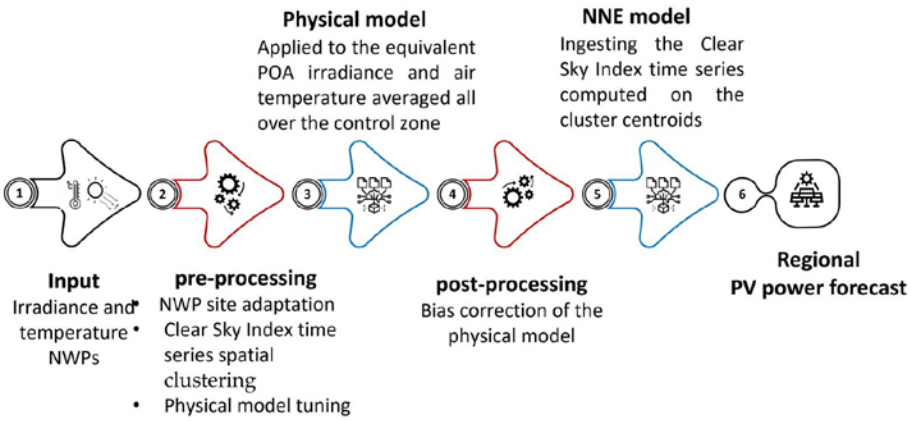

Figure 9-27. Diagram of a hybrid method used to predict regional solar generation

NNE model denotes Neural Network Ensemble model. Image by Eurac Research

Different approaches can also be combined to form hybrid models: A generalized ML model can replace a physical model for a nonmonitored plant or a VPP; physically simulated plants can complement an upscaling approach; and statistical modeling can be restricted to represent only nonmonitored plants, to be combined with data-driven plant forecasts for dynamic aggregation later. Some examples can be found in the literature, e.g., (Gigoni et al. 2018; Pierro et al. 2020a, 2017, 2015), whereas others are proprietary techniques used by commercial forecast providers.

Postprocessing steps are commonly used to improve performance and correct model bias, particularly when there is a target estimate. Different products can finally be combined into a model mix using ML, as is typically performed by a grid operator when receiving data from several forecast providers. Note that such calibrations are not always a better representation of reality because they might only minimize the error to a target estimate that can itself be biased. For instance, this occurs because of the upscaling of unrepresentative plants or the effects of self-consumption and storage.

9.6.2.7 Performance of Regional PV Power Forecasting: Example Evaluation for Italy and Germany

Regional forecasts show much lower uncertainties than single-site forecasts. This also holds for portfolio forecasts for distributed PV systems. By enlarging the footprint of the forecast region of interest, forecast errors are reduced, e.g., (da Silva Fonseca Junior et al. 2014; David et al. 2016a; Hoff and Perez 2012; Kühnert 2015; Lorenz et al. 2009, 2011; Pierro et al. 2020a; Saint-Drenan et al. 2016). This phenomenon, also called regional averaging or smoothing effect, is related to the correlation between the forecast errors at different locations. The larger the region, the less correlated the irradiance conditions are between different sites, and thus also solar forecast errors. This subsequently leads to a higher accuracy of the regional PV power forecasts.

An example is shown in Figure 9-28, which depicts the RMSE of hourly day-ahead forecasts in Italy, obtained by predicting the PV generation of different control areas using averaged model inputs and directly forecasting the power generation at market zone level (Pierro et al. 2020a).

In addition, a measure of PV power variability is displayed in Figure 9-28. With $P(t)$ denoting the PV power output at time *t,* the change in PV power for a given time step, Δt, is defined as:

$$\Delta P_{\Delta t} = P(t) - P(t - \Delta t). \quad (9\text{-}6)$$

Hourly values and a time step, Δt, of 24 hours are specifically considered in Figure 9-28.

The PV power variability in each zone is defined as the standard deviation, $\sigma(\Delta P_{\Delta t})$, as proposed by Perez et al. (2016), which is equivalent to the RMSE of the persistence of PV power:

$$RMSE_{per} = \frac{1}{\sqrt{N}} \sqrt{\sum_{i=1}^{N} (\Delta P_{\Delta t})^2} = \sigma(\Delta P_{\Delta t}). \quad (9\text{-}7)$$

Here, it is commonly assumed that the temporal average of $\Delta P_{\Delta t}$ should be zero.

Both the variability and the forecast errors decrease with an increase in the size of the region and the number of PV systems considered. These quantities can be well fitted either by a hyperbolic function, similar to the one proposed in Perez et al. (2016) or by an exponential function, as proposed by Lorenz et al. (2009). As shown in Figure 9-28, by enlarging the footprint of the forecast region from the prediction of the PV generation in each market zone in Italy to the prediction of the PV generation over all of Italy, the RMSE can decrease from 5.5% (market zones average) to 3.6% (countrywide).

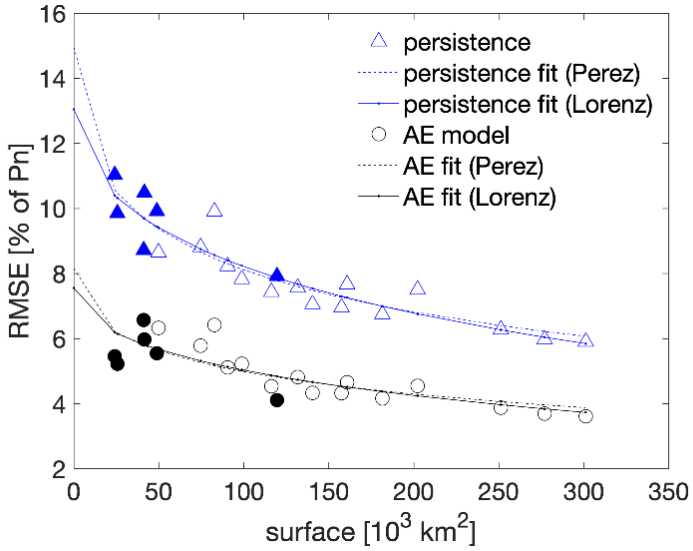

Figure 9-28. Smoothing effect over Italy: Relative RMSE (normalized to the nominal power, Pn) of regional forecasts with an analog ensemble (AE, circles) and persistence (triangles) as a function of the area size of the market zones in Italy (full circles/triangles) and for areas merging several adjacent market zones (empty circles/triangles)

Dashed lines correspond to a fit using the function proposed by Perez et al. (2016), and solid lines correspond to a fit using the function proposed by Lorenz et al. (2009).

Image by Pierro et al. (2020a)

Another important aspect about regional forecasting is that, depending on forecast horizon, performance differences between models and model ranking can change compared to single-site forecasting. An example is illustrated here for the German PV power forecasting system described in Kühnert (2015); see Figure 9-29. Whereas for single sites NWP-based forecasts outperform PV power measurement-based persistence within lead times of less than 1 hour

ahead, measurement-based persistence shows a considerably smaller German-average RMSE than NWP-based forecasts for up to 3 hours ahead. Also, the improvement in the first hours of satellite-based forecasts over NWP-based forecasts is found to be much larger for regional forecasts than for single-site forecasts.

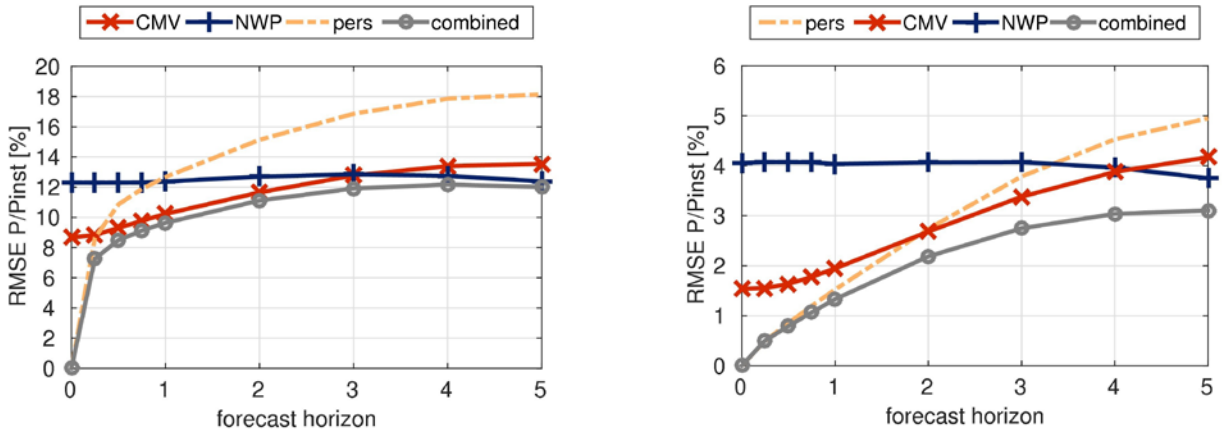

Figure 9-29. Relative RMSE (normalized to the installed PV power, P_{inst}) of 15-minute resolutions over PV power forecasts for lead times up to 5 hours ahead. The results are based on the persistence of PV power measurements (pers), satellite-based CMV (cmv), NWP (ECMWF IFS and DWD COSMO-EU), and a combination of the three (stepwise linear model).

Left: Average single site RMSEs; right: RMSE of aggregated regional PV power considering all sites. Data: 921 PV stations in Germany, May 2013–November 2013, solar zenith angles below 80°.

Image by Kühnert (2015)

Finally, although regional PV power forecasting benefits from spatial averaging because forecast errors decrease especially under variable cloud conditions, challenging weather conditions still remain in regional forecasting. For instance, the large-scale formation and dissipation of fog is difficult to predict and can lead to large regional forecast errors (Köhler et al. 2017). Similarly, snow adhering to PV systems can have a large impact on regional forecast accuracy (Lorenz, Heinemann, and Kurz 2012).

To summarize, regional PV generation exhibits much lower variability and increased forecast accuracy than single PV systems. Exploiting these averaging effects requires a well-developed grid infrastructure and a structure of the energy market adapted to decentralized and variable renewable energy systems.

The accuracy of irradiance forecasts has greatly improved over time, and it has also contributed to reduce uncertainties in the mean irradiance conditions relevant to regional PV feed-in power. The current quality of regional estimates and forecasts thus greatly depends on the quality of PV modeling and the availability of plant data and/or measurements. The procurement of such data is necessary to facilitate a successful energy transition and will require a concerted effort in most countries in the coming years.

9.7 Probabilistic Solar Forecasts

Any forecast is inherently uncertain, and the proper assessment of its associated uncertainty offers grid and plant operators a more informed decision-making framework. For example, a forecast that includes prediction intervals is of genuine added value and, if appropriately incorporated into grid operations, might increase the value of solar power generation (Morales et al. 2014).

This section is restricted to the univariate[60] context that corresponds to those probabilistic forecasts that do not consider the spatiotemporal dependencies generated by stochastic processes such as solar power generation. Two types of solar probabilistic forecasts are considered here: *quantile forecasts* and *ensemble forecasts* (i.e., those using the Ensemble Prediction System (EPS)). Quantile forecasts are quite versatile probabilistic models and, as such, might address a wide range of forecasting time horizons, whereas NWP-based EPS forecasts generally provide probabilistic forecasts for one or several days ahead. Probabilistic forecasting requires a rather complex verification framework, which is introduced in Chapter 10, Section 10.5.1.5. The evaluation framework is based on visual diagnostic tools and a set of scores that mostly originate from the weather forecast verification community (Wilks 2019). What follows constitutes an overview of the basic concepts related to solar probabilistic forecasting methods. Comprehensive overviews regarding forecasting methods and the verification of solar probabilistic forecasts metrics can be found in Antonanzas et al. (2016); Lauret, David, and Pinson (2019); and Van Der Meer, Widén, and Munkhammar (2018).

9.7.1 Nature of Probabilistic Forecasts of Continuous Variables

In contrast to deterministic forecasts, probabilistic forecasts provide additional information about the inherent uncertainty embodied in all forecasting models. The probabilistic forecast of a continuous variable, such as solar power generation or solar irradiance, takes the form of either a cumulative distribution function (CDF), $F(Y)$, or a probability distribution function (PDF), $f(Y)$, of the random variable of interest, Y (e.g., GHI). In particular, the CDF of a random variable, Y, is given as:

$$F(y) = P(Y \leq y) \tag{9-8}$$

where $P(Y \leq y)$ represents the probability that Y is less or equal to y.

The predictive distribution can be summarized by a set of discrete quantiles. The quantile, q_τ, at probability level $\tau \in [0,1]$ is defined as follows:

$$q_\tau = F^{-1}(\tau), \tag{9-9}$$

where F^{-1} is the so-called *quantile function*. A quantile, q_τ, corresponds to the threshold value below which an event, y, materializes with a probability level, τ.

[60] Future work will be devoted to multivariate probabilistic models capable of capturing the spatiotemporal correlations present in irradiance and PV forecasts.

Further, prediction intervals (also called interval forecasts) can be inferred from a set of quantiles. Prediction intervals define the range of values within which the observation is expected to be with a certain probability (i.e., its nominal coverage rate) (Pinson et al. 2007). For example, a central prediction interval with a coverage rate of 95% is estimated by using the quantile $q_{\tau=0.025}$ as the lower bound and $q_{\tau=0.975}$ as the upper bound. Figure 9-30 shows an example of probabilistic forecasts of solar irradiance where prediction intervals have been computed for nominal coverage rates ranging from 20%–80%.

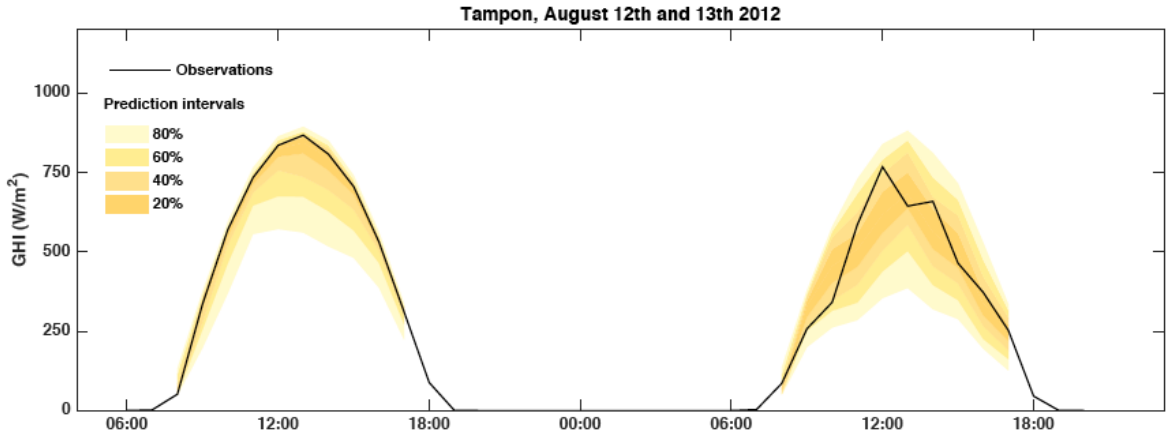

Figure 9-30. Example of probabilistic solar irradiance forecasts: 2 days of measured GHI at Le Tampon, France, and associated 1-hour-ahead forecasts with prediction intervals (yellow) generated with the quantile regression forest model

Image by PIMENT, University of La Reunion

9.7.2 Quantile Forecasts

Two approaches are commonly used in the community to generate quantile forecasts (see Figure 9-31) for different forecast horizons. As input, they use either online ground observations and satellite images for intraday forecasting or NWP deterministic forecasts, which are more effective for day-ahead forecasting. The former approach (e.g., Bacher, Madsen, and Nielsen 2009; Pedro et al. 2018) consists of directly generating the quantiles of the predictive distribution of the variable of interest (e.g., GHI, DNI, or PV power). The latter approach (e.g., David et al. 2016; Grantham, Gel, and Boland 2016; Lorenz et al. 2009; Pierro et al. 2020b) seeks to produce the interval forecasts from the combination of a deterministic (point) forecast and quantiles of the prediction error. In both approaches, the quantiles can be estimated either by assuming a parametric law for the predictive distribution or by nonparametric methods, which make no assumptions about the shape of the predictive distribution.

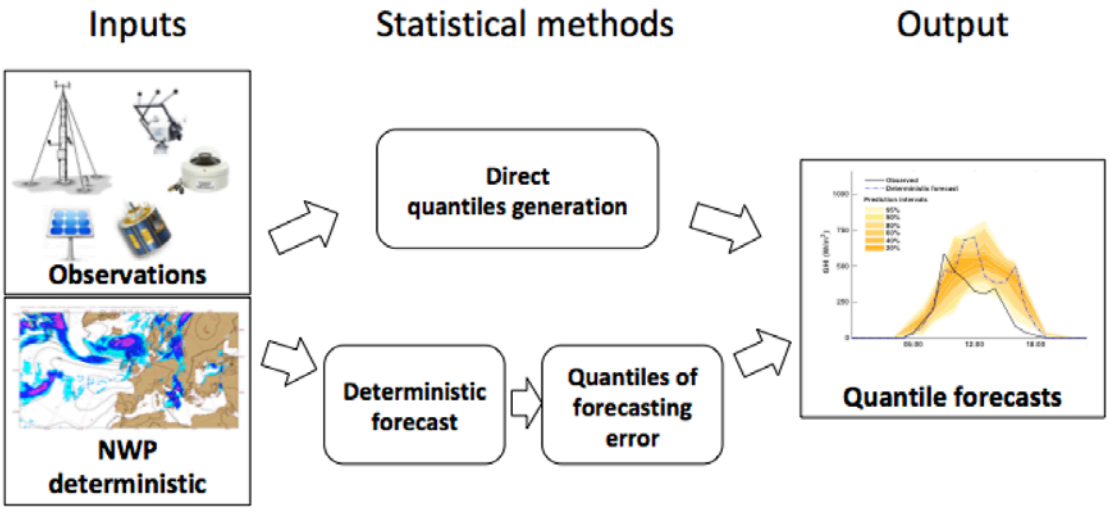

Figure 9-31. Two typical workflows used to generate quantile forecasts from recent past observations and/or deterministic NWP forecasts

Image by PIMENT, University of La Reunion

9.7.2.1 Parametric Methods

Parametric models assume that the variable of interest or the prediction error follows a known law of distribution (e.g., a doubly truncated Gaussian for GHI or a Gaussian for the error distribution). Only a few quantities (e.g., mean and variance) are needed to fully characterize the predictive distribution. Consequently, this approach is particularly interesting in an operational context because it requires low computational effort.

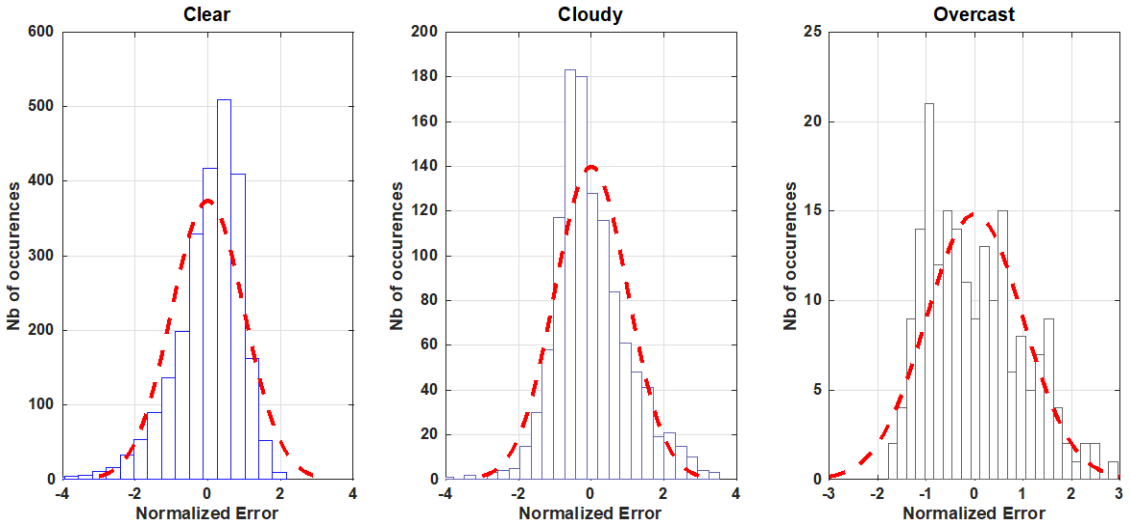

Figure 9-32. PDF of the normalized error (zero mean and unit variance) of the hourly profile of day-ahead forecasts of the clear-sky index provided by ECMWF for three different sky conditions and for the site of Saint-Pierre (21.34°S, 55.49°E), Reunion, France, in 2012

The red dashed line represents the fitted standard normal PDF.

Image from David and Lauret (2018)

In the solar forecasting community, it is very common to fit a Gaussian distribution to the errors even though errors derived from deterministic forecasts of solar irradiance or of the clear-sky index do not usually follow a Gaussian distribution (see Figure 9-32). For instance, Lorenz et al. (2009) developed a probabilistic irradiance forecasting model by assuming a Gaussian distribution of the error of the deterministic GHI forecasts generated by the IFS. More precisely, the predictive CDF was a Gaussian distribution with a mean corresponding to the point forecast and a standard deviation derived from a fourth-degree polynomial function for different classes of cloud index and solar elevation. For intrahour and intraday solar irradiance probabilistic forecasts, David et al. (2016) assumed a Gaussian error distribution of the deterministic forecast to generate a predictive CDF with a Generalized AutoRegressive Conditional Heteroskedasticity (GARCH) model. Instead of fitting a parametric PDF to the error distribution, Fatemi, Kuh, and Fripp (2018) proposed a framework for parametric probabilistic forecasts of solar irradiance using the beta distribution and standard two-sided power distribution.

9.7.2.2 Nonparametric Methods

To circumvent the necessity of making assumptions about the shape of the predictive distribution, numerous nonparametric methods have been proposed in the literature, e.g., Van Der Meer, Widén, and Munkhammar 2018. Examples of techniques include bootstrapping (Efron 1979; Grantham, Gel, and Boland 2016), kernel density estimation (Parzen 1962), and k-nearest neighbors (Pedro et al. 2018). Here, two prominent and simple nonparametric methods are briefly discussed: the quantile regression and the analog ensemble (AnEn) technique.

Quantile regression models relate quantiles of the variable of interest (predictand) to a set of explanatory variables (predictors). Statistical or ML techniques—such as linear quantile regression, quantile regression forest, or gradient boosting (David and Lauret 2018; Van Der Meer, Widén, and Munkhammar 2018)—are commonly used to produce the set of discrete quantiles with probability levels spanning the unit interval (see Figure 9-33).

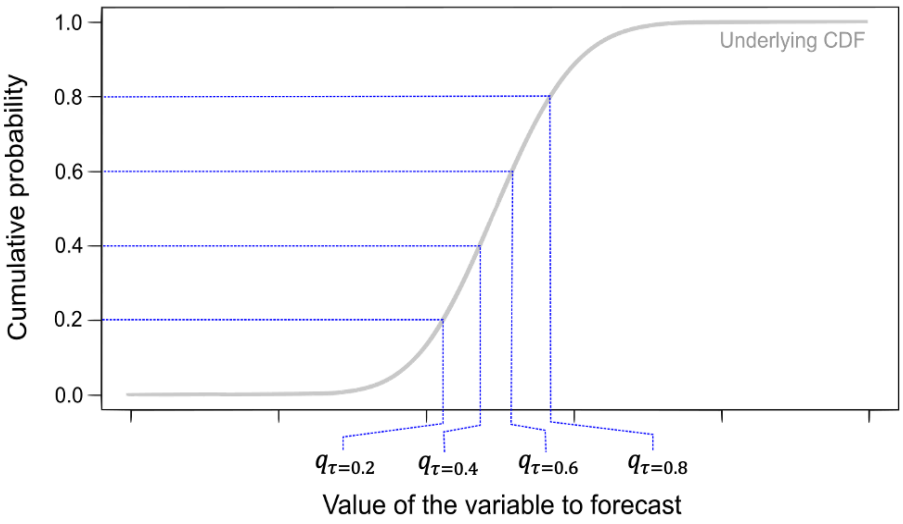

Figure 9-33. Illustration of a set of four discrete quantiles with probabilities ranging from 0.2–0.8

Image by PIMENT, University of La Reunion

The following summarizes the linear quantile regression method first proposed by Koenker and Bassett (1978); see David, Luis, and Lauret (2018) for details about the implementation of other regression methods, including other variants of the linear quantile regression, quantile regression forest, quantile regression neural network, and boosting.

The linear quantile regression technique estimates a set of quantiles of the CDF, F, of some response variable, Y (the predictand), by assuming a linear relationship between the quantiles of Y (q_τ) and a set of explanatory variables, X (the predictors):

$$q_\tau = \beta_\tau X + \epsilon, \tag{9-10}$$

where β_τ is a vector of the parameters to be optimized at each probability level, τ, and ϵ represents a random error term (Koenker and Bassett 1978).

Numerous implementations of the linear quantile regression technique (and of its related variants) have been proposed in the literature to generate quantile forecasts for different forecast horizons and using different types of predictors, X; see, e.g., Bacher, Madsen, and Nielsen (2009), Bakker et al. (2019), and Zamo et al. (2014) for NWP-based forecasts; Lauret, David, and Pedro (2017) for time-series forecasting; Nouri et al. (2023) for ASI forecasting; and Van Der Meer, Widén, and Munkhammar (2018) for a wider review.

The AnEn method (Delle Monache et al. 2013) is a simple nonparametric technique used to build the predictive distributions. The aim is to search for similar forecasted conditions in the historical data and to create a probability distribution with the corresponding observations. Alessandrini et al. (2015) applied an AnEn approach to a set of predicted meteorological variables (e.g., GHI, cloud cover, and air temperature) generated by the Regional Atmospheric Modeling System (RAMS). Note that the AnEn technique is mostly employed for day-ahead forecasting and generates the predictive distribution using NWP deterministic forecasts.

9.7.3 Ensemble Prediction System

9.7.3.1 Definition

The EPS corresponds to a perturbed set of forecasts generated by slightly changing the initial conditions of the control run and of the modeling of unresolved phenomena (Leutbecher and Palmer 2008). Figure 9-34 shows a schematic representation of an ensemble forecast generated by an NWP model. The trajectories of the perturbed forecasts (blue lines) can strongly differ from the control run (red line). The spread of the resulting members (blue-shaded area) represents the forecast uncertainty. For example, the ECMWF provides an ensemble forecast from the IFS model. It consists of 1 control run and 50 “perturbed” members.

Though members of the ensemble are not directly linked to the notion of quantiles, they can be seen as discrete estimates of a CDF when they are sorted in ascending order. Lauret, David, and Pinson (2019) proposed different ways to associate these sorted members to a CDF.

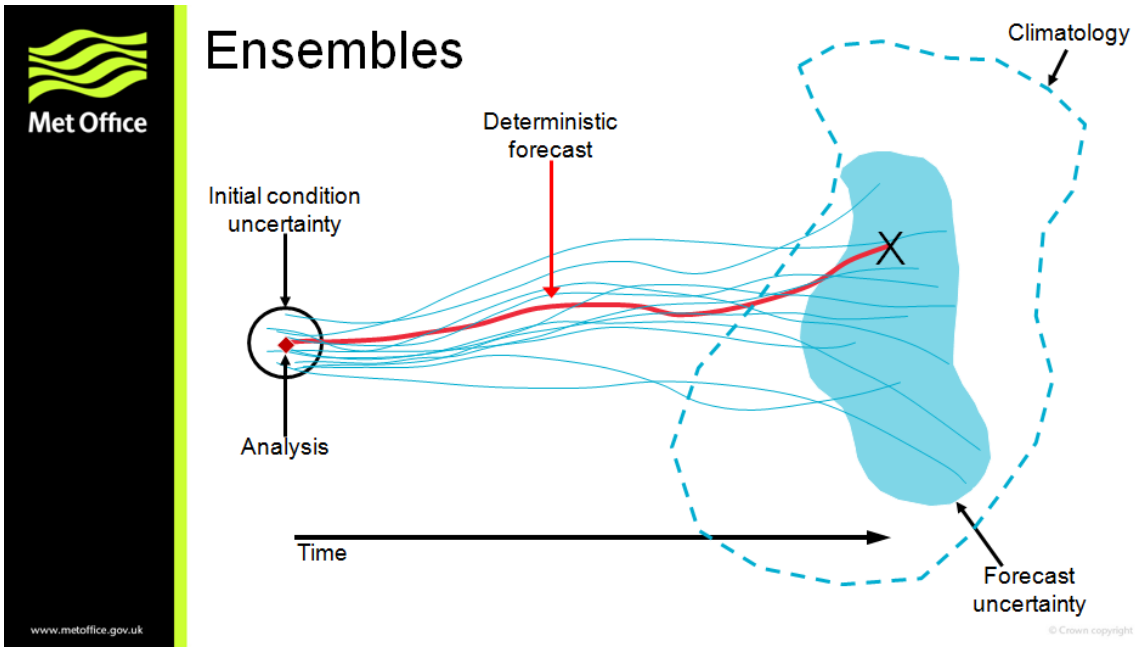

Figure 9-34. A schematic illustration of an ensemble forecast generated with an NWP model

Image from Met Office, © British Crown copyright (2021)

9.7.3.2 Postprocessing of the Ensemble Prediction System

Global and regional NWPs are designed to forecast a large variety of meteorological variables (precipitation and temperature being of utmost importance for society) and have not previously focused on the accurate generation of the different components of solar radiation. Consequently, raw ensembles provided by meteorological centers suffer from a lack of accuracy, a lack of calibration, or both (Leutbecher and Palmer 2008). See, e.g., Yang (2020) for definitions and discussions about the specific meaning of accuracy, calibration, and other specialized terms in the field of forecasting, some of which are further discussed in Chapter 10, Section 10.5.1.5. Overall, raw ensemble forecasts are systematically refined by postprocessing techniques (also called calibration techniques) to further improve their quality.

The aim of postprocessing is to apply a statistical calibration to the PDF drawn by the raw initial ensemble forecasts to optimize a specific metric used to assess the quality of probabilistic forecasts (e.g., the continuous ranked probability score [CRPS] described in Chapter 10, Section 10.5.1.5) In addition to having a coarse spatial resolution, the ensemble forecasts from NWPs are known to be underdispersive. i.e., they exhibit a lack of spread (Leutbecher and Palmer 2008). To address this, Sperati, Alessandrini, and Delle Monache (2016) proposed two different correction methods already used in the realm of wind forecasting: the variance deficit method, designed by Buizza, Richardson, and Palmer (2003) and the ensemble MOS method proposed by Gneiting et al. (2005). Even if these methods cannot be considered parametric, they are based on the characteristics of a normal distribution. Indeed, such a distribution is appealing because it can be assessed with only two parameters: the mean and the standard deviation, which are related to the average bias and the spread of the ensemble, respectively.

Another method of calibration is based on the rank histogram (see Chapter 10, Section 10.6.3.2), which was initially proposed by Hamill and Colucci (1997) for precipitation forecasts. Zamo et

al. (2014) applied this method to the Météo-France EPS, called PEARP, to generate probabilistic solar forecasts. The aim of this method is to build a calibrated CDF from the rank histogram derived from past forecasts and observations. Other techniques of EPS calibration exist in meteorology. For example, Pinson (2012) and Pinson and Madsen (2009) suggested a framework for the calibration of wind ensemble forecasts. Junk, Delle Monache, and Alessandrini (2015) proposed an original calibration model, based on the combination of nonhomogeneous Gaussian regression and AnEn models, for wind speed forecasting applied to ECMWF-EPS predictions. Likewise, Hamill and Whitaker (2006) suggested an adaptation of the AnEn technique for the calibration of ensemble precipitation forecasts using the statistical moments of the distribution, such as the mean and spread of the members as predictors. See Wilks (2019) for a thorough review of univariate ensemble postprocessing methods.

9.7.4 Benchmark Probabilistic Models

This section describes benchmark or baseline probabilistic models used to gauge the performance of new proposed probabilistic methods using skill scores, such as the continuous rank probability skill score. By analogy with the deterministic approach, persistence ensemble (PeEn) models based on GHI (Alessandrini et al. 2015) and on the clear-sky index (David et al. 2016) have been proposed. The empirical CDF of a PeEn forecast is simply built with the most recent k past measurements of solar irradiance. Considering an infinite number of past measurements, the PeEn simply becomes the climatology. In numerous other fields of meteorology, climatology is often considered to be a reference that can be used to test the performance of probabilistic models (Wilks 2019). That is because the climatology is perfectly reliable; however, it has no resolution.

Climatological reference models for probabilistic solar irradiance forecasting should account for the deterministic course of solar irradiance. The complete-history persistence ensemble proposed by Yang (2019) corresponds to a conditional climatology where the time of day is used as a predictor. The so-called clear-sky-dependent climatology (CSD-Clim) (Le Gal La Salle, David, and Lauret 2021)) is based on a similar approach but using the clear-sky irradiance as predictor instead of the time of day. Another simple approach consists of deriving the distribution of the clear-sky index from a long-term dataset and deriving the irradiance distribution by multiplication with clear-sky irradiances (Nouri et al. 2023). A comparison of these baseline models based on clear-sky index distributions derived from a long-term dataset of GHI and DNI in Almeria (Spain) by Nouri et al. (2023) shows only minor differences between the different approaches with a slight advantage for CSD-Clim. Because all three benchmark models consider the current conditions of the sun's position and atmospheric turbidity, the influence of further discretization over the time of day or clear-sky irradiance is small. Finally, for ensemble forecasts, the CRPS of the raw ensemble can serve as a benchmark.

9.8 Summary and Recommendations for Irradiance Forecasting

Solar power forecasting is essential for the reliable and cost-effective system integration of solar energy. It is used for a variety of applications with specific requirements with respect to forecast horizon and spatiotemporal resolution. To meet these needs, different solar irradiance and power forecasting methods have been developed, including physical and empirical models, as well as statistical and ML approaches. Based on these developments, forecasting services of good quality are now available for users.

An overview of the basic characteristics of different forecasting approaches is given in Table 9-2: (1) time-series models based on local measurements, (2) ASI and satellite-based forecasting, and (3) regional and global NWP models. These characteristics include forecast horizon, update frequency, temporal resolution, spatial resolution, and coverage, complemented with some practical information. Beyond using one of these forecasting models, blending of different forecasts using statistical and ML models (Section 9.5) is frequently applied to enhance forecast accuracy.

The different forecasting approaches with their corresponding input data and their applicability for different requirements are summarized in the following, with the spatiotemporal resolution of irradiance forecasts generally decreasing with increasing forecast horizon:

- Short-term forecasting up to approximately 1 hour ahead greatly benefit from the use of local online irradiance or PV power measurements as input; however, pure time-series approaches, based on local measurements only, are outperformed by approaches integrating empirical and/or physical model forecasts from a few minutes to hours onward, depending on the spatiotemporal scale of the forecasts and the climatic conditions of the forecast location.
- Short-term irradiance forecasts up to 20 minutes ahead that resolve irradiance ramps with a temporal resolution of minutes or even less can be derived from ASIs using cloud motion and/or ML-based methodologies. Using information on the local cloudiness around the site under scrutiny, state-of-the-art ASI models outperform persistence based on single-site measurements for high-resolution intrahour forecasting. Local hardware typically consists of a radiometric station, one ASI for point forecasting, and at least two ASIs for spatially resolved irradiance fields.
- Irradiance forecasts up to several hours ahead with typical resolutions from 10–15 minutes are derived from geostationary satellite data covering large areas without requiring local hardware. Satellite-based forecasting models are typically based on cloud motion approaches and increasingly also involve ML techniques. State-of-the-art satellite-based forecasts outperform persistence from approximately 30 minutes onward, and NWP forecasts up to several hours ahead.
- Irradiance forecasts from several hours to days ahead essentially rely on NWP models, with their capability to describe complex atmospheric dynamics, including advection as well as the formation and dissipation of clouds. Typically, NWP forecasts are provided with hourly resolution in the first days; such forecasts cover countries or continents with regional models and the entire Earth with global models.

Table 9-2. Basic Characteristics of Different Forecasting Approaches

	Time-Series Using Local Measurements	All-Sky Imager Based	Satellite Based	NWP Global	NWP Regional
Forecast horizon	Intrahour and intraday: 15 minutes–2 hours	Intrahour: 10–20 minutes	intraday: 4–8 hours	Days ahead: 10–15 days	Days ahead: 2–3 days
Update frequency	1 second to 1 hour	~10 seconds to 1 minute	10–15 minutes	6–24 hours	3–6 hours
Temporal resolution	1 second to 1 hour	~10 seconds to 1 minute	10–15 minutes	1–12 hours	1 hour
Spatial resolution	Point	10–100 m	0.5–3 km at subsatellite point	9–20 km	1–10 km
Coverage	Point	Point to 12 km	Satellite field of view (full Earth disc, continents)	Global	Countries, continents
Local hardware	Radiometric station or meters for PV power measurements	ASI(s) and radiometric station	None	None	None
Forecast providers	Private companies	Private companies	Private companies, some national weather services	National and international weather services	National and private weather services
Comments	Forecast horizon is linked to temporal resolution	Spatially extended forecasts require cloud height measure-ments or multiple ASIs; coverage and forecast horizon depend on cloud conditions	Spatial/ temporal resolutions depend on satellite/ spectral channels; spatial resolution decreases with distance from subsatellite point	Update frequency and temporal resolution might decrease with increasing forecast horizon	

NWP model forecasts are typically provided by international and national weather services, with a list of global NWP models and their providers given in Table 9-1. Regional NWP model

forecasts are provided by numerous national and private weather services. In addition, Table 9-3 gives information on some companies providing ASI-based and/or satellite-based forecasts. It is emphasized that this list is based on the experience of the IEA PVPS Task 16 participants and does not pretend to be exhaustive.

Table 9-3. Examples of Companies Providing Irradiance Forecasts based on ASI or satellite data

Company	Website	ASI	Satellite
CSPServices	https://www.cspservices.de/meteorological-services/	x	
Flucrum3D	https://www.fulcrum3d.com/cloudcam/	x	
meteo for energy	https://www.meteoforenergy.com/en/	x	x
Meteotest	https://solarwebservices.ch/		x
Reuniwatt	https://reuniwatt.com/en/247-all-sky-observation-sky-insight/	x	x
SoDa	https://www.soda-pro.com/		x
SolarAnywhere	https://www.solaranywhere.com/products/solaranywhere-forecast/		x
Solargis	https://solargis.com/products/solar-power-forecast/overview		x
Solcast	https://solcast.com/forecast-accuracy		x
Steadysun	https://www.steady-sun.com/solar-energy-forecasting/	x	x

As a complement to empirical and physical models, statistical and ML methods are widely used in solar irradiance and power forecasting. They also exploit the rapid development in AI techniques along with ever-increasing computational resources:

- Statistical and ML approaches are effectively applied to improve forecasts obtained with empirical or physical models (postprocessing). Through training against high-quality irradiance measurements (ground truth), they can reduce systematic meteorological forecast errors.
- Training of statistical and ML approaches to PV power measurements additionally provides a way to derive plant-specific models that account for the characteristics of a given PV plant or even to replace PV simulation models.
- With the fast advances in computer vision, ML techniques are now successfully applied to the prediction of cloud images (from ASIs or satellites), including algorithms to compute the optical flow in cloud motion approaches. From the predicted cloud image irradiance, forecasts can be derived in a subsequent step.
- Direct ML forecasting approaches can combine all kinds of possible observations (e.g., images from different sources or meteorological measurements of sensor networks) to predict solar irradiance or PV power.

For the training of time-series models, the availability of irradiance and/or PV power measurements is crucial. Great care is essential in the selection and quality control of this ground truth data, depending on the intended model usage. ML models adapt to ground truth as is, including, e.g., potential measurement faults, degradation, and soiling. Depending on the application, this might constitute either a problem (e.g., the irradiance forecasts might be biased if the ground truth originates from soiled sensors) or an advantage (e.g., when predicting the

current status of a PV plant for marketing the produced power, in the presence of soiling and/or degradation). Concerning the postprocessing of NWP model forecasts, satellite-derived data also provide a suitable reference for training.

Overall, the best possible accuracy of irradiance or PV power forecasts can be achieved by integrating different input data and methodologies. Prominent examples include:

- High-resolution intrahour forecasting systems combine local measurements and ASI data with empirical and ML approaches, and possibly also integrate satellite-based forecasts.
- Forecasting systems for the intraday energy market up to several hours ahead integrate online measurements and/or satellite-based forecasts as well as NWP -based forecasts with statistical and/or ML approaches.
- Forecasting systems from several hours to several days ahead use different NWP models as input in combination with statistical and/or ML approaches.

The performance of the different forecast models depends on multiple factors that have different impacts depending on forecast horizon and meteorological conditions:

- The capability of the models to predict changes in clouds and irradiance—for instance, persistence cannot predict approaching clouds.
- The performance of the models for irradiance retrieval/analysis for a forecast lead time of zero—persistence is then error-less, and the satellite-derived irradiance has a lower uncertainty than NWP analysis.
- The model's input data and parameters as well as the area covered by the input data—for instance, the larger the monitored cloud scene, the larger the forecast horizon can be.
- The computer time to execute a model run—the faster a model run, the less time that has passed since the observations fed into the model have been taken at the time of forecast delivery.
- The spatiotemporal resolution of the forecasts
- The capability of the model to correctly predict the AOD, especially for DNI forecasting in arid regions.

Besides forecasting for single PV power plants, the estimation and forecasting of regionally aggregated PV power is important for grid operators. Here, an additional challenge is that the information on all the PV power plants contributing to the overall regional feed-in power is often incomplete. Moreover, for most plants in many countries, the PV power is not monitored at a sufficient temporal resolution. Therefore, regional models, such as upscaling, have been developed and are effectively applied to derive and forecast regionally aggregated PV power. Because of spatial smoothing effects, the forecast errors of regionally aggregated PV power (normalized to the installed power) are much smaller than for single PV plants, depending on the size of the region and the set of contributing PV plants.

Forecast evaluations provide users with the necessary information on forecast accuracy and assist them in selecting between different forecasting services or assessing the risk when a forecast is used as a basis for decisions. In this chapter, different forecasts are compared using RMSE values as a basic score. A more detailed discussion and recommendations for the evaluation and uncertainty assessment of irradiance forecasting are given in Chapter 10.

Compared to deterministic forecasts, probabilistic forecasts have the great advantage to also add specific uncertainty information for each forecast value, depending on weather conditions. Probabilistic forecasts take the form of CDFs or PDFs. They are summarized by quantiles from which prediction intervals can be inferred. Quantiles can be estimated using either a parametric or a nonparametric approach. In the latter case, statistical or ML techniques can be used to estimate the quantiles. Although NWP ensemble members are not directly linked to the notion of quantiles, different propositions exist to infer a CDF from an ensemble.

Finally, forecasting solar power should be evaluated in the context of the system integration of solar power, where elaborate strategies are needed to provide the necessary power to meet the demand at any instant. These strategies include spatial smoothing for grid-integrated PV complemented by wind power and increasingly also the use of storage (batteries), curtailment, and shifting of loads to times with abundant PV generation. Applying these strategies reduces the variability of solar power as well as forecast errors.

References

Aguiar, L. M., B. Pereira, P. Lauret, F. Díaz, and M. David. 2016. "Combining Solar Irradiance Measurements, Satellite-Derived Data and a Numerical Weather Prediction Model to Improve Intra-Day Solar Forecasting." *Renewable Energy* 97: 599–610. https://doi.org/10.1016/j.renene.2016.06.018.

Ahn, H., J. Yu, and J.-M. Yeom. 2022. "Deep Learning-Based Prediction of Solar Surface Irradiance With Geostationary Satellite Images." Presented at the 2022 IEEE 17th Annual System of Systems Engineering Conference (SOSE), Rochester, NY, 311–315. https://doi.org/10.1109/SOSE55472.2022.9812657.

Aicardi, D., P. Musé, and R. Alonso-Suárez. 2022. "A Comparison of Satellite Cloud Motion Vectors Techniques to Forecast Intra-Day Hourly Solar Global Horizontal Irradiation." *Solar Energy* 233: 46–60. https://doi.org/10.1016/j.solener.2021.12.066.

Alessandrini, S., L. Delle Monache, S. Sperati, and G. Cervone. 2015. "An Analog Ensemble for Short-Term Probabilistic Solar Power Forecast." *Applied Energy* 157: 95–110. https://doi.org/10.1016/j.apenergy.2015.08.011.

Alonso-Montesinos, J., and F. J. Batlles. 2015. "Solar Radiation Forecasting in the Short- and Medium-Term Under All Sky Conditions. *Energy* 83: 387–393. https://doi.org/10.1016/j.energy.2015.02.036.

Amaro e Silva, R., and M. C. Brito. 2019. "Spatio-Temporal PV Forecasting Sensitivity to Modules' Tilt and Orientation." *Applied Energy* 255, 113807. https://doi.org/10.1016/j.apenergy.2019.113807.

Amaro e Silva, R., and M. C. Brito. 2017. "Understanding Spatio-Temporal Solar Forecasting."

André, M., R. Perez, T. Soubdhan, J. Schlemmer, R. Calif, and S. Monjoly. 2019. "Preliminary Assessment of Two Spatio-Temporal Forecasting Technics for Hourly Satellite-Derived Irradiance in a Complex Meteorological Context." *Solar Energy* 177: 703–712. https://doi.org/10.1016/j.solener.2018.11.010.

Andrews, R. W., J. H. Stein, C. Hansen, and D. Riley. 2014. "Introduction to the Open Source PV LIB for Python Photovoltaic System Modelling Package." Presented at the 2014 IEEE 4^{0t}h Photovoltaic Specialists Conference (PVSC), Denver, CO, USA, 0170–0174. https://doi.org/10.1109/PVSC.2014.6925501.

Antonanzas, J., D. Pozo-Vázquez, L. A. Fernandez-Jimenez, and F. J. Martinez-de-Pison. 2017. "The Value of Day-Ahead Forecasting for Photovoltaics in the Spanish Electricity Market." *Solar Energy* 158: 140–146. https://doi.org/10.1016/j.solener.2017.09.043.

Antonanzas, J., N. Osorio, R. Escobar, R. Urraca, F. J. Martinez-de-Pison, and F. Antonanzas-Torres. 2016. "Review of Photovoltaic Power Forecasting." *Solar Energy* 136: 78–111. https://doi.org/10.1016/j.solener.2016.06.069.

Arbizu-Barrena, C., D. Pozo-Vázquez, J. A. Ruiz-Arias, and J. Tovar-Pescador. 2015. "Macroscopic Cloud Properties in the WRF NWP Model: An Assessment Using Sky Camera and Ceilometer Data." *JGR Atmospheres* 120. https://doi.org/10.1002/2015JD023502.

Aryaputera, A. W., D. Yang, and W. M. Walsh. 2015. "Day-Ahead Solar Irradiance Forecasting in a Tropical Environment." *Journal of Solar Energy Engineering* 137, 051009. https://doi.org/10.1115/1.4030231.

Bacher, P., H. Madsen, and H. A. Nielsen. 2009. "Online Short-Term Solar Power Forecasting." *Solar Energy* 83: 1772–1783. https://doi.org/10.1016/j.solener.2009.05.016.

Bakker, K., K. Whan, W. Knap, and M. Schmeits. 2019. "Comparison of Statistical Post-Processing Methods for Probabilistic NWP Forecasts of Solar Radiation." *Solar Energy* 191: 138–150. https://doi.org/10.1016/j.solener.2019.08.044.

Bauer, P., A. Thorpe, and G. Brunet. 2015. "The Quiet Revolution of Numerical Weather Prediction." *Nature* 525: 47–55. https://doi.org/10.1038/nature14956.

Benavides Cesar, L., R. Amaro E Silva, M. Á. Manso Callejo, and C.-I. Cira. 2022. "Review on Spatio-Temporal Solar Forecasting Methods Driven by In Situ Measurements or Their Combination With Satellite and Numerical Weather Prediction (NWP) Estimates." *Energies* 15, 4341. https://doi.org/10.3390/en15124341.

Berthomier, L., B. Pradel, and L. Perez. 2020. "Cloud Cover Nowcasting With Deep Learning." Presented at the 2020 IEEE 10th International Conference on Image Processing Theory, Tools, and Applications (IPTA), Paris, France, 1–6. https://doi.org/10.1109/IPTA50016.2020.9286606.

Bessa, R., C. Moreira, B. Silva, and M. Matos. 2014. "Handling Renewable Energy Variability and Uncertainty in Power Systems Operation." *WIREs Energy & Environment* 3: 156–178. https://doi.org/10.1002/wene.76.

Beyer, H.G., A. Drews Betcke Jethro, D. Heinemann, E. Lorenz, G. Heilscher, and S. Bofinger. 2004. "Identification of a General Model for the MPP Performance of PV-Modules for the Application in a Procedure for the Performance Check of Grid Connected Systems."

Bishop, C. M. 1995. *Neural Networks for Pattern Recognition*. Oxford: Clarendon Press, Oxford University Press.

Blanc, P., P. Massip, A. Kazantzidis, P. Tzoumanikas, P. Kuhn, S. Wilbert, D. Schüler, and C. Prahl. 2017. "Short-Term Forecasting of High Resolution Local DNI Maps With Multiple Fish-Eye Cameras in Stereoscopic Mode." Presented at the SOLARPACES 2016: International Conference on Concentrating Solar Power and Chemical Energy Systems, Abu Dhabi, United Arab Emirates, 140004. https://doi.org/10.1063/1.4984512.

Blum, N. B., S. Wilbert, B. Nouri, J. Stührenberg, J. E. Lezaca Galeano, T. Schmidt, D. Heinemann, T. Vogt, A. Kazantzidis, and R. Pitz-Paal. 2022. "Analyzing Spatial Variations of Cloud Attenuation by a Network of All-Sky Imagers." *Remote Sensing* 14, 5685. https://doi.org/10.3390/rs14225685.

Bonavita, M., and P. Lean. 2021. "4D-VAR for Numerical Weather Prediction." *Weather* 76: 65–66. https://doi.org/10.1002/wea.3862.

Bosch, J. L., and J. Kleissl. 2013. "Cloud Motion Vectors From a Network of Ground Sensors in a Solar Power Plant. *Solar Energy* 95, 13–20. https://doi.org/10.1016/j.solener.2013.05.027.

Bottou, L. 1998. "Online Learning and Stochastic Approximations."

Brancucci Martinez-Anido, C., B. Botor, A. R. Florita, C. Draxl, S. Lu, H. F. Hamann, and B.-M. Hodge. 2016. "The Value of Day-Ahead Solar Power Forecasting Improvement." *Solar Energy* 129: 192–203. https://doi.org/10.1016/j.solener.2016.01.049.

Breiman, L. 2001. "Random Forests." *Machine Learning* 45: 5–32. https://doi.org/10.1023/A:1010933404324.

Breiman, L., J. H. Friedman, R. A. Olshen, and C. J. Stone. 2017. *Classification and Regression Trees*, 1st ed. New York: Routledge. https://doi.org/10.1201/9781315139470.

Breitkreuz, H., M. Schroedter-Homscheidt, T. Holzer-Popp, and S. Dech. 2009. "Short-Range Direct and Diffuse Irradiance Forecasts for Solar Energy Applications Based on Aerosol Chemical Transport and Numerical Weather Modeling." *Journal of Applied Meteorology and Climatology* 48: 1766–1779. https://doi.org/10.1175/2009JAMC2090.1.

Bresky, W., and J. Daniels. 2006. "The Feasibility of an Optical Power Flow Algorithm for Estimating Atmospheric Motion."

Bright, J. M., S. Killinger, D. Lingfors, and N. A. Engerer. 2018. "Improved Satellite-Derived PV Power Nowcasting Using Real-Time Power Data From Reference PV Systems." *Solar Energy* 168: 118–139. https://doi.org/10.1016/j.solener.2017.10.091.

Buizza, R., D. S. Richardson, and T. N. Palmer. 2003. "Benefits of Increased Resolution in the ECMWF Ensemble System and Comparison With Poor-Man's Ensembles." *Quarterly Journal of the Royal Meteorological Society* 129: 1269–1288. https://doi.org/10.1256/qj.02.92.

Carrière, T., R. Amaro E. Silva, F. Zhuang, Y.-M. Saint-Drenan, and P. Blanc. 2021. "A New Approach for Satellite-Based Probabilistic Solar Forecasting With Cloud Motion Vectors." *Energies* 14, 4951. https://doi.org/10.3390/en14164951.

Chauvin, R., J. Nou, J. Eynard, S. Thil, and S. Grieu. 2018. "A New Approach to the Real-Time Assessment and Intraday Forecasting of Clear-Sky Direct Normal Irradiance." *Solar Energy* 167: 35–51. https://doi.org/10.1016/j.solener.2018.02.027.

Chauvin, R., J. Nou, S. Thil, and S. Grieu. 2015. "Modelling the Clear-Sky Intensity Distribution Using a Sky Imager." *Solar Energy* 119: 1–17. https://doi.org/10.1016/j.solener.2015.06.026.

Chauvin, R., J. Nou, S. Thil, and S. Grieu. 2016. "Cloud Motion Estimation Using a Sky Imager." Presented at the SOLARPACES 2015: International Conference on Concentrating

Solar Power and Chemical Energy Systems, Cape Town, South Africa, 150003. https://doi.org/10.1063/1.4949235.

Chauvin, R., J. Nou, S. Thil, and S. Grieu. 2017. "Generating High Dynamic Range Images Using a Sky Imager." *IFAC-PapersOnLine* 50: 219–224. https://doi.org/10.1016/j.ifacol.2017.08.037.

Chow, C. W., B. Urquhart, M. Lave, A. Dominguez, J. Kleissl, J. Shields, and B. Washom. 2011. "Intra-Hour Forecasting With a Total Sky Imager at the UC San Diego Solar Energy Testbed." *Solar Energy* 85: 2,881–2,893. https://doi.org/10.1016/j.solener.2011.08.025.

Chu, Y., M. Li, H. T. C. Pedro, and C. F. M. Coimbra. 2015. "Real-Time Prediction Intervals for Intra-Hour DNI Forecasts." *Renewable Energy* 83: 234–244. https://doi.org/10.1016/j.renene.2015.04.022.

Cirés, E., J. Marcos, I. De La Parra, M. García, and L. Marroyo. 2019. "The Potential of Forecasting in Reducing the LCOE in PV Plants Under Ramp-Rate Restrictions." *Energy* 188, 116053. https://doi.org/10.1016/j.energy.2019.116053.

Coimbra, C. F. M., and H. T. C. Pedro. 2013. "Stochastic-Learning Methods." *Solar Energy Forecasting and Resource Assessment*. Elsevier. https://doi.org/10.1016/B978-0-12-397177-7.00015-2.

Cros, S., E. Buessler, L. Huet, N. Sébastien, and N. Schmutz. 2015. "The Benefits of Intraday Solar Irradiance Forecasting to Adjust the Day-Ahead Scheduled PV Power."

Cros, S., J. Badosa, A. Szantaï, and M. Haeffelin. 2020. "Reliability Predictors for Solar Irradiance Satellite-Based Forecast." *Energies* 13, 5566. https://doi.org/10.3390/en13215566.

Cros, S., M. Deroubaix, and N. Schmutz. 2015. "Method and Device for Forecasting Cloudiness by Statistical Processing of Data Selected by Spatial Analysis."

Cros, S., N. Sébastien, O. Liandrat, and N. Schmutz. 2014. "Cloud Pattern Prediction From Geostationary Meteorological Satellite Images for Solar Energy Forecasting." Edited by A. Comerón, E. I. Kassianov, K. Schäfer, R. H. Picard, K. Stein, and J. D. Gonglewski. Presented at the SPIE Remote Sensing, Amsterdam, Netherlands, 924202. https://doi.org/10.1117/12.2066853.

da Silva Fonseca Junior, J. G., T. Oozeki, H. Ohtake, K. Shimose, T. Takashima, and K. Ogimoto. 2014. "Regional Forecasts and Smoothing Effect of Photovoltaic Power Generation in Japan: An Approach With Principal Component Analysis." *Renewable Energy* 68: 403–413. https://doi.org/10.1016/j.renene.2014.02.

Dambreville, R., P. Blanc, J. Chanussot, and D. Boldo. 2014. "Very Short-Term Forecasting of the Global Horizontal Irradiance Using a Spatio-Temporal Autoregressive Model." *Renewable Energy* 72: 291–300. https://doi.org/10.1016/j.renene.2014.07.012.

Das, U. K., K. S. Tey, M. Seyedmahmoudian, S. Mekhilef, M. Y. I. Idris, W. Van Deventer, B. Horan, and A. Stojcevski. 2018. "Forecasting of Photovoltaic Power Generation and Model Optimization: A Review." *Renewable and Sustainable Energy Reviews* 81: 912–928. https://doi.org/10.1016/j.rser.2017.08.017.

David, M., and P. Lauret. 2018. "Solar Radiation Probabilistic Forecasting." In *Wind Field and Solar Radiation Characterization and Forecasting*. Edited by R. Perez. Springer International Publishing. https://doi.org/10.1007/978-3-319-76876-2_9.

David, M., F. Ramahatana, P. J. Trombe, and P. Lauret. 2016. "Probabilistic Forecasting of the Solar Irradiance With Recursive ARMA and GARCH Models." *Solar Energy* 133: 55–72. https://doi.org/10.1016/j.solener.2016.03.064.

David, M., J. Boland, L. Cirocco, P. Lauret, and C. Voyant. 2021. "Value of Deterministic Day-Ahead Forecasts of PV Generation in PV + Storage Operation for the Australian Electricity Market." *Solar Energy* 224: 672–684. https://doi.org/10.1016/j.solener.2021.06.011.

David, M., M. A. Luis, and P. Lauret. 2018. "Comparison of Intraday Probabilistic Forecasting of Solar Irradiance Using Only Endogenous Data." *International Journal of Forecasting* 34: 529–547. https://doi.org/10.1016/j.ijforecast.2018.02.003.

Delle Monache, L., F. A. Eckel, D. L. Rife, B. Nagarajan, and K. Searight. 2013. "Probabilistic Weather Prediction With an Analog Ensemble." *Monthly Weather Review* 141: 3,498–3,516. https://doi.org/10.1175/MWR-D-12-00281.1.

Deng, A., B. Gaudet, J. Dudhia, and K. Alapaty. 2014. "Implementation and Evaluation of a New Shallow Convection Scheme."

Descombes, G., D. Auligne, H.-C. Lin, D. Xu, S. Schwartz, and F. Vandenberghe. 2014. "Multi-Sensor Advection Diffusion nowCast (MADCast) for Cloud Analysis and Short-Term Prediction." https://doi.org/10.5065/D62V2D37.

Dev, S., F. M. Savoy, Y. H. Lee, and S. Winkler. 2019. "Estimating Solar Irradiance Using Sky Imagers." *Atmospheric Measurement Techniques* 12: 5,417–5,429. https://doi.org/10.5194/amt-12-5417-2019.

Diagne, M., M. David, J. Boland, N. Schmutz, and P. Lauret. 2014. "Post-Processing of Solar Irradiance Forecasts From WRF Model at Reunion Island." *Solar Energy* 105: 99–108. https://doi.org/10.1016/j.solener.2014.03.016.

Diagne, M., M. David, P. Lauret, J. Boland, and N. Schmutz. 2013. "Review of Solar Irradiance Forecasting Methods and a Proposition for Small-Scale Insular Grids." *Renewable and Sustainable Energy Reviews* 27: 65–76. https://doi.org/10.1016/j.rser.2013.06.042.

Dittmann, A., N. Holland, and E. Lorenz. 2021. "A New Sky Imager Based Global Irradiance Forecasting Model With Analyses of Cirrus Situations." *metz* 30: 101–113. https://doi.org/10.1127/metz/2020/1024.

Efron, B. 1979. “Bootstrap Methods: Another Look at the Jackknife.” *Annals of Statistics* 7. https://doi.org/10.1214/aos/1176344552.

Erdener, B. C., C. Feng, K. Doubleday, A. Florita, and B.-M. Hodge. 2022. “A Review of Behind-the-Meter Solar Forecasting.” *Renewable and Sustainable Energy Reviews* 160: 112224. https://doi.org/10.1016/j.rser.2022.112224.

Fabel, Y., B. Nouri, S. Wilbert, N. Blum, D. Schnaus, R. Triebel, L. F. Zarzalejo, E. Ugedo, J. Kowalski, and R. Pitz-Paal. 2023. “Combining Deep Learning and Physical Models: A Benchmark Study on All-Sky Imager-Based Solar Nowcasting Systems.” *Solar RRL* solr.202300808. https://doi.org/10.1002/solr.202300808.

Fabel, Y., B. Nouri, S. Wilbert, N. Blum, R. Triebel, M. Hasenbalg, P. Kuhn, L. F. Zarzalejo, and R. Pitz-Paal. 2022. “Applying Self-Supervised Learning for Semantic Cloud Segmentation of All-Sky Images.” Atmospheric Measurement Techniques 15: 797–809. https://doi.org/10.5194/amt-15-797-2022.

Farnebäck, G. 2003. “Two-Frame Motion Estimation Based on Polynomial Expansion.” In *Image Analysis, Lecture Notes in Computer Science*. Edited by J. Bigun and T. Gustavsson. Berlin, Heidelberg: Springer. https://doi.org/10.1007/3-540-45103-X_50.

Fatemi, S. A., A. Kuh, and M. Fripp. 2018. “Parametric Methods for Probabilistic Forecasting of Solar Irradiance.” *Renewable Energy* 129: 666–676. https://doi.org/10.1016/j.renene.2018.06.022.

Friedman, J. H. 2001. “Greedy Function Approximation: A Gradient Boosting Machine.” Annals of Statistics 29. https://doi.org/10.1214/aos/1013203451.

Gallo, R., M. Castangia, A. Macii, E. Macii, E. Patti, and A. Aliberti. 2022. “Solar Radiation Forecasting With Deep Learning Techniques Integrating Geostationary Satellite Images.” *Engineering Applications of Artificial Intelligence* 116, 105493. https://doi.org/10.1016/j.engappai.2022.105493.

Gallucci, D., F. Romano, A. Cersosimo, D. Cimini, F. Di Paola, S. Gentile, E. Geraldi, S. Larosa, S. Nilo, E. Ricciardelli, and M. Viggiano. 2018. “Nowcasting Surface Solar Irradiance With AMESIS via Motion Vector Fields of MSG-SEVIRI Data.” *Remote Sensing* 10, 845. https://doi.org/10.3390/rs10060845.

Gastón, M., E. Lorenz, S. Lozano, D. Heinemann, M. Blanco, and L. Santigosa. 2009. “Comparison of Global Irradiance Forecasting Approaches.”

Gauchet, C., Blanc, P., Espinar, B., Charbonnier, B., Demengel, D. 2012. Surface solar irradiance estimation With low-cost fish-eye camera. Presented at the Workshop on “Remote Sensing Measurements for Renewable Energy.”

Gensler, A., J. Henze, B. Sick, and N. Raabe. 2016. “Deep Learning for Solar Power Forecasting—An Approach Using AutoEncoder and LSTM Neural Networks.” Presented at the

2016 IEEE International Conference on Systems, Man, and Cybernetics (SMC), Budapest, Hungary, 002858–002865. https://doi.org/10.1109/SMC.2016.7844673.

Ghonima, M. S., B. Urquhart, C. W. Chow, J. E. Shields, A. Cazorla, and J. Kleissl. 2012. "A Method for Cloud Detection and Opacity Classification Based on Ground-Based Sky Imagery." *Atmospheric Measurement Techniques* 5: 2,881–2,892. https://doi.org/10.5194/amt-5-2881-2012.

Gigoni, L., A. Betti, E. Crisostomi, A. Franco, M. Tucci, F. Bizzarri, and D. Mucci. 2018. "Day-Ahead Hourly Forecasting of Power Generation From Photovoltaic Plants." *IEEE Transactions on Sustainable Energy* 9: 831–842. https://doi.org/10.1109/TSTE.2017.2762435.

Glahn, H. R., and D. A. Lowry. 1972. "The Use of Model Output Statistics (MOS) in Objective Weather Forecasting." Journal of Applied Meteorology and Climatology 11: 1,203–1,211. https://doi.org/10.1175/1520-0450(1972)011<1203:TUOMOS>2.0.CO;2.

Glorot, X., and Y. Bengio. 2010. "Understanding the Difficulty of Training Deep Feedforward Neural Networks." Presented at the International Conference on Artificial Intelligence and Statistics.

Gneiting, T., A. E. Raftery, A. H. Westveld, and T. Goldman. 2005. "Calibrated Probabilistic Forecasting Using Ensemble Model Output Statistics and Minimum CRPS Estimation." *Monthly Weather Review* 133: 1098–1118. https://doi.org/10.1175/MWR2904.1.

Grantham, A., Y. R. Gel, and J. Boland. 2016. "Nonparametric Short-Term Probabilistic Forecasting for Solar Radiation." *Solar Energy* 133: 465–475. https://doi.org/10.1016/j.solener.2016.04.011.

Gueymard, C., and P. Jiménez. 2018. "Validation of Real-Time Solar Irradiance Simulations Over Kuwait Using WRF-Solar." Presented at the ISES EuroSun 2018 Conference—12th International Conference on Solar Energy for Buildings and Industry, International Solar Energy Society, Rapperswil, 1–11. https://doi.org/10.18086/eurosun2018.09.14.

Gueymard, C., W. Gustafson, A. Etringer, and P. Storck. 2012. "Evaluation of Procedures to Improve Solar Resource Assessments: Optimum Use of Short-Term Data From a Local Weather Station to Correct Bias in Long-Term Satellite-Derived Solar Radiation Time Series."

Hamill, T. M., and J. S. Whitaker. 2006. "Probabilistic Quantitative Precipitation Forecasts Based on Reforecast Analogs: Theory and Application." *Monthly Weather Review* 134: 3,209–3,229. https://doi.org/10.1175/MWR3237.1.

Hamill, T. M., and S. J. Colucci. 1997. "Verification of Eta–RSM Short-Range Ensemble Forecasts." *Monthly Weather Review* 125: 1312–1327. https://doi.org/10.1175/1520-0493(1997)125<1312:VOERSR>2.0.CO;2.

Hammer, A., D. Heinemann, C. Hoyer, R. Kuhlemann, E. Lorenz, R. Müller, and H. G. Beyer. 2003. "Solar Energy Assessment Using Remote Sensing Technologies." *Remote Sensing of Environment* 86: 423–432. https://doi.org/10.1016/S0034-4257(03)00083-X.

Hasenbalg, M., P. Kuhn, S. Wilbert, B. Nouri, and A. Kazantzidis. 2020. "Benchmarking of Six Cloud Segmentation Algorithms for Ground-Based All-Sky Imagers." *Solar Energy* 201, 596–614. https://doi.org/10.1016/j.solener.2020.02.042.

Haupt, S. E., B. Kosović, T. Jensen, J. K. Lazo, J. A. Lee, P. A. Jiménez, J. Cowie, G. Wiener, T. C. McCandless, M. Rogers, S. Miller, M. Sengupta, Y. Xie, L. Hinkelman, P. Kalb, and J. Heiser. 2018. "Building the Sun4Cast System: Improvements in Solar Power Forecasting." *Bulletin of the American Meteorological Society* 99: 121–136. https://doi.org/10.1175/BAMS-D-16-0221.1.

Haupt, S. E., B. Kosovic, T. L. Jensen, J. Lee, P. Jiménez Munoz, K. Lazo, R. Cowie, T. McCandless, M. Pearson, M. Wiener, S. Alessandrini, L. Delle Monache, D. Yu, Z. Peng, D. Huang, J. Heiser, S. Yoo, P. Kalb, S. Miller, M. Rogers, and L. Hinkleman. 2016. *The Sun4Cast® Solar Power Forecasting System: The Result of the Public-Private-Academic Partnership to Advance Solar Power Forecasting*. https://doi.org/10.5065/D6N58JR2.

He, X., C. Yuan, and Z. Yang. 2016. "Performance Evaluation of Chinese Solar Radiation Forecast Based on Three Global Forecast Back Ground Fields."

Hoff, T. E., and R. Perez. 2012. "Modeling PV Fleet Output Variability." *Solar Energy: Progress in Solar Energy* 3 86: 2,177–2,189. https://doi.org/10.1016/j.solener.2011.11.005.

Huang, G.-B., Q.-Y. Zhu, and C.-K. Siew. 2006. "Extreme Learning Machine: Theory and Applications." *Neurocomputing* 70: 489–501. https://doi.org/10.1016/j.neucom.2005.12.126.

Huang, J., M. Korolkiewicz, M. Agrawal, and J. Boland. 2013. "Forecasting Solar Radiation on an Hourly Timescale Using a Coupled AutoRegressive and Dynamical System (CARDS) Model." *Solar Energy* 87: 136–149. https://doi.org/10.1016/j.solener.2012.10.012.

Huang, J., M. M. Khan, Y. Qin, and S. West. 2019. "Hybrid Intra-hour Solar PV Power Forecasting Using Statistical and Skycam-Based Methods." Presented at the 2019 IEEE 4^{6t}h Photovoltaic Specialists Conference (PVSC), Chicago, IL, 2,434–2,439. https://doi.org/10.1109/PVSC40753.2019.8980732.

Inman, R. H., H. T. C. Pedro, and C. F. M. Coimbra. 2013. "Solar Forecasting Methods for Renewable Energy Integration." *Progress in Energy and Combustion Science* 39: 535–576. https://doi.org/10.1016/j.pecs.2013.06.002.

Isvoranu, D., and V. Badescu. 2013. "Comparison Between Measurements and WRF Numerical Simulation of Global Solar Irradiation in Romania." *Annals of West University of Timisoara - Physics* 57: 24–33. https://doi.org/10.1515/awutp-2015-0103.

Jamal, T., C. Carter, T. Schmidt, G. M. Shafiullah, M. Calais, and T. Urmee. 2019. "An Energy Flow Simulation Tool for Incorporating Short-Term PV Forecasting in a Diesel-PV-Battery Off-Grid Power Supply System." *Applied Energy* 254, 113718. https://doi.org/10.1016/j.apenergy.2019.113718.

Jamaly, M., and J. Kleissl. 2017. "Spatiotemporal Interpolation and Forecast of Irradiance Data Using Kriging." *Solar Energy* 158: 407–423. https://doi.org/10.1016/j.solener.2017.09.057.

Jiang, H., N. Lu, J. Qin, W. Tang, and L. Yao. 2019. "A Deep Learning Algorithm to Estimate Hourly Global Solar Radiation From Geostationary Satellite Data." *Renewable and Sustainable Energy Reviews* 114, 109327. https://doi.org/10.1016/j.rser.2019.109327.

Jiménez, P. A., J. Dudhia, G. Thompson, J. A. Lee, and T. Brummet. 2022. "Improving the Cloud Initialization in WRF-Solar With Enhanced Short-Range Forecasting Functionality: The MAD-WRF Model." *Solar Energy* 239: 221–233. https://doi.org/10.1016/j.solener.2022.04.055.

Jiménez, P. A., J. P. Hacker, J. Dudhia, S. E. Haupt, J. A. Ruiz-Arias, C. A. Gueymard, G. Thompson, T. Eidhammer, and A. Deng. 2016. "WRF-Solar: Description and Clear-Sky Assessment of an Augmented NWP Model for Solar Power Prediction." *Bulletin of the American Meteorological Society* 97: 1,249–1,264. https://doi.org/10.1175/BAMS-D-14-00279.1.

Jiménez-Garrote, A., G. Sánchez-Hernández, M. López-Cuesta, and D. Pozo-Vázquez. 2023. "SOWISP—A Retrospective High Spatial and Temporal Resolution Database of the Installed Wind and Solar PV Power in Spain." *Solar Energy* 256: 44–54. https://doi.org/10.1016/j.solener.2023.03.009.

Jones, A. S., and S. J. Fletcher. 2013. "Data Assimilation in Numerical Weather Prediction and Sample Applications." In *Solar Energy Forecasting and Resource Assessment*. Elsevier. https://doi.org/10.1016/B978-0-12-397177-7.00013-9.

Junk, C., L. Delle Monache, and S. Alessandrini. 2015. "Analog-Based Ensemble Model Output Statistics." *Monthly Weather Review* 143: 2,909–2,917. https://doi.org/10.1175/MWR-D-15-0095.1.

Kallio-Myers, V., A. Riihelä, P. Lahtinen, and A. Lindfors. 2020. "Global Horizontal Irradiance Forecast for Finland Based on Geostationary Weather Satellite Data. *Solar Energy* 198: 68–80. https://doi.org/10.1016/j.solener.2020.01.008.

Kamadinata, J. O., T. L. Ken, and T. Suwa. 2019. "Sky Image-Based Solar Irradiance Prediction Methodologies Using Artificial Neural Networks." *Renewable Energy* 134: 837–845. https://doi.org/10.1016/j.renene.2018.11.056.

Karalus, S., B. Köpfer, P. Guthke, S. Killinger, and E. Lorenz. 2023. "Analysing Grid-Level Effects of Photovoltaic Self-Consumption Using a Stochastic Bottom-Up Model of Prosumer Systems." *Energies* 16, 3059. https://doi.org/10.3390/en16073059.

Kaur, A., L. Nonnenmacher, H. T. C. Pedro, and C. F. M. Coimbra. 2016. "Benefits of Solar Forecasting for Energy Imbalance Markets." *Renewable Energy* 86: 819–830. https://doi.org/10.1016/j.renene.2015.09.011.

Kazantzidis, A., P. Tzoumanikas, E. Nikitidou, V. Salamalikis, S. Wilbert, C. Prahl. 2017. "Application of Simple All-Sky Imagers for the Estimation of Aerosol Optical Depth." Presented at the SOLARPACES 2016: International Conference on Concentrating Solar Power and

Chemical Energy Systems, Abu Dhabi, United Arab Emirates, 140012. https://doi.org/10.1063/1.4984520.

Kellerhals, S. A., F. De Leeuw, and C. Rodriguez Rivero. 2022. "Cloud Nowcasting With Structure-Preserving Convolutional Gated Recurrent Units." *Atmosphere* 13, 1632. https://doi.org/10.3390/atmos13101632.

Killinger, S., F. Braam, B. Müller, B. Wille-Haussmann, and R. McKenna. 2016. "Projection of Power Generation Between Differently-Oriented PV Systems." *Solar Energy* 136: 153–165. https://doi.org/10.1016/j.solener.2016.06.075.

Killinger, S., D. Lingfors, Y.-M. Saint-Drenan, P. Moraitis, W. Van Sark, J. Taylor, N. A. Engerer, and J. M. Bright. 2018. "On the Search for Representative Characteristics of PV Systems: Data Collection and Analysis of PV System Azimuth, Tilt, Capacity, Yield, and Shading." *Solar Energy* 173: 1087–1106. https://doi.org/10.1016/j.solener.2018.08.051.

Kingma, D. P., and J. Ba. 2014. "Adam: A Method for Stochastic Optimization." https://doi.org/10.48550/ARXIV.1412.6980.

Kleebauer, M., D. Horst, and C. Reudenbach. 2021. "Semi-Automatic Generation of Training Samples for Detecting Renewable Energy Plants in High-Resolution Aerial Images." *Remote Sensing* 13, 4793. https://doi.org/10.3390/rs13234793.

Kleissl, J. 2013. *Solar Energy Forecasting and resource Assessment*. Academic Press.

Koenker, R., and G. Bassett. 1978. "Regression Quantiles." *Econometrica* 46: 33. https://doi.org/10.2307/1913643.

Köhler, C., A. Steiner, Y.-M. Saint-Drenan, D. Ernst, A. Bergmann-Dick, M. Zirkelbach, Z. Ben Bouallègue, I. Metzinger, and B. Ritter. 2017. "Critical Weather Situations for Renewable Energies—Part B: Low Stratus Risk for Solar Power." *Renewable Energy* 101: 794–803. https://doi.org/10.1016/j.renene.2016.09.002.

Kong, W., Y. Jia, Z. Y. Dong, K. Meng, and S. Chai. 2020. "Hybrid Approaches Based on Deep Whole-Sky-Image Learning to Photovoltaic Generation Forecasting." *Applied Energy* 280, 115875. https://doi.org/10.1016/j.apenergy.2020.115875.

Kosmopoulos, P., D. Kouroutsidis, K. Papachristopoulou, P. I. Raptis, A. Masoom, Y.-M. Saint-Drenan, P. Blanc, C. Kontoes, and S. Kazadzis. 2020. "Short-Term Forecasting of Large-Scale Clouds Impact on Downwelling Surface Solar Irradiation." *Energies* 13, 6555. https://doi.org/10.3390/en13246555.

Kraas, B., M. Schroedter-Homscheidt, and R. Madlener. 2013. "Economic Merits of a State-of-the-Art Concentrating Solar Power Forecasting System for Participation in the Spanish Electricity Market." *Solar Energy* 93: 244–255. https://doi.org/10.1016/j.solener.2013.04.012.

Kriebel, K. T., G. Gesell, M. Ka¨stner, and H. Mannstein. 2003. “The Cloud Analysis Tool APOLLO: Improvements and Validations.” *International Journal of Remote Sensing* 24: 2,389–2,408. https://doi.org/10.1080/01431160210163065.

Kuhn, P., M. Wirtz, N. Killius, S. Wilbert, J. L. Bosch, N. Hanrieder, B. Nouri, J. Kleissl, L. Ramirez, M. Schroedter-Homscheidt, D. Heinemann, A. Kazantzidis, P. Blanc, and R. Pitz-Paal. 2018. “Benchmarking Three Low-Cost, Low-Maintenance Cloud Height Measurement Systems and ECMWF Cloud Heights Against a Ceilometer.” *Solar Energy* 168: 140–152. https://doi.org/10.1016/j.solener.2018.02.050.

Kuhn, P., S. Wilbert, D. Schüler, C. Prahl, T. Haase, L. Ramirez, L. Zarzalejo, A. Meyer, L. Vuilleumier, P. Blanc, J. Dubrana, A. Kazantzidis, M. Schroedter-Homscheidt, T. Hirsch, and R. Pitz-Paal. 2017. “Validation of Spatially Resolved All Sky Imager Derived DNI Nowcasts.” Presented at the SOLARPACES 2016: International Conference on Concentrating Solar Power and Chemical Energy Systems, Abu Dhabi, United Arab Emirates, 140014. https://doi.org/10.1063/1.4984522.

Kühnert, J. 2015. “Development of a Photovoltaic Power Prediction System for Forecast Horizons of Several Hours.”

Kühnert, J., E. Lorenz, and D. Heinemann. 2013. “Satellite-Based Irradiance and Power Forecasting for the German Energy Market.” In *Solar Energy Forecasting and Resource Assessment*. Elsevier. https://doi.org/10.1016/B978-0-12-397177-7.00011-5.

Kurtz, B., and J. Kleissl. 2017. “Measuring Diffuse, Direct, and Global Irradiance Using a Sky Imager.” *Solar Energy* 141: 311–322. https://doi.org/10.1016/j.solener.2016.11.032.

Lara-Fanego, V., J. A. Ruiz-Arias, D. Pozo-Vázquez, F. J. Santos-Alamillos, and J. Tovar-Pescador. 2012. “Evaluation of the WRF Model Solar Irradiance Forecasts in Andalusia (Southern Spain).” *Solar Energy* 86: 2,200–2,217. https://doi.org/10.1016/j.solener.2011.02.014.

Lauret, P., M. David, and H. Pedro. 2017. “Probabilistic Solar Forecasting Using Quantile Regression Models.” *Energies* 10, 1591. https://doi.org/10.3390/en10101591.

Lauret, P., M. David, and P. Pinson. 2019. “Verification of Solar Irradiance Probabilistic Forecasts.” *Solar Energy* 194: 254–271. https://doi.org/10.1016/j.solener.2019.10.041.

Law, E. W., A. A. Prasad, M. Kay, and R. A. Taylor. 2014. “Direct Normal Irradiance Forecasting and its Application to Concentrated Solar Thermal Output Forecasting—A Review. *Solar Energy* 108: 287–307. https://doi.org/10.1016/j.solener.2014.07.008.

Law, E. W., M. Kay, and R. A. Taylor. 2016. “Evaluating the Benefits of Using Short-Term Direct Normal Irradiance Forecasts to Operate a Concentrated Solar Thermal Plant.” *Solar Energy* 140: 93–108. https://doi.org/10.1016/j.solener.2016.10.037.

Le Gal La Salle, J., M. David, and P. Lauret. 2021. “A New Climatology Reference Model to Benchmark Probabilistic Solar Forecasts.” *Solar Energy* 223: 398–414. https://doi.org/10.1016/j.solener.2021.05.037.

LeCun, Y., B. Boser, J. S. Denker, D. Henderson, R. E. Howard, W. Hubbard, and L. D. Jackel. 1989. "Backpropagation Applied to Handwritten Zip Code Recognition." *Neural Computation* 1: 541–551. https://doi.org/10.1162/neco.1989.1.4.541.

Lee, J. A., S. E. Haupt, P. A. Jiménez, M. A. Rogers, S. D. Miller, and T. C. McCandless. 2017. "Solar Irradiance Nowcasting Case Studies Near Sacramento." *Journal of Applied Meteorology and Climatology* 56: 85–108. https://doi.org/10.1175/JAMC-D-16-0183.1.

Leutbecher, M., and T. N. Palmer. 2008. "Ensemble Forecasting." *Journal of Computational Physics* 227: 3,515–3,539. https://doi.org/10.1016/j.jcp.2007.02.014.

Li, J., and A. D. Heap. 2014. "Spatial Interpolation Methods Applied in the Environmental Sciences: A Review." *Environmental Modelling & Software* 53: 173–189. https://doi.org/10.1016/j.envsoft.2013.12.008.

Licciardi, G. A., R. Dambreville, J. Chanussot, and S. Dubost. 2015. :Spatiotemporal Pattern Recognition and Nonlinear PCA for Global Horizontal Irradiance Forecasting." *IEEE Geoscience and Remote Sensing Letters* 12: 284–288. https://doi.org/10.1109/LGRS.2014.2335817.

Lima, F. J. L., F. R. Martins, E. B. Pereira, E. Lorenz, and D. Heinemann. 2016. "Forecast for Surface Solar Irradiance at the Brazilian Northeastern Region Using NWP Model and Artificial Neural Networks." *Renewable Energy* 87: 807–818. https://doi.org/10.1016/j.renene.2015.11.005.

Lin, F., Y. Zhang, and J. Wang. 2023. "Recent Advances in Intra-Hour Solar Forecasting: A Review of Ground-Based Sky Image Methods." *International Journal of Forecasting* 39: 244–265. https://doi.org/10.1016/j.ijforecast.2021.11.002.

Logothetis, S.-A., V. Salamalikis, S. Wilbert, J. Remund, L. F. Zarzalejo, Y. Xie, B. Nouri, E. Ntavelis, J. Nou, N. Hendrikx, L. Visser, M. Sengupta, M. Pó, R. Chauvin, S. Grieu, N. Blum, W. Van Sark, and A. Kazantzidis. 2022. "Benchmarking of Solar Irradiance Nowcast Performance Derived From All-Sky Imagers." *Renewable Energy* 199: 246–261. https://doi.org/10.1016/j.renene.2022.08.127.

Long, C. N., J. M. Sabburg, J. Calbó, and D. Pagès. 2006. "Retrieving Cloud Characteristics From Ground-Based Daytime Color All-Sky Images." *Journal of Atmospheric and Oceanic Technology* 23: 633–652. https://doi.org/10.1175/JTECH1875.1.

Lonij, V. P. A., A. E. Brooks, A. D. Cronin, M. Leuthold, and K. Koch. 2013. "Intra-Hour Forecasts of Solar Power Production Using Measurements From a Network of Irradiance Sensors." *Solar Energy* 97: 58–66. https://doi.org/10.1016/j.solener.2013.08.002.

López-Cuesta, M., R. Aler-Mur, I. M. Galván-León, F. J. Rodríguez-Benítez, and A. D. Pozo-Vázquez. 2023. "Improving Solar Radiation Nowcasts by Blending Data-Driven, Satellite-Images-Based, and All-Sky-Imagers-Based Models Using Machine Learning Techniques." *Remote Sensing* 15, 2328. https://doi.org/10.3390/rs15092328.

Lorenz, E. 2018. “Solar Irradiance Forecasting for System Integration of Solar Energy.”

Lorenz, E., A. Hammer, and D. Heinemann. 2004. “Short-Term Forecasting of Solar Radiation Based on Satellite Data.”

Lorenz, E., and D. Heinemann. 2012. “Prediction of Solar Irradiance and Photovoltaic Power.” In *Comprehensive Renewable Energy*. Elsevier. https://doi.org/10.1016/B978-0-08-087872-0.00114-1.

Lorenz, E., D. Heinemann, and C. Kurz. 2012. “Local and Regional Photovoltaic Power Prediction for Large-Scale Grid Integration: Assessment of a New Algorithm for Snow Detection: Assessment of a New Algorithm for Snow Detection. Progress in Photovoltaics: Research and Applications 20: 760–769. https://doi.org/10.1002/pip.1224.

Lorenz, E., J. Hurka, D. Heinemann, and H. G. Beyer. 2009. “Irradiance Forecasting for the Power Prediction of Grid-Connected Photovoltaic Systems.” *IEEE Journal of Selected Topics in Applied Earth Observations and Remote Sensing* 2: 2–10. https://doi.org/10.1109/JSTARS.2009.2020300.

Lorenz, E., J. Kühnert, D. Heinemann, K. P. Nielsen, J. Remund, and S. C. Müller. 2016. “Comparison of Global Horizontal Irradiance Forecasts Based on Numerical Weather Prediction Models With Different Spatio-Temporal Resolutions.” *Progress in Photovoltaics* 24: 1626–1640. https://doi.org/10.1002/pip.2799.

Lorenz, E., T. Scheidsteger, J. Hurka, D. Heinemann, and C. Kurz. 2011. “Regional PV Power Prediction for Improved Grid Integration.” *Progress in Photovoltaics* 19: 757–771. https://doi.org/10.1002/pip.1033.

Lucas, B., and K. Kanade. 1981. “An Iterative Image Registration Technique With an Application to Stereo Vision (IJCAI).”

Maas, A. L. 2013. “Rectifier Nonlinearities Improve Neural Network Acoustic Models.”

Marcos, J., L. Narvarte, I. Berazaluce, R. González, and J. Samuel. 2013. “Attenuation of Power Fluctuations in Large PV Power Plants: The Use of Prediction to Optimize the Storage System.” Presented at the 28th European Photovoltaic Solar Energy Conference and Exhibition, 4,252–4,255. https://doi.org/10.4229/28THEUPVSEC2013-5BV.7.56.

Marquez, R., and C. F. M. Coimbra. 2011. “Forecasting of Global and Direct Solar Irradiance Using Stochastic Learning Methods, Ground Experiments, and the NWS Database.” *Solar Energy* 85: 746–756. https://doi.org/10.1016/j.solener.2011.01.007.

Marquez, R., and C. F. M. Coimbra. 2013. “Intra-Hour DNI Forecasting Based on Cloud Tracking Image Analysis.” *Solar Energy* 91: 327–336. https://doi.org/10.1016/j.solener.2012.09.018.

Mathiesen, P., and J. Kleissl. 2011. "Evaluation of Numerical Weather Prediction for Intra-Day Solar Forecasting in the Continental United States." *Solar Energy* 85: 967–977. https://doi.org/10.1016/j.solener.2011.02.013.

Mejia, F. A., B. Kurtz, A. Levis, Í De La Parra, and J. Kleissl. 2018. "Cloud Tomography Applied to Sky Images: A Virtual Testbed." *Solar Energy* 176: 287–300. https://doi.org/10.1016/j.solener.2018.10.023.

Miller, S. D., M. A. Rogers, J. M. Haynes, M. Sengupta, and A. K. Heidinger. 2018. "Short-Term Solar Irradiance Forecasting via Satellite/Model Coupling." *Solar Energy* 168: 102–117. https://doi.org/10.1016/j.solener.2017.11.049.

Möhrlen, C., G. Giebel, and J.W. Zack. 2023. *IEA Wind Recommended Practice for the Implementation of Renewable Energy Forecasting Solutions*. Elsevier. https://doi.org/10.1016/C2021-0-03549-5.

Morales, J., M. Zugno, S. Pindea, and P. Pinson. 2014. "Electricity Market Clearing With Improved Scheduling of Stochastic Production." *European Journal of Operational Research* 235: 765–774.

Mueller, R., T. Behrendt, A. Hammer, and A. Kemper. 2012. "A New Algorithm for the Satellite-Based Retrieval of Solar Surface Irradiance in Spectral Bands." *Remote Sensing* 4: 622–647. https://doi.org/10.3390/rs4030622.

Müller, S. C., and J. Remund. 2014. "Satellite-Based Shortest Term Solar Energy Forecast System for Entire Europe for the Next Hours." Presented at the 29th European Photovoltaic Solar Energy Conference and Exhibition, 2,589–2,590. https://doi.org/10.4229/EUPVSEC20142014-5BV.1.6.

Nguyen, D. (Andu), and J. Kleissl. 2014. "Stereographic Methods for Cloud Base Height Determination Using Two Sky Imagers." *Solar Energy* 107: 495–509. https://doi.org/10.1016/j.solener.2014.05.005.

Nielsen, A. H., A. Iosifidis, and H. Karstoft. 2021. "IrradianceNet: Spatiotemporal Deep Learning Model for Satellite-Derived Solar Irradiance Short-Term Forecasting." *Solar Energy* 228: 659–669. https://doi.org/10.1016/j.solener.2021.09.073.

Nonnenmacher, L., and C. F. M. Coimbra. 2014. "Streamline-Based Method for Intra-Day Solar Forecasting Through Remote Sensing." *Solar Energy* 108: 447–459. https://doi.org/10.1016/j.solener.2014.07.026.

Notton, G., M.-L. Nivet, C. Voyant, C. Paoli, C. Darras, F. Motte, and A. Fouilloy. 2018. "Intermittent and Stochastic Character of Renewable Energy Sources: Consequences, Cost of Intermittence, and Benefit of Forecasting." *Renewable and Sustainable Energy Reviews* 87: 96–105. https://doi.org/10.1016/j.rser.2018.02.007.

Nouri, B., K. Noureldin, T. Schlichting, S. Wilbert, T. Hirsch, M. Schroedter-Homscheidt, P. Kuhn, A. Kazantzidis, L. F. Zarzalejo, P. Blanc, Z. Yasser, J. Fernández, and R. Pitz-Paal. 2020. "Optimization of Parabolic Trough Power Plant Operations in Variable Irradiance Conditions

Using All-Sky Imagers." *Solar Energy* 198: 434–453. https://doi.org/10.1016/j.solener.2020.01.045.

Nouri, B., P. Kuhn, S. Wilbert, N. Hanrieder, C. Prahl, L. Zarzalejo, A. Kazantzidis, P. Blanc, and R. Pitz-Paal. 2019. "Cloud Height and Tracking Accuracy of Three All-Sky Imager Systems for Individual Clouds." *Solar Energy* 177: 213–228. https://doi.org/10.1016/j.solener.2018.10.079.

Nouri, B., S. Wilbert, N. Blum, Y. Fabel, E. Lorenz, A. Hammer, T. Schmidt, L. F. Zarzalejo, and R. Pitz-Paal. 2023. "Probabilistic Solar Nowcasting Based on All-Sky Imagers." *Solar Energy* 253: 285–307. https://doi.org/10.1016/j.solener.2023.01.060.

Olmo, F. J., A. Cazorla, L. Alados-Arboledas, M. A. López-Álvarez, J. Hernández-Andrés, and J. Romero. 2008. "Retrieval of the Optical Depth Using an All-Sky CCD Camera." *Applied Optics* 47, H182. https://doi.org/10.1364/AO.47.00H182.

Paletta, Q., G. Arbod, and J. Lasenby. 2021. "Benchmarking of Deep Learning Irradiance Forecasting Models From Sky Images—An In-Depth Analysis." https://doi.org/10.48550/ARXIV.2102.00721.

Paletta, Q., G. Arbod, and J. Lasenby. 2023. "Omnivision Forecasting: Combining Satellite and Sky Images for Improved Deterministic and Probabilistic Intra-Hour Solar Energy Predictions." *Applied Energy* 336, 120818. https://doi.org/10.1016/j.apenergy.2023.120818.

Paragios, N., Y. Chen, and O. Faugeras. 2006. *Handbook of Mathematical Models in Computer Vision*. Boston, MA: Springer. https://doi.org/10.1007/0-387-28831-7.

Parzen, E. 1962. "On Estimation of a Probability Density Function and Mode." *The Annals of Mathematical Statistics* 33: 1,065–1,076. https://doi.org/10.1214/aoms/1177704472.

Pedro, H. T. C., C. F. M. Coimbra, M. David, and P. Lauret. 2018. "Assessment of Machine Learning Techniques for Deterministic and Probabilistic Intra-Hour Solar Forecasts." *Renewable Energy* 123: 191–203. https://doi.org/10.1016/j.renene.2018.02.006.

Pelland, S., G. Galanis, and G. Kallos. 2013. "Solar and Photovoltaic Forecasting Through Post-Processing of the Global Environmental Multiscale Numerical Weather Prediction Model." *Progress in Photovoltaics* 21: 284–296. https://doi.org/10.1002/pip.1180.

Peng, Z., D. Yu, D. Huang, J. Heiser, and P. Kalb. 2016. "A Hybrid Approach to Estimate the Complex Motions of Clouds in Sky Images." *Solar Energy* 138: 10–25. https://doi.org/10.1016/j.solener.2016.09.002.

Peng, Z., D. Yu, D. Huang, J. Heiser, S. Yoo, and P. Kalb. 2015. "3D Cloud Detection and Tracking System for Solar Forecast Using Multiple Sky Imagers." *Solar Energy* 118: 496–519. https://doi.org/10.1016/j.solener.2015.05.037.

Perez, R., and T. E. Hoff. 2013. "Chapter 10: SolarAnywhere Forecasting." In *Solar Energy Forecasting and Resource Assessment*. Edited by J. Kleissl. Boston, MA: Academic Press, Boston. https://doi.org/10.1016/B978-0-12-397177-7.00010-3.

Perez, R., E. Lorenz, S. Pelland, M. Beauharnois, G. Van Knowe, K. Hemker, D. Heinemann, J. Remund, S. C. Müller, W. Traunmüller, G. Steinmauer, D. Pozo, J. A. Ruiz-Arias, V. Lara-Fanego, L. Ramirez-Santigosa, M. Gaston-Romero, and L. M. Pomares. 2013. Comparison of Numerical Weather Prediction Solar Irradiance Forecasts in the U.S., Canada, and Europe." *Solar Energy* 94: 305–326. https://doi.org/10.1016/j.solener.2013.05.005.

Perez, R., J. Schlemmer, S. Kivalov, J. Dise, P. Keelin, M. Grammatico, T. Hoff, and A. Tuohy. 2018. "A New Version of the SUNY Solar Forecast Model: A Scalable Approach to Site-Specific Model Training."

Perez, R., K. Moore, S. Wilcox, D. Renné, and A. Zelenka. 2007. "Forecasting Solar Radiation—Preliminary Evaluation of an Approach Based Upon the National Forecast Database." *Solar Energy* 81: 809–812. https://doi.org/10.1016/j.solener.2006.09.009.

Perez, R., M. David, T. E. Hoff, M. Jamaly, S. Kivalov, J. Kleissl, P. Lauret, and M. Perez. 2016. "Spatial and Temporal Variability of Solar Energy." *Foundations and Trends in Renewable Energy* 1: 1–44. https://doi.org/10.1561/2700000006.

Pierro, M., C. Cornaro, D. Moser, A. Betti, M. Moschella, E. Collino, D. Ronzio, D. Van der Meer, J. Widen, L. Visser, T. A. AlSkaif, and W. Van Sark. 2020a. *Regional Solar Power Forecasting*. No. Report IEA-PVPS T16-01: 2020.

Pierro, M., F. Bucci, C. Cornaro, E. Maggioni, A. Perotto, M. Pravettoni, and F. Spada. 2015. "Model Output Statistics Cascade to Improve Day Ahead Solar Irradiance Forecast." *Solar Energy* 117: 99–113. https://doi.org/10.1016/j.solener.2015.04.033.

Pierro, M., M. De Felice, E. Maggioni, D. Moser, A. Perotto, F. Spada, and C. Cornaro. 2017. "Data-Driven Upscaling Methods for Regional Photovoltaic Power Estimation and Forecast Using Satellite and Numerical Weather Prediction Data." *Solar Energy* 158: 1,026–1,038. https://doi.org/10.1016/j.solener.2017.09.068.

Pierro, M., M. De Felice, F. Maggioni, D. Moser, A. Perotto, F. Spada, and C. Cornaro. 2020b. "Residual Load Probabilistic Forecast for Reserve Assessment: A Real Case Study." *Renewable Energy* 149: 508–522. https://doi.org/10.1016/j.renene.2019.12.056.

Pierro, M., R. Perez, M. Perez, D. Moser, and C. Cornaro. 2020c. "Italian Protocol for Massive Solar Integration: Imbalance Mitigation Strategies." *Renewable Energy* 153: 725–739. https://doi.org/10.1016/j.renene.2020.01.145.

Pinson, P. 2012. "Adaptive Calibration of (u,v)-Wind Ensemble Forecasts." *Quarterly Journal of the Royal Meteorological Society* 138: 1273–1284. https://doi.org/10.1002/qj.1873.

Pinson, P., and H. Madsen. 2009. "Ensemble-Based Probabilistic Forecasting at Horns Rev." *Wind Energy* 12: 137–155. https://doi.org/10.1002/we.309.

Pinson, P., H. Aa. Nielsen, J. K. Møller, H. Madsen, and G. N. Kariniotakis. 2007. "Non-Parametric Probabilistic Forecasts of Wind Power: Required Properties and Evaluation." *Wind Energy* 10: 497–516. https://doi.org/10.1002/we.230.

Prasad, A. A., and M. Kay. 2021. "Prediction of Solar Power Using Near-Real Time Satellite Data." *Energies* 14, 5865. https://doi.org/10.3390/en14185865.

Ramahatana, F., J. La Salle, P. Lauret, and M. David. 2022. "A more efficient microgrid operation through the integration of probabilistic solar forecasts." Sustainable Energy, Grids and Networks 31. https://doi.org/10.1016/j.segan.2022.100783.

Reikard, G. 2009. "Predicting Solar Radiation at High Resolutions: A Comparison of Time Series Forecasts." *Solar Energy* 83: 342–349. https://doi.org/10.1016/j.solener.2008.08.007.

Rigollier, C., M. Lefèvre, and L. Wald. 2004. "The Method Heliosat-2 for Deriving Shortwave Solar Radiation From Satellite Images." *Solar Energy* 77: 159–169. https://doi.org/10.1016/j.solener.2004.04.017.

Ruder, S. 2017. "An Overview of Gradient Descent Optimization Algorithms."

Ruiz-Arias, J. A., J. Dudhia, and C. A. Gueymard. 2014. "A Simple Parameterization of the Short-Wave Aerosol Optical Properties for Surface Direct and Diffuse Irradiances Assessment in a Numerical Weather Model." *Geoscientific Model Development* 7: 1,159–1,174. https://doi.org/10.5194/gmd-7-1159-2014.

Rumelhart, D. E., and J. L. McClelland. 1986. *Parallel Distributed Processing: Explorations in the Microstructure of Cognition. Volume 1, Foundations, Computational Models of Cognition and Perception*. Cambridge, MA: MIT Press.

Saint-Drenan, Y. M., G. H. Good, and M. Braun. 2017. "A Probabilistic Approach to the Estimation of Regional Photovoltaic Power Production." *Solar Energy* 147: 257–276. https://doi.org/10.1016/j.solener.2017.03.007.

Saint-Drenan, Y. M., G. H. Good, M. Braun, and T. Freisinger. 2016. "Analysis of the Uncertainty in the Estimates of Regional PV Power Generation Evaluated With the Upscaling Method." *Solar Energy* 135: 536–550. https://doi.org/10.1016/j.solener.2016.05.052.

Saint-Drenan, Y.-M. 2015. "A Probabilistic Approach to the Estimation of Regional Photovoltaic Power Generation Using Meteorological Data." Kassel, Germany.

Saint-Drenan, Y.-M., L. Wald, T. Ranchin, L. Dubus, and A. Troccoli. 2018. "An Approach for the Estimation of the Aggregated Photovoltaic Power Generated in Several European Countries From Meteorological Data." *Advances in Science and Research* 15: 51–62. https://doi.org/10.5194/asr-15-51-2018.

Saint-Drenan, Y.-M., S. Bofinger, K. Rohrig, and B. Ernst. 2011. "Regional Nowcasting of the Solar Power Production With PV-Plant Measurements and Satellite Images." Presented at the

ISES Solar World Congress 2011, International Solar Energy Society, Kassel, Germany, 1–11. https://doi.org/10.18086/swc.2011.11.09.

Sak, H., A. Senior, and F. Beaufays. 2014. "Long Short-Term Memory Based Recurrent Neural Network Architectures for Large Vocabulary Speech Recognition." https://doi.org/10.48550/ARXIV.1402.1128.

Sánchez-Segura, C. D., L. Valentín-Coronado, M. I. Peña-Cruz, A. Díaz-Ponce, D. Moctezuma, G. Flores, and D. Riveros-Rosas. 2021. "Solar Irradiance Components Estimation Based on a Low-Cost Sky-Imager." *Solar Energy* 220: 269–281. https://doi.org/10.1016/j.solener.2021.02.037.

Sanfilippo, A., L. Martin-Pomares, N. Mohandes, D. Perez-Astudillo, and D. Bachou. 2016. "An Adaptive Multi-Modeling Approach to Solar Nowcasting." *Solar Energy* 125: 77–85. https://doi.org/10.1016/j.solener.2015.11.041.

Scaramuzza, D., A. Martinelli, and R. Siegwart. 2006. "A Toolbox for Easily Calibrating Omnidirectional Cameras." Presented at the 2006 IEEE/RSJ International Conference on Intelligent Robots and Systems, 5,695–5,701. https://doi.org/10.1109/IROS.2006.282372.

Schmidt, T., J. Kalisch, E. Lorenz, and D. Heinemann. 2016. "Evaluating the Spatio-Temporal Performance of Sky-Imager-Based Solar Irradiance Analysis and Forecasts." *Atmospheric Chemistry and Physics* 16: 3,399–3,412. https://doi.org/10.5194/acp-16-3399-2016.

Schroedter-Homscheidt, M., A. Benedetti, and N. Killius. 2017. "Verification of ECMWF and ECMWF/MACC's Global and Direct Irradiance Forecasts With Respect to Solar Electricity Production Forecasts." *Meteorologische Zeitschrift*: 1–19. https://doi.org/10.1127/metz/2016/0676.

Schroedter-Homscheidt, M., and B. Pulvermüller. 2011. "Verification of Direct Normal Irradiance Forecasts for the Concentrating Solar Thermal Power Plant Andasol-3 Location." Presented at the SolarPaces 2011, Granada, Spain.

Schroedter-Homscheidt, M., and S. Wilbert. 2017. "Methods to Provide Meteorological Forecasts for Optimum CSP System Operations." In *The Performance of Concentrated Solar Power (CSP) Systems*. Elsevier. https://doi.org/10.1016/B978-0-08-100447-0.00008-0.

Sengupta, M., P. A. Jiménez, J.-H. Kim, J. Yang, and Y. Xie. 2022. *Probabilistic Cloud Optimized Day-Ahead Forecasting System Based on WRF-Solar (Final Report)*. https://doi.org/10.2172/1855782.

Shaffery, P., A. Habte, M. Netto, A. Andreas, and V. Krishnan. 2020. "Automated Construction of Clear-Sky Dictionary From All-Sky Imager Data." *Solar Energy* 212: 73–83. https://doi.org/10.1016/j.solener.2020.10.052.

Shi, C., Y. Wang, C. Wang, and B. Xiao. 2017. "Ground-Based Cloud Detection Using Graph Model Built Upon Superpixels." *IEEE Geoscience and Remote Sensing Letters* 14: 719–723. https://doi.org/10.1109/LGRS.2017.2676007.

Simoglou, C. K., E. G. Kardakos, E. A. Bakirtzis, D. I. Chatzigiannis, S. I. Vagropoulos, A. V. Ntomaris, P. N. Biskas, A. Gigantidou, E. J. Thalassinakis, A. G. Bakirtzis, and J. P. S. Catalão. 2014. "An Advanced Model for the Efficient and Reliable Short-Term Operation of Insular Electricity Networks With High Renewable Energy Sources Penetration." *Renewable and Sustainable Energy Reviews* 38: 415–427. https://doi.org/10.1016/j.rser.2014.06.015.

Sirch, T., L. Bugliaro, T. Zinner, M. Möhrlein, and M. Vazquez-Navarro. 2017. "Cloud and DNI Nowcasting With MSG/SEVIRI for the Optimized Operation of Concentrating Solar Power Plants." *Atmospheric Measurement Techniques* 10: 409–429. https://doi.org/10.5194/amt-10-409-2017.

Skamarock, C., B. Klemp, J. Dudhia, O. Gill, M. Barker, W. Wang, and G. Powers. 2005. "A Description of the Advanced Research WRF Version 2." https://doi.org/10.5065/D6DZ069T.

Sobri, S., S. Koohi-Kamali, and N. A. Rahim. 2018. "Solar Photovoltaic Generation Forecasting Methods: A Review." *Energy Conversion and Management* 156: 459–497. https://doi.org/10.1016/j.enconman.2017.11.019.

Sosa-Tinoco, I., J. Peralta-Jaramillo, C. Otero-Casal, A. López- Agüera, G. Miguez-Macho, and I. Rodríguez-Cabo. 2016. "Validation of a Global Horizontal Irradiation Assessment From a Numerical Weather Prediction Model in the South of Sonora–Mexico." *Renewable Energy* 90: 105–113. https://doi.org/10.1016/j.renene.2015.12.055.

Sperati, S., S. Alessandrini, and L. Delle Monache. 2016. "An Application of the ECMWF Ensemble Prediction System for Short-Term Solar Power Forecasting." *Solar Energy* 133: 437–450. https://doi.org/10.1016/j.solener.2016.04.016.

Straub, N., W. Herzberg, A. Dittmann, and E. Lorenz. 2023. "Combination of a Novel All Sky Imager Based Approach for High-Resolution Solar Irradiance Nowcasting With Persistence and Satellite Nowcasts for Increased Accuracy." Presented at the EU PVSEC 2023. https://doi.org/10.4229/EUPVSEC2023/4CO.8.3.

Straub, N., W. Herzberg, A. Dittmann, and E. Lorenz. 2024. "Blending of a Novel All Sky Imager Model With Persistence and a Satellite Based Model for High-Resolution Irradiance Nowcasting." *Solar Energy* 269, 112319. https://doi.org/10.1016/j.solener.2024.112319.

Su, F., W. Jiang, J. Zhang, H. Wang, and M. Zhang. 2015. "A Local Features-Based Approach to All-Sky Image Prediction." *IBM Journal of Research and Development* 59 (6): 1–6:10. https://doi.org/10.1147/JRD.2015.2397772.

Sun, D., S. Roth, and M. J. Black. 2010. "Secrets of Optical Flow Estimation and Their Principles."

Sun, Y., G. Szűcs, and A. R. Brandt. 2018. "Solar PV Output Prediction From Video Streams Using Convolutional Neural Networks." *Energy and Environmental Science* 11: 1,811–1,818. https://doi.org/10.1039/C7EE03420B.

Thompson, G., and T. Eidhammer. 2014. "A Study of Aerosol Impacts on Clouds and Precipitation Development in a Large Winter Cyclone." *Journal of the Atmospheric Sciences* 71: 3,636–3,658. https://doi.org/10.1175/JAS-D-13-0305.1.

Tuohy, A., J. Zack, S. E. Haupt, J. Sharp, M. Ahlstrom, S. Dise, E. Grimit, C. Mohrlen, M. Lange, M. G. Casado, J. Black, M. Marquis, and C. Collier. 2015. "Solar Forecasting: Methods, Challenges, and Performance." *IEEE Power and Energy Magazine* 13: 50–59. https://doi.org/10.1109/MPE.2015.2461351.

Ulbricht, R., U. Fischer, W. Lehner, and H. Donker. 2013. "First Steps Towards a Systematical Optimized Strategy for Solar Energy Supply Forecasting."

Urbich, I., J. Bendix, and R. Müller. 2019. "The Seamless Solar Radiation (SESORA) Forecast for Solar Surface Irradiance—Method and Validation." *Remote Sensing* 11, 2576. https://doi.org/10.3390/rs11212576.

Urquhart, B., B. Kurtz, E. Dahlin, M. Ghonima, J. E. Shields, and J. Kleissl. 2015. "Development of a Sky Imaging System for Short-Term Solar Power Forecasting." *Atmospheric Measurement Techniques* 8: 875–890. https://doi.org/10.5194/amt-8-875-2015.

Urquhart, B., C. W. Chow, A. Nguyen, J. Kleissl, M. Sengupta, J. Blatchford, and D. Jeon. 2012. "Towards Intra-Hour Solar Forecasting Using Two Sky Imagers at a Large Solar Power Plant."

Urquhart, B., M. Ghonima, D. (A.) Nguyen, B. Kurtz, C. W. Chow, and J. Kleissl. 2013. "Sky-Imaging Systems for Short-Term Forecasting." In *Solar Energy Forecasting and Resource Assessment*. Elsevier. https://doi.org/10.1016/B978-0-12-397177-7.00009-7.

Van Der Meer, D. W., J. Widén, and J. Munkhammar. 2018. "Review on Probabilistic Forecasting of Photovoltaic Power Production and Electricity Consumption." *Renewable and Sustainable Energy Reviews* 81: 1,484–1,512. https://doi.org/10.1016/j.rser.2017.05.212.

Visser, L., E. Lorenz, D. Heinemann, W. G. J. H. H. Van Sark. 2022. "Solar Power Forecasts." In *Comprehensive Renewable Energy*. Elsevier. https://doi.org/10.1016/B978-0-12-819727-1.00135-7.

Voyant, C., G. Notton, S. Kalogirou, M.-L. Nivet, C. Paoli, F. Motte, and A. Fouilloy. 2017. "Machine Learning Methods for Solar Radiation Forecasting: A Review." *Renewable Energy* 105: 569–582. https://doi.org/10.1016/j.renene.2016.12.095.

Wan, C., J. Zhao, Y. Song, Z. Xu, J. Lin, and Z. Hu. 2015. "Photovoltaic and Solar Power Forecasting for Smart Grid Energy Management." *CSEE Journal of Power and Energy Systems* 1: 38–46. https://doi.org/10.17775/CSEEJPES.2015.00046.

Wang, P., R. Van Westrhenen, J. F. Meirink, S. Van Der Veen, and W. Knap. 2019. "Surface Solar Radiation Forecasts by Advecting Cloud Physical Properties Derived From Meteosat Second Generation Observations." *Solar Energy* 177: 47–58. https://doi.org/10.1016/j.solener.2018.10.073.

Wilks, D. S. 2019. *Statistical Methods in the Atmospheric Sciences*. Elsevier. https://doi.org/10.1016/C2017-0-03921-6.

Winter, K., D. Beinert, S. Vogt, and R. Fritz. 2019. "PV Power Forecast Comparison of Physical and Machine Learning Models."

Wolff, B., J. Kühnert, E. Lorenz, O. Kramer, and D. Heinemann. 2016. "Comparing Support Vector Regression for PV Power Forecasting to a Physical Modeling Approach Using Measurement, Numerical Weather Prediction, and Cloud Motion Data." *Solar Energy* 135: 197–208. https://doi.org/10.1016/j.solener.2016.05.051.

Wolfgang B. 2007. "60 Years Operational Satellites: An Overview From the Beginning of Operational Satellite Applications at an NMS up to 2030."

Xie, W., D. Liu, M. Yang, S. Chen, B. Wang, Z. Wang, Y. Xia, Y. Liu, Y. Wang, and C. Zhang. 2020. "SegCloud: A Novel Cloud Image Segmentation Model Using a Deep Convolutional Neural Network for Ground-Based All-Sky-View Camera Observation." Atmospheric Measurement Techniques 13: 1,953–1,961. https://doi.org/10.5194/amt-13-1953-2020.

Yang, D. 2019. "A Universal Benchmarking Method for Probabilistic Solar Irradiance Forecasting." *Solar Energy* 184: 410–416. https://doi.org/10.1016/j.solener.2019.04.018.

Yang, D. 2020. "Ensemble Model Output Statistics as a Probabilistic Site-Adaptation Tool for Solar Irradiance: A Revisit." *Journal of Renewable and Sustainable Energy* 12, 036101. https://doi.org/10.1063/5.0010003.

Yang, D., and D. Van Der Meer. 2021. "Post-Processing in Solar Forecasting: Ten Overarching Thinking Tools." *Renewable and Sustainable Energy Reviews* 140, 110735. https://doi.org/10.1016/j.rser.2021.110735.

Yang, D., C. Gu, Z. Dong, P. Jirutitijaroen, N. Chen, and W. M. Walsh. 2013. "Solar Irradiance Forecasting Using Spatial-Temporal Covariance Structures and Time-Forward Kriging." *Renewable Energy* 60: 235–245. https://doi.org/10.1016/j.renene.2013.05.030.

Yang, D., H. Quan, V. R. Disfani, and L. Liu. 2017. "Reconciling Solar Forecasts: Geographical Hierarchy." *Solar Energy* 146: 276–286. https://doi.org/10.1016/j.solener.2017.02.010.

Yang, D., J. Kleissl, C. A. Gueymard, H. T. C. Pedro, and C. F. M. Coimbra. 2018. "History and Trends in Solar Irradiance and PV Power Forecasting: A Preliminary Assessment and Review Using Text Mining." *Solar Energy* 168: 60–101. https://doi.org/10.1016/j.solener.2017.11.023.

Yang, D., S. Alessandrini, J. Antonanzas, F. Antonanzas-Torres, V. Badescu, H. G. Beyer, R. Blaga, J. Boland, J. M. Bright, C. F. M. Coimbra, M. David, Â. Frimane, C. A. Gueymard, T. Hong, M. J. Kay, S. Killinger, J. Kleissl, P. Lauret, E. Lorenz, D. van der Meer, M. Paulescu, R. Perez, O. Perpiñán-Lamigueiro, I. M. Peters, G. Reikard, D. Renné, Y.-M. Saint-Drenan, Y. Shuai, R. Urraca, H. Verbois, F. Vignola, C. Voyant, and J. Zhang. 2020. "Verification of Deterministic Solar Forecasts." *Solar Energy* 210: 20–37. https://doi.org/10.1016/j.solener.2020.04.019.

Yang, J., J.-H. Kim, P. A. Jiménez, M. Sengupta, J. Dudhia, Y. Xie, A. Golnas, and R. Giering. 2021. "An Efficient Method to Identify Uncertainties of WRF-Solar Variables in Forecasting Solar Irradiance Using a Tangent Linear Sensitivity Analysis." *Solar Energy* 220: 509–522. https://doi.org/10.1016/j.solener.2021.03.044.

Ye, L., Z. Cao, Y. Xiao, and Z. Yang. 2019. "Supervised Fine-Grained Cloud Detection and Recognition in Whole-Sky Images." *IEEE Transactions on Geoscience and Remote Sensing* 57: 7,972–7,985. https://doi.org/10.1109/TGRS.2019.2917612.

Zamo, M., O. Mestre, P. Arbogast, and O. Pannekoucke. 2014. "A Benchmark of Statistical Regression Methods for Short-Term Forecasting of Photovoltaic Electricity Production. Part II: Probabilistic Forecast of Daily Production." *Solar Energy* 105: 804–816. https://doi.org/10.1016/j.solener.2014.03.026.

Zemouri, N., H. Bouzgou, and C. A. Gueymard. 2019. "Multimodel Ensemble Approach for Hourly Global Solar Irradiation Forecasting." *European Physical Journal Plus* 134: 594. https://doi.org/10.1140/epjp/i2019-12966-5.

Zempila, M.-M., T. M. Giannaros, A. Bais, D. Melas, and A. Kazantzidis. 2016. "Evaluation of WRF Shortwave Radiation Parameterizations in Predicting Global Horizontal Irradiance in Greece." *Renewable Energy* 86: 831–840. https://doi.org/10.1016/j.renene.2015.08.057.

Zhang, J., R. Verschae, S. Nobuhara, and J.-F. Lalonde. 2018. "Deep Photovoltaic Nowcasting." *Solar Energy* 176: 267–276. https://doi.org/10.1016/j.solener.2018.10.024.

Zhao, X., H. Wei, H. Wang, T. Zhu, and K. Zhang. 2019. "3D-CNN-Based Feature Extraction of Ground-Based Cloud Images for Direct Normal Irradiance Prediction." *Solar Energy* 181: 510–518. https://doi.org/10.1016/j.solener.2019.01.096.

10 Principles and Practical Methods for Estimating Uncertainty and Evaluating Solar Irradiance Data

Aron Habte,[1] Christian Gueymard,[2] Stefan Wilbert,[3] Elke Lorenz,[4] José Lorenzo Balenzategui Manzanares,[5] Manajit Sengupta,[1] Daryl Myers,[6] Thomas Stoffel,[7] Frank Vignola,[8†] Jaemo Yang,[1] Philippe Lauret,[9] and Mathieu David[9]

[1] National Renewable Energy Laboratory (NREL), USA
[2] Solar Consulting Services, USA
[4] German Aerospace Center (DLR), Germany
[4] Fraunhofer Institute for Solar Energy Systems, Germany
[5] PVLab-CIEMAT, Spain
[6] NREL (retired), USA
[7] Solar Resource Solutions, LLC, USA
[8] University of Oregon, USA
† *Deceased*
[9] University of La Réunion, France

Executive Summary

The rising investment in solar energy projects has necessitated the development of improved methods to quantify and assess the uncertainty of solar resource data. The practical challenges in this area stem from the instrument used to monitor the measurand, the model and input data used to predict and forecast the measurand, and their interactions. By maintaining the proper traceability, these sources of uncertainty amplify or compensate each other as they propagate from the reference data to prediction and forecast, for example. This propagation of uncertainty has significant impacts on the prediction and forecast data, which subsequently affects the project's financing, as well as the levelized cost of energy (LCOE) and decision making at various steps.

This chapter discusses the uncertainties associated with various forms of solar resource data and how these data impact the predictions of physical or empirical models that use such data. For the purposes of this chapter, solar resource data can be classified into three different categories: experimental data, as those measured at ground stations; modeled data, estimated for past periods using physical, semiempirical, or other radiative models; and forecast data, which use current experimental data and models to estimate the future irradiance for a particular area, season, and time. The latter can be distinguished between short-term forecasting (intrahour, intraday, and days-ahead) and long-term predictions for the next decades.

Accurate measurement, prediction, or forecasting of the solar resource is complicated by the rapidity with which the solar irradiance can change, both in magnitude and spectral distribution, and the varied environmental conditions experienced during measurements.

In the case of predicted and forecasted datasets, it is essential to understand the factors that impact their accuracy relative to ground measurements because of, for example, error propagation. In parallel, the quality of these measured data is key for confidence in the determination of uncertainty in predicted and forecasted datasets. Additional factors can be considered, such as the interannual variability if using only a short dataset of, for example, 12 months or less. Thus, the overall uncertainty of a modeled dataset should include an estimate of the uncertainty of the modeled solar resource, of the ground measurements, and that resulting

from the probable interannual variability. As a general rule, even with improved instrumentation and radiation models, both the measurement and modeling of the incident irradiance can have uncertainties, depending on various factors that cannot be neglected and should be properly taken into consideration.

Sections 10.1 and 10.2 summarize the basic concepts and methods of uncertainty in datasets. Section 10.3 discusses the measurement uncertainty, mainly using the Guide to the Expression of Uncertainty in Measurements (GUM) methodology for quantifying the uncertainty for measured irradiance. Afterward, the uncertainty of modeled and forecasted data is discussed in Sections 10.4 to 10.6. Section 10.7 illustrates some available diagnostic algorithms and tools. Section 10.3 on measurements comes first, because the uncertainty in the modeled data is typically obtained by comparison with reference measurements.

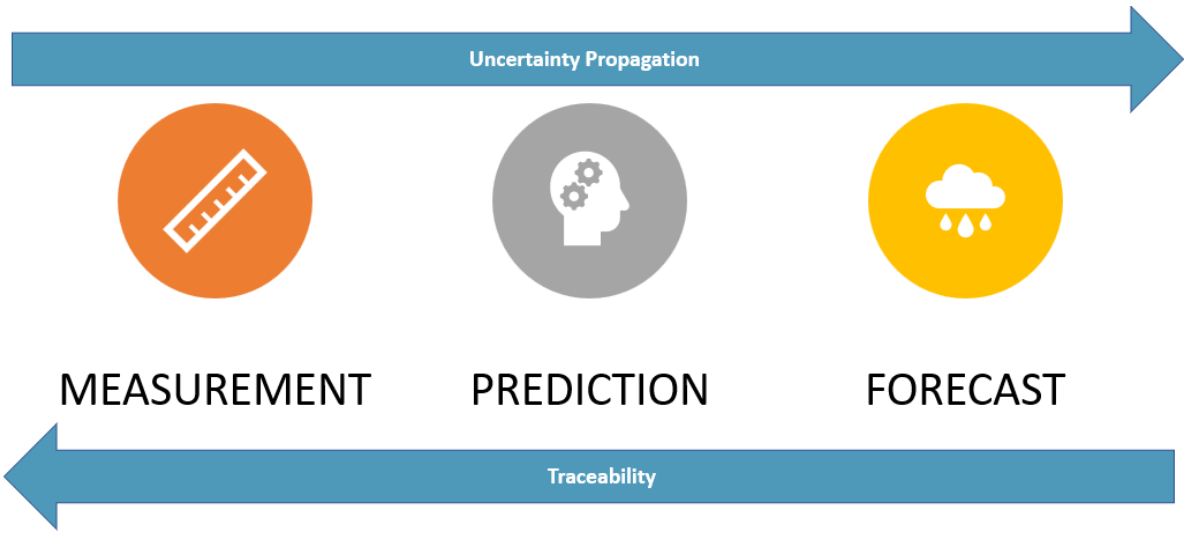

Figure ES 10-1. Traceability and uncertainty propagation for various sources of solar resource data

Image by NREL

10.1 Introductory Outline

Solar irradiance can be measured, modeled, or forecasted with various methods, as described in other chapters. These solar irradiance data are imperfect and thus uncertain.

The actual uncertainty of a dataset strongly depends on the measurement and/or modeling approach, as well as on the considered spatial and temporal scales. Measurements normally serve as a reference baseline for validating modeled data because the latter are expected to have a relatively larger uncertainty. In what follows, the main types of models under scrutiny are those that provide either satellite-derived irradiance estimates or forecasts using numerical weather prediction (NWP).

The following list summarizes a number of common notions and perceptions that are encountered in the solar industry's current practice and provides some initial recommendations based on experience.

- Measurements:
    - Measurements are the data source many users consider “ground truth”; however, measurement uncertainty is frequently not, or not sufficiently, taken into account.
    - Measurement uncertainty strongly depends on instrument specification (e.g., Instrument Class, according to ISO 9060:2018 (ISO 9060 2018)) and quality control (QC); it is essential to evaluate and further consider this uncertainty whenever using measured data.
    - Measurements obtained with Class-A instruments and subject to thorough maintenance program and QC procedures have the lowest possible uncertainty for the site and period under scrutiny. Therefore, they are a suitable reference among other tasks, such as evaluating modeled or forecasted data.
    - Because high-quality irradiance measurements can be sparse, especially for long-term periods, modeled data (of greater uncertainty) are needed in most cases.
- Modeled predictions (satellite- or NWP-based):
    - Definition: Irradiance values for past periods that are inferred using various inputs related to the same site and time through a radiative transfer model or a suite of functions, such as GHI(t)= f(M1(t), M2(t)), where the inputs are retrieved from satellite imagery or meteorological measurements.
    - Uncertainty strongly depends on the time scale of evaluation and decreases with increasing time scales (e.g., hourly values have a higher uncertainty than monthly values or, even more so, long-term mean annual values).
    - The actual uncertainty of predictions strongly depends on the performance of the model itself (or type of model) and time scale; generally, satellite-based modeled data have lower uncertainty than NWP-based irradiance data.
    - The most common way to evaluate the quality of modeled datasets is to compare them to high-quality irradiance measurements for the same location and period; the differences are summarized by some usual statistical indicators of deviation, such as root mean square deviation (RMSD), mean bias deviation (MBD), or mean absolute deviation (MAD) (see Section 10.2.3). The final letter D stands here for “deviation” or “difference” and is used in lieu of “error” to reflect that both datasets have uncertainty, which might be of similar magnitude.
    - The uncertainty of modeled data can be estimated based on statistical metric evaluations. Here, measurement uncertainty is often not properly taken into account because the differences depicted by the metrics between the modeled and measured datasets could move up and down depending on the uncertainty of the measured dataset, and may or may not be significant within these uncertainty intervals; this critical aspect is discussed further below. Note that, in the case of modeled data, accuracy and uncertainty are first a consequence of the quality of the experimental data used for validation and the amount of data available.
    - High-quality satellite-based irradiance predictions are generally considered the next best thing whenever high-quality measurements are not available for a given location and period. In such cases, they might constitute a suitable reference for

the evaluation of other modeled or forecasted data, at least for global horizontal irradiance (GHI).

- Short-term forecasts (intrahour, intraday, and days-ahead):
    - Definition: Future irradiance values that are inferred using present or past inputs: $GHI(t+\Delta t) = f(M1(t), M2(t), N1(t-\Delta t), N2(t-\Delta t))$ Here, short-term forecasting refers to forecasting up to days ahead, in contrast to long term-predictions, as described below.
    - The forecast uncertainty increases with increasing forecast horizon, and also strongly depends on the spatial and temporal scale of evaluation. It decreases with increasing time scales (e.g., minute values have a higher uncertainty than hourly or daily values). It also decreases with increasing spatial resolution (e.g., site-specific or local forecasts have higher uncertainty than regionally averaged or aggregated forecasts).
    - Forecast uncertainty is typically greater than the uncertainty of high-quality measurements or modeled data (suitable for the given spatial and temporal scale).
    - The most common way to evaluate the quality of forecast datasets is by assessing their similarity to high-quality irradiance measurements (or, if not available, high-quality modeled data) and by calculating the usual statistical indicators, such as root mean square error (RMSE), mean bias error (MBE), or mean absolute error (MAE) (see Section 10.2.3), with E denoting "error," which is common practice in meteorological forecasting because the reference measurements are assumed to be of negligible uncertainty compared to that of forecasts.
    - Forecast uncertainty is described by probabilistic forecasts consisting of probability distributions or scenarios of possible future values, depending on the current meteorological situation. As before, the reliability and resolution of these probabilistic forecasts is evaluated against high-quality irradiance measurements (or high-quality modeled data).
- Long-term predictions:
    - Long-term predictions aim to describe irradiance conditions for the next decades, typically 20–30 years for yield assessments, that is, the expected conditions in 2030, 2040, or 2050 toward the preparation of future energy scenarios.
    - Currently, long-term predictions are based on long-term historical measured or modeled data time series, a combination of both, or alternatively on typical meteorological year (TMY) datasets.
    - The accuracy of these long-term predictions is typically estimated from a statistical evaluation of modeled and/or measured data for a specific period in the past. Sometimes, interannual variability and irradiance trends are also taken into account. There is currently no consensus methodology to characterize estimates of the future resource with a precise uncertainty value and a specific confidence interval, contrary to the situation for measurements (see Chapter 6).
    - Long-term trends caused by climate change or regional air-quality measures should additionally be accounted for to estimate the uncertainty of long-term

irradiance predictions. This is a very complex task that requires more research to adequately address (see Chapter 6).

10.2 Basic Uncertainty Concepts

A clear statement of uncertainty should accompany any comprehensive solar radiation dataset to provide the necessary context for understanding the reliability of the data for various solar energy applications. For example, estimation of uncertainty provides a basis to assess confidence in the predicted output of a planned solar conversion system and is thus a key factor when determining the bankability of the project. Uncertainty is a way to specify confidence in the data.

In this preliminary approach, it is worth mentioning two important concepts associated with uncertainty that are sometimes misunderstood or mixed up. The first one is the accuracy of an experimental sensor or of a mathematical model. The accuracy is related to the ability of the sensor/model to determine the correct value of a magnitude, its true value, and how much the readings or estimations are deviated or separated from that value. The uncertainty gives an idea of how much the values of the magnitude provided by the sensor/model can be spread or dispersed around its readings/estimations in repeated measurements or calculations. The second important concept is the calibration (for an experimental sensor) or the evaluation (for an algorithm), which is the procedure or the means by which these deviations are determined and stated. In this step, it is necessary to rely on a reference value given by a standard instrument (for a sensing device) or provided by a set of real data or a function (for a model). A contribution for the overall uncertainty of the value of the magnitude given by the sensor or model is generated during this calibration or evaluation step.

It is important to determine the uncertainty using a standard methodology to provide authoritative results that can be relied on for analysis and comparisons. The GUM (ISO/IEC 2008) is an example of how to determine the uncertainty in measurements. GUM has been formalized by several organizations, including the International Bureau of Weights and Measures (French acronym: BIPM) and published by the International Standards Organization (ISO).

In the case of experimental data, the GUM terminology refers to a quantity (i.e., the value of a physical magnitude) as the measurand. To characterize this measurand, it is necessary to provide a measure of the measurand and its unit. Still, this characterization of the measurand is incomplete without supplying the associated uncertainty. This uncertainty provides an estimate of how well the value of the measurand is known and provides a range of values that would result from equivalent measurements taken under similar circumstances with similar instruments. In general, the measurand has four general sources of uncertainty: the act of measurement, the instrument doing the measurement, the device recording the measurement, and the environment in which the measurements take place. These factors follow a basic metrology's principle, in which the accuracy of the measurement is ensured with some confidence by using common standards.

Therefore, any measurement only approximates the quantity being measured, and it is incomplete without a quantitative statement of uncertainty. Each element of a measurement system contributes to the final uncertainty of the data. For example, the accuracy of solar radiation measurements made at ground stations depends on the radiometer specifications, proper installation and maintenance, data acquisition and accuracy, calibration method and frequency, location and environmental conditions, and possible real-time or a-posteriori adjustment to the data.

A large portion of this overview of uncertainty in measurements of solar radiation made at ground stations is based on Gueymard and Myers (2008); Habte et al. (2014); Habte et al. (2016); Myers et al. (2002); Reda (2011); Stoffel et al. (2000); and Wilcox and Myers (2008).

Similarly, it is desirable that predicted and forecasted datasets be qualified with a specific uncertainty, just like measurements. In this case, the different sources of error/deviation can be classified into six categories: (i) the "imperfections" of the model itself in its mathematical description of the actual physical processes; (ii) the uncertainty in its input data; (iii) the magnitude of the error propagation from input to output, depending on the specific model, location, and period; (iv) the uncertainty in the ground-truth measurements used to validate the modeled predictions; (v) the interannual variability of the predicted dataset, if the model is validated over only a short historical period; and (vi) the possible long-term trends that will affect the predictions in the future, with the latter being most important for long-term predictions. At this point, no general procedure provides a precise quantification of each of these sources of error, let alone a reproducible determination of overall uncertainty, as discussed further in Sections 10.4–10.6. One important reason for this situation is that the first three causes of error are typically site-dependent, which considerably complicates the issue.

10.2.1 Traceability

As with any other quantity or measurand, solar irradiance requires a standard reference value and physical units, which all the measuring instruments can be compared and referred to. In the International System of Units (SI) the units of solar irradiance are those of the radiant power (in W) received by the surface of a device within a given area (in m^2). Although the modern philosophy of SI is to materialize fundamental physical units by means of universal constants, there are still many derived magnitudes based on prototypes or artifacts (a given reference instrument or a given sample of reference material), which realize and implement in practice the real values of these units. This is particularly the case of solar irradiance, which is currently referred by international consensus to a set of reference instruments of high accuracy realizing the unit of W m^{-2}, namely, the World Radiometric Reference (WRR). (As discussed in Section 3.2.3, there is progress toward using the SI-based electric W in radiometry, which will eventually make WRR obsolete.)

According to the World Meteorological Organization (WMO) guide, solar resource measurements are traceable to WRR, which is maintained by the World Radiation Center (WRC) in Davos, Switzerland (see Chapter 3). The International Pyrheliometer Comparison (IPC), which is carried out there every 5 years, is used to maintain the WRR by intercomparing the World Standard Group (WSG) radiometers and evaluating their long-term stability. The WSG is now equipped with a few absolute cavity radiometers, which constitute the group of standard instruments realizing the reference unit of solar irradiance. Their average WRR reduction factor is used to transfer the scale to other participating radiometers. Moreover, during the intervening 5 years, other agencies, such as the National Renewable Energy Laboratory (NREL), organize annual regional intercomparisons to verify and maintain the WRR factor transferred through the IPC. The transfer of calibrations from the WRR to national standards results in an expanded uncertainty for these measurement standards of ±0.45% (Reda et al. 2013).

Various methods and standards are used to transfer the WRR values to field pyrheliometers and pyranometers. The calibration and assessment of calibration and field uncertainties for

pyrheliometers and pyranometers are described in detail in national and international standards, including ASTM E824 (2018); ASTM G167 (2023); ASTM G213 (2017); ISO 9059 (1990); ISO 9060 (2018); ISO 9846 (1993); ISO 9847 (2023); and ISO/TR 9901 (2021). Figure 10-1 illustrates the process of calibration transfer from WRR to any field radiometer, along with the uncertainty added at each step.

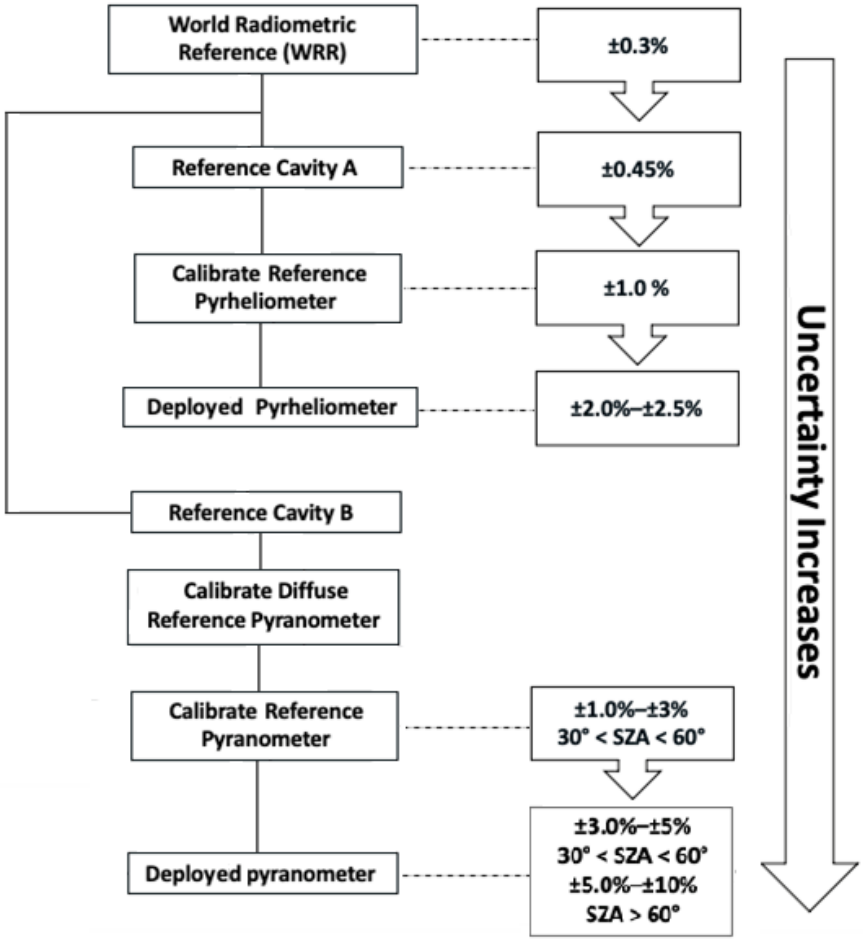

Figure 10-1. Measurement traceability and accumulation of measurement uncertainty for pyrheliometers and pyranometers (coverage factor *k* = 2)

Note: SZA stands for solar zenith angle.

Image by NREL

Similarly, spectral irradiance measurements are traceable to a national metrological laboratory (e.g., National Institute of Standards and Technology [NIST]) that has participated in intercomparisons of standards of spectral irradiance. The traceability chain and associated methods and uncertainties are exemplified in Figure 10-2. This chapter does not cover the uncertainty of spectral data, but this topic may be included in future editions of the handbook.

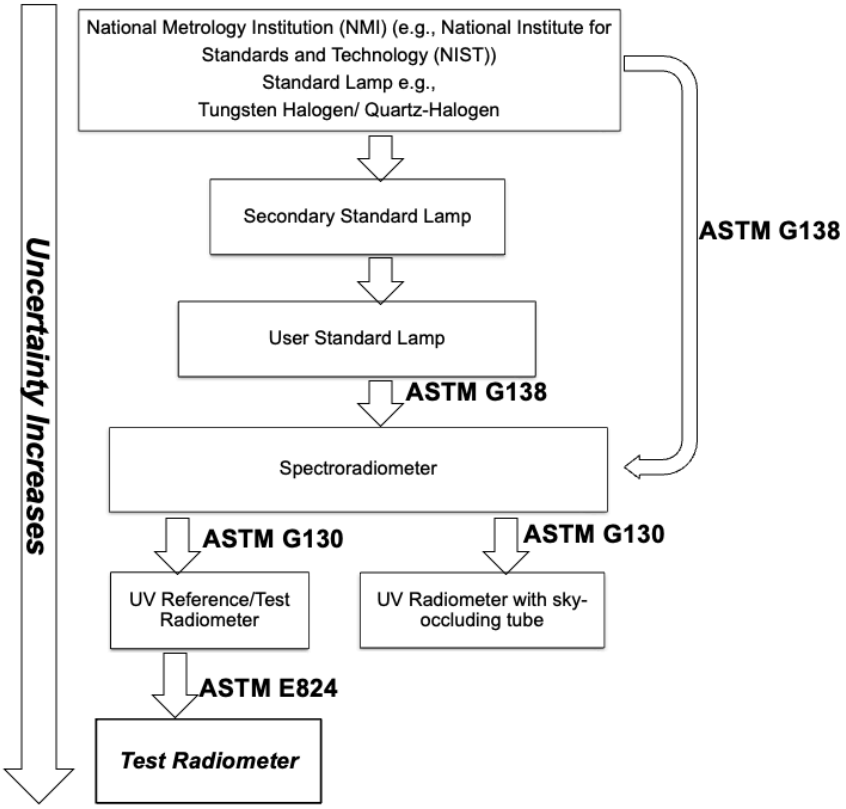

Figure 10-2. Measurement traceability for spectral irradiance

Note: UV stands for ultraviolet.

Image by NREL

Compared to the situation with irradiance measurements just described, the traceability of modeled datasets is not as straightforward. Traceability is either derived from remote-sensing (e.g., satellite or sunphotometer) information, NWP calculations, and/or statistical means. Overall, traceability is maintained through evaluation with ground measurement, as well as ongoing evaluation of uncertainty analysis and error propagation analysis. As noted above, this process is neither rigorous nor standardized yet.

10.2.2 Uncertainty vs. Error/Deviation

The difference between error and uncertainty is well documented. According to GUM (ISO/IEC 2008), the concept of uncertainty analysis supersedes the notion of error analysis. The term uncertainty describes the degree of not knowing the "true value"; it is defined as "a parameter, associated with the result of a measurement, that characterizes the dispersion of the values that could reasonably be attributed to the measurand." This concept can also be applied to predicted and forecast data as well as long-term predictions.

Conversely, error is a signed difference that is the degree of deviation of a measurement from the true value. For example, in GUM (ISO/IEC 2008), the term "error" is described as imperfections in the data that can be reduced. Error can also be explained by random and systematic errors.

Random sources are related to the standard deviation or variance of measured datasets. Biases are estimates of deviations from a "true value," primarily based on engineering judgments of the measurement system performance.

The terms "error" and "deviation" in the context of evaluating any kind of modeled data (including forecasts) typically denote deviation from "reference values" (with uncertainty as low as possible) rather than deviation from the true value. Deviations from the true value can only be approximated by this. Most often, irradiance measurements are used as reference data because they are expected to have lower uncertainty than other data. Despite this uncertainty (see Section 10.3), these data are often referred to as "ground-truth data" if their quality has been confirmed after assessment and possible improvement through appropriate QC processes (see Chapter 4). Alternatively, satellite-retrieved irradiance values, especially in the context of forecasting, or the output of a detailed physical model, might serve as a reference. Depending on the context, either "error" or "deviation" is used in the literature to characterize the difference between the modeled value and the reference value. In this chapter, the term "deviation" is used in the context of modeled historical data. It is used to emphasize the uncertainty in the reference values, for example, ground measurements.

When comparing modeled data to ground measurements, the difference can be considered statistically significant if it is greater than the uncertainty of the latter. In many cases, the uncertainty in ground measurements is not known precisely. That is why reporting the statistical metrics in terms of difference or deviation rather than error is preferred in this context.

To evaluate forecasts, on the other hand, it is preferred to report errors instead of deviations because this is the terminology generally applied in meteorological forecasting. Extrapolating in time to forecast future values adds another source of uncertainty, which leads to deviations from the true value or reference value that increase with longer forecast horizons, making the term "error" a suitable choice in this context.

10.2.3 Statistical Terms and Metrics Used to Define Accuracy

This handbook covers multiple statistical metrics used to define any deviation from the true or reference values. Here, we present the most-used error and deviation measures based on first-order statistics. A more general review is provided by Gueymard (2014) for modeled solar radiation data. A similar overview, but for forecast evaluations, is given in Jolliffe and Stephenson (2011).

10.2.3.1 Deviation of Measurements from True Value

The expected deviation of a measurement from the true value can be estimated by taking a sufficiently large number of measurements. For example, bias provides a measure of the mean overall deviation from the true value. This can be described by the MBE:

$$\mathrm{MBE} = \frac{1}{N}\sum_{N=1}^{N}(X_i - \overline{X}) \tag{10-1}$$

where N is the number of measurements, X_j is the measured value, and $\overline{X}$ is the average of the measured values. Bias can be the result of a systematic error (roughly constant over time) or of different errors that change over time but do not completely compensate for each other in the

long term. Similar to bias, the standard deviation provides a measure of the mean individual deviation from the true value.

10.2.3.2 Deviation of Modeled Historical or Forecasted Data From Reference Values

A time series of N solar radiation values X_i (measured, modeled, or forecasted) at instant i can be characterized by its average:

$$\overline{X} = \frac{1}{N}\sum_{i=1}^{N} X_i \tag{10-2}$$

and by its standard deviation, which provides a measure of the mean individual deviation from its average:

$$\sigma(X) = \sqrt{\frac{\sum_{i=1}^{N}(X_i - \overline{X})^2}{N-1}} \tag{10-3}$$

For the comparison of modeled historical or forecasted solar radiation values X_i (e.g., GHI or direct normal irradiance [DNI]) to reference values X_i^{ref} (e.g., measured GHI or DNI), the following metrics are applied. Here the metrics are introduced using deviation, which is recommended for the evaluation of modeled historical data, as noted above. The corresponding notation using error for forecast data is given between brackets.

The deviation (error) δ_i between a single modeled (forecasted) value and the corresponding reference value (e.g., measurement) is simply:

$$\delta_i = X_i - X_i^{ref} \tag{10-4}$$

To evaluate the agreement between modeled (forecasted) data and a reference value, the RMSD (RMSE) is commonly used:

$$\text{RMSD} = \frac{1}{\sqrt{N}}\sqrt{\sum_{i=1}^{N}\delta_i^2} \tag{10-5}$$

MSD = RMSD^2 (MSE = RMSE^2), is also commonly used to characterize modeled data (forecasts).

Typically, only daytime values are considered for evaluations. Relative errors for modeled historical or forecast irradiance are generally derived by normalization with respect to the mean measured irradiance over a given time interval. In contrast, relative errors of photovoltaic (PV) power forecasts for utility applications are often normalized to the installed power rather than the mean measured value, for example, in Lorenz et al. (2011).

The RMSD (RMSE) metric can be split into two components: (1) systematic, related to the MBD (MBE); and (2) stochastic, related to the standard deviation of the deviations (errors) of single

values. The MBD (MBE) is the difference between the mean of the modeled (forecasted) data and the mean of the reference values (systematic error):

$$\text{MBD} = \overline{X_i} - \overline{X_i^{ref}} = \bar{\delta} = \frac{1}{N}\sum_{i=1}^{N}\delta_i \tag{10-6}$$

A positive MBD (MBE) means the modeled (forecasted) values exceed the reference values on average (overestimation), while a negative MBD (MBE) corresponds to an average underestimation by the modeled (forecasted) data.

The standard deviation of the deviations (errors), SD (SE), is defined as:

$$\text{SD} = \sigma(\delta) = \frac{1}{\sqrt{N}}\sqrt{\sum_{i=1}^{N}(\delta_i - \bar{\delta})^2} \tag{10-7}$$

The SD (SE) metric provides information on the spread of the deviations (errors) around their mean value.

Ultimately, the decomposition of RMSD (RMSE) yields:

$$\text{RMSD}^2 = \text{MBD}^2 + \text{SD}^2 \tag{10-8}$$

For more detailed analyses, the SD (SE) metric might be further decomposed into one part related to the difference between the standard deviation of the modeled (forecasted) time series, $\sigma(X)$, and that of the reference time series, $\sigma(X^{ref})$, and another part related to the correlation coefficient, *r*, of the time series, which is defined as:

$$r = \frac{\sum_{i=1}^{N}(X_i - \bar{X})(X_i^{ref} - \overline{X_i^{ref}})}{\sigma(X)\sigma(X^{ref})} \tag{10-9}$$

Overall, the complete decomposition of RMSD (RSME) yields:

$$\text{RMSD}^2 = \text{MBD}^2 + (\sigma(X) - \sigma(X^{ref}))^2 + 2\sigma(X)\sigma(X^{ref})(1 - r) \tag{10-10}$$

Another common measure to assess the accuracy of modeled (forecasted) data is the mean absolute deviation (MAD):

$$\text{MAD} = \frac{1}{N}\sum_{i=1}^{N}|\delta_i| \tag{10-11}$$

The metrics reviewed above do not have the same importance, depending on application. In solar resource assessments, long-term yield predictions, and various other aspects of solar energy utilization, bias (MBD) can be considered “enemy number one” because it translates into systematic underestimations or overestimations of the solar power plant’s output. In turn, this can have damaging consequences on the plant’s financing, profitability, or viability. A bias in the estimated solar resource of just a few percentage points can make a big difference at the design and financing stages. To characterize random errors, the use of RMSD is more frequent than that of MAD. Because the solar resource is characterized over long periods (1 year to a few decades), and because random errors tend to decrease rapidly as the time integration increases, RMSD

tends to a limit close to |MBD| by virtue of Eq. 10-8, which is another reason why its role is secondary.

The situation is different for the application of short-term forecasting of solar irradiance and power for grid management, energy management, or marketing. Here, the errors of every single forecast value matter because balance between demand and supply must be maintained at all times. Both negative and positive forecast errors have negative consequences, like penalties or need for balancing power that do not balance out over time. This makes MAE and RMSE the most crucial metrics for deterministic forecasting.

MAE is recommended by Hoff et al. (2013) as a preferred measure in solar forecasting, in particular for reporting relative errors. In contrast, RMSE is recommended by Yang et al. (2020). An in-depth discussion on the respective merits of MAE and RMSE is given by Hodson (2022). From a user's point of view, the choice of the most suitable error measure(s) should be based on the impact of the prediction or forecast errors on their application. MAE is appropriate for applications with linear cost functions (i.e., when the costs caused by inaccurate results are proportional to the prediction error). RMSE is more sensitive to large forecast errors and is therefore suitable when small errors are tolerable and larger errors cause disproportionately high costs, which is the case for many applications in the energy market and for grid management issues.

10.2.4 Visual Diagnostics

In addition to the computation of statistical error measures, creating effective figures that demonstrate visual analysis is strongly recommended. These figures are interesting to show a direct comparison between measurements and modeled or forecast data, with the aim of developing a better understanding of the performance. Many scientific papers such as Badosa et al. (2014); Forstinger et al. (2023); Gueymard (2014); Habte et al. (2016); Markovics and Mayer (2022); Sengupta et al. (2018); Vuilleumier et al. (2014); Yang (2020); and Yang et al. (2020) demonstrate effective figures to communicate the result of solar resource and/or solar energy research. Yang (2020) illustrates violin plots that are hybrids of boxplots and kernel density plots and explain summary statistics as well as the density of the variables.

As an example, Figure 10-3 illustrates the combination of a scatterplot with a boxplot. This arrangement explains the complex relationship between the measured and modeled data. The boxplot provides information about the median, lower and upper quartile, and interquartile ranges. Obviously, the scatterplot provides a comprehensive overview of the datasets and illustrates the strength of their relationships. In parallel, the time series plot shows a comparison of successive time intervals, constituting an excellent way to visualize the possible features of a long-term dataset by providing detailed and intuitive information on patterns or relationships caused by, for example, sky conditions, seasonality, or outliers. However, such time-series plots illustrating specific patterns show only a small part of the data. Moreover, the spatial and temporal visualization of aggregated statistical metrics is important to identify any spatial and temporal pattern in relation with geographic or climate signature, for example.

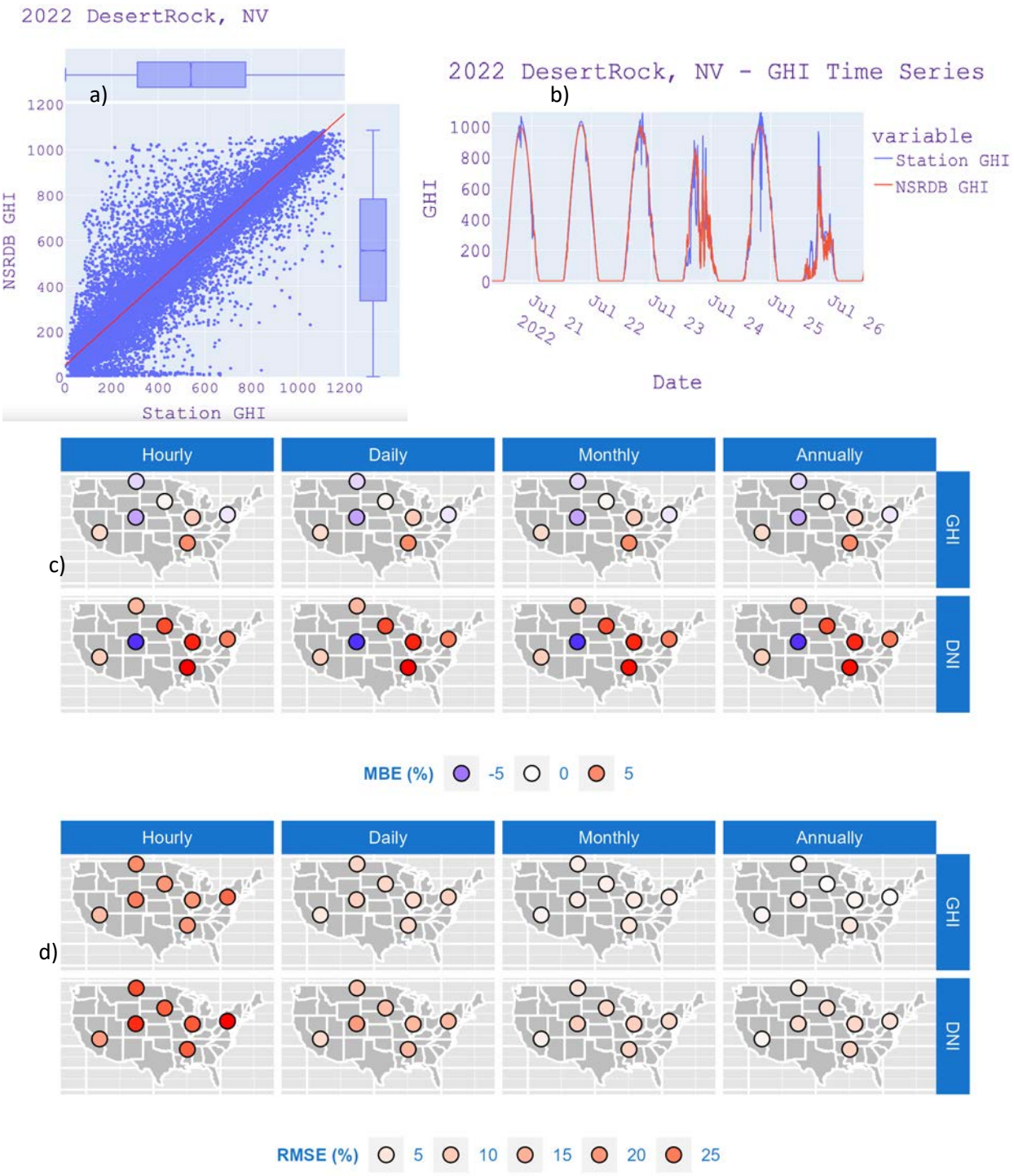

Figure 10-3. Example plots showing various comparisons of National Solar Radiation Database (NSRDB) predictions vs. ground irradiance measurements in the United States: (a) scatterplot and (b) time series plot for GHI at Desert Rock, Nevada; and plots depicting the temporal and spatial distribution of GHI and DNI for seven National Oceanic and Atmospheric Administration (NOAA) Surface Radiation Budget (SURFRAD) locations at different time scales, considering both MBE (c) and RMSE (d).

The 2022 NSRDB data based on the Physical Solar Model (PSM) V4 model was used to generate all plots. Image by NREL

10.3 Estimating Measurement Uncertainty

Uncertainty in solar radiance measurement is dependent on the type of radiometer and on the irradiance component to be measured, such as DNI, GHI, global titled irradiance (GTI), or diffuse horizontal irradiance (DHI). For each component, the measurement equation can be different, and the evaluation of the uncertainty can vary, even when following the same derivation principles. In general, the uncertainty will be estimated as a function of several contributions: calibration of the sensor, its characteristics or specifications, measurement of the output signals, working conditions, etc. Every contribution can have a different weight or relevance, so that not all of them are equally important.

It is important to note here that the uncertainty of the solar irradiance measured by a radiometer is always greater than the uncertainty of its calibration. For instance, in the case of well-maintained, high-quality thermopile radiometers deployed in the field, factors such as accuracy of solar tracking and/or leveling, data logger accuracy, cleanliness of the windows, and frequency of recalibration could contribute more sources of uncertainty. Detailed uncertainty analyses for high-quality field pyrheliometers can be found in ASTM G213 (2017); Balenzategui et al. (2022a; 2022b); Habte et al. (2016; 2017); and Michalsky et al. (2011). Similarly, the study by Vuilleumier et al. (2014) includes field pyranometers, though the term "field instrument" might be misleading here, because most of these studies refer to instruments located at research-class stations and operated under quasi-laboratory conditions (i.e., with optimal calibration and maintenance). In the practice of solar resource assessments, particularly those involving temporary stations under harsh conditions, instruments are typically maintained on a more sporadic schedule, implying that additional uncertainties would apply. In any case, the aforementioned studies show that the uncertainty of calibration is one of the most important contributions to the overall uncertainty for well-maintained high-quality instruments. Calibration of a radiometer usually consists of the determination of its responsivity, R, or the relationship between its output signal (current or voltage) and the incident solar irradiance. Calibration methods depend on the type of radiometer under test and on the type of radiometer used as reference instrument; they are normally specified by international standards (see Chapter 3).

The calibration stability of the present commercially available pyrheliometers and pyranometers is generally satisfactory, as revealed by only a slight change in their R value—typically less than ±0.1% and ±0.2% per year, respectively. When finally deployed in the field, factors such as accuracy of solar tracking and/or proper leveling and orientation, data logger accuracy, cleanliness of the windows and domes, and frequency of recalibration could contribute more sources of uncertainty. Even if these effects are kept low by following measurement and maintenance best practices, expanded uncertainties of ±2.0%–±2.5% in DNI measurements and ±3.0%–±5.0% in GHI measurements have been found from a high-quality measurement system (Reda 2011). As mentioned above, field instruments deployed at solar resource assessment stations in harsh environments can be expected to have greater uncertainties, particularly in the absence of a stringent maintenance program.

Moreover, the ASTM G213 (2017) standard provides guidance and recommended practices for evaluating uncertainties when calibrating and performing irradiance measurements with pyranometers and pyrheliometers. The standard follows the GUM method and attempts to quantify the uncertainty in measuring irradiance. Further, the standard aims to maintain the

measurement traceability through WRR with respect to SI, which ensures that the uncertainty quoted for radiometric measurements can be intercompared, based on documented methods of derivation. Figure 10-4 shows an example of the contribution of uncertainty from each source, expressed either in absolute values or percentages. Some sources of uncertainty contribute more than others, but also, the relative importance of the uncertainty budget varies during the day, with a total uncertainty that increases significantly with SZA, for reasons explained next.

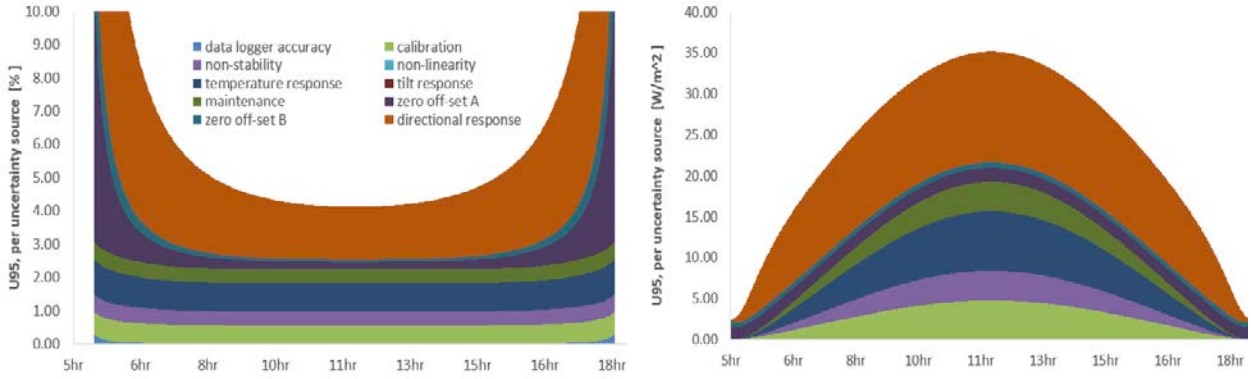

Figure 10-4. Example of expanded uncertainty as a function of time and source of uncertainty contribution, based on ASTM G213 (2017); left image, expressed in percentages, and right, expressed in W m^{-2}

Image by NREL

In addition to being sensitive to the magnitude of GHI, the responsivity of most pyranometers depends on multiple factors such as the angle of incidence of the beam irradiance component. This explains why the typical shade/unshade calibration uncertainty (see, e.g., ISO 9846 [1993]; WMO [2018]) of any thermopile pyranometer placed in a horizontal position with respect to a WRR reference cavity radiometer is ≈0.5% at any very narrow range (±2°–±5°) of SZA (Reda et al. 2008). Typically, during calibration, *R* is selected as an average responsivity for a specified SZA over one or more days. In the field, however, the monitored irradiance is sensed over a wide range of SZAs (up to 0–90°), and the measurement uncertainty over the whole range is larger. As mentioned in Chapter 3, for some pyranometers, *R* can vary by ±3–±10% or even more over this zenith angle interval. These effects then need to be combined with all other potential sources of error in the field (e.g., pyranometer installation, data logger accuracy, cleanliness, spectral dependency, or temperature sensitivity).

If only one *R* is used for a wide range of solar angles, that value is often derived for relatively low SZAs (high solar elevation), thus making the highest irradiance values (on average) associated with the lowest possible uncertainty. Another option, which is the standard procedure at NREL, for instance, is to report *R* for a fixed SZA=45° because that geometry is more representative of all daily situations. The variation of responsivity with SZA and azimuth angles is typically greater for high SZAs; thus, large uncertainties usually occur at high SZAs. These high-SZA-related uncertainties occur throughout parts of the day (early morning and late afternoon) when the available solar resource is much smaller than typical midday values and/or when SZAs are smaller. Because the minimum SZAs vary significantly throughout the year (except close to the equator), the uncertainty in hemispherical radiation data will vary as well. This effect is

especially important for latitudes beyond ±45°, when SZA is rarely smaller than or equal to the SZA at which the responsivity of the pyranometer was determined.

Even when good measurement conditions exist, such as near midday under clear-sky conditions, the uncertainty in hemispherical global or diffuse measurements is typically two to three times that of direct-beam measurements, or ±3–±5% throughout a year, primarily because of seasonal variations in uncertainty. Better instrumentation design and careful applications of correction factors as a function of SZA are ways to improve (reduce) the uncertainty in GHI measurements. The alternative is to use high-quality DNI and DHI measurements using a tracking device (e.g., a disk or a ball) to derive GHI from the closure equation (Michalsky et al. 1999). The expanded uncertainty for this calculated GHI then approaches that of DNI (±2%) for clear-sky measurements. One limitation of this method, however, is that it assumes "perfect" operating conditions, such as correct tracking for both DNI and DHI. Slight misalignments of tracking and complete tracker failures do happen in practice, resulting in large errors in all three components, unless the errors are properly and rapidly detected during the QC procedure, which is difficult in practice.

Figure 10-1 describes the calibration traceability for pyrheliometers used to measure DNI and for pyranometers used to measure GHI or DHI. The figure indicates how uncertainties accumulate from calibration to field deployment. Broad arrow boxes show the accumulated expanded uncertainty at each phase of the process. The resulting uncertainty in field deployment for pyrheliometers is ±2.0–±2.5% in this example, assuming regular and high-quality maintenance. Measurement uncertainties for pyranometers used to measure GHI in the field range from ±3.0–±5% for SZAs between 30° and 60°, but are higher for angles greater than 60°, again assuming regular and high-quality maintenance.

Calibrations of pyranometers can be performed horizontally (for GHI) or at tilt (for GTI). More specifically, pyranometers measuring GHI are calibrated horizontally using either GHI or combined DNI and DHI measurements as a reference. Calibration for a pyranometer intended to sense GTI is done using a reference pyranometer installed on the same exact tilt (ASTM E824 2018). Tilting a pyranometer for GTI measurements can slightly alter its responsivity compared to its horizontal position because of, for example, changes in convection patterns inside the dome or changes in thermal offset. This typically affects the calibration uncertainty of GTI measurements. Some thermopile pyranometers are not designed for tilted measurements, and at certain times of the day, direct sunlight can strike their unshaded bodies, affecting measurements. Shielding can reduce or eliminate this problem. Calibrating a tilted pyranometer with a reference instrument of a different type (or make and model) might also introduce additional uncertainty. To help evaluate the uncertainty in GTI data, the metadata of such datasets should include shielding information.

This caveat also holds for the measurement of upwelling irradiance using a down-facing pyranometer. (This measurement is necessary to obtain the surface albedo by dividing it by GHI, see Chapter 3.)

Digital radiometers have been recently introduced on the market and are now deployed in many solar energy projects. This also brings new challenges in terms of uncertainty quantification. Some digital radiometers, for example, include a built-in temperature compensation feature,

among other things. In such a case, the uncertainty of the calibrated internal sensitivity with temperature coefficients must be applied, and the contribution of the coefficients to the uncertainty should be clearly identified. More research is needed to understand the propagation and relationships of various sources of uncertainty related to digital radiometers.

For rotating shadowband irradiometers (RSIs) and photodiode pyranometers, which are typically used in Tier-2 stations (see Chapter 3), one of the most crucial impacts on uncertainty is the spectral irradiance error. This is because silicon photodiode sensors detect only visible and infrared radiation in the range ≈300–1100 nm and have a spectral response that varies strongly within this wavelength interval (see Chapter 3). Further, the role of using algorithms to reduce systematic effects and the uncertainty introduced by imperfect shading must be considered. A more detailed uncertainty analysis for RSIs following GUM can be found in Wilbert et al. (2016). The study defines a method for the derivation of the spectral error and spectral uncertainties, and presents quantitative values of the spectral and overall uncertainties. The results of this detailed analysis and other studies such as Wilcox and Myers (2008) indicate lower overall uncertainties than those presented in Table 10-2 for silicon photodiode pyranometers because the results in the table assume that no rigorous correction is applied. The expanded measurement uncertainty for subhourly DNI measurements is approximately ±7% for a photodiode RSI radiometer with state-of-the-art correction functions for systematic errors. Similarly, RSI-based GHI measurements are found to be affected by slightly lower uncertainties than DNI (6%, $k = 2$, after application of advanced adjustment functions; see Chapter 3). Moreover, advanced adjustment functions can significantly reduce the uncertainty in both GHI and DNI. In parallel, considering the lower incidence of soiling effects on RSIs than on thermopile pyranometers, the use of advanced adjustment functions can bring RSI measurements at resource assessment stations almost on par with those from reference instruments (Al-Rasheedi et al. 2018).

The average uncertainty of an irradiance time series is expected to vary from one station to another and even from time stamp to time stamp for a specific station. An individual uncertainty analysis per station and time interval is complex and also depends on the applied QC. After detailed QC and the rejection of suspicious data, a significant part of the variation of the uncertainty with station and time is removed. As a simplification, the uncertainty of DNI and GHI at either Tier-1 or Tier-2 stations can be estimated, based on the methods described in this section. In problematic cases and for the most relevant zenith angles, the QC procedure for stations with an independent measurement of the 3 components (GHI, DHI, and DNI) flags data with deviations larger than 8% between calculated (using the closure equation) and measured GHI. Assuming good maintenance, the uncertainty of the used data is expected to be lower than this QC-based limit and close to the mentioned uncertainties.

As indicated above, the standard uncertainty for well-maintained Tier-2 stations is estimated as 7% and 6% for DNI and GHI, respectively. As the three-component test cannot be performed at such stations, the upper uncertainty limit that is related to the QC procedure for these stations is higher than in the case of the Tier-1 stations with independent measurements of DNI, GHI, and DHI, and can be expected to be ≈10%. At Tier-1 stations, the uncertainty is expected to be lower than the QC-related limit and close to the estimations for well-maintained stations.

10.3.1 Method for Quantifying Uncertainty: The GUM Method

The method for estimating uncertainty has changed significantly over the last few decades. The general adaptation to the current methodology takes time, so some outdated terminology and methods still appear in the literature and might be in use by the industry. Even though the use of outdated methodologies is discouraged, short descriptions are provided to help users understand and correctly use uncertainty data based on older methodologies.

10.3.2 Practical Examples

GUM is currently the accepted guide for measurement uncertainty (ISO/IEC 2008). The method provides the expanded uncertainty for a 95% confidence interval by multiplying the combined uncertainty by the coverage factor k (k = 1.96 for a Gaussian distribution for infinite degrees of freedom; it is often approximated as 2, which is also alternatively used in this chapter). GUM defines Type-A uncertainty contributions as derived from statistical methods and Type-B sources as evaluated by other means, such as scientific judgment, experience, specifications, comparisons, and calibration data. GUM defines the concept of a standard uncertainty (u_{std}) for each uncertainty type, which is an estimate of an equivalent standard deviation (of a specified distribution) of the source of uncertainty. To appropriately combine the various uncertainties, the GUM methodology uses a sensitivity coefficient (c) that is calculated from the measurement equation using partial derivatives with respect to each input variable in the equation. GUM removes the historical factor of 2 and introduces the coverage factor k (whose value depends on the known or assumed statistical distribution of uncertainties),[61] which is applied to compute the expanded uncertainty (U_E) as:

$$U_E = k \cdot u_c \tag{10-12}$$

where:

u_C is the combined standard uncertainty, per all the steps of the GUM summary below (points 1–6).

As shown in Figure 10-5, the GUM procedure can be summarized in six steps (Konings and Habte 2016; Reda 2011):

1. ***Define the measurement equation for the calibration and/or measurement system.*** This consists of a mathematical description of the relation between sensor voltage and any other independent variables and the desired output (calibration response or engineering units for measurements). The example equations used to quantify radiometric measurement are:

$$E = \frac{(V - R_{net} \bullet W_{net})}{R} \tag{10-13a}$$

$$E = \text{DNI} \bullet \cos(Z) + \text{DHI} \tag{10-13b}$$

[61] k is 1.96 for a Gaussian distribution for a 95% confidence level. Generally, a 95% confidence level means that 95% of the values will be within the statistical limits defined by the uncertainty.

where:

- E = irradiance, in W m^{-2} (GHI, GTI, DHI, or DNI); in particular, when E stands for DNI, DHI = 0 in Eq. 10-13b and R_{net} ≈0, resulting in a simplified version of Eq. 10-13a: $E = V / R$
- R = responsivity of the radiometer in µV/ (W m^{-2})
- V = sensor output signal (e.g., voltage or current) of the radiometer (e.g., µV, mA)
- R_{net} = net infrared responsivity of the radiometer in µV/(W m^{-2})
- W_{net} = effective net infrared irradiance measured by a collocated pyrgeometer in W m^{-2}.

In the case of GHI, the closure equation (10-13b) applies, in which:

- DNI = beam irradiance measured by a primary or standard reference standard pyrheliometer in W m^{-2}
- Z = SZA, in degrees or radians
- DHI = diffuse horizontal irradiance, measured by a shaded pyranometer (W m^{-2}).

2. ***Determine the sources of uncertainty.*** Most sources of uncertainty are obtained from statistical calculations, specifications from manufacturers, and previously published reports on radiometric data uncertainty or professional experience. Some common sources of uncertainty are associated with the cosine response, spectral response, nonlinearity, temperature response, thermal loss, data logger accuracy, soiling, and calibration, including the drift of the calibration constant(s).

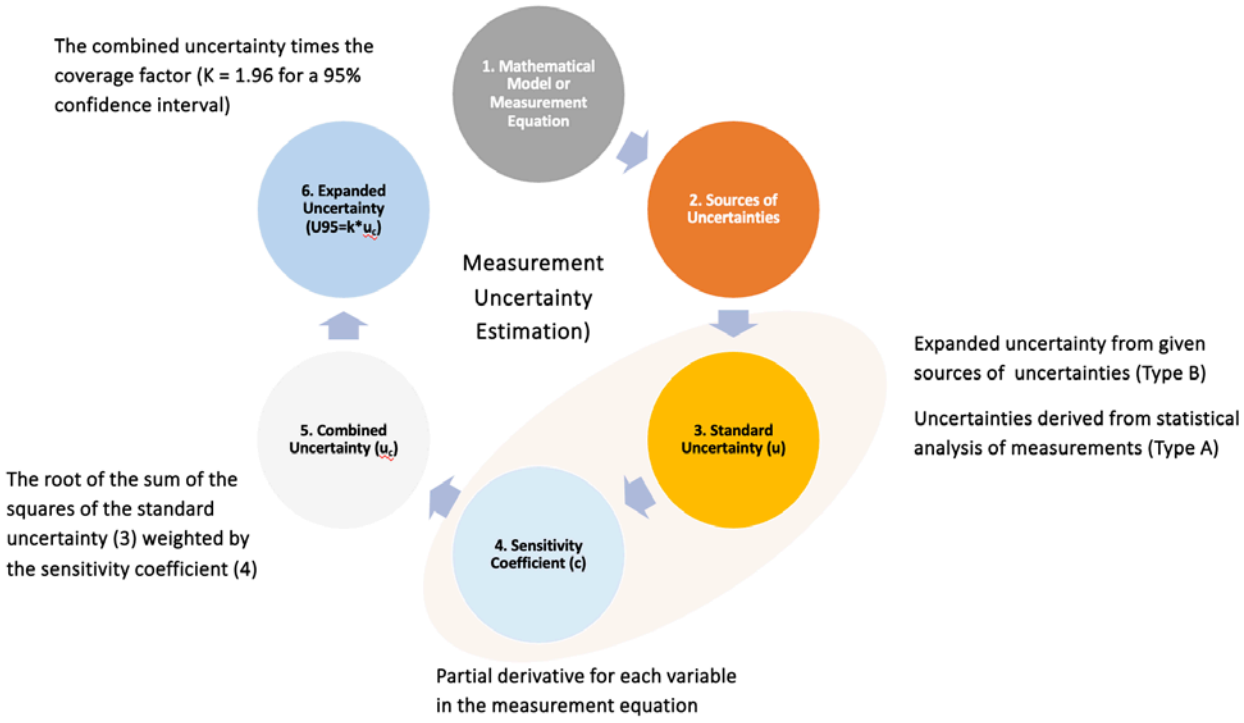

Figure 10-5. Measurement uncertainty estimation flowchart

Image modified from Habte et al. (2016)

3. ***Calculate the standard uncertainty, u.*** In this step, an individual *u* for each variable in the measurement equation is calculated using either a statistical method (Type-A uncertainty component) and/or other methods (Type-B uncertainty component). In the GUM method, the standard uncertainties are calculated by dividing the expanded uncertainty of each source by a factor corresponding to the specific statistical distribution of the experimental data (ASTM G213 2017).

   A. Type-A uncertainty:

      Type-A standard uncertainty (u) is calculated when taking repeated measurements of the input quantity value, from which the sample mean and sample standard deviation (SD or σ) can be calculated, resulting in Eq. 10-13:

$$u^2 = \frac{\sigma^2}{n} \qquad \text{where:} \qquad \sigma^2 = \frac{\sum_{i=1}^{n}(X_i - \overline{X})^2}{n-1} \tag{10-14}$$

   B. Type-B uncertainty:

      Type-B uncertainties are often provided (e.g., in calibration certificates) as an expanded uncertainty (U). To be consistent with Type-A uncertainties, the standard Type-B uncertainties, u, are calculated from the expanded uncertainties, U, using one of the three following methods:

      i. Equation for unknown statistical distribution (common assumption: rectangular distribution): $u = U/\sqrt{3}$, where U is the expanded uncertainty of a variable
      ii. Normal distribution: $u = U/k$, where k is a coverage factor of 2 or, more exactly, 1.96 (ISO/IEC 2008)
      iii. For other statistical distributions, the applicable values for k are used.

4. ***Compute the sensitivity coefficient, c.*** To appropriately combine the various uncertainties in the next step, the uncertainties must be weighted. According to the GUM method, this is done by calculating the sensitivity coefficients (c) of the variables in a measurement equation. These coefficients affect the contribution of each input factor to the combined uncertainty of the irradiance value. Therefore, the sensitivity coefficient for each input is calculated by partial differentiation with respect to each input variable in the measurement equation. Table 10-1 shows those sensitivity coefficients applicable to radiation measurements.

   The sensitivity equations given in Table 10-1 are for two distinct situations. The calibration sensitivity is for calibrations when the reference GHI is calculated from reference DNI and DHI measurements. The second column is for GHI measurements in the field. The calibration sensitivities are related to the inverse of the GHI value, whereas the field sensitivities are related to the inverse of the responsivity.

Table 10-1. Example of Computing Sensitivity Coefficients for GHI Pyranometer Calibration and Measurement Using Partial Derivatives

Calibration Sensitivity Equations	Field Measurement Sensitivity Equations
$c_V = \frac{\partial R}{\partial V} = \frac{1}{\mathrm{DNI}\cos(Z) + \mathrm{DHI}}$	$c_R = \frac{\partial \mathrm{GHI}}{\partial \mathrm{R}} = \frac{-(V - R_{net}\, W_{net})}{R^2}$
$c_{Rnet} = \frac{\partial R}{\partial R_{net}} = \frac{-W_{net}}{\mathrm{DNI}\cos(Z) + \mathrm{DHI}}$	$c_{R_{net}} = \frac{\partial \mathrm{GHI}}{\partial R_{net}} = \frac{-W_{net}}{R}$
$c_{Wnet} = \frac{\partial R}{\partial W_{net}} = \frac{-\mathrm{R_{net}}}{\mathrm{DNI}\cos(Z) + \mathrm{DHI}}$	$c_{W_{net}} = \frac{\partial \mathrm{GHI}}{\partial W_{net}} = \frac{-R_{net}}{R}$
$c_{DNI} = \frac{\partial R}{\partial \mathrm{DNI}} = \frac{-(V - R_{net}\, W_{net})\cos(Z)}{(\,\mathrm{DNI}\cos(Z) + \mathrm{DHI})^2}$	$c_V = \frac{\partial \mathrm{GHI}}{\partial V} = \frac{1}{R}$
$c_{SZA} = \frac{\partial R}{\partial Z} = \frac{\mathrm{DNI}\sin(Z)\,(V - R_{net}\, W_{net})}{(\,\mathrm{DNI}\cos(Z) + \mathrm{DHI})^2}$	
$c_D = \frac{\partial R}{\partial \mathrm{DHI}} = \frac{-(V - R_{net}\, W_{net})}{(\,\mathrm{DNI}\cos(Z) + \mathrm{DHI})^2}$	

5. ***Calculate the combined standard uncertainty, u_c.*** This is the combined standard uncertainty using the propagation of errors formula and quadrature (square root sum of squares) method. It is applicable to both Type-A and Type-B sources of uncertainty. Standard uncertainties (u) in Step 3 multiplied by their sensitivity factors (c) in Step 4 are combined in quadrature to give the combined standard uncertainty, u_c:

$$u_c = \sqrt{\sum_{j=0}^{n} (u_j \bullet c_j)^2} \tag{10-15}$$

   where n is the number of uncertain variables that are used to calculate the combined uncertainty.

6. ***Calculate the expanded uncertainty (U_{95}).*** The expanded uncertainty is calculated by multiplying the combined standard uncertainty by the coverage factor, typically by applying the student's t-analysis to determine the appropriate value of k (typically 1.96 for 95% and 3 for 98% confidence, respectively, for large datasets assuming a Gaussian distribution):

$$U_{95} = k \bullet u_c \tag{10-16}$$

These six steps, also described in Figure 10-5, demonstrate that the uncertainty quantification is a cycle. This means that one can use the expanded uncertainty in Step 6 as an input to a measurement equation. This would be the case, for example, in calculations of the performance ratio of solar conversion systems: to calculate the ratio of system output/solar input, the expanded uncertainty in Step 6 is used as an input to evaluate the denominator (solar input), and the cycle continues to ultimately quantify the expanded uncertainty of the performance ratio.

Further, these steps are applicable to the quantification of the uncertainty in both calibration and field measurements. Uncertainty in measurements begins with the uncertainty in calibration references, calibration processes, and sensor design characteristics. For example, for thermopile sensors, a calibration constant is required to convert the output voltage to the required irradiance, as discussed in Chapter 3. The resulting uncertainty in calibration factors must then be combined with the influence of additional sources of uncertainty in the field measurement instrumentation, installation methods, data acquisition, and operations and maintenance processes (Reda 2011). Overall, estimates of uncertainties for the magnitudes of values (e.g., voltage, R_{net}) need some (documented) experimental, theoretical, or other (specifications) sources. These sources of uncertainty are the magnitudes adjusted in these steps—for example, in the sensitivity coefficients calculation. Such example data are presented in several references (ASTM G213 2017; Habte et al. 2014; Konings and Habte 2016; Reda 2011).

Users must pay close attention to the sources of uncertainty. For instance, the SZA uncertainty includes sources of error such as accuracy in latitude and longitude, air pressure (for refraction corrections), or timekeeping (clock accuracy). The units of these variables must be treated carefully and consistently, whether they are percentages (such as of full scale or reading) or absolute units (such as volts, degrees, or W m^{-2}). Additionally, it is essential to consider the symmetry of the sources of uncertainty. In this section, all sources of uncertainty are considered symmetrical (±); however, some other sources could be asymmetrical or one-sided. For example, Konings and Habte (2016) considered non-stability and zero offset of Type-A as one-sided sources of uncertainty.

Applying the GUM procedure to the case of pyrheliometer and pyranometer calibration, Table 10-2 summarizes the estimated uncertainties that are typically found in practice. In addition, the table identifies the typical sources of uncertainty considered for the overall uncertainty analysis of irradiance measurements from two types of radiometers: radiometers with thermopile detectors and photodiode radiometers with silicon detector (before the application of correction functions for systematic errors). Note that the contribution to uncertainty caused by insufficient maintenance (alignment, leveling, cleaning, etc.) can be much greater than the combined uncertainties for well-maintained instruments. As explained in Chapter 3, instruments with clear optics (such as most thermopile radiometers) are more strongly affected by soiling; therefore, the uncertainty related to their operation in the field directly depends on the regularity and quality of their maintenance over time.

Table 10-2. Example of Estimated Expanded Uncertainties at 95% confidence interval of Responsivities of Field Pyranometers and Pyrheliometers

Modified from Reda (2011)

Type-B Uncertainty Source	Thermopile Pyranometer (%)	Photodiode Pyranometer (%)	Thermopile Pyrheliometer (%)	Photodiode Pyrheliometer (%)
Calibration[a]	3	5	2	3
Zenith Response[b]	2	2	0.5	1
Azimuth Response	1	1	0	0
Spectral Response	1	5	1.5	8
Tilt[c]	0.2	0.2	0	0
Nonlinearity	0.5	1	0.5	1
Temperature Response	1	1	1	1
Aging per Year	0.2	0.5	0.1	0.5
U_{95}	**4.1**	**8.0**	**2.7**	**8.9**

[a] Includes zenith angle responses from 30° to 60°.
[b] Includes zenith angle responses from 0° to 30° and from 60° to 90°.
[c] This uncertainty is set to zero for untilted radiometers.

10.4 Estimating the Uncertainty of Modeled/Predicted Datasets

Solar radiation can be modeled in many ways, depending on the available inputs, origin (ground-based, satellite-based, or NWP-based), application requirements (e.g., clear-sky or all-sky conditions), and degree of detail (broadband or spectral irradiance).

Satellite-based models used to estimate solar radiation can use a physics-based approach relying on radiative transfer modeling, an empirical or semiempirical approach relating the reflected radiance sensed by the satellite sensor directly to surface radiation, or a mix of both (see Chapter 7).

Models developed using empirical or semiempirical correlations between ground-based irradiance measurements and reflected radiance observations from satellite sensors inherently carry the uncertainty of these measurements. This uncertainty is embedded in the ultimate model accuracy, along with the uncertainties associated with the satellite sensors and the modeling process. Models empirically based on ground-based irradiance measurements with 2%, 5%, or 10% uncertainty cannot have a lower uncertainty than the data used to derive and/or validate the model. Similarly, models based on first principles of physics and radiation transfer cannot be validated or verified to a level of accuracy greater than that of the ground-based irradiance measurements. A thoroughly documented uncertainty analysis of these measurements (Gueymard and Myers 2008; 2009; Habte et al. 2016; Vuilleumier et al. 2014) is necessary to ascertain the validity of model accuracy claims. The effect of biases on ground-based irradiance measurements should be part of any model analysis.

An understanding of the differences between the perspectives of satellite-derived irradiance estimates and ground-based measurements is essential when the latter are used to derive and validate satellite-derived irradiance values. Observations of a specific pixel (or grid cell) by a spaceborne radiometer ultimately provide (after substantial modeling) an estimate of surface radiation based on the estimated properties of those clouds and other atmospheric constituents spread throughout that pixel or a larger area. In contrast, surface irradiance observations are made by an instrument viewing the sky from a specific point. If the satellite pixel size is small enough, parallax errors enter into the comparison. Conversely, if it is too large, the radiation field over the pixel might not be homogenous enough for a correct comparison. Terrain effects could also influence a comparison in which cloudiness, elevation, and/or topographic shading could vary within a short distance. Often the data available for satellite modeling lack the exactitude for differentiating fine variations seen by ground-based measurements. Another intricate situation results from the fact that the clear-sky part of a satellite-based radiation model typically has a much coarser spatial resolution than the cloudy part. Whereas the latter is up to 1 km in most modern products, the former is, for example, 0.5 by 0.625° (or ≈65 km) when the atmospheric input data for the clear-sky radiation model are extracted from Modern-Era Retrospective analysis for Research and Applications, Version 2 (MERRA-2). Thus, the actual resolution of the irradiance product ultimately depends on the cloudiness conditions. These issues can be compounded by the fact that ground measurements represent an average irradiance value calculated over a fixed time interval (e.g., 1 minute or 10 minutes), whereas satellite-based model predictions solely rely on instantaneous snapshots taken at different intervals (e.g., every 10 minutes).

10.4.1 Statistical Metrics

To alleviate the absence of any standardized method for accuracy assessment and uncertainty calculation, many possible statistical metrics used in the literature have been reviewed (Gueymard 2014). Still, most authors report only the RMSD and MBD (or RMSE and MBE), that is, randomness and bias (absolute or relative). As an example, the model of Darnell et al. (1988) was used to evaluate surface radiation using cloud information from the International Satellite Cloud Climatology Project C1 cloud database. The results were then compared to surface observations collected by the World Radiation Data Center in Darnell et al. (1992). The RMSD from this comparison was ≈16 W m^{-2}, and the MBD was ≈4 W m^{-2}. Note that the interpretation of the reported sources of uncertainty depends on the spatial and temporal resolution of the data being compared (random errors tend to decrease rapidly with increasing averaging period) and that the relative uncertainties in the modeled DNI are always greater than in GHI—opposite to what occurs with high-quality measurements.

According to Perez et al. (1987), satellite-based retrievals of DNI were accurate to 10–12%. Later, Renné et al. (1999) and Zelenka et al. (1999) found that the target-specific comparison to ground-based observations had a relative RMSD of at least 20%; the time-specific pixel-wide accuracy was 10–12% on an hourly basis at the sites under scrutiny. Most accuracy results contain values that are proportional to the measured values (percentage), given that the measured values are within a certain range and specifications are related to a fixed value in W m^{-2}. The validation of satellite-based irradiance predictions is sometimes performed on a daily (instead of hourly or subhourly) timescale. This might not always be appropriate, however, particularly in areas where strong morning/afternoon cloudiness asymmetries exist (Salazar et al. 2020).

From an application or use of statistical metrics perspective, using both MAD and RMSD is not necessary and can lead to misinterpretations. This stems from considerations of statistical consistency that become important when verifying the accuracy of modeled data—most particularly in the case of forecasts (Section 10.6). In summary, if a model is optimized by minimizing the squared error, RMSD is consistent, but MAD is not (Yang et al. 2024). More in-depth theoretical details are provided by Gneiting (2011).

From a solar resource standpoint, the most important error measure is MBD by far, because any bias in the predicted resource leads to a similar bias in the estimated power production over the long term, which can put the whole project at risk, either at the financing stage or later if the actual production does not meet expectations. Although random errors in modeled irradiance estimates can be large when considering short time intervals (e.g., a few minutes), they decrease rapidly when integrating over time. They normally reach a low value when averaging over one or more years, which is the typical time frame used for resource assessments.

Moreover, bias is actually part of RMSD, per Eq. 10-8. It indicates that, even if a long averaging period is considered, such as ≈15 years, RMSD can approach the absolute value of MBD, |MBD|, but can never be lower. In contrast, good measurements have relatively small random errors, so that their total uncertainty does not change much over time. Thus, when comparing modeled irradiance estimates to reference ground-truth measurements, the RMSD of the former decreases over the averaging time and tends toward a limit that is either the uncertainty of the reference measurements or the |MBD| of the modeled results, whichever is greater. This is exemplified in Figure 10-6, using modeled data from the NSRDB.

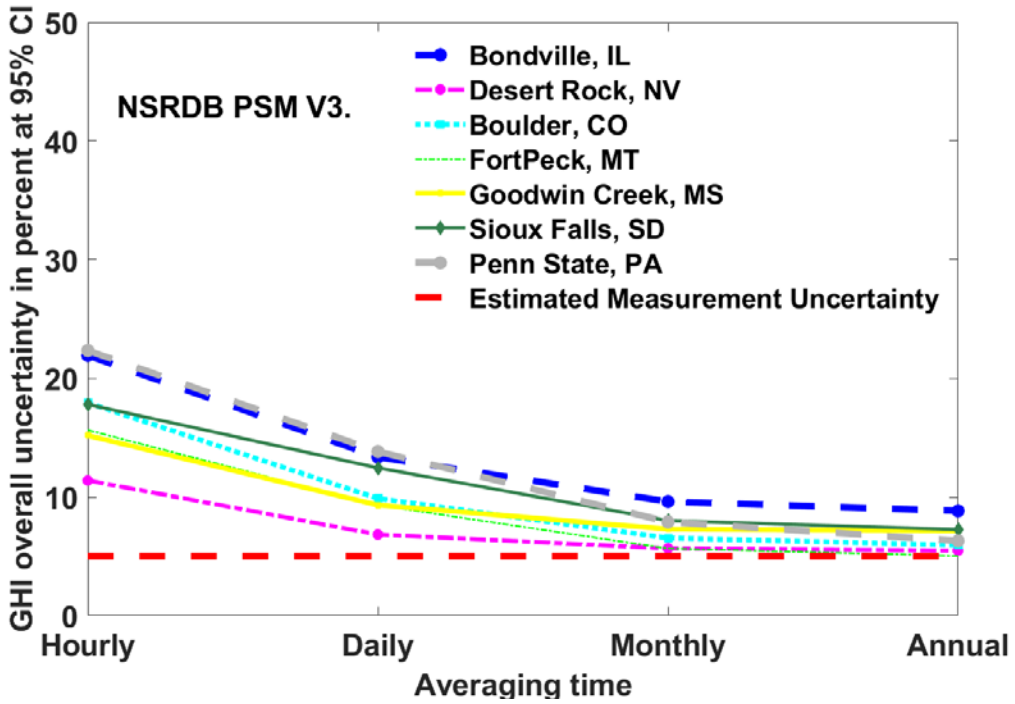

Figure 10-6. Example of decreasing trend of the RMSD of NSRDB-modeled GHI (1998–2018 PSM V3) with averaging time at various U.S. stations in comparison with measurement uncertainty. Y-axis shows the overall uncertainty with 95% confidence interval.

Image by NREL

10.4.2 Practical Examples

To improve modeled data integrity, a comprehensive representation of the model uncertainty method is desirable. As discussed in Section 10.2, no standardized method that would be equivalent to GUM, but specifically addressing modeled estimates, exists yet. Ideally, the assessment of modeled data uncertainty would attempt to replicate the developments made for measurement uncertainty, as detailed in Section 10.1. This means that the individual uncertainty of each of the six sources of error identified above would have to be quantified and ultimately combined in quadrature. This process is still in its infancy, but some considerations are developed in what follows for each source of error.

1. *Intrinsic Model's Uncertainty*

Each radiation model—most notably of an empirical nature—constitutes an approximate (and thus imperfect) mathematical representation of complex physical processes that occur throughout the atmosphere. To accelerate calculations, most models used in practice rely on several simplifying assumptions, parameterizations, look-up tables, interpolation/extrapolation, ad hoc empirical results, etc., which decrease performance. Because this might occur under various, typically unknown, circumstances, and there is essentially no way to verify the model's output without measurements that carry uncertainty, it is difficult to attribute a specific uncertainty to the model itself. The most sophisticated models with a discrete-ordinate solver algorithm (e.g., libRadtran [Emde et al. 2016; Mayer and Kylling 2005]), are considered to provide an "exact" solution to the equation of radiative transfer, and thus should have no intrinsic uncertainty, although this cannot be demonstrated. Moreover, such models cannot normally be used in repetitive calculations because of their considerable computing requirements. Even when they are used in research projects, their irradiance predictions do not necessarily appear better than those of much simpler models, possibly because of the inherent uncertainty in the reference ground truth or error propagation from imperfect inputs (Abreu et al. 2023).

2. *Model's Input Data Uncertainty*

Any radiation model relies on various inputs to provide an irradiance prediction. Some of these inputs are either deterministic (e.g., SZA) or can be measured very accurately, and can thus have an extremely low uncertainty if properly handled. Many important variables, however, can only be retrieved (e.g., through remote sensing) or estimated, in which case their uncertainty can be high and dependent on location and time. This is, for example, the case for all aerosol- and cloud-related variables. If the radiation processes strongly depend on such uncertain variables, the irradiance predictions will be impacted by any error in them. Further, if errors in the atmospheric input data are large over a specific area, a paradoxical situation can occur whereby the predictions of a sophisticated model that uses such inputs can be worse than those of a simple locally developed empirical model that does not depend on them (Sun et al. 2022).

3. *Uncertainty Caused by Error Propagation from Input to Output*

Error propagations depend on the sensitivity of the model to each input, and how these sensitivities interact with each other to result in compensation or amplification of errors.

Ideally, the specific standard deviation, σ_p, for error propagation affecting a model that predicts the irradiance quantity E from n inputs X_i (i = 1, n) would be obtained from:

$$\sigma_p^2 = \left(\Delta X_1 \frac{\delta E}{\delta X_1}\right)^2 + \left(\Delta X_2 \frac{\delta E}{\delta X_2}\right)^2 + \cdots + \left(\Delta X_n \frac{\delta E}{\delta X_n}\right)^2 \quad (10\text{-}17)$$

where the ΔX_i error in input X_i is multiplied by the sensitivity of the modeled output to X_i. This formula, however, might be too pessimistic because it does not take any possible systematic compensation of errors into account. In any case, there is currently no specific data to determine these sensitivities for each model used in practice. Some preliminary studies involving a few clear-sky radiation models have been made, however, either for the particular case of the sensitivity of DNI predictions to aerosol inputs (Gueymard 2003; 2012a; Gueymard and Ruiz-Arias 2015) or for more inputs but with a rigorous radiative transfer model, namely, libRadtran (García et al. 2014). Recently, Wang et al. (2024) analyzed the impact of various key atmospheric variables (including cloud optical depth) on the estimates of hourly all-sky GHI obtained with hybrid combinations of libRadtran and machine-learning algorithms.

4. Uncertainty in Ground-Truth Measurements

As mentioned earlier, the validation of any modeled dataset is normally made by comparison with high-quality ground-based radiometric measurements. Because there is uncertainty involved in those, even a perfect model using perfect inputs would not be attributed an uncertainty lower than that of these reference ground-truth measurements. In the field, the uncertainty of irradiance measurements can be estimated using ASTM G213 (2017), for instance.

Note that many publications mention the term "model uncertainty," but this is a confusing misnomer. Based on the above discussion, a more correct terminology is "modeled prediction uncertainty" because all four sources of error a), b), c), and d) are then explicitly included. It is also important to emphasize that the prediction uncertainty is not necessarily independent from the measurement uncertainty, which complicates the picture, as demonstrated by the following example. Suppose that the predictions from two models, M1 and M2, are compared against GHI measurements obtained with a high-quality pyranometer of assumed 5% uncertainty. Unbeknownst to the analyst, however, that specific instrument is incorrectly calibrated, resulting in a systematic bias of +3% in the measurements. Unbeknownst to the analyst as well, M1 and M2 behave the same in terms of introducing randomness in their outputs, but M1 happens to be perfectly centered (no bias), whereas M2 is biased +3% for the specific inputs used at that specific location. The comparison with ground measurements would lead the analyst to the incorrect conclusion that M2 is better than M1 and that the latter's uncertainty is larger than the former's.

5. Uncertainty Caused by the Interannual Variability

Modeled irradiance predictions are typically validated against ground-based measurements that span a period of only a few months or years. To extrapolate those results to a longer

period, such as the 30-year period of climate normals, additional uncertainty must be added, depending on irradiance component and the specific interannual variability conditions of the area (see Chapter 6). Even though this uncertainty is not negligible in general, most validation results do not take it into account and are thus somewhat optimistic, unfortunately. Note, however, that this uncertainty obviously does not apply to short-term forecasts.

6. Uncertainty Caused by Long-Term Trends

Modeled predictions can only be validated against observational data from the past. Sometimes, the reference measurements that are needed for such validation are years or decades old. Various regions of the world are affected by long-term trends (e.g., dimming and brightening) that typically affect DNI more than GHI. Because what actually matters in solar resource assessments is the accuracy of modeled predictions in future decades, the mismatch between the validation period in the past and the future period of interest must be attributed an additional uncertainty. This specific uncertainty is still not known precisely and has not been considered yet in published validation results. As in the case just above, this uncertainty does not apply to short-term forecasts.

7. Uncertainty Caused by the Sun's Output Variability

As discussed in Chapter 2, the sun's output is not constant but has both short-term (daily) fluctuations and a long-term (≈11-year) cycle. At any moment, the resulting uncertainty is about ±0.2%. It affects the uncertainty of all radiometer calibrations made outdoors because, by chance, an instrument might be calibrated at a moment when the sun's output is exceptionally high or low. For modeled data, however, this source of uncertainty is relatively small and can be neglected.

It is essential to use measurements of solar radiation made at ground stations from regions in various climates (or even microclimates) with the goal of performing a detailed evaluation of the modeled dataset; however, measurements of solar radiation made at ground stations are temporally and spatially sparse, and they are expensive to operate and maintain. Further, to perform an accurate evaluation of the model's predictions, it is critical that these ground-based irradiance measurements be of high quality and rely on low-uncertainty radiometers that follow the best practices for collection, operation, maintenance, and quality assurance.

Studies such as those by Cebecauer et al. (2011b); Gueymard (2014); Habte, Sengupta, and Lopez (2017); Suri and Cebecauer (2014); Thevenard and Pelland (2013) discussed quantification methods aimed at a comprehensive representation of prediction uncertainty. Various error statistics (bias, random error metrics) can be used to evaluate the effective uncertainty of modeled data when also considering the uncertainty in the ground-based irradiance measurements.

Following Gueymard and Wilcox (2011); Habte, Sengupta, and Lopez (2017), the interannual variability metric can be formalized as follows:

$$\mathrm{SD} = \sqrt{\left(\frac{1}{n}\sum_{i=1}^{n}\ (a_i - \hat{a})^2\right)} \tag{10-18}$$

(10-19)

$$U_{inter-annual\ variability}(\%) = \mathrm{COV}(\%) = \frac{\mathrm{SD}}{\hat{a}} \bullet 100$$

where SD is the standard deviation, and a_i is the average irradiance of the individual year, i, of the considered n years. The mean irradiance during the selected long-term period is represented by â.

In parallel, the accuracy of satellite-derived modeled data can be determined using various other statistical indicators, such as the Kolmogorov-Smirnov test (Massey Jr. 1951). The Kolmogorov-Smirnov test is a rigorous nonparametric method that is used for benchmarking satellite-retrieved GHI and DNI against ground-based observations (Espinar et al. 2009; Gueymard 2014). Directly derived from it is the Kolmogorov-Smirnov test integral, which calculates the area differences between two cumulative distribution frequencies to determine the deviation, for example, between satellite-derived data and ground measurements (Espinar et al. 2009; Beyer et al. 2009). Another indicator is OVER (estimate of the area between the CDFs over a critical value distance), which assimilates the original Kolmogorov-Smirnov test; it attempts to find values that are above a specific critical value. Unlike MBD or RMSD, OVER discriminates between values that are either statistically similar or dissimilar (depending on whether they are above a specific critical value). This test has the advantage of being nonparametric and is therefore not distribution-dependent. It compares the two distributions of irradiance to evaluate their resemblance. In the future, more elaborate methods, such as those used in the meteorological community to quantify the performance of weather forecasts (Murphy 1993), can be expected to appear and be adopted more often in large-scale solar resource assessment studies.

10.5 Modeled Data Uncertainty Estimation Challenges

Satellite-derived irradiance datasets have various embedded sources of uncertainty (Cebecauer et al. 2011a; 2011b). Most importantly, irradiance values obtained from satellite-based models use spaceborne observations of clouds. The satellite pixel represents a certain area, typically 1–100 km^2. Depending on that size, some subpixel variability and cloud-induced parallax effects could contribute to higher random errors in both GHI and DNI, as suggested by Cebecauer et al. (2011a); Habte, Sengupta, and Lopez (2017); and Zelenka et al. (1999). In intermittent cloud situations, the resolution of satellite images has limited ability to adequately describe properties of small and scattered clouds. This problem can be exacerbated when a physical retrieval method is used to first characterize the cloud optical properties for a given pixel, which can result in actual partly cloudy periods being classified as cloudless, thus yielding significant positive bias in DNI, for instance (Salazar et al. 2020).

In tropical rainforest climates, it is often challenging to find cloudless situations for characterizing the surface albedo, which is often used as a reference based on which of the pixel's overall cloudiness characteristics can be eventually quantified. Conversely, for geostationary satellite observations at high latitudes, the low satellite viewing angles introduce errors in the detection of cloud position and properties (the satellite sensor most often sees clouds from the side rather than from the top). For intermittent cloud situations, a major part of the observed random errors (evaluated by RMSD) is driven by inadequacies in the cloud-related portions of the radiative transfer algorithms.

Adequate specification of aerosols is another area of concern (Cebecauer et al. 2011b). Aerosols tend to affect DNI three to four times more than GHI, depending on the relative proportions of absorption and scattering for the specific aerosol mixture of the moment and location (Gueymard 2012b). For example, mineral dust is mostly scattering, whereas black carbon is partly absorbing. At any instant, the aerosol optical depth (AOD) varies spectrally, so the common use of a single broadband AOD could result in additional uncertainties (see Chapter 5, Section 5.5 for more information on AOD). When monthly (or "climatological") AOD averages are used, they could introduce significant errors in long-term DNI estimates (Ruiz-Arias et al. 2016). This is more likely to happen over areas of biomass burning, severe urban air pollution, or dust storms, where an aerosol climatology tends to smooth out episodic high-AOD events; therefore, it is advantageous to use AOD data with daily or subdaily resolution in advanced modeling approaches (Cebecauer et al. 2011b; Gueymard et al. 2018).

In regions with variable or complex landscape patterns (e.g., high spatial variability caused by land/water mosaics, complex urbanization, or mountains), the surface reflectance properties change rapidly, both over the space and time domains and even over distances that are shorter than the satellite's spatial resolution (Gueymard et al. 2021) (see Chapter 5, Section 5.11 for more information on this topic). Compared to neighboring rural or natural landscapes, large urban or industrial areas have much higher and temporarily changing concentrations of aerosols and water vapor. Over mountains, rapid changes in elevation also induce rapid changes in the concentration of key atmospheric constituents and in cloud properties. In addition, 3D effects and terrain shading are local complexities that must be considered and approximated by solar radiation models.

Another difficulty inherent to satellite-derived datasets is the poor discrimination between clouds and snow-covered surfaces when using only the visible imagery. This is because both situations have a high reflectance in the visible spectrum; thus, a clear-sky scene over snowy ground might look like an overcast sky, resulting in a strong overestimation or underestimation of both GHI and DNI, depending on the situation (Perez et al. 2002; Vignola and Perez 2004). One such adverse situation is known as the "Eugene syndrome" (Gueymard and Wilcox 2011). The use of multiple channels in the visible and infrared can solve this issue.

Finally, specular reflections of significant intensity, especially from sandy deserts or snowy/icy surfaces during certain times of the day, could result in incorrectly interpreting the satellite image as temporarily cloudy and thus in an underestimation of both GHI and DNI. Theoretically, this issue can be resolved by estimating the probability of specular reflection for such areas and factoring that into the calculation of surface radiation.

10.5.1 Indicative Uncertainty of Modern Satellite-Based Models

As an example, experience based on 189 validation sites shows that state-of the-art semiempirical satellite models can estimate the annual GHI with bias of about ±4% when normalized to daytime irradiation (Suri and Cebecauer 2014). This bias value depends on topography and climate. It can be higher (up to at least ±8%) in: (1) complex tropical regions; (2) areas with high atmospheric pollution, high latitudes, high mountains, or complex terrain; and (3) regions with low sun angles and occurrences of snow. Typical bias for DNI estimates at most sites is approximately twice that of GHI.

Regarding random errors, the main sources of increased uncertainty are clouds and, to a lesser extent, changes in snow cover and increased dynamics of aerosols. Over arid and semiarid areas or during sunny seasons, the RMSD of hourly GHI values normally range from 7–20%. In more cloudy regions with more intricate weather patterns, higher dynamics of atmospheric constituents, complex landscapes, or middle latitudes, the hourly RMSD increases to 15–30%. Over high mountains, high latitudes, or during seasons with low sun angles and frequent occurrences of snow, the relative RMSD for GHI can be 25–35% or more. Similar patterns of RMSD exist for the hourly DNI but with approximately twice the errors mentioned for GHI. In arid and semiarid zones, which are of the highest interest for concentrating solar energy technologies, RMSDs for the hourly DNI ranging from 18–30% are typical. In cloudier regions, with significant dynamics exhibited by aerosols, RMSD can reach 25–45%. Finally, at high latitudes and over mountains, RMSD could exceed 45%.

With continuous progress in satellite sensors and radiation models, it can be expected that the accuracy in satellite-derived databases will continue to improve, as suggested by recent validation results (Babar et al. 2018; 2019; Bright 2019; Kamath and Srinivasan 2020; Shi et al. 2018; Urraca et al. 2018). In Urraca et al. (2017), satellite data are even used to test some aspects of ground measurements using the positive-quality aspects of satellite-based irradiance data. A general validation of this "reverse QC" approach for ground measurements still needs to be undertaken, however.

10.6 Evaluation and Uncertainty of Irradiance and PV Power Forecasts

The evaluation of solar irradiance forecasts provides users with the necessary information about forecast quality and helps them choose from different forecasting products or assess the risk when using a particular forecast as a basis for decisions. This section first addresses the evaluation of deterministic irradiance or solar power forecasts that provides an overall indication of the uncertainty of a specific forecast model. Probabilistic solar forecasts assigning uncertainty estimates to each individual forecast value are described in Chapter 9, Section 9.7. Methods for probabilistic forecast evaluation, including the assessment of reliability, resolution, and sharpness are given below in Section 10.6.3.

As described in Section 10.2, the quality of forecasts, both deterministic and probabilistic, is evaluated by assessing their similarity to reference data. Most often, irradiance measurements are used as reference data. They are commonly referred to as ground-truth data, though they are also affected by a certain degree of uncertainty (see Section 10.3) Alternatively, satellite-retrieved irradiance values or the output of a detailed physical model might serve as reference. The uncertainty of the reference data should always be kept in mind when interpreting the results of forecast evaluations.

An extensive overview of forecast-verification methods is given by Jolliffe and Stephenson (2011). The choice of appropriate metrics and concepts for the evaluation of solar irradiance and power forecasts is the subject of ongoing discussions within the solar forecasting community; see Hoff and Perez (2012); Kleissl et al. (2013). Recently, Yang et al. (2020) proposed applying the well-established Murphy-Winkler framework for distribution-oriented

forecast verification as a standard practice to analyze and compare deterministic solar forecasts. In parallel, Lauret et al. (2019) addressed the evaluation of probabilistic solar forecasts.

In this chapter, the most standard evaluation methods for solar forecasting are outlined. These include: (1) statistical error metrics (Section 10.2.3); (2) basic visual assessment (Section 10.2.4); (3) comparison to reference models using the skill score (Section 10.6.1); (4) analyzing forecasts as a function of different influencing parameters (e.g., location, solar elevation, cloud conditions; Section 10.6.2); and (5) introduction to probabilistic forecast evaluation (Section 10.6.3).

10.6.1 Skill Score

The skill score (also referred to as forecast skill) is used to quantify the forecast performance relative to a reference model. RMSE is normally used for this comparison; other scores, such as MAE or MSE, are also often used. The skill score is defined as the difference between the score of the reference model and the forecast model divided by the difference between the score of the reference model and a perfect model; note that a perfect model yields zero RMSE. For RMSE, the skill score, ss_{RMSE}, is calculated as:

$$ss_{RMSE} = \frac{RMSE_{ref} - RMSE}{RMSE_{ref}}, \tag{10-20}$$

where $RMSE_{ref}$ refers to the reference model, and RMSE refers to the investigated forecasting algorithm (Coimbra and Pedro 2013). The skill score's value of 1 then indicates a perfect forecast, and a skill score of 0 means that the investigated algorithm has the same RMSE as the reference forecast. A negative value indicates performance that is worse than the reference. Skill scores might be applied for comparisons to a simple reference model and also for intercomparisons of different forecasting approaches (i.e., improvement scores).

In solar radiation forecasting, persistence is the simplest and most widely used reference model to evaluate forecast skill. Several definitions of persistence of solar irradiance are given in Chapter 9, Section 9.2.1, including simple persistence, scaled persistence (which accounts for solar geometry changes), and more-advanced concepts, such as smart persistence. Simple persistence, which does not account for solar geometry, is not recommended as a baseline for forecast lead times other than 24 hours (or multiples of it). Scaled or smart persistence are a much better choice in general. Alternatively, if long-term irradiance measurements are available, combinations of climatology and persistence can be used, as recommended by Yang et al. (2020) as an advanced reference model for forecast evaluation.

10.6.2 Analysis of Solar Forecasts Using Statistical Metrics From Different Perspectives

Solar forecasts can be analyzed with statistical metrics calculated over various scales. For example, the statistical metrics described in Section 10.2.3 can be calculated over global, temporal, or spatial scales to assess the performance of solar forecasts. The global-scale metrics computed with all available modeled-observed data across all locations and times are used to evaluate the overall performance of solar forecasts.

It is also useful to group forecast evaluations with respect to forecast lead time (temporal-scale metrics), that is, to compute error metrics with all available data at a given lead time to evaluate

the error evolution as a function of the forecast lead time. Evaluation of forecast performance in dependence of forecast lead time is shown for several examples and a variety of different forecasting algorithms in Chapter 9 (e.g., Figures 9-8, 9-13, 9-19, 9-20). This type of analysis is particularly helpful in identifying the most suitable forecast models for different lead times.

Other important considerations include analyzing forecast quality as a function of space or cloud conditions (Section 10.6.2.1), solar position and time of day (Section 10.6.2.2), or cloud variability and spatiotemporal averaging (Section 10.6.2.3).

10.6.2.1 Spatial Evaluation of Forecasts and Taylor Diagrams for Different Cloud Conditions

For the evaluation of solar forecasts as a function of space, the statistical metrics are calculated with all available pairs of predictions and observations at each location. Figure 10-7 shows an example of 2D maps for R^2, RMSE, MAE, and MBE for the DNI forecasts simulated by the combination of the Fast All-sky Radiation Model for Solar applications with DNI (FARMS-DNI) (Xie et al. 2022; Yang et al. 2022) and WRF-Solar (Jimenez et al. 2016). The NSRDB (Sengupta et al. 2018) was used to analyze the spatial distribution of the statistical metrics. More generally, high-quality satellite-derived solar radiation datasets essentially offer the opportunity to conduct in-depth analyses of the accuracy of gridded solar forecasts over a wide range of regions.

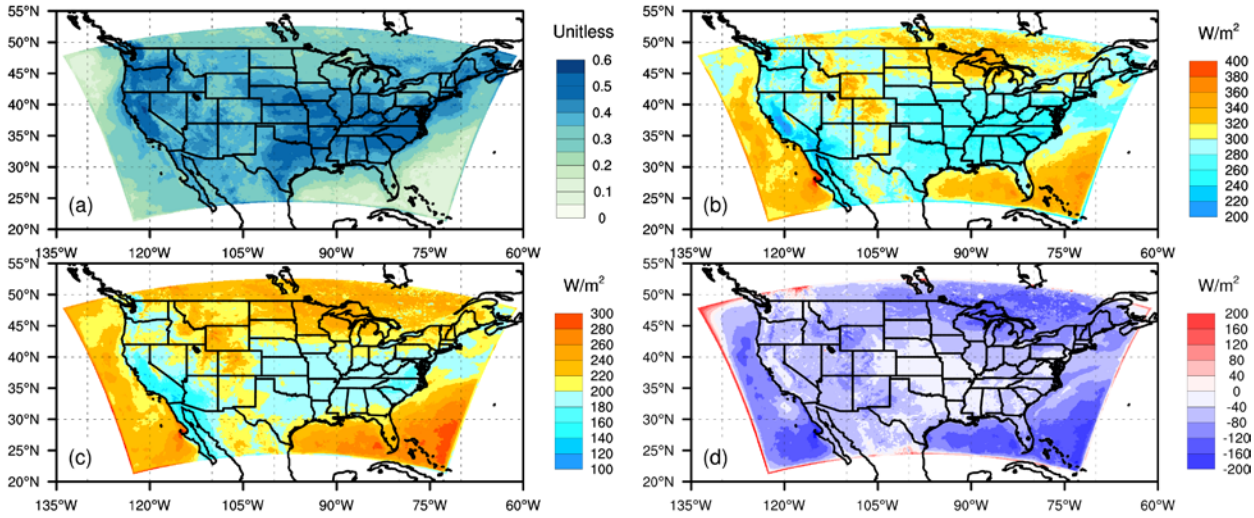

Figure 10-7. 2D maps for (a) R^2, (b) RMSE, (c) MAE, and (d) MBE of DNI forecasts simulated by the combination of FARMS-DNI and WRF-Solar

Statistical metrics of DNI forecasts are calculated against the NSRDB data for each grid point. The evaluation is performed using 365 sets of day-ahead forecasts spanning 2018.

Image by NREL

A statistical summary of model performance for the prediction of solar irradiance can be obtained with the Taylor diagram (Taylor 2001). This diagram quantifies the performance of forecasts (or other modeled data using three statistical metrics computed from modeled-observed pairs: the Pearson correlation coefficient, the standard deviation, and RMSE. Figure 10-8 shows an example of a Taylor diagram (using a normalized standard deviation) representing the performance of each member of ensemble GHI forecasts composed of 20 members simulated

with the WRF-Solar ensemble prediction system (EPS). The member obtaining the best performance is the one that lies closest to the reference point compared to other models. For example, in Figure 10-8, WRF-Solar accurately represents clear-sky scenes (red dots), thus the ensemble members lie much closer to the reference point than for cloudy-sky or all-sky conditions.

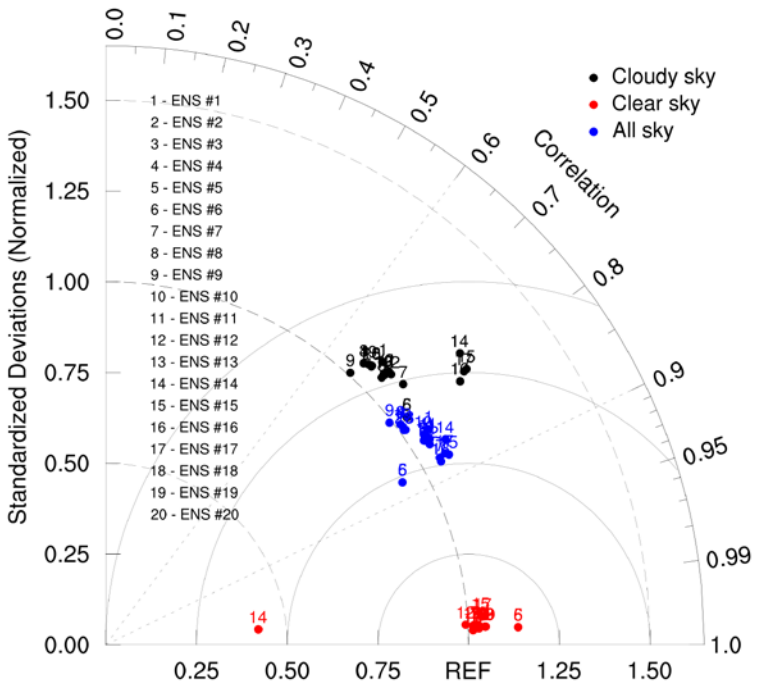

Figure 10-8. Taylor diagram for 20 ensemble members simulated with WRF-Solar under three sky conditions

Data from WRF-Solar EPS development (Sengupta et al. 2022).

10.6.2.2 Analysis of Forecast Error with Respect to Solar Elevation

Solar irradiance has a deterministic component, which results from the daily and seasonal course of the sun, and a nondeterministic component because of, for example, clouds. Both the deterministic and nondeterministic signals influence the forecast error signal. To investigate the solar irradiance forecast errors, valuable additional information is obtained by evaluating not only GHI (or DNI) but also the nondeterministic part of solar radiation, which is primarily caused by errors in the representation of clouds. To this aim, the analyzed variable is often selected to be the forecast error based on the clear-sky index rather than based on GHI.

The forecast performance of the clear-sky index can be illustrated by examples from an observational dataset of hourly pyranometer measurements from 18 weather stations of the German Weather Service (DWD) from March 2013 to February 2014 (Lorenz et al. 2016) and forecasts from two NWP models:

- High-resolution deterministic global Integrated Forecasting System (IFS) model, operated at the ECMWF with a spatial resolution of 0.125° and 3-hourly outputs; here, forecast horizons up to 24 hours are used, issued every day at 00:00 UTC.

- High-resolution Limited Area Model, operated for the area of Scandinavia (HIRLAM-SKA), operated at the Danish Meteorological Institute, with a spatial resolution of 3 km, hourly outputs, and forecast horizons from 4–9 hours ahead, issued daily at 00:00, 06:00, 12:00, and 18:00 UTC.

Figure 10-9 shows the RMSE and MBE of the clear-sky index, K_c, as a function of the cosine of the solar zenith angle (Figure 10-9, left) and the time of day (Figure 10-9, right) for the two different NWP model forecasts (IFS and SKA). The two models show similar behavior: RMSE increases with low SZA or, equivalently, during morning and evening hours, as is also the case with the magnitude of bias. This error pattern is very often caused by deficient modeling of the atmospheric transport of radiation for low solar altitudes. This limitation is a well-known flaw of the two-stream schemes used in most NWP models. Other model limitations also exist, such as 3D effects and atmospheric refraction issues whose impact is enhanced at low solar altitudes.

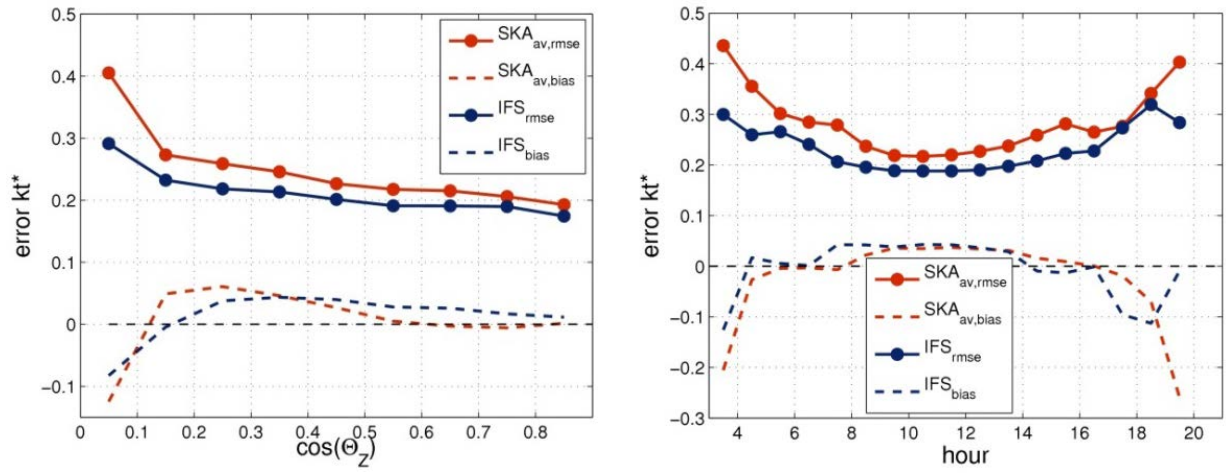

Figure 10-9. Clear-sky index (here noted as kt*) forecast error as a function of (left) cosine of SZA (noted here θ_z) and (right) hour of the day for the forecasts issued by the IFS and SKA NWP models (blue and red lines, respectively)

Solid lines show RMSE, and dashed lines show MBE (bias). The evaluated period is from March 1, 2013 to February 28, 2014.

Image by Elke Lorenz

10.6.2.3 Analysis of Forecast Error with Respect to Cloud Variability and Spatiotemporal Averaging

Forecasts generally show good agreement with measurements during clear-sky periods or even completely overcast days because both basically have a quasi-constant clear-sky index. In contrast, cloud variability strongly impacts solar forecasting accuracy. Thus, considerable deviations from the measurements are typically observed during days with variable cloudiness. An evaluation of the SKA forecast errors as a function of the measurement-derived K_c variability, here represented by the standard deviation of K_c over a 5-hour period, is shown in Figure 10-10. The evaluation also shows this dependence for multiple spatial and temporal averaging configurations of the SKA forecasts.

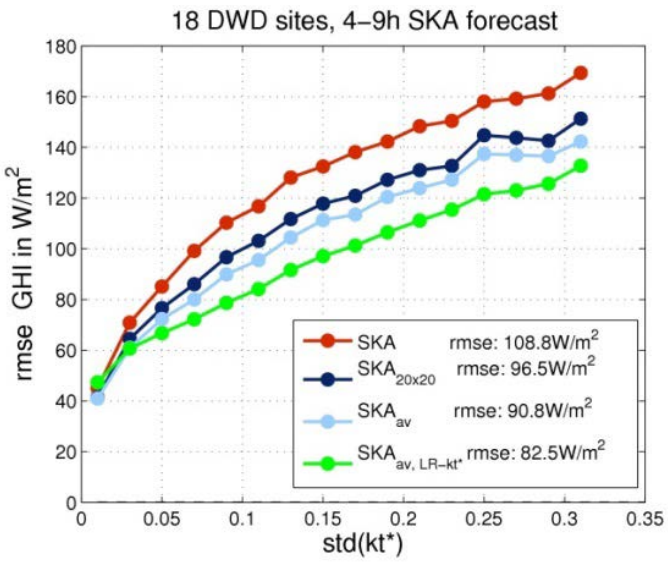

Figure 10-10. RMSE of various versions of the SKA forecasts as a function of the standard deviation of measurement-based clear-sky index, std(kt*)

Red line: SKA, original output. Dark blue: Nearest grid point, SKA_{20x20} averaged throughout 20 by 20 grid points. Light blue: SKA_{av} 5-hour sliding mean of the clear-sky index of the forecasts of the average throughout 20 by 20 grid points. Green: $SKA_{av,\ LR.kt^*}$: linear regression of the clear-sky index of the forecasts applied to SKA_{av}. The evaluated period is from April 3, 2013–February 28, 2014. Training set: Last 30 days, all 18 DWD sites.

Image by Elke Lorenz

Overall, Figure 10-10 shows that:

1. The forecast error increases with enhanced cloud variability.
2. Spatial and temporal forecast averages result in reduced RMSE values, going from negligible reductions under very stable conditions to large reductions under highly variable conditions.

Regarding the first point, the solar radiation forecast error shows a clear dependency with respect to cloud variability and, more generally, with respect to cloud conditions (Figure 10-8). Combining the error trend in the dependence of cloud conditions and the solar elevation has been proposed as an efficient method to reduce the systematic error in NWP model forecasts using a postprocessing model output statistic (MOS). In particular, Lorenz et al. (2009) used a polynomial function with cos(SZA) and K_c as independent variables to parameterize the forecast bias error from historical forecasts relative to observations and ultimately to subtract the parameterized error from operational forecasts. This approach has also been adapted and evaluated for other NWP models and different climates (Mathiesen and Kleissl 2011; Müller and Remund 2010; Pelland et al. 2013).

Regarding the second point, high-resolution irradiance forecasts frequently show phase shifts when compared to measurements, in particular for variable cloud conditions, as described also in Lorenz et al. (2016):

> "Phase shifts are caused by displacement errors in cloud prediction. Even small errors in cloud position can result in large errors for high-resolution forecasts resolving also small-scale cloud features—which is often referred to as 'double

penalty' effect. Spatial as well as temporal averaging reduces large fluctuations and forecast errors in variable situations and consequently also the RMSE."

Looking at this from another perspective, spatial and temporal averaging is in effect a way to create a new forecast by averaging forecasts of neighboring points in space and time. Under variable cloud conditions, the correlations among these forecasts are small, leading to random error cancellations during the averaging process. In contrast, under stable conditions, the correlation among neighboring pixels is high and the cancellation of random errors is reduced.

When using averaging for RMSE reduction, the optimal area size and time interval depend on the correlation structure among neighboring forecasts, both in time and space. Multiple studies have been conducted on this topic. For instance, a detailed evaluation of irradiance forecasts from the Canadian GEM model resulted in a reduction of forecast errors in the range from 10% to 15% when the model outputs were averaged throughout several hundred kilometers (Pelland et al. 2013). A similar improvement was achieved with WRF forecasts provided by Meteotest using averages over an area of 50 km by 50 km (Müller and Remund 2010). In parallel, Mathiesen and Kleissl (2011) reported an averaging area of 100 km by 100 km as suitable for irradiance forecasts using either the GFS or North American Mesoscale forecast system models. The benefit of horizon-dependent smoothing filters for Cloud Motion Vectors (CMV) forecasts was also shown by Lorenz et al. (2004), Aicardi et al. (2022), and Kühnert et al. (2013)

It is emphasized here that spatial and temporal averaging effects also have a strong impact on RSME when comparing solar irradiance forecasts of NWP models with different output resolutions. This should be considered in model intercomparisons, where different models can be compared on a similar spatial and temporal scale in addition to their original output resolution.

Temporal and spatial averaging can be also considered for nowcasts based on an all-sky imager (ASI). It has been found that in a nowcasting system with four ASIs during days with many transient clouds, the DNI RMSE for forecasts that are 10 minutes ahead is reduced in half, from 13.0% to 6.5%, by using averages of 4 km^2 and 15 minutes with respect to pixel-wise forecasts (Kuhn et al. 2018)

Despite the positive impact of spatiotemporal averaging on reducing the RMSE of a forecast, there are also negative effects. A first negative impact exists on the frequency distribution of forecasted data because the averaging process reduces extreme forecasted values and distorts the original frequency distribution of the forecast data. A second impact is that the capability to reproduce irradiance variability by the forecasts is obviously reduced. These different implications of averaging should be considered when evaluating and selecting a forecasting system for a given application. Whereas, for energy trading, RMSE or MAE are the most critical error metrics, ramp forecasting requires forecasts reflecting the high-resolution irradiance variability.

10.6.3 Verification of Probabilistic Solar Forecasts

10.6.3.1 Properties Required for a Skillful Probabilistic System

Several attributes characterize the quality[62] of probabilistic forecasts. Here, the focus is on reliability, resolution, and sharpness—the main properties used to assess the quality of probabilistic forecasts.

Reliability or calibration refers to the statistical consistency between forecasts and observations; in other words, a forecast system has a high reliability if the forecast probability and observed frequency agree. The reliability property is an important prerequisite because nonreliable forecasts would lead to a systematic bias in subsequent decision-making processes (Pinson et al. 2007).

Resolution measures the ability of a forecasting model to generate predictive distributions that depend on forecast conditions. Put differently, the more distinct the observed frequency distributions for various forecast situations are from the full climatological distribution, the more resolution the forecast system has. Climatological forecasts are perfectly reliable but have no resolution. Consequently, a skillful probabilistic forecasting system should issue reliable forecasts and should exhibit high resolution.

Sharpness refers to the concentration of predictive distributions and can be measured by the average width of the prediction intervals. Unlike reliability or resolution, sharpness is a function of only the forecasts and does not depend on the observations. Consequently, a forecasting system can produce sharp forecasts yet be useless if the probabilistic forecasts are unreliable.

10.6.3.2 Probabilistic Verification Tools

A number of visual diagnostic tools and error metrics are used for verifying probabilistic forecasts. Table 10-3 lists the diagnostic tools used to analyze probabilistic forecasts, for which Lauret et al. (2019) provided pros and cons, as well as detailed information about their implementation. Note that some tools were initially designed for a specific type of forecast (i.e., an ensemble or quantile forecast).

[62] Quality refers to the correspondence between forecasts and observations.

Table 10-3. Visual Diagnostic Tools for Probabilistic Forecasts

Diagnostic Tool	Remarks
Reliability Diagram	Initially designed for the reliability assessment of quantile forecasts. Can be used for ensemble forecasts if members are assigned specific probability levels; see Lauret et al. (2019).
Rank Histogram	Initially designed for the reliability assessment of ensemble forecasts. Can be extended to quantile forecasts if quantiles are evenly spaced.
Probability Integral Transform Histogram	Represents a reliability assessment of quantile forecasts
Sharpness Diagram	Plots the average width of the prediction intervals for different nominal coverage rates. Sharpness can only contribute to a qualitative evaluation of the probabilistic forecasts. Even if narrow prediction intervals are preferred, sharpness cannot be seen as a property for verifying the quality of probabilistic forecasts but is more likely the consequence of a high resolution.

Numerical scores provide summary measures for the evaluation of the quality of probabilistic forecasts. Table 10-4 enumerates the main scoring rules for evaluating the quality of probabilistic forecasts of a continuous variable. All the scores listed in the table are proper scoring rules (Gneiting and Raftery 2007), ensuring that perfect forecasts are given the best score value. Lauret et al. (2019) gives a detailed definition of each score.

Table 10-4. Forecast Metrics for Probabilistic Forecasts

Forecast Metric	Remarks
Continuous Ranked Probability Score (CRPS)	Can be normalized to define a skill score (CRPS skill score). Can be further partitioned into the two main attributes: reliability and resolution.
Ignorance Score	Local score (i.e., the score depends only on the value of the predictive distribution at the observation). Cannot be normalized.
Interval Score	Specifically designed for interval forecasts.
Quantile Score	Forecast performance of specific quantiles.

Some frequently used diagnostic tools and numerical scores to evaluate probabilistic forecasts are detailed next (see Lauret et al. [2019] and Yang et al. [2020] for descriptions of other metrics).

10.6.3.2.1 Reliability Diagram

A reliability diagram is a graphical verification display used to assess the reliability attribute of quantile forecasts. Quantile forecasts are evaluated one by one, and their observed frequencies are reported versus their forecast probabilities (Figure 10-11). Such a representation is appealing because the deviations from perfect reliability (the diagonal) can be visually assessed (Pinson et al. 2010); however, because of both the finite number of pairs of observation/forecast and also possible serial correlation in the sequence of forecast-verification pairs, observed proportions are not expected to lie exactly along the diagonal, even if the density forecasts are perfectly reliable. Pinson et al. (2010) proposed a method to add consistency bars to the reliability diagram. This addition can help users gain more confidence in their (possibly subjective) judgment regarding the reliability of the different models. Figure 10-12 shows an example of reliability diagram with consistency bars. In this example, the forecasts cannot be considered reliable because the line Figure 10-11 corresponding to the forecasts falls outside the consistency bars. More elaborate reliability diagrams are proposed by Yang (2019a; 2019b).

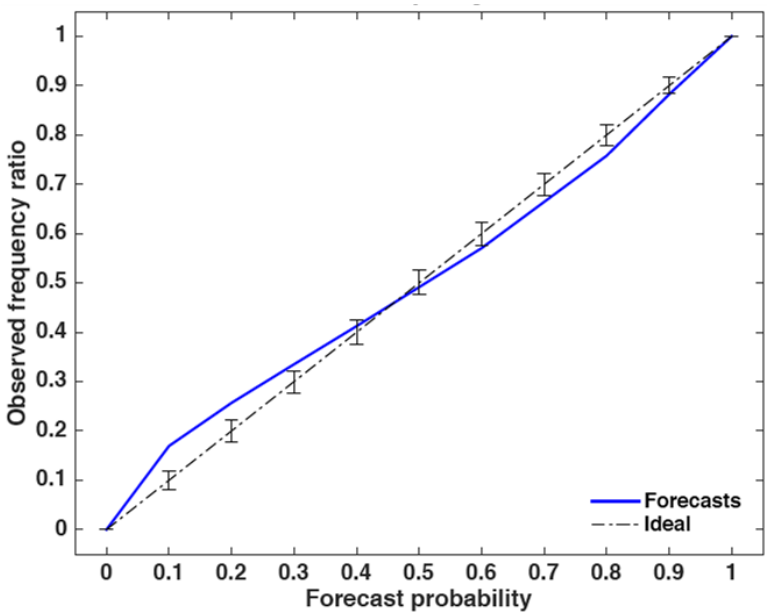

Figure 10-11. Example of a reliability diagram

Consistency bars for a 90% confidence level around the ideal line are individually computed for each nominal forecast probability. Image by University of La Réunion Laboratory of Physics and Mathematical Engineering for ENERGY, the ENVIRONMENT and BUILDINGS (PIMENT)

10.6.3.2.2 Rank Histogram

A rank histogram is a graphical display initially designed for assessing the reliability of ensemble forecasts (Wilks 2011). Rank histograms help users to visually assess the statistical consistency of the ensemble—that is, if the observation can be seen statistically like another member of the ensemble (Wilks 2011). A flat rank histogram is a necessary condition for ensemble consistency and shows an appropriate degree of dispersion of the ensemble. Underdispersed or overdispersed ensembles lead to U-shaped or hump-shaped rank histograms, respectively (Figure 10-12).

In addition, some unconditional biases can be revealed by asymmetrical (triangle-shaped) rank histograms. It must be stressed that one should be cautious when analyzing rank histograms. As

shown by Hamill (2001), a perfectly flat rank histogram does not mean that the corresponding forecast is reliable. Further, when the number of observations is limited, consistency bars can also be calculated with the procedure proposed by Bröcker and Smith (2007).

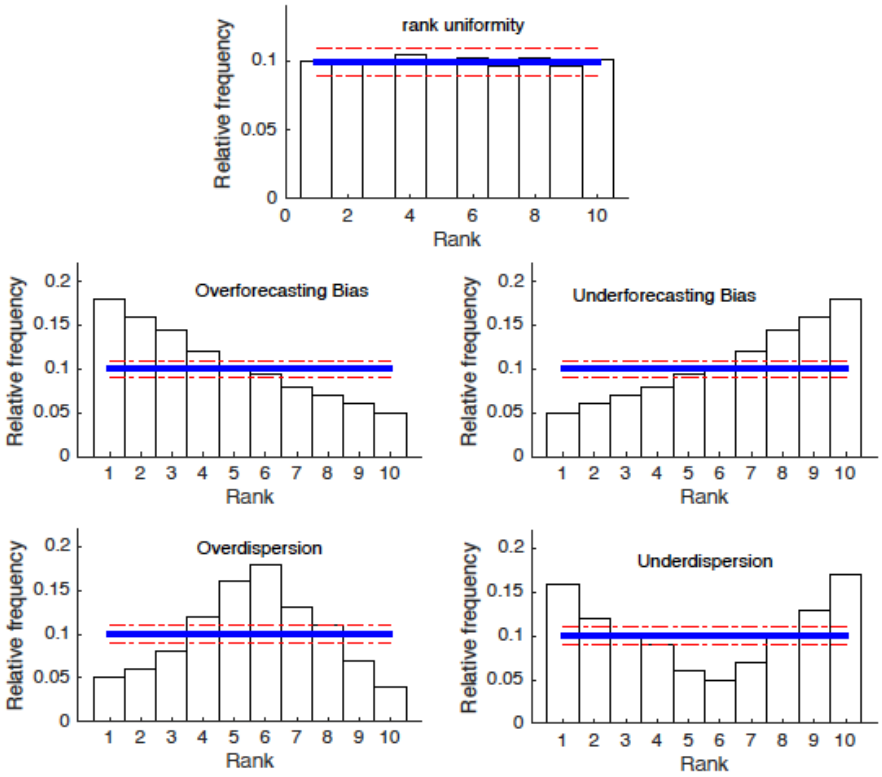

Figure 10-12. Illustrative examples of rank histograms for an ensemble of *M* = 9 members

The horizontal solid blue line denotes the statistical consistency of the ensemble. The dashed-dotted lines represent the consistency bars.

Figure modified from Wilks (2011)

10.6.3.2.3 Overall Skill Assessment With the Continuous Ranked Probability Score

The most common skill score for evaluating the quality of predictive densities of continuous variables is the CRPS, whose formulation is:

$$\mathrm{CRPS} = \frac{1}{N}\sum_{i=1}^{N}\int_{-\infty}^{+\infty}\left[\hat{F}^{i}_{fcst}(y) - F^{i}_{yobs}(y)\right]^{2} dy, \tag{10-21}$$

where $\hat{F}^{i}_{fcst}(y)$ is the predictive cumulative distribution function (CDF) of the variable of interest, x (e.g., GHI), and $F^{i}_{yobs}(y)$ is a CDF of the observation (i.e., a step function that jumps from 0 to 1 at the point where the forecast variable, y, equals the observation, y_{obs}). The squared difference between the two CDFs is averaged over the N forecast/observation pairs. Note that CRPS is negatively oriented (smaller values are better) and has the same dimension as the forecasted variable.

Figure 10-13(a) shows three hypothetical predictive probability density functions (PDFs), and Figure 10-13(b) plots the corresponding predictive CDFs. The black thick line in Figure 10-13(b) represents the CDF of the observation, $F^{i}_{yobs}(y)$. Because CRPS represents the integrated squared difference between the two CDFs, the pair of observation/forecasts labeled "1" will be assigned the best score. Conversely, forecasts indicated by labels 2 and 3 will lead to a higher CRPS. Indeed, although it has the same degree of sharpness as Forecast 1, Forecast 2 is not centered on the observation (i.e., this is a biased forecast). Conversely, Forecast 3 is centered on the observation, but is less sharp than Forecasts 1 or 2. In summary, CRPS rewards the concentration of probability around the step function located at the observed value (Hersbach 2000).

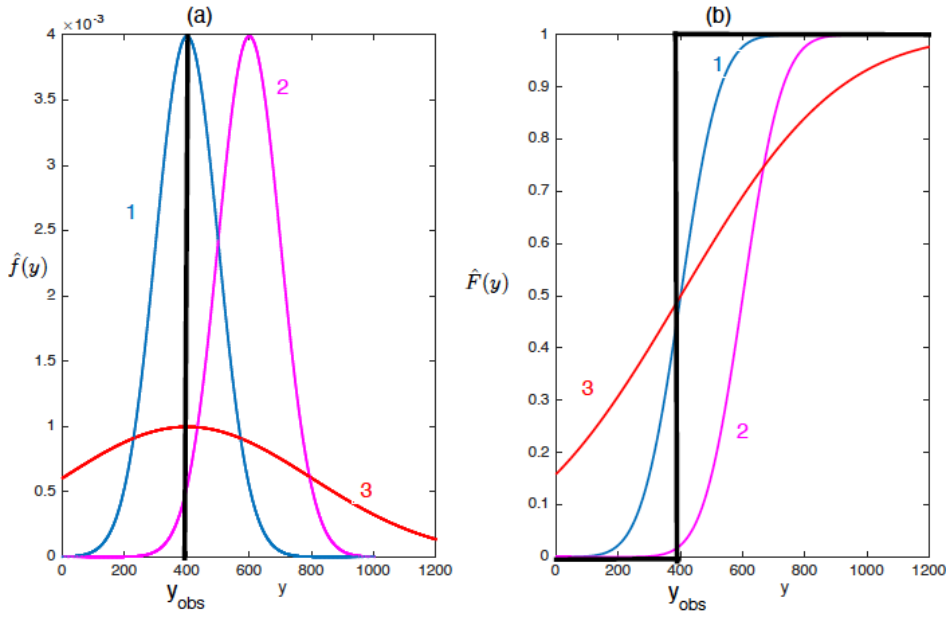

Figure 10-13. Schematic of the CRPS skill score

Three forecast PDFs are shown in relation to the observed variable in (a). The corresponding CDFs are shown in (b), together with the step function CDF of the observation (black heavy line). Forecast 1's PDF would produce a small (i.e., good) CRPS. This would not be the case for Forecast 2 or Forecast 3.

Illustration modified from Wilks (2011)

CRPS can be further partitioned into the two main attributes of probabilistic forecasts described above: reliability and resolution. The decomposition of the CRPS leads to:

$$\text{CRPS} = \text{RELIABILITY} - \text{RESOLUTION} + \text{UNCERTAINTY}. \tag{10-22}$$

The uncertainty term cannot be modified by the forecast system and depends only on the observation's variability (Wilks 2011). Because CRPS is negatively oriented, the goal of a forecast system is to minimize the reliability term and maximize the resolution term as much as possible. Hersbach (2000) and Lauret et al. (2019) detail the procedures for calculating the different terms (reliability and resolution, respectively) for ensemble and quantile forecasts.

It must be stressed that the decomposition of CRPS provides quantitative overall measures of reliability and resolution, providing additional and valuable insight into the performance of a forecasting system.

Similarly, to obtain skill scores used for evaluating deterministic forecasts (Coimbra and Pedro 2013), a CRPS skill score (CRPSS) can be derived to quantify the improvement brought by a new method over a reference easy-to-implement model, such as:

$$\mathrm{CRPSS} = 1 - \frac{\mathrm{CRPS}_{new\ method}}{\mathrm{CRPS}_{Reference}}. \tag{10-23}$$

Negative values of CRPSS indicate that the new proposed method fails to outperform the reference baseline model, and, conversely, positive values of CRPSS mean that the new method outperforms the reference model. Further, the higher the CRPSS, the better the improvement. Note that the uncertainty part of the decomposition of CRPS (which corresponds to the score of the climatology) can be used as a reference baseline model. CRPSS and mean-normalized CRPS are also discussed by Yang (2020).

10.6.3.2.4 Interval Score

The interval score (IS) specifically assesses the quality of interval forecasts. As shown by Eq. 10-24, the interval score rewards narrow prediction intervals but penalizes (with a penalty term that increases with increasing nominal coverage rate) the forecasts for which the observation, x_{obs}, is outside the interval. For a $(1-\alpha)\times 100\%$ nominal coverage rate, the interval score is obtained as:

$$\mathrm{IS}_{\alpha} = \frac{1}{N}\sum_{i=1}^{N}\left(U^{i}-L^{i}\right) + \frac{2}{\alpha}\left(L^{i}-x_{obs}^{i}\right)I_{x_{obs}^{i}<L^{i}} + \frac{2}{\alpha}\left(x_{obs}^{i}-U^{i}\right)I_{x_{obs}^{i}>U^{i}}, \tag{10-24}$$

where I_u is the indicator function (I_u = 1 if U is true and 0 otherwise), and U^i and L^i represent the upper $\left(\tau = 1-\frac{\alpha}{2}\right)$ and lower $\left(\tau = \frac{\alpha}{2}\right)$ quantiles, respectively.

A plot of interval scores for different nominal coverage rates might offer a consistent evaluation of the quality of interval forecasts. Consequently, such a plot could advantageously replace the sharpness diagram.

10.7 Available Diagnostic Tools

To evaluate various datasets, many statistical metrics (e.g., correlation, RMSE, MAE, or MBE) can be calculated by common scripts, given their simple formulas. Moreover, some programming languages provide various user-friendly library functions to calculate the statistical metrics (Table 10-5).

Table 10-5. Functions for Statistical Metrics in R, Python, and MATLAB

Programming Language	Remarks
R	Name of library function: Metrics Documentation: https://cran.r-project.org/web/packages/Metrics/Metrics.pdf Documentation for the Taylor diagram: https://search.r-project.org/CRAN/refmans/plotrix/html/taylor.diagram.html.
Python	Name of library functions: NumPy and scikit-learn Documentation: NumPy: https://numpy.org/doc/stable/ scikit-learn: https://scikit-learn.org/0.21/documentation.html Documentation for Taylor diagrams: https://metplotpy.readthedocs.io/en/develop/Users_Guide/taylor_diagram.html.
MATLAB	Link: https://www.mathworks.com/help/matlab/referencelist.html?type=function&category=descriptive-statistics&s_tid=CRUX_topnav Documentation for the Taylor diagram: https://www.mathworks.com/matlabcentral/fileexchange/20559-taylor-diagram.

References

Abreu, E. F. M., C.A. Gueymard, P. Canhoto, and M.J. Costa. 2023. "Performance assessment of clear-sky solar irradiance predictions using state-of-the-art radiation models and input atmospheric data from reanalysis or ground measurements." *Solar Energy* 252, 309–321. https://doi.org/10.1016/j.solener.2023.01.051.

Aicardi, D., P. Musé, and R. Alonso-Suárez. 2022. "A comparison of satellite cloud motion vectors techniques to forecast intraday hourly solar global horizontal irradiation." *Solar Energy* 233, 46–60. https://doi.org/10.1016/j.solener.2021.12.066.

Al-Rasheedi, M., C.A. Gueymard, A. Ismail, and T. Hussain. 2018. "Comparison of two sensor technologies for solar irradiance measurement in a desert environment." *Solar Energy* 161, 194–206. https://doi.org/10.1016/j.solener.2017.12.058.

ASTM E824. 2018. *ASTM E824-10R18E1 Test Method for Transfer of Calibration From Reference to Field Radiometers*. ASTM International. https://doi.org/10.1520/E0824-10R18E01.

ASTM G167. 2023. *ASTM G167-15 Test Method for Calibration of a Pyranometer Using a Pyrheliometer*. ASTM International. https://doi.org/10.1520/G0167-15.

ASTM G213. 2017. *ASTM G213-17(2023) Standard Guide for Evaluating Uncertainty in Calibration and Field Measurements of Broadband Irradiance with Pyranometers and Pyrheliometers*. ASTM International. https://doi.org/10.1520/G0213-17R23.

Babar, B., R. Graversen, and T. Boström. 2018. "Evaluating CM-SAF solar radiation CLARA-A1 and CLARA-A2 datasets in Scandinavia." *Solar Energy* 170, 76–85. https://doi.org/10.1016/j.solener.2018.05.009.

Babar, B., R. Graversen, and T. Boström. 2019. "Solar radiation estimation at high latitudes: Assessment of the CMSAF databases, ASR and ERA5." *Solar Energy* 182, 397–411. https://doi.org/10.1016/j.solener.2019.02.058.

Badosa, J., J. Wood, P. Blanc, C.N. Long, L. Vuilleumier, D. Demengel, and M. Haeffelin. 2014. "Solar irradiances measured using SPN1 radiometers: Uncertainties and clues for development." *Atmospheric Measurement Techniques* 7(12), 4267–4283. https://doi.org/10.5194/amt-7-4267-2014.

Balenzategui, J. L., J. de Lucas, J. Cuenca, A. González-Leiton, M. Molero, F. Fabero, J.P. Silva, E. Mejuto, R. Muñoz, A. Arce, and E. Prieto. 2022a. "Characterization of absolute cavity radiometers for traceability to SI of solar irradiance." *Measurement Science and Technology* 33(11), 115009. https://doi.org/10.1088/1361-6501/ac849d.

Balenzategui, J. L., M. Molero, J.P. Silva, F. Fabero, J. Cuenca, E. Mejuto, and J. De Lucas. 2022b. "Uncertainty in the Calibration Transfer of Solar Irradiance Scale: From Absolute Cavity Radiometers to Standard Pyrheliometers." *Solar* 2(2), 158–185. https://doi.org/10.3390/solar2020010.

Beyer, H. G., J. Polo Martinez, M. Suri, J.L. Torres, E. Lorenz, S. Müller, C. Hoyer-Klick, and P. Ineichen. 2009. *Report on Benchmarking of Radiation Products* (D1.1.3, Contract No. 038665). https://www.academia.edu/29559582/Report_on_Benchmarking_of_Radiation_Products.

Bright, J. M. 2019. "Solcast: Validation of a satellite-derived solar irradiance dataset." *Solar Energy* 189, 435–449. https://doi.org/10.1016/j.solener.2019.07.086.

Bröcker, J., and L.A. Smith. 2007. "Increasing the Reliability of Reliability Diagrams." *Weather and Forecasting* 22(3), 651–661. https://doi.org/10.1175/WAF993.1.

Cebecauer, T., R. Perez, and M. Šúri. 2011a. *Comparing Performance of Solargis and SUNY Satellite Models Using Monthly and Daily Aerosol Data*. Solar World Congress, Kassel, Germany. https://doi.org/10.18086/swc.2011.24.05.

Cebecauer, T., M. Šúri, and C.A. Gueymard. 2011b. "Uncertainty sources in satellite-derived direct normal irradiance: How can prediction accuracy be improved globally." *Proceedings of the SolarPACES 2011 Conference*, 20–23.

Coimbra, C. F. M., and H.T.C. Pedro. 2013. "Stochastic-Learning Methods." In J. Kleissl (Ed.) *Solar Energy Forecasting and Resource Assessment*. Elsevier. https://doi.org/10.1016/B978-0-12-397177-7.00015-2.

Darnell, W. L., W.F. Staylor, S.K. Gupta, and F.M. Denn. 1988. "Estimation of Surface Insolation Using Sun-Synchronous Satellite Data." *Journal of Climate* 1(8), 820–835. https://doi.org/10.1175/1520-0442(1988)001<0820:EOSIUS>2.0.CO;2.

Darnell, W. L., W.F. Staylor, S.K. Gupta, N.A. Ritchey, and A.C. Wilber. 1992. "Seasonal variation of surface radiation budget derived from International Satellite Cloud Climatology Project C1 data." *Journal of Geophysical Research: Atmospheres* 97(D14), 15741–15760. https://doi.org/10.1029/92JD00675.

Emde, C., R. Buras-Schnell, A. Kylling, B. Mayer, J. Gasteiger, U. Hamann, J. Kylling, B. Richter, C. Pause, T. Dowling, and L. Bugliaro. 2016. "The libRadtran software package for radiative transfer calculations (version 2.0.1)." *Geoscientific Model Development* 9(5), 1647–1672. https://doi.org/10.5194/gmd-9-1647-2016.

Espinar, B., L. Ramírez, A. Drews, H.G. Beyer, L.F. Zarzalejo, J. Polo, and L. Martín. 2009. "Analysis of different comparison parameters applied to solar radiation data from satellite and German radiometric stations." *Solar Energy* 83(1), 118–125. https://doi.org/10.1016/j.solener.2008.07.009.

Forstinger, A., S. Wilbert, A.R. Jensen, B. Kraas, C. Fernandez-Peruchena, C.A. Gueymard, D. Ronzio, D. Yang, E. Collino, J. Polo, et al. 2023. *Worldwide Benchmark of Modelled Solar Irradiance Data*. Report IEA-PVPS T16-05: 2023. IEA PVPS. https://iea-pvps.org/key-topics/worldwide-benchmark-of-modelled-solar-irradiance-data/.

García, R. D., O.E. García, E. Cuevas, V.E. Cachorro, P.M. Romero-Campos, R. Ramos, and A.M. de Frutos. 2014. "Solar radiation measurements compared to simulations at the BSRN Izaña station. Mineral dust radiative forcing and efficiency study." *Journal of Geophysical Research: Atmospheres* 119(1), 179–194. https://doi.org/10.1002/2013JD020301.

Gneiting, T. 2011. "Making and Evaluating Point Forecasts." *Journal of the American Statistical Association* 106(494), 746–762. https://doi.org/10.1198/jasa.2011.r10138.

Gneiting, T., and A.E. Raftery. 2007. "Strictly Proper Scoring Rules, Prediction, and Estimation." *Journal of the American Statistical Association* 102(477), 359–378. https://doi.org/10.1198/016214506000001437.

Gueymard, C. A. 2003. "Direct solar transmittance and irradiance predictions with broadband models. Part II: validation with high-quality measurements." *Solar Energy* 74(5), 381–395. https://doi.org/10.1016/S0038-092X(03)00196-8.

Gueymard, C. A. 2012a. "Temporal variability in direct and global irradiance at various time scales as affected by aerosols." *Solar Energy* 86(12), 3544–3553. https://doi.org/10.1016/j.solener.2012.01.013.

Gueymard, C. A. 2012b. "Visibility, aerosol conditions, and irradiance attenuation close to the ground—Comments on "Solar radiation attenuation in solar tower plants" by J. Ballestrin and A. Marzo." *Solar Energy* 86(5), 1667–1668. https://doi.org/10.1016/j.solener.2011.12.027.

Gueymard, C. A. 2014. "A review of validation methodologies and statistical performance indicators for modeled solar radiation data: Towards a better bankability of solar projects." *Renewable and Sustainable Energy Reviews* 39, 1024–1034.

Gueymard, C. A., A. Habte, M. Sengupta. 2018. "Reducing Uncertainties in Large-Scale Solar Resource Data: The Impact of Aerosols." *IEEE Journal of Photovoltaics* 8(6), 1732–1737. https://doi.org/10.1109/jphotov.2018.2869554.

Gueymard, C. A., V. Lara-Fanego, M. Sengupta, and A. Habte. 2021. "Surface albedo spatial variability in North America: Gridded data vs. local measurements." *Solar Energy* 227, 655–673. https://doi.org/10.1016/j.solener.2021.05.012.

Gueymard, C. A., and D.R. Myers. 2008. "Solar Radiation Measurement: Progress in Radiometry for Improved Modeling." In V. Badescu (Ed.), *Modeling Solar Radiation at the Earth's Surface: Recent Advances*. Springer Berlin Heidelberg. https://doi.org/10.1007/978-3-540-77455-6_1.

Gueymard, C. A., and D.R. Myers. 2009. "Evaluation of conventional and high-performance routine solar radiation measurements for improved solar resource, climatological trends, and radiative modeling." *Solar Energy* 83(2), 171–185. https://doi.org/10.1016/j.solener.2008.07.015.

Gueymard, C. A., and J.A. Ruiz-Arias. 2015. "Validation of direct normal irradiance predictions under arid conditions: A review of radiative models and their turbidity-dependent performance."

Renewable and Sustainable Energy Reviews 45, 379–396. https://doi.org/10.1016/j.rser.2015.01.065.

Gueymard, C. A., and S.M. Wilcox. 2011. "Assessment of spatial and temporal variability in the US solar resource from radiometric measurements and predictions from models using ground-based or satellite data." *Solar Energy* 85(5), 1068–1084. https://doi.org/10.1016/j.solener.2011.02.030.

Habte, A., M. Sengupta, A. Andreas, I. Reda, and J. Robinson. 2016. *The Impact of Indoor and Outdoor Radiometer Calibration on Solar Measurements*. NREL/CP-5D00-66659, National Renewable Energy Laboratory, Golden, CO. https://www.nrel.gov/docs/fy16osti/66659.pdf.

Habte, A., M. Sengupta, A. Andreas, I. Reda, and J. Robinson. 2017. "Radiometer calibration methods and resulting irradiance differences." *Progress in Photovoltaics: Research and Applications* 25(7), 614–622. https://doi.org/10.1002/pip.2812.

Habte, A., M. Sengupta, A. Andreas, S. Wilcox, and T. Stoffel. 2016. "Intercomparison of 51 radiometers for determining global horizontal irradiance and direct normal irradiance measurements." *Solar Energy* 133, 372–393. https://doi.org/10.1016/j.solener.2016.03.065.

Habte, A., M. Sengupta, and A. Lopez. 2017. *Evaluation of the national solar radiation database (NSRDB): 1998-2015*. Golden, CO: NREL. https://www.nrel.gov/docs/fy17osti/67722.pdf.

Habte, A., M. Sengupta, I. Reda, A. Andreas, and J. Konings. 2014. *Calibration and measurement uncertainty estimation of radiometric data*. NREL/CP-5D00-62214, National Renewable Energy Laboratory, Golden, CO. https://www.nrel.gov/docs/fy15osti/62214.pdf.

Hamill, T. M. 2001. "Interpretation of Rank Histograms for Verifying Ensemble Forecasts." *Monthly Weather Review* 129(3), 550–560. https://doi.org/10.1175/1520-0493(2001)129<0550:IORHFV>2.0.CO;2.

Hersbach, H. 2000. "Decomposition of the Continuous Ranked Probability Score for Ensemble Prediction Systems." *Weather and Forecasting* 15(5), 559–570. https://doi.org/10.1175/1520-0434(2000)015<0559:DOTCRP>2.0.CO;2.

Hodson, T. O. 2022. "Root-mean-square error (RMSE) or mean absolute error (MAE): When to use them or not." *Geoscientific Model Development* 15(14), 5481–5487. https://doi.org/10.5194/gmd-15-5481-2022.

Hoff, T. E., and R. Perez. 2012. "Modeling PV fleet output variability." *Solar Energy* 86(8), 2177–2189. https://doi.org/10.1016/j.solener.2011.11.005.

Hoff, T. E., R. Perez, J. Kleissl, D. Renne, and J. Stein. 2013. "Reporting of irradiance modeling relative prediction errors." *Progress in Photovoltaics: Research and Applications* 21(7), 1514–1519. https://doi.org/10.1002/pip.2225.

ISO 9059. 1990. *ISO 9059:1990 Solar energy—Calibration of field pyrheliometers by comparison to a reference pyrheliometer*. https://www.iso.org/standard/16628.html.

ISO 9060. 2018. *ISO 9060:2018 Solar energy—Specification and classification of instruments for measuring hemispherical solar and direct solar radiation*. https://www.iso.org/obp/ui/en/#iso:std:iso:9060:ed-2:v1:en.

ISO 9846. 1993. *ISO 9846:1993 Solar energy—Calibration of a pyranometer using a pyrheliometer*. https://www.iso.org/standard/17724.html.

ISO 9847. 2023. *ISO 9847:2023 Solar energy—Calibration of pyranometers by comparison to a reference pyranometer*. https://www.iso.org/standard/78800.html.

ISO/IEC. 2008. "Uncertainty of measurement: Part 3. Guide to the expression of uncertainty in measurement." In *ISO/IEC Guide 983: 2008*. https://www.iso.org/standard/50461.html.

ISO/TR 9901. 2021. *ISO/TR 9901:2021 Solar energy—Pyranometers—Recommended practice for use*. https://www.iso.org/standard/81937.html.

Jimenez, P. A., J.P. Hacker, J. Dudhia, S.E. Haupt, J.A. Ruiz-Arias, C.A. Gueymard, G. Thompson, T. Eidhammer, and A. Deng. 2016. "WRF-Solar: Description and Clear-Sky Assessment of an Augmented NWP Model for Solar Power Prediction." *Bulletin of the American Meteorological Society* 97(7), 1249–1264. https://doi.org/10.1175/BAMS-D-14-00279.1.

Jolliffe, I. T., and D.B. Stephenson. (Eds.). 2011. *Forecast Verification: A Practitioner's Guide in Atmospheric Science* (2nd ed.). Hoboken: Wiley.

Kamath, H. G., and J. Srinivasan. 2020. "Validation of global irradiance derived from INSAT-3D over India." *Solar Energy* 202, 45–54. https://doi.org/10.1016/j.solener.2020.03.084.

Kleissl, J., C. Coimbra, and R. Marquez. 2013. "Overview of Solar Forecasting Methods and a Metric for Accuracy Evaluation." In J. Kleissl (Ed.) *Solar Energy Forecasting and Resource Assessment*. https://doi.org/10.1016/B978-0-12-397177-7.00008-5.

Konings, J., and A. Habte. 2016. *Uncertainty evaluation of measurements with pyranometers and pyrheliometers*. Solar World Congress, Daegu, Korea. https://doi.org/10.18086/swc.2015.07.15.

Kuhn, P., B. Nouri, S. Wilbert, C. Prahl, N. Kozonek, T. Schmidt, Z. Yasser, L. Ramirez, L. Zarzalejo, A. Meyer, et al. 2018. "Validation of an all-sky imager–based nowcasting system for industrial PV plants." *Progress in Photovoltaics: Research and Applications* 26(8), 608–621. https://doi.org/10.1002/pip.2968.

Kühnert, J., E. Lorenz, and D. Heinemann. 2013. "Satellite-Based Irradiance and Power Forecasting for the German Energy Market." In *Solar Energy Forecasting and Resource Assessment*. Elsevier. https://doi.org/10.1016/B978-0-12-397177-7.00011-5.

Lauret, P., M. David, and P. Pinson. 2019. "Verification of solar irradiance probabilistic forecasts." *Solar Energy* 194, 254–271. https://doi.org/10.1016/j.solener.2019.10.041.

Lorenz, E., A. Hammer, and D. Heinemann. 2004. *Short term forecasting of solar radiation based on satellite data*. https://api.semanticscholar.org/CorpusID:16951232.

Lorenz, E., J. Hurka, D. Heinemann, H.G. Beyer. 2009. "Irradiance Forecasting for the Power Prediction of Grid-Connected Photovoltaic Systems." *IEEE Journal of Selected Topics in Applied Earth Observations and Remote Sensing* 2(1), 2–10. https://doi.org/10.1109/JSTARS.2009.2020300.

Lorenz, E., J. Kühnert, D. Heinemann, K.P. Nielsen, J. Remund, and S.C. Müller. 2016. "Comparison of global horizontal irradiance forecasts based on numerical weather prediction models with different spatio-temporal resolutions." *Progress in Photovoltaics: Research and Applications* 24(12), 1626–1640. https://doi.org/10.1002/pip.2799.

Lorenz, E., T. Scheidsteger, J. Hurka, D. Heinemann, and C. Kurz. 2011. "Regional PV power prediction for improved grid integration." *Progress in Photovoltaics: Research and Applications* 19(7), 757–771. https://doi.org/10.1002/pip.1033.

Markovics, D., and M.J. Mayer. 2022. "Comparison of machine learning methods for photovoltaic power forecasting based on numerical weather prediction." *Renewable and Sustainable Energy Reviews* 161, 112364. https://doi.org/10.1016/j.rser.2022.112364.

Massey Jr, F. J. 1951. "The Kolmogorov-Smirnov test for goodness of fit." *Journal of the American Statistical Association*, 46(253), 68–78. https://doi.org/10.2307/2280095.

Mathiesen, P., and J. Kleissl. 2011. "Evaluation of numerical weather prediction for intraday solar forecasting in the continental United States." *Solar Energy* 85(5), 967–977. https://doi.org/10.1016/j.solener.2011.02.013.

Mayer, B., and A. Kylling. 2005. "Technical note: The libRadtran software package for radiative transfer calculations - description and examples of use." *Atmospheric Chemistry and Physics* 5(7), 1855–1877. https://doi.org/10.5194/acp-5-1855-2005.

Michalsky, J., E.G. Dutton, D. Nelson, J. Wendell, S. Wilcox, A. Andreas, P. Gotseff, D. Myers, I. Reda, and T. Stoffel. 2011. "An Extensive Comparison of Commercial Pyrheliometers under a Wide Range of Routine Observing Conditions." *Journal of Atmospheric and Oceanic Technology* 28(6), 752–766. https://doi.org/10.1175/2010JTECHA1518.1.

Michalsky, J., E. Dutton, M. Rubes, D. Nelson, T. Stoffel, M. Wesley, M. Splitt, and J. DeLuisi. 1999. "Optimal Measurement of Surface Shortwave Irradiance Using Current Instrumentation." *Journal of Atmospheric and Oceanic Technology* 16(1), 55–69. https://doi.org/10.1175/1520-0426(1999)016<0055:OMOSSI>2.0.CO;2.

Müller, S. C., and J. Remund. 2010. "Advances in Radiation Forecast Based on Regional Weather Models MM5 and WRF." *25th European Photovoltaic Solar Energy Conference and Exhibition / 5th World Conference on Photovoltaic Energy Conversion*. https://doi.org/10.4229/25THEUPVSEC2010-4BV.1.75.

Murphy, A. H. 1993. "What is a good forecast? An essay on the nature of goodness in weather forecasting." *Weather and Forecasting* 8(2), 281–293. https://doi.org/10.1175/1520-0434(1993)008<0281:WIAGFA>2.0.CO;2.

Myers, D. R., T.L. Stoffel, I. Reda, S.M. Wilcox, and A.M. Andreas. 2002. "Recent progress in reducing the uncertainty in and improving pyranometer calibrations." *J. Sol. Energy Eng.* 124(1), 44–50. https://doi.org/10.1115/1.1434262.

Pelland, S., G. Galanis, and G. Kallos. 2013. "Solar and photovoltaic forecasting through post-processing of the Global Environmental Multiscale numerical weather prediction model." *Progress in Photovoltaics: Research and Applications* 21(3), 284–296. https://doi.org/10.1002/pip.1180.

Perez, R., P. Ineichen, K. Moore, M. Kmiecik, C. Chain, R. George, and F. Vignola. 2002. "A new operational model for satellite-derived irradiances: Description and validation." *Solar Energy* 73(5), 307–317. https://doi.org/10.1016/S0038-092X(02)00122-6.

Perez, R., R. Seals, P. Ineichen, R. Stewart, D. Menicucci. 1987. "A new simplified version of the perez diffuse irradiance model for tilted surfaces." *Solar Energy* 39(3), 221–231. https://doi.org/10.1016/S0038-092X(87)80031-2.

Pinson, P., P. McSharry, and H. Madsen. 2010. "Reliability diagrams for non-parametric density forecasts of continuous variables: Accounting for serial correlation." *Quarterly Journal of the Royal Meteorological Society* 136(646), 77–90. https://doi.org/10.1002/qj.559.

Pinson, P., H. Nielsen, J.K. Møller, H. Madsen, and G.N. Kariniotakis. 2007. "Non-parametric probabilistic forecasts of wind power: Required properties and evaluation." *Wind Energy* 10(6), 497–516. https://doi.org/10.1002/we.230.

Reda, I. 2011. *Method to Calculate Uncertainty Estimate of Measuring Shortwave Solar Irradiance using Thermopile and Semiconductor Solar Radiometers*. NREL/TP-3B10-52194. National Renewable Energy Laboratory, Golden, CO. https://doi.org/10.2172/1021250.

Reda, I., M. Dooraghi, and A. Habte. 2013. *NREL Pyrheliometer Comparison: September 16 to 27, 2013 (NPC-2013)*. NREL/TP-3B10-60749, National Renewable Energy Laboratory, Golden, CO. https://doi.org/10.2172/1111204.

Reda, I., D. Myers, and T. Stoffel. 2008. "Uncertainty Estimate for the Outdoor Calibration of Solar Pyranometers: A Metrologist Perspective." *NCSLI Measure* 3(4), 58–66. https://doi.org/10.1080/19315775.2008.11721448.

Renné, D., R. Perez, A. Zelenka, C.H. Whitlock, and R.C. DiPasquale. 1999. "Use of Weather and Climate Research Satellites for Estimating Solar Resources." In *Advances in Solar Energy: An Annual Review of Research and Development* (Vol. 13). American Solar Energy Society.

Ruiz-Arias, J. A., C.A. Gueymard, F.J. Santos-Alamillos, and D. Pozo-Vázquez. 2016. "Worldwide impact of aerosol's time scale on the predicted long-term concentrating solar power potential." *Scientific Reports* 6(1), 1–10. https://doi.org/10.1038/srep30546.

Salazar, G., C.A. Gueymard, J.B. Galdino, O. de C. Vilela, and N. Fraidenraich. 2020. "Solar irradiance time series derived from high-quality measurements, satellite-based models, and reanalyses at a near-equatorial site in Brazil." *Renewable and Sustainable Energy Reviews* 117, 109478. https://doi.org/10.1016/j.rser.2019.109478.

Sengupta, M., P.A. Jimenez, J-H Kim, J. Yang, and Y. Xie. 2022. *Probabilistic Cloud Optimized Day-Ahead Forecasting System Based on WRF-Solar (Final Report)*. NREL/TP-5D00-81904, National Renewable Energy Laboratory, Golden, CO. https://doi.org/10.2172/1855782.

Sengupta, M., Y. Xie, A. Lopez, A. Habte, G. Maclaurin, and J. Shelby. 2018. "The National Solar Radiation Data Base (NSRDB)." *Renewable and Sustainable Energy Reviews* 89, 51–60. https://doi.org/10.1016/j.rser.2018.03.003.

Shi, H., W. Li, X. Fan, J. Zhang, B. Hu, L. Husi, H. Shang, X. Han, Z. Song, and Y. Zhang. 2018. "First assessment of surface solar irradiance derived from Himawari-8 across China." *Solar Energy* 174, 164–170. https://doi.org/10.1016/j.solener.2018.09.015.

Stoffel, T. L., I. Reda, D.R. Myers, D. Renne, S. Wilcox, and J. Treadwell. 2000. "Current issues in terrestrial solar radiation instrumentation for energy, climate, and space applications." *Metrologia* 37(5), 399. https://doi.org/10.1088/0026-1394/37/5/11.

Sun, X., D. Yang, C.A. Gueymard, J.M. Bright, and P. Wang. 2022. "Effects of spatial scale of atmospheric reanalysis data on clear-sky surface radiation modeling in tropical climates: A case study for Singapore." *Solar Energy* 241, 525–537. https://doi.org/10.1016/j.solener.2022.06.001.

Suri, M., and T. Cebecauer. 2014. "Satellite-based solar resource data: Model validation statistics versus user's uncertainty." *ASES SOLAR 2014 Conference, San Francisco*.

Taylor, K. 2001. "Summarizing multiple aspects of model performance in a single diagram." *Journal of Geophysical Research* 106, 7183–7192. https://doi.org/10.1029/2000JD900719.

Thevenard, D., and S. Pelland. 2013. "Estimating the uncertainty in long-term photovoltaic yield predictions." *Solar Energy* 91, 432–445. https://doi.org/10.1016/j.solener.2011.05.006.

Urraca, R., A.M. Gracia-Amillo, T. Huld, F.J. Martinez-de-Pison, J. Trentmann, A.V. Lindfors, A. Riihelä, and A. Sanz-Garcia. 2017. "Quality control of global solar radiation data with satellite-based products." *Solar Energy* 158, 49–62. https://doi.org/10.1016/j.solener.2017.09.032.

Urraca, R., T. Huld, A. Gracia-Amillo, F.J. Martinez-de-Pison, F. Kaspar, and A. Sanz-Garcia. 2018. "Evaluation of global horizontal irradiance estimates from ERA5 and COSMO-REA6 reanalyses using ground and satellite-based data." *Solar Energy* 164, 339–354. https://doi.org/10.1016/j.solener.2018.02.059.

Vignola, F., and R. Perez. 2004. *Solar Resource GIS Data Base for the Pacific Northwest using Satellite Data*. University of Oregon.

Vuilleumier, L., M. Hauser, C. Félix, F. Vignola, P. Blanc, A. Kazantzidis, and B. Calpini. 2014. "Accuracy of ground surface broadband shortwave radiation monitoring." *Journal of Geophysical Research: Atmospheres* 119(24), 13,838-13,860. https://doi.org/10.1002/2014JD022335.

Wang, L., Y. Lu, Z. Wang, H. Li, and M. Zhang. 2024. "Hourly solar radiation estimation and uncertainty quantification using hybrid models." *Renewable and Sustainable Energy Reviews* 202: 114727. https://doi.org/10.1016/j.rser.2024.114727.

Wilbert, S., S. Kleindiek, B. Nouri, N. Geuder, A. Habte, M. Schwandt, and F. Vignola. 2016. "Uncertainty of rotating shadowband irradiometers and Si-pyranometers including the spectral irradiance error." *AIP Conference Proceedings* 1734: 150009. https://doi.org/10.1063/1.4949241.

Wilcox, S., and D.R. Myers. 2008. *Evaluation of radiometers in full-time use at the national renewable energy laboratory solar radiation research laboratory*. NREL/TP-550-44627, National Renewable Energy Laboratory, Golden, CO. https://doi.org/10.2172/946331.

Wilks, D. S. 2011. *Statistical methods in the atmospheric sciences* (Vol. 100). Academic press.

WMO, W. 2018. "Guide to instruments and methods of observation." *World Meteorological Organization WMO*. https://library.wmo.int.

Xie, Y., J. Yang, M. Sengupta, Y. Liu, and X. Zhou. 2022. "Improving the prediction of DNI with physics-based representation of all-sky circumsolar radiation." *Solar Energy* 231, 758–766. https://doi.org/10.1016/j.solener.2021.12.016.

Yang, D. 2019a. "On postprocessing day-ahead NWP forecasts using Kalman filtering." *Solar Energy* 182, 179–181. https://doi.org/10.1016/j.solener.2019.02.044.

Yang, D. 2019b. "Standard of reference in operational day-ahead deterministic solar forecasting." *Journal of Renewable and Sustainable Energy* 11(5), 053702. https://doi.org/10.1063/1.5114985.

Yang, D. 2020. "Ensemble model output statistics as a probabilistic site-adaptation tool for solar irradiance: A revisit." *Journal of Renewable and Sustainable Energy* 12(3), 036101. https://doi.org/10.1063/5.0010003.

Yang, D., S. Alessandrini, J. Antonanzas, F. Antonanzas-Torres, V. Badescu, H.G. Beyer, R. Blaga, J. Boland, J.M. Bright, C.F.M. Coimbra, et al. 2020. "Verification of deterministic solar forecasts." *Special Issue on Grid Integration* 210, 20–37. https://doi.org/10.1016/j.solener.2020.04.019.

Yang, D., Y. Gu, M.J. Mayer, C.A. Gueymard, W. Wang, J. Kleissl, M. Li, Y. Chu, and J. Bright. 2024. "Regime-dependent 1-min irradiance separation model with climatology clustering." *Renewable and Sustainable Energy Reviews* 189, 113992. https://doi.org/10.1016/j.rser.2023.113992.

Yang, J., Y. Xie, M. Sengupta, Y. Liu, and H. Long. 2022. “Parameterization of cloud transmittance for expeditious assessment and forecasting of all-sky DNI.” *Journal of Renewable and Sustainable Energy*14(6), 063703. https://doi.org/10.1063/5.0127454.

Zelenka, A., R. Perez, R. Seals, and D. Renné. 1999. “Effective accuracy of satellite-derived hourly irradiances.” *Theoretical and Applied Climatology* 62(3), 199–207. https://doi.org/10.1007/s007040050084.

11 Applying Solar Resource Data to Solar Energy Projects

Wilfried van Sark,[1] Robert Höller,[2] Kristian Pagh Nielsen,[3] Luis F. Zarzalejo,[4] Janine Freeman,[5] Christian Gueymard,[6] Stefan Wilbert,[7] Manuel Silva,[8] Dave Renné,[9] Lourdes Ramírez,[10] David Spieldenner,[11] Rafael Fritz,[12] Mark Mehos,[5] Richard Perez,[13] Aron Habte,[5] Birk Kraas,[14] Lüder von Bremen,[15] and Øyvind Sommer Klyve[16]

[1] *Utrecht University, Copernicus Institute of Sustainable Development, The Netherlands*
[2] *University of Applied Sciences Upper Austria and Energy Development GmbH, Austria*
[3] *Danish Meteorological Institute, Denmark*
[4] *Centro de Investigaciones Energéticas, Medioambientales y Tecnológicas (CIEMAT), Spain*
[5] *National Renewable Energy Laboratory, USA*
[6] *Solar Consulting Services, USA*
[7] *German Aerospace Center (DLR), Germany*
[8] *Universidad de Sevilla, Spain*
[9] *Dave Renné Renewables, LLC, USA*
[10] *Universidad Carlos III de Madrid, Spain*
[11] *First Solar, USA*
[12] *Fraunhofer Institute for Energy Economics and Energy System Technology (Fraunhofer IEE), Germany*
[13] *University at Albany, The State University of New York, USA*
[14] *CSP Services GmbH, Germany*
[15] *German Aerospace Center, Institute of Networked Energy Systems (DLR-NES), Germany*
[16] *Institutt for Energiteknikk (IFE), Norway*

Executive Summary

Solar resource information is essential for the reliable and cost-effective development of solar energy systems. It is used in a variety of applications but most importantly during the initial phases of any solar project. This chapter describes the available information and gives guidance on the types of solar resource information relevant to various stages of a solar project. It also informs readers about specific requirements relative to solar radiation data and how they depend on the type, size, and stage of the solar project.

Table 11-1 summarizes the solar radiation needs at different steps of a hypothetical project. The information provided here is applicable to large solar energy projects, mainly photovoltaics (PV) and concentrating solar thermal (CST),[63] and to building energy performance evaluations.

Maps (from, e.g., the Global Solar Atlas[64] or the Global Atlas for Renewable Energy[65]) as well as typical meteorological year (TMY) data should be used to make a preliminary assessment of the solar resource, depending on system size, cautiously assuming a fairly large potential for error. Geographic information service (GIS) tools and resources are commonly used at this step for convenience. Various spatial resolutions need to be used when addressing projects at the regional or national scale—compared to the neighborhood or city scale. By using these tools, maps of solar radiation, and simple energy production models, the potential energy output from different technologies can be evaluated and compared. When using GIS tools for potential

[63] In this chapter, the terms *concentrating solar thermal* (CST) and *concentrating solar power* (CSP) are both used for concentrating solar thermal electricity generation.
[64] See https://globalsolaratlas.info/map.
[65] See https://www.irena.org/Energy-Transition/Project-Facilitation/Renewable-potential-assessment/Global-Atlas.

assessment, terrain slopes and additional land constraints can also be considered for large projects.

During this screening process, the nature of local aerosols and their spatiotemporal variability might need to be considered. Because widely different sources of information might be available at this stage, it is important to define appropriate parameters that allow for comparisons of the solar resource data sources and to clarify the definitions of *variability*, *error*, and *uncertainty*; thus, variability needs to be identified, mainly at the interannual level, and distinguished from the uncertainty of the modeled data. Ideally, considering the uncertainties from each data source, a common "most probable" range should be obtained based on the expected or "true" value. Temporal and spatial variability are addressed through the coefficient of variation statistic (as discussed in Chapter 6), which can be determined by using long time series of measured or modeled data for the site and its surroundings.

In the feasibility assessment stage, typical solar irradiation series are needed for plant simulation and for economic/profitability analysis. Typical annual time series are provided by a TMY, a typical reference year (TRY), and/or a design reference year (DRY). In addition to the review of typical meteorological data series generation for solar energy simulation, this chapter reviews the proposed procedures for the analysis of the interannual variability and the generation of series of a specific probability of exceedance (POE), such as P90; thus, to evaluate the profitability and payback of a project, simulations of its behavior during bad years are needed. Chapter 7 specifically deals with the issues of combining datasets and reducing their uncertainty through site-adaptation processes. These steps are very important for a precise feasibility assessment and to guarantee bankability, particularly for projects with large associated investments, such as with CST technologies.

Table 11-1. Solar Irradiation Needs for Different Stages of a Hypothetical Project

		System Size		
		Small	Medium	Large
Phase	1. Prefeasibility and planning	• Long-term averages • Monthly data • Solar cadastres/ maps • Simple shading analysis	• TMY • Hourly data • Shading analysis	• Long-term satellite data • Hourly data
	2. Feasibility			• Satellite data • Time series (> 10 years) • Ground measurements (>1 year) • Shading analysis • Further site- and technology-specific meteorological parameters (e.g., albedo, soiling)
	3. Due diligence and finance		• Satellite data • Time series (>10 years) • Minutely data • Shading analysis • Further site- and technology-specific meteorological parameters (e.g., albedo, soiling)	• Satellite data • Time series (>10 years) • Ground measurements (> 1 year) • Minutely data • Shading analysis • Further site- and technology-specific meteorological parameters (e.g., albedo, soiling)
	4. Operations and maintenance	• Simple (inverter) monitoring	• Local measurements • Forecasts	• Local measurements • Forecasts

During and before the plant's construction phase, solar irradiance data are needed to refine the yield estimation and to minimize the expected profitability uncertainties; thus, the value of the energy generated by a solar installation depends on the system's output and on the price offered for that energy at the time it is generated. Methods for the yield estimation of non-concentrating PV projects and of CST projects are discussed in this chapter. Additional meteorological inputs that are necessary for yield estimation, as well as solar radiation characteristics, such as its spectral and angular distribution, are also discussed.

For power plant acceptance and operation, the solar resource information must include high-quality, on-site measurements to qualify the plant's performance. Accurate irradiance forecasts can contribute to optimizing operation and revenue. This chapter's final section discusses the type of solar irradiation data needed for different types of solar projects, such as flat-plate thermal collectors, solar heating and cooling in buildings, smart electric grids, solar desalination, and other chemical applications.

11.1 Introduction and Background

As discussed in previous chapters, solar resource evaluation covers a wide range of topics and applications. Most applications are related to projects involving solar radiation energy conversion. In this chapter, these are referred to as "solar energy projects," and they include electricity production (PV; solar thermal electricity [STE], also referred to as CST, CSP), solar heating applications (central solar heating for district heating, residential and commercial heating and cooling), high-temperature solar process heat, chemistry and solar fuels, water and air applications (disinfection, desalination, decontamination), and energy conservation (for building applications). Figure 11-1 schematically illustrates the rationale behind this chapter.

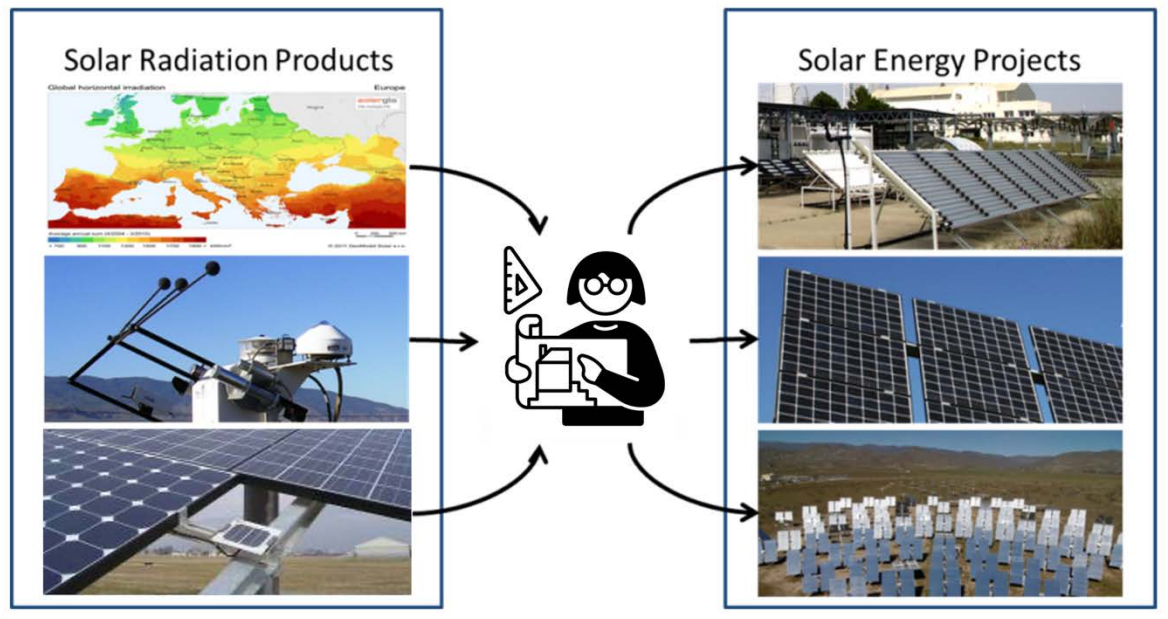

Figure 11-11. (Left) Different solar radiation products or evaluation methodologies described in previous chapters can be applied to (right) various solar energy projects

Photos by Lourdes Ramirez

This chapter focuses on the different requirements, characteristics, and applications of solar resource data in commercial, large-scale solar energy projects. The underlying base case assumption is that of a conventional project development, where professional commercial or institutional entities pursue the goal of realizing a large-scale solar energy project. Therefore, the typical phases in such a project are presented next, and each one is discussed in detail in the following sections. Additionally, there are sections specifically devoted to the selection of suitable datasets, yield estimation methodologies, the variability of the solar resource and how to assess it in a solar energy project, and the bankability of data. There is also a section that

specifically addresses the case of electricity generation projects that do not use only solar energy.

The overall goal in applying solar resource data to solar energy projects is to help the project developer or investor to obtain the optimal solar resource and weather information during each project stage. For large-scale solar projects that need external financing, the bankability of the solar resource data is also crucial. Subsequently, this chapter discusses the currently available information and provides guidance on the types and uses of solar resource data relevant at each project stage. In addition, some information about how to generate datasets for energy simulations is also provided. Sections 11.2–11.5 discuss an idealized project development pathway, corresponding to what is shown in Figure 11-2. Section 11.6 summarizes methodologies used to estimate energy yield of solar systems for which solar data is used. Section 11.7 discusses aspects of power variability and while section 11.8 describes bankability criteria of solar resource datasets. Finally, section 11.9 briefly discusses how solar resource data can be used in other solar projects.

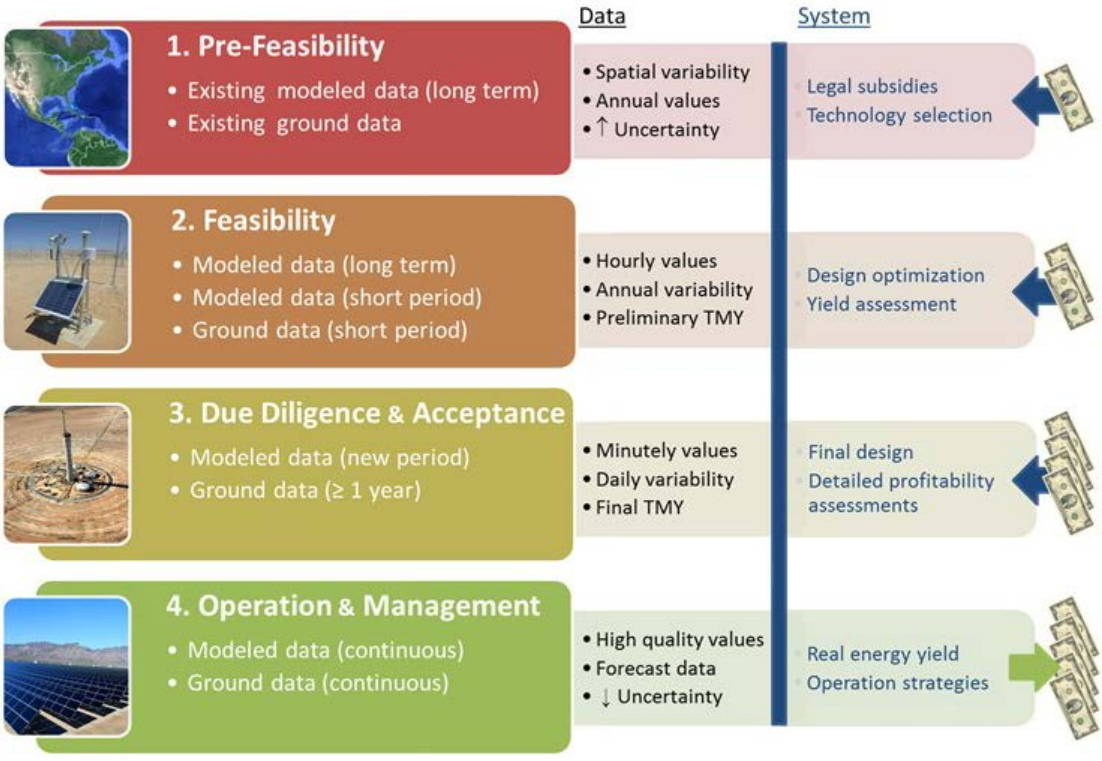

Figure 11-12. Solar resource data at typical stages of a solar power project.

Illustration and photos by Lourdes Ramirez

For any specific project, the precise needs for solar resource data depend on the project's characteristics and how it is financed. In this context, size matters a lot. A small project of a few dozen kilowatts is usually designed with only an appropriate TMY file or long-term monthly solar radiation estimates that can be obtained freely or commercially. Continuous monitoring of the incident irradiance is rarely required during the life of the project. In sharp contrast, a large utility-scale solar power project typically requires several years of high-quality modeled data and

at least 1 year of on-site measured data or satellite-derived data during the final stages of the project execution. The complexity of the situation pertaining to large projects is addressed next.

Figure 11-3 provides a generalized view of solar irradiation data requirements throughout various conceptual stages of a project's life cycle. Stages 2–4, as shown in Figure 11-2, are grouped together because they all invariably address the topic of plant output during the project's life, using different levels of detail and depth. In a solar power project, some questions must be addressed at each stage, as presented in the following sections. Sections 11.2.1–11.2.4 provide some specific information that could help in the interpretation of Figure 11-3.

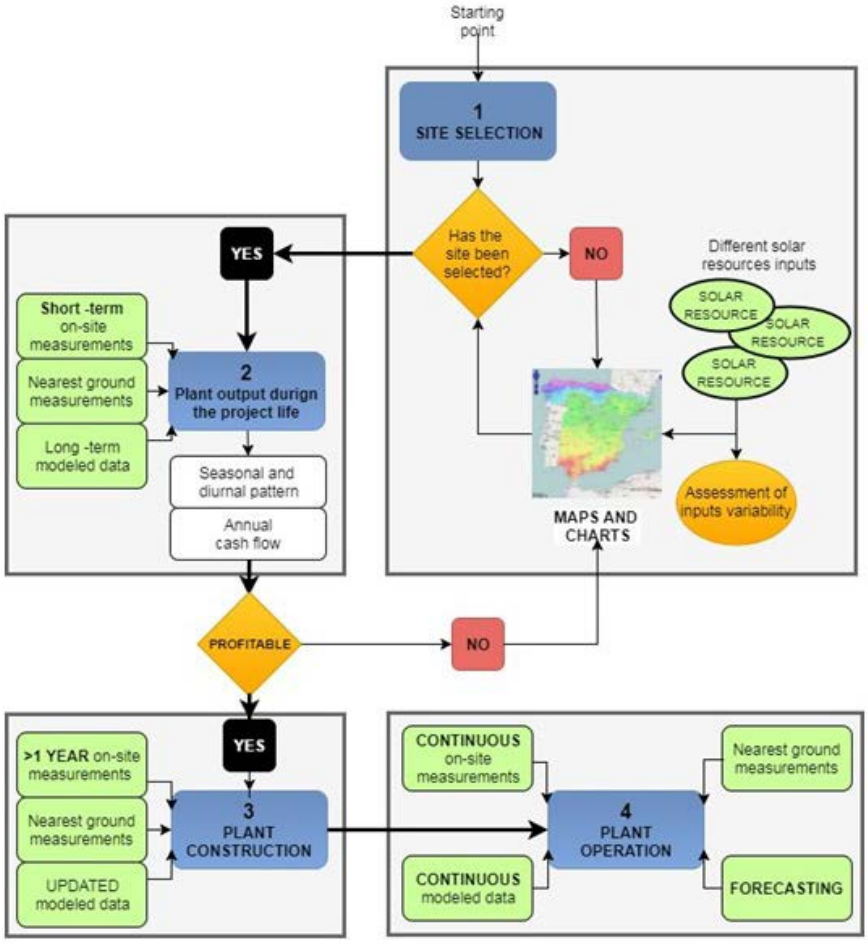

Figure 11-13. Flowchart of the solar radiation data needs (in green) for a hypothetical (large) solar power project

Illustration by Lourdes Ramírez

11.2 Prefeasibility Stage

11.2.1 Prospecting and Site Selection

In the first stage of project development, a prefeasibility assessment of possible sites is typically undertaken. The developer might focus on a specific country or region, but in general is not limited to a certain area, although this depends on the international scope of the company and/or various local subdivisions of that company. A desired outcome at this stage is the estimated annual energy production that could be expected from a solar energy system if installed in various sites. Historical solar resource datasets are generally used at this stage, often in the form of maps (e.g., Global Solar Atlas[66]) or from publicly available or commercial gridded data, such as those discussed in Chapter 5 and Chapter 8. These datasets use a fairly consistent methodology to reliably identify the regions of highest solar potential. Depending on the type of technology used for the solar installation, this potential can refer to global horizontal irradiance (GHI), global tilted irradiance (GTI), or direct normal irradiance (DNI). The maps should be used to make a preliminary assessment of the solar resource, realizing that errors are inherent in this information. For example, for continental Europe far from mountains, the best satellite-based datasets can provide irradiance data with errors below 5%. Over mountainous areas, coasts, islands, and regions with high aerosol optical depth, larger errors are found, up to approximately 10%–12% for GHI or GTI and significantly larger for DNI. This depends on the data provider and region (for quantitative results from an actual benchmark analysis, see Forstinger et al. 2023); thus, if a desirable level of solar resource for a solar power plant project is a daily mean of 7.0 kWh/m^2, sites with mapped resource values down to approximately 6.0 kWh/m^2 should be considered.

About a decade ago, in some cases, a project developer first attempted to build a plant based on concentrating technologies, i.e., CST or concentrating PV (CPV); if the DNI resource turned out to be insufficient, a non-concentrating PV project would be considered instead. Today, however, CPV is not economically viable compared to non-concentrating PV; hence CPV (and CST) is rarely considered anymore. The technical design of the solar energy system at this stage is usually based on a few configuration parameters, e.g., capacity, the orientation of collectors/modules, tracking/non-tracking, or grid connected/non-grid connected. Many prospecting tools offer an initial output calculation with simple parametrizations.

Aside from determining the solar resource, during this stage, a multitude of other parameters need to be considered to exclude nonviable sites. A "first-order" prefeasibility assessment includes the analysis of output potential for various technologies. For example, in the past, studies have been conducted for the southwestern United States by the National Renewable Energy Laboratory's (NREL's) CSP program (Mehos and Perez 2005)[67] to identify the most optimal sites for CSP installations. Using GIS screening techniques, resource maps were developed that highlighted regions potentially suitable for project development after considering various land use constraints, such as protected land areas, sloping terrain, and distance from transmission lines (Figure 11-4). The results of these studies showed that even with these constraints, vast areas in the southwestern United States were potentially suitable for CSP

[66] See https://globalsolaratlas.info/map.
[67] See www.nrel.gov/csp/data-tools.html.

development. Maps such as these are valuable to project developers to highlight specific regions where various levels of site prospecting and prefeasibility analysis can take place.

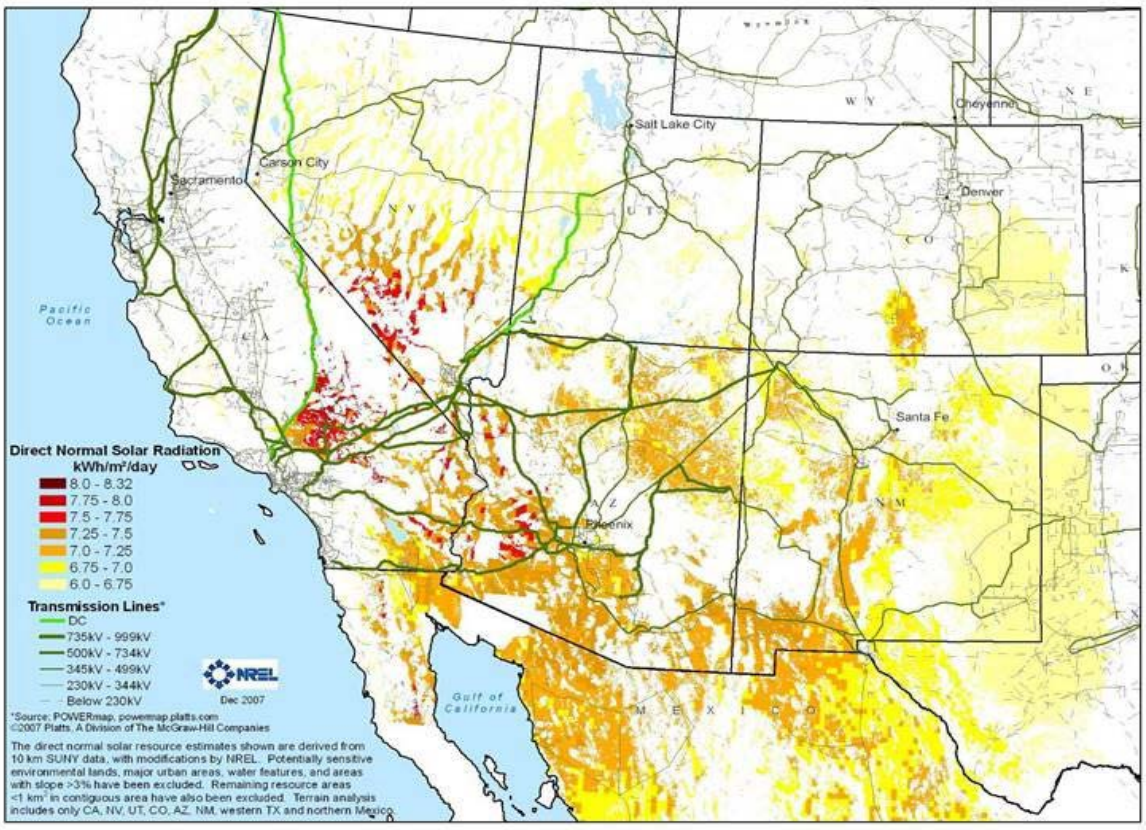

Figure 11-14. CSP prospects of the southwestern United States using GIS analysis for available site selection using the DNI resource, land use, and 3% terrain slope

Image by NREL Mehos and Perez (2005)

In parallel, Navarro et al. (2016) compared various CSP potential assessment methodologies for use in Spain and showed the need for providing intercomparable results while also noting the importance of constraints such as terrain slope. A methodology was proposed, denoted as land constraints, radiation, and slope (LRS), that harmonizes the treatment of these three main inputs. Figure 11.5 shows how the slope consideration (1%, 2%, or 3% of maximum slope) affects the site selection for what became a real CSP power plant in Spain. Only after accepting a maximum slope of 3%, the whole power plant was developed in a suitable area.

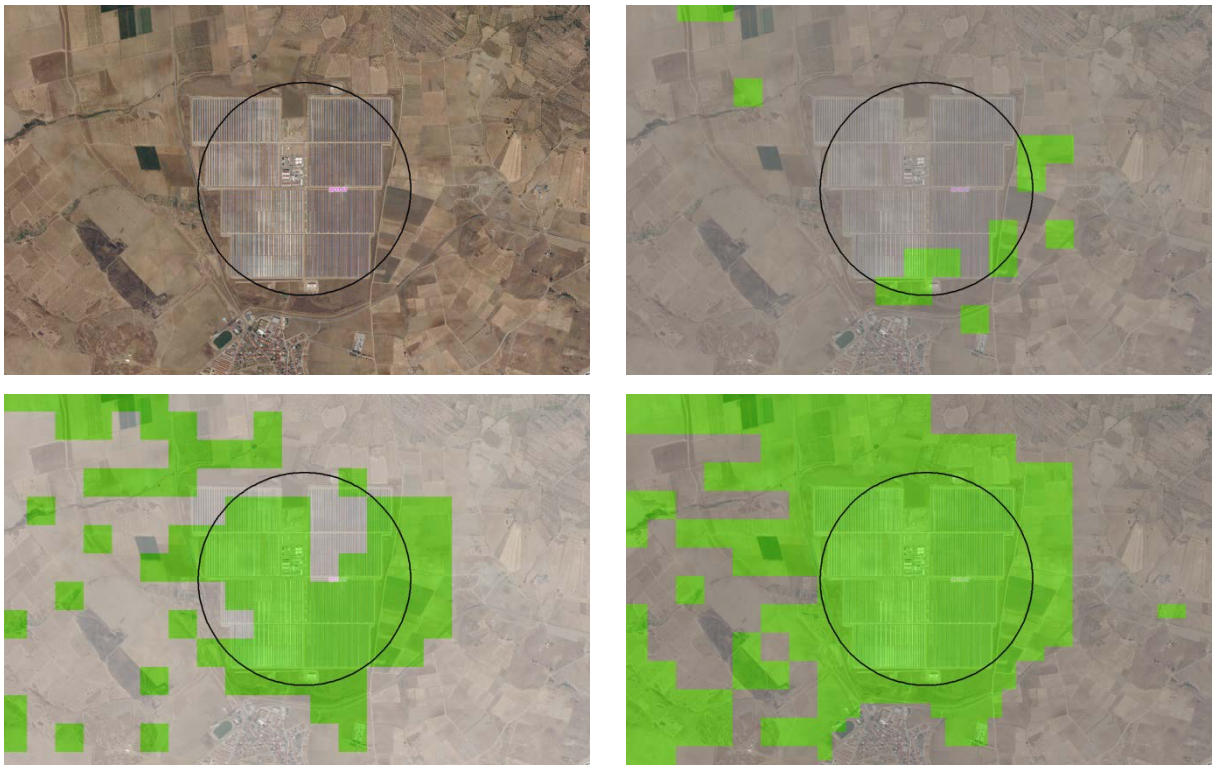

Figure 11-15. (Upper left) Area around the Orellana solar thermal energy plant (Spain) and the suitable areas by the (upper right) LRS1, (bottom left) LRS2, and (bottom right) LRS3 methodologies with maximum slopes of 1%, 2%, and 3%, respectively. Suitable zones are shown in green.

Images from Navarro et al. (2016)

Other studies are being done by various groups to evaluate the solar potential of PV installations on building roofs and façades at the scale of a specific city. Often, these are conducted by administrative bodies to foster solar energy development. Such studies result in the production of solar potential maps (often called "solar cadastres") down to individual building resolution, and they are typically presented as a publicly accessible or commercial online tools offering energy yield estimates for specific locations, usually at the city scale, as shown in Figure 11-6. Examples include solar cadastres for Chrastava, Czech Republic,[68] Podgórzyn, Poland,[69] Los Angeles County, USA,[70] and all cities in Luxemburg.[71] Many other examples exist, but their webpages usually appear only in the local language. For small-scale projects such as residential PV, the information provided by such sources might be sufficient to make an investment decision. The development of cadastres requires GIS data at a very high resolution (better than approximately 1 m), which are usually provided by lidar techniques combined with sophisticated shading analyses (Brito et al. 2012; Huang et al. 2015; Jakubiec and Reinhart 2013; Le et al. 2016; Martínez-Rubio et al. 2016; Mohajeri et al. 2016; Pavlovski 2022; Santos et al. 2014; Tooke et al. 2012).

[68] See https://oneplace.fbk.eu/3d/CZ_PL_solarcadaster/index_chrastava.html.
[69] See https://oneplace.fbk.eu/3d/CZ_PL_solarcadaster/index.html.
[70] See https://apps.gis.lacounty.gov/solar/m/?viewer=solarmap.
[71] See https://map.geoportail.lu/theme/energie.

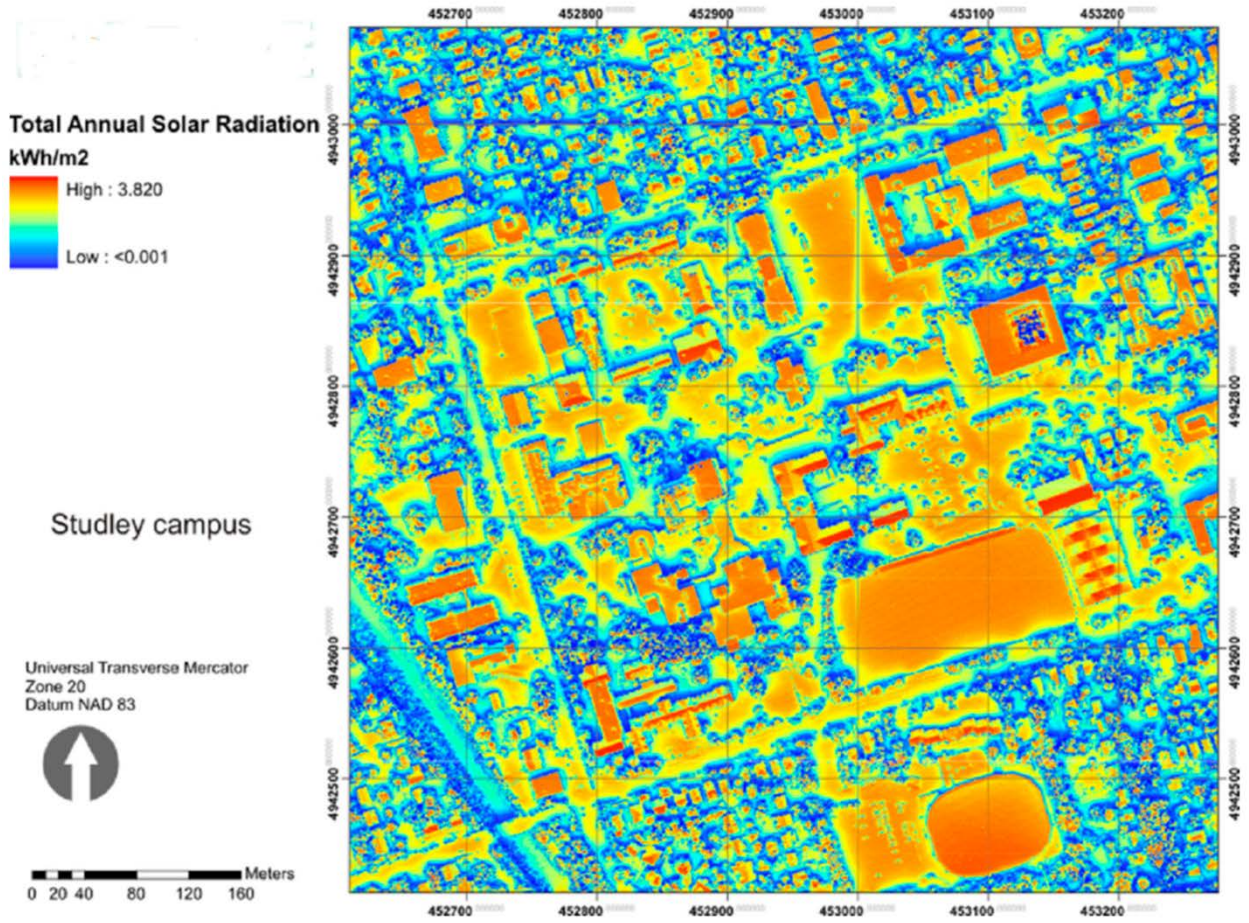

Figure 11-6. Solar potential of rooftops of the Studley campus, Dalhousie University, Halifax, Nova Scotia (red: high potential; yellow/orange: medium potential; blue: low potential)

Image from Pavlovski (2022).

With the introduction of powerful, easy-to-use software tools and webpages—such as the System Advisor Model (SAM),[72] Greenius,[73] RETScreen,[74] Global Atlas for Renewable Energy,[75] Photovoltaic Geographical Information System (PVGIS),[76] Google's Solar API,[77] and Google's Sunroof[78]—many analysts now expect to use maps and time-dependent modeling of the solar systems under study as part of their preliminary analysis. Considerable care must be taken to select the correct irradiance dataset(s) for input to the prospective model. Experts recommend multiple years of at least hourly input data, rather than data from only 1 year or from TMYs, to assess the effects of the interannual variability of the solar resource on year-to-year system performance. Each hourly dataset should be evaluated at a minimum to determine whether the monthly mean values from the hourly data match the best estimate of the monthly

[72] See https://sam.nrel.gov/.
[73] See http://freegreenius.dlr.de/.
[74] See http://www.nrcan.gc.ca/energy/software-tools/7465.
[75] See https://www.irena.org/Energy-Transition/Project-Facilitation/Renewable-potential-assessment/Global-Atlas
[76] See https://joint-research-centre.ec.europa.eu/pvgis-online-tool_en
[77] See https://mapsplatform.google.com/maps-products/solar/
[78] See https://sunroof.withgoogle.com

mean values at the proposed site (Meyer et al. 2008). In many cases, in particular for large utility-scale projects or projects involving tracked collectors and/or bifacial PV, the bankability requires on-site measurements during at least 1 year to validate the long-term modeled time series and to correct them, if needed, using an appropriate site-adaptation technique (see Chapter 7, Section 7.6). More details on bankability can be found in Section 11.8.

11.2.2 Choosing Modeled Irradiation Resource Data

During the first stages of a solar project, solar irradiation information might be available from different sources. Having many sources of irradiance data is better than having none, but the question of selecting the best possible source then arises. This can be done through detailed comparisons between them and validations against high-quality ground measurements. Some concepts related to such tasks are stated in the following. The proposed definitions of *variability* and *error* can aid in better understanding the observed differences among databases (see Chapter 6 and Chapter 10, respectively, for details), though these definitions are not always agreed upon by all analysts or applicable to all possible applications. In addition to these concepts, detailed discussions on uncertainty definition, characterization, and calculation are also provided in Chapter 10.

11.2.3 Variability Impact on Site Selection

Both the temporal variability and the spatial variability are specific to a site (or area) and period. Chapter 6 offers a detailed discussion on solar resource variability.

The spatial variability of the long-term solar resource is a key aspect that needs to be analyzed at this stage and that directly affects the choice of the project site. Using solar resource maps or prospecting tools that visualize the long-term solar resource immediately allows assessing this variability feature. Temporal variability at this project stage is usually analyzed by obtaining long-term monthly mean irradiation data, but assessing multiyear datasets is an effort well invested in case of extremely large project sizes.

11.3 Feasibility Study Stage

In addition to selecting one or more candidate sites for an engineering feasibility assessment, solar power plant project developers need to ensure that they have meteorological datasets, including solar radiation and other meteorological variables, that can guarantee a reliable estimate of the system performance during the project's life. There are different possible situations depending on the availability of measured datasets and/or of other modeled data sources. Because high-quality ground measurements of solar radiation are rarely available for long periods, at least one whole year of local ground measurements and more than 10 years of modeled data are required to guarantee the bankability of large utility-scale projects, especially if using tracked collectors or bifacial PV modules (Leloux et al. 2014).

Solar system software-based simulations often use an annual meteorological dataset intended to be representative of the long-term average meteorological conditions of the project site, usually referred to as either TMY or TRY. Such data files are discussed in Section 8.3. Additionally, it is common practice to use other meteorological annual series representing adverse conditions (e.g., P90; see Section 11.3.2) to assess the project's revenue and financial stress under quasi-worst-case scenario conditions. Sections 11.3.1 and 11.3.2 provide a review of the current

methodologies and possible improvements for the generation of these datasets. Section 11.3.3 discusses the postprocessing and site-adaptation methodologies for reducing uncertainty in the solar resource datasets.

11.3.1 Utilization of Typical Meteorological Data for Solar Energy System Simulations

Typical meteorological datasets are used as the standard input to a wide range of solar energy system simulation software to obtain estimates of the average annual solar energy system yield during the project's lifetime. Such datasets consist of annual time series of hourly or subhourly values of solar radiation and other meteorological variables specifically constructed to be representative of the long-term time series (usually 10–30 years) median values.

TMY datasets are still widely used by building designers and solar energy engineers for basic modeling of renewable energy conversion systems and their preliminary design. These data have natural diurnal and seasonal variations and represent a year of typical climatic conditions for a location and can be useful for such basic tasks. TMYs do not, however, provide all solar resource data needed for solar energy system design, as discussed in more detail in Section 8.3. For example, TMYs do not contain information on interannual variability or meteorological extremes; therefore, TMYs should not be used to predict weather or solar resources for a particular time, for preparing the project's final design, or for evaluating real-time energy production. Because a TMY represents "typical" conditions over a long period, such as 30 years, it is not suited to analyze the system's response to worst-case weather conditions that could occur in the future. An earlier study (Kraas et al. 2011) has exemplarily shown that for CST plants, the simulated electricity yield of individual years of a 10-year measurement period can differ by more than 10% from the simulated yield resulting from a TMY dataset. The magnitude of this difference will vary with technology, project location, and the temporal coverage of available datasets, and it will usually be larger for concentrating solar technologies (because of higher DNI variability), but the spread between individual years might still be significant; hence, a large-scale project should never be designed, planned, or financed based on a TMY file alone, without assessing the interannual variability.

Note also that the simulated performance of the solar energy system might depend on the method followed to construct the TMY file. There are widely different methods of generating TMY files from long-term datasets, including how the variable weighting is handled. For instance, tracked systems typically go into stow mode under high wind speeds; they might not be realistically depicted if the TMY has been created in a manner that correctly represents the long-term solar resource but incorrectly represents the occurrence of high wind speeds that lead to tracker safety shutdown.

11.3.2 Interannual Variability and Probabilities of Exceedance

In the case of large solar energy projects, bankability requirements are stringent (see Section 11.9 for details); hence, reliable profitability and annual payback assessments need to be performed, and thus probabilistic information about the energy output is needed. This must be based on probabilistic solar resource time series that correctly account for extreme situations, which obviously require the statistical examination of long-term time series.

A preliminary step is to first determine the minimum duration of the radiation dataset that is needed to capture the true long-term mean. The interannual variabilities and trends in the resource must be considered (see Chapter 6). A consequence of the high interannual variability of DNI is that CST projects necessarily require scrutiny about the risk of bias in the DNI resource, which can be addressed by using long-term satellite datasets and appropriate site-adaptation techniques. In general, PV projects are less at risk of bias in the GTI resource. Exceptions can occur over regions where the uncertainty in satellite-derived irradiance data is significant and/or in the case of PV installations using tracking systems, which attempt to maximize the DNI fraction of GTI.

Because long-term on-site measurements are still the exception more than the rule, these results underline the importance of relying on an independent long-term dataset, which, in practice, means a modeled dataset derived from satellite images or reanalysis of numerical weather prediction (NWP) results. This is necessary to reduce the uncertainty in the long-term average DNI estimates for a proposed CST site, most particularly, and to provide reasonable due diligence of a plant's estimated performance throughout the life of the project. This and additional concepts related to the development of specialized TMYs or annual series for energy simulation are described by Vignola et al. (2012).

A common way to address the risks associated with the uncertainty of the long-term estimates of the mean annual GHI or DNI values is to consider the annual POE. POE, which is also simply denoted by "P," is the complementary value of a percentile value. In the case of P50, its value matches the 50^{th} percentile and is the result of achieving an annual energy production based on the long-term median resource value. For this value, the probability of reaching a higher energy value is 50%. For example, TMYs are meant to represent the P50 value. In contrast, P90 corresponds to the 10^{th} percentile; hence, the risk that an annual energy value is not reached is 10% (or, reciprocally, 90% of all values in a distribution exceed the P90 value). Depending on the project's size and the practices of the financial institution involved, the solar resource's "bad years" can be examined using various Ps—from relatively lax (P75), to stringent (P90 or P95), to very stringent (P99).

Although the irradiance magnitude is the largest source of uncertainty in P estimates, those estimates must also include other sources of uncertainty, including modeling uncertainty, uncertainty in the system parameters, and reliability uncertainty. High uncertainty is always an issue, even if the P results appear favorable. The combination of probabilistic performance modeling and the uncertainty inherent in the various components of the system (including the solar resource) requires specialized approaches, such as detailed in Ho, Khalsa, and Kolb (2011) and Ho and Kolb (2010).

Figure 11-7, taken from a study by Moody's Investors Services (2010) and reproduced in Renné (2016, 13–41), conceptually demonstrates how improving knowledge of the true long-term solar resource at a site serves to reduce financial risks. By assuming that a long-term annual dataset follows a Gaussian or normal distribution (which is not necessarily the case), Figure 11-7 shows that the standard deviation of the true long-term mean based on only 1 year of data is expected to be much higher than that with 10 years of data because a 10-year dataset contains much more actual information regarding the interannual variability at the site. Assuming that the median value (P50) of the distributions is the same for both the 1-year and the 10-year distribution

curves, the P90 value increases with the additional knowledge (higher confidence) associated with having a 10-year dataset. In turn, that 10-year P90 value reduces the financial risk of the project (or, in other words, is more bankable) because the yield estimates are higher when more data are available. In addition to the uncertainty due to interannual variability, the uncertainty in the irradiance estimates (from modeling or measurement) must also be considered and corrected, if necessary, to evaluate the uncertainty in P; for details, see Hirsch et al. (2017).

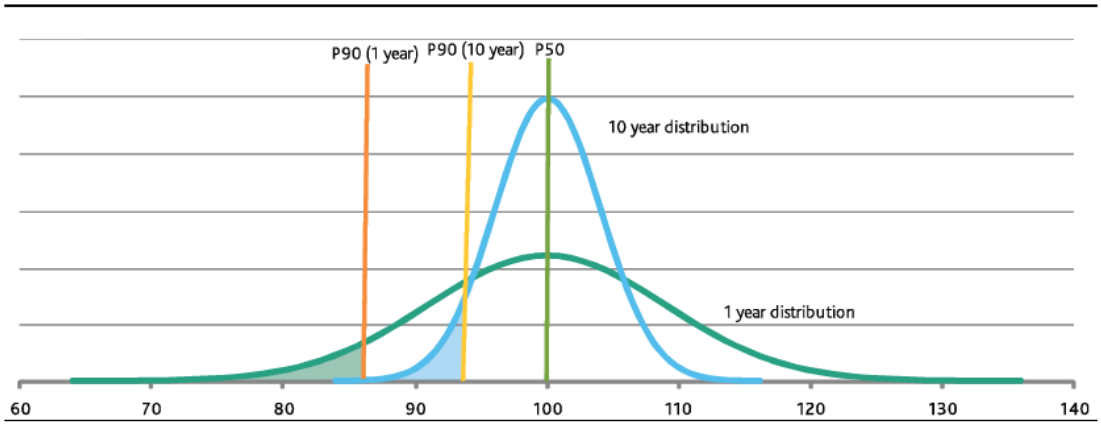

Figure 11-7. The uncertainty of the value of the true long-term mean is much higher with only 1 year of data (green curve) than with 10 years of data (blue curve).

Image from Moody's Investors Services (2010) as presented in Renné (2016)

The statistical calculations of P values often assume that long-term irradiance data follow a normal (or Gaussian) distribution; however, this assumption might not be correct. For example, Dobos, Gilman, and Kasberg (2012) considered long-term measured and modeled updated National Solar Radiation Database (NSRDB) GHI and DNI data for Phoenix, Arizona (Wilcox 2012), and produced cumulative distribution functions (CDFs) based on 30 separate annual datasets to illustrate the concept of P50 and P90. Figure 11-8 shows that if the annual Phoenix data were fit to a normal distribution (solid line) at CDF = 0.1 (which corresponds to the P90 value), an annual GHI of 1.96 MWh/m^2 would be exceeded 90% of the years (or, conversely, the solar resource would fall below this value 10% of the years). Similarly, for DNI, the annual solar resource exceeds 2.2 MWh/m^2 for 90% of the years. For Phoenix, however, the long-term solar data do not appear to follow a normal distribution, but other types of distributions (such as Weibull) have not been assessed for the study. Figure 11-8 shows that the P90 value is somewhat less in Phoenix when determined from an empirical instead of a normal distribution. Further discussion on these points can be found in Renné (2016; 2017).

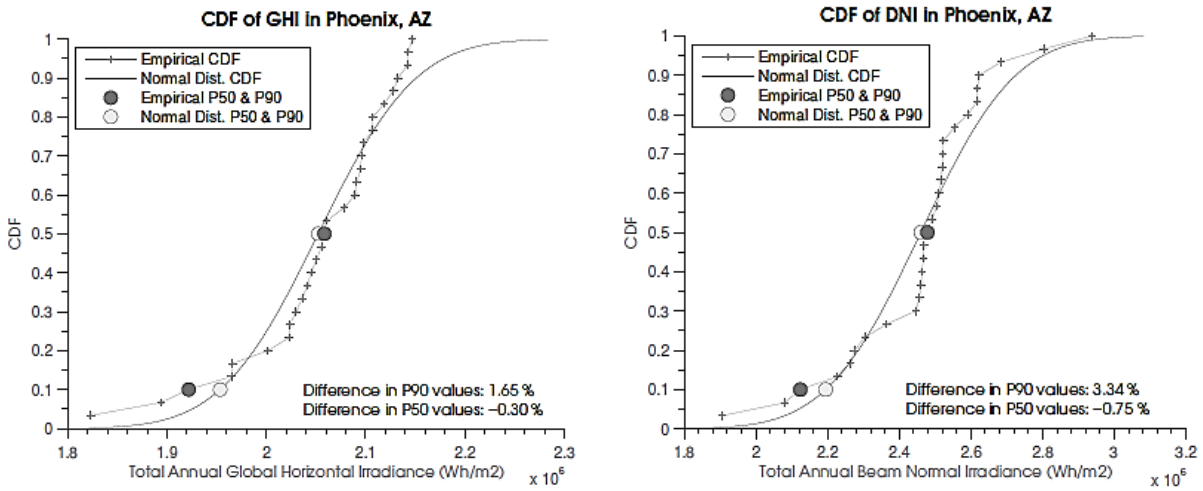

Figure 11-8. (Left) Annual GHI and (right) DNI data fitted to a normal distribution (solid line) for Phoenix, Arizona. Note that each gray circle covers a marker (+).

Image from Dobos, Gilman, and Kasberg (2012)

As discussed by Pavón et al. (2016) and Ramírez et al. (2017), there are several issues related to a P estimate. The first is the assumption that, for instance, an irradiance at the P90 level is proportional to the P90 of the solar system energy output, or yield, which constitutes only an approximation. Additional elements are thus needed (1) to identify the most appropriate P value and (2) to construct a specific 1-year time series for that P using hourly or subhourly data whose sum is that specified P value. A statistically based estimation of the P value depends on the assumed probability distribution. This probability distribution can be approximated with the normal distribution in the case of annual GHI. For DNI, however, there is no evidence that a normal, a log-normal, or a Weibull distribution would always be the best choice. When 10 (or preferably more than 20) whole years of local measurements or modeled estimates are available, methodologies based on the CDF should be used, such as those proposed by Peruchena et al. (2016). In addition, new techniques are developed to construct meteorological years for bankability scenarios that correspond to P90—for example, Dobos, Gilman, and Kasberg (2012).

An additional issue is the resolution of the data time series used for energy simulations. For CST projects, for instance, the yield and probabilistic predictions obtained with hourly data could substantially differ from those using 1-minute or 5-minute data (Hirsch et al. 2010; Meybodi, Ramírez-Santigosa, and Beath 2017). Depending on satellite sensor and period, satellite-derived irradiance time series are not available at a temporal resolution better than 5–60 minutes. Some stochastic methods have been proposed to derive 1-minute or 5-minute irradiance from data at a coarser resolution (Grantham et al. 2017; Hofmann et al. 2014), which can be helpful (see Chapter 6 for details). Instead of using a limited number of yearly datasets for simulation, Nielsen et al. (2017) proposed using Monte Carlo methodologies to generate an unlimited number of yearly series. This methodology allows the solar resource assessment—and thus the energy output calculation—to be performed in a way that is similar to that currently used for estimating other essential variables in the economic assessment of solar power plants. The generation of hundreds of such plausible years has been demonstrated by Larrañeta et al. (2019), Fernández-Peruchena et al. (2015), and Meybodi, Ramírez-Santigosa, and Beath (2017). Other authors—Ho, Khalsa, and Kolb (2011) and Ho and Kolb (2010)—have found issues with the Monte Carlo approach and suggested the Latin hypercube sampling method instead.

Another alternate approach is to completely avoid the step of generating solar resource time series with certain characteristics such as a Pxx value. This approach is based on running the energy yield simulation with the complete available multiyear time series and analyzing the output instead of manipulating the input data to these simulations. From the output, which corresponds to a simulation of operating the planned solar energy system over the available historical period, a variety of information can be extracted. This approach has several distinct advantages:

- It does not require manipulating the available solar resource data to obtain a predefined input dataset (other than reformatting the input files to conform to the simulation software's input data format); thus, it avoids the complications of identifying a suitable dataset generation method, programming highly advanced computational methods that might not be available in the public domain, and other practical complications.
- It does not depend on the TMY generation method or variable weighting.
- It preserves the physical/meteorological patterns that have actually occurred as long as they have been correctly recorded in the dataset. Any other method that generates artificial datasets is at risk of resulting in physically/meteorologically inconsistent datasets. A prominent example is that in a monthly based concatenation method, such as the TMY3 method, the last day in a month might be followed by the first day of a month that had completely different conditions, e.g., a cyclone pressure system immediately followed by an anticyclone. In this alternate method, extreme years are not excluded and can be used for financial projections of debt servicing.
- It preserves information on many non-solar resource meteorological events, such as wind speeds (relevant for module performance and tracking system safety shutdowns), rain events (useful for soiling analysis), or temperature (relevant to plant performance).
- It is a very intuitive method that is easy to explain to any third-party reviewer, shareholder, or investor: "If this power plant had been built 20 years ago, it would have performed like this."
- It is supported by the wide availability of long-term solar resource datasets covering almost 30 consecutive years over various regions.
- The method is compatible with using several input datasets for different time periods and with different temporal resolutions. In a simplified approach, each dataset can be used for independent yield simulations, and the results can be reconciled by averaging the outputs, weighed with a confidence factor for each dataset.
- Very intuitive results can be extracted, such as average annual yield (P50), P90 yield, worst yield in a calendar year, or longest period of electricity generation below a certain threshold.

A practical obstacle to this method is that most system simulation software in common use do not support the modeling of more than one consecutive year at a time; hence, in the worst case, this means preparing up to approximately 30 single-year datasets, manually running the simulation, and compiling the results. NREL SAM is among the simulation software that offer this multiyear option as an integrated feature, in addition to offering a P50/P90 analysis for sites covered by the U.S. NRSDB (Dobos, Gilman, and Kasberg 2012).

Including long-term trends derived from the effect of climate change and other local or regional singularities (such as the increase of atmospheric aerosols derived from pollution) on solar

radiation might improve the value of the solar power plant yield prediction (i.e., during the complete solar facility lifetime). For instance, the Meteonorm[79] software includes the effect of climate change estimated from the Intergovernmental Panel on Climate Change models for three different scenarios. Aerosol pollution scenarios are also important for future GHI and DNI resources. For instance, a decrease in the solar resource has occurred in many Asian countries during the recent past, and this trend could continue into the foreseeable future (see other causes of future changes in Chapter 6).

11.3.3 Combining Data Sets: Site Adaptation to Improve Data Quality and Completeness

Long-term solar resource datasets always have uncertainty. If the magnitude can be precisely evaluated, investors can derive the risk of the project and evaluate whether the performance of the system could be lower than desired. Reducing uncertainty in solar resource data is thus a key step toward bankable projects. The general process of combining modeled datasets with site observations is called postprocessing in various fields (Janotte et al. 2017). In solar applications, this is generally referred to as *site adaptation,* consisting of a wide variety of methodologies that are applied to improve direct model or retrieval outputs and reduce uncertainty. A detailed description of these methods is given in Chapter 7, Section 7.6.

11.4 Due Diligence and Acceptance Stage

When a utility-scale power plant is built, typically there is a period during which the "engineering, procurement, and construction" (EPC) contractor operates the power plant. In practice, this period is usually 1 or 2 years. During this time, the EPC must prove the warranted power plant performance to the owner before the owner (or a third party entitled by the owner) takes charge of the power plant operation.

To correctly establish the true power plant performance, it is necessary to record accurate solar irradiance and meteorological readings. Generally, all meteorological and other parameters that influence the power plant's electricity yield must be determined with a high degree of accuracy. This is of extreme importance because the acceptance of the plant—including all economic and legal consequences, such as warranty claims or liquidated damages—depends on a correct performance assessment. Any ambiguity of the reference measurement data, or lack of agreement on the method of establishing the reference dataset, can potentially lead to severe disputes and legal confrontations.

Therefore, in the EPC contract, the following should be exactly determined:

- The parameters that must be measured
- The instrumentation that shall be used and the number of measurement locations in the plant
- The parameters that influence the power plant electricity yield that have been established based on models, estimates and assumptions, the method to derive them, the sensitivity of the power plant to these parameters, and how to treat changes to these parameters that might be discovered during the acceptance stage

[79] See http://www.meteonorm.com/.

- The required documentation (calibration certificates and history, instruments, installation report, etc.)
- The data format and temporal resolution that shall be used
- The party responsible of providing, installing, and commissioning the instrumentation
- The maintenance procedures and the frequency and documentation thereof
- The data acquisition procedures
- The data quality control procedures, including data completeness rates and rates of data passing all quality control methods
- The virtual power plant performance model (of the digital twin) that will be used and how the measurement data are fed into this model.

Specific care should be taken of parameters that, at the time of the EPC contract signature and potentially also afterward, were/are only available as modeled values or assumptions or might undergo notable change. Prominent examples for this are ground albedo (relevant for tracked/bifacial PV plants), atmospheric attenuation (relevant in CSP central receiver plants), or sunshape (relevant for concentrating technologies).

In tracked PV plants, an independent measurement or model of tracked plane-of-array (POA) irradiance might be necessary if the EPC provider or tracker manufacturer claims a specific performance gain over astronomical tracking by proprietary tracking algorithms. The same consideration should be made to verify claimed bifacial gains in bifacial PV.

Additionally, it is important to precisely identify which meteorological datasets were used for the technical design (design operating conditions) and the procedure to establish filter criteria by which periods with non-design operating conditions shall be removed from the performance assessment.

For each of these points, some recommendations are included in chapters 3, 4, and 5 as well as in this chapter.

Given the importance of accurate and unbiased measurements during the acceptance stage, and considering the inherent conflict of interest (the EPC has control over the power plant and usually the measurement equipment, but it has no incentive to obtain accurate data because any lack of data will support covering low plant performance), both parties might consider involving an external expert to write the specifications in the contract; to conduct the measurements on-site; and/or to perform a third-party review of instruments, documentation, and measurement data. As practice has shown, if this is applied, this should be done early because low-quality measurement data cannot usually be restored to a satisfying degree of uncertainty.

11.5 Operation Stage

This section discusses a variety of approaches for monitoring the solar resource at an *existing* solar power plant to better understand its performance. The performance of a solar energy system is directly linked to the local meteorological conditions. For flat-plate thermal collectors and PV, the production is roughly proportional to the incident GTI; for concentrating technologies, the incident DNI is the driving input. For bifacial PV, the in-plane rear-side irradiance also needs to be considered. In all cases, additional meteorological variables need to

be monitored because they play a modulating role. In summary, the real-time monitoring of meteorological conditions at the system's location is important to:

- Evaluate a performance guarantee (acceptance testing; see also Section 11.4)
- Assess the power plant's performance to improve yield predictions and to gain knowledge toward improvements in future plants
- Identify conditions of poor performance, including evidence of soiling, shading, hardware malfunction, or degradation, which could lead to warranty replacement, etc.

In nearly all cases, data recorded from on-site measurements of the solar resource are necessary. The required and recommended measurands and radiometers are discussed in Section 3.5. For PV monitoring with lower accuracy requirements, remote meteorological data or satellite data are also acceptable for GHI, ambient temperature, wind speed, and precipitation (IEC 2021).

11.5.1 Performance Guarantee

Different methods exist to evaluate a plant's performance guarantee (Kurtz et al. 2014). In all cases, data recorded from on-site measurements of the solar resource are necessary. In the case of concentrating technologies, datasets derived from good-quality, on-site DNI measurements are usually required as inputs to the models used for performance guarantee. For flat-plate thermal collectors and PV, the yield prediction is generally based on GHI (even though the actual resource corresponds to GTI); hence, it is also common for a performance guarantee to use GHI as the basis for determining whether a plant has performed as promised. Some companies, however, have noted that the performance characterization of a PV plant can be accomplished with a lower uncertainty by using GTI instead. That is because this approach reduces the uncertainty inherent to the approximate transposition procedure that transforms GHI into GTI. Moreover, specific irradiance sensors, such as reference cells or reference modules that closely match the PV module response, can be chosen to match the expected response of the PV modules, which thus reduces the angle-of-incidence and spectral effects. Specifying GHI remains the best option if, for instance, a PV system comprises sections with different in-plane irradiances (POA irradiances) as a result of different tilts or azimuths, which might be the case over complex terrain. If the performance guarantee is specified in terms of GTI, the plant efficiency characterized during the performance guarantee evaluation could differ from the efficiency estimated in an earlier step with a model rather than using historical GHI data. Also, the placement of all sensors must (1) be in the correct plane (which is easy to confirm when the sensor is in the horizontal plane but not as easy for other orientations) and (2) experience the expected local conditions (ground albedo and potential shading of sensors) if the sensor is not in the horizontal plane (Kurtz et al. 2014).

Additional meteorological variables must be measured for yield predictions, as discussed next. Depending on the solar system's size, more than one measurement point must be considered, as sky conditions will continuously vary. Even under clear-sky conditions, but especially under partly cloudy conditions, irradiance variations across a solar system will lead to performance variations (Janotte, Lüpfert, and Pitz-Paal 2012; Kearney 2009, 2013).

11.5.2 Power Plant Performance Monitoring and Forecasting

During power plant operations, knowledge of the current meteorological conditions and real-time status of the plant is of high importance. In addition, the future meteorological conditions

directly influence the power output forecasts, which are important to maximize the plant's revenue and are also often mandated by the grid regulators; therefore, both solar resource measurements and forecasts are essential data streams for many large solar systems. Real-time DNI, wind, and temperature data are essential for the operation of CST plants, and thus they need to be continuously monitored. Although many PV plants can successfully operate with only episodic intervention, measurements and forecasts can also be advantageous. For example, controlled cleaning of a PV array as a function of meteorological conditions (e.g., frequency of recent precipitation) has benefits. Moreover, equipment malfunctions can be detected more quickly if the PV plant output is being continually compared to the expected output based on actual meteorological conditions.

11.5.3 Solar Radiation Forecasting Needs for Solar Power Project Operations and Maintenance

Forecasting the production of a solar power plant can considerably improve its profitability (Ramírez and Vindel 2017). Accurate predictions of the plant's average solar resource are needed for both solar thermal and PV power plants. The most important parameter to forecast is GHI in the case of flat or tilted PV plants and DNI in the case of concentrating systems. A GTI forecast is highly desirable, but it can be derived from a GHI forecast using transposition models. Wind velocity and direction are also relevant for the operation of tracking systems and for the temperature of PV modules in the plant.

Detailed explanations of solar radiation forecasting methodologies and the current state of the art are provided in Chapter 9. The specific forecasting needs depend on the intended application. Essentially, solar radiation forecasts can be used for either planning maintenance downtime or for optimizing operations. Moreover, grid regulators increasingly tend to make them mandatory for grid stability and management reasons.

11.5.3.1 Planning Maintenance

Maintenance work is needed in all types of solar power plants. Examples include technical closure, replacing defective components, cleaning collectors, or conducting characterization tests. Depending on the expected duration of the maintenance work, the required forecasts correspond to different time horizons. Usually, a technical plant closure must be planned ahead of time and occurs on a fixed date based on the long-term forecasting on a monthly basis, whereas minor maintenance work is decided based on day-ahead forecasts.

11.5.3.2 Optimizing Operation and Revenue

To optimize operation, forecasting knowledge will help improve electricity sales by better matching production with demand if the plant is equipped with storage, particularly in the case of CST projects. In that case, the plant's annual revenue is conditioned by the quality of the solar forecasts (Ferretti et al. 2016); thus, especially when subject to a fluctuating electricity market, the plant's revenue can be maximized if production is appropriately predicted. Aside from increasing the revenue by maximizing the electricity sales prices, high-quality forecasts can also help to reduce incurred penalties for failing to match projected production schedules in specific market environments.

If there are ramp rate or connection capacity limitations defined by the grid operator, the yield of a PV plant with batteries can be improved by storing the excess PV energy during positive ramps and using energy from the batteries during negative ramps. Forecasts can help manage the battery storage for this application and help limit the required storage capacity. Figure 11-9 shows the role of meteorological variables in forecasting demand and energy generation.

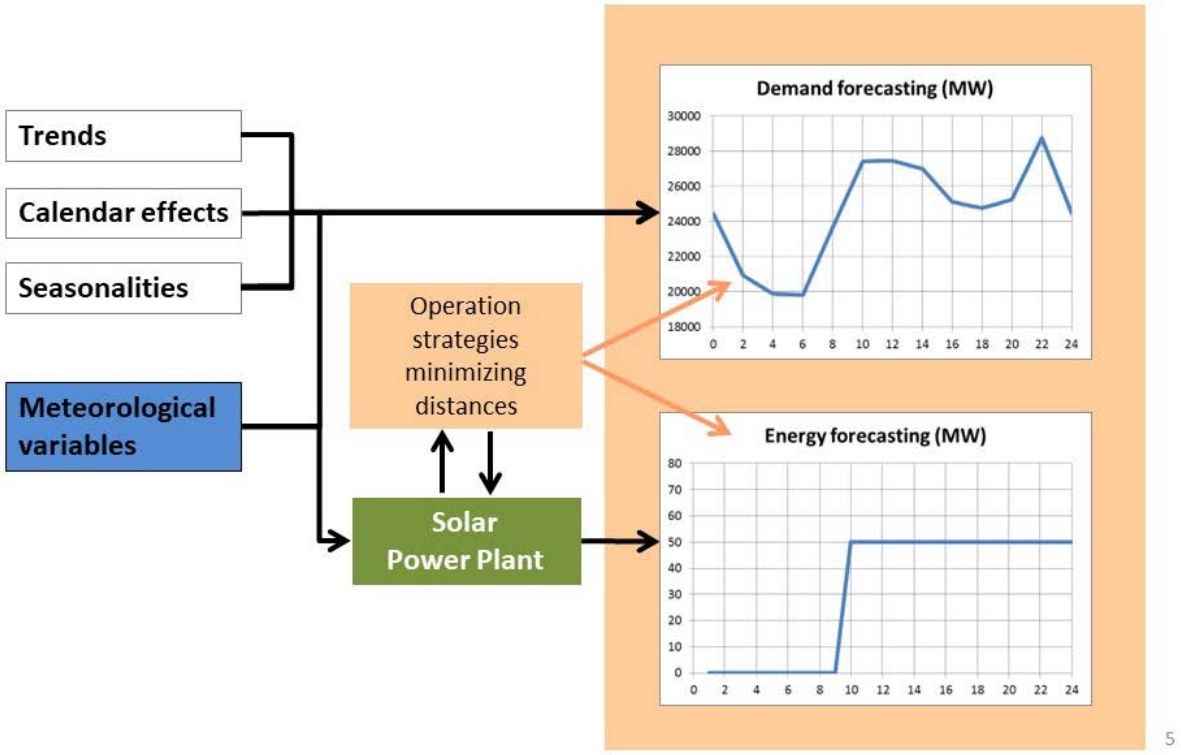

Figure 11-9. Importance of weather variables in forecasting demand and energy production

Image from Ramírez and Vindel (2017)

11.5.4 Economic Value of Solar Radiation and Photovoltaic Forecasting

Beyond general information on forecast applications, the economic value of applying forecast models for markets and the grid integration of solar power is of interest to forecast users. Here, some studies on the economic value of forecasting are summarized.

11.5.4.1 Economic Value of Photovoltaic Power Forecasting in Markets: A Case Study for the Scandinavian Electricity Market

In energy markets that have mandatory market gate closures, production from variable renewable energy assets, such as PV, must be forecasted prior to delivery. In many of these markets, e.g., Scandinavia (Klyve et al. 2023), imbalances between the contractual market agreements made at the market gate closures and the actual physical delivery must be financially accounted for on a hourly basis through a so-called *imbalance settlement*. Because the issued forecasts at the market gate closures determine the final imbalances that need to be financially settled, the forecast accuracy provides economic value. The income loss for PV producers that issue inaccurate forecasts in the Scandinavian day-ahead and intraday markets are quantified using historical

market prices, meteorological data, and NWP estimates from 2017–2021 (Klyve et al. 2023). This study assumed that PV producers participated in the Scandinavian day-ahead and intraday markets. Moreover, the producers were assumed to submit their bids to the day-ahead auction daily at the day-ahead market gate closure time of 12:00 CET D-1 (day before delivery), i.e., a forecasting horizon of 12–36 hours. Then at the gate closure of the intraday market, i.e., D-0–60 minutes (1 hour prior to a given settlement period), the PV producers use their updated intraday forecasts to sell or buy what they estimate the day-ahead forecast error will be. Note that PV power generation time series for synthetic 10-MWp plants are modeled using irradiance, temperature, and wind speed data from 11 meteorological weather stations across Scandinavia. Further, market forecasts for the same locations are generated using a NWP model, i.e., the Integrated Forecasting System (IFS) from the European Centre for Medium-Range Weather Forecasts (ECMWF) combined with a smart persistence forecast (SPF) model. Figure 11-10 illustrates how the SPF data are generated.

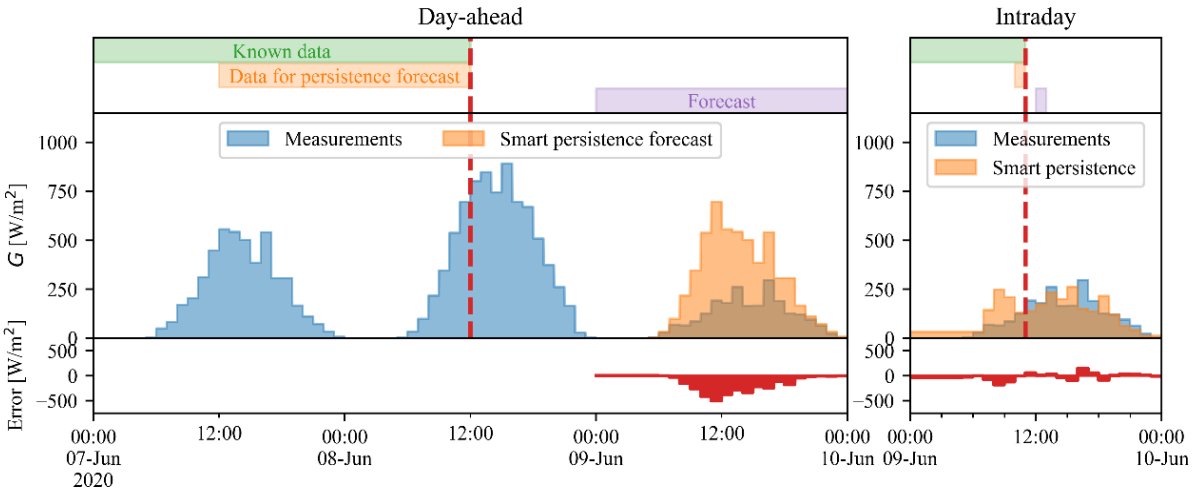

Figure 11-10. Generation of SPF irradiance forecasts for the (left) day-ahead and (right) intraday markets in Scandinavia. For the day-ahead market gate closure (dotted, red line), the forecasts are issued for the entire day of June 9, 2020. The illustrated intraday market gate closure represents only the gate closure for the settlement period from 12:00–13:00 CET on June 9, 2020. The imbalance between the measured energy generation and the market committed schedule is shown (in red) in the lower part of the figure.

Image from Klyve et al. (2023)

Further, it is assumed that all PV producers are price takers in the markets, such that the historical day-ahead prices, weighted-average intraday prices, and regulating prices (used in the imbalance settlement) are used to quantify the income loss caused by the forecast errors. Finally, four cases are defined to quantify the value of PV forecasts under the past (1), present (2), and future (3, 4) Scandinavian market structures.

- Case 1: Old market (until 2021-11-01)—Imbalance settlement at hourly resolution and a dual-price structure (imbalance surpluses and deficits are priced differently). The intraday gate closure is set 60 minutes prior to delivery.
- Case 2: Present market (2021-11-01 to 2025-01-01)—Same as Case 1 but with a single-price imbalance settlement structure

- Case 3: Short-term future market (beyond 2025-01-01)—As with Case 2 but with the day-ahead market, intraday market, and imbalance settlement conducted at 15-minute resolutions.
- Case 4: Future market with extended intraday trading—Same as Case 3 but with the intraday gate closure set to 1 second before the beginning of the settlement period.

The income losses relative to providing perfect forecasts to the markets are given in Figure 11-11 using the ECMWF's IFS for the day-ahead forecasts and SPF for the intraday forecasts. The main takeaways from this work are:

- The value of providing accurate forecasts is largest under the dual-price imbalance settlement structure (Case 1—abolished, old market).
- The transition from 60-minute to 15-minute settlement periods under the single-price imbalance settlement has little effect on the forecast value (from Case 2 to Case 3 or Case 4).
- Extending the intraday gate closure to the beginning of a settlement period generally reduces the income losses (Case 3 to Case 4).
- When bidding in the day-ahead market and trading the forecasted imbalances in the intraday market, the income losses for the modeled PV power plants range:
    - From 0.1–2.3% when bidding with SPF in the day-ahead and intraday market
    - From 0.6–2.4% when bidding with the ECMWF's IFS in the day-ahead and intraday market
    - From -0.1–2.6% when bidding with the ECMWF's IFS in the day-ahead and SPF in the intraday market.

Klyve et al. (2023) clearly showed the importance of accurate PV forecasts for the profitability of PV power plants in the Scandinavian markets. The same analysis should be done for other markets to determine whether investing in more sophisticated forecasting methods would influence the overall profitability of solar power plants.

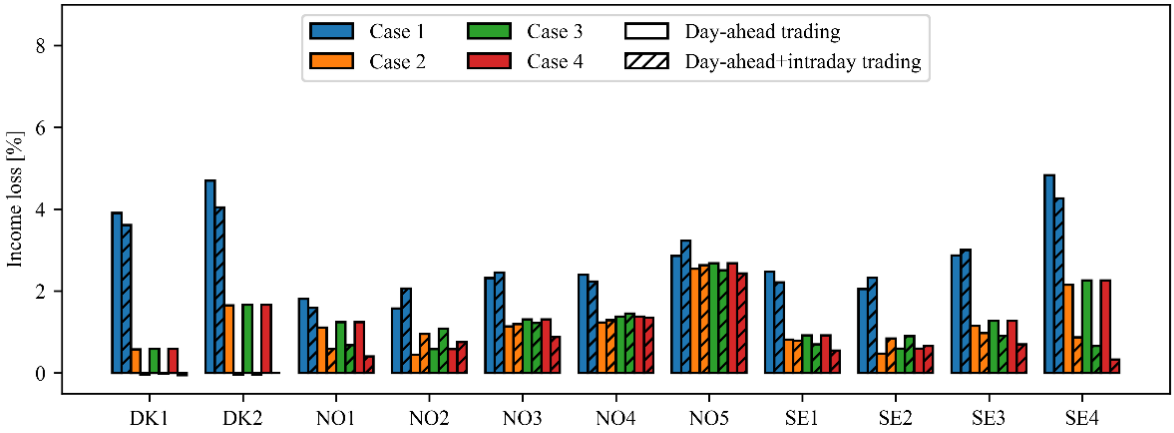

Figure 11-11. Income losses of the modeled Scandinavian PV power plants when bidding with the ECMWF's IFS in the day-ahead market and SPF in the intraday market relative to bidding with perfect forecasts for these markets. The case studies represent the past (1), present (2), and future (3, 4) energy markets as well as the imbalance settlement structures.

Image from Klyve et al. (2023)

11.5.4.2 Value of Short-Term Forecast Uncertainty Information in Stochastic Photovoltaic Power System Dispatch Optimization: A German Case Study

In the German research project SOLREV,[80] a tool from DLR-Oldenburg that was designed to assess the value of probabilistic feed-in forecasts for wind plants (Buller 2023) was used to study an example power network including PV systems, hence one fluctuating generator. This study focuses on the expected balancing costs at the time of delivery that would reduce the total system costs in a power system network. The expected balancing costs are estimated from the probabilities of PV feed-in scenarios. Details of the stochastic optimization problem are provided in Buller (2023).

The specific network is shown in Figure 11-12 (Morales et al. 2014) and consists of a 100-MW PV system sited at each of the two buses that are connected via a 100-MW link. The static loads are set to 80 MW and 90 MW, respectively. Further, a 30-MW storage with a capacity of 180 MWh is added to Bus 2. Optionally, the network can be modeled without storage. The flexible generator G1 has the highest marginal costs (35 $/MWh), and the inflexible generators have lower marginal costs of 30 and 10 $/MWh, respectively. The marginal costs of PV and storage are assumed to be very small.

[80] See https://www.enargus.de/pub/bscw.cgi/?op=enargus.eps2&q=Deutsches%20Zentrum%20für%20Luft-%20und%20Raumfahrt%20e.V.%20(DLR)&m=1&v=10&id=1224264.

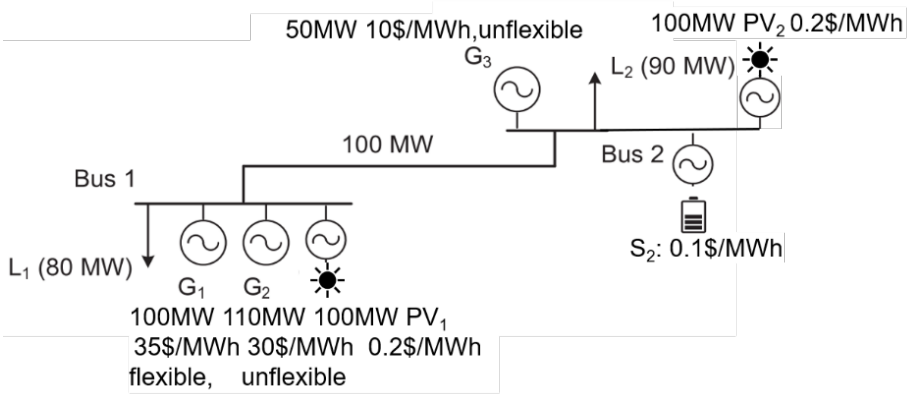

Figure 11-12. Exemplary power system network with two PV systems and short-term storage

Image modified from Morales et al. (2014)

The simulations were carried out for an entire year using intraday PV forecasts for two grid points in southern Germany. The probabilistic PV forecasts are based on ECMWF GHI forecasts from July 2015–June 2016 and consist of 50 ensemble members. For simplicity, a random member of the ensemble is used as the observed PV power to determine the deviation between the dispatched (planned) PV power and the delivered PV power.

At the beginning of each day, the dispatch of each plant (including storage) for the entire day is computed using stochastic dispatch optimization. At the time of delivery, the balancing module is activated to balance any deviation between the dispatch and the real feed-in. In case of imbalances, the following actions are possible in the order of the related marginal costs: The storage is used, PV power is curtailed, the flexible power plant G1 is ramped upward or downward at slightly higher costs than 35 $/MWh (including balancing premiums), or, finally, the load is shed at a cost of 200 $/MWh. These costs are called balancing costs.

The results of the stochastic dispatch optimization are evaluated in terms of total system costs that are the sum of the initial dispatch costs and the balancing costs. The reference case is the economic dispatch using a deterministic forecast for the PV systems. In this case, the merit order principle is clearly followed, i.e., stored energy is taken first, followed by PV, generator G3, G2, and, last, G1. The first ensemble member is always chosen as the deterministic forecast.

Figure 11-13 shows an increase in the daily cost savings over the normalized mean absolute error of the deterministic PV forecast error. This is expected because high deterministic forecast errors require more expensive balancing. In those cases, the stochastic dispatch optimization dispatches more power from G1, G2, and G3 plus PV than actually needed (i.e., exceeding the static load) and ramps down the flexible G1 if enough PV is available at the time of delivery.

The simulated storage (green crosses in Figure 11-13) more efficiently reduces the total system costs for the economic dispatch using deterministic forecasts; however, the use of probabilistic information in stochastic dispatch optimization is still more valuable, i.e., leads to lower costs. Without storage, the yearly average cost is 21.49 $/MWh for the stochastic dispatch optimization and 21.93 $/MWh for the economic dispatch. Using the 180-MWh short-term storage, the costs decrease to 21.26 and 21.35 $/MWh for the stochastic and economic dispatches, respectively. In case no PV is considered in the network, the average costs are 24.41 $/MWh, whereas in case no

PV forecast errors occur (perfect foresight), the average costs are 21.19 $/MWh (without storage).

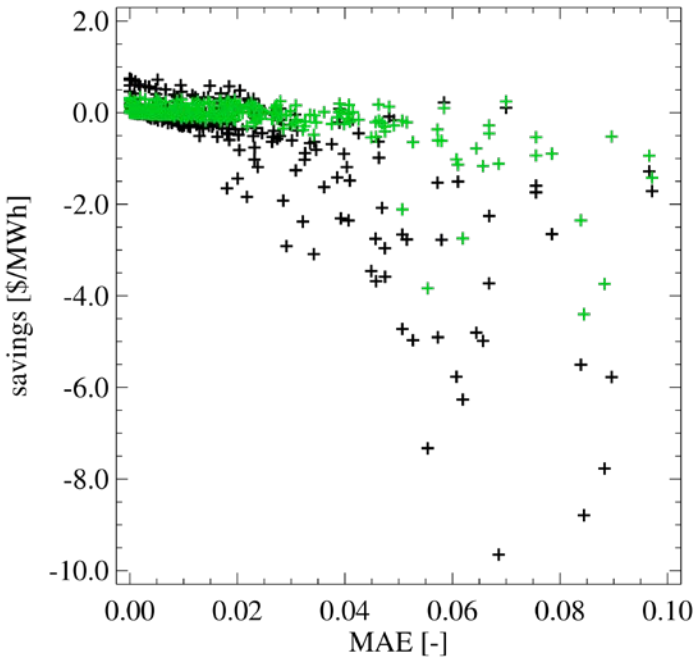

Figure 11-13. Daily cost savings [$/MWh] using stochastic dispatch optimization compared to economic dispatch without storage (black) and with 180 MWh of storage (green).

Image by DLR Institute of Networked Energy Systems

11.6 Yield Estimation Methodologies

This section provides a summary of the general approaches that use solar resource data to estimate the yield of solar energy systems. The resource data considered here include not only solar radiation but also other meteorological parameters (such as wind speed and temperature). First, PV systems are discussed, followed by CST systems.

11.6.1 Yield Estimation of Non-Concentrating Photovoltaic Projects

The value of electricity generated by a PV system depends on the amount of electricity generated and on the grid's need (market driven) for that electricity at the time it is generated (i.e., its load curve). For small- to medium-size residential and commercial systems up to approximately 100-kWp capacity, the generated electricity will normally be consumed directly behind the meter of the premises where the system is located. In contrast, larger-size systems are connected directly to the grid to supply electricity directly to that grid. A quantitative understanding of the specific solar resource for the intended location and orientation of the PV system is essential to evaluate the former's quantity. The relevant solar input for yield calculation is the irradiance incident on the POA (i.e., GTI), although other variables (particularly ambient temperature, wind, and soiling) also impact the system's output. This section provides a high-level overview; more detailed descriptions of PV system modeling can be found in Ellis, Behnke, and Barker (2011) and Holmgren, Hansen, and Mikofski (2018).

Three general approaches exist to estimating a PV system's yield. These are presented in order of increasing accuracy.

11.6.1.1 Performance Ratio Method

The output of a PV plant can be characterized by the performance ratio (PR) metric (Reich et al. 2012), which is the ratio of the electricity generated by the plant relative to its theoretical output during the same period.

When using this method, the first step is to determine the theoretical annual output of the system. The nameplate rating for PV systems refers to the system power output evaluated under standard test conditions (GTI of 1000 W/m^2 at 25°C), and it is primarily a function of the efficiency, η, and area, A, of the PV modules in the system to convert incoming solar radiation to DC power output. The rated power, P_0, of the system is given by:

$$P_0\,[\mathrm{kW_p}] = A\,[\mathrm{m^2}] \cdot 1000\,[\mathrm{W/m^2}] \cdot \eta. \tag{11-1}$$

The reference annual energy yield, Y_R, of the module is then determined from the actual annual GTI [kWh/m^2] at the site:

$$Y_R\,[\mathrm{kWh}] = P_0\,[\mathrm{kW}] \cdot \mathrm{GTI}\,[\mathrm{kWh/m^2}] \,/\, 1000\,[\mathrm{W/m^2}]. \tag{11-2}$$

The annual performance ratio is then applied to Eq. 11-2 to determine the actual energy produced by the PV system, also called the final yield, Y_F, which is typically less than its theoretical energy output because of a variety of factors (as described next):

$$Y_F\,[\mathrm{kWh}] = \mathrm{PR} \cdot Y_R\,[\mathrm{kWh}] \tag{11-3}$$

where the PV plant size is derived from the sum of each module's nameplate rating. The specific or normalized yield, y_F [kWh/kW$_p$] = Y_F / P_0, is the normalized final yield of the system, which is mostly reported. Note that the performance ratio is usually calculated from the measured final and reference yields (Reich et al. 2012). In practice, deviations from this estimate can be expected because of the interannual variability of the solar resource and the variability of the performance ratio (van Sark et al. 2012).

Typically, for most recent PV power plants, the performance ratio ranges from 0.8–0.9. Factors that contribute to lower performance ratios include:

- Shading losses
- Soiling or snow cover losses
- Nonideal system orientations
- Wiring losses
- Lower module efficiencies under high-temperature operations
- Undersized inverters, making them "clip" the plant's output part of the time
- Older plants that have experienced module degradation, including potential-induced and light-induced degradation
- Modules whose performance is less than expected because of incorrect nameplate information. The situation has changed over time. In past years, manufacturers often

placed modules in the bin with the larger nameplate value. Currently, many manufacturers now bin modules so that the actual performance is equal to or greater than (up to 3%) the nameplate value. Only measurements of the PV module power corrected to standard test conditions can provide correct values of the performance ratio.
- In (residential) areas with high penetrations of PV systems, voltage limits are violated at high feed-in, which leads to the shutdown of inverters, thus lowering the performance ratio.
- Any curtailment, either required by grid operators in support of grid reliability or used by PV system operators for economic reasons, leads to yield loss.

Some factors that contribute to high observed performance ratios include:

- Operation in cold climates
- Modules with low-temperature coefficients. Typically, cadmium telluride (CdTe), copper-indium-gallium-selenide, and high-efficiency silicon heterojunction modules tend to have the lowest temperature coefficients (Louwen et al. 2017). In this case, the power output degrades less when the temperature rises; hence, the modules will produce a higher energy yield. Such modules are the preferred option in high-temperature environments.
- Modules that generate power above the nameplate rating (based on 1000 W/m²) as a result of high atmospheric transparency, cloud enhancement, and/or high ground reflection
- Modules that have bifacial sensitivity, adding up to approximately 5–10% to annual yield (Stein et al. 2021), depending on ground albedo
- Soiling or miscalibration of the radiation sensor, making it underestimate the incident irradiance and overestimate the performance ratio; therefore, regular cleaning and maintenance of the sensor is very important (see Chapter 4).
- Time resolution. Due to varying irradiance intensity distributions as well as temperature variations over a year, the performance ratio is sensitive to the period over which it is determined. A graph of monthly or daily performance ratio reveals seasonal effects. A boxplot showing the average annual performance ratio as well as quantiles and outliers is very informative for system operators.

Other impacts on the performance ratio are the choice of the irradiation sensor (thermopile pyranometer versus photodiode detector or reference cell, or even GHI from meteorological stations/services) and the methodology used to determine the PV system power (nameplate power, manufacturer flasher measurement, and/or on-site measurements).

The performance ratio method is simple, but it might not be accurate in all cases. For instance, van Sark et al. (2012) found a few older PV systems with performance ratios surprisingly less than 50%. The method is particularly useful, however, to compare the performance of existing systems or to quickly use solar resource data that might not be available to the alternate performance models, which are presented in the next sections. Otherwise, using a more sophisticated performance model is most likely the better approach.

11.6.1.2 Simple Photovoltaic Performance Models

Among simple PV modeling tools, NREL's PVWatts®[81] or the European Commission's Joint Research Centre PVGIS[82] are free online tools that provide estimates of the electric energy production of roof- or ground-mounted PV systems based on a few simple inputs. The user needs to enter a street address or the geographic coordinates of the system's location (latitude, longitude) and specify the main characteristics, including the installed power (kWp), array inclination (tilt) and orientation, and the module technology type. For PVGIS, four satellite irradiation sources can be selected (depending on location)—the Satellite Application Facility on Climate Monitoring (CM SAF) Surface Solar Radiation Data Set – Heliosat (SARAH), SARAH2, NSRDB, and ERA5 (see Chapter 8)—whereas PVWatts relies exclusively on the NSRDB. Both tools can model tracking PV systems, and PVGIS also provides estimates for off-grid systems. As output, both tools provide hourly and yearly estimates of energy incident on the PV installation and of the corresponding electricity production. The monetary value of the produced electricity is also calculated, for which the user needs to provide information about the system's cost and the grid's electricity consumer price.

By default, for locations in the United States, PVWatts uses a TMY created from the NREL NSRDB Physical Solar Model (PSM) datasets, both labeled "tmy-2020," and derived from the PSM Version TMY and the Himawari PSM V3 TMY, where the year corresponds to the latest year in the dataset. Advanced users can change the default assumptions for losses caused by shading, soiling, and other factors. Earlier versions of PVWatts were based on algorithms from Dobos (2014), but the recent Version 8 update includes improved internal models of the PV module, module thermal effects, and inverter, which are consistent with implementations in NREL's more detailed SAM.[83] Note that some parts of PVWatts have been recently ported to the pvlib environment.[84]

PVGIS provides hourly values of solar resource data and PV performance estimates for different technologies and system configurations based on averages of hourly calculations for time periods of more than 10 years. The effects of the irradiance spectral content, angle-of-incidence reflectance, and PV efficiency at low-irradiance or high-temperature conditions are considered as one lump loss parameter, as are other general losses.[85] PVGIS uses automatically derived horizon profiles by default, which can be adapted by the user to the case of interest. PVGIS was originally developed for Europe, but it has been extended to Africa, and at present it offers data for most of Asia and America as well, thanks to the Joint Research Centre's collaboration with NREL and the European Organisation for the Exploitation of Meteorological Satellites (EUMETSAT) CM SAF. PVGIS also offers TMY data following the ISO 15927-4 methodology.

These simple tools provide a very convenient and more accurate analysis method than the performance ratio described in the previous section and are thus recommended when a quick estimate is needed.

---

[81] See http://pvwatts.nrel.gov.
[82] See https://joint-research-centre.ec.europa.eu/pvgis-online-tool_en.
[83] See https://sam.nrel.gov/.
[84] See https://nrel-pysam.readthedocs.io/en/main/index.html.
[85] See https://joint-research-centre.ec.europa.eu/pvgis-online-tool/getting-started-pvgis/pvgis-user-manual_en.

11.6.1.3 Detailed Photovoltaic System Performance Models

Even more accurate estimates of PV system performance can be obtained by setting up a detailed 3D model of the PV plant that includes the appropriate selection of specific modules and inverters, an array layout, detailed losses, and shading (horizon, row-to-row) analysis. An increasing number of public domain and commercial tools are available to perform these detailed analyses. These elaborate models allow the user to have more control over the many submodels (constituting a "model chain") necessary to go from irradiance to power output. These tools usually include options for:

- Specifying irradiance and meteorological data sources
- Transposing the irradiance data from horizontal to the POA
- Modeling the impact of shading from both external objects and inter-row (self-) shading
- Modeling or specifying loss percentages for soiling and snow cover
- Modeling the impact of the irradiance's spectral distribution on PV technologies
- Modeling reflections from the cover of the PV module
- Modeling the temperature of the PV module
- Modeling the power output from the PV module based on the effective irradiance reaching the PV cells and the module temperature
- Modeling or specifying losses resulting from a mismatch between the modules and the DC wiring
- Modeling the inverter's conversion of power from DC to AC
- Modeling or specifying AC wiring losses and transformer losses
- Specifying losses for planned or unplanned system maintenance and outages.

Examples of freely available programs that include such detailed PV performance models are NREL's SAM,[86] First Solar's PlantPredict,[87] RETScreen,[88] and Greenius.[89] A set of software tools written in Python is pvlib.[90] It is based on a toolbox developed in MATLAB at Sandia National Laboratories but is further developed with community support in the framework of the PV Performance Modeling Collaborative.[91]

Some popular commercially available options include PVsyst,[92] PV*SOL,[93] Aurora Solar,[94] HelioScope,[95] and archelios Pro.[96] Some programs are desktop tools, whereas others are web tools performing cloud-based applications. For software programmers, SAM, PlantPredict, and PVWatts include options for accessing calculations from various programming languages via an

[86] See https://sam.nrel.gov/.
[87] See https://plantpredict.com/.
[88] See https://www.nrcan.gc.ca/maps-tools-publications/tools/data-analysis-software-modelling/retscreen/7465.
[89] See https://www.dlr.de/sf/en/desktopdefault.aspx/tabid-11688/20442_read-44865/.
[90] See https://pvlib-python.readthedocs.io/en/stable/.
[91] See https://pvpmc.sandia.gov.
[92] See https://www.pvsyst.com/.
[93] See https://valentin-software.com/en/products/pvsol-premium/.
[94] See https://www.aurorasolar.com/.
[95] See https://www.helioscope.com/.
[96] See https://www.trace-software.com/archelios-pro/solar-pv-design-software/.

application programming interface (API). Further, SAM's code is open source, allowing interested parties to examine the underlying algorithms in great detail.

All detailed PV modeling tools require not only irradiance but also meteorological parameters (most importantly ambient temperature and wind speed) to evaluate the power output. Because the incident irradiance is one of the biggest sources of uncertainty in the final modeled power output, care should be taken to minimize uncertainty in the irradiance resource data selected for PV modeling. Additional considerations for selecting the most appropriate input irradiance data can depend on the PV technology. For example, thin-film PV modules respond to a different part of the irradiance spectrum than crystalline modules, making spectral corrections important for accurately modeling thin-film technologies (Huld and Amilio 2015)

Evolving module technologies make it hard for modeling software to keep up with technological advancements. For example, when modeling thin-film CdTe modules, optimal results might not be obtained from conventional modeling software packages. PlantPredict has specifically focused on properly modeling thin-film CdTe modules, but it is not limited to the CdTe technology; it can also be used to model mono-passivated emitter and rear cell, bifacial, and other thin-film module technologies.

The accuracy of predictions from these detailed PV modeling tools is very important to system feasibility and financing. Freeman et al. (2014) compared predicted outputs from multiple PV modeling tools to measured outputs for nine different systems. In parallel, Axaopoulos, Fylladitakis, and Gkarakis (2014) performed the same kind of comparison—but using a different set of modeling tools and measured data—for only one PV system. Recently, Riedel-Lyngskær et al. (2020) and Theristis et al. (2023) compared the predictions obtained with various PV simulation software against actual results from a few instrumented experimental systems and underlined the various sources of disagreement. Many of them were found at the level of the irradiance-related submodels mentioned in Chapter 7, which emphasizes the importance of following the best practices in terms of solar radiation modeling.

11.6.2 Yield Estimation of Concentrating Solar Thermal Technology Projects

Yield estimation models for CST plants cover the calculation of the concentrating optics performance; the conversion of concentrated light to electricity, process heat, or chemical energy; and the management of the storage systems, if included.

In general, DNI is by far the most critical solar input for yield calculation in concentrating technologies. Moreover, the variability of DNI is much higher (and ramps faster) than GHI, which impacts the forecast errors of CSP plant output. Other meteorological variables are also usually required: dry air temperature, relative humidity (or, alternatively, wet-bulb temperature), and wind speed. Wind direction, precipitation, and snow height are also recommended to better characterize local conditions (Hirsch et al. 2017).

Below are brief descriptions of the available types of optical performance models oriented to yield calculation. Some models are integrated with others for conversion into electricity, including storage, or with additional specialized modules for cost calculations (e.g., SAM, Greenius). Optical performance models can be separated into different categories: ray-tracing

tools, analytical optical performance models, and models that determine the optical performance with lookup tables.

11.6.2.1 Monte Carlo Ray-Tracing Tools

The incident solar irradiance can be described as a multitude of solar rays transmitted from the sun to the concentrators (or heliostats in the case of CSP systems of the central tower type) and finally to the receiver. Although ray-tracing tools *can* provide highly accurate results, they are also highly demanding in terms of computing resources; thus, their use is usually limited to detailed design calculations (for example, calculation of the flux distribution on the receiver surfaces in central receiver systems) or to the elaboration of lookup tables or incidence angle modifiers for line-concentrating technologies; however, improvements in computational algorithms combined with additional tools might pave the way for the use of ray-tracing tools for design purposes (Blanco et al. 2021).

Ray-tracing tools—such as the Solar Tower Ray Tracing Laboratory (STRAL) (Belhomme et al. 2009), SolTrace (Wendelin 2003), MIRVAL (Leary and Hankins 1979), the Solar Power Ray-Tracing tool (SPRAY) (Buck 2010), Tonatiuh (Blanco et al. 2009; Cardoso et al. 2018), Tonatiuh++,[97] or Heliosim (Potter et al. 2018)—calculate the path of the sun's rays from the sun's disk and the circumsolar region to the target by application of physical laws. Monte Carlo techniques are often implemented to achieve reasonable calculation times.

For illustration, one method of ray tracing that is available in SPRAY is explained here. The method selects one concentrator element after another, and it traces a given number of rays from the current element. After calculating the vector to the center of the sun, the appropriate *sunshape* is included. (For details, see Chapter 2, Section 2.7.1, and Chapter 7, Section 7.9, respectively.) The specific ray under scrutiny is then related to a power calculated as the product of the incident DNI and the projected area of the current concentrator element divided by the number of rays per element. Then the path of the ray is followed until it reaches the receiver. This ray-tracing method can be based on actual measurements of the concentrator geometry or on its design geometry affected by typical optical errors.

11.6.2.2 Analytical Optical Performance Models

Analytical optical performance models are generally based on cone-optics convolution methods. One example of a calculation method that uses an analytical approach is the Bendt-Rabl model (Bendt et al. 1979; Bendt and Rabl 1981). To accelerate calculations, analytical equations are derived and solved to describe the ray's path throughout the optical system. For example, the model can be used for parabolic troughs and solar dishes. First, an angular acceptance function is determined from the design geometry. The angular acceptance function is defined by the fractional number of rays incident on the aperture at a specific angle that ultimately reach the receiver. Second, an effective source is determined that includes both the user-defined sunshape and any possible deviation from the design geometry. The optical errors of concentrators are described as Gaussian-distributed independent uncertainties. Their combination is also a Gaussian distribution with a standard deviation, which is often called an optical error. Third, the function that describes the optical errors is then combined with the sunshape using convolution. For line-focusing systems, such as parabolic troughs, a further integration step is required

[97] See https://zenodo.org/record/7105107/.

because the effect of circumsolar radiation on the incident irradiance strongly depends on angle. Finally, the intercepted radiation can be determined by summing the product of the effective source and the acceptance function over all angles. Similar analytical methods are used in HELIOS (Vittitoe and Biggs 1981), DELSOL (Kistler 1986), HFLCAL (Schwarzbözl, Pitz-Paal, and Schmitz 2009), and Solar Power tower Integrated Layout and Optimization Tool (SolarPILOT) (Wagner and Wendelin 2018).

11.6.2.3 Lookup Table-Based Optical Performance Models

The fastest way to determine the optical performance of a CST collector uses only parameterizations or lookup tables that describe the change in optical performance with solar position. The necessary parameters can be derived from experimental data, analytical performance models, or ray-tracing tools. Such lookup tables or parameterizations are used in some SAM submodels (Blair et al. 2014) and in Greenius (Dersch, Schwarzbözl, and Richert 2011; Quaschning et al. 2001).

11.7 Power Output Variability

From an application perspective, the solar resource variability translates into power production variability, which could impact the stability of electric grids or the economics of the facility. One important question that has received specific attention is: How much is the temporal variability at one solar power plant site correlated with that at another site some distance away? A high correlation would tend to destabilize the grid and thus needs to be addressed in detail.

11.7.1 Photovoltaic Applications

Based on extensive studies (Hoff and Perez 2012), it appears that the output's variability of a fleet of N PV plants over a given region will be reduced by the inverse of the square root of N if the plants' output variability is uncorrelated and if the plants experience similar natural variability. This is a consequence of the *spatial smoothing effect* noted by many (Elsinga and van Sark 2014; Marcos et al. 2011; Murata, Yamaguchi, and Otani 2009; Wiemken et al. 2001; Woyte, Belmans, and Nijs 2007). This result means that nearby locations are highly correlated, experiencing the same ramp rates at nearly the same time and varying in sync. In contrast, the time series from distant locations are uncorrelated. Partial correlation exists between these two extremes. Hoff and Perez (2012) used hourly satellite-derived irradiances over the continental United States. They observed a similar asymptotic decay with distance and a predictable dependence of this decay upon Δt for time intervals of 1, 2, and 3 hours. They also noted that the rate of decrease of correlation with distance was different for various U.S. regions and attributed these differences to prevailing regional cloud speeds, as confirmed by personal communications with T. E. Hoff and N. Norris in 2010. Perez, Kivalov, and Hoff (2011) analyzed high-resolution, high-frequency, satellite-derived irradiances (1 km, 1 minute) in climatically distinct regions of North America and Hawaii to investigate the site-pair correlation decay as a function of distance, timescale, and mean monthly regional cloud speed (see Figure 11-14), itself independently derived from satellite cloud motion vectors. Interestingly, as shown in this figure for various areas and periods, the rate of decrease of this correlation with distance is a strong function of the data's temporal resolution. A distance of approximately 5 km might be sufficient to smooth out fluctuations on a 1-minute timescale, whereas distances greater than 50 km would be needed to smooth out hourly fluctuations. See also Remund et al. (2015) for examples pertaining to other regions in the world.

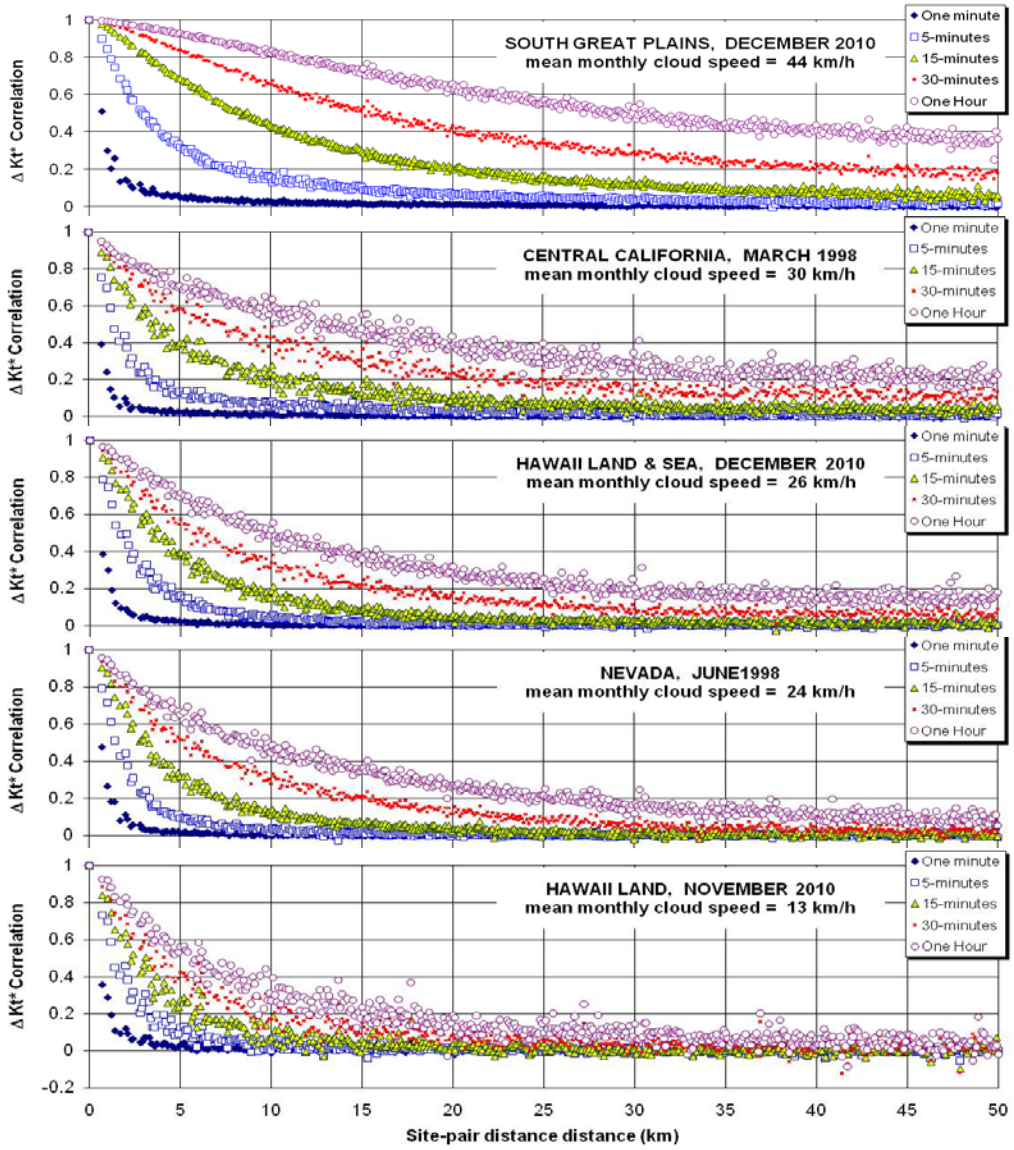

Figure 11-14. Site-pair correlations as a function of time and distance for sample regions in North America and Hawaii. Mean monthly cloud speed was estimated from satellite-derived cloud motion vectors computed for each data point.

Image from Perez, Kivalov, and Hoff (2011)

11.7.2 Quantifying Photovoltaic Output Variability

The variability quantifying metric should adapt to a wide range of temporal and spatial scales and embed (1) the *physical quantity* that varies, (2) the variability *timescale*, and (3) the *time span* during which variability is assessed.

11.7.2.1 Physical Quantity

For energy producers and grid operators, the pertinent quantity is the power output, ***p***, of a power plant or of a fleet of power plants at a given point in time. The power output variability reflects the underlying variability of irradiance impinging on the plant(s); therefore, understanding and quantifying the variability of irradiance amounts to quantifying and understanding the variability

of $\boldsymbol{p}$. DNI's variability is relevant for concentrating technologies, whereas the variability in GHI or GTI is representative of flat-plate technologies. This section focuses on the latter.

The solar geometry-induced variability is fully predictable. Here, the focus is on cloud/weather-induced variability that is stochastic in nature. To better understand this variability component, it is useful to first remove the solar geometry effects. The *clearness index*, *Kt* (ratio between GHI and its extraterrestrial counterpart), or *the clear-sky index*, *Kc* (ratio between GHI and its clear-sky counterpart), both embed the stochastic variability of irradiance but are largely independent of solar geometry. The use of *Kc* is preferable in general because it more effectively removes solar geometry effects at low solar elevations (Perez et al. 1990). Nevertheless, its use implies that the clear-sky irradiance can be accurately estimated, which represents an additional step that many analysts try to avoid.

11.7.2.2 Timescale

The intuitive temporal example presented here suggests that the temporal scale of the selected physical quantity's time series, Δt, is a fundamental factor. Depending on the application, Δt can range from 1 second or less to hours and more. A variation in *Kc* corresponding to the selected timescale Δt is noted $\Delta Kc_{\Delta \boldsymbol{t}}$. On short scales (milliseconds to minutes), this change is often referred to as the *ramp rate*.

11.7.2.3 Time Span

A proper measure of variability should include ramp events covering a statistically significant *time span*. This time span should be a large multiple of Δt.

11.7.2.4 Nominal Variability Metric

Nominal variability refers to the variability of the dimensionless clear-sky index. The maximum or mean $\Delta Kc_{\Delta \boldsymbol{t}}$ ramp rate over a given time span has been proposed as such a measure (Hoff and Perez 2010); however, most authors have recently settled on the ramp rate's variance, or its square root—the ramp rate's standard deviation—over a given time span as the preferred metric for variability. Eq. 11-7 describes a nominal dimensionless metric:

$$\text{Nominal variability} = \sigma(\Delta Kc_{\Delta \boldsymbol{t}}) = \sqrt{Var[\Delta Kc_{\Delta \boldsymbol{t}}]} \tag{11-4}$$

11.7.2.5 Power Output (Absolute) Variability Metric

When dealing with power generation, it is necessary to scale up the nominal metric and to quantify the power variability in absolute terms. This is expressed by Eq. 11-5:

$$\text{Power variability} = \sigma(\Delta \boldsymbol{p}_{\Delta \boldsymbol{t}}) = \sqrt{Var[\Delta \boldsymbol{p}_{\Delta \boldsymbol{t}}]} \tag{11-5}$$

Recall that $\boldsymbol{p}$ can be modeled from *Kc* via extraction of GHI, extrapolation to POA irradiance (GTI), and inclusion of PV specifications (i.e., without changing the inherent cause of variability); hence, Eq. 11-5 does not include additional intrinsic variability information relative to Eq. 11-4.

11.8 Data Bankability

The bankability of solar radiation datasets is crucial for securing financing and insurance for solar energy projects. An accurate assessment of a project's risks and potential returns will lead to increased confidence in the project, which will lead to increased investment in solar energy projects and the broader adoption of renewable energy sources. The bankability of solar radiation datasets refers to the level of confidence and reliability that lenders and investors have in using these datasets to assess the feasibility and financial viability of solar energy projects. In the context of solar power projects, accurate solar resource data are crucial for estimating the energy generation potential, determining project performance, and conducting financial analysis (Vignola, McMahan, and Grover 2013).

Key criteria that contribute to the bankability of solar radiation datasets include:

- Data source and quality: The bankability of solar radiation datasets heavily depends on the source of the data and its quality. Data obtained from reputable meteorological agencies or well-known commercial vendors are generally considered more reliable.
- Data quality control: A robust quality control process is necessary to identify and correct any anomalies or errors in the data. Quality control ensures that only reliable data are used for analysis. Ground-based sensors must be regularly cleaned and calibrated (see Chapter 4).
- Long-term and historical data: Solar projects have a long lifespan, of 20–25 years or more; therefore, bankable datasets should provide historical solar radiation data over an extended period (typically at least 10–20 years) to support accurate long-term energy yield predictions.
- Validation and calibration: The historical dataset must undergo validation and calibration processes to ensure accuracy. Bankable commercial vendors of solar resource datasets need to provide calibration and validation reports for them. For satellite or reanalysis model datasets, this means that the model should be validated against, and possibly calibrated with, existing ground measurement data in the region of the project location. For utility-scale projects in particular, validation information related to solar and meteorological data from nearby sites should be included to support the bankability of the assessment. On-site measurements, when available, can be integrated into the analysis to reduce uncertainty (site adaptation, see Chapter 7, Section 7.6) and give higher confidence to financial institutions. If a site adaptation is conducted, the input data and site-adaptation method that were used should be documented, and a comparison of the dataset with and without site adaptation including validation statistics should be performed.
- Geographic coverage: The dataset should cover the specific geographic location of the solar project. Accurate solar radiation data at the project site or nearby locations are crucial for project planning and energy production estimations.
- Temporal resolution: High-temporal-resolution data, such as hourly or subhourly measurements, are preferred because they capture short-term fluctuations and help provide accurate energy production estimations.
- Transparency and documentation: Transparent documentation of data collection methods, sources, and any adjustments made during the calibration or quality control processes is essential. This helps financial investors understand the dataset's reliability and make

informed decisions. For ground measurements, documentation recommendations are summarized in Chapter 3, Section 3.6.

- Availability and accessibility: Bankable solar radiation datasets should be readily available to all relevant stakeholders, including investors, lenders, and project developers. Open access to such data promotes transparency and encourages investment in solar projects. The budgetary implications should be considered early enough to allocate resources.
- Acceptance by industry standards: The datasets should conform to industry standards, as described in detail in this handbook, and should be widely accepted within the solar energy industry. This recognition by experts and professionals provides additional credibility and confidence in the data.
- Consistency and consensus: Bankability is also influenced by the consistency of solar radiation data with other related datasets, such as temperature, humidity, and wind speed. Consensus among multiple datasets can further validate the reliability of the information.

Meeting these key requirements enhances the bankability of solar resource data, increasing confidence among financial institutions, investors, and project developers to invest in solar energy projects. It facilitates accurate energy yield predictions, risk assessments, and financial modeling, ultimately supporting the growth and adoption of solar power as a sustainable energy source.

As already described in this chapter, for large utility-scale solar power projects, a bankable solar resource assessment might require on-site measurements of at least 1 year to validate the long-term modeled time-series data and to correct them using an appropriate site-adaptation technique. There is no fixed threshold as to which project size requires an on-site measurement, but in practice it is often done for project sizes exceeding 100 MW, unless they are located in a region with abundant reference projects, good data availability, and low uncertainty of model datasets. For utility-scale CSP projects, on-site measurements are always recommended because DNI uncertainty in modeled datasets is typically larger and can be significantly reduced by site adaptation.

For most PV projects, even including large-scale, multimegawatt power plants, financial institutions do not generally require ground-based measurements at the project's site during the development stage until it is time to run the business. In most cases, a high-quality solar resource dataset from an institution that is accepted by the bank and that fulfills these criteria suffices to be bankable. Individual banks have their own requirements with regard to POE values, which thus need to be clarified case by case.

11.9 Applying Solar Resource Data to Other Types of Solar Energy Projects

11.9.1 Projects Using Flat-Plate Thermal Collectors

Energy simulation tools for flat-plate thermal collector systems usually include a suite of modules describing the thermal receiver and the thermal losses of the piping, parasitic losses,

and thermal storage. Some typical tools for these simulations are Polysun[98] and T*Sol[99]; however, some of the aforementioned general software tools also include these types of systems. For example, this is the case with RETScreen, SAM, and Greenius. Although the irradiance in the flat-plate collector plane (GTI) is the physically relevant irradiance, the separate specification of DNI and diffuse horizontal irradiance (DHI) can be of interest. Individual incidence angle modifiers can be used to determine the efficiency of the DNI and DHI energy conversion, respectively, for a given solar position.

11.9.2 Solar Heating and Cooling in Buildings

Solar heating and cooling in buildings (Sørensen 2012), smart cities, and smart grids are projects that include solar systems among other energy systems or energy conservation measures. Solar radiation data are still needed for sizing, simulation, and evaluation. Note, in particular, that TMYs and TRYs/DRYs (Crawley 1998; Hall et al. 1978; Lund 1974) were originally developed for building applications. The Transient System Simulation Tool (TRNSYS)[100] software (University of Wisconsin) has also traditionally been applied to buildings.

11.9.3 Smart Electric Grids

Electric grids benefit from high-quality solar radiation data in both grid operation (now, later today, and the next days) and grid planning (over the next months to years). For example, solar radiation and forecasting data are used in grid operation for:

- Power system state estimation
- Unit commitment and scheduling of power plants and storage units
- Congestion forecasting and management
- Forward coordination among various stakeholders (e.g., transmission and distribution grid operators, plant operators, and other market players).

The further the integration of solar PV into the grid proceeds, the more important it is to integrate information about current and upcoming electrical power production and feed-in into operation processes. Regulations such as the European System Operation Guideline[101] define the need for data. Grid-connected PV power plants of a relevant size (e.g., more than 1 MWp) typically provide real-time measurement data and a regular schedule of the planned feed-in. Further, for a detailed congestion forecast in grid operation, one needs an additional estimate for the possibly large number of small grid-connected installations. Because even smart meters do not always provide real-time data to grid operators, due to privacy concerns, among other reasons, those not receiving the data need to generate or buy an estimation of regional feed-in, typically based on some upscaling method. To do so, radiation data from NWP and satellite observations are a valuable source of information. Forecasting providers, making use of sophisticated statistical or even machine-learning models, usually process these inputs. For this, they rely on detailed master data about the individual plant or the large number of plants behind the meter. An extensive database (per grid and/or per nation) that collects and provides such master data should be available (van Sark 2023). In contrast to grid operation, where individual

[98] See http://www.velasolaris.com/.
[99] See http://www.valentin-software.com/.
[100] See https://www.trnsys.com.
[101] See https://www.europex.org/eu-legislation/sogl/.

estimates and forecasts are permanently integrated into the processes, grid planning is based on a historical radiation dataset, and simultaneity factors within a portfolio of installed or expected power plants are assumed.

An alternative to operational approaches intended to blend with standard transmission system operator (TSO) practice, such as those just described, is termed *firm power* (Perez et al. 2023). This is achieved by adding and operating dedicated hardware and controls to PV plants or fleets of plants so that the output seen by the grid operator exactly amounts to the forecast output. The hardware consists of optimized storage and plant oversizing to make up for all instances of forecast over- or underestimation as well as controls to equate actuals and predictions in real time. In addition to being a prospectively cost-effective operational forecast strategy for TSOs, the real value of this strategy lies in opening the door to least-cost firm power generation, hence the possibility of ultrahigh solar penetration at the lowest possible cost.

- *A prospectively cost-effective operational forecast strategy for TSOs*: Firm forecast operations have been analyzed for individual Surface Radiation Budget Network (SURFRAD) locations in the United States as well as for a simulated fleet in California comprising 16 power plants—one in each state's climatic region (Perez 2019a; Perez et al. 2019b). Applying the State University of New York (SUNY) forecast model to the California fleet would result in achieving a firm forecast cost less than $150/kWp today (i.e., an approximate 10% premium on current large-scale turnkey PV costs) for firm day-ahead forecasts. Future PV and storage costs anticipated in 10–15 years are expected to reduce the cost of entirely eliminating solar supply-side imbalances to less than $50 per kWp. Pierro et al. (2020) recently showed that such a firm forecast strategy could already be cost-effective for ratepayers today in Italy, compared to the existing market for load imbalance corrections, even including seasonal variations in PV power generation.
- *A least-cost ultrahigh penetration transition strategy*: The same operational strategy—optimized storage plus overbuilding—applied on a larger scale has been shown to be the key to achieving firm, effectively dispatchable PV production at the least possible cost. A series of recent publications (Perez 2019a; 2019b) showed that 2040-targeted, firm, 24/7 electricity production levelized cost of energy (LCOE) on the order or less than U.S. $0.05 per kWh were realistic targets in the central United States, Italy, and the island grid of La Reunion, France. Figure 11-15 illustrates how PV overbuilding can sufficiently reduce storage requirements to achieve an acceptably low firm power generation LCOE. Pierro et al. (2021) showed that the entry-level firm forecast strategy can be gradually expanded over time, following technology costs and TSO practice learning curves to transition from low-level firmness requirements—meeting forecast production—to more stringent requirements, until meeting demand 24/7/365 becomes economically achievable with only minimal reliance on conventional resources.

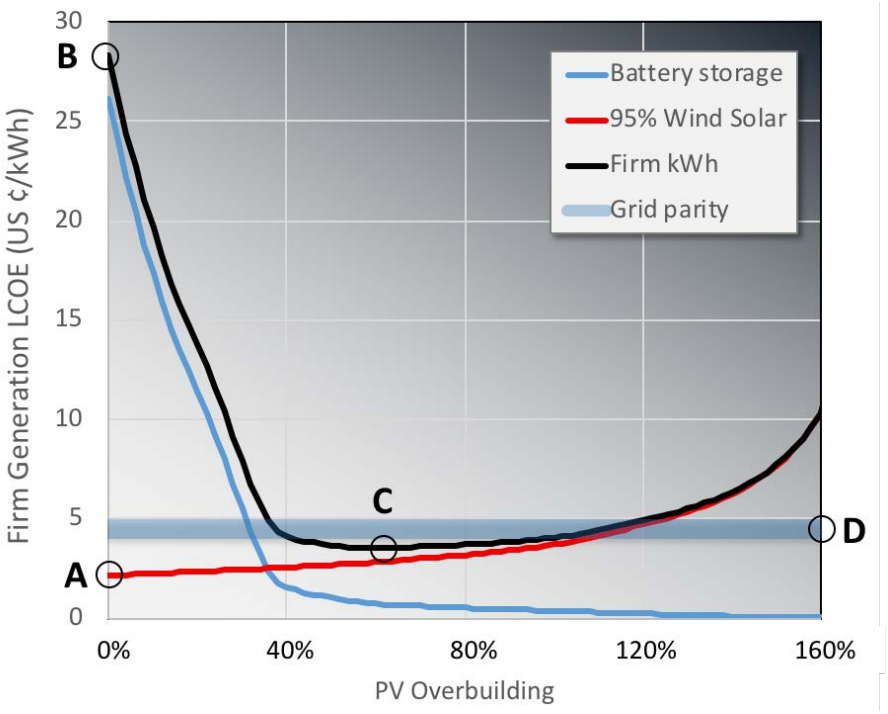

Figure 11-15. Impact of PV overbuilding on firm power generation LCOE

Whereas unconstrained PV (A) is inexpensive (apparently below grid parity), firming PV to meet demand 24/7/365 with storage alone (B) is unrealistically expensive. Overbuilding PV fleets reduces storage requirements to the point (C) where firm PV power generation can achieve true grid parity (D). *Image from Perez et al. 2019b.*

11.9.4 Chemical Applications

Solar resource data are required for several chemical applications. These can be divided into two main topics because of their different use of the solar resource: solar desalination and solar photochemical applications.

11.9.4.1 Solar Desalination

Global demand for freshwater is continuously increasing because of population growth and economic development. To meet this increasing demand, desalination has become the most important source of freshwater for drinking and agriculture in some world regions with huge solar energy potential, such as the Middle East and North Africa (Isaka 2012).

Seawater solar thermal desalination via multistage flash or multi-effect distillation uses solar heat as the energy input. This methodology is the most promising desalination process based on renewable energy. As previously discussed, the CST part of the desalination project needs several years of high-quality, on-site data for simulation and design optimization or site-adapted data time series that are similar to the required data for CST plants.

Many small PV-based membrane desalination systems have been installed worldwide, especially in remote areas and islands. As in the case of a standard PV plant, GHI and/or GTI data are needed as the most relevant solar inputs for these systems.

11.9.4.2 Solar Photocatalysis: Detoxification and Disinfection of Fluids

Solar photocatalytic detoxification and disinfection processes constitute a solution for the treatment of contaminated groundwater, industrial wastewater, air, or soil (Malato 2004). The development of these processes has reached a point where the solar technology can be competitive with conventional treatment methods, particularly at isolated locations with high solar potential, which can be the case with many agricultural farms.

Solar photochemistry can be defined as the technology that collects solar photons and introduces them in an adequate reactor volume to promote specific chemical reactions (Blanco and Malato 2010). The equipment that performs this function is a solar collector—specifically, a compound parabolic collector with a relatively large acceptance angle; hence, they can use DNI and the part of DHI that emanates from the circumsolar region. The requirements for solar photochemical reactors are similar to any other photochemical reactor, with the particularity that their light input comes from the sun rather than from a lamp. For this reason, and according to the working temperature, the collector must be tilted or mounted on a tracking system with one or two axes. Figure 11-16 illustrates two different photoreactors installed at Plataforma Solar de Almería (CIEMAT), Spain.[102] Depending on the type of solar collector, tilted or direct ultraviolet solar irradiance data will be needed. In the most general case that ultraviolet radiation is not measured locally, these variables must be empirically derived from DNI and/or GHI data (Habte et al. 2019).

Figure 11-16. Compound parabolic collector photoreactors installed at Plataforma Solar de Almería for solar water disinfection and phytopathogen elimination from wastewater applications: (left) compound parabolic collector and (right) phytopathogen elimination system

Photos from Plataforma Solar de Almería, CIEMAT

[102] See http://www.psa.es/en/instalaciones/aguas.php.

References

Axaopoulos, P. J., E. D. Fylladitakis, and K. Gkarakis. 2014. "Accuracy Analysis of Software for the Estimation and Planning of Photovoltaic Installations." *International Journal of Energy and Environmental Engineering* 5 (71). https://doi.org/10.1007/s40095-014-0071-y.

Belhomme, B., R. Pitz-Paal, P. Schwarzbözl, and S. Ulmer. 2009. "A New Fast Ray Tracing Tool for High-Precision Simulation of Heliostat Fields." *Journal of Solar Energy Engineering*, 131 (3). https://doi.org/10.1115/1.3139139.

Bendt, P., A. Rabl, H. W. Gaul, and K. A. Reed. 1979. *Optical Analysis and Optimization of Line Focus Solar Collectors*. Office of Scientific and Technical Information (OSTI). https://doi.org/10.2172/900712.

Bendt, P., and A. Rabl. 1981. "Optical Analysis of Point Focus Parabolic Radiation Concentrators." *Applied Optics* 20 (4): 674. https://doi.org/10.1364/ao.20.000674.

Blair, N., A. P. Dobos, J. Freeman, T. Neises, M. Wagner, T. Ferguson, P. Gilman, and S. Janzou. 2014. *System Advisor Model, SAM 2014.1.14: General Description*. NREL/TP-6A20-61019, National Renewable Energy Laboratory, Golden, CO. https://www.nrel.gov/docs/fy14osti/61019.pdf.

Blanco, J., and S. Malato. 2010. "Solar Energy Conversion and Photoenergy System—Thermal Systems and Desalination Plants: Vol. 3." In *Encyclopedia of Life Support Systems*. EOLSS Publishers Co. Ltd. https://www.eolss.net/.

Blanco, M. J., A. Mutuberria, P. Garcia, R. Gastesi, and V. Martin. 2009. "Preliminary Validation of Tonatiuh." Proc. SolarPACES Conference, Berlin, Germany.

Blanco, M., V. Grigoriev, K. Milidonis, G. Tsouloupas, M. Larrañeta, and M. Silva. 2021. "Minimizing the Computational Effort to Optimize Solar Concentrators with the Open Source Tools SunPATH and Tonatiuh++." *Energies* 14: 4412. https://doi.org/10.3390/en14154412.

Brito, M. C., N. Gomes, T. Santos, and J. A. Tenedório. 2012. "Photovoltaic Potential in a Lisbon Suburb Using LiDAR Data." *Solar Energy* 86 (1): 283–288. https://doi.org/10.1016/j.solener.2011.09.031.

Buck, R. 2010. *Solar Power Raytracing Tool, SPRAY, User Manual, Version 2.6*. DLR.

Buller, C. 2023. *Optimizing Energy Dispatch Leveraging Uncertainty Information in Short-Term Wind Power Forecasts*. Constructor University Bremen. https://elib.dlr.de/195357/.

Cardoso, J. P., A. Mutuberria, C. Marakkos, P. Schoetti, T. Osorio, and I. Les. 2018. "New Functionalities for the Tonatiuh Ray-Tracing Software." In *AIP Conference Proceedings* 2033: 210010. https://doi.org/10.1063/1.5067212.

Crawley, D. B. 1998. "Which Weather Data Should You Use for Energy Simulations of Commercial Buildings?" *ASHRAE Transactions* 104 (2): 498–515.

Dersch, J., P. Schwarzbözl, and T. Richert. 2011. "Annual Yield Analysis of Solar Tower Power Plants With GREENIUS." *Journal of Solar Energy Engineering* 133 (3), 031017. https://doi.org/10.1115/1.4004355.

Dobos, A., P. Gilman, and M. Kasberg. 2012. "P50/P90 Analysis for Solar Energy Systems Using the System Advisor Model." World Renewable Energy Forum, Denver, Colorado. NREL/CP-6A20-54488. https://www.nrel.gov/docs/fy12osti/54488.pdf.

Dobos, A. P. 2014. "PVWatts Version 5 Manual." NREL/TP-6A20-62641. National Renewable Energy Laboratory, Golden, CO. https://www.nrel.gov/docs/fy14osti/62641.pdf.

Ellis, A., M. Behnke, and C. Barker. 2011. "PV System Models for Grid Planning Studies." 37th IEEE Photovoltaic Specialists Conference, Seattle, WA. https://doi.org/10.1109/PVSC.2011.6186478.

Elsinga, B., and W. van Sark. 2014. "Spatial Power Fluctuation Correlations in Urban Rooftop Photovoltaic Systems." *Progress in Photovoltaics: Research and Applications* 23: 1390–1397. https://doi.org/10.1002/pip.2539.

Fernández-Peruchena, C. M., M. Gastón, M. Sánchez, J. García-Barberena, M. Blanco, and A. Bernardos. 2015. "MUS: A Multiscale Stochastic Model for Generating Plausible Meteorological Years Designed for Multiyear Solar Energy Yield Simulations." *Solar Energy* 120: 244–256. https://doi.org/10.1016/j.solener.2015.07.037.

Ferretti, F., C. Hogendijk, V. Aga, and A. Ehrsam. 2016. "Addressing Forecast Uncertainty Impact on CSP Annual Performance." *AIP Conference Proceedings* 1850: 030015. https://doi.org/10.1063/1.4984358.

Forstinger, A., S. Wilbert, A. Jensen, B. Kraas, C. M. Fernández-Peruchena, C.A. Gueymard, D. Ronzio, D. Yang, E. Collino, J. Polo, J.A. Ruiz-Arias, N. Hanrieder, P. Blanc, and Y.M. Saint-Drenan. 2023. *Worldwide Benchmark of Modelled Solar Irradiance Data.* Report IEA-PVPS T16-05: 2023. IEA PVPS. https://iea-pvps.org/key-topics/worldwide-benchmark-of-modelled-solar-irradiance-data/.

Freeman, J., J. Whitmore, N. Blair, and A. Dobos. 2014. *Validation of Multiple Tools for Flat Plate Photovoltaic Modeling Against Measured Data*. NREL/TP-6A20-61497. National Renewable Energy Laboratory, Golden, CO. https://doi.org/10.2172/1150179.

Grantham, A. P., P. J. Pudney, L. A. Ward, M. Belusko, and J. W. Boland. 2017. "Generating Synthetic Five-Minute Solar Irradiance Values From Hourly Observations." *Solar Energy* 147: 209–221. https://doi.org/10.1016/j.solener.2017.03.026.

Habte, A., M. Sengupta, C. A. Gueymard, R. Narasappa, O. Rosseler, and D. M. Burns. 2019. "Estimating Ultraviolet Radiation from Global Horizontal Irradiance." *IEEE Journal of Photovoltaics* 9 (1): 139–146. https://doi.org/10.1109/JPHOTOV.2018.2871780.

Hall, I. J. R., R. R. Prairie, H. E. Anderson, and E. C. Boes. 1978. *Generation of Typical Meteorological Years for 26 SOLMET Stations*. SAND78-1601. Sandia National Laboratories, Albuquerque, NM.

Hirsch, T., H. Schenk, N. Schmidt, and R. Meyer. 2010. "Dynamics of Oil-Based Parabolic Trough Plants—Impact of Transient Behaviour on Energy Yield." Proc, SolarPACES Conference, Perpignan, France.

Hirsch, T., J. Dersch, T. Fluri, J. Garcia-Barberena, S. Giuliano, F. Hustig, R. Meyer, M. Seitz, and E. Yildiz. 2017. *SolarPACES Guideline for Bankable STE Yield Assessment*. http://www.solarpaces.org/wp-content/uploads/SolarPACES_Guideline_for_Bankable_STE_Yield_Assessment_-_Version_2017.pdf.

Ho, C. K., and G. J. Kolb. 2010. "Incorporating Uncertainty into Probabilistic Performance Models of Concentrating Solar Power Plants." *Journal of Solar Energy Engineering* 132 (3): 031012. https://doi.org/10.1115/1.4001468.

Ho, C. K., S. S. Khalsa, and G. J. Kolb. 2011. "Methods for Probabilistic Modeling of Concentrating Solar Power Plants." *Solar Energy* 85 (4): 669–675. https://doi.org/10.1016/j.solener.2010.05.004.

Hoff, T. E., and R. Perez. 2010. "Quantifying PV Power Output Variability." *Solar Energy* 84 (10): 1782–1793. https://doi.org/10.1016/j.solener.2010.07.003.

Hoff, T. E., and R. Perez. 2012. "Modeling PV Fleet Output Variability." *Solar Energy* 86 (8): 2177–2189. https://doi.org/10.1016/j.solener.2011.11.005.

Hofmann, M., S. Riechelmann, C. Crisosto, R. Mubarak, and G. Seckmeyer. 2014. "Improved Synthesis of Global Irradiance with One-Minute Resolution for PV System Simulations." *International Journal of Photoenergy* 2014: 1–10. https://doi.org/10.1155/2014/808509.

Holmgren, W. F., C. W. Hansen, and M. A. Mikofski. 2018. "Pvlib Python: A Python Package for Modeling Solar Energy Systems." *Journal of Open Source Software* 3 (29): 884. https://doi.org/10.21105/joss.00884.

Huang, Y., Z. Chen, B. Wu, L. Chen, W. Mao, F. Zhao, J. Wu, J. Wu, and B. Yu. 2015. "Estimating Roof Solar Energy Potential in the Downtown Area Using a GPU-Accelerated Solar Radiation Model and Airborne LiDAR Data." *Remote Sensing* 7 (12): 17212–17233. https://doi.org/10.3390/rs71215877.

Huld, T., and A. G. Amilio. 2015. "Estimating PV Module Performance Over Large Geographical Regions: The Role of Irradiance, Air Temperature, Wind Speed and Solar Spectrum." *Energies* 8: 5159–5181. https://doi.org/10.3390/en8065159.

International Electrotechnical Commission (IEC). 2021. *IEC 61724-1:2021 Photovoltaic System Performance – Part 1: Monitoring*. Geneva, Switzerland. https://webstore.iec.ch/en/publication/65561.

Isaka, M. 2012. *Water Desalination Using Renewable Energy. Technology Brief*. IEA-ETSAP and IRENA.

Jakubiec, J. A., and C. F. Reinhart. 2013. "A Method for Predicting City-Wide Electricity Gains from Photovoltaic Panels Based on LiDAR and GIS Data Combined with Hourly Daysim Simulations. *Solar Energy* 93: 127–143. https://doi.org/10.1016/j.solener.2013.03.022.

Janotte, N., E. Lüpfert, and R. Pitz-Paal. 2012. "Acceptance Testing and Advanced Evaluation Strategies for Commercial Parabolic Trough Solar Fields." Proc. SolarPACES Conference, Marrakech, Morocco.

Janotte, N., S. Wilbert, F. Sallaberry, M. Schroedter-Homscheidt, and L. Ramírez. 2017. "2 – Principles of CSP Performance Assessment." In P. Heller (Ed.) *The Performance of Concentrated Solar Power (CSP) Systems*. https://doi.org/10.1016/B978-0-08-100447-0.00002-X.

Kearney, D. 2009. *Utility-Scale Parabolic Trough Solar Systems: Performance Acceptance Test Guidelines: April 2009—December 2010*. NREL/SR-5500-48895. National Renewable Energy Laboratory, Golden, CO. https://www.nrel.gov/docs/fy11osti/48895.pdf.

Kearney, D. 2013. *Utility-Scale Power Tower Solar Systems: Performance Acceptance Test Guidelines*. NREL/SR-5500-57272. National Renewable Energy Laboratory, Golden, CO. https://www.nrel.gov/docs/fy13osti/57272.pdf.

Kistler, B. 1986. *A User's Manual for DELSOL3: A Computer Code for Calculating the Optical Performance and Optimal System Design for Solar Thermal Central Receiver Plants*. SAND86-8018. Sandia National Laboratories, Albuquerque, NM. https://doi.org/10.2172/7228886.

Klyve, O. S., M. M. Nygard, H. N. Riise, J. Fagerstrom, and E. S. Marstein. 2023. "The Value of Forecasts for PV Power Plants Operating in the Past, Present, and Future Scandinavian Energy Markets." *Solar Energy* 255: 208–221. https://doi.org/10.1016/j.solener.2023.03.044.

Kraas, B., C. Hoyer-Klick, T. Hirsch, M. Moser, N. Geuder, and E. Lüpfert. 2011. "Comparison of Different Methods to Derive Appropriate Meteorological Data Sets for Yield Assessment for Concentrating Solar Power Plants." Proc. SolarPACES Conference, Granada, Spain.

Kurtz, S., P. Krishnani, J. Freeman, R. Flottemesch, E. Riley, T. Dierauf, J. Newmiller, L. Ngan, D. Jordan, and A. Kimber. 2014. "PV System Energy Test." In *Proceedings of the 2014 IEEE 40th Photovoltaic Specialist Conference (PVSC)*: 0879–0884. https://doi.org/10.1109/PVSC.2014.6925055.

Larrañeta, M., C. Fernandez-Peruchena, M. A. Silva-Pérez, I. Lillo-bravo, A. Grantham, and J. Boland. 2019. "Generation of Synthetic Solar Datasets for Risk Analysis." *Solar Energy* 187: 212–225. https://doi.org/10.1016/j.solener.2019.05.042.

Le, T., D. Kholdi, H. Xie, B. Dong, and R. Vega. 2016. "LiDAR-Based Solar Mapping for Distributed Solar Plant Design and Grid Integration in San Antonio, Texas." *Remote Sensing* 8 (3): 247. https://doi.org/10.3390/rs8030247.

Leary, P. L., and J. D. Hankins. 1979. *User's Guide for MIRVAL: A Computer Code for Comparing Designs of Heliostat-Receiver Optics for Central Receiver Solar Power Plants*. Albuquerque, NM: Sandia National Laboratories. https://doi.org/10.2172/6371450.

Leloux, J., E. Lorenzo, B. García-Domingo, J. Aguilera, and C. A. Gueymard. 2014. "A Bankable Method of Assessing the Performance of a CPV Plant." *Applied Energy* 118: 1–11. https://doi.org/10.1016/j.apenergy.2013.12.014.

Louwen, A., A. C. De Waal, R. E. I. Schropp, A. P. C. Faaij, and W. G. J. H. M. van Sark. 2017. "Comprehensive Characterisation and Analysis of PV Module Performance Under Real Operating Conditions." *Progress in Photovoltaics: Research and Applications* 25: 218–232.

Lund, H. 1974. "The 'Reference Year,' A Set of Climatic Data for Environmental Engineering." Also published as *Report no. 32, Thermal Insulation Laboratory, Technical University of Denmark*. In *Second Symposium on the Use of Computers for Environmental Engineering Related to Building Proceedings*: 12.

Malato, S. 2004. "Photocatalitic Reactors for the Treatment of Liquid Wastewater in the Presence of Solar Radiation." In *1st Seminar of Advanced Oxidation Methods of the Treatment of Liquid and Air Waste Proceedings*: 16.

Marcos, J., L. Marroyo, E. Lorenzo, and M. García. 2011. "Smoothing of PV Power Fluctuations by Geographical Dispersion." *Progress in Photovoltaics: Research and Applications* 20 (2): 226–237. https://doi.org/10.1002/pip.1127.

Martínez-Rubio, A., F. Sanz-Adan, J. Santamaría-Peña, and A. Martínez. 2016. "Evaluating Solar Irradiance Over Facades in High Building Cities, Based on LiDAR Technology." *Applied Energy* 183: 133–147. https://doi.org/10.1016/j.apenergy.2016.08.163.

Mehos, M., and R. Perez. 2005. "Mining for Solar Resources: U.S. Southwest Provides Vast Potential." *Imaging Notes 20* (2): 12–15. *NREL/JA-550-37799*.

Meybodi, M. A., L. Ramírez-Santigosa, and A. C. Beath. 2017. "A Study on the Impact of Time Resolution in Solar Data on the Performance CSP Plants." *Renewable Energy*. http://dx.doi.org/10.1016/j.renene.2017.03.024.

Meyer, R., N. Geuder, E. Lorenz, A. Hammer, C. Von Ossietzky, U. Oldenburg, and H. G. Beyer. 2008. "Combining Solar Irradiance Measurements and Various Satellite-Derived Products to a Site-Specific Best Estimate." In *SolarPaces Conference Proceedings*: 1–8.

Mohajeri, N., G. Upadhyay, A. Gudmundsson, D. Assouline, J. Kämpf, and J.-L. Scartezzini. 2016. "Effects of Urban Compactness on Solar Energy Potential." *Renewable Energy* 93: 469–482. https://doi.org/10.1016/j.renene.2016.02.053.

Moody's Investors Services. 2010. "PV Solar Power Generation Projects. Special Comment." July 28, 2010.

Morales, J., M. Zugno, S. Pindea, and P. Pinson. 2014. "Electricity Market Clearing With Improved Scheduling of Stochastic Production." *European Journal of Operational Research* 235: 765–774.

Murata, A., H. Yamaguchi, and K. Otani. 2009. "A Method of Estimating the Output Fluctuation of Many Photovoltaic Power Generation Systems Dispersed in a Wide Area." *Electrical Engineering in Japan* 166 (4): 9–19. https://doi.org/10.1002/eej.20723.

Navarro, A. A., L. Ramírez, P. Domínguez, M. Blanco, J. Polo, and E. Zarza. 2016. "Review and Validation of Solar Thermal Electricity Potential Methodologies." *Energy Conversion and Management* 126: 42–50. https://doi.org/10.1016/j.enconman.2016.07.070.

Nielsen, K. P., P. Blanc, F. Vignola, L. Ramírez, M. Blanco, and R. Meyer. 2017. "Discussion of Currently Used Practices for 'Creation of Meteorological Data Sets for CSP/STE Performance Simulations.'" In *SolarPaces Conference Proceedings*.

Pavlovski, A. 2022. "Solar Architecture in Energy Engineering." *Encyclopedia 2:* 1432–1452. https://doi.org/10.3390/encyclopedia2030097.

Pavón, M., C. M. Fernández, M. Silva, S. Moreno, M. V. Guisado, and A. Bernardos. 2016. "Statistical Analysis of CSP Plants by Simulating Extensive Meteorological Series." *SolarPaces Conference Proceedings*.

Perez, M., R. Perez, K. Rabago, and M. Putnam. 2019a. "Achieving 100% Renewables: Supply-Shaping Through Curtailment." *PVTech*, May 15, 2019. https://www.pv-tech.org/technical-papers/achieving-100-renewables-supplyshaping-through-curtailment/.

Perez, M., R. Perez, K. Rabago, and M. Putnam. 2019b. "Overbuilding and Curtailment: The Cost-Effective Enablers of Firm PV Generation." *Solar Energy* 180: 412–422.

Perez, R., M. Perez, J. Remund, K. Rabago, M. Putnam, M. Pierro, M. G. Prina, D. Moser, C. Cornaro, J. Schlemmer, J. Dise, T. E. Hoff, A. Swierc, P. Kellin, J. Boland, E. Tapaches, M. David, P. Lauret, R. Van Eldik, W. van Sark, J. Lopez-Laurente, G. Makrides, and G. Georghiou. 2023. *Firm Power Generation*. IEA PVPS. IEA-PVPS T16-04:2023. https://iea-pvps.org/wp-content/uploads/2023/01/Report-IEA-PVPS-T16-04-2023-Firm-Power-generation.pdf.

Perez, R., M. Perez, M. Pierro, J. Schlemmer, S. Kivalov, J. Dise, P. Keelin, M. Grammatico, A. Swierc, J. Ferreira, A. Foster, M. Putnam, and T. Hoff. 2019a. "Operationally Perfect Solar Power Forecasts: A Scalable Strategy to Lowest-Cost Firm Solar Power Generation." In *Proceedings of the 2019 IEEE 46th Photovoltaic Specialists Conference (PVSC)*. https://doi.org/10.1109/pvsc40753.2019.9198973.

Perez, R., M. Perez, M. Pierro, J. Schlemmer, S. Kivalov, J. Dise, P. Keelin, M. Grammatico, A. Swierc, J. Ferreira, P. Schmid, M. Putnam, and T. E. Hoff. 2019b. "Perfect Operational Solar Forecasts: A Scalable Strategy Toward Firm Power Generation." In *Proceedings of the ISES Solar World Congress 2019*. https://doi.org/10.18086/swc.2019.45.07.

Perez, R., R. Seals, A. Zelenka, and P. Ineichen. 1990. "Climatic Evaluation of Models That Predict Hourly Direct Irradiance From Hourly Global Irradiance: Prospects for Performance Improvements." *Solar Energy* 44 (2): 99–108. https://doi.org/10.1016/0038-092x(90)90071-j.

Perez, R., S. Kivalov, and T. Hoff. 2011. "Spatial-Temporal Characteristics of Solar Radiation Variability." *Proceedings of the ISES Solar World Congress 2011*. https://doi.org/10.18086/swc.2011.24.23.

Peruchena, C. M. F., L. Ramírez, M. Silva, V. Lara, D. Bermejo, M. Gastón, S. Moreno, J. Pulgar, J. Liria, S. Macías, R. Gonzalez, A. Bernardos, N. Castillo, B. Bolinaga, R. X. Valenzuela, and L. Zarzalejo. 2016. "A Methodology for Calculating Percentile Values of Annual Direct Normal Solar Irradiation Series." *SolarPaces Conference Proceedings* 391 (2012): 150005. https://doi.org/10.1063/1.4949237.

Pierro, M., R. Perez, M. Perez, D. Moser, and C. Cornaro. 2020. "Italian Protocol for Massive Solar Integration: Imbalance Mitigation Strategies." *Renewable Energy* 153: 725–739. https://doi.org/10.1016/j.renene.2020.01.145.

Pierro, M., R. Perez, M. Perez, M. G. Prina, D. Moser, and C. Cornaro. 2021. "Italian Protocol for Massive Solar Integration: From Solar Imbalance Regulation to Firm 24/365 Solar Generation." *Renewable Energy* 169: 425–436. https://doi.org/10.1016/j.renene.2021.01.023.

Potter, D. F., J.-S. Kim, A. Khassapov, R. Pascual, L. Hetherton, and Z. Zhang. 2018. "Heliosim: An Integrated Model for the Optimisation and Simulation of Central Receiver CSP Facilities." *AIP Conference Proceedings*. https://doi.org/10.1063/1.5067213.

Quaschning, V., W. Ortmanns, R. Kistner, and M. Geyer. 2001. "Greenius: A New Simulation Environment for Technical and Economical Analysis of Renewable Independent Power Projects." In *Solar Forum 2001 Proceedings*: 413–418.

Ramírez, L., and J. M. Vindel. 2017. "Forecasting and Nowcasting of DNI for Concentrating Solar Thermal Systems." In *Advances in Concentrating Solar Thermal Research and Technology*. Edited by M. J. Blanco & L. Ramírez Santigosa. Elsevier. https://doi.org/10.1016/B978-0-08-100516-3.00013-7.

Ramírez, L., K. Pagh, F. Vignola, M. Blanco, P. Blanc, R. Meyer, and S. Wilbert. 2017. "Road Map for Creation of Advanced Meteorological Data Sets for CSP Performance Simulations." http://www.solarpaces.org/wp-content/uploads/SolarPACES-T5_BeyondTMY_Road_Map.pdf.

Reich, N. H., B. Mueller, A. Armbruster, W. G. J. H. M. van Sark, K. Kiefer, and C. Reise. 2012. "Performance Ratio Revisited: Is PR > 90% Realistic?" *Progress in Photovoltaics: Research and Applications* 20 (6): 717–726. https://doi.org/10.1002/pip.1219.

Remund, J., C. Calhau, L. Perret, and D. Marcel. 2015. *Characterization of the Spatio-Temporal Variations and Ramp Rates of Solar Radiation PV*. IEA-PVPS. https://iea-pvps.org/key-topics/characterization-of-the-spatio-temporal-variations-and-ramp-rates-of-solar-radiation-and-pv-2015/.

Renné, D. S. 2016. “Resource Assessment and Site Selection for Solar Heating and Cooling Systems.” In *Advances in Solar Heating and Cooling*. Elsevier. https://doi.org/10.1016/b978-0-08-100301-5.00002-3.

Renné, D. S. 2017. “Effective Solar Resource Methodologies for Sustainable PV Applications.” In R. Z. Wang and T. S. Ge (Eds.) *Photovoltaics for Sustainable Electricity and Buildings*. Springer International Publishing. https://doi.org/10.1007/978-3-319-39280-6_3.

Riedel-Lyngskær, N., D. Berrian, D. Alvarez Mira, A. Aguilar Protti, P. B. Poulsen, J. Libal, and J. Vedde. 2020. “Validation of Bifacial Photovoltaic Simulation Software Against Monitoring Data from Large-Scale Single-Axis Trackers and Fixed-Tilt Systems in Denmark.” *Applied Sciences* 10 (23): 8487. https://doi.org/10.3390/app10238487.

Santos, T., N. Gomes, S. Freire, M. C. Brito, L. Santos, and J. A. Tenedório. 2014. “Applications of Solar Mapping in the Urban Environment.” *Applied Geography* 51: 48–57. https://doi.org/10.1016/j.apgeog.2014.03.008.

Schwarzbözl, P., R. Pitz-Paal, and M. Schmitz. 2009. “Visual HFLCAL—A Software Tool for Layout and Optimisation of Heliostat Fields.” Proc. SolarPACES Conference, Berlin, Germany.

Sørensen, P. A. 2012. *Solar District Heating Guidelines*. https://www.solarthermalworld.org/sites/default/files/story/2015-04-03/sdh-wp3-d31-d32_august2012_0.pdf.

Stein, J. S., C. Reise, J. Bonilla Castro, G. Friesen, G. Maugeri, E. Urrejola, and S. Ranta. 2021. *Bifacial Photovoltaic Modules and Systems: Experience and Results from International Research and Pilot Applications*. IEA-PVPS T13-14:2021. https://iea-pvps.org/wp-content/uploads/2021/04/IEA-PVPS-T13-14_2021-Bifacial-Photovoltaic-Modules-and-Systems-report.pdf.

Theristis, M., N. Riedel-Lyngskær, J. S. Stein, L. Deville, L. Micheli, A. Driesse, W. B. Hobbs, S. Ovaitt, R. Daxini, D. Barrie, M. Campanelli, H. Hodges, J. R. Ledesma, I. Lokhat, B. McCormick, B. Meng, B. Miller, R. Motta, E. Noirault, … C. Zhao. 2023. “Blind Photovoltaic Modeling Intercomparison: A Multidimensional Data Analysis and Lessons Learned.” *Progress in Photovoltaics: Research and Applications*. https://doi.org/10.1002/pip.3729.

Tooke, T. R., N. C. Coops, A. Christen, O. Gurtuna, and A. Prévot. 2012. “Integrated Irradiance Modelling in the Urban Environment Based on Remotely Sensed Data.” *Solar Energy* 86: 2923–2934. https://doi.org/10.1016/j.solener.2012.06.026.

van Sark, W. 2023. “Photovoltaics Performance Monitoring Is Essential in a 100% Renewables-Based Society.” *Joule* 7: 1,388–1,393.

van Sark, W. G. J. H. M., N. H. Reich, B. Müller, A. Armbruster, K. Kiefer, and C. Reise. 2012. “Review of PV Performance Ratio Development.” *World Renewable Energy Congress* 6: 1–6. https://doi.org/10.13140/2.1.2138.7204.

Vignola, F. E., A. C. McMahan, and C. N. Grover. 2013. "Bankable Solar-Radiation Datasets." In J. Kleissl (Ed.) *Solar Energy Forecasting and Resource Assessment*. Elsevier. https://doi.org/10.1016/b978-0-12-397177-7.00005-x.

Vignola, F., C. Grover, N. Lemon, and A. McMahan. 2012. "Building a Bankable Solar Radiation Dataset." *Solar Energy* 86 (8): 2,218–2,229. https://doi.org/10.1016/j.solener.2012.05.013.

Vittitoe, C., and F. Biggs. 1981. *User's Guide to HELIOS: A Computer Program for Modeling the Optical Behavior of Reflecting Solar Concentrators. Part I. Introduction and Code Input*. Sandia National Laboratories, Albuquerque, NM. https://doi.org/10.2172/6239002.

Wagner, M. J., and T. Wendelin. 2018. "SolarPILOT: A Power Tower Solar Field Layout and Characterization Tool." *Solar Energy* 171: 185–196. https://doi.org/10.1016/j.solener.2018.06.063.

Wendelin, T. 2003. "SolTRACE: A New Optical Modeling Tool for Concentrating Solar Optics." *Solar Energy*. https://doi.org/10.1115/isec2003-44090.

Wiemken, E., H. G. Beyer, W. Heydenreich, and K. Kiefer. 2001. "Power Characteristics of PV Ensembles: Experiences From the Combined Power Production of 100 Grid-Connected PV Systems Distributed Over the Area of Germany." *Solar Energy* 70 (6): 513–518. https://doi.org/10.1016/s0038-092x(00)00146-8.

Wilcox, S. M. 2012. *National Solar Radiation Database 1991–2010 Update: User's Manual*. NREL/TP-5500-54824. National Renewable Energy Laboratory, Golden, CO. https://www.nrel.gov/docs/fy12osti/54824.pdf.

Woyte, A., R. Belmans, and J. Nijs. 2007. "Fluctuations in Instantaneous Clearness Index: Analysis and Statistics." *Solar Energy* 81 (2): 195–206. https://doi.org/10.1016/j.solener.2006.03.001.

12 Future Work

Jan Remund,[1] Carlos Fernandez Peruchena,[2] Stefan Wilbert,[3] Kristian Pagh Nielsen,[4] Manajit Sengupta,[5] and Elke Lorenz[6]

[1] *Meteotest, Switzerland*
[2] *Society of Renewable Energy Resources and Meteorological Intelligence, Spain*
[3] *German Aerospace Center (DLR), Germany*
[4] *Danish Meteorological Institute (DMI), Denmark*
[5] *National Renewable Energy Laboratory (NREL), USA*
[6] *Fraunhofer ISE, Germany*

12.1 Introduction

Advancing solar energy generation and its application will require improvements in our understanding, determination, and forecasts of solar radiation resources. This chapter briefly describes areas of research and development identified as emerging technology needs. The International Energy Agency (IEA) Photovoltaic Power System (PVPS) Task 16 work plan for its third phase (2023–2026) on "solar resource for high penetration and large-scale applications" seeks to address significant parts of the research and development needs presented in this chapter.

The third phase of Task 16 will include the following new focus areas:

1. Meteorological data for advanced, integrated, and upcoming technologies like agrivoltaics and floating photovoltaics (PV), including albedo for bifacial modules
2. Analysis of climate model results and descriptions of how to optimally use them:
    A. Exploiting new machine-learning techniques for the forecasting of solar radiation and solar power before and behind the meter, or
    B. Exploiting new machine-learning techniques for the forecasting of solar radiation, solar power generation, and feed-in to electricity grids.

Aside from the new focus areas of Task 16, participants will continue to work on many ongoing topics.

Models must be updated regularly to include ongoing solar satellite innovations, like additional spectral channels or higher resolutions (e.g., Meteosat Third Generation or aerosol measurements with EUMETSAT Polar System-Second Generation (EPS-SG) Multi-Viewing Multi-Channel Multi-Polarization Imaging).

With the increasing diversity and complexity of solar resource data, it is necessary to invest significant effort in the application, evaluation, and standardization of these data. Users need to know which datasets are most suitable for their applications, and this requires readily available evaluations of existing products. A first evaluation of this kind was published in a report prepared by Task 16 participants (Forstinger et al. 2023), but regular updates would certainly be useful to the whole solar industry. In parallel, the ground irradiance measurements that are necessary to validate modeled products must be of the highest possible quality. Forstinger et al. (2023) describe a detailed quality-control algorithm, and a separate report (Blanc and Silva 2023) discusses some preliminary developments aimed at filling data gaps in measurement time series.

Follow-up efforts toward even more sophisticated quality-control and gap-filling algorithms, to be made publicly accessible, have already started.

To create an efficient market, best practices and standards for the creation, documentation, and application of the resource data are needed. Task 16 contributes to relevant work in international standardization bodies, such as the International Organization for Standardization, International Electrotechnical Commission, and ASTM International. The standardization activities are related to solar spectra, radiation measurements, calibration and test methods, radiation forecasts, data formats, and meteorological measurements for power plant performance measurement.

Some resource products are currently not used to their full extent. The potential benefits of their full applications might be understood by most stakeholders, but methods to use the data are yet to be developed or implemented. Examples of such resource products include diverse quantities such as time series of soiling rates; spectral mismatch factors; or circumsolar radiation data that are often included only as an approximation in solar power plant models. Other examples are probabilistic forecasts or spatially highly resolved forecasts based on sky cameras. Users and data providers must collaborate closely to create the best datasets and to fully exploit the potential of such resource data. In the area of forecasting, the Task is collaborating with IEA Wind Task 51.

Work on firm power generation will be continued. This work shows how to build and run cost-efficient energy systems based on deep knowledge of renewable resources and their temporal and spatial variability. The findings of this work have great effects on other topics like regulations of curtailment or supporting schemes for PV. Therefore, close collaboration will expand with IEA PVPS Tasks 1 (markets and policy), Task 14 (grid and inverter modeling and regulations), and Task 18 (edge-of-the-grid modeling).

12.2 Meteorological Data for Advanced, Integrated, and Upcoming Technologies

The ongoing development of solar energy technologies also brings the need for different and additional meteorological data. In particular, advanced, integrated, and upcoming technologies such as floating PV, agrivoltaics, and building- or vehicle-integrated PV require further developments of the resource data.

Solar irradiance is still the most important meteorological input variable for solar yield analysis of such new technologies, but the characteristics of the needed irradiance data is different. For example, the role of the ground-reflected or rear-side irradiance and surface albedo is particularly complex and/or relevant for agrivoltaics, floating PV, and building-integrated PV. Cost-efficient and bankable ways to include these complex contributions to the yield modeling and its uncertainty must be found. Bi-directional reflectance distribution functions (BRDF) and enhanced sky radiance data might be used by experts to provide the required data for yield estimations.

Further, several additional quantities besides the irradiance must be provided at high spatial and/or temporal resolution for accurate yield analysis. For the economic success of a solar project, especially when involving the newest technologies, the role of variables such as temperature, wind loads, soiling, or precipitation is remarkable. Further, such data must be

derived and provided in a way that fits the requirements of the specific technology of interest. For instance, temperature data obtained from a weather model or a meteorological station next to a lake contemplated for a floating PV power plant might significantly differ from that of the water body. In agrivoltaic projects, the important variables do not only affect the PV installation but also the crop yield, so the different effects must be considered as a whole in the project.

Overall, there are many reasons why various parameters must be studied in more detail in the future and methods must be developed to adapt the available data to the specific needs of solar projects. Even for well-known technologies, such as monofacial PV or solar thermal systems, some parameters still require significant further research. For example, accurate, robust, and low-maintenance soiling measurements are still under development, and soiling forecast models based on meteorological data must be improved. Research and development are also required to prepare recommendations and procedures so that these data become truly applicable in the context of commercial solar projects and enable the fast growth of the solar energy sector. Evaluations and comparisons of existing and new datasets, as well as prediction methods, are needed to empower users toward selecting the most adequate data and methods for their projects. Task 16's future work will then necessarily focus on the evaluation of the related uncertainties and their impacts.

12.3 Effects of Climate Change on Radiation and Solar Energy Production

Task 16 will have a new focus on climate model scenarios (e.g., SSP5-8.5; IPCC 2021) with respect to long-term solar resource assessments. In essence, the quality of the results of global and regional climate models will be analyzed with a particular focus on historical long-term dimming and brightening periods. Task 16 will review the future aerosol scenarios, including volcanic aerosols and cloud-aerosol effects. Other factors, like regional impacts of shifts in cloud cover and optical thickness, temperature, or heat waves caused by increased greenhouse gas emissions in the climate model scenarios will also be investigated because future aerosol scenarios related to anthropogenic emissions, with their associated cloud-aerosol effects, can lead to future dimming and brightening periods. It is anticipated that such effects will be better modeled in forthcoming climate models and therefore will be more realistic. It is also important to develop more representative typical and reference yearly datasets, for reasons explained in (Müller et al. 2014). For instance, these new developments would include:

- A review of methods used to generate "plausible" or realistic artificial multiyear solar datasets, such as that in Fernández-Peruchena et al. (2015). These methods will be assessed with respect to the realism of their statistical properties, particularly as a function of the intrayear variability of the solar resource.
- Evaluation of how extreme weather conditions will change in the future. This is because, for example, severe storms and hailstorms can damage solar PV modules and the mirrors in concentrating solar power systems. How the frequency of these events will change with global climate change varies regionally and will be reviewed on a regional basis. This work will be done in collaboration with PVPS Task 13.

Additionally, statistical characteristics of interannual and non-stochastic variability (induced by, e.g., climate trends or volcanic activity) will be examined.

12.4 Forecasting Solar Radiation and Solar Power, Before and Behind the Meter, Based on New Machine-Learning Techniques

Solar power forecasting will be an essential component of the future energy supply system, which will use large amounts of variable solar power. Presently, solar power forecasting systems already contribute to the successful integration of considerable amounts of solar power to the electric grid, and solar power forecasting receives unprecedented attention from various scientific communities. The solar resource variability must be properly managed for various reasons, such as to increase the share of solar power into the energy mix, to maintain the stability of the grid, and to guarantee optimal grid effectiveness in terms of unit commitments and economic dispatch. Consequently, new techniques and approaches will be proposed to improve the accuracy of the models to provide solar radiation and power forecasts.

These new developments will build on existing data sources and models, including irradiance and PV power measurements, all-sky imagers, and satellite data and numerical weather predictions. Major changes are expected in the combination of solar power plants with local storage and demand and enhancing forecasts with machine-learning models.

The usage of solar power forecasting in combination with local storage and energy management systems will strongly impact the feed-in characteristics of solar power and forecast requirements. In many countries, the current situation is that large shares of the generated solar power are directly fed into the grid. Thus, grid management is largely based on the result of using forecasts of regionally aggregated solar generation over the grid area. With the fast expansion of storage facilities combined with solar power plants, as well as the increasing share of self-consumption in urban areas, the solar power that is actually fed to the grid might increasingly deviate from its local generation. This poses new challenges for forecasting solar power feed-in to the grids, though in the long run energy management and storage evidently are essential for balancing fluctuating generation and therefore also for the large-scale system integration of solar power. In addition to forecasting solar generation, self-consumption and storage must be considered when forecasting regionally aggregated PV power feed-in. Here, irradiance data with high spatiotemporal resolution are required to properly model solar generation, and thus will play an important role in complementing measurements at the feed-in point for behind-the-meter applications. Further, high-resolution local forecasts for local and small-scale energy management systems are also considered more critically important.

With the growing need for accurate predictions (both site-specific and regionwide), the scientific community has become increasingly aware of recent advanced data processing techniques aimed at exploiting the ever-increasing amounts of meteorological data in a large-scale spatiotemporal context (Schultz et al. 2021). The key elements that tend to push this transition to a data-driven approach are as follows:

3. The massive parallel processing power now offered by graphics processing units (GPUs), which has considerably enhanced all computing capabilities
4. The increased number of irradiance datasets available for benchmarks—an important topic within Task 16 (see Forstinger et al. 2023)
5. The specialized data processing techniques that make analyses more efficient through enhanced combinations of satellite-based or ground-based images with numerical data.

Among these techniques, it is worth mentioning AutoML (auto machine learning), which has become a hot topic thanks to its high accuracy, deployment simplicity, and time efficiency.

With the aim of providing a comprehensive overview of the performance of new solar radiation and power forecasting models to forecast users, their evaluation in benchmark studies will be an essential part of Task 16's future work.

References

Blanc, P., and R.A. Silva. 2023. *Framework for Benchmarking of GHI Gap-Filling Methods.* Report IEA-PVPS T16-03:2023. IEA-PVPS. https://iea-pvps.org/wp-content/uploads/2023/06/Report-IEA-PVPS-T16-03-2023-Framework-for-benchmarking-of-GHI-gap-filling-methods-1.pdf.

Fernández-Peruchena, C.M., M. Gastón, M. Sánchez, J. García-Barberena, M. Blanco, and A. Bernardos. 2015. "MUS: A Multiscale Stochastic Model for Generating Plausible Meteorological Years Designed for Multiyear Solar Energy Yield Simulations." *Sol. Energy* 120, 244–256. https://doi.org/10.1016/j.solener.2015.07.037.

Forstinger, A., S. Wilbert, A.R. Jensen, B. Kraas, C.M.F. Peruchena, C.A. Gueymard, D. Ronzio, D. Yang, J. Polo Martinez, J.A. Ruiz-Arias, et al. 2023. *Worldwide Benchmark of Modelled Solar Irradiance Data 2023.* Report IEA-PVPS T16-05: 2023. IEA-PVPS. https://iea-pvps.org/wp-content/uploads/2023/06/IEA-PVPS-T16-05-2023-Worldwide-Benchmark-Modelled-Solar.pdf.

IPCC (Intergovernmental Panel on Climate Change). 2021. "Summary for Policymakers." In: *Climate Change 2021: The Physical Science Basis. Contribution of Working Group I to the Sixth Assessment Report of the Intergovernmental Panel on Climate Change*. Masson-Delmotte, V., P. Zhai, A. Pirani, S.L. Connors, C. Péan, S. Berger, N. Caud, Y. Chen, L. Goldfarb, M.I. Gomis, M. Huang, K. Leitzell, E. Lonnoy, J.B.R. Matthews, T.K. Maycock, T. Waterfield, O. Yelekçi, R. Yu, and B. Zhou (Eds.). Cambridge University Press, pp. 3−32, https://doi.org/10.1017/9781009157896.001.

Müller, B., M. Wild, A. Driesse, and K. Behrens. 2014. "Rethinking Solar Resource Assessments in the Context of Global Dimming and Brightening." *Sol. Energy* 99: 272–282. https://doi.org/10.1016/j.solener.2013.11.013.

Schultz, M.G., C. Betancourt, B. Gong, F. Kleinert, M. Langguth, L.H. Leufen, A. Mozaffari, and S. Stadtler. 2021. "Can Deep Learning Beat Numerical Weather Prediction?" *Philos. Trans. R. Soc. Math. Phys. Eng. Sci.* 379: 20200097. https://doi.org/10.1098/rsta.2020.0097.

Glossary

In the definition column, words in italics refer to another entry in the column labeled "Term."

Term	Definition
Absolute cavity radiometer (ACR)	An instrument used as part of a primary reference measurement procedure for solar *irradiance*. It absorbs *radiation* on a blackened conical receiver and is electrically self-calibrating. It provides the reference from which other *radiometers* are calibrated.
Absolute humidity	ρ_v [g/m^3] A measure of the actual amount of *water vapor* in the air.
Absorption	When the quantity of interest is captured by a substance, reducing the amount available. For example, *solar radiation* is absorbed by some atmospheric molecules, solar *collectors*, and the ocean.
Aerosol	Excluding cloud droplets and related precipitation, any small particle that tends to stay in the air, such as smoke, dust, salt, or pollen.
Aerosol optical depth (AOD)	[unitless] Extinction per unit path length due to *aerosols* alone. This is typically obtained at any *wavelength* λ by evaluating the total atmospheric extinction and subtracting the extinction of as many of the other constituents as possible (*water vapor* [w], ozone [o], mixed gases [g], nitrogen dioxide (n), and atmospheric molecules [m]). The *transmittance*, T, and *optical depth*, τ, of an atmospheric constituent are related as follows: $T_\lambda = \exp(-\tau_\lambda m)$, or $\tau_\lambda = -\ln(T_\lambda)/m$ where m is the *airmass*. Based on this, the AOD at λ can be derived as: $\tau_{a\lambda} = \tau_\lambda - (\tau_{w\lambda} + \tau_{o\lambda} + \tau_{g\lambda} + \tau_{n\lambda} + \tau_{m\lambda})$ where τ_λ is the total *optical depth* of the *atmosphere*, typically sensed by a *sunphotometer* or *spectroradiometer*. See also *Atmospheric turbidity* and *Langley*.

Term	Definition
Airmass	AM or *m* [unitless]; also called optical air mass or relative air mass. The path length of the direct solar beam *irradiance* through an ideal *atmosphere* composed of only air molecules, relative to its vertical height. When the sun is at the zenith, i.e., directly above a location, the path length is defined as airmass 1 (AM 1.0). AM 1.0 is not synonymous with *solar noon* because the sun is usually not directly overhead at solar noon in most seasons and locations. AM0 is the term conventionally used to denote the conditions at the *Top of atmosphere*. When the *solar zenith angle* increases, the airmass increases approximately by its secant, i.e., 1/cos(SZA). Formulas of various complexity have been proposed to evaluate AM from SZA (*Rapp-Arrarás and Domingo-Santos 2011)*. The optical mass of specific atmospheric constituents, such as *water vapor*, ozone, or *aerosols*, is somewhat different from AM because they do not have the same vertical profiles as air molecules (Gueymard 2019).
Albedo	The fraction of *solar radiation* that is reflected by a surface (e.g., ground, vegetation, water, or snow) or atmospheric constituent (e.g., air or cloud). For the solar energy community, albedo usually refers to just the surface surrounding a solar installation.
Albedometer	A combination of two *pyranometers* specifically designed to measure *albedo*. One instrument faces up and the other faces down.
Ambient temperature	The air temperature measured with a thermometer, similar to *dry-bulb temperature*.
Angle of incidence	[rad or °] The angle that a ray (of *solar radiation,* for example) makes with a line perpendicular to the surface. For example, a surface that directly faces the sun has a solar angle of incidence of 0°, whereas if the surface is parallel to the sun (for example, sunrise striking a horizontal rooftop), the angle of incidence is 90°. At any instant, the angle of incidence can be calculated from sun position and the surface's tilt and azimuth (Iqbal 2012).
Angle of refraction	[rad or °] The angle that a ray (of *solar radiation*, for example) makes with a line perpendicular to the boundary separating two media after bending caused by *refraction.*

Term	Definition
Angular response characterization	Quantification of the effects of the irradiance *incidence angle* on *pyranometer* measurement performance. If a pyranometer is rotated while a beam of light is shined upon it, it will record the maximum *energy* when it is directly facing the beam, and the energy will fall to zero when it is sideways to (or facing away from) the beam. If the instrument were perfect, its signal should vary like the cosine of the *angle of incidence*. Pyranometers have imperfections that keep them from following this pattern. The actual *cosine response* of the instrument thus needs to be characterized.
Anisotropic	See *Isotropy.*
Astronomical unit (AU)	A unit of length defined by the International Astronomical Union exactly as 149,597,870.7 km, representing the approximate mean Sun-Earth distance. See *Solar constant*.
Atmosphere	Gaseous envelope surrounding a planet or a star.
Atmospheric pressure	[mb or hPa] The pressure (force per area) created by the weight of the *atmosphere*. At higher elevations, the atmospheric pressure is lower because there is less air.
Atmospheric turbidity	Haziness in the *atmosphere* caused by various kinds of *aerosol* particles. If turbidity is zero, the sky has no aerosols. In the past, turbidity was defined by the Linke turbidity factor or the Ångström turbidity coefficient. Currently, it is more precisely quantified by the *aerosol optical depth* at one (typically 550 nm) or more *wavelengths*.
Attenuation	In atmospheric physics, loss of radiation by optical phenomena. For example, solar *irradiance* attenuates through scattering and *absorption* as it passes through the *atmosphere* to the surface of the Earth. See also *Scattered radiation.*
Azimuth angle	Ψ [rad or °] The angle between the horizontal direction (of the sun, for example) and a reference direction (normally north, although some authors incorrectly measure the solar azimuth angle from due south).
Barometer	An instrument that measures *atmospheric pressure*, also called *barometric pressure*.

Term	Definition
Barometric pressure	[mb or hPa] The pressure (force per area) created by the weight of the *atmosphere*, measured by a *barometer*. At higher elevations, the atmospheric pressure is lower because there is less air.
Beam radiation	A synonym for *direct normal irradiance*, the amount of *solar radiation* from the direction of the sun.
Bias	An indication of the average deviation of the predicted from the measured values.
Bidirectional reflectance distribution function	Angular function describing the distribution of reflected light at a surface in a specific direction for all possible *angles of incidence* of the incoming *radiation*.
Bird clear-sky model	Named after Dr. Richard Bird, a scientist at the National Renewable Energy Laboratory. This radiation model uses properties of the *atmosphere*—such as *albedo*, *atmospheric turbidity*, and *precipitable water*—to determine the amount of *solar radiation* striking the Earth's surface under a cloudless sky (Bird and Hulstrom 1981).
Blackbody	The theoretical "perfect" absorber of *electromagnetic radiation* at all *wavelengths*. As blackbodies heat up, they emit a characteristic double-exponential light frequency (*energy*) curve, which is imperfectly seen in nature.
Broadband Outdoor Radiometer Calibration (BORCAL)	A method of calibrating *pyrheliometers* and *pyranometers* based on the summation technique at NREL's Solar Radiation Research Laboratory. Up to 3 days of clear-sky solar *irradiance* measurements taken at 30-second intervals from sunrise to sunset are used to compute the individual *radiometer* responsivities.
Broadband solar irradiance	[W m^{-2}] Theoretically, the *solar radiation* arriving at the Earth from all frequencies or *wavelengths*, but in practice limited to the spectral range of *radiometers*, typically *wavelengths* from 290 nm to ≈3000 nm (for *pyranometers*), ≈4000 nm (for *pyrheliometers*), or infinite (for windowless ***absolute cavity radiometers***). Meteorologists often refer to this band as *shortwave radiation*.
Calibration	The process of comparing an instrument's output signal to that of a reference. Instruments that measure solar energy tend to "drift"—that is, their output signals do not mean the same thing from one time period to another. Because of this, they are periodically (e.g., annually) recalibrated against more reliable reference instruments.

Term	Definition
Campbell-Stokes sunshine recorder	A clear glass sphere that focuses the sun's rays onto a special strip chart, producing a charred path when there is bright *sunshine*. The length of the path determines the bright *sunshine duration*. The lower limit for bright sunshine (based on a Campbell-Stokes recorder) might vary between ≈70 W/m^2 (very dry air) and ≈280 W/m^2 (very humid air).
Circumsolar radiation	The amount of *solar radiation* coming from a circle in the sky centered on the sun's disk. In radiometry, the region of most interest has a radius up to ≈3°, depending on the type of instrument being used to measure the *beam radiation* (broadband or spectral). This region can be smaller or wider in concentrating solar applications, depending on the concentration ratio.
Clear-sky index	K_c [unitless] Ratio between the observed or predicted *global horizontal irradiance* and its ideal clear-sky counterpart at any instant: $K_c = \mathrm{GHI} / \mathrm{GHI_{cs}}$ where $\mathrm{GHI_{cs}}$ is estimated by a clear-sky *radiation* model. See *Bird clear-sky model.*
Clearness index	K_t **[**unitless**]** The global transmittance of the atmosphere, i.e, the ratio between *global horizontal irradiance* and *top-of-atmosphere horizontal irradiance (also called extraterrestrial irradiance*) at any instant: $K_t = \mathrm{GHI} / \mathrm{ETH} = K_n + K_d$ where K_n and K_d are the direct and diffuse transmittances of the atmosphere, respectively.
Climate	The typical or expected (average) *weather* pattern over a long period, as opposed to the actual weather at any given instant.
Cloud type	The type of clouds (e.g., altostratus, cumulonimbus) that form each layer of the *sky dome*. Clouds are classified in 10 main groups, called genera. Each observed cloud is a member of one, and only one, genus.
Collector	A device that receives *solar radiation* and converts it to useful *energy* forms.

Term	Definition
Concentrating parabolic trough	A *collector* system that tracks the path of the sun by pivoting on one axis (typically east-west or north-south) using shiny *parabolic collector troughs* to heat the collector fluid that passes through a tube at the focus.
Concentrator	A *collector* that enhances *solar radiation* by focusing it onto a smaller area through mirrored surfaces or lenses.
Cosine response	The effects of the *irradiance incidence angle* on pyranometer measurement performance, compared to the expected angular response for an ideal instrument. See *Angular response characterization*.
Dewpoint	[K or °C] The temperature at which the *water vapor* in the *atmosphere* will condense as drops on a surface.
Diffuse fraction	*K* [unitless] The ratio between *diffuse horizonal irradiance* and *global horizontal irradiance* at any instant: K = DHI / GHI
Diffuse horizontal irradiance (DHI)	[W m^{-2}] The *irradiance* generated by *diffuse sky radiation* when incident on a horizontal surface.
Diffuse sky radiation	[W m^{-2}] The radiation component that emanates from a point in the sky after scattering, in practice excluding *circumsolar radiation*. Low diffuse sky radiation exists at high-elevation sites under cloudless skies or at any location under thick cloudiness (e.g., strong thunderstorms). High values are produced by a turbid cloudless *atmosphere* or by intense scattering from clouds.
Diffuse transmittance	K_d [unitless] The ratio between *diffuse horizontal irradiance* and *extraterrestrial (top-of-atmosphere) horizontal irradiance* at any instant: K_d = DHI / ETH, See *Clearness index.*
Direct horizontal irradiance (DIR)	[W m^{-2}] The amount of direct *solar radiation* that is incident on a horizontal surface, i.e., DNI cos(SZA), where SZA is the *Solar zenith angle*.
Direct normal irradiance (DNI)	[W m^{-2}] A synonym for *beam radiation*, the amount of *solar radiation* from the direction of the sun collected at normal incidence.

Term	Definition
Direct transmittance	K_n [unitless] The ratio between *direct normal irradiance* and *extraterrestrial (top-of-atmosphere) normal irradiance* at any instant: K_n = DNI / ETN. See *Clearness index.*
Diurnal	Refers to the daily cycle. A diurnal plot is usually a representative midnight-to-midnight graph of values measured at a smaller time interval (e.g., hourly or 5-minute values).
Dry-bulb temperature	[K or °C] The air temperature measured with a thermometer, similar to ambient temperature. The term dry-bulb distinguishes it from the *wet-bulb temperature* measured by a psychrometer to determine relative humidity.
Electromagnetic radiation	A form of *energy* propagation where *photons* travel at the speed of light.
Electromagnetic spectrum	The entire *energy* range of *electromagnetic radiation* specified by frequency, *wavelength*, or *photon* energy.
Emissivity	[unitless] The ratio of the actual amount of *electromagnetic radiation* emitted by an object to the amount emitted by an ideal *blackbody* at the same temperature.
Energy	[J or kWh] An amount of *power* that has been at work during a specified period.
Equation of time (EqT)	[minutes] The annual east-west swing of the location of the sun, which can be detected by noting the position of the sun at the same time (such as noon) each day. This motion is caused by the libration (wobble) of the Earth. It varies between about –14 and +16 minutes during the year and is usually calculated with high accuracy by sun position algorithms. It can also be estimated (in minutes) by the simple formula of (Spencer 1971): $EqT = 229.18\,(0.000075 + 0.001868\cos D - 0.032077\sin D - 0.014615\cos 2D - 0.040849\sin 2D)$ where: $D = n_D\,(360° / 365)$ and n_D is the day number (e.g., n_D = 32 for Feb. 1). See *Local standard time.*

Term	Definition
Equinox	Literally "equal night," a day when the number of hours of daylight equals the number of hours of night. In the Northern Hemisphere, the vernal equinox, usually March 21, signals the onset of spring, and the autumnal equinox, usually Sept. 21, signals the onset of autumn.
Extraterrestrial irradiance	[W m^{-2}] Also known as "*top-of-atmosphere*" *irradiance*, the amount of radiation that a location on Earth would receive if there was no *atmosphere* or *clouds* (i.e., in outer space). This number is typically used as the reference amount against which actual *solar radiation* measurements are compared.
Fixed-tilt array	A set (array) of solar power collectors that are permanently installed on a fixed structure. They are usually mounted on an equator-facing tilted structure that maximizes the annual amount of *energy* that they can produce.
Flat-plate collector	A solar power *collector* with a flat surface that absorbs *solar radiation* without concentrating or refocusing it.
Global horizontal irradiance (GHI)	[W m^{-2}] Also called global (or total or surface) *solar radiation*; the sum of *diffuse horizontal irradiance* and *direct horizontal irradiance*: $GHI = DHI + DNI \cos(SZA)$ where SZA is the *solar zenith angle*.
Global tilted irradiance (GTI)	[W m^{-2}] Also called POA *irradiance*. The sum of direct tilted irradiance, diffuse tilted irradiance (DTI, the diffuse sky *radiance* integrated over the visible fraction of the sky), and surface-reflected irradiance (RTI): $GTI = DNI \cos(\theta) + DTI + RTI$ where θ is the *angle of incidence*.
Ground-reflected radiation	The radiation from the sun that is reflected back into the *atmosphere* after striking the surface.
Heliosat	A modeling method originally developed by Cano et al. (1986) for the determination of *global horizontal irradiance* from meteorological satellite imagery. Various improved versions have followed.

Term	Definition
Heliostat	A large flat mirror, usually on a 2-axis tracker so that it can continuously reflect the sun's rays onto the central receiver of a concentrating solar power (CSP) plant. A typical central receiver system requires hundreds of heliostats.
Hemispherical	Describing properties related to a half sphere, represented by a 2π-sr solid angle.
Humidity	(See *Absolute humidity*, *Relative humidity*, *Specific humidity*.)
Illuminance	[lux] Photometric quantity representing the total luminous flux incident on a surface, per unit area. This corresponds to the *solar radiation* in the visible region of the *solar spectrum* to which the human eye responds.
Incidence angle	[°] See *Angle of incidence.*
Incident radiation	The incoming *radiation*, i.e., radiation that strikes a surface.
Infrared radiation	The radiation with *wavelengths* beyond ≈750 nm, i.e., greater than those of the *visible radiation* but shorter than those of microwaves (at ≈800 μm). Infrared radiation is associated with heat *energy*. The near infrared contains wavelengths in the *shortwave* range ≈750–4000 nm.
Irradiance	E [W m^{-2}] The rate at which *radiant energy* impinges on a specific area of surface during a specific time interval. This is also known as *radiant flux* density.
Irradiation	H [J m^{-2} or kWh m^{-2}] The *energy* accumulated on a unit area surface during a specific period (1 kWh m^{-2} = 3.6 MJ m^{-2}).
Isotropy	Characterizes an emission or reflection process in which the *radiance* is the same in all directions. To simplify calculations, the diffuse sky radiance and the reflectance of materials or ground surfaces are often considered isotropic, but this typically constitutes an oversimplification (Kamphuis et al. 2020). A process that is not isotropic is called anisotropic.

Term	Definition
Lambertian	A Lambertian radiating surface is one whose intensity varies with angle according to Lambert's law [Johann H. Lambert, 1728–1777]. This applies to the characterization of the *reflectance* and *albedo* of a surface. The *radiance* of a Lambertian radiating surface is independent of the angle from which it is viewed. Hence, such a surface radiates isotropically. In particular, the radiance of a *blackbody* is Lambertian.
Langley	Samuel P. Langley (1834–1906) was an American astronomer and physicist who invented the bolometer. He dedicated substantial efforts to the evaluation of the *solar constant* and its possible variations, based on bolometer observations made at high-altitude observatories and airmass-based extrapolations to AM0 (*Top of atmosphere*; see also *Airmass*). In sunphotometry, this "Langley extrapolation" or "Langley plot" technique is used systematically to calibrate *sunphotometers* against the sun with a high degree of confidence (Shaw 1983). The "Langley ratio method" (Almansa et al. 2024) is also used to transfer the calibration of sunphotometers. In his honor, an irradiation unit (Langley or Ly) was named after him but is now deprecated. By definition, 1 Ly = 1 cal cm^{-2} = 41.84 kJ m^{-2}. In terms of *irradiance*, 1 Ly min^{-1} = 697.33 W m^{-2}.
Latitude	[**°**] The angular distance from the equator to the pole, counted positively toward the North Pole (+90°). Hence, the South Pole is 90° south, or –90°.
Light	The visual portion of the electromagnetic spectrum between the ultraviolet (≈380 nm) and the infrared (≈750 nm). The term is sometimes used as a synonym for all *electromagnetic radiation*, at least in the *shortwave*. See also *Visible radiation.*
Local apparent time	LAT [hour]. Also called True Solar Time, or simply Solar Time. The time of day strictly based on the movement of the sun. See *Solar noon*.
Local standard time	LST [hour]. The time of day based on the local time zone, irrespective of any daylight savings correction. The correspondence between LST and LAT depends on the local *longitude* (L), its time zone (TZ), and the *Equation of time* (EqT): LST = LAT + 4 (15 TZ – L) + EqT

Term	Definition
Longitude	[°] The east-west angular distance of a locality from the Prime Meridian. The Prime Meridian originates from the Greenwich Observatory in England. Longitudes are counted positively toward the east, up to +180°, and negatively toward the west, down to –180°. The ±180° Meridian is where the date changes by one day.
Longwave radiation	See *Infrared radiation*.
Macroclimate	The general climate of a large region such as the Rocky Mountains or the Northern Great Plains in the U.S., or the Alps in Europe.
Measurand	A quantity intended to be measured.
Measurement uncertainty	The bounds that should be placed on a measurand because of uncertainties in the measurement. If there are several factors pertaining to the measurement, such as voltage bias *and* temperature bias *and* the precision of the measurement scale, the total measurement uncertainty can be difficult to calculate and might be larger than the largest individual uncertainty of any one factor depending on the sensitivity of the measurement to the significant factors. There is no such thing as a perfect measurement, although some measurements are so precise that errors are negligible. Solar irradiance measurements are notoriously unreliable with the best usual methods having 1%–3% uncertainty.
Megawatt	[MW] A unit of *power* equal to 1 million (10^6) watts.
Mesoclimate	The *climate* that is peculiar to a small natural feature, such as a hill or a small lake, with typical distances in the range 1–100 km. This climate tends to be different from the general climate of the region in predictable ways. A statement such as "it snows more at the airport than downtown" characterizes a mesoclimate.
Microclimate	The local *climate* near the ground that is peculiar to a very small area, i.e., with a radius less than a kilometer and possibly as small as a millimeter. A microclimate region is defined by changes in behavior of the atmosphere's surface boundary layer and not by obvious physical features.
Mie scattering	The scattering of *solar radiation* by ideal spherical particles in the *atmosphere* that have the same approximate size as the *wavelength* of light, analyzed by Gustav Mie. Although *Rayleigh scattering* explains the blue sky, Mie scattering explains why hazy (turbid) skies are whiter than dry, mountainous skies.

Term	Definition
Nadir	Vertical direction oriented straight down (toward the center of the Earth), typically from a satellite sensor.
Normal radiation	*Radiation* striking a surface that is facing the sun. Global (total) normal *irradiance* is all *solar radiation* that strikes a flat surface that faces the sun at normal incidence, whereas *direct normal irradiance* excludes all radiation that does not come from the direction of the sun, but in practice includes the *Circumsolar radiation* emanating from a region of ≈2.5° around the sun center.
Optical depth	[unitless] Also called optical thickness. The natural logarithm of the ratio of incident to transmitted *radiant flux* through a material (e.g., the *atmosphere*). See also *Aerosol optical depth*.
Orientation	[°] The direction that a solar energy *collector* faces, also referred to as geometry. The two components of orientation are the tilt angle and the *azimuth angle* (the angles the active surface of the collector makes from the horizontal and from north, respectively.
Ozone layer	The layer in the *atmosphere* with the most ozone, usually at an altitude of ≈25 km. Ozone is created from oxygen by *ultraviolet radiation* bombardment. Because ozone tends to absorb and block ultraviolet radiation, a substantial ozone layer reduces the risk of skin cancer.
Parabolic collector trough	A system that tracks the path of the sun by pivoting on one axis (typically east-west or north-south), using reflective parabolic troughs to heat the collector fluid that passes through a tube at the focus.
Peak power	[W] The maximum amount of *power* produced or demanded in a time interval.
Photoelectric	Pertaining to the conversion of *light* (radiant *energy*) to electricity.
Photon	The fundamental particle or quantum of *electromagnetic radiation* (*radiant energy*).
Photovoltaic	A technology for converting sunlight directly into electricity, usually with *photovoltaic cells*.
Photovoltaic array	A *photovoltaic module* or (most usually) set of modules used for converting *solar radiation* into electric energy.

Term	Definition
Photovoltaic cell	A single semiconducting element of small size (for example, 1–100 cm^2) that absorbs light or other bands of the electromagnetic spectrum and produces electricity.
Photovoltaic module	A unit, comprised of several *photovoltaic cells*, that is the principal unit of a photovoltaic array. A photovoltaic module's size is on the order of 1–2 m^2, although its size is governed by convenience and application. All modules in an array must be electrically connected in series or parallel.
Physikalisch-Meteorologisches Observatorium Davos/World Radiation Center	Located in Davos, Switzerland, this institution (also known as PMOD) is mandated by the World Meteorological Organization to determine and maintain worldwide radiometric standards for the measurement of *solar radiation*, including the *World Radiometric Reference*.
Power	[W] The amount of work or *energy* expended in a given amount of time. The watt is defined as a joule per second.
Precipitable water	[mm, cm, or kg m^{-2}] Also called integrated *water vapor*, characterizes the amount of water vapor in a vertical column of *atmosphere*. The unit of measure is typically the depth to which the water vapor would fill the vertical column if it were condensed to a liquid. For example, 6 cm of precipitable water indicates a very moist atmosphere, as opposed to less than 0.5 cm for a dry one.
Pyranometer	An instrument with a hemispherical field of view, used for measuring total or global *solar radiation*, specifically *global horizontal irradiance* or *global tilted irradiance*. A pyranometer with a shadowband or shading disk blocking the direct beam measures the *diffuse sky radiation*. A pyranometer mounted downward (facing the ground) measures the reflected radiation from the ground (see *Albedo*).
Pyrheliometer	A *radiometer* with a narrow field of view (≈2.5° half-angle) that measures *direct normal irradiance*. Pyrheliometers are mounted on sun-following trackers so that the instrument is always aimed at the sun.
Radiance	*L* [W m^{-2} sr^{-1}] The flux density of *radiant energy* per unit solid angle per unit of projected source area. This applies to the diffuse radiance emitted from any point in the sky. The total radiance emitted from all source points in the visible sky (minus the circumsolar region) determines the diffuse sky *irradiance*.

Term	Definition
Radiant emittance	M [W m^{-2}] The *radiant energy* emitted from a surface.
Radiant energy	Q [J] A portion of *radiation* in the form of *photons* or electromagnetic waves that are emitted by the *atmosphere*.
Radiant flux	Φ [W] The amount of *radiant energy* per unit of time in the form of *photons* or electromagnetic waves.
Radiant intensity	I [W sr^{-1}] The *radiant energy* emitted by a source per unit solid angle.
Radiation	Synonymous with *electromagnetic radiation*, or the *energy* produced by an oscillating electrical (and magnetic) field, transmitted by *photons*. See *Electromagnetic spectrum*.
Radiometer	Instrument constructed to measure *electromagnetic radiation* over a limited or unlimited spectral range.
Rayleigh scattering	The scattering of *solar radiation* by ideally spherical particles in the *atmosphere* that are much smaller than the *wavelength* of light, as analyzed by Lord Rayleigh. Rayleigh scattering explains the blue color of the cloudless sky and the reddening of the sun at sunrise/sunset.
Reanalysis	A meteorological data assimilation method based on a numerical *weather* prediction (forecast) model that is run for the past and provides physical estimates of Earth System variables at any location and at any point in time consistent with the model physics. It assimilates historical atmospheric observational data spanning an extended period, using a single consistent assimilation (or "analysis") scheme throughout the period, which can span many decades.
Receiver	A device that receives *solar radiation* and converts it to useful *energy* forms.
Reference cell	A *photovoltaic* cell mounted in a suitable enclosure and used as a *radiometer* to measure the photovoltaic-matched *irradiance*, which is sometimes also called the effective irradiance or photovoltaic resource.

Term	Definition
Reflectance	The fraction or percentage of a particular frequency or *wavelength* of *electromagnetic radiation* that is incident at a specific *angle of incidence* onto a surface and reflected by it without being absorbed or transmitted. When considering radiation emanating from the whole sky hemisphere rather than a specific direction, see *Albedo*.
Refraction	The bending of *electromagnetic radiation* by its passage through a medium of a high refractive index. *Light* is refracted by passing through a lens, water, or the *atmosphere*.
Relative humidity	[%] The amount of *water vapor* in the air expressed as the ratio between the measured amount and the maximum possible amount (the saturation point at which water condenses as dew).
Rotating shadowband radiometer	An instrument that determines the total *solar radiation* and *diffuse sky radiation* by periodically shading the total sky sensor from the sun with a rotating shadowband. Typically once every minute, the curved black shadowband rotates 180° to obscure the sun for a few seconds and then returns to its resting position.
Saturated air	Air that contains the maximum possible amount of *water vapor*; any increase in water vapor would then cause condensation.
Scattered radiation	*Radiation* that has interacted with particles, to the effect of disrupting the original direction of the incident beam.
Semiconductor	A material that has much lower resistance to the flow of electrical current in one direction than in another. Diodes, transistors, and many *photovoltaic* cells contain semiconductive materials, such as silicon.
Shading disk	A small disk attached on a tracking arm that permanently blocks the *direct normal irradiance* so that a *pyranometer* can only sense the *diffuse sky radiation*.
Shadowband	An adjustable metal strip that blocks the direct radiation so that a *pyranometer* can only sense the *diffuse sky radiation*. It must be adjusted manually on a ≈daily basis.
Shortwave radiation	The principal portion of the *solar spectrum* that spans from approximately 290 nm to 4000 nm in the *electromagnetic spectrum*.

Term	Definition
Silicon sensor	A *photovoltaic* cell that is being used to measure solar *irradiance*. Because its spectral response is not flat, its signal depends on the instantaneous characteristics of the *solar spectrum*.
Sky dome	Refers to the appearance of the entire sky, from horizon to zenith in all directions.
Sky radiation	See *Diffuse sky radiation*.
Solar absorber	A sheet of material—usually copper, aluminum, or steel—that forms the surface of a solar *collector*. It collects and retains *solar radiation*, which is passed to a heat transfer medium.
Solar cell	A *photovoltaic* cell that is used to convert solar energy into electricity.
Solar collector	A device that receives solar energy and converts it to useful *energy* forms (usually heat).
Solar concentrator	A solar *collector* that enhances solar energy by focusing it onto a smaller area through mirrored surfaces or lenses.
Solar constant	[W m^{-2}] Long-term average amount of the *Total solar irradiance* received at the *Top of atmosphere* by a normal surface after passing through the mean Earth orbit. The currently accepted value, based on satellite measurements, is 1361.1 W m^{-2} (ASTM 2022). Note that Earth-based *pyrheliometers* record lower values of solar power flux because of atmospheric attenuation.
Solar irradiance	[W m^{-2}] The amount of solar energy that is incident on a specific area of a surface during a specific time interval (*radiant flux* density).
Solar noon	The time at which the position of the sun is at its highest elevation in the sky. It is also the moment when the sun apparently crosses the local longitude. This time can be quite different from noon according to *local standard time*.
Solar radiation	The *electromagnetic radiation* emitted by the sun.
Solar spectrum	The electromagnetic spectral distribution emitted by the sun or received by a *collector* or instrument on Earth. In meteorology, the shortwave spectrum and the longwave spectrum correspond to *wavelengths* below and above ≈4 μm, respectively.

Term	Definition
Solar thermal electric	A technology for using the sun's *energy* to produce steam to run turbines that generate electricity.
Solar zenith angle (SZA)	[rad or °] The angle between the sun and the zenith (directly overhead). It is usually calculated at any instant with a sun position algorithm.
Spatial	Pertaining to space or to distance, such as *spatial variation* (variation over distance).
Specific humidity	$\boldsymbol{q}$ [g kg^{-1}] The mass of *water vapor* per unit mass of humid air, usually expressed as grams of water vapor per kilogram of air.
Spectral irradiance	E_λ or $E(\lambda)$ [$W \cdot m^{-2} \cdot nm^{-1}$ or $W \cdot m^{-2} \cdot \mu m^{-1}$] The amount of *radiant energy* flux expressed in terms of the *solar spectrum*. Spectral *irradiance* is typically measured with a *spectroradiometer*.
Spectroradiometer	An instrument designed to measure *spectral irradiance*.
Stratosphere	The relatively isothermal (constant temperature) layer of the *atmosphere* above the *troposphere* and below the mesosphere.
Sunphotometer	An instrument designed to measure *spectral irradiance* at a few selected *wavelengths* and then derive the spectral *aerosol optical depth* and/or *precipitable water*. This type of instrument requires very precise calibration. See *Langley*.
Sunshine	Used interchangeably with the more precise term "bright sunshine", when the sun casts an obvious shadow or when a sunshine recorder is recording. The World Meteorological Organization defines sunshine duration as the period during which the *direct normal irradiance* exceeds 120 W m^{-2}. A previous definition used a higher value of 210 W m^{-2} (Iqbal 2012). Sunshine is measured by a sunshine recorder. Whereas modern instruments exist, most historical data have been obtained with the *Campbell-Stokes sunshine recorder.*
Sunshine duration	[hour] The length of time over which the sun casts an obvious shadow or when a sunshine recorder is recording. See also *Sunshine* and *Campbell-Stokes sunshine recorder.*
Sun position	The location of the sun in the sky, expressed in terms of solar *azimuth angle* and *solar zenith angle*. The sun position can be obtained from an ephemeris or astronomical almanac. In solar energy practice, it is calculated by a sun position algorithm.

Term	Definition
Suns	An ad hoc unit (typically 1 kW m^{-2}) that multiplies the amount of *power* a solar *concentrator* can receive from the sun. For example, a concentrator might focus the *energy* of 40 suns onto a central receiver. A high-performance solar cell can be tested at "1000 suns" if developed for concentrators.
Temporal	Pertaining to time, such as *temporal variation* (variation over time).
Terrestrial radiation	The electromagnetic *longwave radiation* that is emitted by the Earth, as opposed to the *solar radiation* that is emitted by the sun.
Thermopile	A set of thermocouple junctions connected in series to boost the voltage to a meaningful amount (usually measured in millivolts). A *thermocouple* is a metallic strip or wire that produces an electromagnetic potential (voltage) when the two ends (junctions) are at different temperatures. The "cold" junctions of thermopile *radiometers* are painted white to reflect *radiation*, and the "hot" junctions are painted black to absorb radiation.
Top of atmosphere (TOA)	Term frequently used in meteorology and atmospheric sciences, with the same meaning as "extraterrestrial" used more frequently in solar applications. See *Extraterrestrial irradiance, Solar constant*, and *Total solar irradiance*.
Total solar irradiance (TSI)	[W m^{-2}] Full-spectrum solar *irradiance* emitted by the Sun at any instant, and corrected to correspond to the average Sun-Earth distance (≈1 AU). See *Astronomical unit* and *Solar constant*.
Total solar radiation	See *Global horizontal irradiance.*
Transmittance	[unitless] The fraction of a particular wavelength or waveband of electromagnetic radiation that passes through a substance without being absorbed or reflected.
Troposphere	The lowest region of the *atmosphere* between the surface of the Earth and the *stratosphere*. In the troposphere, the temperature usually decreases with increasing altitude.
Trough	See *Parabolic collector trough.*
Turbidity	A measure of the optical opacity of the cloudless *atmosphere*. See *Atmospheric turbidity.*

Term	Definition
Typical meteorological year	A "typical" year of hourly solar and meteorological values that is designed to simulate the expected *climate* of a location throughout a year.
Ultraviolet radiation	The range of radiation between ≈1 and 400 nm. In solar and other terrestrial applications, two different UV regions are considered: UV-A (315 or 320 nm to 400 nm) and UV-B (280 nm to 315 or 320 nm).
Uncertainty	The expression of the amount of doubt that remains after a result is obtained. See *Measurement uncertainty.*
Visible radiation	The radiation *wavelengths* that are visible to the human eye, covering the approximate range 380–750 nm. See also *Light*.
Volt	The metric unit of electric potential.
Water vapor	Gaseous water (individual water molecules) in the *atmosphere*. See also *Precipitable water* and *Relative humidity.*
Watt	A unit of power defined as a joule per second.
Watt-hour	A unit of *energy* (symbol Wh) equal to 3600 joules. A kWh is 1000 Wh or 3.6 MJ.
Wavelength	The distance between adjacent peaks or troughs of an electromagnetic wave. Wavelengths of light are typically expressed in terms of micrometers (10^{-6} m) or nanometers (10^{-9} m).
Weather	The state of the *atmosphere* at any given time. This includes temperature, *relative humidity*, cloudiness, precipitation type, *wind*, and the presence of *aerosols* or meteors.
Wet-bulb temperature	The temperature to which air will cool when water is evaporated into unsaturated air; measured by a wet-bulb thermometer, which has a wet cloth sleeve that covers its bulb. Wet-bulb temperature and *dry-bulb temperature* are used to compute *relative humidity*.
Wind	The horizontal motion of air near the surface of the Earth.
Wind rose	Polar graphs that indicate the speed and relative frequency of *wind* according to its direction. Wind roses are useful for determining the most prevalent direction of winds of desired strength.

Term	Definition
World Radiometric Reference (WRR)	Provides the basis for all measurements by *radiometers* in the world. Every 5 years, many of the best *absolute cavity radiometers* undergo an intercomparison at the *Physikalisch-Meteorologisches Observatorium Davos/World Radiation Center* in Davos, Switzerland. The most stable, accurate, and precise instruments provide the WRR for the coming years. Any credible radiometer measurement must be traceable to the WRR.
World Standard Group (WSG)	Maintained by the *World Meteorological Organization's Physikalisch-Meteorologisches Observatorium Davos/World Radiation Center* (WRC). The WSG is a group of seven well-characterized *absolute cavity radiometers* used to define the *World Radiometric Reference* (WRR). International intercomparisons of national standard pyrheliometers with the WSG are held every 5 years at the WRC to transfer the WRR to national centers. The WRR has an uncertainty of ≈0.3%. This means that the best possible measurements of *direct normal irradiance* have at least this uncertainty.

References

Almansa, A.F., A. Barreto, N. Kouremeti, R. González, R., A. Masoom, A., C. Toledano, J. Gröbner, R.D. García, Y. González, S. Kazadzis, S. Victori, O. Álvarez, F. Maupin, V. Carreño, V.E. Cachorro, and E. Cuevas, E. 2024. "The Langley Ratio Method, a New Approach for Transferring Photometer Calibration from Direct Sun Measurements." *Atmospheric Measurement Techniques* 17: 659–675. https://doi.org/10.5194/amt-17-659-2024.

ASTM 2022. "Solar Constant and Zero Air Mass Solar Spectral Irradiance Tables." Standard E490-22, ASTM International. https://www.astm.org/e0490-00ar06.html.

Bird, R.E., and R.L. Hulstrom. 1981. Review, Evaluation, and Improvement of Direct Irradiance Models. *Journal of Solar Energy Engineering* 103: 182–192. https://doi.org/10.1115/1.3266239.

Cano, D., J.M. Monget, M. Albuisson, H. Guillard, N. Regas, and L. Wald. 1986. "A Method for the Determination of the Global Solar Radiation from Meteorological Satellite Data." *Solar Energy* 37, 31–39. https://doi.org/10.1016/0038-092X(86)90104-0.

Gueymard, C.A. 2019. Clear-sky radiation models and aerosol effects. In: Polo, J., Martin-Pomares, L., Sanfilippo, A. (Eds.) Solar Resources Mapping – Fundamentals and Applications, Springer. https://doi.org/10.1007/978-3-319-97484-2.

Iqbal, M. 2012. *An Introduction to Solar Radiation*. Elsevier.

Kamphuis, N.R., C.A. Gueymard, M.T. Holtzapple, A.T. Duggleby, and K. Annamalai. 2020. "Perspectives on the origin, derivation, meaning, and significance of the isotropic sky model." Solar Energy 201: 8–12. https://doi.org/10.1016/j.solener.2020.02.067.

*Rapp-Arrarás, I., and J.M. Domingo-Santos. 2011. "*Functional Forms for Approximating the Relative Optical Air Mass*." Journal of Geophysical Research 116: D24308.* https://doi.org/10.1029/2011JD016706.

Shaw, G. E. 1983. "Sun Photometry." *Bulletin of the American Meteorological Society* 64: 4–10. https://doi.org/10.1175/1520- 0477(1983)064<0004:SP>2.0.CO;2.

Spencer, J. W. 1971. "Fourier Series Representation of the Position of the Sun." Search 2 (5): 172.